INNOVATIVE APPROACHES IN COMPUTATIONAL STRUCTURAL ENGINEERING

EDITED BY: George C. Tsiatas and Vagelis Plevris

PUBLISHED IN: Frontiers in Built Environment

frontiers Research Topics

frontiers

ISSN 1664-8714
ISBN 978-2-88963-607-5
DOI 10.3389/978-2-88963-607-5

About Frontiers

Frontiers is more than just an open-access publisher of scholarly articles: it is a pioneering approach to the world of academia, radically improving the way scholarly research is managed. The grand vision of Frontiers is a world where all people have an equal opportunity to seek, share and generate knowledge. Frontiers provides immediate and permanent online open access to all its publications, but this alone is not enough to realize our grand goals.

Frontiers Journal Series

The Frontiers Journal Series is a multi-tier and interdisciplinary set of open-access, online journals, promising a paradigm shift from the current review, selection and dissemination processes in academic publishing. All Frontiers journals are driven by researchers for researchers; therefore, they constitute a service to the scholarly community. At the same time, the Frontiers Journal Series operates on a revolutionary invention, the tiered publishing system, initially addressing specific communities of scholars, and gradually climbing up to broader public understanding, thus serving the interests of the lay society, too.

Dedication to Quality

Each Frontiers article is a landmark of the highest quality, thanks to genuinely collaborative interactions between authors and review editors, who include some of the world's best academicians. Research must be certified by peers before entering a stream of knowledge that may eventually reach the public - and shape society; therefore, Frontiers only applies the most rigorous and unbiased reviews.
Frontiers revolutionizes research publishing by freely delivering the most outstanding research, evaluated with no bias from both the academic and social point of view. By applying the most advanced information technologies, Frontiers is catapulting scholarly publishing into a new generation.

What are Frontiers Research Topics?

Frontiers Research Topics are very popular trademarks of the Frontiers Journals Series: they are collections of at least ten articles, all centered on a particular subject. With their unique mix of varied contributions from Original Research to Review Articles, Frontiers Research Topics unify the most influential researchers, the latest key findings and historical advances in a hot research area! Find out more on how to host your own Frontiers Research Topic or contribute to one as an author by contacting the Frontiers Editorial Office: researchtopics@frontiersin.org

INNOVATIVE APPROACHES IN COMPUTATIONAL STRUCTURAL ENGINEERING

Topic Editors:
George C. Tsiatas, University of Patras, Greece
Vagelis Plevris, OsloMet – Oslo Metropolitan University, Norway

Nowadays, numerical computation has become one of the most vigorous tools for scientists, researchers and professional engineers, following the enormous progress made during the last decades in computing technology, in terms of both computer hardware and software development. Although this has led to tremendous achievements in computer-based structural engineering, the increasing necessity of solving complex problems in engineering requires the development of new ideas and innovative methods for providing accurate numerical solutions in affordable computing times.

This collection aims at providing a forum for the presentation and discussion of state-of-the-art innovative developments, concepts, methodologies and approaches in scientific computation applied to structural engineering. It involves a wide coverage of timely issues on computational structural engineering with a broad range of both research and advanced practical applications.

This Research Topic encompasses, but is not restricted to, the following scientific areas: modeling in structural engineering; finite element methods; boundary element methods; static and dynamic analysis of structures; structural stability; structural mechanics; meshless methods; smart structures and systems; fire engineering; blast engineering; structural reliability; structural health monitoring and control; optimization; and composite materials, with application to engineering structures.

Citation: Tsiatas, G. C., Plevris, V., eds. (2020). Innovative Approaches in Computational Structural Engineering. Lausanne: Frontiers Media SA.
doi: 10.3389/978-2-88963-607-5

Table of Contents

frontiers in Built Environment

EDITORIAL
published: 08 April 2020
doi: 10.3389/fbuil.2020.00039

Editorial: Innovative Approaches in Computational Structural Engineering

George C. Tsiatas[1] *and Vagelis Plevris*[2]*

[1] Department of Mathematics, University of Patras, Rio, Greece, [2] Department of Civil Engineering and Energy Technology, OsloMet—Oslo Metropolitan University, Oslo, Norway

Keywords: structural engineering, innovation, computational, FEM, BEM, meshless methods

Editorial on the Research Topic

Innovative Approaches in Computational Structural Engineering

Over the last few decades, tremendous development has been made in the field of computing technology, in terms of both computer hardware and software development. As a result of this progress, numerical computation has now become one of the most effective tools for scientists, researchers, and professional engineers around the world. Although this has led to great achievements in computer-based structural engineering, the increasing necessity to solve complex problems in engineering requires the development of new ideas and innovative methods for providing accurate numerical solutions in affordable computing times (Plevris and Tsiatas, 2018).

The Research Topic "Innovative Approaches in Computational Structural Engineering" aims to provide a forum for the presentation and discussion of state-of-the-art innovative developments, concepts, methodologies, and approaches in scientific computation applied to structural engineering. It involves a wide coverage of timely issues on computational structural engineering with a broad range of research and practical applications.

The collection includes both research and advanced applied topics, with particular emphasis on innovation in computational structural mechanics and engineering. The contributions come from 58 leading researchers and professionals from 10 countries around the world who are actively involved in the field of computational structural engineering. The papers in the collection cover various relevant scientific areas such as modeling in structural engineering; finite element methods; boundary element methods; static and dynamic analysis of structures; performance-based design; structural optimization; meshless methods; modeling of advanced and innovative materials such as shape memory alloys; non-linear structural analysis; system identification methods; structural stability; GPU computing; earthquake engineering; seismic vulnerability; incremental dynamic analysis; structural damage assessment; smart structures and systems; structural reliability; structural health monitoring and control; optimization; and composite materials, with application to engineering structures.

PAPERS IN THE COLLECTION

In the 1st paper of the collection, Mitropoulou et al. present a methodology to identify the most appropriate damage index, able to provide a reliable description of the structural damage level. A performance-based design framework is formulated based on this damage index, which is to be used as a design tool for achieving safer and more economic designs. For each damage index under consideration, design optimization problems for structural systems are solved by means of a popular metaheuristic search algorithm.

OPEN ACCESS

Edited and reviewed by:
Georgios Eleftherios Stavroulakis, Technical University of Crete, Greece

Correspondence:
Vagelis Plevris
vageli@oslomet.no

Specialty section:
This article was submitted to Computational Methods in Structural Engineering, a section of the journal Frontiers in Built Environment

Received: *05 March 2020*
Accepted: *19 March 2020*
Published: *08 April 2020*

Citation:
Tsiatas GC and Plevris V (2020) Editorial: Innovative Approaches in Computational Structural Engineering. Front. Built Environ. 6:39. doi: 10.3389/fbuil.2020.00039

Next, Charalampakis and Tsiatas examine three uniaxial phenomenological models, i.e., the Graesser-Cozzarelli model, the Wilde-Gardoni-Fujino model, and the Zhang-Zhu model, which are currently used for the description of a Shape Memory Alloy (SMA) behavior. The examination process reveals several limitations and drawbacks, including the large number of parameters and the unclear effect of specific parameters in the overall response. Based on this analysis, powerful metaheuristics are employed for system identification and a new simple rate-independent model is proposed, which addresses all issues in a unified manner producing excellent fit with the experimental data.

The 3rd paper by Yiotis and Katsikadelis deals with the solution to the vibration problem of cylindrical shell panels using the Meshless Analog Equation Method (MAEM). The method is based on the principle of the analog equation, converting the original equations into three substitute ones, two Poisson's and one biharmonic, which are solved using a meshless method. The use of integrated Multiquadric—Radial Basis Functions (MQ-RBFs) to approximate the fictitious sources allows the approximation of the solutions sought by new RBFs, which accurately approximate both the solution and its derivatives. Several shell panels are analyzed using the method, and the numerical results demonstrate its efficiency and accuracy.

Tsalkatidis et al. study the mechanical behavior of bolted hybrid connections that consist of a square hollow steel column (SHS) and a glulam timber beam. A reference model is constructed and verified by comparison to experimental and numerical data from the literature. Several parameters that affect the response of the connection are modified in order to investigate and quantify their effect, resulting in seven different case studies. A proposed optimal configuration of the hybrid connection is investigated and presented.

In the next paper, Tsiatas et al. present a new layered approach to the non-linear analysis of initially straight Euler-Bernoulli rectangular beams by the Boundary Element Method (BEM). The formulation of the problem is based on the displacements, and the equations of equilibrium, derived from the principle of minimum total potential energy, being coupled and non-linear. The beam is discretized in both the longitudinal direction and the cross-sectional plane, and the governing differential equations are solved using the Analog Equation Method (AEM) in conjunction with an iterative numerical process. Various representative examples are examined that not only take geometrical non-linearity into account but material non-linearity as well. The reliability and effectiveness of the proposed method are validated by comparing the results obtained with those presented in the literature or derived by other Finite Element (FE) models.

Arailopoulos et al. propose an integrated reverse engineering methodology for a large-scale fully operational steam turbine rotor, addressing issues that include developing the CAD and FE model of the structure, as well as the applicability of model updating techniques based on experimental modal analysis procedures. The FE model of the turbine was developed using tetrahedral solid elements resulting in 55 million DOFs. Experimentally identified modal modes and modal frequencies were compared to the FE model predictions, and CMA-ES optimization was used to fine-tune the material parameters, such as modulus of elasticity and density. A simplified FE model was also developed and used for the turbine rotordynamic analysis.

In the 7th paper, Mascolo et al. developed a FE model of the Moderate Rotation Theory (MRT) of laminated composite beams. The proposed model describes laminated composite beams with arbitrary curvature of the beam axis taking into account shear deformation, warping effects, and in-plane and out-of-plane instability. The stability analysis is performed through a path-following procedure and a bordering algorithm. Several numerical results are presented and comparisons are made with classical beam theories and other theories available in the relevant literature.

Jena and Chakraverty investigate the free vibration of the variable cross-section (non-uniform) Single-Layered Graphene Nano-Ribbons (SLGNRs) by using the Differential Quadrature Method (DQM). The Euler–Bernoulli beam theory is considered in conjunction with Eringen's non-local elasticity theory. A convergence study is carried out to illustrate the efficiency of the method and the obtained results are validated with known results.

In the paper by Molina-Moya et al., a parallel iterative solver based on the Generalized Minimum Residual Method (GMRES) with complex-valued coefficients is explored, with applications to BEM. The proposed approach does not require modifications in the main program, which computes the system matrix and the right vector, allowing the use of standard BEM codes, with the solver task being transferred to the Graphic Processing Unit (GPU). The CUDA programming language is used, exploiting the particular architecture of the GPU device for complex-valued systems. The parallelized GMRES solver shows reductions in computing times when compared with its CPU implementation.

In the 10th paper, Panagiotopoulos et al. present a unified methodology to solve problems of frictionless unilateral contact as well as adhesive contact between linear elastic solids. The methodology is based on energetic principles and is applied to a minimization problem of the total potential energy. To solve the quadratic problem, two algorithms are developed, which are both variants of the well-known conjugate gradient algorithm. Both symmetric and non-symmetric formulations of this matrix are presented and discussed, showing that the non-symmetric formulation provides more accurate results. The framework is found to be very useful in cases where dissipative mechanisms also exist on the boundaries or common interfaces of elastic bodies.

Blasi et al. present a work aimed at developing a hybrid approach to consider the effect of concrete cracking on the hysteretic response of RC frames. The smeared cracking approach is employed, while discrete cracking

surfaces are included in the geometrical model where the interface behavior is defined by the combination of contact and cohesive elements. The proposed approach is adopted in ABAQUS to simulate an experimental test on a double cantilever column for the calibration of the numerical model. Numerical and experimental results are compared in terms of hysteretic force-displacement behavior and cumulative dissipated energy, to assess the reliability of the proposed model in simulating the energy dissipation capacity of RC members subjected to lateral cyclic loading.

In the 12th paper by Zhao et al., three different strategies are proposed to identify the general hysteretic behavior of a typical shear structure subjected to external excitations. Different case studies are presented to analyze the dynamic responses of a time-varying shear structural system with the early version of the Bouc-Wen-Baber-Noori (BWBN) hysteresis model. Various computational techniques are utilized. The results show that Intelligent Parameter Varying (IPV) performs superior computational efficiency and system identification accuracy in comparison to Genetic algorithm (GA), and Transitional Markov Chain Monte Carlo (TMCMC) approaches.

The subject of the 13th work of the collection, by Giordano et al., is Sant' Agostino Sanctuary in Offida, central Italy. The village and the sanctuary itself was severely damaged by the seismic events of August 2016. A finite element model using non-linear static analysis (Pushover) is employed to estimate the vulnerability of the sanctuary and its dynamic response, considering the non-linear behavior of masonry with a homogenized material and a smeared cracking and crushing constitutive law. The structure is shown to be prone to massive damage leading to collapse.

Repapis and Zeris investigate the vulnerability assessment of non-conforming infilled RC structures of the 1960s and 1970s. The seismic performance of typical bare and infilled structures was evaluated. The results from Static Pushover analyses are extended with Incremental Dynamic Analysis predictions using a large number of recorded base excitations from recent destructive earthquakes in Greece and internationally. The analysis shows that fully or partially infilled RC frames can perform well, while frames with an open floor usually have the worst performance due to the formation of an unintentional soft story.

In the 15th paper, Juárez-Luna and Caballero-Garatachea study the nonlinear behavior of RC circular, elliptic, and triangular isolated slabs using computational mechanics. The concrete was modeled with a damage model which includes softening, while the behavior of the reinforcing steel was simulated with a 1D bilinear plasticity model. Validation was done by comparing the computed numerical results with the experimental results reported in the literature. The coefficient method is proposed for its simplicity to calculate design bending moments in slabs with arbitrary geometries.

Soroushian and Farahani apply a technique proposed in 2008 by Soroushian (2008) to the FE analysis of assemblies of beam-columns subjected to continuous static loads. These loads may be computationally expensive especially when they are densely digitized. It is shown that the adapted technique might considerably reduce the computational cost with only a negligible change in accuracy. Furthermore, the good performance of the adapted technique is demonstrated from different points of view and is compared with the performance of the technique in time integration analysis.

In the 17th paper, Marakakis et al. review the current state of the art in shunt piezoelectric systems for noise and vibration control. In fact, resonant shunts have proved to be very efficient and stable for the reduction of vibration on smart piezoelectric structures, such as beams and plates. From the numerous applications which were reviewed it is evident that shunt piezoelectric systems can be very effective for several different purposes such as control of vibrations on hard drives, noise reduction on acoustic applications, improvement of image quality and scan rate of tapping mode Atomic Force Microscopy.

In the last paper of the collection, Papazafeiropoulos et al. propose a novel spectra-matching framework, which employs a linear combination of raw ground motion records to generate artificial acceleration time histories for matching a target spectrum taking not only the acceleration into account, but also the seismic input energy equivalent velocity. The procedure of selection and scaling of the suite of ground motion records to fit a given target spectrum is formulated by means of an optimization problem. The optimization results have shown that there is good agreement between the target and optimized spectra for the different matching scenarios examined, regardless of the nature of the target spectrum.

In closing this editorial, we would like to thank the contributing authors, the reviewers, the staff at Frontiers and all the other people we have worked closely with in trying to make this Research Topic a success. Once again, it has been proven that computational methods are at the forefront of real-world applications. Especially in the structural engineering discipline, the applications are numerous and cover a wide range of topics. Although very powerful capabilities are now available for the simulation and analysis of structures, there are still many exciting research challenges. The field of computational structural engineering will continue to grow and increasingly contribute to technological development in the future, influencing and enriching the engineering profession and our lives in general.

AUTHOR CONTRIBUTIONS

GT and VP handled manuscripts and edited the Research Topic. Both authors have made a substantial, direct and intellectual contribution to the work, and approved it for publication.

REFERENCES

Plevris, V., and Tsiatas, G. (2018). Computational structural engineering: past achievements and future challenges. *Front. Built Environ.* 4:21. doi: 10.3389/fbuil.2018.00021

Soroushian, A. (2008). A technique for time integration analysis with steps larger than the excitation steps. *Commun. Numer. Methods Eng.* 24, 2087–2111. doi: 10.1002/cnm.1097

Conflict of Interest: The authors declare that the research was conducted in the absence of any commercial or financial relationships that could be construed as a potential conflict of interest.

frontiers in Built Environment

ORIGINAL RESEARCH
published: 04 July 2018
doi: 10.3389/fbuil.2018.00032

Damage Index-Based Lower Bound Structural Design

Chara Ch. Mitropoulou[1], *Giuseppe C. Marano*[2,3] *and Nikos D. Lagaros*[4]*

[1] ACE-Hellas, Athens, Greece, [2] College of Civil Engineering, Fuzhou University, Fuzhou, China, [3] Department of Civil Engineering and Architectural Science, Technical University of Bari, Bari, Italy, [4] Veltion Engineering and Applied Sciences Optimization Lab, Department of Structural Engineering, School of Civil Engineering, Institute of Structural Analysis & Antiseismic Research, National Technical University of Athens, Athens, Greece

The scope of the work is to detect the most appropriate damage index, able to provide a reliable description of the structural damage level. This damage index is used to formulate a performance-based design framework to be used as a design tool for achieving safer and more economic designs. This objective is achieved by comparing alternative structural systems that comply with the design demands in the most cost-efficient approach, i.e., those requiring less material volume for concrete and steel reinforcement. In this direction, design optimization problems for structural systems are defined for each damage index under consideration and the structural optimization problems at hand are solved by means of a popular metaheuristic search algorithm.

Keywords: performance-based design, structural optimization, damage indices, reinforced concrete structures, PSO algorithm

OPEN ACCESS

Edited by:
Vagelis Plevris, OsloMet—Oslo Metropolitan University, Norway

Reviewed by:
Makoto Ohsaki, Kyoto University, Japan
Francesco Tornabene, Università degli Studi di Bologna, Italy
Flavia De Luca, University of Bristol, United Kingdom

***Correspondence:**
Nikos D. Lagaros
nlagaros@central.ntua.gr

Specialty section:
This article was submitted to Computational Methods in Structural Engineering, a section of the journal Frontiers in Built Environment

Received: *17 April 2018*
Accepted: *15 June 2018*
Published: *04 July 2018*

Citation:
Mitropoulou CC, Marano GC and Lagaros ND (2018) Damage Index-Based Lower Bound Structural Design. Front. Built Environ. 4:32. doi: 10.3389/fbuil.2018.00032

INTRODUCTION

Performance-based design (PBD) framework was presented throughout the past couple of decades, for designing structural systems exposed to non-deterministic earthquake loading conditions, aiming at increasing structural safety against earthquake hazard. In accordance to performance-based earthquake engineering the structures need to be able resisting various earthquake loading scenarios in a measurable fashion and sustaining potential damages corresponding to desirable performance levels (Vanzi et al., 2015). The contemporary PBD engineering state-of-practice, among others, can be found in US design codes such as FEMA-445 (2006), ASCE-41 (2006), ATC-58 (2009), and FEMA-P-58-1 (2012). Aiming to achieve the PBD engineering goals, these design guidelines suggest that in seismic-prone areas require implementing higher-order analysis methods for performing structural assessment and design of existing or new structural systems, respectively. Structural optimization can provide a highly-effective design framework, yet computationally intensive, exploiting the benefits provided by nonlinear dynamic or static analysis methods. Structural design optimization problems formulated on the basis of PBD frameworks became a topic of growing interest, over the last years, where interesting results have been reached. The progress in structural optimization has facilitated passing from design procedures of trial-and-error basis toward fully automatic ones using advanced design space exploration algorithms (Marano et al., 2009; Quaranta et al., 2014; Fiore et al., 2016a; Greco et al., 2016). Partly, this transition should be credited to metaheuristic search algorithms that last decades developed rapidly. These search algorithms are capable of dealing with optimization problems of high complexity. Furthermore, structural optimization matured from simple academic problems to become the core of contemporary design in case of extremely complicated structural systems (Marano and Greco, 2006; Marano et al., 2006, 2007, 2008; Lagaros, 2014a, 2018; Greco et al., 2015).

So far, many researchers have integrated the PBD concept into design optimization procedures for achieving better designs. Indicatively, Ganzerli et al. (2000) suggested a PBD optimization practice for reinforced concrete (RC) framed structures relying on mathematical programming search algorithms. Esteva et al. (2002) recommended a formulation for life-cycle cost (LCC) aiming to define optimized mechanical properties of structures subjected to earthquake risk. Li and Cheng (2003) presented a design concept based on damage reduction and was implemented into structural optimization problems and exhibited that this idea leads to improved designs with respect to structural performance in terms of both maximum interstory drift and life-cycle cost performance. Chan and Zou (2004) presented an improved approach for RC building structures subject to seismic loading aiming to improve elastic and inelastic interstory drifts into structural optimization problems. Liu et al. (2005) presented a design optimization approach for multiple-objectives using Genetic Algorithm (GA) for the case of steel framed structures taking into account various criteria; for two performance levels the resulting maximum interstory drift, material weight, and design complexity ones. Fragiadakis et al. (2006) presented PBD optimization practice for steel moment-resisting frames (MRFs) based on FEMA-350 (2000) probabilistic framework. An overview for the PBD framework state-of-the-art was presented by Foley et al. (2007) and implemented such a design framework into multiple-objective structural optimization problem formulations for single and multi-story steel framed structures having fully and partially restrained connections. European seismic code recommendations were assessed by Lagaros and Papadrakakis (2007), when adopted for designing 3D RC building structures, within a PBD multi-objective optimization concept. Aiming to deal with complex optimization problems, confidence levels were integrated with the objective criterion together with the material cost for various optimized design scenarios, the GA search algorithm was adopted by Rojas et al. (2007). Lagaros et al. (2010) presented an automated PBD approach that was implemented for designing RC building structures, examining the effect of infill walls, in this direction PBD approach alternatives were tested relying on non-linear static or dynamic analyses. In the work by Lagaros and Fragiadakis (2011) a comparative study is performed over the state-of-practice on nonlinear static analysis approaches, recommended by the European and US code provisions, were implemented within PBD optimization formulations; while aiming to examine the parameters that affect LCC estimation of structures, multi-objective LCC optimization problems were formulated by Mitropoulou et al. (2011).

The concept of defining the condition of structural loss using an engineering compatible quantity taking values on specific scale by means of a damage index (DI) is appealing due to its ease of implementation. So far several researchers have proposed several DIs for the case of RC or steel structural systems (i.e., Ghobarah, 2004; Estekanchi and Arjomandi, 2007). This work aims at exploring and assessing alternative designs, exhibiting a required performance monitored by a damage index, that comply with design codes according to the utmost economical way, i.e., having lower material volume requirements for concrete and steel reinforcement. In this direction, performance-based structural design optimization problems are formulated for various damage indices and the designs obtained are subsequently assessed

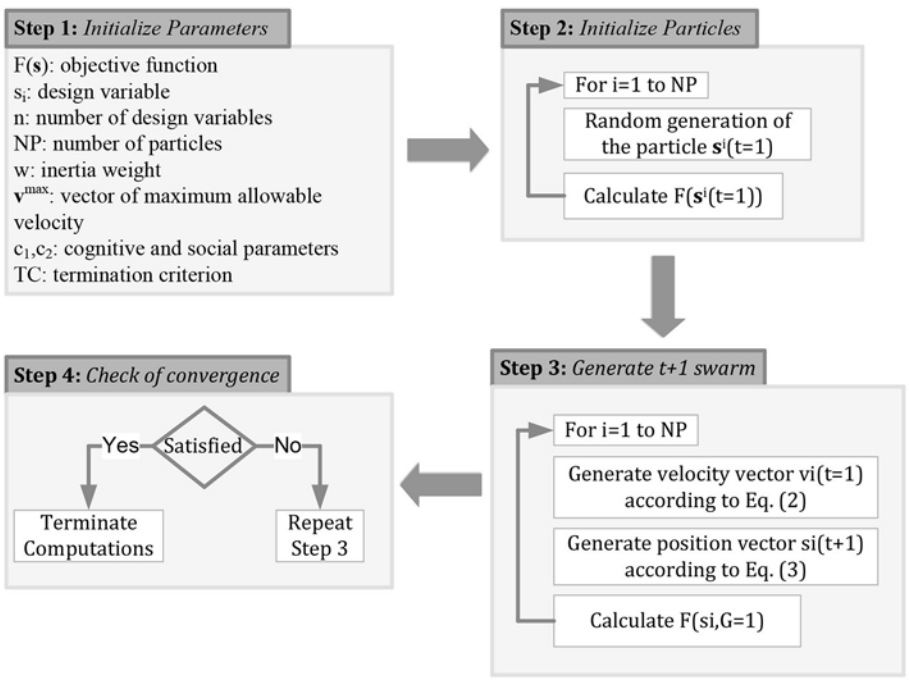

FIGURE 1 | Schematic representation of PSO algorithm.

under a set of seismic records properly selected. The main objective is to detect the most appropriate damage index, able to provide a reliable description of the structural damage level. This damage index is used to formulate a performance-based design framework to be used as a design tool for achieving safer and more economic designs. The resulting structural optimization problems are solved using a well-known metaheuristic optimization algorithm, namely the particle swarm optimization method, while the limit states implemented for the formulation of the performance-based design procedures, which describe the status of structural integrity, are based on calibrated values obtained from a former study of the authors (Mitropoulou et al., 2014).

LOCAL AND GLOBAL DAMAGE INDICES

Damage indices can be classified into two groups (Grigoriu, 1987): (a) DIs based on strength; and (b) those based on response. Strength-based DIs do not require response analyses (Shiga et al., 1982; Khashaee, 2005). However, they need to be calibrated with reference to observed damage based on rather large experimental databases. The performance of structures against seismic loading is generally correlated to the ability to sustain inelastic deformations (Resta et al., 2013), while experimental studies have shown that indices of structural performance (like ductility as well as others), which rely only on the fatigue concept of low-cycle, do not appear to offer an acceptable indicator for structural loss due to seismic loads (Banon and Veneziano, 1982). These observations are in agreement with the notion that brittle systems' failure is developed due to significant deformation demands, while ideal ductile structures' failure begun when inelastic deformations are observed repeatedly (Fiore et al., 2016b). Damage indices used to characterize the performance of structural systems that are not ideal ductile or brittle, need to consider for losses due to repeated and increased inelastic deformations (Park and Ang, 1985; Greco et al., 2017). Thus, more wide-ranging applicable and reliable indices are required to characterize structural performance.

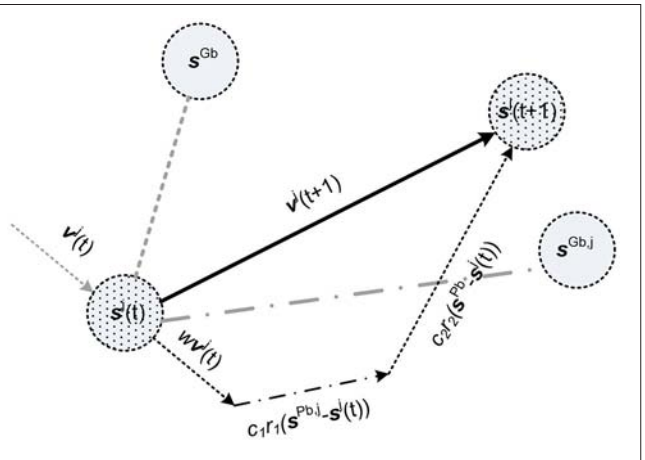

FIGURE 2 | Graphic description of particle's positioning indicatively for the 2D design space.

According to Ghobarah et al. (1999) the DIs based on response are classified in three sets based on what DI accounts for: (a) maximum deformation (Mahin and Bertero, 1974; Saiidi and Sozen, 1981; Toussi and Yao, 1982; Roufaiel and Meyer, 1987; Powell and Allahabadi, 1988); (b) cumulative damage (Banon and Veneziano, 1982; Allahabadi and Powell, 1988); and (c) combination of cumulative damage and maximum deformation. In this work DIs accounting for both cumulative damage and maximum deformation are implemented. In particular, (i) the local DI by Park and Ang (1985), (ii) its alternative presented by Kunnath et al. (1992), (iii) local DI by Chung et al. (1987, 1989), (iv) together with the final and maximum softening DIs presented by DiPasquale and Çakmak (1987, 1988) are evaluated in the current study. For their implementation the local DIs are transformed into global ones by combining the local values of the DIs of the structural elements using weight coefficients.

Several damage indices account for the local damage induced to individual structural elements. Monitoring of local damage indices helps in the identification of the weak or vulnerable members that need to be rehabilitated. Nevertheless, it is not an easy task to obtain clear view for the structure's response provided the input earthquake record out of a list of members DIs. Currently, safety and residual strength of damaged structural systems rely on single or global DIs. The global ones are usually implemented for reliability studies, post-earthquake evaluation of structures, and performance-based design applications. Global DIs could be defined by combining local ones; the weighting scheme is the simplest approach for combining local damage indices (Kunnath et al., 1992). The weighting factors can predict the relative importance and/or the replacement cost of a structural element or part of the structure in preserving safety of the entire structure. However, employing weighted average procedures in order to define global DIs does not justify appropriately the concentration locally of the damages, does not distinguish between different structural elements, and might lead to misrepresentative conclusions. There are cases that for a few structural elements of the structural system to have undergone severe damage deprived of this being reflected in by a DI.

For the reasons described previously DIs expressed using weighting factors have not been considered; however, for purposes of completeness such DIs are briefly outlined below. Direct implementation of the damage model to the overall structural system, a single story frame or a structural member requires determining the corresponding overall structural system, story or member ultimate deformations. Nonlinear behavior is limited to plastic regions close to the structural joints; therefore, it is difficult to establish the relation between member, story or top story structural system deformations, with the rotations of the local plastic zone. Two other global and story damage indices were proposed (Kunnath et al., 1992), which are calculated using weighting factors, these factors rely on the hysteretic energy dissipated at story and component levels,

respectively:

$$DI_{storey} = \sum_{i=1}^{n_{el}} (\lambda_i)_{element}(DI_i)_{element} \quad (1)$$

$$(\lambda_i)_{element} = \frac{E_i}{\sum_{i=1}^{n_{el}} E_i} i = 1, \ldots, n_{el}(\text{over the elements}) \quad (2)$$

and

$$DI_{overall} = \sum_{i=1}^{n_{st}} (\lambda_i)_{storey}(DI_i)_{storey} \quad (3)$$

$$(\lambda_i)_{storey} = \frac{E_i}{\sum_{i=1}^{n_{st}} E_i} i = 1, \ldots, n_{st}(over\ the\ stories) \quad (4)$$

λ_i denotes the energy weight factor for story i; E_i represents the overall energy absorbed by the ith story or component, while n_{st} and n_{el} denote the total number of stories and components/elements, respectively.

LOWER BOUND DESIGN OF STRUCTURES

This work concerns the production of lower-bound optimized designs, which comply with design requirements by a cost-efficient means (i.e., those requiring less material volume for concrete and steel reinforcement) and subsequently to be compared. These designs are then used as the basis of comparison for identifying the best design procedure. Therefore, structural optimization problems are formulated and optimized designs obtained are subsequently evaluated.

Design of Reinforce Concrete Structures

Aiming to evaluate the performance of different designs of RC framed structures; structural optimization problems were formulated as below:

$$\begin{aligned} &minimize && C_{IN}(t, \boldsymbol{s}) \\ &subject\ to && g_j^{SERV}(\boldsymbol{s}) \le 0 j = 1, ..., k \\ & && g_j^{ULT}(\boldsymbol{s}) \le 0 j = k+1, ..., m \end{aligned} \quad (5)$$

The design variables comprising of the dimensions of cross-sectional for groups of beams and columns considered for formulating the optimization problem are defined by vector $\boldsymbol{s}$, F represents the feasible part of the design space where all serviceability and ultimate limit state design requirements implemented as constraint functions (i.e., the series of constraint functions $g_j^{SERV}(s)$ *and* $g_j^{ULT}(s)$) are satisfied:

$$F = \left\{ \boldsymbol{s} \in R^D \left| g_j^{SERV}(\boldsymbol{s}) \le 0, j = 1, ..., k \text{ and } g_j^{ULT}(\boldsymbol{s}) \le 0\, j = k+1, ..., m \right. \right\} \quad (6)$$

where R^D represents the discrete design set where design vectors $\boldsymbol{s}$ take values. The structural materials cost C_{IN} of the design is the objective function considered. Aiming to deal with the optimization problem the well-known metaheuristic search algorithm called as particle swarm optimization (PSO) method is implemented.

Swarm Intelligence

According to the optimization algorithm particle swarm (Kennedy and Eberhart, 1995), various design vectors collaborate. Every vector of unknowns is labeled as "*particle*" characterized by its velocity and position, both defined in the D-dimensional design domain, while a sum of particles constitutes the so termed "*swarm.*" During the search procedure where an optimized design vector is on the hunt, a particle "*flies*" in the design space of the problem. During the search procedure, velocity and position vectors are adjusted for every particle based on personal "*experience*" as well as that of the others (neighboring particles). Memorizing and tracking the best positions encountered construct particles' experience. PSO algorithm relies on joint search locally (self-experience) with global one (neighboring experience), trying to control exploitation with exploration. Every particle maintains its two basic characteristic vectors, i.e., velocity and position (or location), in the D-dimensional domain which are iterated as below:

$$\boldsymbol{v}^j(t+1) = w\boldsymbol{v}^j(t) + c_1\boldsymbol{r}_1 \cdot \left(\boldsymbol{s}^{Pb,j} - \boldsymbol{s}^j(t)\right) + c_2\boldsymbol{r}_2 \cdot \left(\boldsymbol{s}^{Gb} - \boldsymbol{s}^j(t)\right) \quad (7)$$

$$\boldsymbol{s}^j(t+1) = \boldsymbol{s}^j(t) + \boldsymbol{v}^j(t+1) \quad (8)$$

$\boldsymbol{v}^j(t)$ refers to the jth particle's velocity at time t, $\boldsymbol{s}_j(t)$ denotes the jth particle's position vector at time t, the self-best location of jth particle is labeled as $\boldsymbol{s}^{\mathrm{Pb},j}$, and the best position obtained

TABLE 1 | 2D test example-Damage state with reference to crack width.

Damage state	DI_{ms}	DI_{fs}	DI_{PA}	DI_{KRL}	DI_{CMS}
No damage	0.05	0.06	0.06	0.07	0.03
Slight	0.13	0.21	0.14	0.21	0.05
Moderate	0.44	0.66	0.52	0.75	0.06
Extensive	0.57	0.77	1.40	1.51	0.38

TABLE 2 | Definition of the limit states.

Design procedure	50/50	10/50	2/50
$DI_{\theta max}$	0.400	1.800	3.000
DI_{ms}	0.046	0.443	0.566
DI_{fs}	0.061	0.655	0.765
DI_{PA}	0.056	0.524	1.400
DI_{KRL}	0.071	0.751	1.510
DI_{CMS}	0.035	0.060	0.377

globally is denoted with the vector $\boldsymbol{s}^{\mathrm{Gb}}$. Coefficients c_1 and c_2 denoted as acceleration ones, refer to the level of confidence with the best vector achieved by a specific particle (c_1 is labeled as cognitive coefficient) and by entire swarm (c_2 is denoted as social coefficient), respectively. Vectors r_1 and r_2 are composed by arbitrary elements distributed uniformly in [0,1]. Flowchart of **Figure 1** describes the basic steps of PSO algorithm, while particle's motion indicatively for the case of the two-dimensional design space is depicted in **Figure 2**. The lower left dotted circle of **Figure 2** represents present position vector $\boldsymbol{s}^j(t)$ at time t, and the upper right dotted bold circle denotes new location vector $\boldsymbol{s}^j(t+1)$ at time $t+1$. The means that the particle's transition into the D-dimensional search domain is affected by: (i) velocity vector $\boldsymbol{v}^j(t)$; (ii) self-best found location vector ($\boldsymbol{s}^{\mathrm{Pb},j}$); and (iii) swarm's global-best location achieved so far ($\boldsymbol{s}^{\mathrm{Gb}}$) is presented in **Figure 2**.

DAMAGE INDEX-BASED DESIGN

In this work the performance degree are denoted in terms of structural deformation and cumulative energy, using different damage indices apart from maximum interstory drift that has been exclusively used in the past in PBD. More specifically Park and Ang DI and its reformed version as presented by Kunnath et al. (1992), as well as the Chung et al. DI, together with the final maximum and softening DIs suggested by DiPasquale and Çakmak (1988), have been considered for the definition of the performance levels. These five DIs account for cumulative damage and maximum deformation. These damage indices were calibrated in a recent study by the authors (Mitropoulou et al., 2014) relying on the crack openings' width. In particular, incremental dynamic analysis was employed for developing an archive of the DIs' values using a coarse modeling of structures employing column-beam 1D elements.

Six optimization problems are pursued within, following the PBD framework based on (i) interstory drift (DI_θ), (ii) Park and Ang (DI_{PA}); (iii) its alternative presented by Kunnath et al. (DI_{KRL}); (iv) Chung et al. (DI_{CMS}); (v) maximum softening (DI_{ms}) as well as (vi) final softening (DI_{fs}). Moreover, DIs statistical features were calculated implementing horizontal statistics combined with the method of maximum likelihood function together with a properly selected search technique. The values provided in **Table 1** (Mitropoulou et al., 2014) represent calibrated damage states and they are used for defining the performance objective introduced in the proposed design framework.

Performance-Based Design

Several distinctive features for PBD seismic design procedure with respect to design procedures imposed by the prescriptive codes: (i) Permits structural engineers to select both appropriate seismic hazard level and the analogous performance of the structure, (ii) series of performance objectives are used for designing a structural system. PBD design procedure represents a design procedure relying on displacements where design measures and capacity demands are formulated considering displacements rather than using forces (Sullivan et al., 2003).

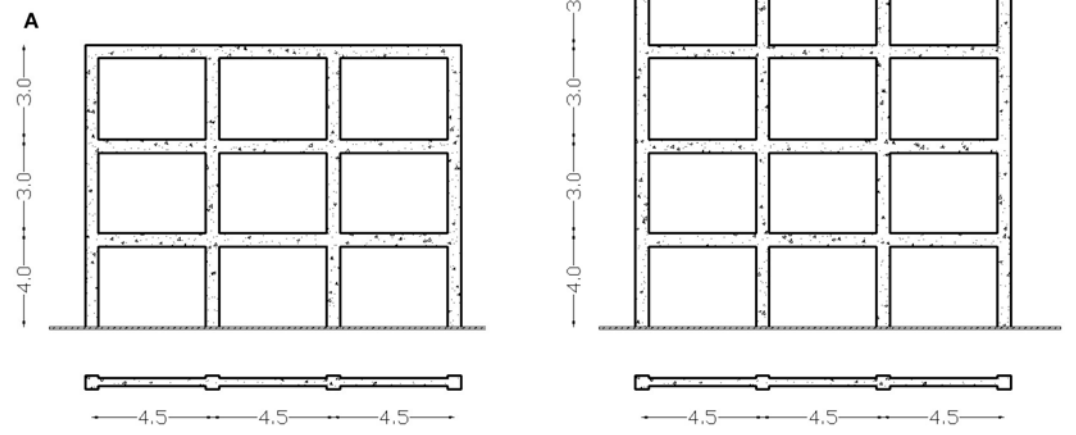

FIGURE 3 | RC test examples—**(A)** three-story and **(B)** six-story.

PBD implies that structural elements are selected, as well as the assessment; construction and maintenance studies are operated on the construction aiming to meet the purposes imposed by owners/users as well as society (Krawinkler and Miranda, 2004). When designing against seismic hazard, the aim is to construct structural systems having predictable performance capable to withstand seismic loading with measurable metrics. Hence, contemporary conceptual approach for structural design is that structural systems need to achieve performance objectives for several seismic levels varying in the rage of seismic event having low intensity and return period, to more damaging earthquake incidents having larger return periods. The contemporary state-of-practice for PBD structural engineering is offered by the various design codes (ASCE-41, 2006; FEMA-445, 2006; ATC-58, 2009; FEMA-P-58-1, 2012), that theoretically do not vary besides adopt techniques that represent the first significant difference with respect to prescriptive-based guidelines. Several of the contemporary design guidelines applied to design studies for new build structures can be considered as merely PBD ones, as these design guidelines combine all measures into a single level of performance, frequently the collapse prevention or life safety level. The definition of performance objectives represents the most important ingredient of a PBD seismic procedure.

DI-Based Design Concept for Safe and Economic Seismic Resistant Structures

The main scope of this step is to incorporate the DIs calibrated in a recent work by the authors into a performance-based design framework and to propose an innovative design concept leading to safe and economic earthquake resistant RC structures. For this purpose, the DIs selected in Mitropoulou et al. (2014) will be used to define different DI-based designs into structural optimization problems. The formulation of the DI-based concept can be stated as follows:

$$\begin{aligned} DI^{i}_{HL1}(\boldsymbol{s}) &\leq DI^{allow,i}_{HL1} \\ DI^{i}_{HL2}(\boldsymbol{s}) &\leq DI^{allow,i}_{HL2} \\ &\vdots \\ DI^{i}_{HLn}(\boldsymbol{s}) &\leq DI^{allow,i}_{HLn} \end{aligned} \tag{9}$$

which represent the performance-based design constraints [denoted as $g^{ULT}(\boldsymbol{s})$ in Equation 5]. The DI should be less or equal to the allowable upper bounds for a number of hazard levels (*HL1, HL2,…,HLn*) while i denotes the DI considered in the formulation (i=1,2,…,m). The boundaries of the feasible part of the design space are defined using the calibrated values of the *DIs* defined in Mitropoulou et al. (2014) which are given in **Table 2**. Therefore, in order to identify the DI that represents better the structural behavior, various minimum initial material cost DI-based design optimization problems are formulated according to Equation (5), where the PBD checks are implemented according to Equation (9).

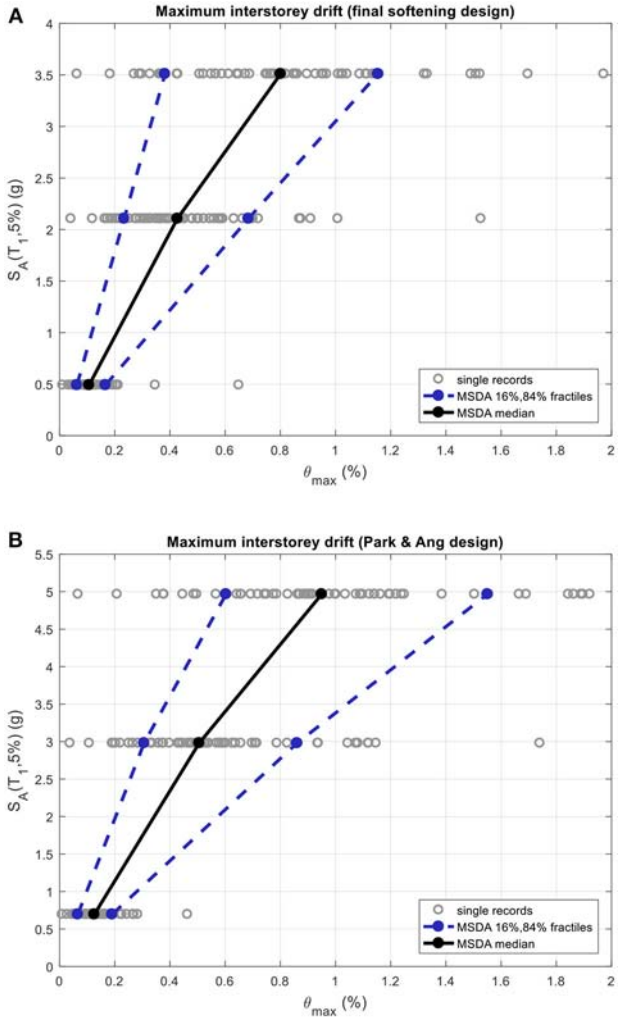

FIGURE 4 | Three-story—multi-stripe dynamic analysis with reference to the maximum drift for **(A)** final softening and **(B)** Park and Ang designs.

NUMERICAL TESTS

The objective of this work is to incorporate several damage indices examined in former study by the authors (Mitropoulou et al., 2014) into a performance-based design framework and to identify the best choice to be used for designing reinforced concrete structures.

Description of the Test Examples

The two 2D RC moment resisting framed (MRF) building structures shown in **Figure 3** have been taken into account aiming to study the effect of incorporating DI within the design framework of RC building structures. The foremost test example refers to a three-story concrete building while the second one is a six-story one. Class of concrete C20/25 and of steel S500 are assumed. The thickness of the slabs was taken equal to 15 cm for both test examples and their contribution to the moment of inertia of the beams through

TABLE 3 | Three-story test example: Concrete volume and steel weight corresponding to the optimized designs based on six DIs.

Design procedure	Columns		Beams		$C_{IN,Frame}$ (MU)
	Concrete (m^3)	Steel (kg.)	Concrete (m^3)	Steel (kg.)	
$D_{DI=\theta}$	10.00	1810.0	5.06	715.0	8110.0
$D_{DI=ms}$	8.46	1730.0	6.75	1800.0	10600.0
$D_{DI=fs}$	8.46	1930.0	7.16	1630.0	10800.0
$D_{DI=PA}$	14.88	4210.0	8.98	2540.0	19700.0
$D_{DI=KRL}$	13.00	2240.0	6.62	1190.0	11000.0
$D_{DI=CMS}$	7.06	1270.0	6.08	954.0	9990.0

TABLE 4 | Six-story test example: Concrete volume and steel weight corresponding to the optimized designs based on six DIs.

Design procedure	Columns		Beams		$C_{IN,Frame}$ (MU)
	Concrete (m^3)	Steel (kg.)	Concrete (m^3)	Steel (kg.)	
$D_{DI=\theta}$	19.65	2110.0	12.69	1890.0	13900.0
$D_{DI=ms}$	27.32	4580.0	14.51	2050.0	21600.0
$D_{DI=fs}$	28.34	3290.0	16.46	1550.0	17500.0
$D_{DI=PA}$	29.9	3500.0	14.85	1870.0	18800.0
$D_{DI=KRL}$	30.74	3840.0	12.69	2590.0	21300.0
$D_{DI=CMS}$	31.46	4440.0	19.53	2760.0	24100.0

effective flange width is taken into account. Due to floor finishing-partitions permanent loading of 2 kN/m^2 and moving one equal to 1.5 kN/m^2, are applied further to the self-weight of beams and slabs, where an effective zone 10 × 15 m^2 is considered for each story. The nominal imposed and permanent loads are combined using the load factors 1.50 and 1.35, respectively.

Columns and beams were simulated adopting the inelastic force-based fiber finite element. The simulation with this type of elements exhibits better accuracy than the plastic hinge formulation (Lagaros, 2014b). The structural analyses required in the framework the study were performed using OpenSEES (McKenna and Fenves, 2009) software. For steel reinforcement pure kinematic hardening bilinear material model was implemented, considering also geometric nonlinearities explicitly. The extended Kent-Park model as modified by Scott et al. (1982) was used for simulating concrete. Despite its relatively simple formulation, the specific model offers for acceptable forecasts of the needs for flexure-dominated RC members. The cyclic inelastic behavior of bars reinforcement was implemented with Menegotto-Pinto model (Menegotto and Pinto, 1973).

Analysis Procedure

During seismic structural design and/or assessment a wide-ranging earthquake events and multiple structural response levels are required for accounting the uncertainties that earthquake hazard introduces into performance-based earthquake engineering (PBEE) assessment or design. Methods implemented for PBEE assessment by means of nonlinear dynamic analyses are classified into single and multiple hazard level ones. Incremental dynamic analysis (IDA) and multi-stripe dynamic analysis (MSDA), their single and multicomponent (Lagaros, 2010) variants, represent the most appropriate ones. The numerical study performed consists of two stages, the optimization and the structural assessment ones, for both multi-stripe dynamic analysis (MSDA) was implemented for calculating the maximum inter-story drift.

Similar to IDA the purpose of MSDA studies is to form the relationship among earthquake intensity level and the correlative maximum structural performance. Earthquake ranking and performance of the structural system are defined through intensity measures (IM) and engineering demand parameters (EDP), correspondingly. MSDA implementation involves multiple inelastic dynamic analyses (stripes) executed in various spectral acceleration stages (see **Figure 4** for the case of the final softening and Park and Ang designs). In every stripe various inelastic dynamic analyses are executed for the seismic records considered, all are scaled to specific spectral acceleration. The group of seismic records adopted for deriving each stripe should preferably be representative of the seismic hazard at specific spectral acceleration; nevertheless, although not necessarily always justified (e.g., Jalayer and Cornell, 2009), it is common to implement the same group of records for all spectral acceleration levels.

Formulation of the Optimization Problems

The problem is expressed mathematically as single-objective minimization problem and is shown below:

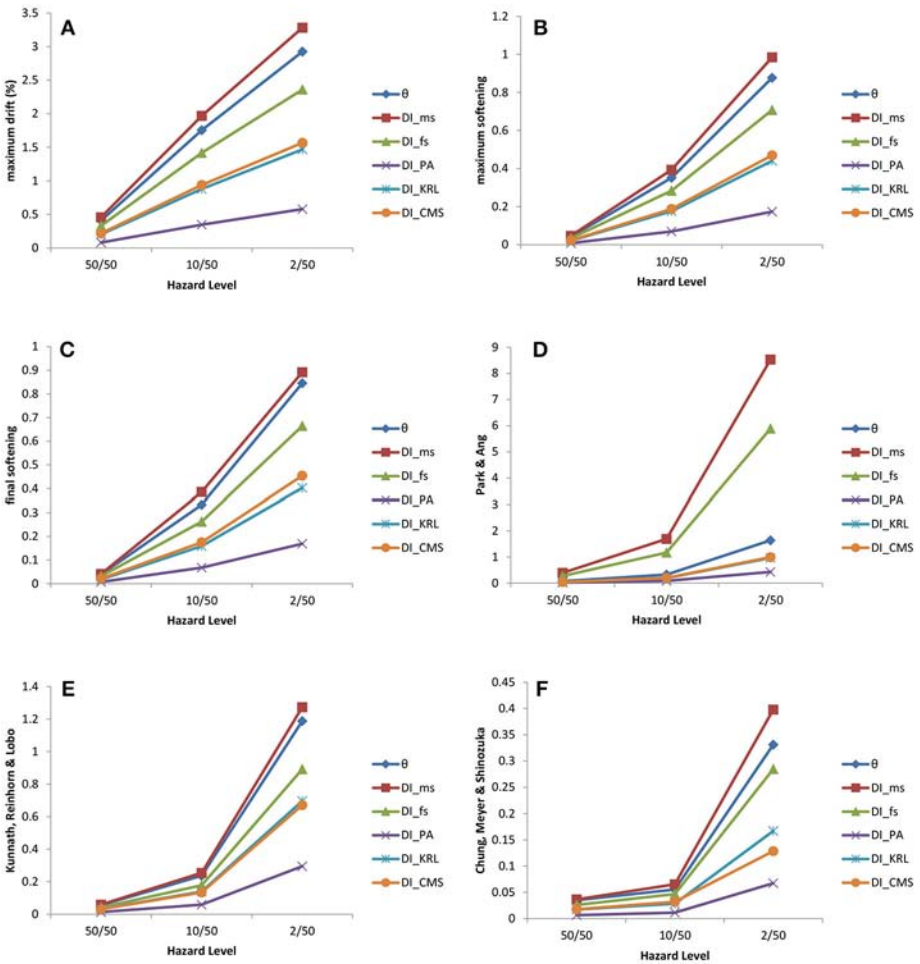

FIGURE 5 | Three-story test example—performances of the optimized designs (i.e., $DI_{\theta max}$, DI_{ms}, DI_{fs}, DI_{PA}, DI_{KRL}, and DI_{CMS}) for three hazard levels compared with respect **(A)** maximum drift, **(B)** maximum softening, **(C)** final softening, **(D)** Park and Ang damage index, **(E)** Kunnath et al. damage index, and **(F)** Chung et al. damage index.

$$\begin{aligned} \min_{s\in F} \quad & C(\boldsymbol{s}) \\ \text{where} \quad & C(\boldsymbol{s}) = C_b(\boldsymbol{s}) + C_{sl}(\boldsymbol{s}) + C_{cl}(\boldsymbol{s}) + C_{ns}(\boldsymbol{s}) \\ \text{subject to} \quad & DI^i_{HL1}(\boldsymbol{s}) \le DI^{allow,i}_{HL1} \\ & DI^i_{HL2}(\boldsymbol{s}) \le DI^{allow,i}_{HL2} \\ & \quad \vdots \\ & DI^i_{HLn}(\boldsymbol{s}) \le DI^{allow,i}_{HLn} \end{aligned} \tag{10}$$

subject to the constraints of Equation (9) (Quaranta et al., 2014; Fiore et al., 2016a). The total initial structural material cost $C(\boldsymbol{s})$ is the objective criterion considered, and $C_{cl}(\boldsymbol{s})$, $C_b(\boldsymbol{s})$, $C_{sl}(\boldsymbol{s})$, and $C_{ns}(\boldsymbol{s})$ are the total material cost of columns, slabs, beams ,and nonstructural members, correspondingly. The ith DI for several hazard levels (HL_1, HL_2, …, HL_n) should remain below the allowable upper bounds ($DI^i_{HLj}(s) \le DI^{allow,i}_{HLj}$). The limits of the feasible region are given in **Table 2** (Mitropoulou et al., 2014). The PSO algorithm is adopted for dealing with the resulting structural design optimization problems. The boundaries for the maximum interstory drift were obtained by Ghobarah (2004).

The optimized design is computed by applying the PSO method with the following characteristic parameters for both test examples as suggested by the parametric study of Pedersen (2010): Number of particles NP is equal to 100, inertia weight w is equal to −0.6, cognitive and social parameters c_1 is equal to −0.65 and c_2 is equal to 2.65, respectively. Rectangular cross-sectional shape is adopted for both columns and beams, which are separated into different sets. The beams/columns dimensionality together with the longitudinal reinforcing bars represent the design parameters, which are allocated to every set of the beams/columns. The structural members (columns and beams) are divided in two sets for the three-story and three sets for the six-story test examples, resulting into five and seven design variables, respectively.

The optimized designs obtained are labeled as $D_{DI=i}$ associated with the damage index used (i–vi). The optimized

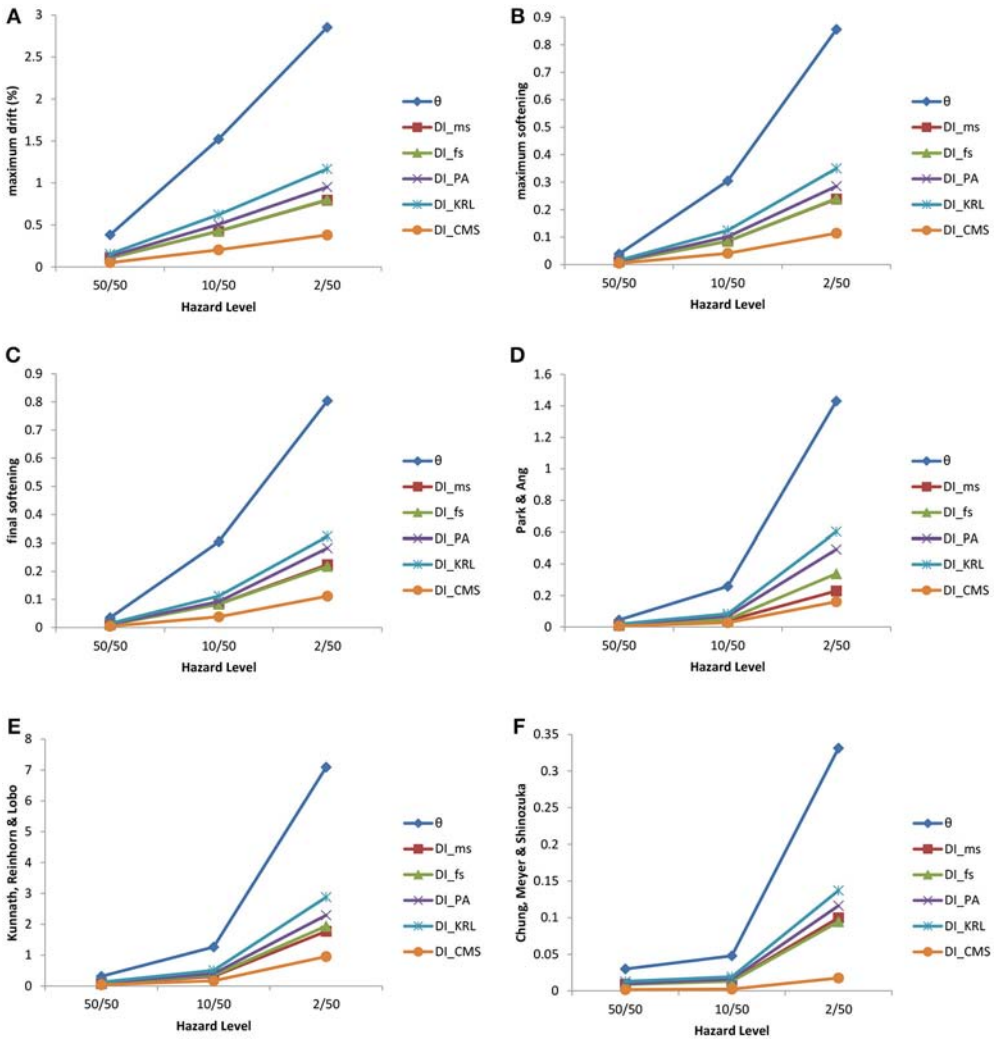

FIGURE 6 | Six-story test example—performances of the optimized designs (i.e., $DI_{\theta max}$, DI_{ms}, DI_{fs}, DI_{PA}, DI_{KRL}, and DI_{CMS}) for three hazard levels compared with respect **(A)** maximum drift, **(B)** maximum softening, **(C)** final softening, **(D)** Park and Ang damage index, **(E)** Kunnath et al. damage index, and **(F)** Chung et al. damage index.

designs obtained for different DI considerations with reference to steel and concrete material demands are shown in **Tables 3**, **4**, respectively. According to **Tables 3**, **4** it looks that $D_{DI=ms}$, $D_{DI=fs}$, and $D_{DI=CMS}$ are leading to smaller columns for the three-storys but it does not apply to the six-story where $D_{DI=\theta}$ is the one leading to smaller columns. With respect to beams, it looks that $D_{DI=\theta}$ and $D_{DI=CMS}$ are leading to smaller beams for the three-stories and $D_{DI=\theta}$ and $D_{DI=KRL}$ are leading ones for the six-story. Compared to design $D_{DI=\theta}$, it can be seen that, the initial material construction cost of the other five designs is increased by 23–145% for the three-story and by 26–75% for the six-story test example.

Assessment of the Optimized Designs

Aiming to evaluate the capacity of the optimized designs achieved by means of the six design PBD procedures described previously, a multi-stripe analyses is performed over a properly selected bin 100 natural records from the list of records provided in Mitropoulou et al. (2015). Seismic records were chosen from PEER (2010) database in agreement with the subsequent characteristics: (i) Records chosen in particular geographical zone (latitude 32–41°, longitude −124° to −115°). (ii) Magnitude (M) to be greater or equal to 5. (iii) Distance from the epicenter (R) is <150 km. **Figures 5**, **6** depict the median values of maximum interstory drifts, maximum softening, final softening, Park and Ang damage index, Kunnath et al. damage index, and Chung et al. damage index. These quantities are obtained for three hazard levels namely 50/50, 10/50, and 2/50 (corresponding to probabilities of exceedance equal to 50, 10, and 2% in 50 years, respectively) and for the optimized designs achieved according to the design frameworks discussed above. Indicatively the multi-stripe analysis results for the three-story

with reference to the maximum drift for final softening and Park and Ang designs that were used to derive the corresponding for these two designs median curves of **Figure 5A** are provided in **Figure 4**. In **Figure 5A** is represented the structural performance of the three-stories optimized designs (i.e., $DI_{\theta max}$, DI_{ms}, DI_{fs}, DI_{PA}, DI_{KRL}, and DI_{CMS}) for the three hazard levels based only on maximum drift; the different lines are representing the different design.

The measure of the performance of one DI over the others is the structural performance achieved by each optimized design compared to the other ones, i.e., the design that has on average the better structural performance for all DIs. For the three-story test model it is the design obtained according to Park and Ang damage index that shows an overall better performance with reference to the six engineering demand parameters. On the other hand, for the six-story test model it is the design achieved according to Chung et al. damage index that exhibits the best performance, with reference to the six engineering demand parameter. Furthermore, for both test examples the maximum interstory drift appear to increase smoothly based on the abscissa escalation for all optimized designs in consideration of the hazard levels, while the structural behavior of the six designs is nonlinear with reference to the other damage indices. In general, it can be said that, for the two test examples considered, it is the Chung et al. damage index that shows an overall good performance with reference to the performance criteria considered. This is because for both test examples the designs obtained through the design formulation with the Chung et al. DI corresponds to the lower DI values, with reference to all six damage indices considered.

CONCLUSIONS

In this work we aim to incorporate a number of damage indices previously assessed by Mitropoulou et al. (2014) into a performance-based design framework and to identify the most suitable one for designing reinforced concrete framed structures. In this direction, structural optimization problems are formulated with performance-based design criteria corresponding to six damage indices for two reinforced concrete buildings.

An investigation was performed on the influence of these six damage indices incorporated into a performance-based design procedure. This was achieved by means of lower bound performance-based design. The ultimate objective was to compare lower-bound designs that satisfying in the most cost-efficient way the design code requirements, i.e., those requiring less material volume for concrete and steel reinforcement. The optimized designs obtained were subsequently assessed on the basis of their performance on a number of properly selected earthquakes with increasing intensity.

From the results obtained it was observed that, compared to design $D_{DI=\theta}$ based on interstory drift, the initial construction cost of the other five designs is enlarged by 23–145% for the three-story test example and by 26–75% for the six-story one. It can also be concluded that for the two test examples considered it is the Chung et al. damage index that shows an overall good performance with reference to the performance criteria considered.

AUTHOR CONTRIBUTIONS

All authors listed have made a substantial, direct and intellectual contribution to the work, and approved it for publication.

ACKNOWLEDGMENTS

This research was supported by the OptArch project: Optimization Driven Architectural Design of Structures (No: 689983) belonging to the Marie Skłodowska-Curie Actions (MSCA) Research and Innovation Staff Exchange (RISE) H2020-MSCA-RISE-2015.

REFERENCES

Allahabadi, R., and Powell, G. H. (1988). *DRAIN-2DX User Guide.* Technical Report No. UCB/EERC-88-06, Earthquake Engineering Research Center, University of California, Berkeley, CA.

ASCE-41 (2006). *Seismic Rehabilitation of Existing Buildings*. American Society of Civil Engineers ASCE/SEI Standard 41-06, Reston, VA.

ATC-58 (2009). *Guidelines for Seismic Performance Assessment of Buildings.* Applied Technology Council, Redwood City, CA.

Banon, H., and Veneziano, D. (1982). Seismic safety of reinforced members and structures. *Earthq. Eng. Struct. Dyn.* 10, 179–193. doi: 10.1002/eqe.4290100202

Chan, C.-M., and Zou, X.-K. (2004). Elastic and inelastic drift performance optimization for reinforced concrete buildings under earthquake loads. *Earthq. Eng. Struct. Dyn.* 33, 929–950. doi: 10.1002/eqe.385

Chung, Y. S., Meyer, C., and Shinozuka, M. (1987). *Seismic Damage Assessment of Reinforced Concrete Members*. Report NCEER-87-0022, National Center for Earthquake Engineering Research, State University of New York, Buffalo, NY.

Chung, Y. S., Meyer, C., and Shinozuka, M. (1989). Modelling of concrete damage. *ACI Struct. J.* 86, 259–271. doi: 10.1016/B978-012443341-0/50056-9

DiPasquale, E., and Çakmak, A. S. (1987). *Detection and Assessment of Seismic Structural Damage.* Report NCCER-87-O015, National Center for Earthquake Engineering Research State University of New York, Buffalo, NY.

DiPasquale, E., and Çakmak, A. S. (1988). *Identification of the Serviceability Limit State and Detection of Seismic Structural Damage.* Report NCEER-88-0022, National Center for Earthquake Engineering Research State University of New York, Buffalo, NY.

Estekanchi, H. E., and Arjomandi, K. (2007). Comparison of damage indexes in nonlinear time history analysis of steel moment frames. *Asian J. Civil Eng.* 8, 629–646. Available online at: http://www.sid.ir/En/Journal/ViewPaper.aspx?ID=103772

Esteva, L., Díaz-López, O., García-Pérez, J., Sierra, G., and Ismael, E. (2002). Life-cycle optimization in the establishment of performance-acceptance parameters for seismic design. *Struct. Saf.* 24, 187–204. doi: 10.1016/S0167-4730(02)00024-3

FEMA-350 (2000). *Recommended Seismic Design Criteria for New Steel Moment-Frame Buildings.* Federal Emergency Management Agency, Washington, DC.

FEMA-445 (2006). *Next-Generation Performance-Based Seismic Design Guidelines, Program Plan for New and Existing Buildings.* Federal Emergency Management Agency, Washington, DC.

FEMA-P-58-1. (2012). *Seismic Performance Assessment of Building.* Federal Emergency Management Agency, Washington, DC.

Fiore, A., Marano, G. C., Greco, R., and Mastromarino, E. (2016a). Structural optimization of hollow-section steel trusses by differential evolution algorithm. *Int. J. Steel Struct.* 16, 411–423. doi: 10.1007/s13296-016-6013-1

Fiore, A., Spagnoletti, G., and Greco, R. (2016b). On the prediction of shear brittle collapse mechanisms due to the infill-frame interaction in RC buildings under pushover analysis. *Eng. Struct.* 121, 147–159. doi: 10.1016/j.engstruct.2016.04.044

Foley, C. M., Pezeshk, S., and Alimoradi, A. (2007). Probabilistic performance-based optimal design of steel moment-resisting frames. I: formulation. *J. Struct. Eng.* 133, 757–766. doi: 10.1061/(ASCE)0733-9445(2007)133:6(757)

Fragiadakis, M., Lagaros, N. D., and Papadrakakis, M. (2006). Performance-based earthquake engineering using structural optimization tools. *Int. J. Reliab. Saf.* 1, 59–76. doi: 10.1504/IJRS.2006.010690

Ganzerli, S., Pantelides, C. P., and Reaveley, L. D. (2000). Performance-based design using structural optimization. *Earthq. Eng. Struct. Dyn.* 29, 1677–1690. doi: 10.1002/1096-9845(200011)29:1drd1<1677::AID-EQE986>3.0.CO;2-N

Ghobarah, A. (2004). "On drift limits associated with different damage levels," in *International Workshop on Performance-Based Seismic Design* (Bled).

Ghobarah, A., Abou-Elfath, H., and Biddah, A. (1999). Response-based damage assessment of structures. *Earthq. Eng. Struct. Dyn.* 28, 79–104. doi: 10.1002/(SICI)1096-9845(199901)28:1<79::AID-EQE805>3.0.CO;2-J

Greco, R., Lucchini, A., and Marano, G. C. (2015). Robust design of tuned mass dampers installed on multi-degree-of-freedom structures subjected to seismic action. *Eng. Optim.* 47, 1009–1030. doi: 10.1080/0305215X.2014.941288

Greco, R., Marano, G. C., and Fiore, A. (2016). Performance–cost optimization of tuned mass damper under low-moderate seismic actions. *Struct. Design Tall Spec. Build.* 25, 1103–1122. doi: 10.1002/tal.1300

Greco, R., Marano, G. C., and Fiore, A. (2017). Damage-based inelastic seismic spectra. *Int. J. Struct. Stabil. Dyn.* 17:1750115. doi: 10.1142/S0219455417501152

Grigoriu, M. (1987). *Damage Models for Seismic Analysis.* Technical Report 87-4, Department of Structural Engineering, Cornell University, Ithaca, NY.

Jalayer, F., and Cornell, C. A. (2009). Alternative non-linear demand estimation methods for probability-based seismic assessments. *Earthq. Eng. Struct. Dyn.* 38, 951–972. doi: 10.1002/eqe.876

Kennedy, J., and Eberhart, R. (1995). "Particle swarm optimization," in *IEEE International Conference on Neural Networks* (Piscataway, NJ), 1942–1948.

Khashaee, P. (2005). Damage-based seismic design of structures. *Earthq. Spect.* 21, 371–387. doi: 10.1193/1.1896366

Krawinkler, H., and Miranda, E. (2004). "Performance-based earthquake engineering," in *Earthquake Engineering: From Engineering Seismology to Performance-Based Earthquake Engineering,* eds Y. Bozorgnia and Vitelmo V. Bertero (Boca Raton, FL: CRC Press), 9–59.

Kunnath, S. K., Reinhorn, A. M., Lobo, R. F. (1992). *IDARC Version 3.0: a Program for the Inelastic Damage Analysis of Reinforced Concrete Structures.* Technical Report NCEER-92-0022, National Center for Earthquake Engineering Research, Buffalo, NY.

Lagaros, N. D. (2010). Multicomponent incremental dynamic analysis considering variable incident angle. *J. Struct. Infrastruct. Eng.* 6, 77–94. doi: 10.1080/15732470802663805

Lagaros, N. D. (2014a). A general purpose real-world structural design optimization computing platform. *Struct. Multidiscip. Optim.* 49, 1047–1066. doi: 10.1007/s00158-013-1027-1

Lagaros, N. D. (2014b). Risk assessment of steel and steel-concrete composite 3D buildings considering sources of uncertainty. *Earthq. Struct.* 6, 19–43. doi: 10.12989/eas.2014.6.1.019

Lagaros, N. D. (2018). The environmental and economic impact of structural optimization. *Struct. Multidiscip. Optim.* doi: 10.1007/s00158-018-1998-z. [Epub ahead of print].

Lagaros, N. D., and Fragiadakis, M. (2011). Evaluation of ASCE-41, ATC-40 and N2 static pushover methods based on optimally designed buildings. *Soil Dyn. Earthq. Eng.* 31, 77–90. doi: 10.1016/j.soildyn.2010.08.007

Lagaros, N. D., Naziris, I. A., and Papadrakakis, M. (2010). The influence of masonry infill walls in the framework of the performance-based design. *J. Earthq. Eng.* 14, 57–79. doi: 10.1080/13632460902988976

Lagaros, N. D., and Papadrakakis, M. (2007). Seismic design of RC structures: a critical assessment in the framework of multi-objective optimization. *Earthq. Eng. Struct. Dyn.* 36, 1623–1639. doi: 10.1002/eqe.707

Li, G., and Cheng, G. (2003). Damage-reduction-based structural optimum design for seismic RC frames. *Struct. Multidiscip. Optim.* 25, 294–306. doi: 10.1007/s00158-003-0299-2

Liu, M., Burns, S. A., and Wen, Y. K. (2005). Multiobjective optimization for performance-based seismic design of steel moment frame structures. *Earthq. Eng. Struct. Dyn.* 34, 289–306. doi: 10.1002/eqe.426

Mahin, S. A., and Bertero, V. V. (1974). Nonlinear seismic response evaluation - Charaima building. *J. Struct. Eng.* 100, 1225–1242.

Marano, G. C., and Greco, R. (2006). Damage and ductility demand spectra assessment of hysteretic degrading systems subject to stochastic seismic loads. *J. Earthq. Eng.* 10, 1–26. doi: 10.1080/13632460609350612

Marano, G. C., Greco, R., and Palombella, G. (2008). Stochastic optimum design of linear tuned mass dampers for seismic protection of high towers. *Struct. Eng. Mech.* 29, 603–622. doi: 10.12989/sem.2008.29.6.603

Marano, G. C., Quaranta, G., and Greco, R. (2009). Multi-objective optimization by genetic algorithm of structural systems subject to random vibrations. *Struct. Multidiscip. Optim.* 39, 385–399. doi: 10.1007/s00158-008-0330-8

Marano, G. C., Trentadue, F., and Greco, R. (2006). Optimum design criteria for elastic structures subject to random dynamic loads. *Eng. Optim.* 38, 853–871. doi: 10.1080/03052150600913028

Marano, G. C., Trentadue, F., and Greco, R. (2007). Stochastic optimum design criterion of added viscous dampers for buildings seismic protection. *Struct. Eng. Mech.* 25, 21–37. doi: 10.12989/sem.2007.25.1.021

McKenna, F., and Fenves, G.L. (2009). *The OpenSees Command Language Manual - Version 2.0.* Pacific Earthquake Engineering Research Centre, University of California, Berkeley, CA.

Menegotto, M., and Pinto, P. E. (1973). Method of analysis for cyclically loaded reinforced concrete plane frames including changes in geometry and non-elastic behaviour of elements under combined normal force and bending," in *IABSE Symposium on Resistance and Ultimate Deformability of Structures Acted on by Well Defined Repeated Loads* (Lisbon), 15–22.

Mitropoulou, CCh., Lagaros, N. D., and Papadrakakis, M. (2011). Life-cycle cost assessment of optimally designed reinforced concrete buildings under seismic actions. *Reliab. Eng. Syst. Saf.* 96, 1311–1331. doi: 10.1016/j.ress.2011.04.002

Mitropoulou, CCh., Lagaros, N. D., and Papadrakakis, M. (2014). Numerical calibrations of damage indices. *Adv. Eng. Softw.* 70, 36–50. doi: 10.1016/j.advengsoft.2014.01.007

Mitropoulou, CCh., Lagaros, N. D., and Papadrakakis, M. (2015). Generation of artificial accelerograms for efficient life-cycle cost analysis of structures. *Eng. Struct.* 88, 138–153. doi: 10.1016/j.engstruct.2015.01.029

Park, Y. J., and Ang, A. H.-S. (1985). A mechanistic seismic damage model for reinforced concrete. *J. Struct. Eng.* 111, 722–739. doi: 10.1061/(ASCE)0733-9445(1985)111:4(722)

Pedersen, M. E. H. (2010). *Good Parameters for Particle Swarm Optimization*. Hvass Laborato-ries Technical Report no. HL1001, Southampton.

Powell, G. H., and Allahabadi, R. (1988). Seismic damage prediction by deterministic methods: concepts and procedures. *Earthq. Eng. Struct. Dyn.* 16, 719–734. doi: 10.1002/eqe.4290160507

Quaranta, G., Fiore, A., and Marano, G. C. (2014). Optimum design of prestressed concrete beams using constrained differential evolution algorithm. *Struct. Multidiscip. Optim.* 49, 441–453. doi: 10.1007/s00158-013-0979-5

Resta, M., Fiore, A., and Monaco, P. (2013). Non-Linear finite element analysis of masonry towers by adopting the damage plasticity constitutive model. *Adv. Struct. Eng.* 16, 791–803. doi: 10.1260/1369-4332.16.5.791

Rojas, H. A., Pezeshk, S., and Foley, C. M. (2007). Performance-based optimization considering both structural and nonstructural components. *Earthq. Spectra* 23, 685–709. doi: 10.1193/1.2754002

Roufaiel, M. S. L., and Meyer, C. (1987). Analytical modelling of hysteretic behaviour of RC frames. *J. Struct. Eng.* 113, 429–443. doi: 10.1061/(ASCE)0733-9445(1987)113:3(429)

Saiidi, M., and Sozen, M. A. (1981). Simple nonlinear seismic analysis of RC structures. *J. Struct. Eng.* 107, 937–952.

Scott, B. D., Park, R., and Priestley, M. J. N. (1982). Stress–strain behavior of concrete confined by overlapping hoops at low and high strain rates. *ACI J.* 79, 13–27.

Shiga, T., Shibata, A., and Hirosawa, M. (1982). "Outline of research on estimation of damages and repairs of the buildings damaged by the Miyagi-Ken-Oki earthquake, June, 1978," in *Seminar on Repair and Retrofit of Structures* (Ann Arbor, MI), 147.

Sullivan, T. J., Calvi, G. M., Priestley, M. J. N., and Kowalsky, M. J. (2003). The limitations and performances of different displacement based design methods. *J. Earthq. Eng.* 7, 201–241. doi: 10.1080/13632460309350478

Toussi, S., and Yao, J. T. P. (1982). Hysteresis identification of existing structures. *J. Eng. Mech.* 109, 1189–1203. doi: 10.1061/(ASCE)0733-9399(1983)109:5(1189)

Vanzi, I., Marano, G. C., Monti, G., and Nuti, C. (2015). A synthetic formulation for the Italian seismic hazard and code implications for the seismic risk. *Soil Dyn. Earthq. Eng.* 77, 111–122. doi: 10.1016/j.soildyn.2015.05.001

Conflict of Interest Statement: The authors declare that the research was conducted in the absence of any commercial or financial relationships that could be construed as a potential conflict of interest.

frontiers in Built Environment

ORIGINAL RESEARCH
published: 28 August 2018
doi: 10.3389/fbuil.2018.00046

A Simple Rate-Independent Uniaxial Shape Memory Alloy (SMA) Model

Aristotelis E. Charalampakis[1]* *and George C. Tsiatas*[2]

[1] School of Civil Engineering, National Technical University of Athens, Athens, Greece, [2] Department of Mathematics, University of Patras, Rio, Greece

In this paper, three specific uniaxial phenomenological models commonly used for the description of a Shape Memory Alloy (SMA) behavior are examined in detail. In particular, the models examined are the Graesser-Cozzarelli model, the Wilde-Gardoni-Fujino model, and the Zhang-Zhu model. The pertinent model parameters are examined with respect to their physical representation, if any. Based on this analysis, a new simple rate-independent model is proposed which addresses all issues in a unified manner. Finally, powerful metaheuristics are employed for system identification, producing excellent fit with experimental data while revealing valuable information regarding the relative sensitivity of the proposed model parameters.

Keywords: Shape Memory Alloy (SMA), identification, hysteresis, rate-independent model, phenomenological model

OPEN ACCESS

Edited by:
Nikos D. Lagaros, National Technical University of Athens, Greece

Reviewed by:
Dimitrios Giagopoulos, University of Western Macedonia, Greece
Savvas Triantafyllou, University of Nottingham, United Kingdom

***Correspondence:**
Aristotelis E. Charalampakis
achar@mail.ntua.gr

Specialty section:
This article was submitted to Computational Methods in Structural Engineering, a section of the journal Frontiers in Built Environment

Received: *11 June 2018*
Accepted: *30 July 2018*
Published: *28 August 2018*

Citation:
Charalampakis AE and Tsiatas GC (2018) A Simple Rate-Independent Uniaxial Shape Memory Alloy (SMA) Model. Front. Built Environ. 4:46. doi: 10.3389/fbuil.2018.00046

INTRODUCTION

Throughout history, humanity has sought shelter from natural phenomena. Natural shelters, such as caves, were abandoned for artificial structures made of primitive materials, i.e., wood, stone, and brick. The building blocks were held in place by either sole gravity or by primitive paste. In the classical era, the Romans used *opus caementicium*, a pozzolanic concrete-like material, to build arches, vaults, and domes. Following a prolonged period of stagnation, new materials were introduced around 1800–1850 (i.e., cast iron and, later on, wrought iron and structural steel, as well as Portland cement), causing a revolution in the construction industry. Nowadays, the extensive use of high-strength steel and concrete, as well as the combination of them (as in composite structures), has led to an explosion in the capacity, performance, and size of structures that are feasible. Nevertheless, there is a consensus that, more or less, these materials have been fully exploited and groundbreaking development is unlikely to be observed.

Seeking the next revolution in the construction industry, researchers drew their attention to the so-called smart materials. These materials exhibit extraordinary properties, ranging from piezoelectricity and pH-sensitivity to magnetostriction and self-healing. A popular class of these materials, commonly known as Shape Memory Alloys (SMAs), exhibit physical and mechanical characteristics that allow their integration into structures. SMAs are capable of sustaining large inelastic strains that can be recovered by heating or unloading, depending on prior loading history. The origin of this unusual behavior is the ability of SMAs to undergo a first-order solid-solid diffusionless, and reversible phase change called *martensitic transformation* between a parent phase called austenite (A), stable at high temperature and low stress, and a product phase called martensite (M), metastable at low temperature and high stress (Olson and Cohen, 1982; Cisse et al., 2016). The martensitic transformation is at the origin of the two main effects observed in SMAs, namely the *shape-memory effect* and *superelasticity*.

Various innovative systems and devices, mainly using NiTi and Cu-based SMAs, have been developed for seismic energy absorption, damping control, structural retrofit. Several

prototypes of SMA braces for the seismic protection of structures have been designed, numerically assessed and experimentally tested (Clark et al., 1995; Auricchio et al., 2006; Andrawes and DesRoches, 2007; Zhu and Zhang, 2008; Asgarian and Moradi, 2011). Hybrid devices, comprising of a combination of SMA and other components such as precompressed springs (Ma and Cho, 2008; Miller et al., 2012), or struts and steel tubes (Walter Yang et al., 2010) have been presented. Also, SMA-based isolation devices have been developed finding various applications on buildings or bridge structures (Krumme et al., 1995; Wilde et al., 2000). These devices exploit the hysteretic nature of SMA materials aiming to absorb structural vibrating energy and mitigate seismic effects. Gur and Mishra (2013) proposed a combination of steel-Teflon surface isolation device with superelastic SMA restrainers for energy dissipation and simultaneous minimization of isolator displacements and superstructure accelerations. Ozbulut and Hurlebaus (2010) introduced a sliding-type isolation system, optimally designed with the help of a multi-objective genetic algorithm, which consists of a steel Teflon sliding bearing and a NiTi SMA device, providing vertical load capacity, damping, and self-centering at the same time. Other applications of SMA materials in structural engineering include damping devices for bridge structures (Fujino et al., 1993; Ben Mekki and Auricchio, 2011; Torra et al., 2013), SMA-based structural connections in steel structures (Leon et al., 2001; Speicher et al., 2011; Fang et al., 2014) and reinforced concrete frames (Youssef et al., 2008; Muntasir Billah and Shahria Alam, 2012), structural retrofit of buildings and bridges (DesRoches and Delemont, 2002; Andrawes et al., 2010), use of SMA as reinforcement material in concrete structures (Deng et al., 2006; Zafar and Andrawes, 2013) as well as self-rehabilitation of structural elements (Li et al., 2006, 2008).

Obviously, proper modeling of the extraordinary behavior of SMAs is important and, thus, several models have been proposed in the literature. These can be broadly categorized into microscopic thermodynamic models, based on the Ginzburg-Landau theory or molecular dynamics; micro-macro models, based on micromechanics, micro-planes or micro-spheres; and macroscopic models, based on the theory of plasticity, thermodynamic potentials, finite strains or statistical physics (Cisse et al., 2016). For applications in structural engineering, however, uniaxial phenomenological models are of special interest as integration with existing reliable FEM codes, e.g., OpenSees (Mazzoni et al., 2006), is straightforward. Falling under this category, the Graesser-Cozzarelli model (Graesser and Cozzarelli, 1991), the Wilde-Gardoni-Fujino model (Wilde et al., 2000), and the Zhang-Zhu model (Zhang and Zhu, 2007) are examined herein in detail. Their parameters are examined concerning their physical representation, if any. This process reveals several limitations and drawbacks, most prominent of which is the large number of parameters and the unclear effect of specific parameters in the overall response. These are addressed in a unified manner in a new rate-independent model proposed herein. Finally, metaheuristic algorithms are employed for the identification of unknown parameter values. This process reveals valuable information regarding the relative sensitivity of the parameters as well as the mathematical consistency of the model.

BASIC SMA BEHAVIOR

The primary forms of SMA behavior which are pertinent to the applications examined in this study are shown in **Figure 1**. In particular, **Figure 1A** shows the hysteretic loop observed at ambient temperatures $T < M_f$, where M_f is the temperature at which the microstructure of the material is fully martensitic. Although the loop strongly resembles the one observed in most conventional steels, the hysteretic mechanism is quite different. In steels, hysteresis in cyclic loading is due to dislocation glide but in SMAs it is due to twinning deformation of martensite that occurs by rotation, growth, and shrinkage of individual variants of martensite (Graesser and Cozzarelli, 1991). By application of sufficient strain, only one martensitic variant remains. This variant reverts to the original parent crystal orientation upon the application of heat, thus the term *shape-memory effect*.

Figure 1B shows the hysteretic loop observed at ambient temperatures $T > A_f$, where A_f is the temperature at which the microstructure of the material is fully austenitic. This behavior exhibits two very important properties, i.e., energy dissipation and zero residual strain upon unloading, and thus it is termed *superelastic*. According to this, the stable austenitic

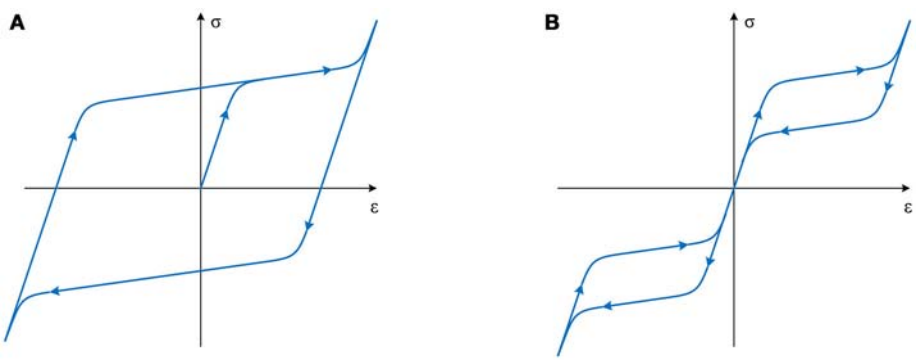

FIGURE 1 | Schematic representation SMA behavior **(A)** twinning hysteresis ($T < M_f$), **(B)** superelasticity ($T > A_f$).

microstructure is loaded elastically up to a threshold stress level, at which a transformation from austenite to martensite is initiated. The transformation is accompanied by the reduced modulus, as compared to the initial elastic loading, which strongly resembles the plastic yielding of steels. Gradually, the volume ratio of martensite is increased within the microstructure until it becomes dominant. Further loading of the now fully martensitic microstructure leads to elastic loading with a modulus smaller than the one of the elastic austenite, yet significantly higher than the one during transformation. Upon unloading, the inverse process is observed but at a significantly lower stress plateau. Ideally, the material returns to its exact original form (Graesser and Cozzarelli, 1991).

THE GRAESSER-COZZARELLI MODEL

By modifying Ozdemir's model (Ozdemir, 1973), which is a particular case of the well-known Bouc-Wen hysteretic model (Bouc, 1967; Wen, 1976), Graesser and Cozzarelli (1991) proposed a one-dimensional phenomenological law to describe both twinning hysteresis and superelasticity, which is described by the following equations:

$$\dot{\sigma} = E\left[\dot{\varepsilon} - |\dot{\varepsilon}|\left(\frac{\sigma-\beta}{Y}\right)^n\right], \tag{1}$$

$$\beta = E\alpha\left[\varepsilon_{in} + f_T|\varepsilon|^c erf\left(\bar{a}\varepsilon\right) u\left(-\varepsilon\dot{\varepsilon}\right)\right], \tag{2}$$

where, $(\dot{})$ = ordinary time derivative, σ = stress, ε = strain, β = backstress, E = initial elastic modulus, Y = yield stress, $\alpha = E_y/\left(E-E_y\right)$ = parameter controlling the post-elastic slope of the curve (E_y = post-elastic modulus), n = parameter controlling the abruptness of transition from the elastic to post-elastic branch, $\varepsilon_{in} = \varepsilon - \sigma/E$ = inelastic strain, f_T, $\bar{a}$, c are model parameters, $erf\,(\cdot)$ is the error function defined by:

$$erf\,(x) = \frac{2}{\sqrt{\pi}}\int_0^x e^{-t^2}dt, \tag{3}$$

and $u\,(\cdot)$ is the Heaviside step function defined by:

$$u\,(x) = \begin{cases} 1, & x \geq 0 \\ 0, & x < 0 \end{cases}. \tag{4}$$

Note that parameter $\bar{a}$ is used in Equation (2) to avoid confusion between parameters a and α in the original paper. Also, in Equation (1) the term $(\sigma - \beta)$ may be negative, which is problematic when n takes real rather than integer values. This problem is addressed in a similar manner as in Zhang and Zhu (2007) in the proposed model which will be presented later.

Rate-Independency

The Graesser and Cozzarelli model is rate-independent, as is the Bouc-Wen model (Charalampakis and Koumousis, 2008b; Charalampakis, 2015). This means that in strain-controlled experiments, as the ones shown next, the same hysteretic loop will be traced irrespective of the rate of loading. In fact, the input does not even need to be sinusoidal; any input history with the specific sequence of local maxima and minima, i.e., $0 \rightarrow \varepsilon_{max} \rightarrow -\varepsilon_{max} \rightarrow \varepsilon_{max} \rightarrow \ldots$, will produce the same result.

Twinning Hysteresis

Twinning hysteresis in the Graesser and Cozzarelli model is observed by setting $f_T = 0$ in Equation (2). The base model shown in **Figure 2A** was used in the original paper (Graesser and Cozzarelli, 1991), where $E = 28,500\ ksi$; $Y = 30ksi$; $\alpha = 0.0197$; $n = 3$. The input history is sinusoidal with $\varepsilon_{max} = 0.016$.

In **Figure 2B**, the effect of varying parameter E is shown. Apart from the initial stiffness, which is clearly controlled by E, the post-elastic stiffness E_y is also affected since $E_y = \alpha E/\left(1+\alpha\right)$.

In **Figure 2C** the effect of varying parameter Y is examined. Obviously, Y controls the yield stress. Note that the term "yield stress" should be used rather loosely in our context. In SMA, it corresponds to the stress level at which stress induced phase transformation takes place in the material and has nothing to do with plastic deformation. Nevertheless, it will be used for reasons of simplicity.

In **Figure 2D** the effect of varying parameter α is shown. Clearly, α controls the post-elastic stiffness E_y without affecting the initial stiffness E.

In **Figure 2E** the effect of varying the exponential parameter n is shown. As is the case of the Bouc-Wen model, n controls the abruptness of transition between the initial (elastic) and post-elastic branches. Small values of n lead to a smooth transition and vice versa. Note that the sensitivity of the model with respect to this parameter becomes negligible when $n \geq 3$. In the figure, the responses for $n = 3$ and $n = 5$ are practically the same.

Superelasticity

Superelasticity in the Graesser and Cozzarelli model is observed by setting $f_T > 0$ in Equation (2). The base model shown in **Figure 3A** was used in the original paper (Graesser and Cozzarelli, 1991), where $E = 28{,}500\ ksi$; $Y = 30\ ksi$; $\alpha = 0.0197$; $n = 3$; $f_T = 0.07$; $\bar{a} = 2{,}500$; and $c = 0.001$. The input history is sinusoidal with $\varepsilon_{max} = 0.016$. In **Figure 3B**, the effect of varying parameter f_T is shown. It is observed that high values of f_T reduce the size of the energy-dissipating loops exhibited during the material transformations. Apparently, the sensitivity of the model with respect to f_T is high. In **Figure 3C** the effect of varying parameter $\bar{a}$ is examined. As is the case with n, high values of $\bar{a}$ do not alter the response significantly. For small values of $\bar{a}$, the response becomes smooth around the origin, yielding residual deformations upon unloading. In **Figure 3D** the effect of varying parameter c is shown. In general, the sensitivity of the model with respect to this parameter is very small. **Figure 3E** shows the variation of the quantity $|\varepsilon|^c$ during the experiment. The responses for $c = 0.001$ and $c = 0.00001$ are practically the same, because $|\varepsilon|^c \cong 1$ for $\varepsilon \neq 0$. For $c = 0.1$, the graph of $|\varepsilon|^c$ takes a form not radically different from the error function $erf\,(\cdot)$ used in the same expression, i.e., Equation (2). Thus, the response observed for $c = 0.1$, can also be obtained by appropriate values of f_T, n, and $\bar{a}$. To demonstrate this, the optimum values of f_T, n and $\bar{a}$ have been obtained which produce a similar curve as the one with c = 0.1 (**Figure 3F**) using metaheuristics. In this regard, the term $|\varepsilon|^c$ in Equation (2) is deemed redundant and will be removed in the proposed model which will be presented later.

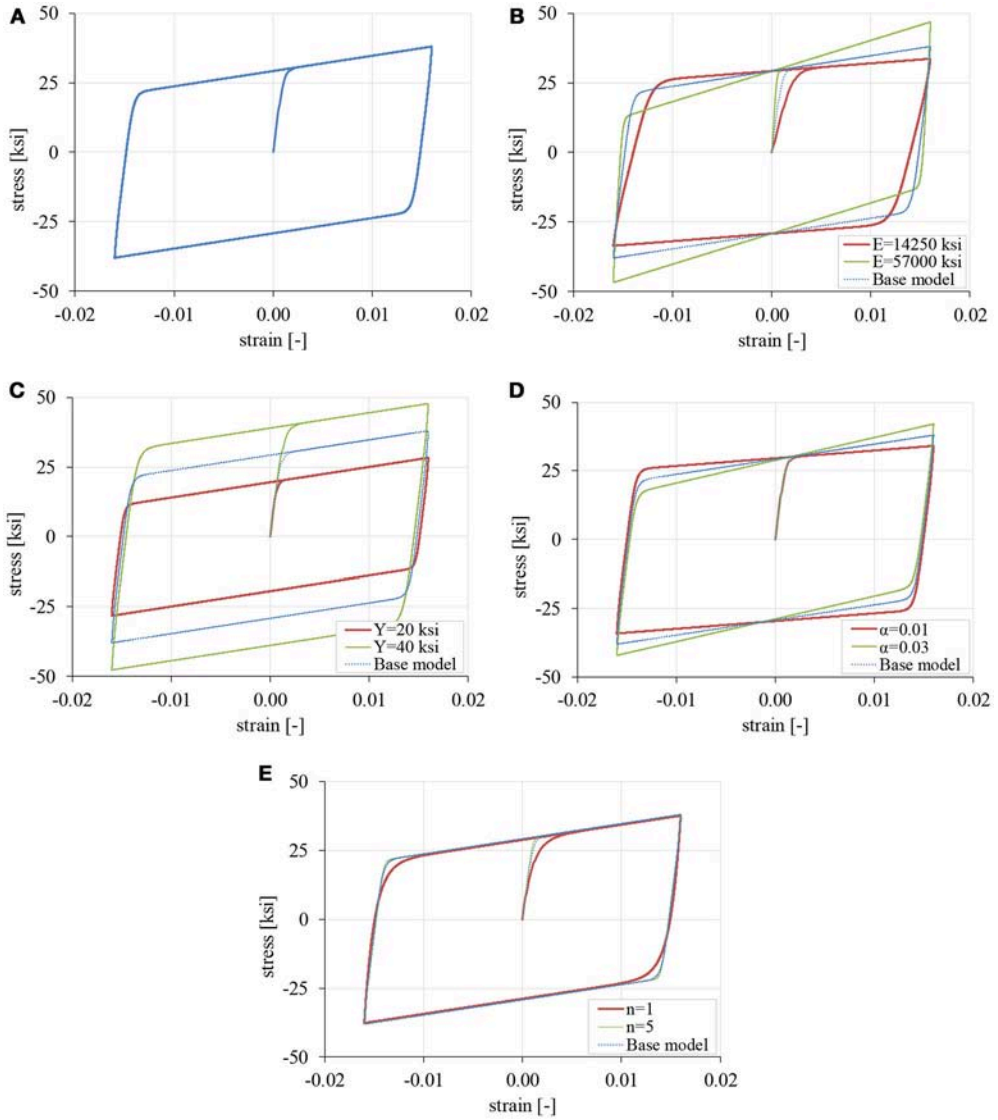

FIGURE 2 | Twinning hysteresis ($f_T = 0$) with the Graesser-Cozzarelli model, **(A)** base model with $E = 28{,}500$ ksi, $Y = 30$ ksi, $\alpha = 0.0197$, $n = 3$ **(B)** variation in E **(C)** variation in Y **(D)** variation in α **(E)** variation in n.

Error Function

The final note on the Graesser-Cozzarelli model refers to the error function itself. As the evaluation of this function is cumbersome [see Equation (3)], its substitution with the hyperbolic tangent is proposed herein. The hyperbolic tangent is remarkably similar to the error function but more comfortable to evaluate, e.g., by using:

$$\tanh(x) = 1 - \frac{2}{1 + e^{2x}}. \tag{5}$$

In **Figure 4**, the similarity of $erf\,(\bar{a}\varepsilon)$ to $\tanh\left(\hat{a}\varepsilon\right)$ is illustrated. Three levels of strain coefficients, i.e., $\bar{a} = \{2,500;\ 500;\ 100\}$ are matched manually to $\hat{a} = \{3,000;\ 625;\ 125\}$ to produce similar curves.

THE WILDE—GARDONI—FUJINO MODEL

The Wilde-Gardoni-Fujino model (Wilde et al., 2000) is an extension of the Graesser-Cozzarelli model which takes into account the elastic behavior of the martensite which is activated after a particular strain level. The following equations describe it:

$$\begin{aligned}\dot{\sigma} &= E\left[\dot{\varepsilon} - |\dot{\varepsilon}|\left(\frac{\sigma-\beta}{Y}\right)^n\right] u_I(\varepsilon) + E_m\dot{\varepsilon}\,u_{II}(\varepsilon) \\ &\quad + \left(3\alpha_1\dot{\varepsilon}\varepsilon^2 + 2\alpha_2\,\mathrm{sgn}(\varepsilon)\,\dot{\varepsilon}\varepsilon + \alpha_3\dot{\varepsilon}\right) u_{III}(\varepsilon), \qquad (6)\\ \beta &= E\alpha\left[\varepsilon_{in} + f_T|\varepsilon|^c erf\,(\bar{a}\varepsilon)\,u\,(-\varepsilon\dot{\varepsilon})\right], \qquad (7)\end{aligned}$$

where the functions $u_I(\varepsilon)$, $u_{II}(\varepsilon)$, and $u_{III}(\varepsilon)$ are given by:

$$u_I(\varepsilon) = 1 - u_{II}(\varepsilon) - u_{III}(\varepsilon), \tag{8}$$

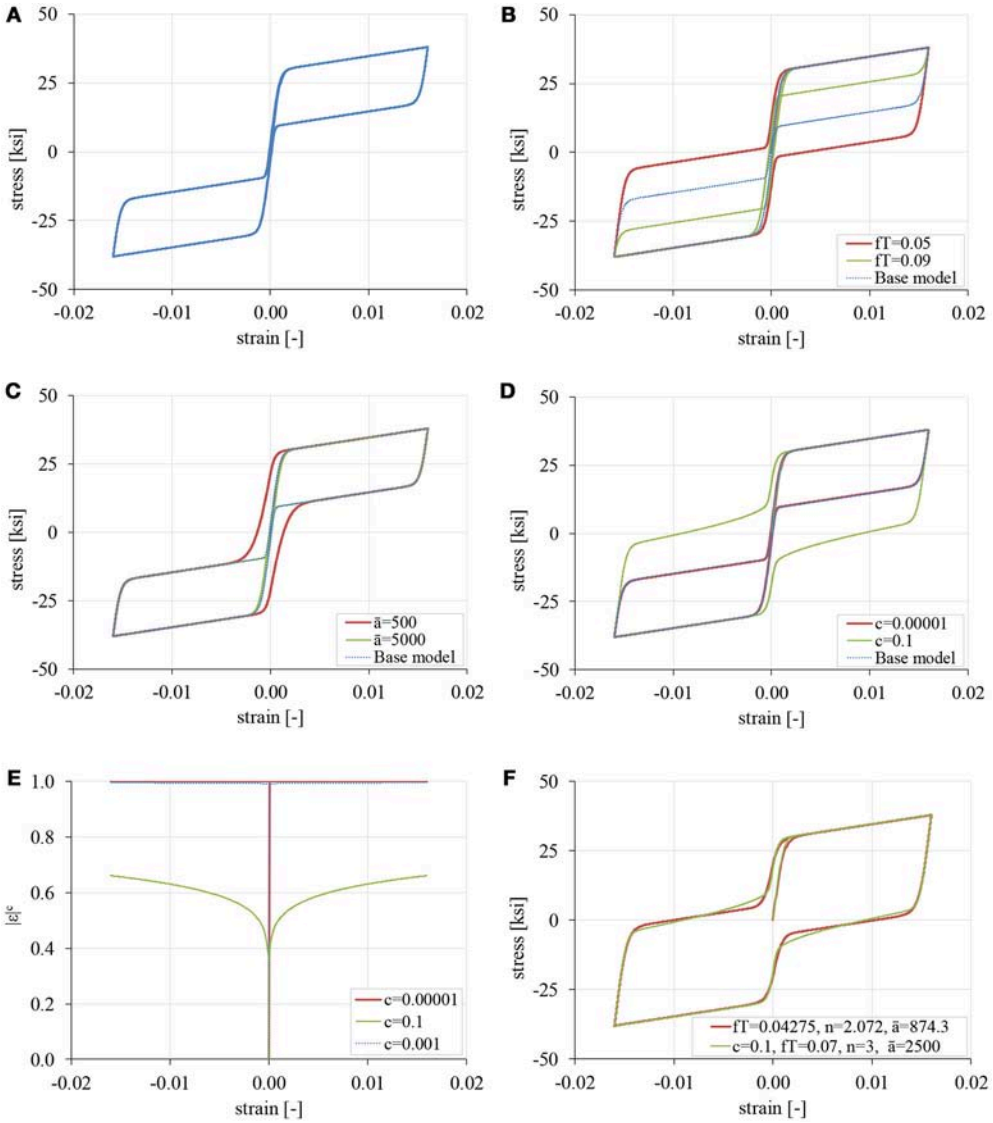

FIGURE 3 | Superelasticity ($f_T > 0$) with the Graesser-Cozzarelli model, **(A)** base model with $E = 28{,}500$ ksi, $Y = 30$ ksi, $\alpha = 0.0197$, $n = 3$, $f_T = 0.07$, $\bar{a} = 2{,}500$, $c = 0.001$ **(B)** variation in f_T **(C)** variation in $\bar{a}$ **(D)** variation in c, **(E)** value of $|\varepsilon|^c$ for various values of c, **(F)** curve-fit of the response obtained with c = 0.1 by altering f_T, n, and $\bar{a}$ only (c = 0).

$$u_{II}(\varepsilon) = \begin{cases} 1, & |\varepsilon| \geq \varepsilon_m \\ 0, & \text{otherwise} \end{cases}, \tag{9}$$

$$u_{III}(\varepsilon) = \begin{cases} 1, & \dot{\varepsilon}\varepsilon > 0 \text{ and } \varepsilon_1 < |\varepsilon| < \varepsilon_m \\ 0, & \text{otherwise} \end{cases}, \tag{10}$$

In this model, the response is divided into separate regions which are activated or deactivated by the flags described by Equations (8)–(10). The strain ε_m defines the point at which the transformation from austenite to martensite is completed. Beyond this strain, the response is linear elastic with modulus equal to E_m, due to the term $E_m \dot{\varepsilon} u_{II}(\varepsilon)$ in Equation (6). A smooth transition is achieved during loading only, due to the term activated by $u_{III}(\varepsilon)$.

Although the model is capable of simulating the martensitic phase of the SMA, its usage is cumbersome. For instance, the coefficients a_1, a_2, and a_3 do not have physical representation and plausible value ranges are not easy to establish. As is the case with the Graesser-Cozzarelli model, the term $(\sigma - \beta)$ may be negative, which is problematic when n takes real rather than integer values. Smooth transition between austenitic and martensitic phases can be realized with simpler and more elegant relations, as illustrated in the proposed model described later on.

THE ZHANG—ZHU MODEL

The Zhang-Zhu model (Zhang and Zhu, 2007) is a modification of the Wilde-Gardoni-Fujino model which aims to enhance the

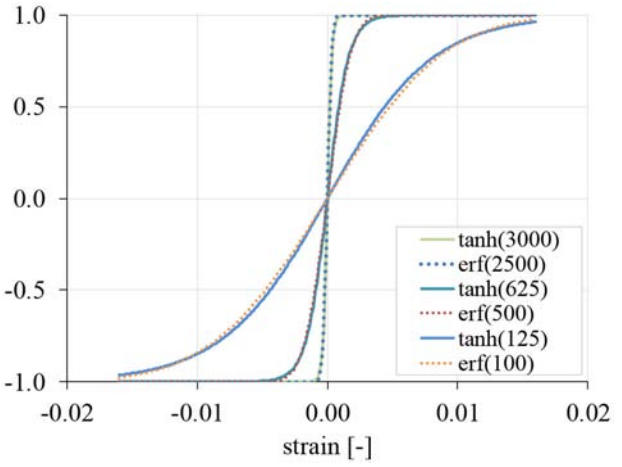

FIGURE 4 | Comparison of the error and hyperbolic tangent functions.

stability of numerical simulation and speed up the computation time. The following equations describe it:

$$\dot{\sigma} = E\left[\dot{\varepsilon} - K(\varepsilon)\,|\dot{\varepsilon}|\,\mathrm{sgn}(\sigma-\beta)\left(\frac{|\sigma-\beta|}{Y}\right)^{n}\right]u_I(\varepsilon) + E_m\dot{\varepsilon}\,u_{II}(\varepsilon) + \left(E_y\frac{\varepsilon_m-\varepsilon}{\varepsilon_m-\varepsilon_1} + E_m\frac{\varepsilon-\varepsilon_1}{\varepsilon_m-\varepsilon_1}\right)\dot{\varepsilon}\,u_{III}(\varepsilon), \quad (11)$$

$$\beta = E\alpha\left[\varepsilon_{in} + f_T u(-\varepsilon\dot{\varepsilon})\,sgn(\varepsilon)\,g\left(\bar{a}\varepsilon_{in} + sgn(\varepsilon)\,b\right)\right], \quad (12)$$

where the functions $u_I(\varepsilon)$, $u_{II}(\varepsilon)$, $u_{III}(\varepsilon)$, $K(\varepsilon)$, $g(t)$ are given by:

$$u_I(\varepsilon) = 1 - u_{II}(\varepsilon) - u_{III}(\varepsilon), \quad (13)$$

$$u_{II}(\varepsilon) = \begin{cases} 1, & \dot{\varepsilon}\varepsilon > 0 \text{ and } |\varepsilon| \geq \varepsilon_m \\ 0, & \text{otherwise} \end{cases}, \quad (14)$$

$$u_{III}(\varepsilon) = \begin{cases} 1, & \dot{\varepsilon}\varepsilon > 0 \text{ and } \varepsilon_1 < |\varepsilon| < \varepsilon_m \\ 0, & \text{otherwise} \end{cases}, \quad (15)$$

$$K(\varepsilon) = \begin{cases} 1, & \dot{\varepsilon}\varepsilon > 0 \\ u(\varepsilon_{in}\varepsilon), & \text{otherwise} \end{cases}, \quad (16)$$

$$g(t) = 1 - e^{-t^2}, \quad (17)$$

and the signum function is defined as

$$\mathrm{sgn}(x) = \begin{cases} 1, & x > 0 \\ 0, & x = 0 \\ -1, & x < 0 \end{cases}. \quad (18)$$

Note that parameters α, E, and n can take different values for loading and loading phases. Thus, the model contains up to fourteen parameters. The main improvements with respect to the Wilde-Gardoni-Fujino are the following:

- The problem with the potentially negative term $(\sigma - \beta)$ has been addressed.
- The coefficients a_1, a_2, and a_3 have been replaced.
- The error function has been replaced.

The following, however, can be listed as disadvantages of the model:

- The number of parameters is high.
- Plausible value ranges are not provided for the parameters not having a physical representation.
- The response is still divided into many phases controlled with on/off flags.

PROPOSED MODEL

Based on the observations above, a simple rate-independent uniaxial phenomenological model is proposed herein which is described by the following terms:

$$\dot{\sigma} = (1 - s(\varepsilon))\,E\left[\dot{\varepsilon} - |\dot{\varepsilon}|\,\mathrm{sgn}(\sigma-\beta)\left(\frac{|\sigma-\beta|}{Y}\right)^{n}\right] + s(\varepsilon)\,E_m\dot{\varepsilon}, \quad (19)$$

$$\beta = E\alpha\left[\varepsilon - \sigma/E + f_T \tanh(\bar{a}\varepsilon)\,u(-\varepsilon\dot{\varepsilon})\right], \quad (20)$$

$$s(\varepsilon) = \frac{\tanh(c(|\varepsilon| - \varepsilon_t)) + 1}{2}, \quad (21)$$

where, $s(\varepsilon)$ is a smooth logistic function which yields 0 for $|\varepsilon| \ll \varepsilon_t$ and 1 for $|\varepsilon| \gg \varepsilon_t$. Note that $s(\varepsilon_t) = 0.5$, i.e., at this level of strain the weights of the Graesser-Cozzarelli term and the elastic martensitic term in Equation (19) are equal. The coefficient c controls the abruptness of transition. For high values of c, the transition is abrupt, as evidenced by **Figure 5A**.

In total, the model contains only nine parameters (E, Y, α, n, f_T, $\bar{a}$, E_m, ε_t, c) as opposed to the thirteen parameters of the Wilde-Gardoni-Fujino model (E, E_m, Y, α, n, f_T, c, $\bar{a}$, ε_m, ε_1, α_1, α_2, α_3) and the eleven to fourteen parameters of the Zhang-Zhu model (E_l, E_u, E_m, Y, E_Y, α_l, α_u, n_l, n_u, f_T, $\bar{a}$, ε_m, ε_1, b). A brief description of the model parameters and their effect on the overall response, based on the evidence examined earlier, is summarized in **Table 1**. The last three parameters refer to the martensitic phase.

TABLE 1 | Brief description of proposed model parameters and their effect on the overall response.

Parameter	Description/Effect
E	Initial modulus during the austenitic phase
Y	"Yield" stress
α	Control of post-elastic stiffness
n	Control of abruptness of transition between initial elastic and post-elastic phases
f_T	Control between twinning hysteresis and superelasticity
$\bar{a}$	Smoothness around the origin during cyclic loading
E_m	Modulus during the fully martensitic phase
ε_t	Strain of middle point of transition between Graesser-Cozzarelli and martensitic terms
c	Control of abruptness of transition between Graesser-Cozzarelli and martensitic terms

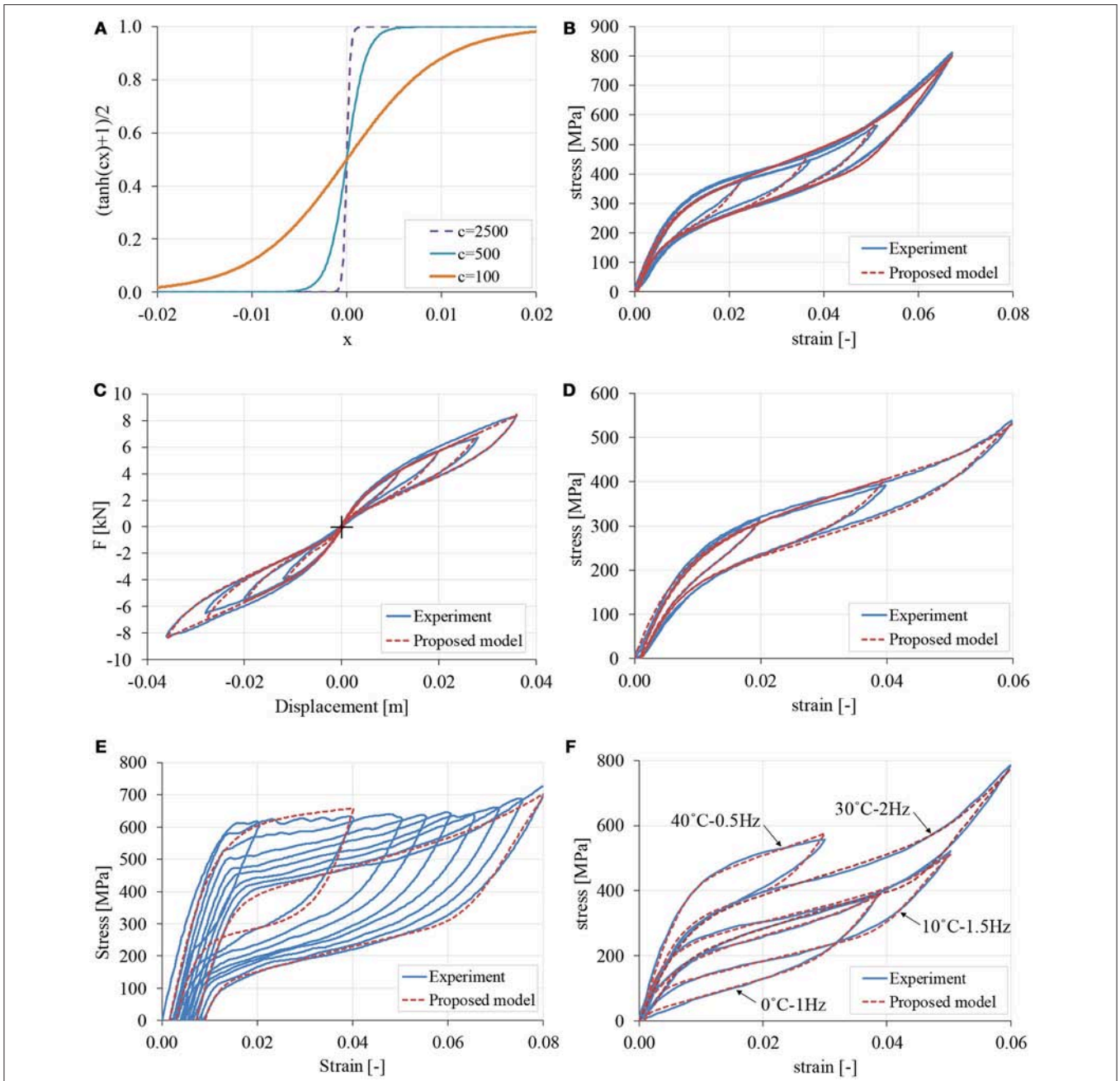

FIGURE 5 | (A) Logistic function $f(x) = (\tanh(cx) + 1)/2$ for various values of coefficient c, and curve fit of the proposed model with experimental data obtained from **(B)** Zhang and Zhu (2007), **(C)** Zhuang et al. (2016), **(D)** Ozbulut et al. (2010), **(E)** Auricchio et al. (2003), **(F)** Ozbulut and Hurlebaus (2010).

Despite its simplicity, the proposed model can accurately capture all the pertinent characteristics of the response curve. System identification based on metaheuristics produces excellent fit with experimental data obtained from the literature, as will be demonstrated. The optimum (best) parameter values were evaluated by Differential Evolution, a powerful metaheuristic algorithm (Storn and Price, 1997). The DE/rand/1/bin configuration was used with population size $P = 50$, $F = 0.5$ and $C_r = 0.9$. Ten independent runs were conducted with different random seeds. Each run was terminated after 20000 function evaluations. The sum of squares of the difference between the measured and the predicted time history of stress is used as the objective function to be minimized. Cast in discrete form, this function can be written as

$$OF(\mathbf{p}) = \sum \left(\sigma(t_i) - \widehat{\sigma}(t_i|\mathbf{p})\right)^2, \tag{22}$$

where $\mathbf{p}$ is the parameter vector.

TABLE 2 | Statistical analysis of identified parameters of the proposed model for the experimental data obtained from Zhang and Zhu (2007) shown in **Figure 5B**.

Parameter	Lower bound	Upper bound	Best	Min	Max	Average	Standard Deviation	Coefficient of variation
E [MPa]	10,000	60,000	46,823.455	34,519.290	46,823.455	42,422.809	3,534.132	0.083
Y [MPa]	200	500	314.844	311.916	317.408	315.654	1.929	0.006
α	0	1	0.148	0.148	0.218	0.168	0.020	0.118
n	0.5	3	1.327	1.327	2.926	1.726	0.452	0.262
f_T	0.1	1	0.064	0.061	0.066	0.064	0.001	0.021
$\bar{a}$	1	1,000	194.224	194.224	225.739	202.093	8.711	0.043
E_m [MPa]	10,000	60,000	19,291.590	18,991.328	19,906.820	19,230.288	263.735	0.014
ε_t	0.01	0.08	0.052	0.050	0.052	0.051	0.000	0.006
c	1	1,000	99.135	96.101	107.987	98.857	3.439	0.035

TABLE 3 | Statistical analysis of identified parameters of the proposed model for the experimental data obtained from Zhuang et al. (2016) shown in **Figure 5C**.

Parameter	Lower bound	Upper bound	Best	Min	Max	Average	Standard deviation	Coefficient of variation
E [kN/m]	100	2,000	584.159	584.159	587.764	586.236	1.530	0.003
Y [kN]	1	10	4.255	4.253	4.260	4.256	0.002	0.000
α	0	1	0.395	0.390	0.395	0.392	0.002	0.006
n	0.5	3	1.399	1.382	1.399	1.389	0.007	0.005
f_T	0.1	1	0.017	0.017	0.017	0.017	0.000	0.004
$\bar{a}$	1	1,000	665.339	663.530	671.228	666.635	3.191	0.005

In **Figure 5B** the case of tensional tests on cold-drawn nitinol wires with a diameter of 0.58 mm obtained from Zhang and Zhu (2007) is shown. A statistical analysis of the identified parameters is summarized in **Table 2**. It is noted that the initial side constraints are quite relaxed, yet the identification process was found to be straightforward. It is also observed that some parameters are very sensitive to the considered experimental data set, i.e., parameters ε_t, Y, E_m, f_T, and c, while the others are not so. In general, however, all runs were obviously guided to the same optimum region of the search space, which is a strong indication of a well-behaved model with uniquely defined parameters, each one with a distinct role in the response curve. If needed, the insensitive parameters can be accurately identified with other experiments which focus on the pertinent characteristics of the response curve, e.g., parameter E with a linear elastic experiment with small strains. Improved results can also be obtained by gradual tightening of the side constraints based on trial analyses, as in Charalampakis and Koumousis (2008a), but this lies beyond the scope of the present study and will be pursued in future research.

Figure 5C shows excellent fit in the case of the single SMA helical spring with hook-like ends obtained from Zhuang et al. (2016). Being phenomenological, the proposed model can be easily used with force-displacement curves instead of stress-strain curves, with the necessary semantic changes concerning parameters E and Y. By inspection, it is clear that the experimental data does not include any stress-induced martensitic phase. Therefore, the pertinent parameters (E_m, ε_t, c) cannot be identified. This fact is manifested clearly in the results of the identification, where the metaheuristic algorithm selects arbitrary values for these parameters in order to disable them (i.e., $\varepsilon_t > 0.037$, any E_m, and large c). In this specific case, we can use $s(\varepsilon) = 0$ instead of Equation (21), or repeat the experiment with a larger displacement to record martensitic phase data. A statistical analysis of the identified parameters is summarized in **Table 3**, where small coefficients of variation are observed.

Figure 5D shows an excellent fit for the case of NiTi SMA wires with a diameter of 1 mm. The data refers to the response of different strain levels at a frequency of 1 Hz and has been obtained from Ozbulut et al. (2010). A value of 0.005 has been subtracted from all strains to compensate for the lack of complete tautness. The wires have been trained with a set of 10 load cycles with a strain amplitude of 6% at 0.04 Hz. A statistical analysis of the identified parameters is summarized in **Table 4**, where, again, small coefficients of variation are observed.

In **Figure 5E**, the experimental stress-strain response of an untrained commercial Ni-Ti wire with a diameter of 2.01 mm is shown. The loading cycles are characterized by an increasing value of the maximum elongation that varies from 2 to 8%. The data has been obtained from Auricchio et al. (2003), and an excellent fit can be observed for the second and last cycle, indicatively. Apparently, the values differ significantly, which is the result of the progressive decrement of the initial and final stress thresholds of the phase transformations during the training of a specimen (Auricchio et al., 2003). In similar fashion, in **Figure 5F** very good fit is observed for the experimental data obtained from Ozbulut and Hurlebaus (2010). The data refer to NiTi wires with a diameter of 1.5 mm which are subjected to tensile tests with various temperatures and strain rates. The identified model parameters for the latter cases are summarized in **Table 5**. By appropriate interpolation of model parameters, it may be possible that aspects which are not covered presently,

TABLE 4 | Statistical analysis of identified parameters of the proposed model for the experimental data obtained from Ozbulut et al. (2010) shown in **Figure 5D**.

Parameter	Lower bound	Upper bound	Best	Min	Max	Average	Standard deviation	Coefficient of variation
E [MPa]	10,000	60,000	39,286.352	32,783.866	40,068.672	36,609.716	2,971.842	0.081
Y [MPa]	200	500	284.271	282.443	290.882	285.069	2.691	0.009
α	0	1	0.130	0.124	0.165	0.144	0.015	0.108
n	0.5	3	1.112	1.018	1.678	1.315	0.254	0.193
f_T	0.1	1	0.081	0.078	0.085	0.080	0.002	0.028
$\bar{a}$	1	1,000	135.944	130.274	150.642	140.804	7.059	0.050
E_m [MPa]	10,000	60,000	12,084.968	10,988.091	12,690.244	12,122.933	508.070	0.042
ε_t	0.01	0.08	0.054	0.054	0.055	0.055	0.000	0.007
c	1	1,000	181.706	172.829	217.115	190.377	12.437	0.065

TABLE 5 | Identified parameters of the proposed model for the experimental data shown in **Figures 5E,F**.

Parameter	Auricchio et al. (2003) **2nd cycle**	Auricchio et al. (2003) **last cycle**	Ozbulut and Hurlebaus (2010) **0°C−1 Hz**	Ozbulut and Hurlebaus (2010) **10°C−1.5 Hz**	Ozbulut and Hurlebaus (2010) **30°C−2 Hz**	Ozbulut and Hurlebaus (2010) **40°C−0.5 Hz**
E [MPa]	72,478.332	56,469.931	38,944.849	60,000.000	40,754.313	60,000.000
Y [MPa]	619.072	385.812	204.114	243.092	338.771	444.085
α	0.023	0.075	0.164	0.088	0.174	0.120
n	1.682	2.249	1.076	1.141	2.083	2.550
f_T	0.530	0.114	0.031	0.061	0.071	0.100
$\bar{a}$	179.385	254.366	1,000.000	382.420	178.101	208.790
E_m [MPa]	–	14,899.926	14,932.520	16,418.358	22,441.737	10,000.000
ε_t	–	0.059	0.036	0.042	0.048	0.032
c	–	58.753	150.688	144.455	142.488	108.515

TABLE 6 | Statistical analysis of identification results for the Wilde-Gardoni-Fujino model with data obtained from Zhang and Zhu (2007).

Parameter	Lower bound	Upper bound	Best	Min	Max	Average	Standard deviation	Coefficient of variation
E [MPa]	10,000	100,000	35,995.179	35,048.908	53,552.683	44,130.931	7,752.798	0.176
E_m [MPa]	10,000	100,000	16,072.799	10,000.000	16,072.799	11,360.786	2,483.071	0.219
Y [MPa]	100	800	359.596	172.570	417.298	308.840	89.187	0.289
ε_m	0.01	0.08	0.064	0.010	0.065	0.037	0.020	0.544
ε_1	0.01	0.08	0.043	0.010	0.078	0.058	0.023	0.393
f_T	0.1	1	0.180	0.103	0.997	0.558	0.341	0.612
α	0.01	1	0.139	0.033	0.152	0.081	0.046	0.565
n	1	2	1.939	1.160	2.000	1.737	0.302	0.174
$\bar{a}$	1	5,000	283.772	271.270	4,982.904	3,102.826	2,097.170	0.676
c	0.0001	1	0.143	0.102	0.368	0.255	0.096	0.376
α_1	0	100,000	26,367.269	825.089	99,018.466	36,926.151	33,488.155	0.907
α_2	0	100,000	27,821.814	0.000	94,387.750	37,703.847	34,095.015	0.904
α_3	0	100,000	9,386.547	0.000	97,085.336	28,741.415	35,912.720	1.250
Objective function			5.211E+05	5.211E+05	1.055E+07	4.834E+06	3.825E+06	0.791

such as strain-rate and temperature dependency, or training process, are taken into account. This, however, lies beyond the scope of the present study and will be pursued in future research.

In order to demonstrate the advantages of the proposed model, the same identification procedure is applied to the Wilde-Gardoni-Fujino model with data obtained from Zhang and Zhu (2007). The results are summarized in **Table 6**, where great variability in parameter values and quality of solutions can be observed.

CONCLUSIONS

In this paper, three specific uniaxial phenomenological models commonly used for the description of a Shape Memory Alloy (SMA) behavior were examined in detail, and a new simple rate-independent model was proposed which addresses all issues in a unified manner. From the presented analysis and the numerical results, the following main conclusions can be drawn:

a) In total, the proposed model contains only nine parameters as opposed to the thirteen parameters of the Wilde-Gardoni-Fujino model and the eleven to fourteen parameters of the Zhang-Zhu model.
b) Despite its simplicity, the proposed model can accurately capture all the pertinent characteristics of the response curve.
c) For the proposed model, system identification based on metaheuristics produced excellent fit with experimental data obtained from the literature.
d) Apart from the best result, all runs produced quality solutions in the same region of the design space, and the identified parameters had small coefficients of variation. This is a strong indication of a well-behaved model, with uniquely defined parameters, each one with a distinct role in the response curve.
e) On the contrast, the application of the same identification process to the Wilde-Gardoni-Fujino model yielded significantly inferior results, i.e., great variability in parameter values and quality of solutions.
f) A significant advantage of the proposed uniaxial model is that it can be incorporated within a Finite Element code such as OpenSees straightforwardly.

AUTHOR CONTRIBUTIONS

AC had the research idea, drafted the article, and contributed to the derivation of the numerical examples. GT contributed to the conception of the work and interpretation of the results. Both authors contributed to the writing of the manuscript.

REFERENCES

Andrawes, B., and DesRoches, R. (2007). Effect of hysteretic properties of superelastic shape memory alloys on the seismic performance of structures. *Struct. Control Heal. Monit.* 14, 301–320. doi: 10.1002/stc.159

Andrawes, B., Shin, M., and Wierschem, N. (2010). Active confinement of reinforced concrete bridge columns using shape memory alloys. *J. Bridg. Eng.* 15, 81–89. doi: 10.1061/(ASCE)BE.1943-5592.0000038

Asgarian, B., and Moradi, S. (2011). Seismic response of steel braced frames with shape memory alloy braces. *J. Constr. Steel Res.* 67, 65–74. doi: 10.1016/j.jcsr.2010.06.006

Auricchio, F., Fugazza, D., and Desroches, R. (2006). Earthquake performance of steel frames with nitinol braces. *J. Earthq. Eng.* 10, 45–66. doi: 10.1080/13632460609350628

Auricchio, F., Marfia, S., and Sacco, E. (2003). Modelling of SMA materials: training and two way memory effects. *Comput. Struct.* 81, 2301–2317. doi: 10.1016/S0045-7949(03)00319-5

Ben Mekki, O., and Auricchio, F. (2011). Performance evaluation of shape-memory-alloy superelastic behavior to control a stay cable in cable-stayed bridges. *Int. J. Non. Linear. Mech.* 46, 470–477. doi: 10.1016/j.ijnonlinmec.2010.12.002

Bouc, R. (1967). "Forced vibrations of a mechanical system with hysteresis," in *Proceedings of the 4th Conference on Non-Linear Oscillations* (Prague).

Charalampakis, A. E. (2015). The response and dissipated energy of Bouc–Wen hysteretic model revisited. *Arch. Appl. Mech.* 85, 1209–1223. doi: 10.1007/s00419-014-0937-8

Charalampakis, A. E., and Koumousis, V. K. (2008a). Identification of Bouc–Wen hysteretic systems by a hybrid evolutionary algorithm. *J. Sound Vib.* 314, 571–585. doi: 10.1016/j.jsv.2008.01.018

Charalampakis, A. E., and Koumousis, V. K. (2008b). On the response and dissipated energy of Bouc–Wen hysteretic model. *J. Sound Vib.* 309, 887–895. doi: 10.1016/j.jsv.2007.07.080

Cisse, C., Zaki, W., and Ben Zineb, T. (2016). A review of constitutive models and modeling techniques for shape memory alloys. *Int. J. Plast.* 76, 244–284. doi: 10.1016/j.ijplas.2015.08.006

Clark, P. W., Aiken, I. D., Kelly, J. M., Higashino, M., and Krumme, R. (1995). "Experimental and analytical studies of shape-memory alloy dampers for structural control," in *Proceedings Volume 2445, Smart Structures and Materials 1995: Passive Damping* (San Diego, CA), 241–251. doi: 10.1117/12.208891

Deng, Z., Li, Q., and Sun, H. (2006). Behavior of concrete beam with embedded shape memory alloy wires. *Eng. Struct.* 28, 1691–1697. doi: 10.1016/j.engstruct.2006.03.002

DesRoches, R., and Delemont, M. (2002). Seismic retrofit of simply supported bridges using shape memory alloys. *Eng. Struct.* 24, 325–332. doi: 10.1016/S0141-0296(01)00098-0

Fang, C., Yam, M. C. H., Lam, A. C. C., and Xie, L. (2014). Cyclic performance of extended end-plate connections equipped with shape memory alloy bolts. *J. Constr. Steel Res.* 94, 122–136. doi: 10.1016/j.jcsr.2013.11.008

Fujino, Y., Warnitchai, P., and Pacheco, B. M. (1993). Active stiffness control of cable vibration. *J. Appl. Mech.* 60:948. doi: 10.1115/1.2901006

Graesser, E. J., and Cozzarelli, F. A. (1991). Shape-memory alloys as new materials for aseismic isolation. *J. Eng. Mech.* 117, 2590–2608. doi: 10.1061/(ASCE)0733-9399(1991)117:11(2590)

Gur, S., and Mishra, S. K. (2013). Multi-objective stochastic-structural-optimization of shape-memory-alloy assisted pure-friction bearing for isolating building against random earthquakes. *Soil Dyn. Earthq. Eng.* 54, 1–16. doi: 10.1016/j.soildyn.2013.07.013

Krumme, R., Hayes, J., and Sweeney, S. (1995). "Structural damping with shape-memory alloys: one class of device," in *Proceedings Volume 2445, Smart Structures and Materials 1995: Passive Damping* (San Diego, CA), 225–240. doi: 10.1117/12.208890

Leon, R. T., DesRoches, R., Ocel, J., and Hess, G. (2001). "Innovative beam column connections using shape memory alloys," in *Proceedings Volume 4330, Smart Structures and Materials 2001: Smart Systems for Bridges, Structures, and Highways. Event: SPIE's 8th Annual International Symposium on Smart Structures and Materials* (Newport Beach, CA), 227–237. doi: 10.1117/12.434122

Li, H., Liu, Z. Q., and Ou, J. P. (2006). Behavior of a simple concrete beam driven by shape memory alloy wires. *Smart Mater. Struct.* 15, 1039–1046. doi: 10.1088/0964-1726/15/4/017

Li, H., Liu, Z. Q., and Ou, J. P. (2008). Experimental study of a simple reinforced concrete beam temporarily strengthened by SMA wires followed by permanent strengthening with CFRP plates. *Eng. Struct.* 30, 716–723. doi: 10.1016/j.engstruct.2007.05.020

Ma, H., and Cho, C. (2008). Feasibility study on a superelastic SMA damper with re-centring capability. *Mater. Sci. Eng. A* 473, 290–296. doi: 10.1016/j.msea.2007.04.073

Mazzoni, S., McKenna, F., Scott, M. H., and Fenves, G. L. (2006). *OpenSees Command Language Manual*. Available online at: http://opensees.berkeley.edu/OpenSees/manuals/usermanual/OpenSeesCommandLanguageManualJune2006.pdf (Accessed July 18, 2018).

Miller, D. J., Fahnestock, L. A., and Eatherton, M. R. (2012). Development and experimental validation of a nickel–titanium shape memory alloy self-centering buckling-restrained brace. *Eng. Struct.* 40, 288–298. doi: 10.1016/j.engstruct.2012.02.037

Muntasir Billah, A. H. M., and Shahria Alam, M. (2012). Seismic performance of concrete columns reinforced with hybrid shape memory alloy (SMA) and fiber reinforced polymer (FRP) bars. *Constr. Build. Mater.* 28, 730–742. doi: 10.1016/j.conbuildmat.2011.10.020

Olson, G. B., and Cohen, M. (1982). Stress-assisted isothermal martensitic transformation: application to TRIP steels. *Metall. Trans. A* 13, 1907–1914. doi: 10.1007/BF02645934

Ozbulut, O. E., and Hurlebaus, S. (2010). Evaluation of the performance of a sliding-type base isolation system with a NiTi shape memory alloy device considering temperature effects. *Eng. Struct.* 32, 238–249. doi: 10.1016/j.engstruct.2009.09.010

Ozbulut, O. E., Roschke, P. N., Lin, P. Y., and Loh, C. H. (2010). GA-based optimum design of a shape memory alloy device for seismic response mitigation. *Smart Mater. Struct.* 19:065004. doi: 10.1088/0964-1726/19/6/065004

Ozdemir, H. (1973). *Nonlinear Transient Dynamic Analysis of Yielding Structure*. Available online at: https://ci.nii.ac.jp/naid/10007658537/ (Accessed April 29, 2018).

Speicher, M. S., DesRoches, R., and Leon, R. T. (2011). Experimental results of a NiTi shape memory alloy (SMA)-based recentering beam-column connection. *Eng. Struct.* 33, 2448–2457. doi: 10.1016/j.engstruct.2011.04.018

Storn, R. M., and Price, K. V. (1997). Differential evolution–a simple and efficient heuristic for global optimization over continuous spaces. *J. Glob. Optim.* 11, 341–359. doi: 10.1023/A:1008202821328

Torra, V., Auguet, C., Isalgue, A., Carreras, G., Terriault, P., and Lovey, F. C. (2013). Built in dampers for stayed cables in bridges via SMA. The SMARTeR-ESF project: a mesoscopic and macroscopic experimental analysis with numerical simulations. *Eng. Struct.* 49, 43–57. doi: 10.1016/j.engstruct.2012.11.011

Walter Yang, C. S., DesRoches, R., and Leon, R. T. (2010). Design and analysis of braced frames with shape memory alloy and energy-absorbing hybrid devices. *Eng. Struct.* 32, 498–507. doi: 10.1016/j.engstruct.2009.10.011

Wen, Y. K. (1976). Method for random vibration of hysteretic systems. *J. Eng. Mech. Div.* 102, 249–263.

Wilde, K., Gardoni, P., and Fujino, Y. (2000). Base isolation system with shape memory alloy device for elevated highway bridges. *Eng. Struct.* 22, 222–229. doi: 10.1016/S0141-0296(98)00097-2

Youssef, M. A., Alam, M. S., and Nehdi, M. (2008). Experimental investigation on the seismic behavior of beam-column joints reinforced with superelastic shape memory alloys. *J. Earthq. Eng.* 12, 1205–1222. doi: 10.1080/13632460802003082

Zafar, A., and Andrawes, B. (2013). Experimental flexural behavior of SMA-FRP reinforced concrete beam. *Front. Struct. Civ. Eng.* 7, 341–355. doi: 10.1007/s11709-013-0221-y

Zhang, Y., and Zhu, S. (2007). A shape memory alloy-based reusable hysteretic damper for seismic hazard mitigation. *Smart Mater. Struct.* 16, 1603–1613. doi: 10.1088/0964-1726/16/5/014

Zhu, S., and Zhang, Y. (2008). "Performance based seismic design of steel braced frame system with self-centering friction damping brace," in *Structures Congress 2008* (Reston, VA: American Society of Civil Engineers), 1–13.

Zhuang, P., Xue, S., Nie, P., and Wang, W. (2016). Experimental and numerical study on hysteretic performance of SMA spring-friction bearings. *Earthq. Eng. Eng. Vib.* 15, 597–609. doi: 10.1007/s11803-016-0351-z

Conflict of Interest Statement: The authors declare that the research was conducted in the absence of any commercial or financial relationships that could be construed as a potential conflict of interest.

The handling editor declared a shared affiliation, though no other collaboration, with one of the authors AC at time of review.

frontiers in Built Environment

ORIGINAL RESEARCH
published: 12 September 2018
doi: 10.3389/fbuil.2018.00040

A Meshless Solution to the Vibration Problem of Cylindrical Shell Panels

Aristophanes J. Yiotis and John T. Katsikadelis*

School of Civil Engineering, National Technical University of Athens, Athens, Greece

The Meshless Analog Equation Method (MAEM) is a purely mesh-free method for solving partial differential equations (PDEs). In the present study, the method is applied to the dynamic analysis of cylindrical shell structures. Based on the principle of the analog equation, MAEM converts the three governing partial differential equations in terms of displacements into three uncoupled substitute equations, two of 2nd order (Poisson's) and one of 4th order (biharmonic), with fictitious sources. The fictitious sources are represented by series of Radial Basis Functions (RBFs) of multiquadric (MQ) type, and the substitute equations are integrated. The integration allows the representation of the displacements by new RBFs, which approximate the displacements accurately and also their derivatives involved in the governing equations. By inserting the approximate solution in the governing differential equations and taking into account the boundary and initial conditions and collocating at a predefined set of mesh-free nodal points, we obtain a system of ordinary differential equations of motion. The solution of the system gives the unknown time-dependent series coefficients and the solution to the original problem. Several shell panels are analyzed using the method, and the numerical results demonstrate its efficiency and accuracy.

Keywords: MAEM, Meshless Analog Equation Method, cylindrical shells, dynamic analysis, radial basis functions, partial differential equations

OPEN ACCESS

Edited by:
Vagelis Plevris, OsloMet—Oslo Metropolitan University, Norway

Reviewed by:
Andreas Kampitsis, Imperial College London, United Kingdom
Aristotelis E. Charalampakis, National Technical University of Athens, Greece

****Correspondence:***
Aristophanes J. Yiotis
fgiotis@otenet.gr

Specialty section:
This article was submitted to Computational Methods in Structural Engineering, a section of the journal Frontiers in Built Environment

Received: *13 March 2018*
Accepted: *04 July 2018*
Published: *12 September 2018*

Citation:
Yiotis AJ and Katsikadelis JT (2018) A Meshless Solution to the Vibration Problem of Cylindrical Shell Panels. Front. Built Environ. 4:40. doi: 10.3389/fbuil.2018.00040

INTRODUCTION

Thin shell structures have an outstanding efficiency in fully utilizing the structural material and have been extensively used in many engineering applications including aircraft structures, pressure vessels, and others. Static and dynamic analysis is essential for the analysis and design of shell structures. Various numerical methods, such as the Finite Difference Method (FDM) and especially the Finite Element Method (FEM) have been used (Lee and Han, 2001) for the dynamic analysis of linear elastic thin shells characterized by complex geometry, loading and boundary conditions. Both methods have been employed successfully for the solution of a variety of static and dynamic shell problems. The Boundary Element Method (BEM) is an efficient alternative to the domain type methods, especially for thin elastic shallow shells (Beskos, 1991), or combined with the AEM for cylindrical shells (Yiotis and Katsikadelis, 2000).

Such methods require the generation of a mesh which can be an incredibly tedious and time-consuming process, while their convergence rate is of 2nd order (Cheng et al., 2003). On the other hand, Meshless Methods (MMs) present an attractive alternative to FEM or BEM, especially for shell structures that are complex regarding both the governing equations and the geometry representation. Comprehensive descriptions of different MMs are presented by Liu (2002); Liu and Gu (2005) and in a review paper by Nguyen et al. (2008).

There are several papers on dynamic analysis of shells using MM. Homogeneous shells are studied using various versions of MM in Liu et al. (2006), Ferreira et al. (2006b), and Dinis et al. (2011). Functionally graded (FG) cylindrical thin shells have also been treated by this method (Ferreira et al., 2006a; Zhao et al., 2009; Roque et al., 2010), as well as thick cylindrical shells (Pilafkan et al., 2013) have been analyzed by this method.

The mesh-free multiquadric radial basis functions (MQ-RBFs) method presented in Kansa (2005) has attracted the interest of researchers, due to its exponential convergence and its easiness of implementation. The significant drawbacks of the method are the ill-conditioning of the coefficient matrix and the inability to accurately approximate the derivatives of the sought solution which renders the method inappropriate for a strong formulation of the problem. These drawbacks of the standard MQ-RBF method, are overcome by a new RBF method presented recently by Katsikadelis (2006, 2008a,b, 2009) and Yiotis and Katsikadelis (2008, 2013, 2015a,b). Another critical issue is the implementation of multiple boundary conditions for equations of order higher than 2nd. In this investigation, the δ-technique is employed (Jang et al., 1989) for the 4th order equation. The problem of multiple boundary conditions is not present when the shell is modeled as a 3D body (Katsikadelis and Platanidi, 2007).

In this paper, the MAEM is extended to the dynamic problem of cylindrical shell panels as described by section MAEM Solution. A first approach to this problem was attempted in a previous work (Yiotis and Katsikadelis, 2015b), where some preliminary results only for the eigenfrequency analysis were presented. In section Problem Statement, the statement of the problem is presented, while several example problems are worked out in section Numerical Examples, which illustrate the applicability of the method and demonstrate its efficiency and section Conclusions contains certain conclusions drawn from this investigation.

PROBLEM STATEMENT

We consider a thin cylindrical shell with parametric lines x ($s = const.$) and s ($x = const.$) which are assumed to be lines of curvature, as well; x is measured along the x lines of the shell and s along the s lines, while z is measured along the normal to the middle surface of the shell, as shown in **Figure 1**. R is the radius of curvature and h is the thickness.

In this investigation we use the Flügge equations for the thin shell theory, based on the following assumptions (Love, 1944):

1. The thickness of the shell is small compared with (i) its other dimensions; (ii) the smallest radius of the shell curvature.
2. Strains and displacements are sufficiently small and as a result quantities of 2nd and higher order of magnitude in the strain-displacement relations can be neglected.
3. The normal transverse stress is relatively small, compared with the other normal stresses, and can be neglected.
4. Lines normal to the undeformed middle surface remain straight and normal to the deformed middle surface.

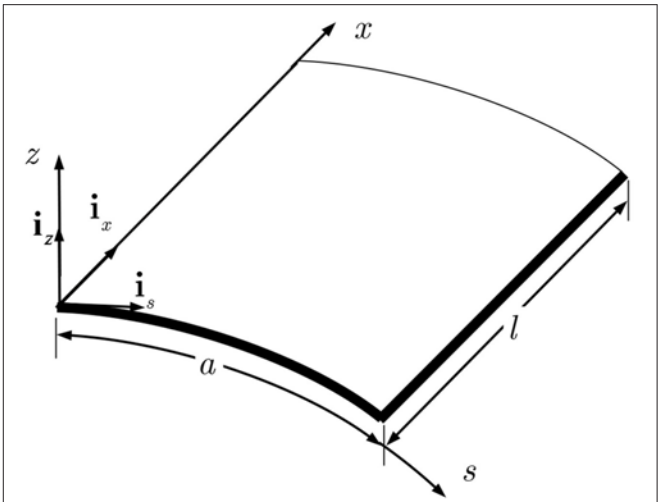

FIGURE 1 | Cylindrical shell.

The first assumption defines the meaning of "thin shells," whereas the second one implies that all calculations refer to the original undeformed configuration and subsequently leads to linear differential equations. Further, the assumption $z/R << 1$ is adopted in deriving the stress resultants in integrating the stresses through the thickness of the shell. The 4th assumption is known as Kirchhoff's hypothesis yielding

$$\gamma_{xz} = 0, \tag{1a}$$

$$\gamma_{sz} = 0, \tag{1b}$$

$$e_z = 0, \tag{1c}$$

which implies $\sigma_{xz} = \sigma_{sz} = 0$ (Leissa, 1973).

The equations of motion for the case of the thin cylindrical shell can be derived using Hamilton's principle as follows

$$\delta\left[\int_{t_0}^{t_1}(\Pi - K)dt - \int_{t_0}^{t_1} W_{nc}dt\right] = 0, \tag{2}$$

where Π is the total potential energy given by

$$\Pi = U_0 - W_1 - W_2, \tag{3}$$

in which U_0, is the strain energy

$$U_0 = \frac{1}{2}\int_{\nu}(\sigma_x e_x + \sigma_s e_s + \sigma_{xs}\gamma_{xs} + \sigma_{xz}\gamma_{xz} + \sigma_{sz}\gamma_{sz})dxdsdz, \tag{4}$$

and W_1, W_2 the works produced by the loading and the boundary forces, i.e.,

$$W_1 = \int_S (q_x u + q_s v + q_z w)dxds, \tag{5}$$

$$W_2 = \int_s (\bar{N}_x u + \bar{N}_{xs} v + \bar{Q}_x w + \bar{M}_x\theta_x + \bar{M}_{xs}\theta_s)ds + \int_x (\bar{N}_{sx} u + \bar{N}_s v + \bar{Q}_s w + \bar{M}_{sx}\theta_x + \bar{M}_s\theta_s)dx, \tag{6}$$

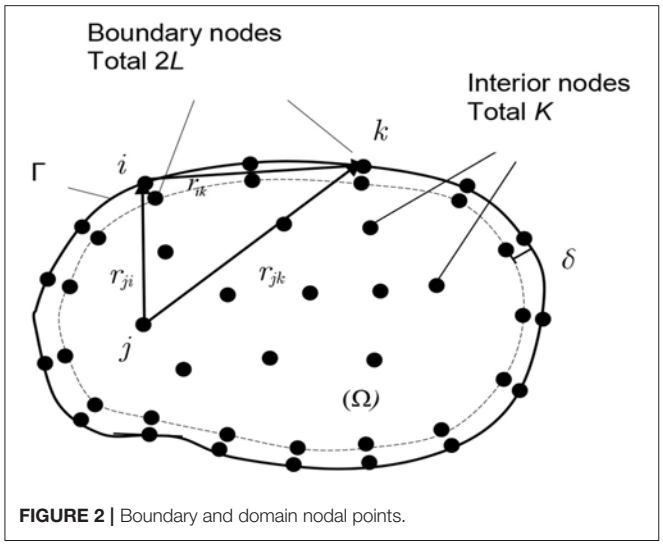

FIGURE 2 | Boundary and domain nodal points.

In Equation (4) σ_x, σ_s are the normal stresses, σ_{xs} the tangential shear stress, σ_{xz}, σ_{sz} the transverse (in the z direction) shear stresses and e_x, e_s, γ_{xs}, γ_{xz}, γ_{sz} the respective strains at an arbitrary point of shell cross-section.

In Equation (5), $q_x(t)$, $q_s(t)$, and $q_z(t)$ are the three components of the loading in the axial, circumferential and normal to the middle surface directions, respectively, while u, v, and w represent the axial, circumferential and normal displacements at the middle surface of the shell.

In Equation (6) the quantities $\bar{N}_x$, $\bar{N}_{xs}$, $\bar{Q}_x$, $\bar{M}_x$, $\bar{M}_{xs}$, and $\bar{N}_{sx}$, $\bar{N}_s$, $\bar{Q}_s$, $\bar{M}_{sx}$, $\bar{M}_s$ denote prescribed boundary forces along an edge ($x = const.$) and an edge ($s = const.$) respectively; u, v and w represent the axial, circumferential and normal displacements at the boundary and θ_x, θ_s are the rotations of the normal to the middle surface about the s and x axes respectively.

Furthermore, in Equation (2) the quantity K is the kinetic energy of the body and is given regarding the shell variables as

$$K = \frac{h\rho}{2}\int_x\int_s [\dot{u}^2 + \dot{v}^2 + \dot{w}^2 + \frac{h^2}{12}(\dot{\theta}_x^2 + \dot{\theta}_s^2)]dxds, \tag{7}$$

where ρ is the mass density of the material of the shell.

The quantity δW_{nc} represents the work of the damping forces, non-conservative forces, due to the virtual displacements and is given by the relation

$$\delta W_{nc} = \int_x\int_s (\eta\dot{u}\delta u + \eta\dot{v}\delta v + \eta\dot{w}\delta w)dxds, \tag{8}$$

where η is the damping coefficient.

Neglecting the contribution from the rotatory inertia terms $\rho h^3\theta_x/12$ and $\rho h^3\theta_s/12$ in Equation (7), inserting Equation (3) and taking the variation (Katsikadelis, 2016), we obtain the Flügge type differential equations (Flügge, 1962; Kraus, 1967), in terms of the displacements as well as the associated boundary and initial conditions

(a) Differential equations

$$u_{,xx} + \frac{1-\nu}{2}u_{,ss} + \frac{1+\nu}{2}v_{,xs} + \frac{\nu}{R}w_{,x} - \frac{h^2}{12}\frac{1}{R}\left[w_{,xxx} - \frac{1-\nu}{2}R\left(\frac{w_{,xs}}{R} + \frac{u_{,s}}{R^2}\right)_{,s}\right] - \eta\dot{u} = -\frac{1-\nu^2}{Eh}(q_x - \rho h\ddot{u}), \tag{9a}$$

$$v_{,ss} + \frac{1-\nu}{2}v_{,xx} + \frac{1+\nu}{2}u_{,xs} + \left(\frac{w}{R}\right)_{,s} + \frac{h^2}{12}\frac{1}{R^2}\left[\frac{3(1-\nu)}{2}v_{,xx} - \frac{(3-\nu)}{2}Rw_{,xxs} - R_{,s}(w_{,ss} + \frac{w}{R^2} + \frac{R_{,s}}{R^2}v)\right] - \eta\dot{v} = -\frac{1-\nu^2}{Eh}(q_s - \rho h\ddot{v}), \tag{9b}$$

$$\nabla^4 w + \frac{w_{,ss}}{R^2} + \left(\frac{w}{R^2}\right)_{,ss} + \frac{w}{R^4} - \frac{1}{R}u_{,xxx} + \frac{1-\nu}{2}\left(\frac{u_{,xs}}{R}\right)_{,s} - \frac{3-\nu}{2}\left(\frac{v}{R}\right)_{,xxs} + \left(\frac{R_{,s}}{R^2}v\right)_{,ss} + \frac{R_{,s}}{R^4}v + \frac{12}{h^2}\frac{1}{R}\left(v_{,s} + \frac{w}{R} + \nu u_{,x}\right) + \eta\dot{w} = -\frac{12(1-\nu^2)}{Eh^3}\left(-q_z + \rho h\ddot{w}\right), \tag{9c}$$

where $\nabla^4 = \frac{\partial^4}{\partial x^4} + \frac{2\partial^4}{\partial x^2\partial s^2} + \frac{\partial^4}{\partial s^4}$ is the biharmonic operator E is the modulus of elasticity and ν is Poisson's ratio.

(b) The boundary conditions (Kraus, 1967)

On a curved edge ($x = 0$ *or* $x = l$)

$$u = \bar{u} \text{ or } N_x = \bar{N}_x, \tag{10a}$$
$$v = \bar{v} \text{ or } T_{xs} = \bar{T}_{xs}, \tag{10b}$$
$$w = \bar{w} \text{ or } V_x = \bar{V}_x, \tag{10c}$$
$$\theta_x = \bar{\theta}_x \text{ or } M_x = \bar{M}_x, \left(\theta_x = -\frac{\partial w}{\partial x}\right). \tag{10d}$$

On a straight edge ($s = 0$ or $s = a$)

$$u = \bar{u} \text{ or } T_{sx} = \bar{T}_{sx}, \tag{10e}$$
$$v = \bar{v} \text{ or } N_s = \bar{N}_s, \tag{10f}$$
$$w = \bar{w} \text{ or } V_s = \bar{V}_s, \tag{10g}$$
$$\theta_s = \bar{\theta}_s \text{ or } M_s = \bar{M}_s, \left(\theta_s = \frac{v}{R} - \frac{\partial w}{\partial s}\right). \tag{10h}$$

Besides, the following corner conditions must be satisfied (Leissa, 1973)

$$w = \bar{w} \text{ or } (M_{xs} - M_{sx})_k = \bar{F}_k, \quad k = 1, 2, 3, 4. \tag{10i}$$

(c) The initial conditions

$$w(x, 0) = g_3(x), \quad \dot{w}(x, 0) = h_3(x), \tag{11a-b}$$

$$u(x, 0) = g_1(x), \quad \dot{u}(x, 0) = h_1(x), \tag{11c-d}$$

$$v(x, 0) = g_2(x), \quad \dot{v}(x, 0) = h_2(x), \tag{11e-f}$$

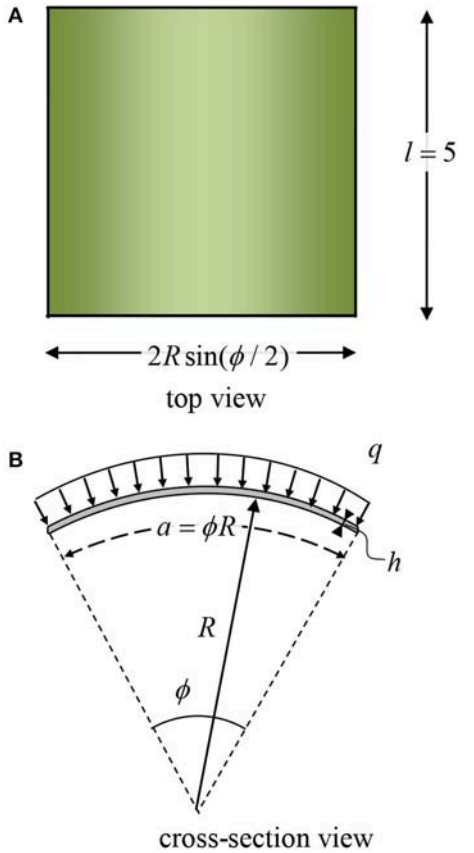

FIGURE 3 | The circular cylindrical shell and its geometry.

where $g_i(\mathrm{x}), h_i(\mathrm{x})$ $(i = 1,2,3)$ are specified functions and $(\mathrm{x}) = (x, s)$.

The stress resultants $N_x, N_s, N_{xs}, N_{sx}, M_x, M_s, M_{xs}, M_{sx}, Q_x, Q_s$ are expressed in terms of the displacements as

$$N_x = \frac{Eh}{1-\nu^2}\left[u_{,x} + \nu\left(v_{,s} + \frac{w}{R}\right) - \frac{h^2}{12}\frac{1}{R}w_{,xx}\right], \tag{12a}$$

$$N_s = \frac{Eh}{1-\nu^2}\left[v_{,s} + \frac{w}{R} + \nu u_{,x} + \frac{h^2}{12}\frac{1}{R}\left(w_{,ss} + \frac{w}{R^2} + \frac{R_{,s}}{R^2}v\right)\right], \tag{12b}$$

$$N_{xs} = \frac{Eh}{2(1+\nu)}\left[u_{,s} + v_{,x} - \frac{h^2}{12}\frac{1}{R}\left(w_{,xs} - \frac{1}{R}v_{,x}\right)\right], \tag{12c}$$

$$N_{sx} = \frac{Eh}{2(1+\nu)}\left[u_{,s} + v_{,x} + \frac{h^2}{12}\frac{1}{R}\left(w_{,xs} + \frac{1}{R}u_{,s}\right)\right], \tag{12d}$$

$$M_x = -D\{w_{,xx} + \nu\left[w_{,ss} - \left(\frac{v}{R}\right)_{,s}\right] - \frac{1}{R}u_{,x}\}, \tag{12e}$$

$$M_s = -D\left(w_{,ss} + \frac{w}{R^2} + \frac{R_{,s}}{R^2}v + \nu w_{,xx}\right), \tag{12f}$$

$$M_{xs} = -D(1-\nu)\left(w_{,xs} - \frac{1}{R}v_{,x}\right), \tag{12g}$$

$$M_{sx} = -D\frac{(1-\nu)}{2}\left(2w_{,xs} - \frac{v_{,x}}{R} + \frac{u_{,s}}{R}\right), \tag{12h}$$

$$Q_x = -D\left[w_{,xxx} + w_{,xss} - \frac{u_{,xx}}{R} + \frac{(1-\nu)}{2}\left(\frac{u_{,s}}{R}\right)_{,s} - \frac{1+\nu}{2R}\left(\frac{v}{R}\right)_{,xs}\right], \tag{12i}$$

$$Q_s = -D\left[w_{,sss} + w_{,xxs} + \left(\frac{w}{R^2}\right)_{,s} - \frac{(1-\nu)}{R}v_{,xx} + \left(\frac{R_{,s}}{R^2}v\right)_{,s}\right], \tag{12j}$$

where $D = E/12(1-\nu^2)$ and, T_{xs} V_x the effective tangential membrane and transverse shear forces at the edges $x = 0, l$ given as

$$T_{xs} = N_{xs} + \frac{M_{xs}}{R} = \frac{Eh}{2(1+\nu)}\left[u_{,s} + v_{,x} + \frac{h^2}{4}\frac{1}{R}\left(\frac{v_{,x}}{R} - w_{,xs}\right)\right], \tag{13a}$$

$$V_x = Q_x + \frac{\partial M_{xs}}{\partial s} = -D\left[w_{,xxx} + (2-\nu)w_{,xss} - \frac{u_{,xx}}{R} + \frac{(1-\nu)}{2}\left(\frac{u_{,s}}{R}\right)_{,s} - \frac{3-\nu}{2}\left(\frac{v_{,x}}{R}\right)_{,s}\right]. \tag{13b}$$

Similarly, T_{sx} and V_s represent the effective tangential membrane, and transverse shear force at the edges $s = 0, a$ and are given as

$$T_{sx} = N_{sx} = \frac{Eh}{2(1+\nu)}[u_{,s} + v_{,x} + \frac{h^2}{12}\frac{1}{R}(w_{,xs} + \frac{1}{R}u_{,s})], \tag{14a}$$

$$V_s = Q_s + \frac{\partial M_{sx}}{\partial x} = -D[w_{,sss} + (2-\nu)w_{,xxs} - \frac{3(1-\nu)}{2}\frac{v_{,xx}}{R} + \left(\frac{R_{,s}\nu}{R^2}\right)_{,s} + \left(\frac{w}{R^2}\right)_{,s} + \frac{(1-\nu)}{2}\frac{u_{,xs}}{R}]. \tag{14b}$$

MAEM SOLUTION

MAEM (Katsikadelis, 2002) is used for the solution of the initial boundary problem (9), (10), (11), as shown in the following. Let u, v and w be the solution to the problem. Since Equations (9) are of the 2nd order with respect to u, v and of the 4th order with respect to w, the analog equations which are convenient to use are

$$\nabla^2 u = b_1(\mathrm{x}, t), \quad \nabla^2 v = b_2(\mathrm{x}, t), \quad \nabla^4 w = b_3(\mathrm{x}, t), \tag{15a,b,c}$$

where $b_i = b_i(\mathrm{x}, t)$ $(i = 1,2,3)$ are unknown fictitious sources depending on time, which, however, is treated as a parameter, i.e., Equations (15a,b,c) are quasi-static, treated as static at each instant. The fictitious sources can be established as follows.

The fictitious sources are approximated with MQ-RBFs series. Thus we have

$$\nabla^2 u \simeq \sum_{j=1}^{K+L} a_j^{(1)}(t) f_j(r), \quad \nabla^2 v \simeq \sum_{j=1}^{K+L} a_j^{(2)}(t) f_j(r), \quad \nabla^4 w \simeq \sum_{j=1}^{K+2L} a_j^{(3)}(t) f_j(r) \tag{16a,b,c}$$

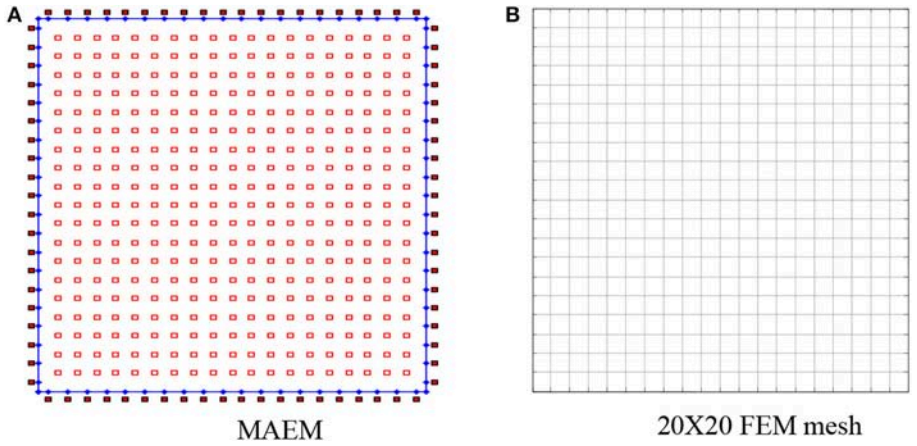

FIGURE 4 | (A) Shell collocation scheme MAEM. **(B)** Shell discretization FEM.

where c is the shape parameter; K, L represent the number of collocating points inside Ω and on Γ, respectively; $f_j(r) = \sqrt{r^2 + c^2}$, $r = |\mathrm{x} - \mathrm{x}_j|$ (see **Figure 2**), and $a_j^{(1)}$, $a_j^{(2)}$, $a_j^{(3)}$ time-dependent coefficients to be determined. Note that, while the derivatives of the membrane displacements u, v are collocated at K domain and L boundary points, the derivatives of the normal displacement w according to the δ-technique (Ferreira et al., 2005) are collocated in K domain and $2L$ boundary nodal points placed on the auxiliary boundary $\tilde{\Gamma}$ at a small distance δ from the actual one.

Equations (16) can be directly integrated to yield

$$u \simeq \sum_{j=1}^{K+L} a_j^{(1)}(t)\hat{u}_j, \quad v \simeq \sum_{j=1}^{K+L} a_j^{(2)}(t)\hat{v}_j, \quad w \simeq \sum_{j=1}^{K+2L} a_j^{(3)}(t)\hat{w}_j, \tag{17a,b,c}$$

where $\hat{u}_j(r)$, $\hat{v}_j(r)$, $\hat{w}_j(r)$ are solutions of the equations

$$\nabla^2\hat{u}_j = f_j(r), \quad \nabla^2\hat{v}_j = f_j(r), \quad \nabla^4\hat{w}_j = f_j(r). \tag{18a,b,c}$$

Since the functions $f_j(r)$ depend only on the radial distance r, the solution of Equations (18) can be obtained after writing them in polar coordinates. For the 2nd order equations, we have

$$\nabla^2\hat{u}_j = \frac{1}{r}\frac{d}{dr}\left(r\frac{d\hat{u}_j}{dr}\right) = f_j(r), \tag{19}$$

which after integration gives

$$\hat{u}_j = \frac{1}{9}f_j{}^3 + \frac{1}{3}f_j c^2 - \frac{c^3}{3}\ln\left(c + f_j\right) + G_1\ln(r) + H_1. \tag{20}$$

Similarly, we have

$$\hat{v}_j = \frac{1}{9}f_j{}^3 + \frac{1}{3}f_j c^2 - \frac{c^3}{3}\ln\left(c + f_j\right) + G_2\ln(r) + H_2. \tag{21}$$

The regularity condition at $r = 0$ demands $G_1 = G_2 = 0$. The remaining constants H_1, H_2 together with the shape parameter c, if not arbitrarily specified, can be determined with an optimization procedure, such as to ensure the regularity of coefficients matrix (control of the condition number) and the error minimization. It has been shown that the coefficient matrix resulting from the new RBFs is always invertible (Sarra, 2006), and as a result, we take in this analysis $H_1 = H_2 = 0$ for convenience. Thus only c, the shape parameter is involved in the error minimization procedure (Katsikadelis, 2008a).

TABLE 1 | Eigenfrequency parameters of the shell in Example 1.

Mode	c	$\Omega_f = R\omega\sqrt{(1-\nu^2)\rho/E}$	
		MAEM	**FEM**
1	0.06	0.6944	0.6969
2		0.8677	0.8672
3		1.0469	1.0440
4		1.1111	1.1220
5		1.2044	1.2113
6		1.4421	1.4452

For the 4th order equation, one can write

$$\nabla^4\hat{w} = \nabla^2(\nabla^2\hat{w}) = f_j. \tag{22}$$

Integrating Equation (22), and removing the singular terms and the terms including the arbitrary constants (Yao et al., 2010) yield

$$\hat{w}_j = -\frac{7}{60}c^4 f_j + \frac{2}{45}c^2 f_j{}^3 + \frac{1}{225}f_j{}^5 + \frac{2c^2 - 5r^2}{60}c^3\ln(c + f_j) + \frac{1}{12}r^2c^3. \tag{23}$$

Direct differentiation of Equations (17) obtains the derivatives of the displacements involved in the governing equations (9a,b,c).

$$u_{,ikl} \simeq \sum_{j=1}^{K+L} a_j^{(1)}(t)\hat{u}_{j,ikl}, \quad v_{,ikl} \simeq \sum_{j=1}^{K+L} a_j^{(2)}(t)\hat{v}_{j,ikl}, \quad w_{,ikl} \simeq \sum_{j=1}^{K+2L} a_j^{(3)}(t)\hat{w}_{j,ikl}, \tag{24a,b,c}$$

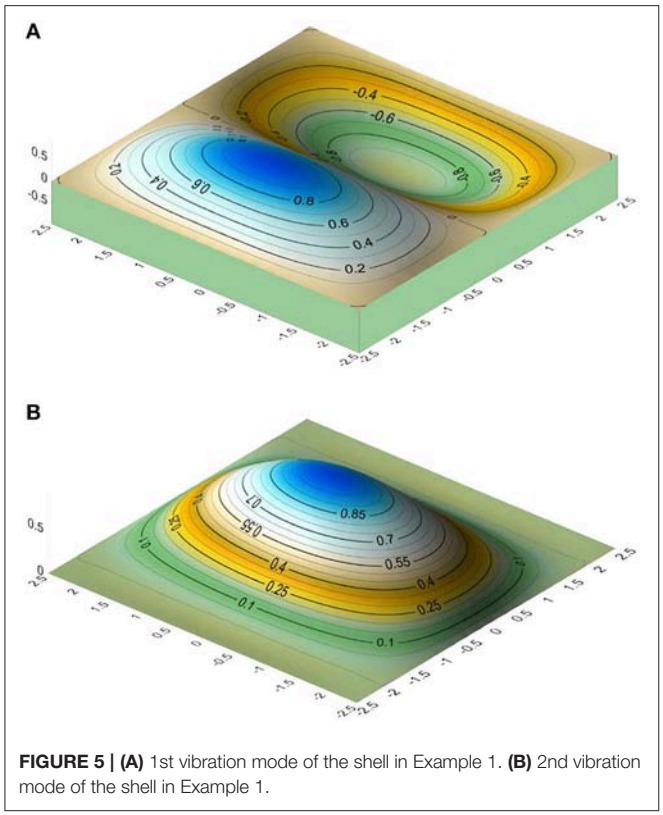

FIGURE 5 | (A) 1st vibration mode of the shell in Example 1. **(B)** 2nd vibration mode of the shell in Example 1.

where i, k, l stand for x, s.

Furthermore, the derivatives of the displacements with respect to time can also be obtained by direct differentiation of Equations (17). Thus we have

$$\dot{u} \simeq \sum_{j=1}^{K+L} \dot{a}_j^{(1)}(t)\hat{u}_j, \quad \dot{v} \simeq \sum_{j=1}^{K+L} \dot{a}_j^{(2)}(t)\hat{v}_j, \dot{w} \simeq \sum_{j=1}^{K+2L} \dot{a}_j^{(3)}(t)\hat{w}_j, \tag{25a,b,c}$$

$$\ddot{u} \simeq \sum_{j=1}^{K+L} \ddot{a}_j^{(1)}(t)\hat{u}_j, \quad \ddot{v} \simeq \sum_{j=1}^{K+L} \ddot{a}_j^{(2)}(t)\hat{v}_j, \quad \ddot{w} \simeq \sum_{j=1}^{K+2L} \ddot{a}_j^{(3)}(t)\hat{w}_j. \tag{26a,b,c}$$

Collocating Equations (9) at the K nodal points inside Ω and the four boundary conditions, Equations (10), at the L boundary nodal points (**Figure 2**) using the well-known δ-technique for multiple boundaries (Yiotis and Katsikadelis, 2015a), and inserting Equations (17) and (24) to (26) in the resulting expressions, a system of ordinary differential equations is obtained, namely

$$\mathbf{M}\ddot{\mathbf{a}} + \mathbf{C}\dot{\mathbf{a}} + \mathbf{K}\mathbf{a} = \mathbf{g}, \tag{27}$$

where $\mathbf{M}$, $\mathbf{C}$, and $\mathbf{K}$ are known square matrices having dimension $3K + 4L$; $\mathbf{g}$ is a vector including the $3K$ values of the external load $g(\mathbf{x}, t)$ and $\mathbf{a}$ is the vector of the $3K + 4L$ values of the unknown time-dependent coefficients $a_j^{(1)}(t)$, $a_j^{(2)}(t)$, $a_j^{(3)}(t)$.

Equation (27) is the semi-discretized equation of motion of the cylindrical shell with $\mathbf{M}$, $\mathbf{C}$, and $\mathbf{K}$ representing the generalized mass, damping and stiffness matrices, respectively. It can be solved numerically, using any time step integration technique to establish the time-dependent unknown coefficients. Here the method presented in Katsikadelis (2014a,b) is employed. The initial conditions of Equation (27) result from Equations (17) and (25) on the basis of Equations (11) as follows:

$$\mathbf{a}^{(1)}(\mathbf{0}) = \hat{\mathbf{u}}^{-1}\mathbf{g}_1(\mathbf{x}), \quad \dot{\mathbf{a}}^{-1}(\mathbf{0}) = \hat{\mathbf{u}}^{-1}\mathbf{h}_1(\mathbf{x}), \tag{28a}$$

$$\mathbf{a}^{(2)}(\mathbf{0}) = \hat{v}^{-1}\mathbf{g}_2(\mathbf{x}), \quad \dot{\mathbf{a}}^{(2)}(\mathbf{0}) = \hat{v}^{-1}\mathbf{h}_2(\mathbf{x}), \tag{28b}$$

$$\mathbf{a}^{(3)}(\mathbf{0}) = \hat{\mathbf{w}}^{-1}\mathbf{g}_3(\mathbf{x}), \quad \dot{\mathbf{a}}^{(3)}(\mathbf{0}) = \hat{\mathbf{w}}^{-1}\mathbf{h}_3(\mathbf{x}). \tag{28c}$$

Once the coefficients $a_j^{(1)}(t)$, $a_j^{(2)}(t)$, $a_j^{(3)}(t)$ have been computed, the field functions u, v, w, their derivatives, and the stress resultants can be evaluated from Equations (17), (24) to (26) and (12) to (14).

TABLE 2 | Eigenfrequency parameters of the shell in Example 2.

Mode	c	$\Omega_f = R\omega\sqrt{(1-\nu^2)\rho/E}$	
		MAEM	FEM
1	0.06	0.9026	0.9039
2		0.9086	0.9139
3		1.2032	1.1939
4		1.3662	1.3751
5		1.5473	1.5649
6		1.7498	1.7487

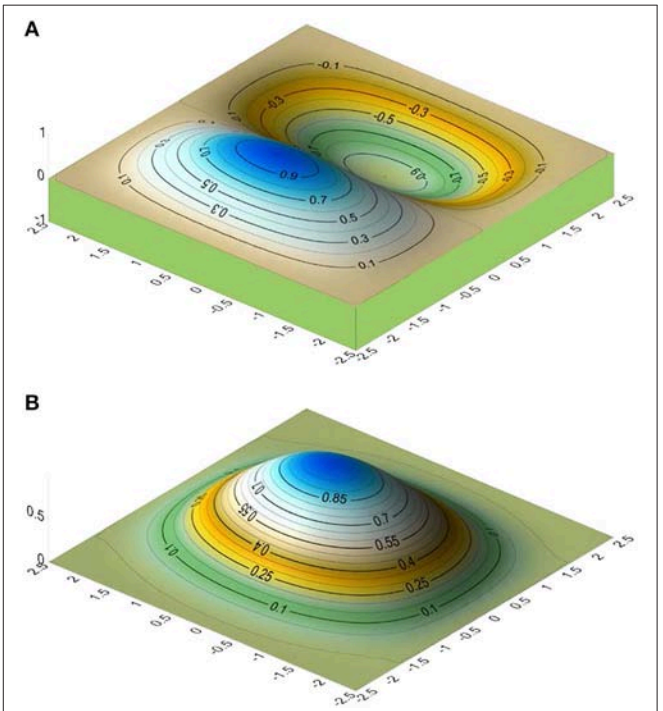

FIGURE 6 | (A) 1st vibration mode of the shell in Example 2. **(B)** 2nd vibration mode of the shell in Example 2.

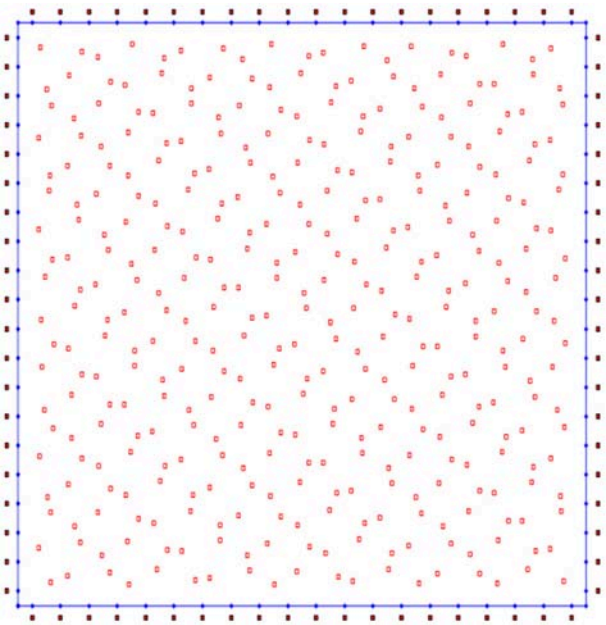

FIGURE 7 | Shell irregular collocation scheme: MAEM.

TABLE 3 | Eigenfrequency parameters of the shell in Example 3: case (a).

Mode	c	$\Omega_f = \frac{2l\omega R\sin(\phi/2)}{h}\sqrt{12\times(1-\nu^2)\rho/E}$	
		MAEM	**Lim and Liew (1994)**
1	0.05	99.716	99.263
2		118.227	119.00
3		150.854	151.13
4		155.536	156.35
5		171.666	172.52
6		190.027	192.43
7		200.254	201.67
8		205.107	207.80

For free vibrations it is $\mathbf{C} = \mathbf{g}(\mathbf{x}, t) = \mathbf{0}$ and the equation of motion, Equation (27), takes the form

$$\mathbf{M\ddot{a}} + \mathbf{Ka} = \mathbf{0}, \tag{29}$$

while the essential boundary conditions, Equations (10), become homogeneous.

By setting

$$\mathbf{a}(t) = \alpha e^{i\omega t}, \tag{30}$$

Equation (29) results in the eigenvalue problem

$$\left[\mathbf{K} - \omega^2\mathbf{M}\right]\alpha = \mathbf{0}, \tag{31}$$

which gives the eigenfrequencies ω_i and the eigenvectors $\boldsymbol{\alpha} = [\boldsymbol{\alpha}^{(1)}, \boldsymbol{\alpha}^{(2)}, \boldsymbol{\alpha}^{(3)}]^T$, where $\boldsymbol{\alpha}^{(1)} = [\alpha_1^{(1)}, \alpha_2^{(1)}, ..., \alpha_{K+L}^{(1)}]^T$, $\boldsymbol{\alpha}^{(2)} = [\alpha_1^{(2)}, \alpha_2^{(2)}, ..., \alpha_{K+L}^{(2)}]^T$, $\boldsymbol{\alpha}^{(3)} = [\alpha_1^{(3)}, \alpha_2^{(3)}, ..., \alpha_{K+2L}^{(3)}]^T$.

TABLE 4 | Eigenfrequency parameters of the shell in Example 3: case (b).

Mode	c	$\Omega_f = \frac{2l\omega R\sin(\phi/2)}{h}\sqrt{12\times(1-\nu^2)\rho/E}$	
		MAEM	**Lim and Liew (1994)**
1	0.05	45.909	46.241
2		73.250	74.300
3		79.160	79.239
4		109.855	110.14
5		130.664	132.35
6		136.049	135.51
7		165.271	165.57
8		167.891	166.82

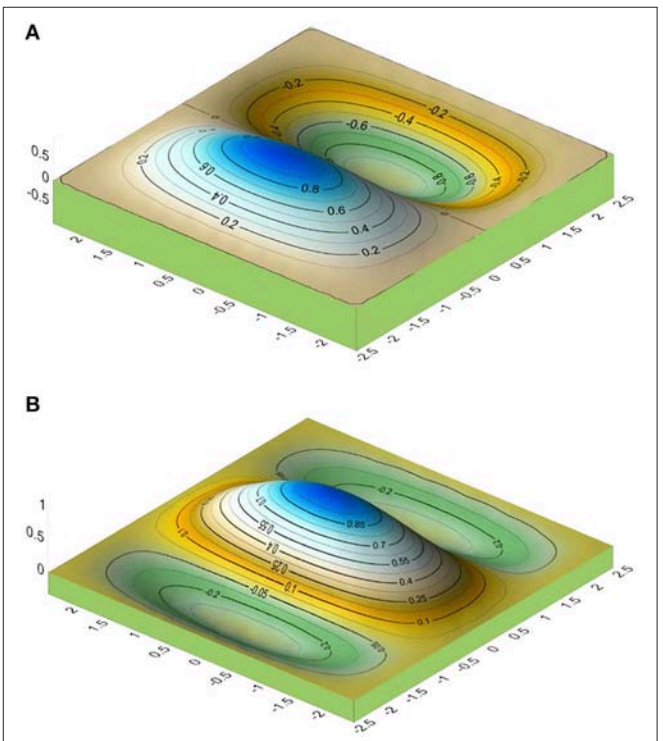

FIGURE 8 | (A) 1st vibration mode of the shell in Example 3-case (a). **(B)** 2nd vibration mode of the shell in Example 3-case (a).

The elements of these vectors are the three sets of coefficients corresponding to the functions u, v, and w, respectively. Subsequently, the mode shapes are obtained by substituting $\boldsymbol{\alpha} = [\boldsymbol{\alpha}^{(1)}, \boldsymbol{\alpha}^{(2)}, \boldsymbol{\alpha}^{(3)}]^T$ in Equations (17).

The accuracy of the approximation (9) depends heavily on c (see Equations 20-21-23). This was also verified in the problem at hand. Thus we come across to the problem of selecting a "*good*" value for c, that is, a value of the shape parameters that produces results of acceptable accuracy. Several methods have been suggested (Hardy, 1971; Franke, 1982; Foley, 1994; Rippa, 1999; Katsikadelis, 2009) for selecting a good value for c in 2D problems. Katsikadelis (2006, 2008b) proposed the minimization of the functional (total potential) for obtaining

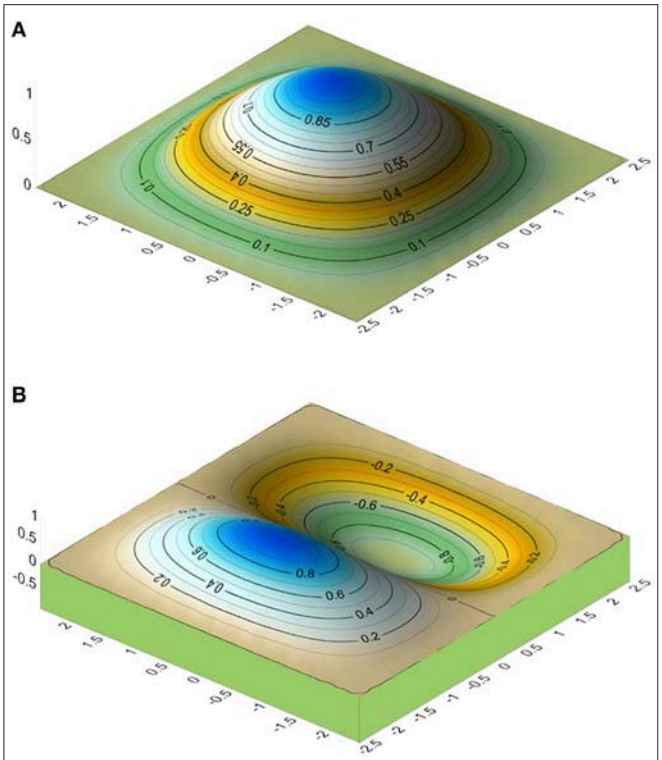

FIGURE 9 | (A) 1st vibration mode of the shell in Example 3-case (b). **(B)** 2nd vibration mode of the shell in Example 3-case (b).

an optimal value for c. For the present problem, the optimal value is obtained by the search method as the value of c which yields the minimum value of the eigenfrequencies ω_i. It was observed that the optimum c giving the minimum 1st eigenfrequency differs negligibly from that yielding the higher minimum eigenfrequencies. Therefore the same optimum value of c can be used to avoid the search method for higher eigenfrequencies.

NUMERICAL EXAMPLES

On the basis of the above analysis, a Fortran program has been written. The expressions of the derivatives involved in Equations (9) to (11) and Equations (12) to (14) have been obtained using the symbolic language MAPLE. Though the method applies to cylindrical shell of variable radius of curvature, for reasons of simplicity, the efficiency and accuracy of the developed method are demonstrated by studying the forced and free vibrations of circular cylindrical panels, (**Figure 3**), under different sets of boundary conditions. The NASTRAN FEM code and a model with 400 rectangular elements (**Figure 4B**) are used to compare the results. In all examples the employed material constants are: $E = 21 \times 10^6 kN/m^2$, $\nu = 0.30$. The results have been obtained running the relevant programs on an Intel Core 1.6 GHz with RAM 4 GB computer.

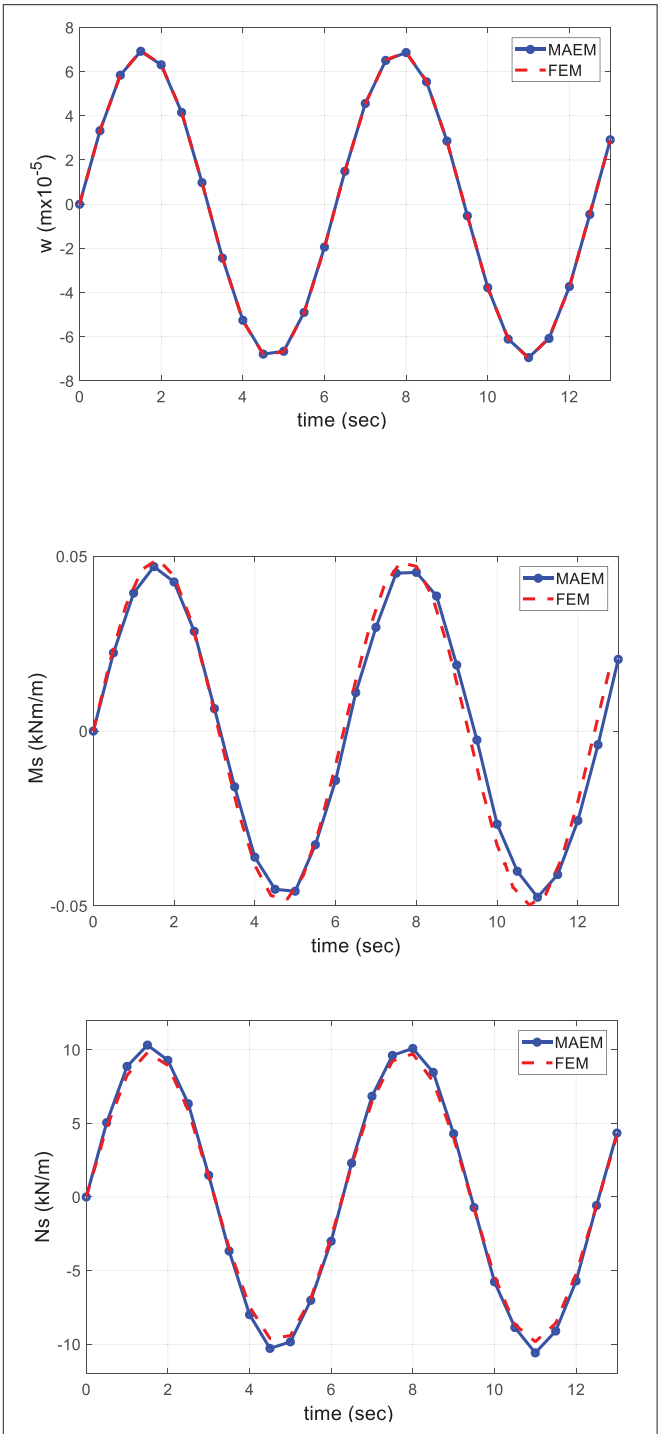

FIGURE 10 | Time history of the normal displacement w, bending moment M_S, and membrane force Ns at the center of the shell in Example 4.

Example 1

We study the dimensionless eigenfrequency parameter $\Omega_f = R\omega\sqrt{(1-\nu^2)\rho/E}$ of a simply supported circular cylindrical shell panel with movable curved edges in the axial direction ($N_x = v = w = M_x = 0$ along the curved edges and $u = v = w =$

$M_s = 0$ along the straight edges). The first six eigenfrequency parameters from MAEM are given in **Table 1** and are compared with a FEM solution. The 1st and 2nd vibration modes for the normal displacement are shown in **Figure 5**, respectively. The numerical results have been obtained with the parameters $L = 80$, $K = 361$ and $\delta = 1.e-6$ as shown in **Figure 4A**. The optimal value $c_{opt} = 0.06$ corresponds to the 1st mode and has also been used for the other five modes. This value is close to that obtained by the formula $c = 2/\sqrt{(K+2L)} = 0.088$ proposed in Ferreira et al. (2006b). The employed geometrical data are: $h = 0.10$ m, $R = 10.00$ m, $l = 5.00$ m, $a = 5.00$ m. The CPU time for the FEM solution was 10 s, while for the MAEM was 85 s. Note that the employed code has not been optimized.

Example 2

In this example the same shell as in Example 1 is analyzed under the following boundary conditions: $N_x = v = w = \theta_x = 0$ along the curved edges and $u = v = w = \theta_s = 0$ along the straight edges. The same collocation points as in the Example 1 have been used. The first six eigenfrequency parameters are shown in **Table 2** as compared again with those obtained from a FEM solution. The 1st and 2nd vibration modes for the normal displacement are shown in **Figure 6** respectively. The value $c_{opt} = 0.06$ was employed to obtain results for the first six modes. The CPU time for the FEM solution was 10 s, while for the MAEM was 88 s.

Example 3

In this example, a cylindrical shell panel with geometrical data $R = 9.896$ m, $l = 4.949$ m, $a = 5.00$ m is analyzed. Two cases with regard to the thickness have been considered: (a) $2R\sin(\phi/2)/h = 100$ and (b)$2R\sin(\phi/2)/h = 20$. All edges are clamped, i.e., $u = v = w = \theta_x = 0$ along the curved edges and $u = v = w = \theta_s = 0$ along the straight edges. The numerical results have been obtained with $L = 80$, $K = 361$ randomly distributed as shown in **Figure 7**, that is using an irregular distribution, and $\delta = 1.e-6$. In both cases, the search method resulted $c_{opt} = 0.05$. The first eight eigenfrequency parameters are shown in **Tables 3**, **4** as compared with those obtained from an analytical solution (Lim and Liew, 1994). The 1st and 2nd vibration modes for the normal displacement are shown in **Figure 8** for case (a) and in **Figure 9** for case (b), respectively. These figures show that that the vibration modes are influenced by the thickness of the shell, which is verified in (Webster, 1968; Lim and Liew, 1994).

Example 4

In this example, the forced vibrations of a simply supported circular cylindrical shell panel ($u = v = w = M_x = 0$ along the curved edges and $u = v = w = M_s = 0$ along the straight edges) with zero initial conditions ($u(x,0) = \dot{u}(x,0) = v(x,0) = \dot{v}(x,0) = w(x,0) = \dot{w}(x,0) = 0$) has been studied. Its geometrical data are those of Example 1. The applied load is the normal pressure given by $q_z = \sin(t)\ kN/m^2$. The mass density is $\rho = 2.446 kNm^{-4}sec^2$. The numerical results have been obtained with $L = 80$, $K = 361$ distributed as shown in **Figure 4A** and $\delta = 1.e-6$. The employed optimal value is $c_{opt} = 0.06$. The time history of the normal displacement w, the bending moment M_s and the membrane force N_s at the center of the shell are shown in **Figure 10** as compared with those obtained by a FEM solution. The CPU time for the FEM solution was 40 s, while for the MAEM was 325 s.

CONCLUSIONS

The Meshless Analog Equation Method, a truly meshless method, has been applied to the dynamic analysis of thin cylindrical shell panels in the present study. MAEM is based on the principle of the analog equation, converting the original equations into three substitute equations, two Poisson's and one biharmonic, which are solved using a meshless method. The use of integrated MQ-RBFs to approximate the fictitious sources allows the approximation of the sought solutions by new RBFs, which approximate both the solution and its derivatives accurately. This way the strong formulation of the problem avoids the drawbacks inherent in the conventional MQ-RBFs, while maintaining all the advantages of a truly mess-free method. A method is presented to obtain optimum values for the shape parameter, eliminating the uncertainty in its choice. It was observed that the optimum value of the shape parameter for the 1st mode differs negligibly from those of higher modes and therefore the same value can be used to obtain the eigenfrequencies of higher modes. The solution algorithm is straightforward and quite reasonably easy to program. The numerical examples presented demonstrate the efficiency and accuracy of the proposed method and show that MAEM can be used as an efficient solver for challenging problems in engineering analysis.

AUTHOR CONTRIBUTIONS

AY has implemented the MAEM (Meshless Analog Equation Method) for the solution of problems governing by fourth order differential equations (plates-shells etc.). JK has invented the AEM (Analog Equation Method), which is a general method for the solution of various engineering problems.

REFERENCES

Beskos, D. E. (1991). "Static and dynamic analysis of shells," in *Boundary Element Analysis of Plates and Shells*, ed D. E. Beskos (Berlin: Springer-Verlag), 93–140.

Cheng, A. H. D., Golbeg, M. A., Kansa, E. J., and Zammito, G. (2003). Exponential1 convergence and h-c multiquadric collocation method for partial differential equations. *Numerical Methods Partial Differential Equations* 19, 571–594. doi: 10.1002/num.10062

Dinis, L. M. J. S., Natal Jorge, R. M., and Belinha, J. (2011). A natural neighbour meshless method with a 3D shell-like approach in the dynamic analysis of thin 3D structures. *Thin-Walled Structures* 49, 185–196. doi: 10.1016/j.tws.2010.09.023

Ferreira, A. J. M., Roque, C. M. C., and Jorge, R. M. M. (2006a). Modelling cross-ply laminated elastic shells by a higher-order theory and multiquadrics. *Comput. Struct.* 84, 1288–99. doi: 10.1016/j.compstruc.2006.01.021

Ferreira, A. J. M., Roque, C. M. C., and Jorge, R. M. M. (2006b). Static and free vibration analysis of composite shells by radial basis functions. *Eng. Anal. Bound.Elements* 30, 719–733. doi: 10.1016/j.enganabound.2006.05.002

Ferreira, A. J. M., Roque, C. M. C., and Martins, P. A. L. S. (2005). Analysis of thin isotropic rectangular and circular plates with multiquadrics. *Strength Mater*. 37, 163–173. doi: 10.1007/s11223-005-0029-7

Flügge, W. (1962). *Stresses in Shells*. Berlin: Springer-Verlag.

Foley, T. A. (1994). Near optimal parameter selection for multiquadric interpolation. *J. Appl. Sci. Comput*. 1, 54–69.

Franke, R. (1982). Scattered data interpolation: tests of some methods. *Math. Comput*. 38, 181–200.

Hardy, R. L. (1971). Multiquadric equations of topography and other irregular surfaces. *J. Geophys. Res*. 76, 1905–1915. doi: 10.1029/JB076i008p01905

Jang, S. K., Bert, C. W., and Striz, A. G. (1989). Application of differential quadrature to static analysis of structural components. *Int. J. Num. Methods Eng*. 28, 561–577. doi: 10.1002/nme.1620280306

Kansa, E. J. (2005). "Highly accurate methods for solving elliptic partial differential equations," in *Boundary Elements XXVII*, eds C. A. Brebbia, E. Divo, and D. Poljak (Southampton: WIT Press), 5–15.

Katsikadelis, J. T. (2002). The analog equation method. A boundary-only integral equation method for nonlinear static and dynamic problems in general bodies. *Int. J. Theor. Appl. Mech. Arch. Appl. Mech*. 27, 13–38. doi: 10.2298/TAM0227013K

Katsikadelis, J. T. (2006). "The meshless analog equation method. A new highly accurate truly mesh-free method for solving partial differential equations," in *Boundary Elements and Other Mesh Reduction Methods XXVIII*, eds C. A. Brebbia and J. T. Katsikadelis (Southampton: WIT Press), 13–22. doi: 10.2495/BE06002

Katsikadelis, J. T. (2008a). A generalized Ritz method for partial differential equations in domains of arbitrary geometry using global shape functions. *Eng. Anal. Bound. Elem*. 32, 353–367. doi: 10.1016/j.enganabound.2007.09.001

Katsikadelis, J. T. (2008b). The 2D elastostatic problem in inhomogeneous anisotropic bodies by the meshless analog equation method MAEM. *Eng. Anal. Bound. Elem.*32, 997–1005. doi: 10.1016/j.enganabound.2007.10.016

Katsikadelis, J. T. (2009). The meshless analog equation method: I. Solution of elliptic partial differential equations. *Arch. Appl. Mech*. 79, 557–578. doi: 10.1007/s00419-008-0294-6

Katsikadelis, J. T. (2014a). A new direct time integration method for the equations of motion in structural dynamics. *Zeitschrift Angewandte Math Mech*. 94, 757–774. doi: 10.1002/zamm.201200245

Katsikadelis, J. T. (2014b). *Boundary Element Method for Plate Analysis*. Oxford, UK: Academic Press; Elsevier.

Katsikadelis, J. T. (2016). *The Boundary Element Method for Engineers and Scientists, 2nd Edn*. Oxford, UK: Academic Press; Elsevier.

Katsikadelis, J. T., and Platanidi, J. G. (2007). "3D analysis of thick shells by the meshless analog equation method," in *Proceedings of the 1st International Congress of Serbian Society of Mechanics*, (Kopaonik), 475–484.

Kraus, H. (1967). *Thin Elastic Shells. An Introduction to the Theoretical Foundations and the Analysis of Their Static and Dynamic Behavior*. New York, NY; London; Sydney: John Wiley and Sons.

Lee, S. J., and Han, S. E. (2001). Free-vibration analysis of plates and shells with a nine-node assumed natural degenerated shell element. *J. Sound Vibr.* 241, 605–633. doi: 10.1006/jsvi.2000.3313

Leissa, A. W. (1973). *Vibrations of Shells, Scientific and Technical Information Office*. Washington, DC: NASA.

Lim, C. W., and Liew, K. M. (1994). A pb-2 Ritz formulation for flexural vibration of shallow cylindrical shells of rectangular planform. *J. Sound. Vibr*. 173, 343–375. doi: 10.1006/jsvi.1994.1235

Liu, G. R. (2002). *Meshfree Methods: Moving Beyond the Finite Element Method*. New York, NY: CRC Press.

Liu, G. R., and Gu, Y. T. (2005). *An Introduction to Meshfree Methods and Their Programming*. Dordrecht: Springer.

Liu, L., Chua, L. P., and Ghista, D. N. (2006). Element free Galerkin method for static and dynamic analysis of spatial shell structures. *J. Sound Vibr.* 295, 388–406. doi: 10.1016/j.jsv.2006.01.015

Love, A. E. H. (1944). *A Treatise on the Mathematical Theory of Elasticity, 4th Edn*. New York, NY: Dover Pub Inc.

Nguyen, V. P., Rabczuk, T., Bordas, S., and Duflot, M. (2008). Meshless methods: a review and computer implementation aspects. *Math. Comput Simul*. 79, 763–813. doi: 10.1016/j.matcom.2008.01.003

Pilafkan, R., Folkow, P. D., Darvizeh, M., and Darvizeh, A. (2013). Three dimensional frequency analysis of bidirectional graded thick cylindrical shells using a radial point interpolation method (RPIM). *Eur. J. Mech. A/Solids* 39, 26–34. doi: 10.1016/j.euromechsol.2012.09.014

Rippa, S. (1999). An algorithm for selecting a good value for the parameter c in radial basis function approximation. *Adv. Comput. Math*. 11, 193–210. doi: 10.1023/A:1018975909870

Roque, C. M. C., Ferreira, A. J. M., Neves, A. N. A., Fasshauer, G. E., Soares, C. M. M., and Jorge, R. M. N. (2010). Dynamic analysis of functionally graded plates and shells by radial basis functions. *Mech. Adv. Mater. Struct*. 17, 636–652. doi: 10.1080/15376494.2010.518932

Sarra, S. A. (2006). Integrated multiquadric radial basis function approximation methods. *Comput. Math. Appl.* 51, 1283–1296. doi: 10.1016/j.camwa.2006.04.014

Webster, J. J. (1968). Free vibrations of rectangular curved panels. *Int. J. Mech. Sci.* 10, 571–582. doi: 10.1016/0020-7403(68)90058-1

Yao, G., Tsai, C. H., and Chen, W. (2010). The comparison of three meshless methods using radial basis functions for solving fourth-order partial differential equations. *Eng. Analysis Bound. Elem*. 34, 625–631. doi: 10.1016/j.enganabound.2010.03.004

Yiotis, A. J., and Katsikadelis, J. T. (2000). Static and dynamic analysis of shell panels using the analog equation method. *Comput. Model. Eng. Sci*. 2, 95–103. doi: 10.3970/cmes.2000.001.255

Yiotis, A. J., and Katsikadelis, J. T. (2008). "The Meshless Analog Equation Method for the solution of plate problems," in *Proceedings of the 6th GRACM International Congress on Computational Mechanics* (Thessaloniki).

Yiotis, A. J., and Katsikadelis, J. T. (2013). Analysis of cylindrical shell panels. A Meshless Solution. *Eng. Anal. Bound. Elem.* 37, 928–935. doi: 10.1016/j.enganabound.2013.03.005

Yiotis, A. J., and Katsikadelis, J. T. (2015a). Buckling of cylindrical shell panels. A MAEM solution. *Arch. Appl. Mech*. 85, 1545–1557. doi: 10.1007/s00419-014-0944-9

Yiotis, A. J., and Katsikadelis, J. T. (2015b). "The dynamic analysis of cylindrical shell panels. A MAEM solution," in *Book of Abstracts of the 8th GRACM International Congress on Computational Mechanics, July 12–15,* eds N. Pelekasis and E. G. Stavroulakis (Volos), 147.

Zhao, X., Lee, Y. Y., and Liew, K. M. (2009). Thermoelastic and vibration analysis of functionally graded cylindrical shells. *Int. J. Mech. Sci.* 51, 694–707. doi: 10.1016/j.ijmecsci.2009.08.001

Conflict of Interest Statement: The authors declare that the research was conducted in the absence of any commercial or financial relationships that could be construed as a potential conflict of interest.

The reviewer AC declared a shared affiliation, with no collaboration, with the authors to the handling editor at time of review.

frontiers in Built Environment

ORIGINAL RESEARCH
published: 27 September 2018
doi: 10.3389/fbuil.2018.00048

Numerical Investigation of Bolted Hybrid Steel-Timber Connections

Themistoklis Tsalkatidis[1]*, *Youcef Amara*[2], *Samuel Embaye*[2] and *Einar Nathan*[1]

[1] Faculty of Science and Technology, Norwegian University of Life Sciences, Ås, Norway, [2] UnionConsult, Oslo, Norway

Hybrid steel to timber connections are found in many buildings and bridges. These connections offer several advantages such as ease of construction and energy dissipation. This research paper aims to study the mechanical behavior of bolted hybrid connections that consists of a square hollow steel column (SHS) and a glulam timber beam. The connection between the two structural members is achieved by means of angles and preloaded bolts. A reference model is constructed and verified by comparison to experimental and numerical data from the international literature. Additionally, several parameters that affect the response of the connection are modified in order to investigate and quantify their effect, resulting in seven different case studies. These parameters are the size of the bolts, the thickness of the angles and the addition of stiffener. The moment-rotation curve of each case study is constructed and the results are commented. Finally, a proposed optimal configuration of the hybrid connection is presented.

Keywords: FEM analysis, parametric investigation, hybrid steel-timber connections, bolted connections, hollow sections

OPEN ACCESS

Edited by:
George C. Tsiatas,
University of Patras, Greece

Reviewed by:
Mario D'Aniello,
Università degli Studi di Napoli Federico II, Italy
Massimo Latour,
Università degli Studi di Salerno, Italy

***Correspondence:**
Themistoklis Tsalkatidis
themistoklis.tsalkatidis@nmbu.no

Specialty section:
This article was submitted to Computational Methods in Structural Engineering, a section of the journal Frontiers in Built Environment

Received: *02 July 2018*
Accepted: *29 August 2018*
Published: *27 September 2018*

Citation:
Tsalkatidis T, Amara Y, Embaye S and Nathan E (2018) Numerical Investigation of Bolted Hybrid Steel-Timber Connections. Front. Built Environ. 4:48. doi: 10.3389/fbuil.2018.00048

INTRODUCTION

Steel and wood are materials that have been extensively used in constructions worldwide, even from ancient times. Nowadays, the need for a sustainable built environment encourages structural engineers to think of new design options that can maximize the benefits of the aforementioned materials. By combining the strength and ductility of steel with the low weight of wood, environmental friendly structures are achieved. The structural members in this type of constructions are connected using hybrid solutions. In countries like Norway where the access to wood resources is easy, these hybrid structures could become the norm for future lightweight structures.

METHODS

Problem Formulation

Connections between steel and concrete or steel and timber structural elements are referred as hybrid. In general, the design of connections between members is always a challenge for the structural engineers. Loads and stresses need to be transferred from one structural member to another. In the presented paper, finite element modeling is used as a tool to investigate the behavior of hybrid bolted steel- timber connections considering several proposals made in technical literature, such as Amara and Embaye (2017). This type of connections has not been thoroughly examined. The numerical simulations of the hybrid connections under study are governed by the contact conditions at the steel-timber interface. Emphasis is placed on the construction of moment-rotation curves of the connections. Only the elastic stiffness of the connection is determined since elastic design is traditionally selected in the case of connections. The reference beam to column hybrid connection is depicted in **Figure 1**.

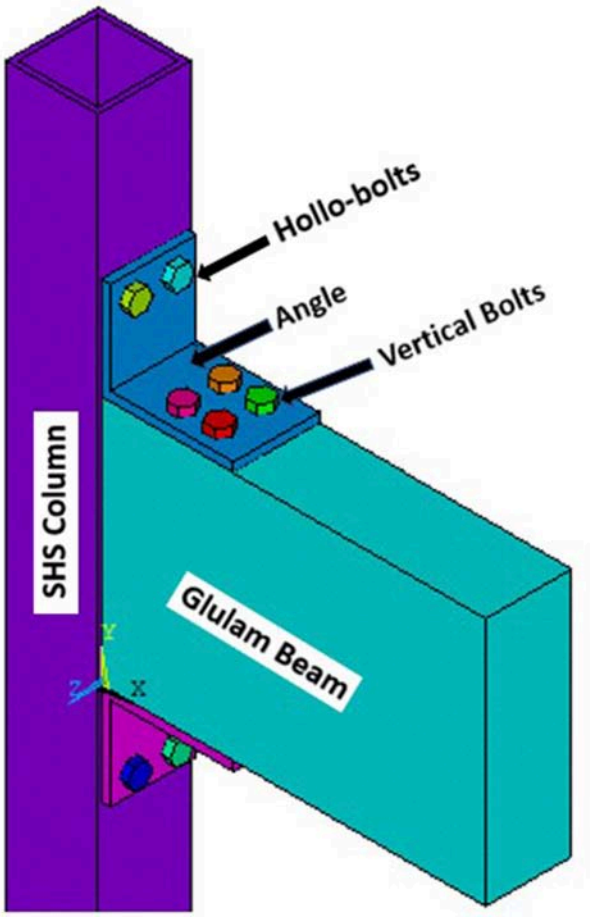

FIGURE 1 | Rendering of the reference connection, figure based on Karagiannis et al. (2017).

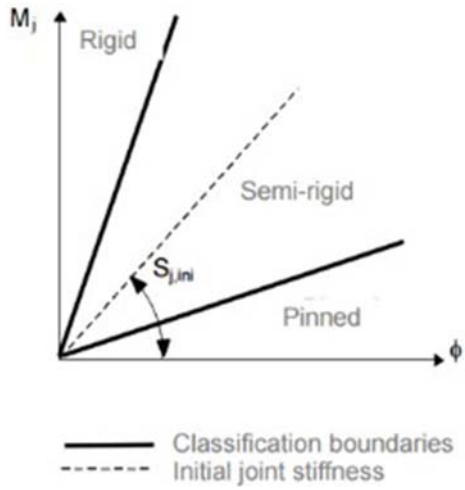

FIGURE 2 | Connection classification by initial rotational stiffness, figure from Eurocode (EN 1993-1-8, 2005).

Moment-Rotation Curve

In structural engineering, the behavior of a certain structure under design load situations is represented by unique action-deformation curves. If the structure is examined at member level then the moment-rotation (M-ϕ) curve represents the behavior of a certain connection between structural members. The rotational stiffness of the connection is equal to the slope of the curve and the initial value of this stiffness is used for the classification of the connection, which is important for the design of MRFs. According to Eurocode 3 part 1.8 (EN 1993-1-8, 2005), a connection can be classified as pinned, semi-rigid or rigid, if it satisfies the respective criteria presented below in Equations (1)–(5):

$$\text{Nominally pinned} \quad S_{j,ini} < 0.5EI_b/L_b \quad (1)$$

$$\text{Semi-rigid} \quad 0.5\,EI_b/Lb < S_j < 8EI_b/L_b \text{ (braced frame)} \quad (2)$$

$$0.5EI_b/L_b < Sj < 25EI_b/L_b \text{ (unbraced frame)} \quad (3)$$

$$\text{Rigid} \quad S_{j,ini} > 8EI_b/L_b \text{(braced frame) or} \quad (4)$$

$$S_{j,ini} > 25EI_b/L_b \text{(unbraced frame)} \quad (5)$$

where:

$S_{j,ini}$ is the initial rotational stiffness of the connection (kN/mrad)

EI_b is the bending stiffness of the beam (kN/mrad)

L_b is the span of the beam (mm)

The classification of the joint according to the initial rotational stiffness presented in Eurocode 3 (EN 1993-1-8, 2005) and Eurocode 5 (EN 1995-1-1, 2004) is depicted in **Figure 2**. The M-ϕ curve can be either non-linear or have a simplified tri-linear or even bi-linear form as described in Eurocode 3. In our analysis, only the first linear branch of the M-ϕ curve is plotted since it is adequate to classify the hybrid connections when performing elastic analysis of connections at the Serviceability Limit State (SLS).

Analytical Solution

The general procedure for determining the rotational stiffness of a connection proposed by Eurocode (EN 1993-1-8, 2005) is the component method. The key idea of this method is to calculate the stiffness of all the components of a connection and then the total stiffness by assembling a mechanical model of the whole system of elementary springs. The components of a connection are the connected parts and the connecting elements. Of course, the identification of the active components of the connection and the evaluation of their contribution according to Porteous and Kermani (2013) must be done in the beginning. The problem with this method is that it cannot be applied in hybrid connections without assumptions. These assumptions are often very conservative thus leading to overdesigned connection solutions. Therefore, the following method is used. First, the rotation ϕ of the connection is calculated, for every load step, using the

trigonometric Equation (6), neglecting the elastic deformation of the column:

$$\phi = \arctan(\Delta e/d_b) \quad (6)$$

where:

ϕ is the rotation of the connection (mrad)

Δe is the elastic deformation of the beam (mm)

d_b is the depth of the beam (mm)

Then, the reaction force P_e, as shown in **Figure 3**, is calculated using the Eq. (7):

$$P_e = 12EI/g_1^{3*}(g_1 + g_{2/g1} + 4g_2)^*\Delta_e \quad (7)$$

where:

P_e is the reaction force (kN)

g_1 is the gauge distance parallel to the column (mm)

g_2 is the gauge distance parallel to the beam (mm)

Finally, the elastic moment of the connection is found, using the Equation (8):

$$M = (P_e^* l_e)^*(d_b + g_1)^*(d_b/\Delta_e)^*\phi \quad (8)$$

where:

M is the elastic moment of the connection (kNm)

l_e is the effective length of the angle (mm)

Equations (7) and (8) together with the corresponding **Figure 3**, are empirical analytical formulas that are valid for semi-rigid connections with angles. These formulas were proposed by Lee and Moon (2002) and predict accurately the early response of the connection.

The final step is to construct the moment-rotation curve and to calculate the initial rotational stiffness, which is equal to the slope of the M-ϕcurve. The calculation is done using the Equation (9):

$$S_{j,ini} = \arctan(M/\phi) \quad (9)$$

where:

$S_{j,ini}$ is the initial rotational stiffness of the connection (kN/mrad)

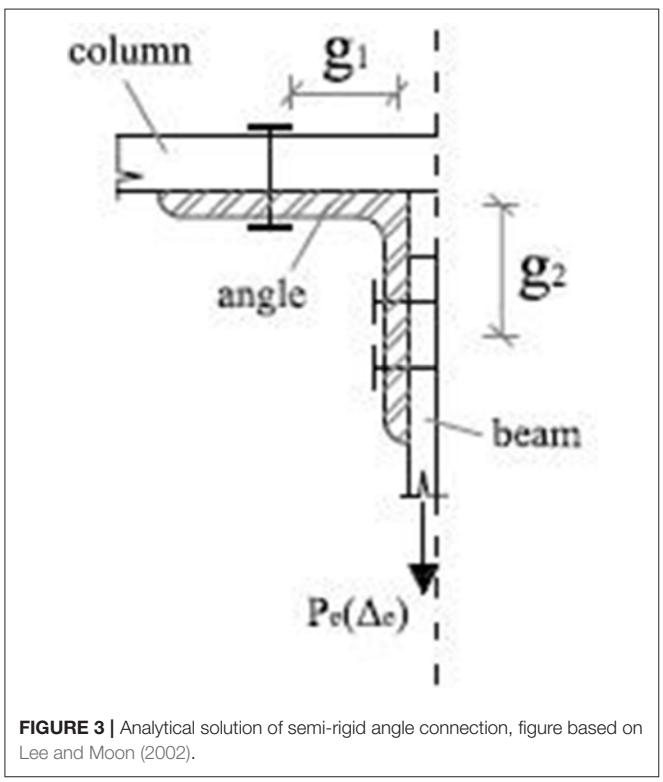

FIGURE 3 | Analytical solution of semi-rigid angle connection, figure based on Lee and Moon (2002).

NUMERICAL ANALYSIS

Reference Model

The reference beam-column hybrid connection consists of glulam beam and a steel SHS column. The beam has a height of 405 mm and width of 140 mm, whereas the column is 150 mm wide and 10 mm thick. Top and seat angles are 150*200 mm, 15 mm thick and they are connected using M12 HR bolts to the glulam beam and M16 HR bolts to the tubular steel column, respectively. The steel grade of the column is S355, of the top and seat angle is S275 and of the bolts. Glulam is of category GL28h. The model is constructed according to the geometric and mechanical characteristics of an experimental specimen found in the international literature by Karagiannis et al. (2017). The

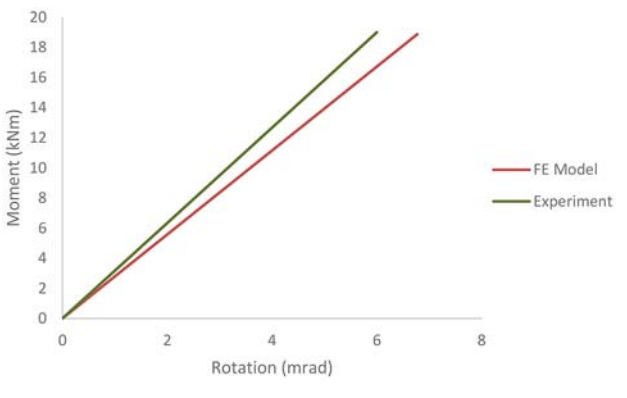

FIGURE 4 | Verification of numerical model.

TABLE 1 | Case studies examined.

Nr	Description
1	Reference model
2	Thickness of the top and seat angle equal to 18 mm
3	Thickness of the top and seat angles equal to 20 mm
4	Diameter of the vertical bolts equal to 16 mm
5	Diameter of the vertical bolts equal to 20 mm
6	Reduction of 20 mm in the width of the top and seat angle
7	Thickness of the top and seat angle equal to 12 mm and use of a 14 mm stiffener in the middle of the top angle

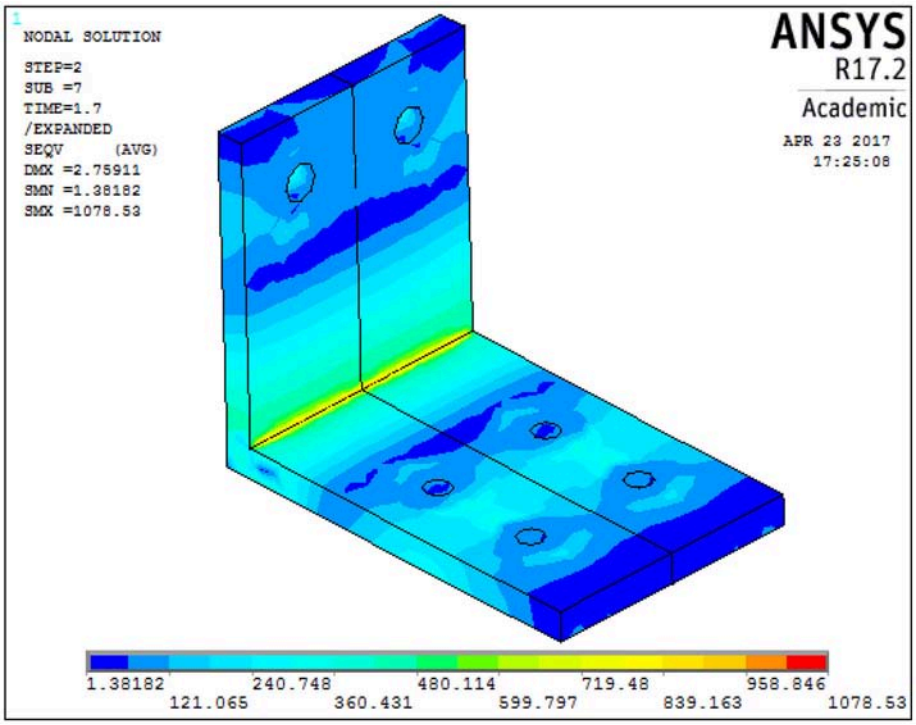

FIGURE 5 | Von Mises stress distribution in the top angle for case 1.

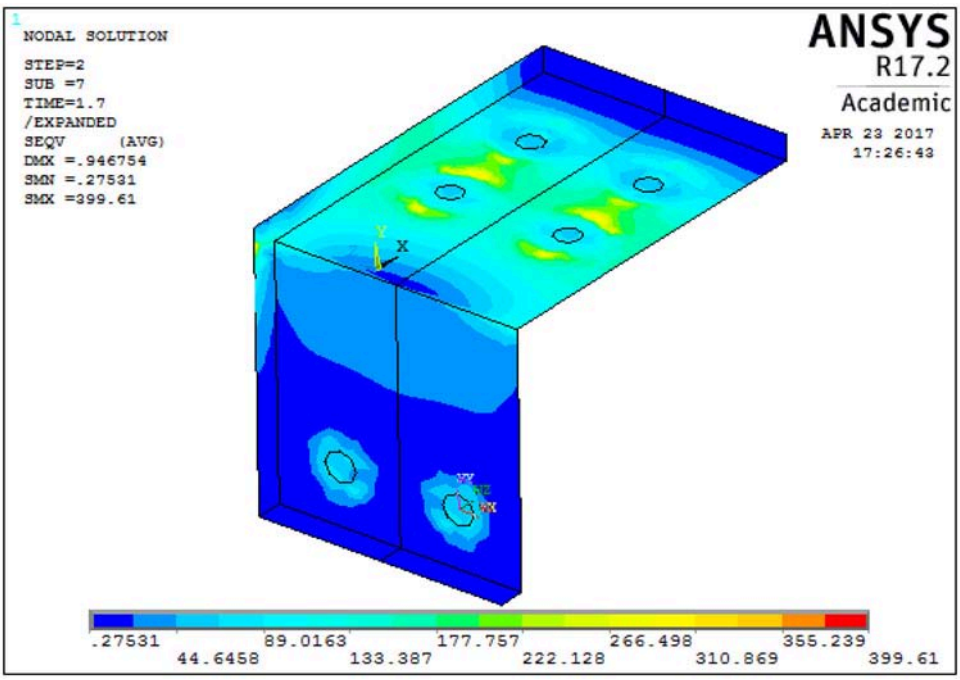

FIGURE 6 | Von Mises stress distribution in the seat angle for case 1.

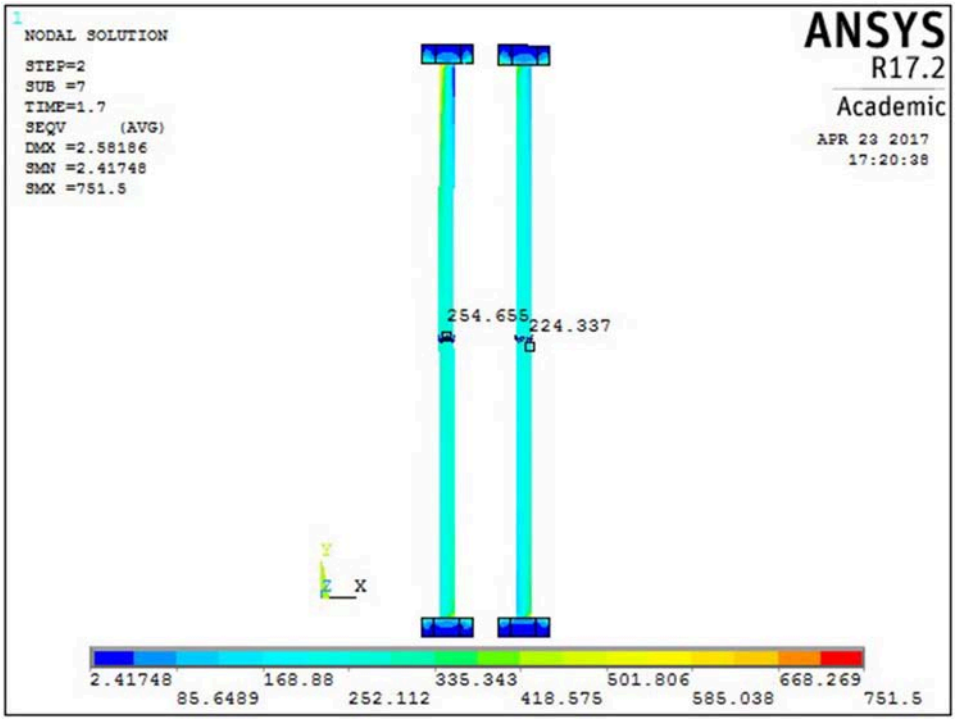

FIGURE 7 | Von Mises stress distribution in the vertical bolts for case 1.

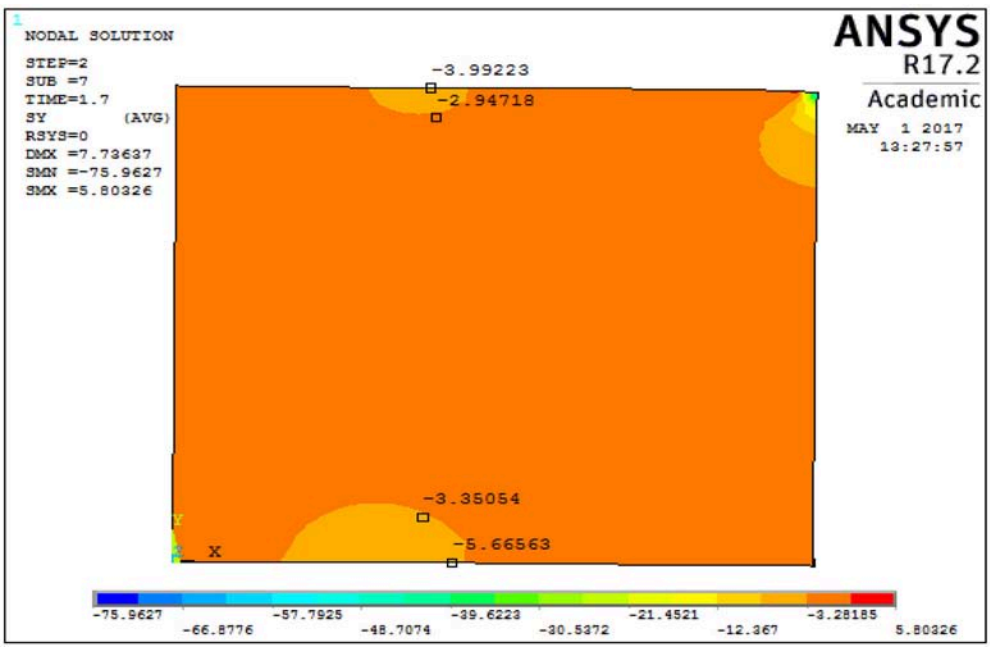

FIGURE 8 | Von Mises stress distribution in the glulam beam for case 1.

reference model does not have blind bolts penetrating the SHS column for simplicity reasons although mechanical models that describe the behavior of blind-bolted angle connections have been proposed by Malaga-Chuquitaype and Elghazouli (2010). In this paper, the focus is on the effect of the different components on the connection by Anwar and Najam (2016), in relation to the strength and the rotational stiffness of the joint. The support and loading conditions of the three-dimensional finite element simulation are the same as the experiment by Karagiannis et al. (2017) for verification purposes.The displacement-induced load at the end of the beam is limited to 7mm in order the behavior of the joint to remain elastic. Only one quarter of the joint is modeled due to symmetry. The model is constructed using ANSYS version 17.2 finite element package (Ansys Inc., 2017). **Figure 4** depicts the comparison of the moment-rotation curve between the numerical and the experimental analysis, within the elastic response of the connection.

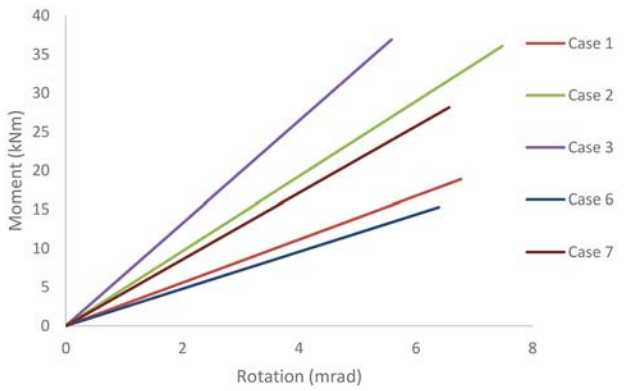

FIGURE 9 | Numerical moment-rotation curves.

The beam, the column and the angles are simulated with three-dimensional structural solid finite elements and the contact interfaces with surface-to-surface contact elements. Contact, itself, is a complex phenomenon that adds nonlinearities to a finite element simulation as presented by Bathe (1996) and Mistakidis and Stavroulakis (1998). In the case of hybrid connections, the interaction of different materials adds an extra level of difficulty. ANSYS software offers the option of pair-based contact where one surface is regarded as the contact and the other as the target one. The interface behavior is set as bonded with a Coulomb coefficient of friction equal to 0.7 in order to simulate unilateral frictional contact conditions described by Popov (2010) and Tsalkatidis and Avdelas (2010). The contact elements overlay the solid elements and the contact is detected at Gauss points. The pretension of the bolts and the resulting clamping forces are modeled by using the PRETS179 element from the ANSYS library. As stated before, the blind bolts of the experimental specimen are replaced by bolts with nuts.

Case Studies

A total number of seven case studies is examined by Amara and Embaye (2017), as presented in the **Table 1**. The parameters examined are the thickness of the angles (case studies 2, 3, and 7), the diameter of the vertical bolts (case studies 4 and 5), the width

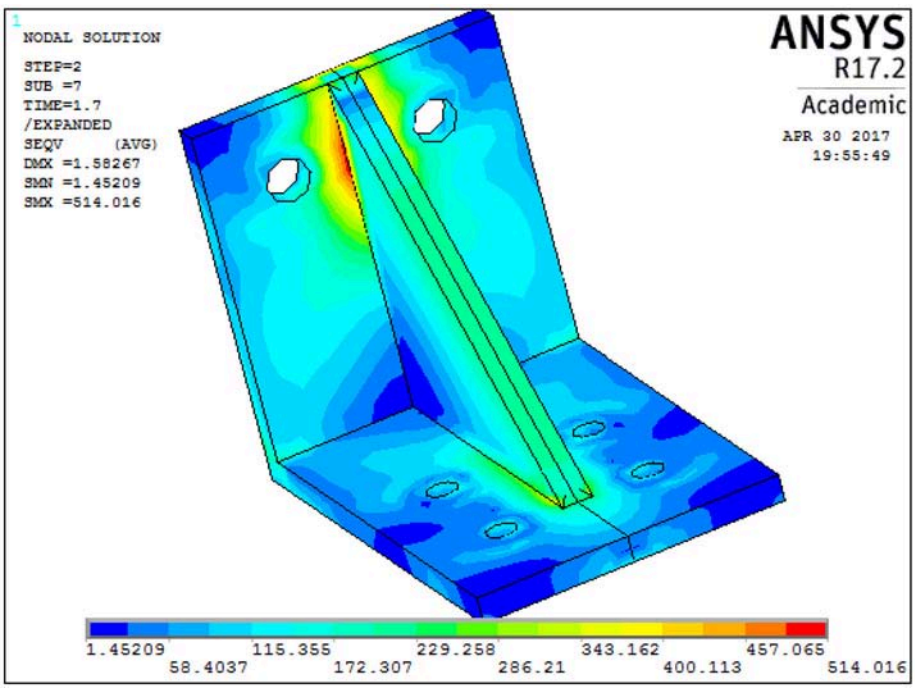

FIGURE 10 | Von Mises stress distribution in the top angle for case 7.

of the angles (case study 6) and the addition of stiffener (case study 7). The aforementioned parameters have been examined in several research studies such as Theofanous et al. (2015), Tartaglia et al. (2018), and Gil et al. (2015).

RESULTS

The main results of the numerical analysis are the moment-rotation curves together with the corresponding initial rotational stiffness and the von Mises stresses that develop in the connection. The results are presented in **Figures 5–10**.

DISCUSSION AND CONCLUSION

The numerical analysis of the hybrid steel-timber connection focuses on the initial rotational stiffness and the developing von Mises stresses in the top angle.

Effect of angle thickness

- By changing the thickness of the top and the seat angles from 15 mm (case study 1) to 18 mm (case study 2) or to 20 mm (case study 3), the rotational stiffness of the connection increases. For case 2 the increase is 73% and for case 3 is 137%, in comparison to case 1. This denotes that even a small increase in thickness of the angles has a significant effect on the rotational stiffness of the connection. As expected, the connection becomes stiffer when the thickness of the angles is increased. Moreover, the maximum von Mises stress in the top angle is decreased by 12.2% in case 2 and by 15.5 % in case 3. The increase in the amount of steel used is 21 and 35.2%, respectively.

Effect of bolt diameter

- By changing the diameter of the vertical bolts from12 mm (case study 1) to 16 mm (case study 4) or to 20 mm (case study 5), the rotational stiffness of the connection is not affected. The change in the diameter of the bolts is reciprocal to the change in the pretension force. Moreover, the maximum von Mises stress in the top angle is decreased by 20.7% in case 4 and by 32.7% in case 5. The increase in the amount of used steel is higher by 21 and 35.2%, respectively.

Effect of angle width

- By reducing the width of the of the top and the seat angles from 150 mm (case study 1) to 130 mm (case study 6), the rotational stiffness of the connection is reduced by 14.15%. Moreover, the maximum von Mises stress in the top angle increases by 14.28%.

Effect of stiffener

- By adding a stiffener at the top angle (case study 7), the rotational stiffness of the connection increases by 53.6% in relation to the reference model. The addition of stiffener leads to the development of high von Mises stresses in the seat angle near the bolt heads due to bending of the horizontal leg of the seat angle. After the pretension of the bolt, the stiffener also enhances the clamping forces at the bolt-angle interface.
- Local surface crushing of the glulam beam is present in all models, due to compression from the top and seat angle. The effect is more significant when the stiffness of the angle is higher, thus resulting in a huge difference in deflection between the beam and the angle.
- The connection in all the case studies remains semi-rigid, as assumed. Case studies 2, 3, and 7 have the higher values of initial rotational stiffness. The von Mises stress in case study 5 has its minimum value.
- The recommended connection is a combination of case studies 3 and 5. The geometry of the joint remains the same, as in the reference model, but the thickness of both angles and the diameter of the bolts are set equal to 20 mm. This design option increases the initial rotational stiffness of the connection by 137%, whereas the von Mises stress decreases by at least 32.7%. The aforementioned benefits in the response of the connection by far outweigh the increase in steel use.

AUTHOR CONTRIBUTIONS

TT, YA, and SE contributed conception, design of the study, and performed the analysis; TT wrote the first draft of the manuscript; TT, YA, SE, and EN wrote sections of the manuscript. All authors read and approved the submitted manuscript version.

REFERENCES

Amara, Y., and Embaye, S. (2017). *Analyzing the Behaviour of a Hybrid Steel to Timber Connection by Modifying Different Parameters.* dissertation/master's thesis, Norwegian University of Life Sciences, Ås.

Ansys Inc. (2017). *Ansys Manual v17.2*. Canonsburg, PA.

Anwar, N., and Najam, F. (2016). *Structural Cross-Sections: Analysis and Design*. Oxford: Elsevier.

Bathe, K. J. (1996). *Finite Element Procedures*. Upper Saddle River, NJ: Prentice Hall.

EN 1993-1-8 (2005). *Eurocode 3: Design of Steel Structures, Part 1–8: Design of Joints.* Brussels: CEN.

EN 1995-1-1 (2004). *Eurocode 5: Design of Timber Structures, Part 1–1: General Common Rules and Rules for Buildings.* Brussels: CEN.

Gil, B., Bijlaard, F., and Bayo, E. (2015). T-stub behavior under out-of-plane bending. II: parametric study and analytical characterization. *Eng. Struct*. 98, 242–250. doi: 10.1016/j.engstruct.2015.03.039

Karagiannis, V., Malaga-Chuquitaype, C., and Elghazouli, A. Y. (2017). Behavior of hybrid timber beam-to-column moment connections. *Eng. Struct*. 131, 243–263. doi: 10.1016/j.engstruct.2016.11.006

Lee, S. S., and Moon, T. S. (2002). Moment rotational model of semi rigid connection with angles. *Eng. Struct*. 24, 227–237. doi: 10.1016/S0141-0296(01)00066-9

Malaga-Chuquitaype, C., and Elghazouli, A. Y. (2010). Component-based mechanical models for blind-bolted angle connection. *Eng. Struct*. 32, 3048–3067. doi: 10.1016/j.engstruct.2010.05.024

Mistakidis, E. S., and Stavroulakis, G. E. (1998). *Non Convex Optimization and its Applications: Non Convex Optimization in Mechanics*. Dordrecht: Kluwer Academic Publishers. doi: 10.1007/978-1-4615-5829-3

Popov, V. L. (2010). *Contact Mechanics and Friction*. Berlin: Springer-Verlag. doi: 10.1007/978-3-642-10803-7

Porteous, J., and Kermani, A. (2013). *Structural Timber Design to Eurocode*. Oxford: Wiley-Blackwell.

Tartaglia, R., D'Aniello, M., and Landolfo, R. (2018). The influence of rib stiffeners on the response of extended end-plate joints. *J. Const. Steel Res*. 148, 669–690. doi: 10.1016/j.jcsr.2018.06.025

Theofanous, M., Liew, A., and Gardner, L. (2015). Experimental study of stainless steel angles and channels in bending. *Structures* 4, 80–90. doi: 10.1016/j.istruc.2015.10.004

Tsalkatidis, T., and Avdelas, A. (2010). The unilateral contact problem in composite slabs. Experimental study and numerical treatment. *J. Const. Steel Res*. 66, 480–486. doi: 10.1016/j.jcsr.2009.10.012

Conflict of Interest Statement: The authors declare that the research was conducted in the absence of any commercial or financial relationships that could be construed as a potential conflict of interest.

frontiers in Built Environment

ORIGINAL RESEARCH
published: 09 October 2018
doi: 10.3389/fbuil.2018.00052

A Layered Boundary Element Nonlinear Analysis of Beams

George C. Tsiatas[1], Antonis G. Siokas[2] and Evangelos J. Sapountzakis[3]*

[1] Department of Mathematics, University of Patras, Rio, Greece, [2] School of Civil Engineering, National Technical University of Athens, Athens, Greece, [3] School of Civil Engineering, National Technical University of Athens, Athens, Greece

This work aims to introduce a new layered approach to the nonlinear analysis of initially straight Euler-Bernoulli beams by the Boundary Element Method (BEM). The beam is studied in the context of both geometrical and material nonlinearity. The governing differential equations, derived by applying the principle of minimum total potential energy, are coupled and nonlinear, while the boundary conditions are the most general and may include elastic support or restraint. The boundary value problem, regarding the axial and transverse displacements, is solved using the Analog Equation Method (AEM), a BEM based method, together with an iterative procedure. Although a direct solution to the geometrical nonlinear problem has already been presented, in this work an alternative layered analysis is proposed. The discretization is applied in both the longitudinal direction and the cross-sectional plane, and an iterative process is commenced. First, initial fictitious load distributions are assumed at beam's each cross-section, and the displacements, as well as their derivatives, are computed using the AEM. Second, the two stress resultants, i.e., the axial force and bending moment, are evaluated by appropriate integration over the cross-section. In the end, the derivatives of the stress resultants are evaluated, and the equilibrium of the governing equations is checked. If the equilibrium is satisfied, the process is terminated. Otherwise, the fictitious load distributions are updated, and the procedure starts over again. Several representative examples are studied, and the results are compared with those presented in the literature, validating the reliability and effectiveness of the proposed method.

Keywords: beams, geometrical nonlinear analysis, material nonlinear analysis, Boundary Element Method (BEM), layered analysis, shape memory alloys (SMA)

OPEN ACCESS

Edited by:
Raffaele Barretta, Università degli Studi di Napoli Federico II, Italy

Reviewed by:
S. Ali Faghidian, Islamic Azad University, Iran
Giovanni Romano, Università degli Studi di Napoli Federico II, Italy

****Correspondence:***
George C. Tsiatas
gtsiatas@upatras.gr

Specialty section:
This article was submitted to Computational Methods in Structural Engineering, a section of the journal Frontiers in Built Environment

Received: *11 July 2018*
Accepted: *04 September 2018*
Published: *09 October 2018*

Citation:
Tsiatas GC, Siokas AG and Sapountzakis EJ (2018) A Layered Boundary Element Nonlinear Analysis of Beams. Front. Built Environ. 4:52. doi: 10.3389/fbuil.2018.00052

INTRODUCTION

Beam elements have historically found applications in the process of structural modeling and analysis in a wide range of engineering disciplines, from civil (e.g., buildings, bridges) to mechanical (e.g., shafts, wind turbine parts, nuclear reactor components) to aeronautical (e.g., aircraft wings, spacecraft parts) (Hodges, 2006) to name only a few. For this reason, considerable research has been directed at studying the static and dynamic structural behavior of beams. Over the years, the exponential growth in computational power in conjunction with significant advances in numerical methods have led to more sophisticated simulations; the initially simplifying modeling assumptions have been gradually diminished, and more realistic nonlinear formulations are employed.

In general, two conventional sources of nonlinearity may affect the response of structural elements: material and geometrical (Reddy, 2005a). On the one hand, material nonlinearity stems

from the inherent nonlinear constitutive behavior of several materials. In this case, the stress-strain relation may be a function of the combined or individual stress, strain or strain rate and may also be path dependent about the load history. Nonlinear material behavior in solid mechanics can be rate-independent or rate-dependent (Taylor, 1996). On the other hand, the geometrical nonlinearity results from maintaining the square of the slope in the strain-displacement relations (Katsikadelis and Tsiatas, 2003). In this case, the transverse deflection affects the axial force, and the resulting governing equations are coupled nonlinear with variable coefficients.

An analytical solution to the mathematical model describing the behavior of the beam cannot be obtained when general boundary conditions are imposed at its ends; therefore, a numerical approach should be adopted (Katsikadelis and Tsiatas, 2003). The most widely used numerical methods in Computational Mechanics are the Finite Element Method (FEM), the Boundary Element Method (BEM), and the Finite Difference Method (FDM) (Banerjee and Butterfield, 1981; Becker, 1992). Firstly, FDM can be applied to any system of differential equations by substituting the differential operators with algebraic ones at representative nodes after the problem domain discretization. It is the simplest of the three methods and relatively easy to program. However, it is not suitable for problems with irregular domain geometries and rapidly changing variables, due to the difficulty of establishing a non-uniform grid of nodes. Secondly, according to FEM, the domain of the solution is decomposed into a finite number of smaller subdomains, called finite elements. On each subdomain the behavior of the whole body is approximated, and then continuity and balance rules are applied at the boundaries of the elements to obtain the solution for the entire domain (Plevris and Tsiatas, 2018). FEM is appropriate for problems with geometrical complex solution domains. However, discretizing the whole body results in a large number of finite elements leading to significant computational cost. Lastly, BEM, applying the concept of the Fundamental Theorem of Calculus, transforms the governing differential equations into equivalent integral ones, thus transferring the solution domain to its boundary, where a discretization scheme is then established. In this respect, the dimension of the problem is reduced by one order while the number of unknowns is also significantly reduced (Plevris and Tsiatas, 2018). Moreover, the BEM allows the evaluation of the derivatives of the solution at any point of the original solution domain (before the initial integration), whereas it is suitable for the analysis of structures with complex boundaries and geometric peculiarities, such as cracks (Katsikadelis, 2016).

To the problem at hand, FEM has been adopted by many researchers for the materially and/or geometrical nonlinear analysis of beams. In particular, Mondkar and Powell (1977), examined structures accounting for large displacements with finite strains and formulated the incremental equations of motion using the principle of virtual displacements. Argyris et al. (1978a,b, 1979), to circumvent the complications emerging from the noncommutative nature of rotations about fixed distinct axes, presented the concept of semi-tangential rotation in the matrix displacement analysis of geometrically nonlinear structures. Bathe and Bolourchi (1979) studied the behavior of a beam element undergoing large displacements and large rotations formulating a total Lagrangian and an updated Lagrangian approach. Yang and McGuire (1986) presented a nonlinear analysis of beams with a doubly symmetric cross-section employing an updated Lagrangian finite element formulation. Cai et al. (2009) performed a large deformations-large rotations finite element analysis of a three-dimensional frame with members of arbitrary cross-sections by the nonlinear Von Karman theory of deformation.

Furthermore, linear and nonlinear analysis of beams has also been performed employing BEM. Banerjee and Butterfield (1981) and Providakis and Beskos (1986) employed BEM in order to solve the static and dynamic problems of Euler-Bernoulli beams, respectively. Further, the Analog Equation Method (AEM), a numerical technique based on BEM, was applied to the nonlinear static (Katsikadelis and Tsiatas, 2003) and dynamic (Katsikadelis and Tsiatas, 2004) flexural analysis of beams with variable cross-section. Sapountzakis and Mokos (2008) and Sapountzakis and Panagos (2008) studied the nonlinear flexural behavior of beams of doubly symmetric constant and variable cross-section using BEM and adopting the assumptions of the Timoshenko beam theory. Tsiatas (2010) examined the nonlinear problem of non-uniform beams resting on a nonlinear elastic foundation presenting a boundary integral equation solution. Sapountzakis and Dourakopoulos (2010) formulated a BEM solution to the moderate large deflections flexural-torsional analysis of Timoshenko beams of a constant cross-section of arbitrary shape under general boundary conditions. Sapountzakis and Dikaros (2011) adopted a BEM methodology to examine the effects of warping and rotary inertia to the moderate large deflections and twisting rotations flexural-torsional dynamic analysis of beams.

In formulating a one-dimensional element for the linear or nonlinear analysis of beams, two considerations have to be made: First, the prediction of the cross-sectional response. Second, the integration of the cross-sectional response over the length of the element to obtain its response regarding the available degrees of freedom (Izzuddin et al., 2002). Although the latter consideration has been extensively presented in the previous works, an open issue remains regarding the former consideration.

As far as cross-sectional response is concerned, three main approaches have been widely adopted (Izzuddin et al., 2002): According to the first one, explicit expressions for cross-sectional response parameters (e.g., stress-strain functions) are provided. The second one utilizes interaction relationships based mainly on principles of plasticity. The third approach, known as the fiber approach, utilizes a cross-sectional decomposition into a finite number of subdomains adequately small to readily evaluate stresses and strains at representative points. The fiber approach is the most general, as it can be applied even in cases where the stress-strain relation is not a priori known, or even if a mathematical function can not explicitly describe it, but only by sets of experimental data.

In this respect, the fiber model has been extensively applied in the analysis and design of beams. Kaba and Mahin (1984) first introduced a beam element divided into fibers for the analysis of reinforced concrete or steel members assuming

that plane sections remain plane. They used both force and displacement shape functions to compute the element flexibility and the element-resisting forces, respectively. Filippou et al. (1991) presented a FEM solution for the problem of reinforced concrete members under cyclic loading conditions that induce biaxial bending and axial force. Zbiciak (2010) presented a formulation of an initial-boundary-value problem for the Euler-Bernoulli beam made of pseudoelastic shape memory alloy (SMA). A 2D finite difference discretization scheme was established in the longitudinal sense and on the cross-sectional plane dividing the cross-section into layers of constant thickness. More recently, Sapountzakis and Kampitsis (2017) developed a hybrid domain BEM formulation for the geometrical nonlinear analysis of inelastic Euler-Bernoulli beams resting on viscous inelastic Winkler foundation, employing an inelastic redistribution modeled through a fiber approach. Finally, Tsiatas et al. (2018) presented a first step toward the solution of the problem presented in this work, employing a fiber approach to the large deflections analysis of beams by BEM. In this solution, the material nonlinearity of the beam was not considered.

In this work, a layered approach to the nonlinear analysis of initially straight Euler-Bernoulli beams by BEM is presented. The beam is studied in the context of both geometrical and material nonlinearity. It must be noted that in the current analysis, the cross-sections under consideration are rectangular. In this case, the fiber model can be reduced to a layered model; more specifically, fibers can be substituted by layers of constant thickness. The formulation of the problem is based on the displacements, and the equations of equilibrium, derived from the principle of minimum total potential energy, are coupled and nonlinear. The solution to the system of those equations is achieved using AEM according to which the obtained equations of equilibrium are substituted by the same number of uncoupled linear equations (Analog Equations) of the same order of differentiation for each displacement component, i.e., a second order for the axial deformation and fourth order for the transverse deformation respectively. It is worth noting that, from a physical point of view, each substitute linear equation describe the response of a beam with unit stiffness, for the axial and bending problem respectively, subjected to unknown fictitious loads (Katsikadelis and Tsiatas, 2003). Although a direct solution to the problem at hand has already been presented by Katsikadelis and Tsiatas (2003), in this work, an alternative layered analysis is proposed. In this case, a discretization is applied in both the longitudinal direction and the cross-sectional plane, and an iterative numerical process is commenced. First, initial fictitious load distributions are assumed at beam's each cross-section and the displacements and their derivatives are computed using AEM. Consequently, the stress resultants are evaluated by appropriate integration over the cross-section. In the end, the derivatives of the stress resultants are evaluated, and the equilibrium of the governing equations is checked. If the equilibrium is satisfied, the process is terminated. Otherwise, the fictitious load distributions are updated, and the procedure starts over again. Several representative examples are examined considering not only geometrical nonlinearity but material nonlinearity as well. The reliability and effectiveness of the proposed method are validated by comparing the obtained results with those presented in the literature or produced by other Finite Element models.

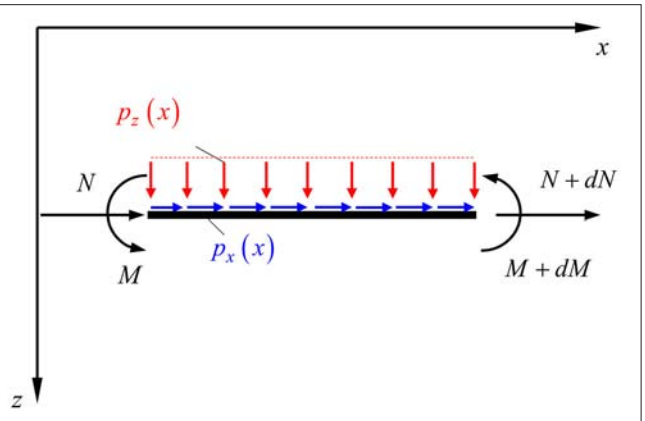

FIGURE 1 | Forces and moments acting on the element.

STATEMENT OF THE PROBLEM

Kinematics

An initially straight beam of length L is considered. The beam has variable axial and bending stiffness EA and EI (**Figure 1**), respectively, which may result from the variation of the cross-section, $A = A(x)$ and $I = I(x)$, and/or from the inhomogeneous nature of the linearly elastic material, $E = E(x)$. The x axis of the beam is assumed to coincide with its neutral axis. The beam is subjected to the combined action of the distributed loads $p_x = p_x(x)$ and $p_z = p_z(x)$, along with the x and z-direction, respectively, and it is bent in its plane of symmetry xz (Katsikadelis and Tsiatas, 2003).

The bending of the beam is studied in the context of the Euler-Bernoulli beam theory, according to which plane cross-sections of the beam perpendicular to the beam axis before deformation remain (i) plane, (ii) rigid, and (iii) perpendicular to the (deformed) axis after deformation. Following these assumptions, the displacement field is written as.

$$\bar{u}(x,y,z) = u(x) - z w_{,x}(x), \tag{1}$$

$$\bar{v}(x,y,z) = 0, \tag{2}$$

$$\bar{w}(x,y,z) = w(x), \tag{3}$$

where $(\cdot)_{,x}$ denotes differentiation with respect to x; $\bar{u}, \bar{v}, \bar{w}$ are the displacements of an arbitrary point of the beam along the x, y, z axes respectively and u, w are the displacements of a point on the neutral axis.

The components of the three-dimensional Green-Lagrange strain tensor are given (Reddy, 2005a)

$$\varepsilon_{xx} = \bar{u}_{,x} + \frac{1}{2}\left[(\bar{u}_{,x})^2 + (\bar{v}_{,x})^2 + (\bar{w}_{,x})^2\right], \tag{4}$$

$$\varepsilon_{yy} = \bar{v}_{,y} + \frac{1}{2}\left[(\bar{u}_{,y})^2 + (\bar{v}_{,y})^2 + (\bar{w}_{,y})^2\right], \tag{5}$$

$$\varepsilon_{zz} = \bar{w}_{,z} + \frac{1}{2}\left[(\bar{u}_{,z})^2 + (\bar{v}_{,z})^2 + (\bar{w}_{,z})^2\right], \quad (6)$$

$$\gamma_{xy} = 2\varepsilon_{xy} = \left(\bar{v}_{,x} + \bar{u}_{,y}\right) + \left(\bar{u}_{,x}\bar{u}_{,y} + \bar{v}_{,x}\bar{v}_{,y} + \bar{w}_{,x}\bar{w}_{,y}\right), \quad (7)$$

$$\gamma_{yz} = 2\varepsilon_{yz} = \left(\bar{w}_{,y} + \bar{v}_{,z}\right) + \left(\bar{u}_{,y}\bar{u}_{,z} + \bar{v}_{,y}\bar{v}_{,z} + \bar{w}_{,y}\bar{w}_{,z}\right), \quad (8)$$

$$\gamma_{zx} = 2\varepsilon_{zx} = (\bar{u}_{,z} + \bar{w}_{,x}) + (\bar{u}_{,z}\bar{u}_{,x} + \bar{v}_{,z}\bar{v}_{,x} + \bar{w}_{,z}\bar{w}_{,x}). \quad (9)$$

Assuming that the strains are small, the terms $(\bar{u}_{,x})^2$, ε_{zz}, $\bar{u}_{,x}\bar{u}_{,z}$ are negligible compared to $u_{,x}$ (Reddy, 2005a) and substituting the displacement components from Equations (1)–(3) to the strain-displacement relations (4)–(9) the only non-vanishing component of the strain tensor is

$$\varepsilon_{xx}(x,z) = u_{,x} + \frac{1}{2}(w_{,x})^2 - zw_{,xx}. \quad (10)$$

Furthermore, the only non-vanishing stress component of the second Piola-Kirchhoff stress tensor is

$$S_{xx} = E\varepsilon_{xx}. \quad (11)$$

Governing Equations of the Problem and Boundary Conditions

To establish the equations of equilibrium of the beam, the principle of minimum total potential energy is employed. To this end, the total potential energy of the elastic beam is

$$\Pi(u,w) = U + V, \quad (12)$$

where U, V are the strain energy of the beam and the potential of the external forces, respectively. The strain energy per unit volume is given by the integral

$$U_o = \int_0^{\varepsilon_{xx}} S_{xx} d\varepsilon_{xx} = \int_0^{\varepsilon_{xx}} E\varepsilon_{xx} d\varepsilon_{xx} = \frac{1}{2}E\varepsilon_{xx}^2, \quad (13)$$

and the total strain energy of the beam is

$$U = \int_V U_o dV = \int_V \frac{1}{2}E\varepsilon_{xx}^2 dV. \quad (14)$$

The potential of the external forces applied to the beam is equivalent to the work done on the beam by them

$$V = \int_0^l \left[-p_x u - p_z w\right] dx. \quad (15)$$

The stress resultants, namely the axial force N and the bending moment M are defined as

$$N = \int_A S_{xx} dA \quad M = \int_A S_{xx} z dA. \quad (16)$$

According to the principle of minimum total potential energy, the first variation of the total potential energy of the beam must be equal to zero

$$\delta\Pi = \delta U + \delta V = 0. \quad (17)$$

Substituting Equations (14), (15) in Equation (17) and by virtue of Equations (10), (11), (16) leads to

$$\int_0^l \{N\left[(\delta u)_{,x} + w_{,x}(\delta w)_{,x}\right] - M(\delta w)_{,x}\} + \int_0^l \left(-p_x\delta u - p_z\delta w\right) dx = 0. \quad (18)$$

By applying the Gauss-Green theorem (integration by parts) and collecting the coefficients δu and δw, we obtain

$$\int_0^l \left\{\left(-N_{,x} - p_x\right)\delta u + \left[-(Nw_{,x})_{,x} - M_{,xx} - p_z\right]\delta w\right\} dx + \left[N\delta u + (Nw_{,x} + M_{,x})\,\delta w + M\delta(w_{,x})\right]_0^l = 0 \quad (19)$$

Since δu, δw are arbitrary and independent of each other in the interval $(0, l)$, by virtue of the fundamental lemma of calculus of variations the governing equations become

$$-N_{,x} - p_x(x) = 0, \quad (20)$$

$$-(Nw_{,x})_{,x} - M_{,xx} - p_z(x) = 0. \quad (21)$$

In case the stress-strain relation is a known function, and analytical integration can be performed on Equation (16), then with respect to Equation (10) the stress resultants in terms of the displacements are written as

$$N = EA\left[u_{,x} + \frac{1}{2}(w_{,x})^2\right], \quad (22)$$

$$M = -EIw_{,xx}. \quad (23)$$

Using Equations (22), (23) the governing equations take the form

$$\left[EA\left(u_{,x} + \tfrac{1}{2}w_{,x}^2\right)\right]_{,x} = -p_x(x), \quad (24)$$

$$-(EIw_{,xx})_{,xx} + \left[EA\left(u_{,x} + \tfrac{1}{2}w_{,x}^2\right)w_{,x}\right]_{,x} = -p_z(x). \quad (25)$$

Examining now the boundary terms of Equation (19), we conclude that (Reddy, 2005b):

- δu, δw, $\delta w_{,x}$ are the primary variables, and their specification constitutes the essential boundary conditions of the problem.
- N, $Nw_{,x} + M_{,x}$, M are the secondary variables, and their specification constitutes the natural boundary conditions of the problem.

Among the values comprising the pairs (u, N), $(w, Nw_{,x} + M_{,x})$, $(w_{,x}, M)$ only one can be prescribed.

Moreover, the boundary conditions of the problem can be written as (Katsikadelis and Tsiatas, 2003)

$$a_1 u(0) + a_2 N(0) = a_3, \quad (26)$$

$$\overline{a_1} u(l) + \overline{a_2} N(l) = \overline{a_3}, \quad (27)$$

$$\beta_1 w(0) + \beta_2 (Nw_{,x} + M_{,x})(0) = \beta_3, \quad (28)$$

$$\overline{\beta_1} w(l) + \overline{\beta_2} (Nw_{,x} + M_{,x})(l) = \overline{\beta_3}, \quad (29)$$

$$\gamma_1 w_{,x}(0) + \gamma_2 M(0) = \gamma_3, \tag{30}$$

$$\overline{\gamma_1} w_{,x}(l) + \overline{\gamma_2} M(l) = \overline{\gamma_3}, \tag{31}$$

where α_κ, $\bar{\alpha}_\kappa$, β_κ, $\overline{\beta}_\kappa$, γ_κ, $\overline{\gamma}_\kappa$ ($\kappa = 1, 2, 3$) are known constants. In Equations (26)–(31) the most general boundary conditions of the problem are described. It is worth noting that they include the case of elastic support of the beam, as well.

Equations (20), (21) in terms of stress resultants or (24), (25) in terms of displacements, along with Equations (26)–(31) constitute the boundary value problem that describes the nonlinear bending of the beam. Analytical solution of the problem is somewhat cumbersome, so a numerical scheme has to be introduced.

NUMERICAL FORMULATION

The AEM Solution

A direct solution to the boundary value problem described by the coupled Equations (24) and (25) together with the boundary conditions (26)–(31) is achieved on the basis of the AEM formulation for the large deflection analysis of beams of variable stiffness as developed in Katsikadelis and Tsiatas (2003). Briefly discussed, let $u = u(x)$ and $w = w(x)$ be the sought solutions of the problem, having continuous derivatives up to the 2nd and 4th order respectively in $(0, L)$. According to the analog equation principle, the two coupled nonlinear equations can be substituted by the following analog equations

$$u_{,xx} = b_1(x), \tag{32}$$

$$w_{,xxxx} = b_2(x), \tag{33}$$

applying the linear differential operators of the second and fourth order respectively to $u = u(x)$ and $w = w(x)$. Both operators have known fundamental solutions. It is noteworthy that Equations (32) and (33) are attributed independently to the linear response of a beam of constant unit stiffness under the fictitious loads b_1 and b_2 for the axial and bending problem respectively. According to the AEM, the solution of the system of Equations (24) and (25) can be achieved by solving the uncoupled system of Equations (32) and (33) under the same boundary conditions (26)–(31), after the determination of the fictitious load distributions b_1, b_2. Accordingly, a procedure can be developed by the integral equation method. In this sense, the integral representations of the solutions of Equations (32) and (33) take the following form

$$u(x) = c_1 x + c_2 + \int_0^l G_1(x,\xi)\, b_1(\xi)\, d\xi, \tag{34}$$

$$w(x) = c_3 x^3 + c_4 x^2 + c_5 x + c_6 + \int_0^l G_2(x,\xi)\, b_2(\xi)\, d\xi, \tag{35}$$

where c_i ($i = 1, 2, \ldots 6$) are arbitrary integration constants that will be determined from the boundary conditions and

$$G_1 = \tfrac{1}{2}|x-\xi|, \tag{36}$$

$$G_2 = \tfrac{1}{12}|x-\xi|(x-\xi)^2, \tag{37}$$

are the fundamental solutions (free space Green's functions) of Equations (32) and (33), respectively.

By direct differentiation of Equations (34) and (35) the derivatives of u and w can be obtained as

$$u_{,x}(x) = c_1 + \int_0^l G_{1,x}(x,\xi)\, b_1(\xi)\, d\xi, \tag{38}$$

$$u_{,xx}(x) = b_1(x), \tag{39}$$

$$w_{,x}(x) = 3c_3 x^2 + 2c_4 x + c_5 + \int_0^l G_{2,x}(x,\xi)\, b_2(\xi)\, d\xi, \tag{40}$$

$$w_{,xx}(x) = 6c_3 x + 2c_4 + \int_0^l G_{2,xx}(x,\xi)\, b_2(\xi)\, d\xi, \tag{41}$$

$$w_{,xxx}(x) = 6c_3 + \int_0^l G_{2,xxx}(x,\xi)\, b_2(\xi)\, d\xi, \tag{42}$$

$$w_{,xxxx}(x) = b_2(x). \tag{43}$$

Substituting Equations (38)–(43) into Equations (24) and (25) they can be written in terms of the unknown fictitious sources b_1 and b_2.

The next step of the AEM requires the discretization of the domain $(0, L)$ into N elements, not necessarily equal. On each element the variation of each fictitious load b_1 and b_2 is approximated by a predefined law (constant, linear, parabolic, etc.). In what follows, the elements are considered equal and the constant law is adopted (constant elements).

Subsequently, the integral representation of Equations (34) and (35) can be written in matrix form as

$$u(x) = \mathbf{H}_1(x)\mathbf{c}_1 + \mathbf{G}_1(x)\mathbf{b}_1, \tag{44}$$

$$w(x) = \mathbf{H}_2(x)\mathbf{c}_2 + \mathbf{G}_2(x)\mathbf{b}_2, \tag{45}$$

where $\mathbf{G}_1(x)$ and $\mathbf{G}_2(x)$ are $1 \times N$ known matrices obtained by integrating the kernels $G_1(x,\xi)$ and $G_2(x,\xi)$ on the constant elements, respectively; $\mathbf{H}_1(x) = \begin{bmatrix} x & 1 \end{bmatrix}$ and $\mathbf{H}_2(x) = \begin{bmatrix} x^3 & x^2 & x & 1 \end{bmatrix}$; $\mathbf{c}_1 = \{c_1, c_2\}^T$; $\mathbf{c}_2 = \{c_3, c_4, c_5, c_6\}^T$; $\mathbf{b}_1$, $\mathbf{b}_2$ are vectors containing unknown fictitious loadings at the N nodes. Likewise, Equations (38)–(43) can be written as

$$u_{,x}(x) = \mathbf{H}_{1x}(x)\mathbf{c}_1 + \mathbf{G}_{1x}(x)\mathbf{b}_1, \tag{46}$$

$$u_{,xx}(x) = \mathbf{b}_1, \tag{47}$$

$$w_{,x}(x) = \mathbf{H}_{2x}(x)\mathbf{c}_2 + \mathbf{G}_{2x}(x)\mathbf{b}_2, \tag{48}$$

$$w_{,xx}(x) = \mathbf{H}_{2xx}(x)\mathbf{c}_2 + \mathbf{G}_{2xx}(x)\mathbf{b}_2, \tag{49}$$

$$w_{,xxx}(x) = \mathbf{H}_{2xxx}(x)\mathbf{c}_2 + \mathbf{G}_{2xxx}(x)\mathbf{b}_2, \tag{50}$$

$$w_{,xxxx}(x) = \mathbf{b}_2, \tag{51}$$

where $\mathbf{G}_{1x}(x)$, $\mathbf{G}_{2xx}(x)$,… $\mathbf{G}_{2xxx}(x)$ are $1 \times N$ known matrices, stemming from the integration of the derivatives of the kernels $G_1(x,\xi)$, $G_2(x,\xi)$ on the elements; $\mathbf{H}_{1x}(x)$ is a 1×2 known matrix resulting from the differentiation of $\mathbf{H}_1(x)$, whereas $\mathbf{H}_{2x}(x)$, $\mathbf{H}_{2xx}(x)$, $\mathbf{H}_{2xxx}(x)$ are 1×4 known matrices resulting from the differentiation of $\mathbf{H}_2(x)$.

The final step of the AEM is the collocation of the Equations (24) and (25) at the N internal nodal points and the substitution of the displacements and their derivatives according to the Equations (44)–(51)

$$\mathbf{F}_1(\mathbf{b}_1, \mathbf{b}_2, \mathbf{c}) = -\mathbf{p}_x, \tag{52}$$

$$\mathbf{F}_2(\mathbf{b}_1, \mathbf{b}_2, \mathbf{c}) = -\mathbf{p}_z, \tag{53}$$

where $\mathbf{F}_i(\mathbf{b}_1, \mathbf{b}_2, \mathbf{c})$ are generalized stiffness vectors, and $\mathbf{c} = \{c_1, c_2, \ldots c_6\}^T$. Equations (52) and (53) constitute a system of $2N$ nonlinear algebraic equations of $2N + 6$ unknowns. The additional six equations required to solve the system can be derived from the exploitation of the boundary conditions of the problem. To this end, the related derivatives are substituted into Equations (26)–(31) to give

$$\mathbf{f}_i(\mathbf{b}_1, \mathbf{b}_2, \mathbf{c}) = \mathbf{0} \quad (i = 1, 2, \ldots 6). \tag{54}$$

The nonlinear Equations (52)–(53) in combination with the Equations (54) constitute a system of $2N + 6$ algebraic equations with respect to the unknown vectors $\mathbf{b}_1, \mathbf{b}_2$ and $\mathbf{c}$. The solution of the system by any numerical technique provides the values of the fictitious loads at the internal nodal points.

However, when the stress resultants and their derivatives cannot be evaluated analytically, the following layered analysis should be employed.

The Layered Analysis

As a first step to the layered analysis, an appropriate number of monitoring cross-sections is defined along the length of the beam. For convenience purposes, the position of each cross-section coincides with the nodal points of the longitudinal discretization and the two points that correspond to the ends of the beam. Consequently, each cross-section is decomposed into a number of layers of constant height. At the center of each layer, the strain is expressed in terms of the nodal displacement components. Next, given the strain expressions, stresses are computed and employing an appropriate integration scheme, stress resultants are evaluated. The discretization scheme is depicted in **Figure 2**.

An odd number of layers k is selected so as the center of the beam's cross-section is located at the middle of the $(k+1)/2$ layer. The constant height of the layers is Δh. The z coordinate of the center of the i-th layer is written as

$$z_i = \left(\frac{k+1}{2} - i\right)\Delta h. \tag{55}$$

The axial force N_i and the bending moment M_i for each layer can be computed as

$$N_i = S^i_{xx}\Delta A_i, \tag{56}$$

$$M_i = S^i_{xx} z_i \Delta A_i, \tag{57}$$

where S^i_{xx}, ΔA_i are the stress component at the center of each layer and the area of each layer respectively. Therefore, the stress resultants can be approximated as

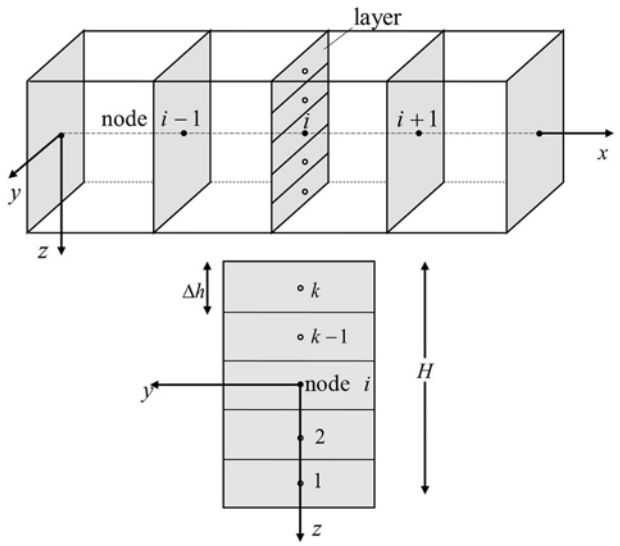

FIGURE 2 | Discretization of the beam into monitoring cross-sections and cross-section layers.

$$N = \sum_{i=0}^{k} S^i_{xx}\Delta A, \tag{58}$$

$$M = \sum_{i=0}^{k} S^i_{xx} z_i \Delta A_i. \tag{59}$$

After evaluating the axial force and the bending moment at each nodal point, their derivatives must be computed to check if the equations of equilibrium hold. To this end, the procedure thoroughly described in Tsiatas and Charalampakis (2017) is adopted.

Having established the numerical expressions of the stress resultants and their derivatives in terms of the unknown fictitious loads, the nonlinear Equations (52)–(54) are solved iteratively. The first iteration starts with an initial guess for the unknown fictitious loads. Next, the displacements and their derivatives are evaluated at all the defined monitoring cross-sections of the beam using the respective integral representations. Subsequently, the stress resultants are computed at each layer using Equations (56), (57) and the whole cross-section by applying Equations (58), (59). Lastly, the governing Equations (20) and (21) are checked for equilibrium. In case the equilibrium is satisfied, the process is terminated. Otherwise, the fictitious load distributions are updated, and the procedure continues with further iterations.

NUMERICAL EXAMPLES

Based on the presented numerical procedure, a computer program has been developed, and representative examples have been studied to demonstrate the accuracy and the efficiency of the proposed method of nonlinear analysis.

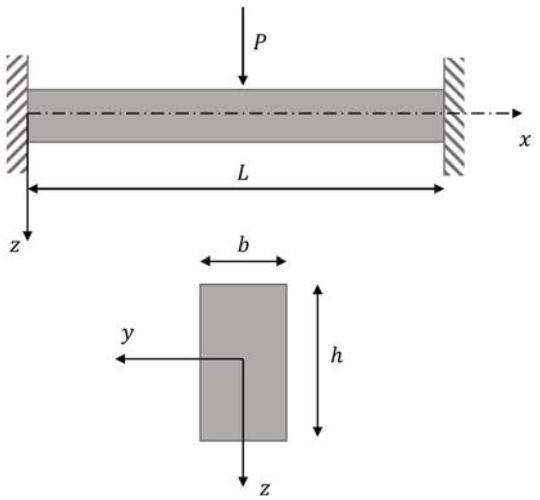

FIGURE 3 | Fixed beam in Example 1.

Example 1: Beam With Fixed Ends Under Concentrated Loading

The first example deals with the geometrical nonlinear static analysis of a fully fixed beam under concentrated loading applied at the midspan. The cross-section of the beam is rectangular $b \times h$ and its length is L. The geometrical characteristics of the beam and the cross-section are shown in **Figure 3**. The beam is made of a linearly elastic material. The employed data for the elastic properties of the material and the geometry of the beam are: $E = 2.07 \times 10^8 kN/m^2$, $b = 0.0254\,m$, $h = 0.003175\,m$, and $L = 0.508\,m$.

The present example has been also examined in the studies of Katsikadelis and Tsiatas (2003) and Mondkar and Powell (1977). It is noted that in the study of Katsikadelis and Tsiatas (2003) a BEM scheme for the longitudinal problem is also established, but an analytical procedure to obtain the stress resultants is adopted. Furthermore, Mondkar and Powell (1977) modeled the half of the beam using five eight-node plane stress elements and applied a 2×2 Gauss quadrature. Results from both these works are used herein for comparison purposes.

Figures 4A,B show the profiles for the vertical and horizontal displacements respectively, corresponding to load value $P_z = 3.11kN$. The results of the proposed method are compared with those presented by Katsikadelis and Tsiatas (2003); it can be seen that they are in excellent agreement. In **Figure 5**, the variation of vertical displacements w at the middle of the beam with respect to the force P_z is presented for the layered approach as well as for both the references above; the identification of the results is noteworthy. In **Table 1**, deflections at the middle of the beam length are presented for several numbers of longitudinal elements and layers; it can be observed that satisfactory convergence can be achieved for a small number of layers. Finally, **Figures 6A–C** depict the bending, axial, and shear stress resultants respectively.

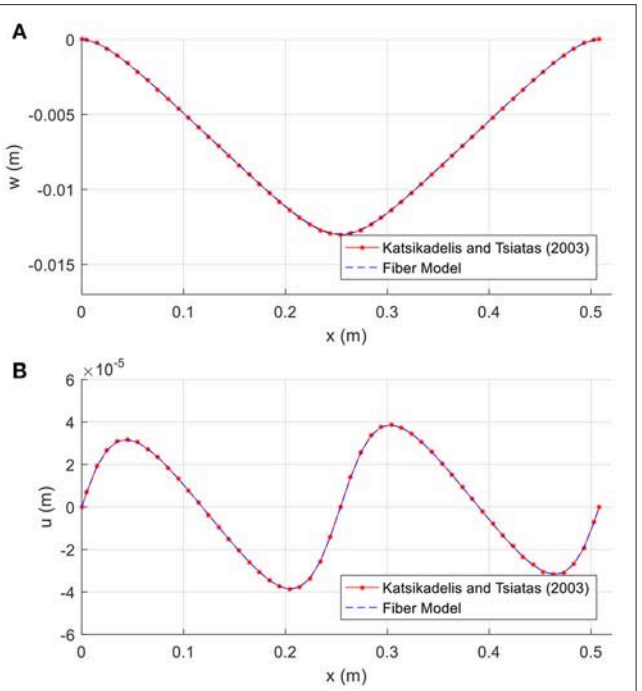

FIGURE 4 | Profiles of the **(A)** deflection and **(B)** axial displacement in Example 1.

TABLE 1 | Deflection at the midspan in Example 1.

Number of Fibers k	Number of beam elements N				
	31	41	51	61	71
	Deflection at the midspan				
5	−0.012828	−0.012945	−0.013008	−0.013047	−0.013073
7	−0.012817	−0.012933	−0.012996	−0.013035	−0.013060
9	−0.012813	−0.012928	−0.012991	−0.013029	−0.013055
11	−0.012810	−0.012926	−0.012989	−0.013027	−0.013052
13	−0.012809	−0.012925	−0.012987	−0.013025	−0.013050
15	−0.012808	−0.012924	−0.012986	−0.013024	−0.013049
17	−0.012808	−0.012923	−0.012986	−0.013024	−0.013049
19	−0.012808	−0.012923	−0.012985	−0.013023	−0.013048
21	−0.012807	−0.012922	−0.012985	−0.013023	−0.013048
23	−0.012807	−0.012922	−0.012985	−0.013023	−0.013048
25	−0.012807	−0.012922	−0.012985	−0.013023	−0.013048

Example 2: Simply Supported Beam Made of Nonlinear Material

For comparison reasons, in the second example an initially straight beam made of a nonlinear elastic material is examined. The cross-section of the beam is rectangular $b \times h$ and its length is L. It is pinned at its both ends and is subjected to a uniformly distributed vertical load p_z. The employed geometrical data, as shown in **Figure 7**, is: $b = 0.10\,m$, $h = 0.50\,\text{m}$, $L = 2.0\,\text{m}$. The constitutive law of the nonlinear elastic material is given by the

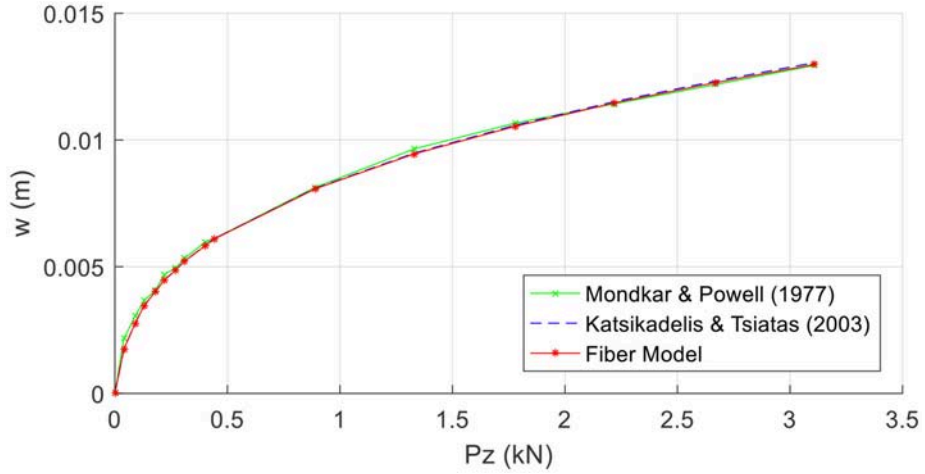

FIGURE 5 | Deflection versus Load at the center of the beam in Example 1.

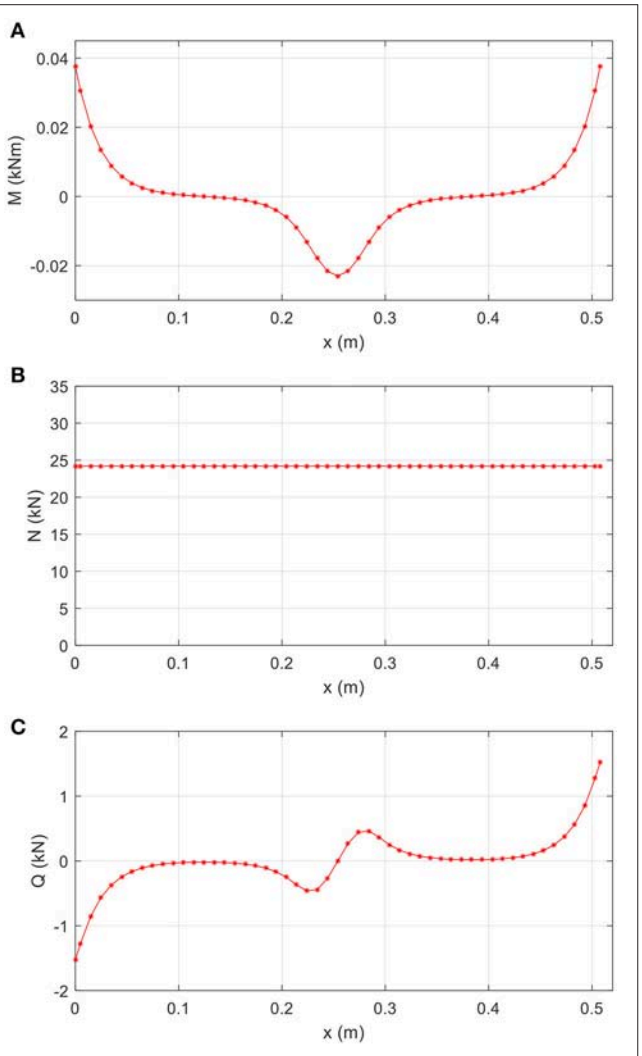

FIGURE 6 | Profile of the **(A)** bending moment, **(B)** axial force, and **(C)** shear force in Example 1.

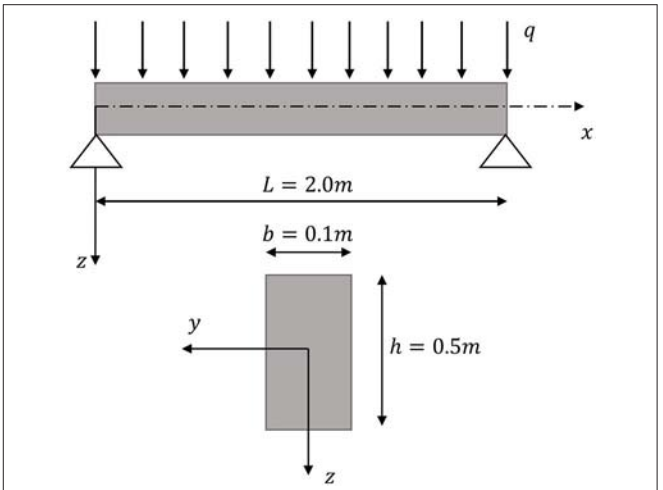

FIGURE 7 | Simply supported beam in Example 2.

relation

$$\sigma = \sigma_0 \frac{\varepsilon}{\sqrt{\varepsilon^2 + \varepsilon_0^2}}, \tag{60}$$

where $\sigma_0 = 410000$ kPa, $\varepsilon_0 = 0.017143512$. The stress-strain curve is depicted in **Figure 8**. In this example, the geometrical nonlinear effect is not considered.

In the context of the presented layered methodology, static geometrical linear-material nonlinear analyses are performed for several loading values. The beam length is discretized into 51 elements, and the cross-section is decomposed into 21 layers. The obtained results are compared with corresponding results obtained from two FEM models: (i) a FEM model with 51 beam elements, and (ii) a solid FEM model comprising 12500 hexahedral 8-node elements.

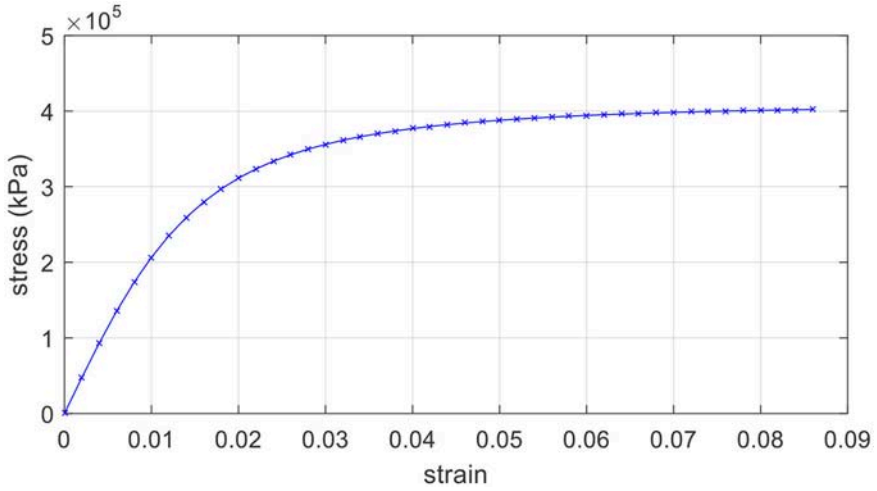

FIGURE 8 | Stress-strain curve for the nonlinear material in Example 2.

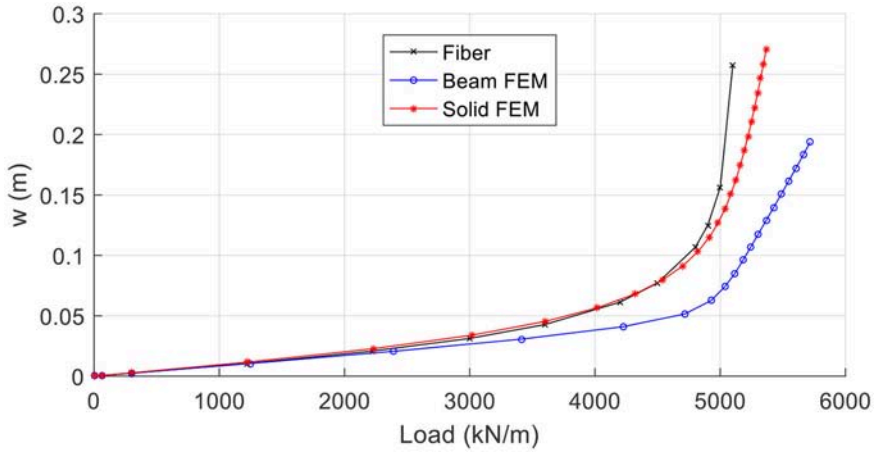

FIGURE 9 | Deflection at the middle of the beam vs. load in Example 2.

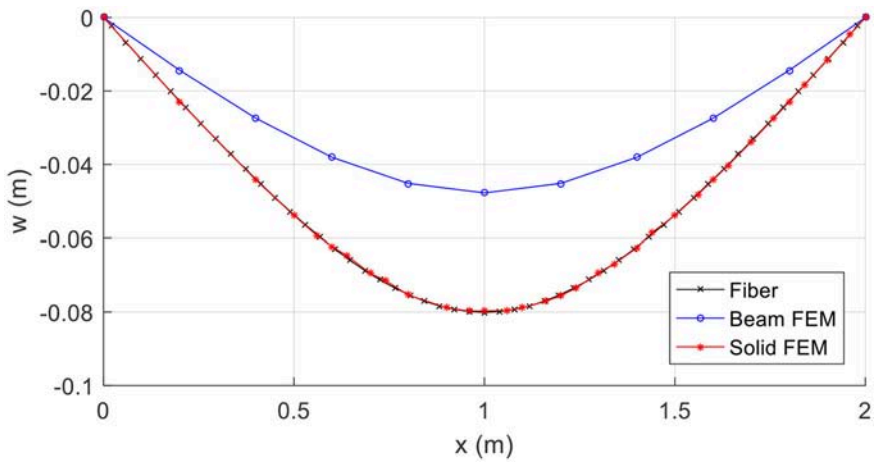

FIGURE 10 | Profile of deflections for $p_z = 4541.42$kN/m in Example 2.

Figure 9 presents the vertical deflections at the middle of the beam versus the vertical load p_z. It can be readily observed that the layered model satisfactorily converges to the solid FEM solution, while the beam FEM solution exhibits significant discrepancies for a relatively low value of loading. In **Figure 10** the deflection profile for $p_z = 4541.42$kN/m is shown. It is remarkable that the layered analysis yields deflections along the beam that are in excellent agreement with the ones obtained from the solid model.

Example 3: Shape Memory Alloy Beam Under Concentrated Loading

In order to demonstrate the range of applications of the proposed methodology of analysis, in this final example, an initially straight clamped beam made of a superelastic Shape Memory Alloy (SMA) is considered. One of the most important mechanical property of SMAs is that they can undergo large inelastic strains recoverable upon load removal (Superelasticity). The SMA's stress-strain relation adopted herein was obtained by interpolating the experimental curve presented in Charalampakis and Tsiatas (2018).

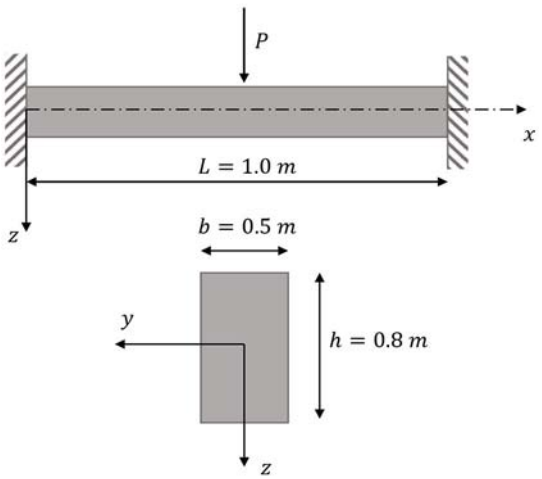

FIGURE 11 | Fixed beam in Example 3.

The beam under consideration has a uniform rectangular cross-section $b \times h$, and length L, as shown in **Figure 11**. It is fixed at its both ends and is subjected to a concentrated vertical load P_z at the middle of its length. The geometrical data is: $b = 0.50\,m$, $h = 0.80$ m, and $L = 1.0$ m. The beam is divided into 51 elements along its length, and the cross-section is discretized into 21 layers.

In this example two cases of analysis are performed, for several loading values: (i) geometrical linear analysis, and (ii) geometrical nonlinear analysis. It is noted that material nonlinearity is taken into account in both cases, and the stress-strain relation is depicted in **Figure 12**. In **Figure 13**, the deflections at the midspan vs. the loading variation are presented for both cases of analysis. The effect of geometrical nonlinearity in the decrease of the central deflection for a specific loading range is verified. This effect can also be verified in the comparison of the stress resultants. More specifically, **Figure 14A** shows the bending moment profiles ($P_z = 400kN$) where it can be readily observed the decrease of the bending moment, in case of the geometrical nonlinear case, due to the contribution of the axial forces to the loading carriage. Finally, **Figure 14B** shows the axial force profile ($P_z = 400kN$) only for the geometrical nonlinear case since in the geometrical linear analysis the axial force is zero.

CONCLUSIONS–FUTURE RESEARCH

In this work, a layered approach to the nonlinear analysis of beams has been presented. The beam is studied considering both geometrical and material nonlinearity. The governing differential equations were obtained with a variational approach and their system was solved using the AEM in conjunction with an iterative numerical process. To this end, a discretization scheme was

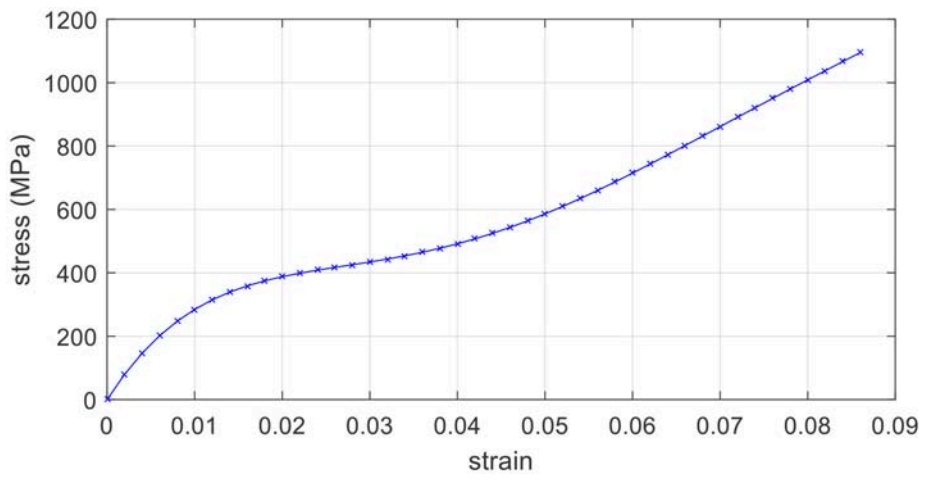

FIGURE 12 | Stress-strain curve for the nonlinear SMA material in Example 3.

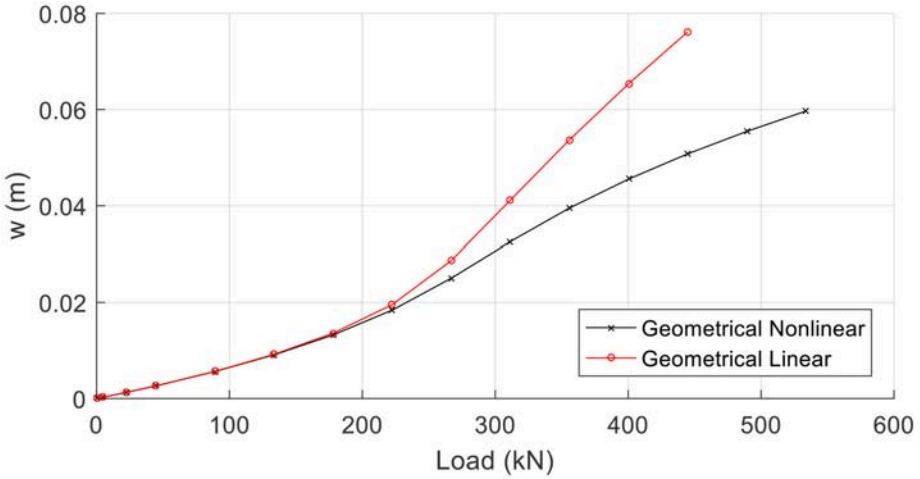

FIGURE 13 | Deflection at the middle of the beam vs. load in Example 3.

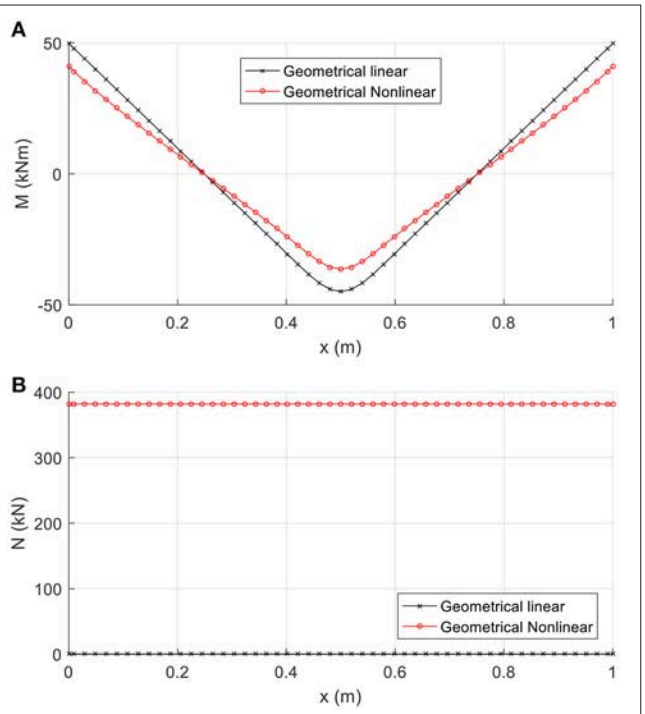

FIGURE 14 | Profile of the **(A)** bending moment, and **(B)** axial force, for $P_Z = 400kN$ in Example 3.

established in both the longitudinal sense and the cross-sectional plane. According to the presented analysis and the numerical results, the following main conclusions can be drawn:

a) The layered method has proven to be very competent and together with the AEM can be employed in the solution of difficult nonlinear coupled problems.
b) The method can treat both geometrical and material nonlinearity in a more general context, as compared to existing direct solution methods which are confined only to handling geometrical nonlinearity.
c) The numerical solution is efficient and stable, while a small number of line elements and layers are adequate to achieve significant accuracy for the displacements and the stress resultants.
d) In comparison with the FEM beam model, the layered approach model is capable of giving results that better converge to the ones obtained by a FEM solid model.
e) The proposed layered approach can be easily extended to solve problems of curved beams, as well as beams with arbitrary cross-sections.
f) Furthermore, the limitation of the number of monitoring cross-sections only in locations of high-stress concentration (e.g., beam supports) can be considered as a future application of the layered approach.

AUTHOR CONTRIBUTIONS

GT had the research idea, contributed to the theoretical analysis, and interpretation of the results. AS drafted the article, and contributed to the derivation of the numerical examples. ES supervised the research. All the authors contributed to the writing of the manuscript.

REFERENCES

Argyris, J. H., Dunne, P. C., Malejannakis, G., and Scharpf, D. W. (1978a). On large displacement - small strain analysis of structures with rotational degrees of freedom. *Comput. Methods Appl. Mech. Eng.* 15, 99–135. doi: 10.1016/0045-7825(78)90008-7

Argyris, J. H., Dunne, P. C., Malejannakis, G., and Scharpf, D. W. (1978b). On large displacement - small strain analysis of structures with rotational

degrees of freedom. *Comput. Methods Appl. Mech. Eng.* 14, 401–451. doi: 10.1016/0045-7825(78)90076-2

Argyris, J. H., Hilpert, G. A., Malejannakis, G., and Scharpf, D. W. (1979). On the geometrical stiffness of a beam in space. a consistent V. W. approach. *Comput. Methods Appl. Mech. Eng.* 20, 105–131. doi: 10.1016/0045-7825(79)90061-6

Banerjee, P. K., and Butterfield, R. (1981). *Boundary Element Methods in Engineering Sciences.* London: Mc Graw - Hill.

Bathe, K. J., and Bolourchi, S. (1979). Large displacement analysis of three-dimensional beam structures. *Int. J. Numer Methods Eng.* 14, 961–986. doi: 10.1002/nme.1620140703

Becker, A. A. (1992). *The Boundary Element Method in Engineering: A Complete Course*. New York, NY: Mc Graw - Hill.

Cai, Y., Paik, J. K., and Atluri, S. N. (2009). Large deformation analyses of space - frame structures, with members of arbitrary cross-section, using explicit tangent stiffness matrices, based on a Von Karman type nonlinear theory in rotated reference frames. *Comput. Model. Eng. Sci.* 53, 117–145. doi: 10.3970/cmes.2009.053.123

Charalampakis, A. E., and Tsiatas, G. C. (2018). A simple rate-independent Uniaxial Shape Memory Alloy (SMA) model. *Front. Built Environ.* 4:46. doi: 10.3389/fbuil.2018.00046

Filippou, F. C., Taucer, F. F., and Spacone, E. (1991). *A Fiber Beam Column Element for Seismic Response Analysis of Reinforced Concrete Structures.* EERC Report 91/17, UC Berkeley, Earthquake Engineering Research Center.

Hodges, D. H. (2006). "Progress in astronautics and aeronautics," in *Nonlinear Composite Beam Theory* (Reston, VA: AIAA). doi: 10.2514/4.866821

Izzuddin, B. A., Siyam, A. F., and Lloyd Smith, D. (2002). An efficient beam-column formulation for 3D reinforced concrete frames. *Comput. Struct.* 80, 659–676. doi: 10.1016/S0045-7949(02)00033-0

Kaba, S., and Mahin, S. A. (1984). *Refined Modeling of Reinforced Concrete Columns for Seismic Analysis.* EERC Report 84/03, UC Berkeley, Earthquake Engineering Research Center.

Katsikadelis, J. T. (2016). *The Boundary Element Method for Engineers and Scientists.* Oxford: Academic Press, Elsevier.

Katsikadelis, J. T., and Tsiatas, G. C. (2003). Large deflection analysis of beams with variable stiffness. *Acta Mech.* 164, 1–13. doi: 10.1007/s00707-003-0015-8

Katsikadelis, J. T., and Tsiatas, G. C. (2004). Nonlinear dynamic analysis of beams with variable stiffness. *J. Sound Vib.* 270, 847–863. doi: 10.1016/S0022-460X(03)00635-7

Mondkar, D. P., and Powell, G. H. (1977). Finite element analysis of nonlinear static and dynamic response. *Int. J. Numer. Methods Eng.* 11, 499–520. doi: 10.1002/nme.1620110309

Plevris, V., and Tsiatas, G. C. (2018). Computational structural engineering: past achievements and future challenges. *Front. Built Environ.* 4:21. doi: 10.3389/fbuil.2018.00021

Providakis, C. P., and Beskos, D. E. (1986). Dynamic analysis of beams by the boundary element methods. *Comput. Struct.* 22, 957–964. doi: 10.1016/0045-7949(86)90155-0

Reddy, J. N. (2005a). *An Introduction to Nonlinear Finite Element Analysis.* New York, NY: Oxford University Press.

Reddy, J. N. (2005b). *An Introduction to the Finite Element Method, 3rd Edn*. New York, NY: Mc Graw - Hill.

Sapountzakis, E. J., and Dikaros, I. C. (2011). Nonlinear Flexural-Torsional dynamic analysis of beams of arbitrary cross section by BEM. *Int. J. Non Linear Mech.* 46, 782–794. doi: 10.1016/j.ijnonlinmec.2011.02.012

Sapountzakis, E. J., and Dourakopoulos, J. A. (2010). Flexural-Torsional nonlinear analysis of Timoshenko beam-column of arbitrary cross section by BEM. *Comput. Mater. Continua* 18, 121–153. doi: 10.3970/cmc.2010.018.121

Sapountzakis, E. J., and Kampitsis, I. C. (2017). Dynamic analysis of beam-soil interaction systems with material and geometrical nonlinearities. *Int. J. Non Linear Mech.* 90, 82–89. doi: 10.1016/j.ijnonlinmec.2017.01.007

Sapountzakis, E. J., and Mokos, V. G. (2008). Shear deformation effect in nonlinear analysis of spatial beams. *Eng. Struct.* 30, 653–663. doi: 10.1016/j.engstruct.2007.05.004

Sapountzakis, E. J., and Panagos, D. G. (2008). Nonlinear analysis of beams of variable cross section including shear deformation effect. *Arch. Appl. Mech.* 78, 687–710. doi: 10.1007/s00419-007-0182-5

Taylor, G. A. (1996). *A Vertex Based Discretization Scheme Applied to Material Non-Linearity Within a Multiphysics Finite Volume Framework*. London: University of Greenwich.

Tsiatas, G. C. (2010). Nonlinear analysis of non-uniform beams on nonlinear elastic foundation. *Acta Mech.* 209, 141–152. doi: 10.1007/s00707-009-0174-3

Tsiatas, G. C., and Charalampakis, A. E. (2017). Optimizing the natural frequencies of axially functionally graded beams and arches. *Composite Struct.* 160, 256–266. doi: 10.1016/j.compstruct.2016.10.057

Tsiatas, G. C., Siokas, A. G., and Sapountzakis, E. J. (2018). "A fiber approach to the large deflections analysis of beams by BEM," in *9th GRACM, International Congress on Computational Mechanics* (Chania).

Yang, Y., and McGuire, W. (1986). Stiffness matrix for geometric nonlinear analysis. *J. Struct. Eng. ASCE* 112, 853–877. doi: 10.1061/(ASCE)0733-9445(1986)112:4(853)

Zbiciak, A. (2010). Dynamic analysis of pseudoelastic SMA beam. *Int. J. Mech. Sci.* 52, 56–64. doi: 10.1016/j.ijmecsci.2009.10.003

Conflict of Interest Statement: The authors declare that the research was conducted in the absence of any commercial or financial relationships that could be construed as a potential conflict of interest.

frontiers in Built Environment

ORIGINAL RESEARCH
published: 22 October 2018
doi: 10.3389/fbuil.2018.00055

Integrated Reverse Engineering Strategy for Large-Scale Mechanical Systems: Application to a Steam Turbine Rotor

Alexandros Arailopoulos, Dimitrios Giagopoulos, Ilias Zacharakis and Eleni Pipili*

Department of Mechanical Engineering, University of Western Macedonia, Kozani, Greece

OPEN ACCESS

Edited by:
Vagelis Plevris, OsloMet – Oslo Metropolitan University, Norway

Reviewed by:
Alfredo Raúl Carella, OsloMet – Oslo Metropolitan University, Norway
Manolis S. Georgioudakis, National Technical University of Athens, Greece

****Correspondence:***
Dimitrios Giagopoulos
dgiagopoulos@uowm.gr

Specialty section:
This article was submitted to Computational Methods in Structural Engineering, a section of the journal Frontiers in Built Environment

Received: *08 May 2018*
Accepted: *24 September 2018*
Published: *22 October 2018*

Citation:
Arailopoulos A, Giagopoulos D, Zacharakis I and Pipili E (2018) Integrated Reverse Engineering Strategy for Large-Scale Mechanical Systems: Application to a Steam Turbine Rotor. Front. Built Environ. 4:55. doi: 10.3389/fbuil.2018.00055

An integrated reverse engineering methodology is proposed for a large-scale fully operational steam turbine rotor, considering issues that include developing the CAD and FE model of the structure, as well as the applicability of model updating techniques based on experimental modal analysis procedures. First, using an integrated reverse engineering strategy, the digital shape of the three sections of a steam turbine rotor was designed and the final parametric CAD model was developed. The finite element model of the turbine was developed using tetrahedral solid elements resulting in fifty-five million DOFs. Imposing impulsive loading in a free-free state, measured acceleration time histories were used to obtain the dynamic responses and identify the modal characteristics of each section of the complete steam turbine. Experimentally identified modal modes and modal frequencies compared to the FE model predicted ones constitute the actual measure of fit. CMA-ES optimization algorithm is then implemented in order to finely tune material parameters, such as modulus of elasticity and density, in order to best match experimental and numerical data. Comparing numerical and experimental results verified the reliability and accuracy of the applied methodology. The identified finite element model is representative of the initial structural condition of the turbine and is used to develop a simplified finite element model, which then used for the turbine rotordynamic analysis. Accumulated knowledge of the dynamic behavior of the specific steam turbine system, could be implemented in order to evaluate stability or instability states, fatigue growth in the turbine blades, changes in the damping of the bearing system and perform necessary scheduled optimal and cost-effective maintenance strategies. Additionally, upon a series of scheduled experimental data collection, a permanent output-only vibration SHM system could be installed and even a proper dynamic balancing could be investigated and designed.

Keywords: integrated reverse engineering, system identification, large scale models, FE model updating, rotordynamic analysis

INTRODUCTION

The largest proportion of electricity worldwide is produced using some kind of turbine (Steam, Hydro, Nuclear, etc.) As large density of energy flows through the turbines, the rotation speeds are extremely high, large inertia loads are developed, shaft and blade deform extensively, blades corrode and high levels of vibration occur, all leading to strong dynamic instabilities (Bavastri et al., 2008). Instability problems of turbines, especially when rotating at high speeds, can result in partial failures or system shutdown. Taking into account the size of these structures, it is necessary to avoid interruptions due to system failure, but most importantly, accidents that, in addition to financial damage, can cause serious injuries or even fatalities. This implies that detailed study and development of each turbine in various operating scenarios combined to proper maintenance, even outside the limits of normal use, are necessary.

Moreover, in the fast paces of today's most developed societies, industries are constantly trying to cope with rapid technological developments, increasing technology penetration in our everyday life, and enormous competition soaring as a result of globalization. Thus, it is imperative to minimize the time and cost, from design to production and maintenance, for a product to be developed and function as intended. So either for competition reasons, safety or reliability enhancements in addition to lack of information about a product, a widespread methodology is used, i.e., reverse engineering (Abella et al., 1994; Várudy et al., 1997; Wang et al., 2012; Ouamer-Ali et al., 2014; Dagli and Idowu, 2015). Reverse engineering is this process in which we extract knowledge, design information about the parts that make up a machine and the way they function. Issues that include developing the CAD and FE model of the examined structure, as well as experimental modal analysis procedures and the application of robust and effective computational finite element model updating techniques are taken into account.

The main objective of the present work is to demonstrate the advantages of a reverse engineering strategy applying a developed model updating computational framework (Giagopoulos and Arailopoulos, 2017) to handle large-scale linear and nonlinear models. The applicability of the framework is examined by calibrating the structural parameters of a high-fidelity FE model of a steam turbine rotor with several millions degrees of freedom, using experimentally identified modal parameters. Modal identification techniques (Eykhoff, 1974; Beck and Katafygiotis, 1998; Beck, 2011) are used to extract natural frequencies and modal damping ratios from acceleration measurements. Measured and predicted modal parameters are used to quantify the discrepancy between numerical and experimental models, defining both modal and response residuals (Giagopoulos and Arailopoulos, 2015a,b, 2016; Arailopoulos and Giagopoulos, 2016), in a single-objective optimization problem. Next, a free distribution of the non-gradient, non-intrusive optimization algorithm, Covariance Matrix Adaptation—Evolution Strategy (CMA-ES) (Hansen et al., 2003; Hansen, 2006, 2011), within Π4U framework (Hadjidoukas et al., 2015), coupled to robust and accurate FE Analysis software (DTECH, 2013) are applied in parallel computing, based on a parallel computing library, i.e., TORC (Hadjidoukas et al., 2012). Structural material model parameters, such as modulus of elasticity and density are tuned, in order to best match experimental and analytical data.

Moreover, in this work a simplified numerical model based on the updated full large-scale FE model of the steam turbine is introduced, in order to get deep insight of the rotordynamic behavior and gyroscopic phenomena of the examined rotor. The main purpose is to examine the axial, lateral, and torsional dynamic characteristics, so as to evaluate shaft's vibration levels and acquire experience of the acceptable vibration limits and the limits at which maintenance is needed. System stability and critical speeds are also being determined by plotting the Campbell diagram (Campbell, 1924; Meher-Homji and Prisell, 2005) of turbine's response spectrum as a function of spin speed. Its tolerance to normal or even abnormal vibration levels on critical speeds, define the adequacy of the turbine's performance. Hence, as damping bearing properties influence significantly the turbine's levels of vibration, an optimum design could be adopted by minimizing the imbalances in operational rotation speeds. Accumulated knowledge of the dynamic behavior of the steam turbine system, could be later implemented in order to evaluate stability or instability states, fatigue growth in the turbine blades, changes in the damping of the bearing system and perform necessary scheduled optimal and cost-effective maintenance strategies (Bavastri et al., 2008; Booysen et al., 2015; Plesiutschnig et al., 2016). Additionally, upon a series of scheduled experimental data collection, a permanent output-only vibration Structural Health Monitoring system could be installed and even a proper dynamic balancing could be investigated and designed.

The work deals with the study of a steam turbine rotor operating in the IV unit of a Greek Public Power Corporation (PPC) power plant. The steam turbine is a Leningradsky Metallichesky Zavod© (LMZ) K-300-170-1 steam turbine system of maximum nominal output power of 310 MW. The examined turbine shaft consists mainly of three rotors, high, intermediate, and low pressure, starting from left to right as shown in **Figure 1**. Between the intermediate and low pressure turbines there is a cylindrical part used to join the two sections together. The length of the high, intermediate, and low pressure turbines is 5.7, 6.9, and 5.9 m, consisting of 10, 17, and 10 stages (discs) that host 954, 1,948 and 1,224 blades, respectively. The total length of the turbine is 18.5 m, but in the assembly of the whole turbine system additional components may apply, in order to secure connection to the generator. So at 310 MW power output there are 37 stages with a total number of 4,126 blades. The stages of the right half of the low pressure turbine, consist of the same last five stages of the intermediate pressure turbine. On the other hand, the left half is consisted of the same stages, in a mirrored arrangement so that the induced momentum is the same as the momentum of the rest of the turbine. So for convenience, the blades of the low pressure will be referred to by names already given in the intermediate pressure shaft.

The organization of this work is set as follows. The theoretical formulation of the actual measure of fit of the updating methodology based on modal modes, modal frequencies and frequency response functions is briefly presented in section

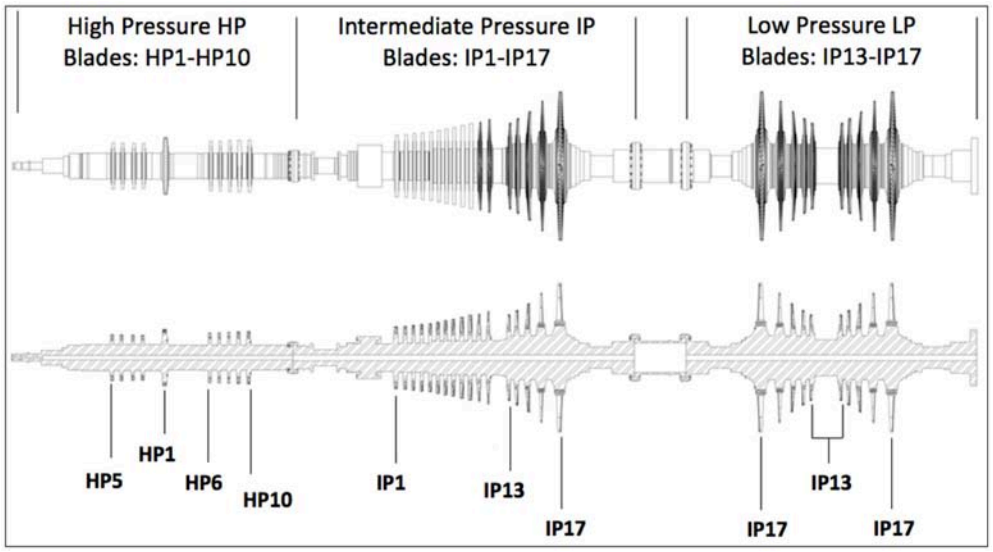

FIGURE 1 | High, intermediate and low pressure turbines with numbered stages.

Formulation of Objective Function. Section Linear FE Model Updating Framework presents the implemented FE model updating methodology. Section Reverse Engineering Strategy presents the 3D digitization of the blades and the 2D designing of the three shafts of the individual sections of the complete turbine, as well as their combination leading to the final parametric CAD model. Next, the experimental modal identification procedure is described, in order to identify modal modes and frequencies of the actual structures of the intermediate pressure sections. The updating results of the parameterized intermediate pressure turbine is presented in section Finite Element Model Updating. Section Rotordynamic Analysis of the Simplified Equivalent Model of the Complete Steam Turbine presents a brief formulation and a rotordynamic analysis of the introduced simplified FE model based on Timoshenko beam and disk elements. Finally, some conclusions about the applicability and future work are summarized in section Conclusions.

FORMULATION OF OBJECTIVE FUNCTION

Modal Measure of Fit

We consider the data $D = \{\hat{\lambda}_r, \underline{\hat{\varphi}_r} \in R^{N_{o,r}}, r = 1, \cdots, m\}$ to be the squared of the measured modal frequencies, $\hat{\lambda}_r = \hat{\omega}_r^2$ and the respective mode shapes $\underline{\hat{\varphi}_r}$ of the examined turbines, where $N_{o,r}$ is the number of measured components for each r and m is the number of identified modes. Consider a parameterized linear FE model of the structures and let $\underline{\theta} \in R^{N_\theta}$ be a vector of free material model parameters to be tuned. The objective is to estimate the values of the parameter set $\underline{\theta}$ so that the predicted modal frequencies and mode shapes $\{\lambda_r(\underline{\theta}), \underline{\varphi_r}(\underline{\theta}) \in R^{N_{0,r}}, r = 1, \cdots, m\}$ at the corresponding $N_{0,r}$ DOFs, diminishes discrepancies between modal frequencies identified in D. Thus, the modal frequency and mode shape residualsh are formulated as Mottershead et al. (2011); Giagopoulos and Arailopoulos (2015a,b, 2016), and Arailopoulos and Giagopoulos (2016):

$$\varepsilon^2_{\lambda_r}(\underline{\theta}) = \frac{\left(\lambda_r(\underline{\theta}) - \hat{\lambda}_r\right)^2}{\hat{\lambda}_r^2} \text{ and } \varepsilon^2_{\underline{\phi_r}}(\underline{\theta}) = \frac{\left\|\beta_r(\underline{\theta})\underline{\phi_r}(\underline{\theta}) - \underline{\hat{\phi}_r}\right\|^2}{\left\|\underline{\hat{\phi}_r}\right\|^2} \quad (1)$$

where $||\underline{Z}||^2 = \underline{Z}^T\underline{Z}$ is the usual Euclidean norm, and $\beta_r(\underline{\theta}) = \underline{\hat{\phi}_r}^T\underline{\phi_r}(\underline{\theta})/\left\|\underline{\phi_r}(\underline{\theta})\right\|^2$ is a normalization constant that guaranties that the measured mode shape $\underline{\hat{\phi}_r}$ at the measured DOFs is closest to the model mode shape $\beta_r(\underline{\theta})\underline{\phi_r}(\underline{\theta})$ predicted by the particular value of $\underline{\theta}$.

$J_1(\underline{\theta})$ and $J_2(\underline{\theta})$ are selected to represent the measure of fit between the measured and the model predicted frequencies and modes in the form:

$$J_1(\underline{\theta}) = \sum_{r=1}^{m} \varepsilon^2_{\lambda_r}(\underline{\theta}) \text{ and } J_2(\underline{\theta}) = \sum_{r=1}^{m} \varepsilon^2_{\underline{\phi}_r}(\underline{\theta}) \quad (2)$$

Frequency Response Measure of Fit

A global shape correlation coefficient between experimentally identified and numerically predicted FRFs may be used (Grafe, 1995, 1999) for any measured frequency point λ_k as follows:

$$x_s(\lambda_k) = \frac{\left|\left\{H_X(\lambda_k)\right\}^H \left\{H_A(\lambda_k)\right\}\right|^2}{\left(\left\{H_X(\lambda_k)\right\}^H \left\{H_X(\lambda_k)\right\}\right)\left(\left\{H_A(\lambda_k)\right\}^H \left\{H_A(\lambda_k)\right\}\right)} \quad (3)$$

where $\left\{H_X(\lambda_k)\right\}$ is the experimentally identified FRFs whereas as $\left\{H_A(\lambda_k)\right\}$ are the numerically computed FRFs at matching

excitation locations and response directions. As the MAC value, $x_s(\lambda_k)$ assumes a value between zero and unity and indicates perfect correlation with $x_s(\lambda_k) = 1$. For $x_s(\lambda_k) = 1$, experimental and numerical data perfectly correlate contrary to the value of zero pertaining to no correlation at all. If only one measurement is utilized, $\{H_X(\lambda_k)\}$ and $\{H_A(\lambda_k)\}$ are reduced from column vectors to scalar and $x_s = 1$ across the full frequency spectrum for uncorrelated FRFs.

Thus, a supplementary amplitude correlation coefficient $x_a(\lambda_k)$, for any measured frequency point λ_k is implemented quantifying the discrepancies in amplitude defined as:

$$x_a(\lambda_k) = \frac{2\left|\{H_X(\lambda_k)\}^H \{H_A(\lambda_k)\}\right|}{\left(\{H_X(\lambda_k)\}^H \{H_X(\lambda_k)\}\right) + \left(\{H_A(\lambda_k)\}^H \{H_A(\lambda_k)\}\right)} \quad (4)$$

defined to lie between zero and unity only if $\{H_A(\lambda_k)\} = \{H_X(\lambda_k)\}$.

$J_3(\underline{\theta})$ and $J_4(\underline{\theta})$ are selected to represent the measure of fit corresponding to the identified and predicted FRFs of the system:

$$J_3(\underline{\theta}) = \sum_{r=1}^{m}\left[1 - x_s(\hat{\lambda}_r, \underline{\theta})^2\right] \text{ and } J_4(\underline{\theta}) = \sum_{r=1}^{m}\left[1 - x_a(\hat{\lambda}_r, \underline{\theta})^2\right] \quad (5)$$

Objective Function

The overall measure of fit is formulated by a single objective function as follows:

$$J(\underline{\theta}; \underline{w}) = w_1 J_1(\underline{\theta}) + w_2 J_2(\underline{\theta}) + w_3 J_3(\underline{\theta}) + w_4 J_4(\underline{\theta}) \quad (6)$$

using the weighting factors $w_i \geq 0$, $i = 1,2,3,4$, with $w_1 + w_2 + w_3 + w_4 = 1$. The choice of weights scales each measure of fit according to the confidence in the experimental and FE predicted

FIGURE 2 | (A) High pressure turbine. **(B)** Intermediate pressure turbine. **(C)** Low pressure turbine.

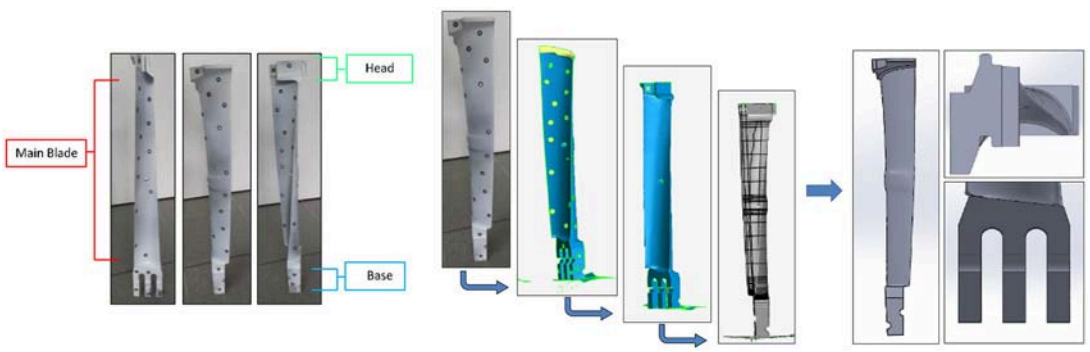

FIGURE 3 | Digitization and final 3D CAD model of a single blade at stage IP 15 of the intermediate pressure turbine.

data, highly affecting the global minimum and the optimized solutions for the parameter set $\underline{\theta}$ for given $\underline{w}$ are denoted by $\hat{\underline{\theta}}(\underline{w})$ (Christodoulou et al., 2008; Ntotsios and Papadimitriou, 2008; Papadimitriou et al., 2012; Giagopoulos et al., 2013).

LINEAR FE MODEL UPDATING FRAMEWORK

As the objective function $J(\underline{\theta})$ is not an analytical expression, a stochastic black box search algorithm, namely the Covariance Matrix Adaptation Evolution Strategy (CMA-ES) (Hansen et al., 2003; Hansen, 2006, 2011) is implemented in this work as has been previously successfully applied for tuning linear and nonlinear FE models (Giagopoulos and Arailopoulos, 2017). The aim is to iteratively find the candidate solutions of the parameter set $\underline{\theta} \in \Re^n$ that produce the minimum $J(\underline{\theta})$, where the function values are sampled from a multivariate normal distribution in each iteration (Hansen, 2006, 2011).

CMA-ES avoids entrapment in local minima, reaching the global optimum of the sampled objective function. The algorithm is coupled to a commercial FE solver Dynamis (DTECH, 2013) surpassing the need of model reduction or sub-structuring techniques and taking advantage of the raw experimental measurements for increased accuracy. Thus, having the ability to compare modal modes and frequency response functions node

FIGURE 4 | (A) Rotor shaft and complete 3D CAD assembly of the high pressure turbine. **(B)** Rotor shaft and complete 3D CAD assembly of the intermediate pressure turbine. **(C)** Rotor shaft and complete 3D CAD assembly of the low pressure turbine. **(D)** Final 3D CAD of the complete steam turbine.

by node and modal frequencies in a large frequency range overall fidelity of the updated FE models to the real structures is highly maintained. Moreover, due to the extremely large scale of the developed FE models and the numerous iterations needed to convergence a parallel computing scheme is applied in order to compensate for the computation time. Details on the formulation sequence of CMA-ES and the applied framework can be found in Giagopoulos and Arailopoulos (2017).

The minimum offsprings become parents in the next set of iterations and statistical values (mean and covariance matrix) are updated in a sequence of iterations with improved fitness values. The described framework runs in parallel in order to sample the prescribed population at once, in order to produce the total runs of each generation. Next, convergence criteria are checked. Introduced criteria include a given threshold of the objective function $J(\underline{\theta}) = 0$, being practically inapplicable and the difference of the best values of two consecutive sets of iterations $\Delta J(\underline{\theta}) = 10^{-3}$.

REVERSE ENGINEERING STRATEGY

An integrated reverse engineering methodology is presented in total in this section on the steam turbine system currently

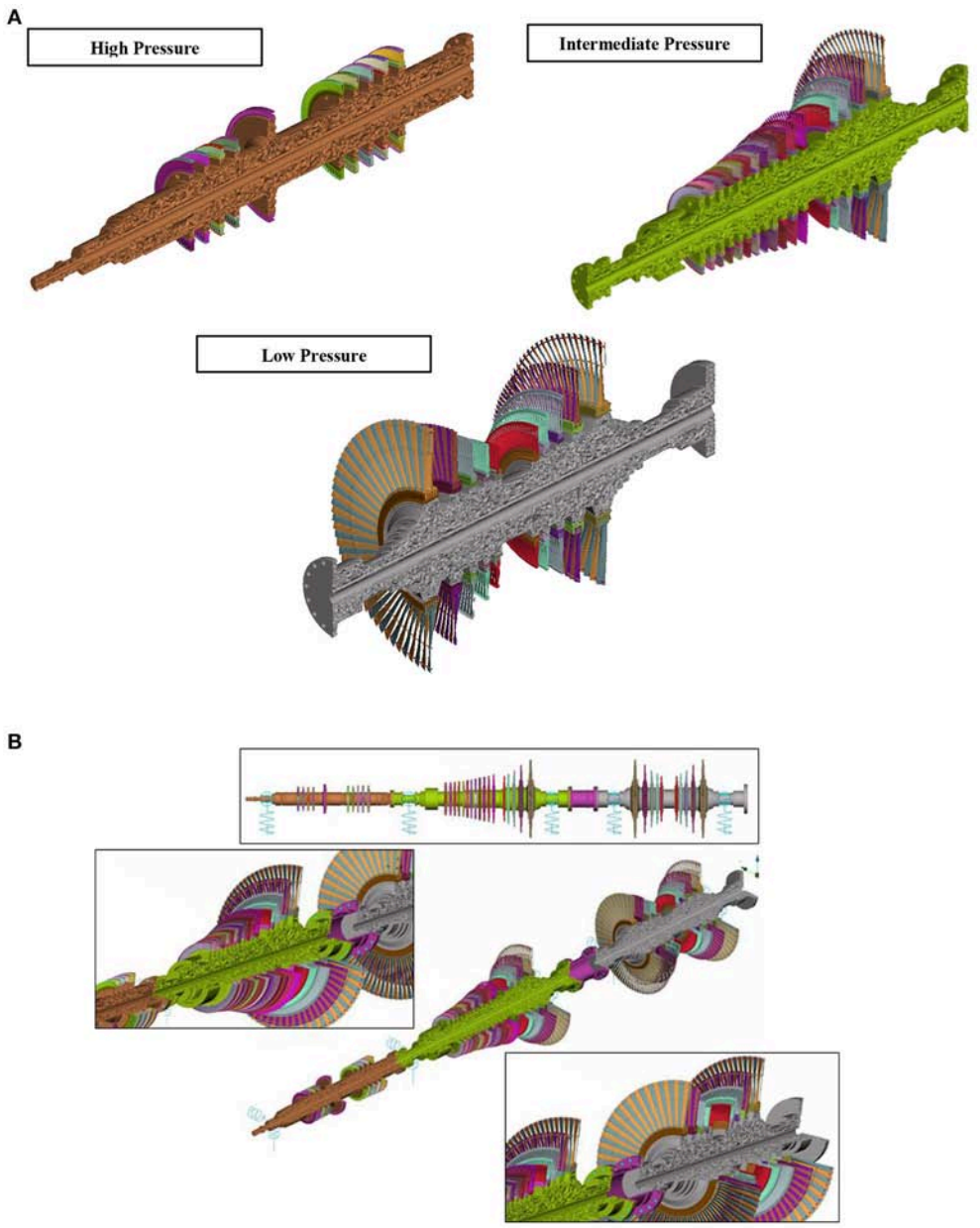

FIGURE 5 | (A) Detailed FE models of the high, intermediate, and low pressure turbines. **(B)** Detailed FE models of the complete steam turbine.

operating at a thermal power plant of the Greek Public Power Corporation. The methodology combines modern techniques for geometry representation and development of the CAD and FE models, contemporary methods of modal identification and estimation of the dynamic characteristics of the physical structure from acceleration measurements and state-of-the-art model updating techniques, in order to produce a high fidelity FE model adequately simulating the steam turbine system.

The high, intermediate, and low pressure turbines are presented in **Figures 2A–C** respectively, under regular maintenance. The structure is made of steel with Young's modulus $E = 210GPa$, Poisson's ratio v = 0.3 and density $\rho = 7850kg/m^3$ (Giagopoulos et al., 2017).

Digitization and CAD Model of the Steam Turbine

At first, using two types of 3D scanner devices, i.e., a structured light and a laser scanner, the digital shape of each blade was reconstructed. The collection of the raw data and the consecutive processing to the development of the final CAD model are completed in four basic steps as demonstrated in **Figure 3**. First, the geometry of each blade was captured, so as to collect a raw stereo-lithography (STL) file. Due to various flaws and imperfections of the initial design such as holes, humps, coarse and non-continuous surfaces, the second step was to use compatible software in order to design the final STL file of the captured geometry, before designing the CAD model (Béchet et al., 2002; Bianconi, 2002; Rypl and Bittnar, 2006). The next step

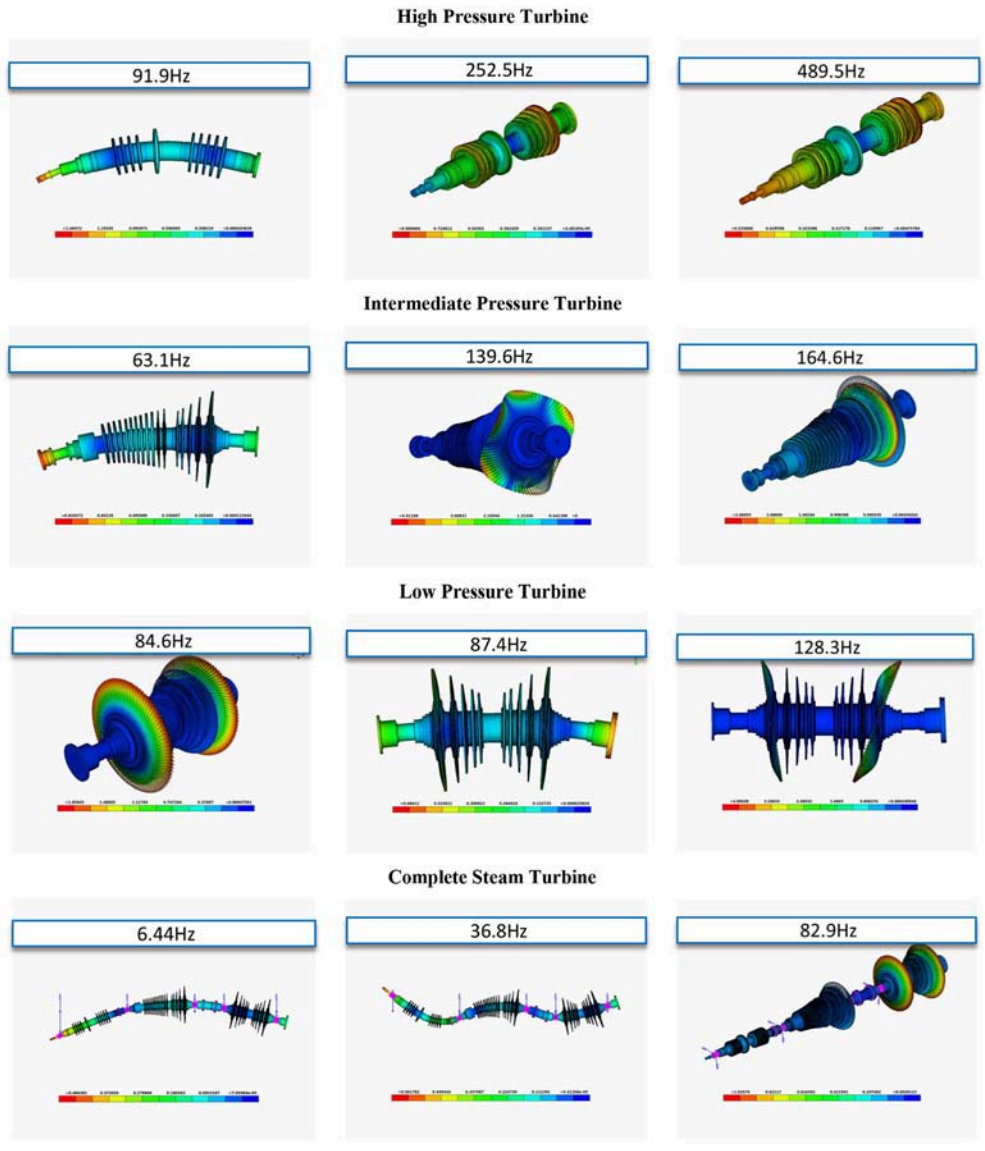

FIGURE 6 | Indicative eigenmodes of the high, intermediate and low pressure sections and the complete steam turbine predicted by the nominal FEM.

FIGURE 7 | Experimental set-up of the intermediate pressure turbine.

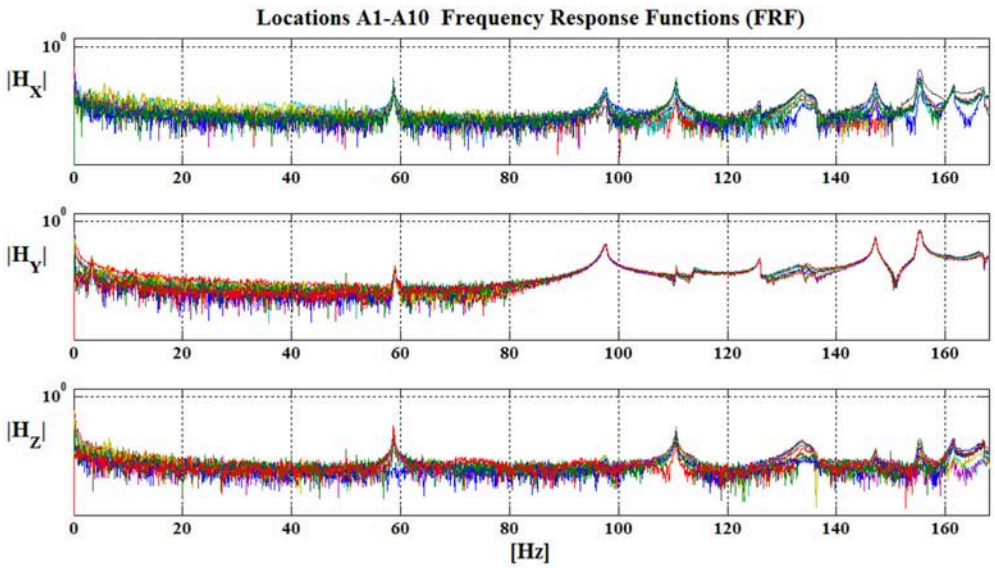

FIGURE 8 | Typical elements of the experimental FRF matrix for the intermediate pressure rotor.

was the preparation of the consecutive foil sections that represent each blade. After aligning the scanned geometry, automated curves were created by section along the length of the main body of the blade at varying increments, depending on its length and complexity as well as on designing needs. These curves were parallel to each other as well as to base of the blades. Last, step was to select the most representable curves of each blade and use them to reconstruct the CAD models.

On top of designing the main body of the blades, bases, and heads were designed from scratch under meticulous measurements. Four blades were cover by heads that were designed separately and placed on top of the main body using vertical curves, in order to succeed the finest positioning. Additionally, all bases of the blades were designed separately taking into consideration their slight curvature, in order to tangently fit around the

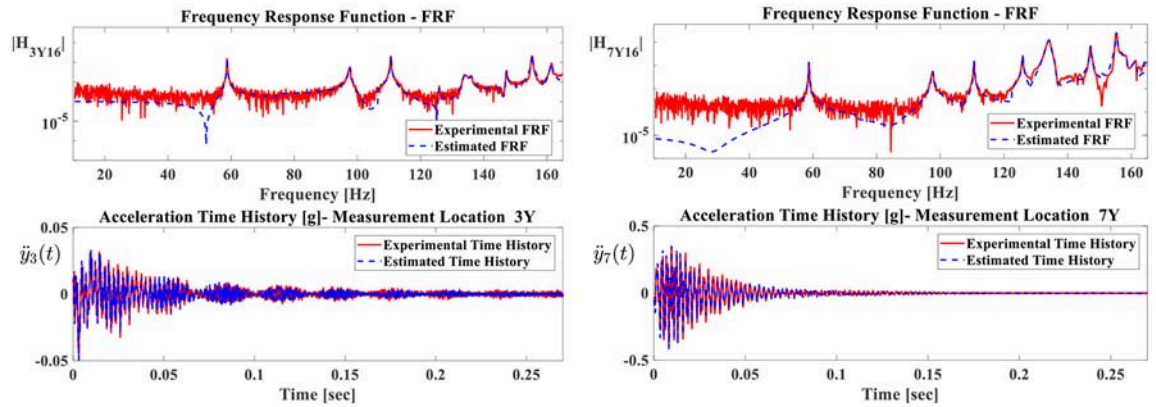

FIGURE 9 | Comparison of FRFs and time histories of accelerations corresponding to frequency response functions $|H_{3Y16}|$ and $|H_{7Y16}|$ of accelerometers A3 and A7 at local direction Y.

TABLE 1 | Identified and nominal FEM predicted modal frequencies and modal damping ratios of the intermediate pressure turbine.

Mode	Identified modal frequency	Nominal FE predicted modal frequency	Difference between identified and FE Predicted modal frequencies	Identified modal damping ratio
–	ω_{rE} [Hz]	$\omega_{rN_{FE}}$ [Hz]	$\frac{\omega_{rN_{FE}}-\omega_{rE}}{\omega_{rN_{FE}}}100\%$	ζ_{rE} (%)
1	58.70	63.04	6.88%	0.21
2	101.30	89.52	13.16%	0.19
3	110.60	127.22	13.06%	0.12
4	126.10	131.62	4.19%	0.08
5	134.80	134.85	0.04%	0.13
6	135.01	135.92	0.67%	0.13
7	142.32	144.24	1.33%	0.12
8	147.40	148.64	0.83%	0.16
9	156.77	154.22	1.65%	0.16
10	161.30	160.04	0.79%	0.35

rotor shaft. Finally, the top of each base was designed flat in order to fit perfectly with the main body of the blade.

In order to design the rotor shafts of the steam turbine, the technical drawings were used. The blueprints were hardcopies of the high, intermediate, and low pressure turbines in manageable scale used in order to produce the 2D axisymmetric design of the shafts.

Combining the complete CAD models of the blades with the three rotor shafts, the final CAD model of the complete steam turbine was created. The following **Figures 4A–C** present the rotor shafts and the complete 3D CAD models of the high, intermediate and low pressure turbines respectively. Furthermore, the final 3D CAD model of the complete steam turbine is presented in **Figure 4D**.

FE Models of Steam Turbine Rotor

The geometry of the turbine sections is discretized by solid elements (tetrahedral). Due to the complex geometry of the structure, the total number of degrees of freedom of the high, intermediate, and low pressure sections were about 10,000,000, 20,000,000, and 19,500,000 respectively, whereas the resulting complete rotor model was about 55,000,000 degrees of freedom, including the connection parts between the sections. The detailed FE models of the high, intermediate and low pressure turbines are presented in **Figure 5A** respectively and **Figure 5B** depicts the final finite element model of the complete steam turbine. FE pre-processor software and FE analysis software were used in order to develop and analyze the FE model (DTECH, 2013; BETA CAE Systems, 2018). Indicative mode shapes of the three sections in a free-free state and the complete model with typical supports are presented in **Figure 6**.

Experimental Modal Analysis

In this section the dynamic characteristics of the complete steam turbine are identified in order to compute the measure of fit between numerical FE model and actual structure. In order to quantify the dynamic characteristics of the complete steam

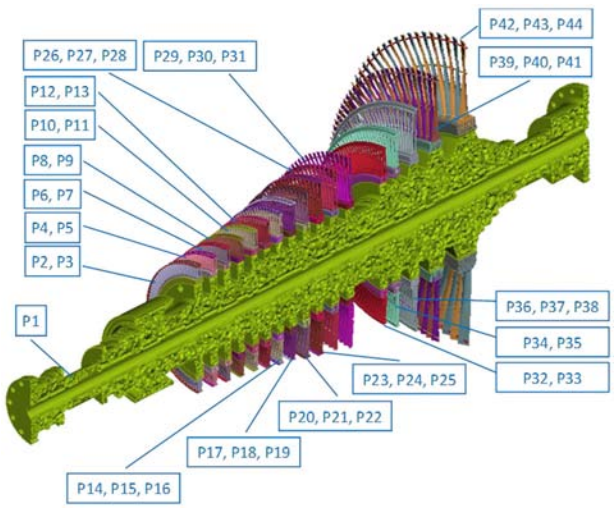

FIGURE 10 | Parts of the parameterized FE models of the intermediate pressure turbines.

TABLE 2 | Optimized parameter values of material properties for rotor shaft and indicative blades of the intermediate pressure turbine.

Number of parameter	Part		Optimized value	Lower bound	Upper bound
1	P1	$E_1 \cdot 10^2$ [GPa]	2.181		
2		$\rho_1 \cdot 10^3 \left[kg/m^3\right]$	7.987		
3	P3	$E_2 \cdot 10^2$ [GPa]	1.932		
4		$\rho_2 \cdot 10^3 \left[kg/m^3\right]$	7.400		
5	P9	$E_3 \cdot 10^2$ [GPa]	1.922		
6		$\rho_3 \cdot 10^3 \left[kg/m^3\right]$	8.156		
7	P27	$E_4 \cdot 10^2$ [GPa]	2.123		
8		$\rho_4 \cdot 10^3 \left[kg/m^3\right]$	7.988	1.89 for E_i	2.31 for E_i
9	P30	$E_5 \cdot 10^2$ [GPa]	2.030	7.065 for ρ_i	8.635 for ρ_i
10		$\rho_5 \cdot 10^3 \left[kg/m^3\right]$	8.145		
11	P33	$E_6 \cdot 10^2$ [GPa]	2.001		
12		$\rho_6 \cdot 10^3 \left[kg/m^3\right]$	7.887		
13	P35	$E_7 \cdot 10^2$ [GPa]	2.225		
14		$\rho_7 \cdot 10^3 \left[kg/m^3\right]$	7.899		
15	P43	$E_8 \cdot 10^2$ [GPa]	2.145		
16		$\rho_8 \cdot 10^3 \left[kg/m^3\right]$	8.456		

turbine, an experimental modal analysis of the three turbine sections was performed. Due to large size of the results, it is selected to present the results only for the intermediate pressure rotor.

An industrial size crane was used to mount each turbine separately, simulating a support-free state for the experimental procedure. Impulsive loading was imposed at various locations and directions on the structure in order to estimate the elements of the FRF matrix—Equation (7) (Ewins, 1984; Mohanty and Rixen, 2005; Giagopoulos and Natsiavas, 2007, 2015; Spottswood and Allemang, 2007).

$$\begin{bmatrix} \ddot{u}_1 \\ \ddot{v}_1 \\ \ddot{w}_1 \\ \cdots \\ \ddot{w}_n \end{bmatrix} = \begin{bmatrix} Hu_1u_1 & \cdots & Hu_1w_n \\ Hv_1u_1 & \cdots & Hv_1w_n \\ Hw_1u_1 & \cdots & Hw_1w_n \\ \vdots & \ddots & \vdots \\ Hw_nu_1 & \cdots & Hw_nw_n \end{bmatrix}_{3n\times 3n} \begin{bmatrix} Fu_1 \\ \vdots \\ Fw_n \end{bmatrix}_{3n\times 3n} \quad (7)$$

The frequency range of 0–2048 Hz was obtained during measurements, including the numerical frequency range of interest, i.e., 0–200 Hz including the first ten modal frequencies. A schematic illustration of the measurement geometry for the modal analysis of the intermediate pressure rotor, with the real experimental set up of this test is presented in **Figure 7**. For instance, **Figure 8** presents the magnitude of representative elements of the FRF matrix.

The Rational Fraction Polynomial Method (RFPM) (Richardson and Formenti, 1985; Friswell and Penny, 1990; Ntotsios and Papadimitriou, 2008) was used in order to estimate the experimental natural frequencies and the damping ratios of the intermediate pressure turbine, based on the measured FR functions.

Indicatively, two typical elements of the experimentally measured FRF matrix of the intermediate pressure turbines are compared to the estimated RFPM contours as presented in **Figure 9**. The same figure also presents the experimentally measured and analytically estimated time histories. The FR functions corresponding to accelerometers A3 and A7 of the intermediate pressure section at Y local component are presented in **Figure 9**. The red line corresponds to the experimentally measured FRF and time history compared to the dashed blue line corresponding to the estimated contour filtered with Welch's (1967) method. Additionally, all experimentally modal mode shapes are identified, in order to be used in the formulation of the measure of fit passed to the optimization algorithm.

Table 1 summarizes the experimental modal analysis results for the intermediate pressure turbine. The values of the lowest natural frequencies ω_{rE}, are presented in the second column of **Table 1** whereas the fifth column list the corresponding damping ratios. The values of the natural frequencies predicted from the numerical model $\omega_{rN_{FE}}$ using nominal material parameters using lumped mass matrix implemented in solver Dynamis (DTECH, 2013), are listed in the third column whereas a comparison is presented in the fourth column. The underestimation of the predicted natural frequencies of the nominal FE model, is attributed to the way Dynamis handles mass matrix. In spite of the fairly insignificant discrepancies between the nominal FE model and the experimental data, a subsequent FE model updating process is necessary to diminish these errors.

The accuracy of the experimental measurements highly depends on the quality of the experimental devices and the abilities of the users. Inaccurate measurement data could be produce by a defective apparatus or user mishandling. The reliability of the collected data during the experimental procedures was checked, from the small variation of the data. Such an examination is imperative as the experimental results highly affect the accuracy of the overall technique.

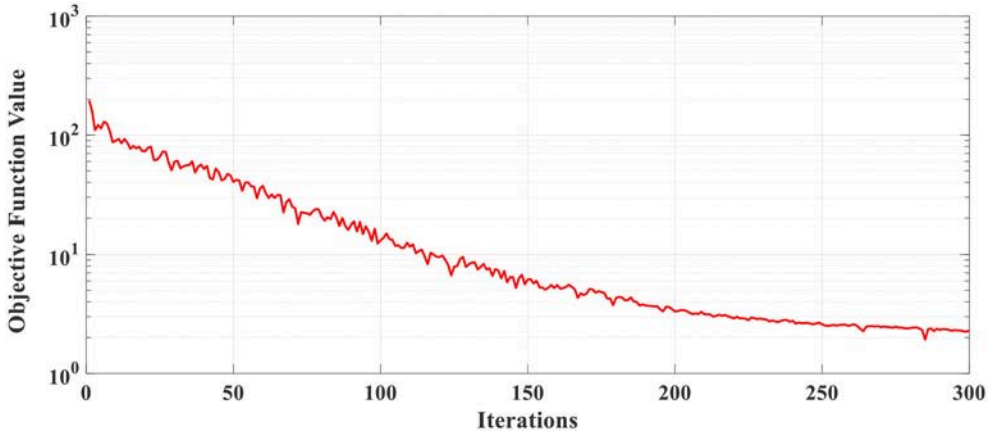

FIGURE 11 | Objective function values diagram of intermediate pressure turbine.

TABLE 3 | Identified and optimized FE predicted modal frequencies of the intermediate pressure turbine.

Mode	Identified modal frequency	Optimized FE predicted modal frequency	Difference between identified and FE predicted modal frequencies
–	ω_{rE} [Hz]	$\omega_{rO_{FE}}$ [Hz]	$\frac{\omega_{rO_{FE}}-\omega_{rE}}{\omega_{rO_{FE}}}100\%$
1	58.70	59.45	1.26%
2	101.30	99.62	1.69%
3	110.60	112.22	1.44%
4	126.10	128.62	1.96%
5	134.80	134.85	0.04%
6	135.01	135.92	0.67%
7	142.32	144.24	1.33%
8	147.40	148.64	0.83%
9	156.77	154.22	1.65%
10	161.30	160.04	0.79%

FINITE ELEMENT MODEL UPDATING

Parameterization of FE Models

In this section, the parameterization of the finite element model of the intermediate section is introduced in order to apply the updating methodology. This model consists of about 23 million degrees of freedom. The parameterized model consisting of 44 parts which is shown in **Figure 10**. At each of these parts are used as design variables the Young's modulus and the density. Thus, the final number of the design parameters are eighty-eight (88) variables. The first parts describe the rotor shafts whereas each stage is modeled with two or three parts. Two parts are used to model the blades and their circumferential ring at small diameter stages, whereas three parts are used to model eight large diameter stages of the intermediate pressure assigning two parts for the blades and one for the circumferential ring. Although both the rotor shaft and the turbine blades have been built from a single material, steel, the mechanical treatment that all parts undertake in order to take their final form and shape as well as their assembly may change the overall stiffness of the structure related to an FE model where assumption are made beforehand. Specifically, molding of the steel during industrial manufacturing of the turbine parts may result in slight variation of the modulus of elasticity and density of the actual used material. Additionally, remaining stresses may develop that increase stiffness. Furthermore, the tight assembly of the blades on the rotor shaft and between each other, result in additional remaining stresses that could not be modeled in the FEM and could only be handled by tuning the material propertied. In this direction the parameter space for each design variable, was selected in the range of $\pm$ 10% of the nominal values, introducting the upper and lower constraints of material properties, in order to maintain realistic values and keep their physical meaning.

The finite element model is updated using the ten identified modal frequencies and mode shapes shown in **Table 1**. Components at all 17 sensor locations are used in identification of the mode shapes of the structure. Moreover, the total weight of the FE model is defined as a global behavioral design constraint, apart from the box constraints of the design variables in the optimization process. This global behavioral constraint was implemented in order to reject and resample the material parameters chosen from the design space of the boxed (lower and upper bound) constraints, that produce a total weight of the FE model that varies significantly from the actual weight of the structure.

Model Update Results and Verification

The CMA-ES framework introduced in previous work (Giagopoulos and Arailopoulos, 2017) is applied to update the developed FE models. During FE model analyses, no model reduction or sub-structuring methodologies were applied in order to increase accuracy with regard to the real structures. Furthermore, the large number of degrees of freedom of each FE model in conjunction with the numerous amount of sampling

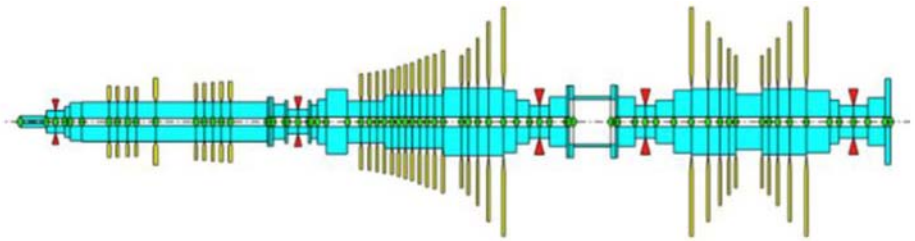

FIGURE 12 | Schematic illustration of simplified FE model of the complete steam turbine.

TABLE 4 | Comparison between modal frequencies of the simplified FE model at idle state and the full-scale FE model.

Mode	Frequencies [Hz]		Deviation
–	Simplified FE model	Full-scale FE model	
1	1.49	1.21	23.1%
2	1.93	1.72	12.0%
3	6.64	6.44	3.10
4	16.05	16.02	0.2%
5	38.13	36.87	3.4%
6	60.49	58.08	4.1%
7	94.66	92.77	2.0%

needed by CMA-ES for convergence, required prohibitive time, at high computational cost. Thus, a parallelized scheme of the applied algorithm, coupling FE solver Dynamis (DTECH, 2013) to CMA-ES was implemented, as has been previously demonstrated in Giagopoulos and Arailopoulos (2017), in order to counterbalance computational cost effectiveness and render possible and applicable such an optimization methodology at an extremely large scale FE model. Indicatively, the optimization process was running for ∼15 days for the intermediate pressure turbine. The computer that was used, hosts two (2) Intel® Xeon® Processors E5-2630 v3 (20M Cache, 2.40 GHz) with 8-cores and 16-threads, resulting in a total number of thirty-two (32) logical (virtual) cores and 64 GB of RAM, on Linux Ubuntu 16.04 Operating System.

Table 2 presents the design vector of the optimized material properties of indicative parts of the intermediate pressure turbine. Part P1 corresponds to the rotor shaft, and the optimized parameters lie close to the nominal parameter values of steel, as it is the only part of the turbine that is almost intact and unaffected by its long time operation. Parts P3, P9, P27, P30, P33, P35, and P43 correspond to the optimized material properties that showed maximum deviation from the nominal values. All parts are related to blades. Blades are the most vulnerable parts of the turbine that corrode during operation and need regular maintenance. Additionally, all blades are tightly fixed with steel rods producing remaining stresses that increase stiffness.

Convergence has been achived with respect to the objective function using the convergence critterion as defind in section Linear FE Model Updating Framework being the difference of the best values of two consecutive sets of iterations $\Delta J(\underline{\theta}) = 10^{-3}$. In order to equally consider the contribution of the four residuals, equal weighting factors were chosen. Different weighting factors would account for increased reliability of the formulation of one of the four residuals, arisen from experience or experimental confidence.

Figure 11 presents the history of convergence, where the objective function value is presented against number of iterations where we can see the fast convergence rate and **Table 3** presents the updated modal frequencies along a comparison between the identified (ω_{rE}) and optimized FE predicted modal frequencies ($\omega_{r\,O_{FE}}$). A slight difference between optimal and experimental modal frequencies is inevitable due to various uncontrolled uncertainties.

ROTORDYNAMIC ANALYSIS OF THE SIMPLIFIED EQUIVALENT MODEL OF THE COMPLETE STEAM TURBINE

The analyses presented refer to the system in free oscillation, having omitted the rotation speed of the rotor and having no knowledge of the effect of gyroscopic and shear phenomena due to rotation. The large scale of the developed finite element model renders the rotordynamic analysis from extremely computationally expensive to impossible. Thus, a simplified model of the turbine, which takes into account the gyroscopic phenomena occurring during the rotation of the turbine, was introduced in Matlab (Mathworks, 2016) using the freeware scripts of rotor software (Friswell et al., 2010b) developed for analyzing the dynamics of rotating machines (Friswell et al., 2010a). The simplified model was tested for the accuracy of its results with the developed complete finite element model by modal analysis in idle position. Based on the full-scale steam turbine, the simplified FE model consists of 73 Timoshenko beam elements simulating the shaft and 37 disk elements simulating the stages of the blade elements of the turbine. The total number of nodes was 74 and at 5 nodes isotropic bearing elements were placed in all directions that refer to the bearing point of the rotor. **Figure 12** illustrates the simplified model of the steam turbine, where cyan color is the shaft elements, green dots refer to the nodes, yellow color represents the

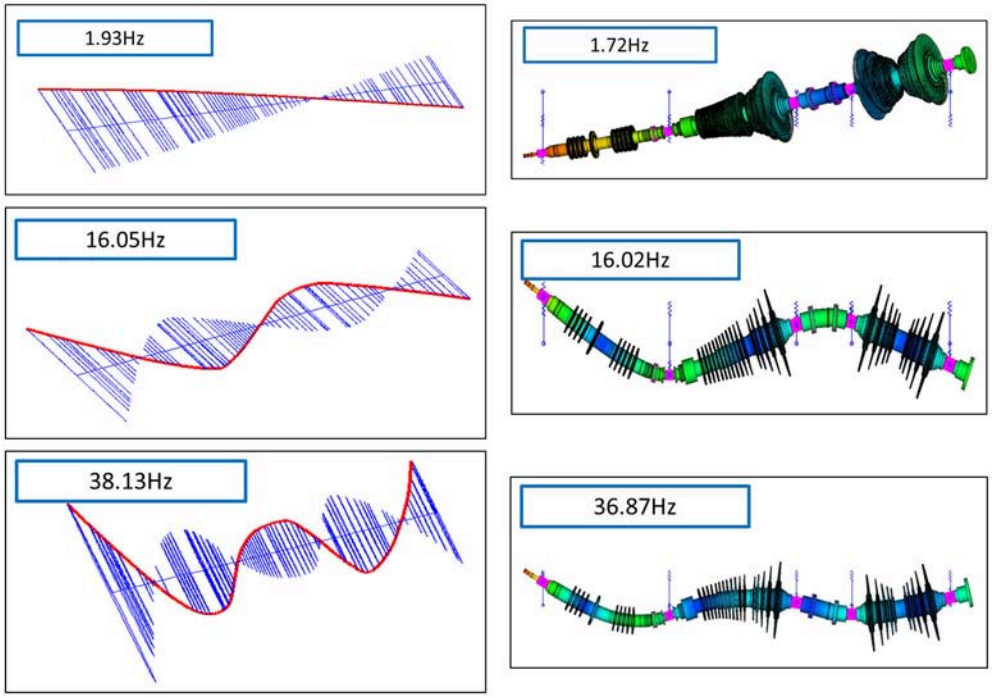

FIGURE 13 | 2nd, 4, and 5th eigenmodes of the simplified FE model at idle state at 1.93, 16.05, and 38.13 Hz and equivalent eigenmodes of the full-scale FE model at 1.72, 16.02, and 36.87 Hz.

blades of each stage and red triangles show the bearing of the rotor.

The updated material parameters of the full model of the turbine were used, for the axis properties. The only difference is in the density of the disks. As each stage consists of a large number of blades that obviously have a gap between them, they cannot be modeled as solid disc. Thus, the density of the disk was adjusted according to the actual volume and the actual mass of the stage from the full-scale FE model. Firstly, frequencies of the simplified model at zero rotational speed (idle) were compared to those of the complete FE model as presented in **Table 4**. Specifically, the second and third columns present the frequencies of the simplified and full-scale FE models, whereas the last column presents the deviation between them.

Indicatively the 2nd, 4, and 5th modes of the full-scale and the simplified for zero rotation speed, FE models are presented in **Figure 13**. We notice that the modes are very similar to both models. Coloring the results of the simplified and full-scale model based on displacements, helps us understand the movement of the body at each mode. Thus, the coloration of the simplified model in red line correspond to the shaft and the blue lines to the displacements of the internal nodes, whereas the coloration of the full-scale FE model is depicted on the colored legend.

Moreover, at 50 Hz, which is the electric current frequency, the turbine will rotate at 3,000 rpm. **Table 5** summarizes the 30 first rotational frequencies of the simplified model at 3,000 rpm rotational speed. Indicative modes are presented in **Figure 14**. The simplified FE model could be further updated in regard to the bearings for increased accuracy and fidelity to the real steam turbine structure at working state. Specifically, experimental vibration measurements could be collected at all bearing points under real working conditions, in order to update the stiffness and damping parameters at all supporting directions during rotation of the steam turbine at operational spin speed. The thick black line represents the rotor axis while the vertical circular lines represent the orbits of the nodes in a period of rotation.

TABLE 5 | Rotational eigenfrequencies of the simplified model at 3,000 rpm rotational speed.

Mode	Rotational frequencies	Mode	Rotational frequencies	Mode	Rotational frequencies
1	1.48	11	58.82	21	194.93
2	1.49	12	62.16	22	228.99
3	1.83	13	92.05	23	236.48
4	2.03	14	97.27	24	261.54
5	6.43	15	108.91	25	268.63
6	6.86	15	116.48	26	298.63
7	15.13	17	160.48	27	310.81
8	17.02	18	160.66	28	352.23
9	37.34	19	165.40	29	360.95
10	44.51	20	184.32	30	361.21

Finally, **Figure 15** presents the Campell diagram (Campbell, 1924; Meher-Homji and Prisell, 2005) of turbine's response spectrum as a function of spin speed, at a range of 0–4,500 rpm which represents the variation of the rotational frequencies as the rotation speed changes.

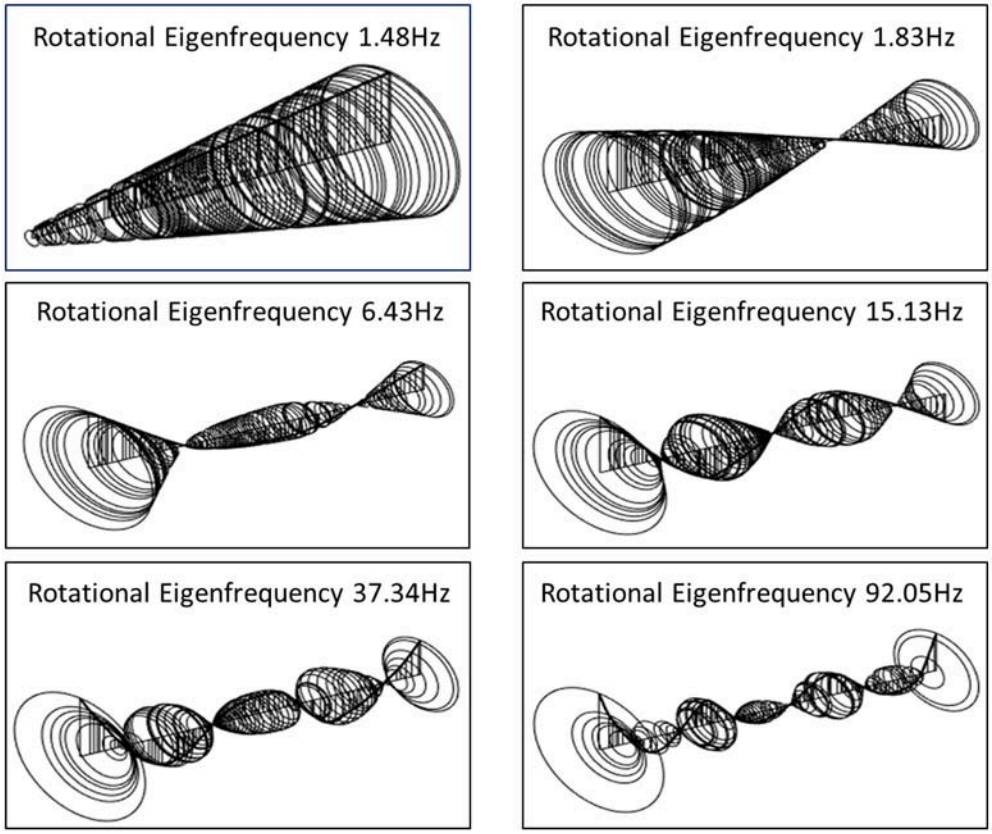

FIGURE 14 | Indicative rotational eigenmodes 1, 3, 5, 7, 9, and 13 corresponding to 1.48, 1.83, 6.43, 15.13, 37.34, and 92.05 Hz of the simplified FE model at 3,000 rpm rotational speed.

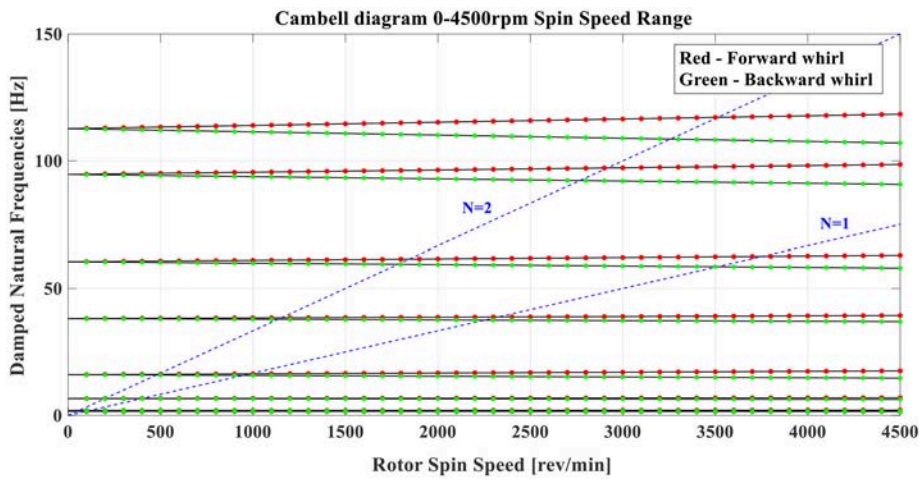

FIGURE 15 | Cambell diagram at 0–4.500 rpm spin speed range.

CONCLUSIONS

An integrated reverse engineering methodology is presented in this work on a large-scale steam turbine rotor, taking into account issues related to the development of the CAD and FE model, experimental modal analysis procedures and the application of robust and effective computational finite element model updating techniques. Numerical and experimental

methodologies were implemented in order to identify the model parameters and develop a high fidelity finite element model of the examined structure. An extensible framework of CMA Evolution Strategy for complex and computationally demanding physical models is implemented in order to finely tune material parameters, such as modulus of elasticity and density, in order to best match experimental and numerical data. Moreover, a simplified FE model based on the updated full large-scale FE model of the steam turbine is introduced, in order to get deep insight of the rotordynamic behavior and gyroscopic effects of the examined rotor. Accumulated knowledge of the dynamic behavior of the steam turbine system, could be later implemented in order to evaluate stability or instability states, fatigue growth in the turbine blades, changes in the damping of the bearing system and perform necessary scheduled optimal and cost-effective maintenance strategies. Additionally, upon a series of scheduled experimental data collection, a permanent output-only vibration SHM system could be installed and even a proper dynamic balancing could be investigated and designed.

AUTHOR CONTRIBUTIONS

DG was involved in the development of the computational framework, finite element models and experimental modal analysis, AA with the development of the computational framework and the finite element model updating, while IZ and EP with the scanning of the surfaces and the development of three-dimensional geometry.

REFERENCES

Abella, R. J., Daschbach, J. M., and McNichols, R. J. (1994). Reverse engineering industrial applications. *Comp. Indus. Eng.* 26, 381–385. doi: 10.1016/0360-8352(94)90071-X

Arailopoulos, A., and Giagopoulos, D. (2016). "Finite element model updating techniques of complex assemblies with linear and nonlinear components," in *34th IMAC, A Conference and Exposition on Structural Dynamics, 2016* (Orlando, FL: Springer New York LLC).

Bavastri, C. A., Ferreira, E. M. D. S., Espíndola, J. J. D., and Lopes, E. M. D. O. (2008). Modeling of dynamic rotors with flexible bearings due to the use of viscoelastic materials. *J. Br. Soc. Mech. Sci. Eng.* 30, 22–29. doi: 10.1590/S1678-58782008000100004

Béchet, E., Cuilliere, J. C., and Trochu, F. (2002). Generation of a finite element MESH from stereolithography (STL) files. *Comput. Aided Des.* 34, 1–17. doi: 10.1016/S0010-4485(00)00146-9

Beck, J. L. (2011). "Bayesian updating, model class selection and robust stochastic predictions of structural response," in *Proceedings of the 8th International Conference on Structural Dynamics, EURODYN 2011* (Leuven).

Beck, J. L., and Katafygiotis, L. S. (1998). Updating models and their uncertainties. I: Bayesian statistical framework. *J. Eng. Mech.* 124, 455–461.

BETA CAE Systems, S.A. (2018). *ANSA and META-Post.* Thessaloniki: BETA CAE Systems. S.A.

Bianconi, F. (2002). Bridging the gap between CAD and CAE using STL files. *Int. J. CAD CAM* 2, 55–67.

Booysen, C., Heyns, P. S., Hindley, M. P., and Scheepers, R. (2015). Fatigue life assessment of a low pressure steam turbine blade during transient resonant conditions using a probabilistic approach. *Int. J. Fatig.* 73, 17–26. doi: 10.1016/j.ijfatigue.2014.11.007

Campbell, W. (1924). *Protection of Steam Turbine Disk Wheels from Axial Vibration.* Schenectady, NY: General electric Co.

Christodoulou, K., Ntotsios, E., Papadimitriou, C., and Panetsos, P. (2008). Structural model updating and prediction variability using Pareto optimal models. *Comp. Methods Appl. Mech. Eng.* 198, 138–149. doi: 10.1016/j.cma.2008.04.010

Dagli, C. H., and Idowu, M. A. (2015). "Instantaneous modelling and reverse engineering of data-consistent prime models in seconds," in *Procedia Computer Science Complex Adaptive Systems* (San Jose, CA), 373–380.

DTECH (2013). *DYNAMIS 3.1.1.* Thessaloniki: DTECH.

Ewins, D. J. (1984). *Modal Testing: Theory and Practice.* Somerset: Research Studies Press.

Eykhoff, P. (1974). *System Identification Parameter and State Estimation.* London, UK: John Wiley & Sons, Inc.

Friswell, M. I., and Penny, J. E. T. (1990). Updating model parameters from frequency domain data via reduced order models. *Mech. Syst. Signal Process.* 4, 377–391. doi: 10.1016/0888-3270(90)90064-R

Friswell, M. I., Penny, J. E. T., Garvey, S. D., and Lees, A. W. (2010a). *Dynamics of Rotating Machines. Cambridge Aerospace Series.* Cambridge, CA: Cambridge University Press.

Friswell, M. I., Penny, J. E. T., Garvey, S. D., and Lees, A. W. (2010b). *Rotordynamics Software Manual, in Dynamics of Rotating Machines.* Cambridge: Cambridge University.

Giagopoulos, D., and Arailopoulos, A. (2015a). "Finite element model updating of geometrically complex structure through measurement of its dynamic response," in *1st ECCOMAS Thematic Conference on Uncertainty Quantification in Computational Sciences and Engineering, UNCECOMP 2015* (Crete Island: National Technical University of Athens).

Giagopoulos, D., and Arailopoulos, A. (2015b). "Parameter identification of complex structures using finite element model updating techniques," in *ASME 2015 International Design Engineering Technical Conferences and Computers and Information in Engineering Conference, IDETC/CIE 2015* (Boston, MA: American Society of Mechanical Engineers (ASME)).

Giagopoulos, D., and Arailopoulos, A. (2016). "Parameter estimation of nonlinear large scale systems through stochastic methods and measurement of its dynamic response," in *7th European Congress on Computational Methods in Applied Sciences and Engineering, ECCOMAS Congress 2016* (Crete Island: National Technical University of Athens).

Giagopoulos, D., and Arailopoulos, A. (2017). Computational framework for model updating of large scale linear and nonlinear finite element models using state of the art evolution strategy. *Comp. Struct.* 192, 210–232. doi: 10.1016/j.compstruc.2017.07.004

Giagopoulos, D., Arailopoulos, A., Zacharakis, I., and Pipili, E. (2017). "Finite element model developed and modal analysis of large scale steam turbine rotor: quantification of uncertainties and model updating," in *2nd ECCOMAS Thematic Conference on Uncertainty Quantification in Computational Sciences and Engineering (UNCECOMP)* Rhodes Island: ECCOMAS.

Giagopoulos, D., and Natsiavas, S. (2007). Hybrid (numerical-experimental) modeling of complex structures with linear and nonlinear components. *Nonlinear Dynam.* 47, 193–217. doi: 10.1007/s11071-006-9067-3

Giagopoulos, D., and Natsiavas, S. (2015). Dynamic response and identification of critical points in the superstructure of a vehicle using a combination of numerical and experimental methods. *Exp. Mech.* 55, 529–542. doi: 10.1007/s11340-014-9966-z

Giagopoulos, D., Papadioti, D.-C., Papadimitriou, C., and Natsiavas, S. (2013). "Bayesian uncertainty quantification and propagation in nonlinear structural dynamics," in *Topics in Model Validation and Uncertainty Quantification, Volume 5: Proceedings of the 31st IMAC, A Conference on Structural Dynamics, 2013*, eds T. Simmermacher, S. Cogan, B. Moaveni, and C. Papadimitriou (New York, NY: Springer), 33–41.

Grafe, H. (1995). *Review of Frequency Response Function Updating Methods.* BRITE-URANUS BRE2-CT94-0946.

Grafe, H. (1999). *Model Updating of Large Structural Dynamics Models Using Measured Response Function.* London: Department of Mechanical Engineering, Imperial College.

Hadjidoukas, P. E., Angelikopoulos, P., Papadimitriou, C., and Koumoutsakos, P. (2015). Π4U: a high performance computing framework for Bayesian uncertainty quantification of complex models. *J. Comput. Phys.* 284, 1–21. doi: 10.1016/j.jcp.2014.12.006

Hadjidoukas, P. E., Lappas, E., and Dimakopoulos, V. V. (2012). "A runtime library for platform-independent task parallelism," in *2012 20th Euromicro International Conference on Parallel, Distributed and Network-based Processing.* (Garching).

Hansen, N. (2006). The CMA evolution strategy a comparing review. *Towards New Evol. Comput.* 192, 75–102. doi: 10.1007/3-540-32494-1_4

Hansen, N. (2011). *The CMA Evolution Strategy: A Tutorial.* Research centre Saclay –Île-de-France Universite Paris-Saclay, LRI.

Hansen, N., Müller, S. D., and Koumoutsakos, P. (2003). Reducing the time complexity of the derandomized evolution strategy with covariance matrix adaptation (CMA-ES). *Evol. Comput.* 11, 1–18. doi: 10.1162/106365603321828970

Mathworks (2016). *MATLAB*, Natick, MA: Mathworks Inc.

Meher-Homji, C. B., and Prisell, E. (2005). Dr. Max Bentele—pioneer of the jet age. *J. Eng. Gas Turb. Power* 127, 231–239. doi: 10.1115/1.1807412

Mohanty, P., and Rixen, D. J. (2005). Identifying mode shapes and modal frequencies by operational modal analysis in the presence of harmonic excitation. *Exp. Mech.* 45, 213–220. doi: 10.1007/BF02427944

Mottershead, J. E., Link, M., and Friswell, M. I. (2011). The sensitivity method in finite element model updating: a tutorial. *Mech. Syst. Signal Process.* 25, 2275–2296. doi: 10.1016/j.ymssp.2010.10.012

Ntotsios, E., and Papadimitriou, C. (2008). "Multi-objective optimization algorithms for finite element model updating," in *International Con- ference on Noise and Vibration Engineering (ISMA2008).* Leuven: Katholieke Universiteit Leuven, 66–80.

Ouamer-Ali, M.-I., Laroche, F., Bernard, A., and Remy, S. (2014). "Toward a methodological knowledge based Approach for partial automation of reverse engineering," in *24th CIRP Design Conference* (Elsevier), 270-275. doi: 10.1016/j.procir.2014.03.190

Papadimitriou, C., Ntotsios, E., Giagopoulos, D., and Natsiavas, S. (2012). Variability of updated finite element models and their predictions consistent with vibration measurements. *Struct. Control Health Monit.* 19, 630–654. doi: 10.1002/stc.453

Plesiutschnig, E., Fritzl, P., Enzinger, N., and Sommitsch, C. (2016). Fracture analysis of a low pressure steam turbine blade. *Case Stud. Eng. Fail. Anal.* 5–6, 39–50. doi: 10.1016/j.csefa.2016.02.001

Richardson, M. H., and Formenti, D. L. (1985). "Global curve fitting of frequency response measurements using the rational fraction polynomial method," in *Third IMAC Conference* (Orlando, FL).

Rypl, D., and Bittnar, Z. (2006). Generation of computational surface meshes of STL models. *J. Comput. Appl. Math.* 192, 148–151. doi: 10.1016/j.cam.2005.04.054

Spottswood, S. M., and Allemang, R. J. (2007). On the investigation of some parameter identification and experimental modal filtering issues for nonlinear reduced order models. *Exp. Mech.* 47, 511–521. doi: 10.1007/s11340-007-9047-7

Várudy, T., Martin, R. R., Cox, J., Várady, T., Martin, R. R., and Cox, J. (1997). Reverse engineering of geometric modelsreverse engineering of geometric models—an introduction. *Comput. Aided Des.* 29, 255–268. doi: 10.1016/S0010-4485(96)00054-1

Wang, J., Gu, D., Yu, Z., Tan, C., and Zhou, L. (2012). A framework for 3D model reconstruction in reverse engineering. *Comp. Ind. Eng.* 63, 1189–1200. doi: 10.1016/j.cie.2012.07.009

Welch, P. (1967). The use of fast Fourier transform for the estimation of power spectra: a method based on time averaging over short, modified periodograms. *IEEE Trans. Audio Electroacoust.* 15, 70–73. doi: 10.1109/TAU.1967.1161901

Conflict of Interest Statement: The authors declare that the research was conducted in the absence of any commercial or financial relationships that could be construed as a potential conflict of interest.

The reviewer, ARC, and handling editor declared their shared affiliation.

frontiers in Built Environment

ORIGINAL RESEARCH
published: 23 October 2018
doi: 10.3389/fbuil.2018.00057

A Finite Element Analysis of the Stability of Composite Beams With Arbitrary Curvature

Ida Mascolo[1], *Mariano Modano*[2], *Ada Amendola*[1] *and Fernando Fraternali*[1]*

[1] *Department of Civil Engineering, University of Salerno, Fisciano, Italy,* [2] *Department of Structures for Engineering and Architecture, University of Naples Federico II, Naples, Italy*

A finite element approximation of a theory recently proposed for the geometrically nonlinear analysis of laminated curved beams is developed. The application of the given finite element model to the computation of stability points and post-buckling behavior of beams with arbitrary curvature is also carried out, on taking into account the influences of shear deformation and warping effects on the in-plane and out-plane responses of the beam. The stability analysis is performed through a path-following procedure and a bordering algorithm. Several numerical results are given and comparisons with classical beam theories and other theories available in the relevant literature are established. The given results highlight that the proposed finite element model is well suited to study the stability of structures that incorporate laminated composite beams, such as, e.g., light-weight roof structures and arch bridges.

Keywords: composite laminates, curved beams, fiber-reinforced composites, buckling-analysis, finite element method

OPEN ACCESS

Edited by:
Vagelis Plevris, OsloMet–Oslo Metropolitan University, Norway

Reviewed by:
Georgios A. Drosopoulos, University of KwaZulu-Natal, South Africa
Francesco Tornabene, Università degli Studi di Bologna, Italy

***Correspondence:**
Fernando Fraternali
f.fraternali@unisa.it

Specialty section:
This article was submitted to Computational Methods in Structural Engineering, a section of the journal Frontiers in Built Environment

Received: *28 July 2018*
Accepted: *28 September 2018*
Published: *23 October 2018*

Citation:
Mascolo I, Modano M, Amendola A and Fraternali F (2018) A Finite Element Analysis of the Stability of Composite Beams With Arbitrary Curvature. Front. Built Environ. 4:57. doi: 10.3389/fbuil.2018.00057

INTRODUCTION

Laminated composite (fiber-reinforced) structures are increasingly used in a wide range of engineering applications (naval, aeronautical, automation, mechanical, civil, medical engineering, etc.), due to the outstanding proprieties that such structures may exhibit when a proper design of the material and the lamination scheme are employed: light weight, high stiffness-to-weight and tensile strength-to-weight ratios, high damping, excellent corrosion, thermal and high impact resistance (Fraternali et al., 2011, 2012; Bencardino et al., 2012). Nowadays, laminated composite structures play a crucial role in the production of various innovative structures or products, which include: light-weight roof structures, arch bridges, impact energy mitigation and vibration isolation devices, just to name a few examples. In order to capture the puzzling mechanical response of such structures, various theoretical and numerical approaches have been proposed in the literature, including zig-zag displacement-based theories and stress-based methods, with special attention on the modeling of anisotropy, warping, fracture and damage (Feo and Fraternali, 2000; Roberts and Al-Ubaidi, 2001; Fraternali et al., 2002, 2010, 2011, 2012; Fraternali, 2007; Schmidt et al., 2009; Feo and Mancusi, 2010; Bencardino et al., 2012; Markkula et al., 2013; Viera et al., 2013; Özütok and Madenci, 2017). Shear deformation and warping effects may be rather important in composite beams. At this regard (Özütok and Madenci, 2017) by Özütok and Madenci analyses the effects of a non-linear distribution of the shear stress through the beam thickness within a higher-order shear deformation theory; Roberts and Al-Ubaidi develop in Roberts and Al-Ubaidi (2001) an approximate theory for assessing the influence of shear deformation on restrained torsional

warping of pultruded bars; while Viera et al. develop a thin-walled beam model able to simulate warping and higher order effects in Viera et al. (2013). For what concerns stability phenomena, which are of peculiar interest in the case of composite beams due to the characteristic slenderness of such structures, it is worth mentioning the non-linear elastic approaches proposed in Ascione et al. (2011, 2013); Fraternali et al. (2013); Mascolo and Pasquino (2016); Özütok and Madenci (2017), and Mascolo et al. (in press). The recent study illustrated in Fraternali et al. (2013) presents a geometrically nonlinear theory of laminated curved beams, which assumes that cross-section rotations and shear strains are moderately large, while axial strains are infinitesimal. Due to its minor complexity with respect to the finite elasticity theory, the model presented in Fraternali et al. (2013) is particularly convenient for computing the first stability point of a composite laminated beam and studying its behavior near such a point.

In the present paper, we develop a comprehensive finite-element approximation of the mechanical model given in Fraternali et al. (2013), which is founded upon the use of Lagrangian isoparametric elements (section Finite Element Model). The adopted model proves to be a robust and versatile tool that allows to model the geometrically non-linear response and the buckling behavior of laminated composite beams with arbitrary curvature. It takes into account both shear deformations and warping effects, which are essential to accurately predict in-plane and out-plane buckling loads. The proposed stability analysis employs the path-following procedure proposed by Bathoz and Dhatt (1979) and the algorithm for computing stability points proposed by Simo and Wriggers (1990) (section Finite Element Analysis of the Stability of Composite Curved Beams). The accuracy of the proposed finite-element model is assessed by presenting different numerical results relative to the stability of isotropic and composite beams and establishing comparisons with the corresponding results of classical beam theories and other theories available in the relevant literature (section Numerical Results). We end with concluding remarks and directions for future work in section Concluding Remarks.

$$R_e^h = \frac{\left[\left(Z_{2_e}^h\right)_{,\xi}^2 + \left(Z_{3_e}^h\right)_{,\xi}^2\right]^{3/2}}{\left[\left(Z_{2_e}^h\right)_{,\xi}\left(Z_{3_e}^h\right)_{,\xi\xi} - \left(Z_{2_e}^h\right)_{,\xi\xi}\left(Z_{3_e}^h\right)_{,\xi}\right]} = \frac{\left[\left(\sum_{I=1}^n N_{I,\xi}\, Z_{2_I}\right)^2 + \left(\sum_{I=1}^n N_{I,\xi}\, Z_{3_I}\right)^2\right]^{3/2}}{\left[\left(\sum_{I=1}^n N_{I,\xi}\, Z_{2_I}\right)\left(\sum_{J=1}^n N_{J,\xi\xi}\, Z_{3_J}\right) - \left(\sum_{I=1}^n N_{I,\xi\xi}\, Z_{2_I}\right)\left(\sum_{J=1}^n N_{J,\xi}\, Z_{3_J}\right)\right]}. \quad (5)$$

FINITE ELEMENT MODEL

Let us denote by C^h a finite-element discretization of axis curve of a laminated beam, and let us assume that the elements $C_1, \ldots, C_n$ belong to the Lagrange family (Reddy, 1992) (see **Figure 1**)

$$C^h = \bigcup_{e=1}^{n_e} C_e. \quad (1)$$

On adopting an isoparametric finite-element approximation (Reddy, 1992) we use the same shape functions to approximate both the geometry and the (generalized) displacement field over the generic element C_e

$$Z_{2_e}^h = \sum_{I=1}^n N_I Z_{2_I},\; Z_{3_e}^h = \sum_{I=1}^n N_I Z_{3_I},\; \hat{\boldsymbol{u}}_e^h = \sum_{I=1}^n N_I \hat{\boldsymbol{u}}_I. \quad (2)$$

In Equation (2) N_I is the shape function corresponding to the node I and consists of a complete polynomial of order $n-1$; Z_{2I} and Z_{3I} are the coordinates of I with respect to the global frame $\{0, Z_1, Z_2, Z_3\}$ (**Figure 1**); $\hat{\boldsymbol{u}}_I$ is the generalized displacement vector relative to the same node.

In particular, for a four-node Lagrangian element, we represent in **Figure 2** the transformation $(2)_{1,2}$ which maps the master element onto a curved (cubic) element.

The Jacobian of the transformation from the local coordinate ξ (**Figure 2**) to the global coordinate X_3 (**Figure 1**) is given by Nomizu and Kobayashi (1963)

$$J = \frac{dX_3}{d\xi} = \sqrt{\left(\frac{dZ_{2_e}^h}{d\xi}\right)^2 + \left(\frac{dZ_{3_e}^h}{d\xi}\right)^2} = \sqrt{\left(\sum_{I=1}^n N_{I,\xi} Z_{2_I}\right)^2 + \left(\sum_{I=1}^n N_{I,\xi} Z_{3_I}\right)^2} \quad (3)$$

$N_{I,\,\xi}$ being the derivative of N_I with respect to ξ. Denoting by $(\cdot)'$ the derivative with respect to X_3, we have:

$$N_I{}' = \frac{dN_I}{dX_3} = J^{-1} N_{1,\,\xi}. \quad (4)$$

By making use of Equation $(2)_{1,2}$, we obtain the following approximation of the curvature radius R (Nomizu and Kobayashi, 1963)

Coming back to Equation $(2)_3$, we now observe that it can be written in the following compact form

$$\hat{\boldsymbol{u}}_e^h = \boldsymbol{N}\boldsymbol{U}_e \quad (6)$$

where $\boldsymbol{U}_e$ is the M-dimensional vector collecting nodal, generalized, displacements of

$$C_e\left(\boldsymbol{U}_e = \left[\hat{\boldsymbol{u}}_1^T,\, \hat{\boldsymbol{u}}_2^T,\, \ldots, \hat{\boldsymbol{u}}_n^T\right]^T\right), \quad (7)$$

while $\boldsymbol{N}$ is the following matrix

$$\boldsymbol{N}_{[m\times M]} = [\boldsymbol{N}_1,\, \boldsymbol{N}_2,\, \ldots, \boldsymbol{N}_n], \quad (8)$$

whose blocks are diagonal submatrices

$$\boldsymbol{N}_{I_{[m\times m]}} = diag\,(N_I\, N_I \ldots N_I). \quad (9)$$

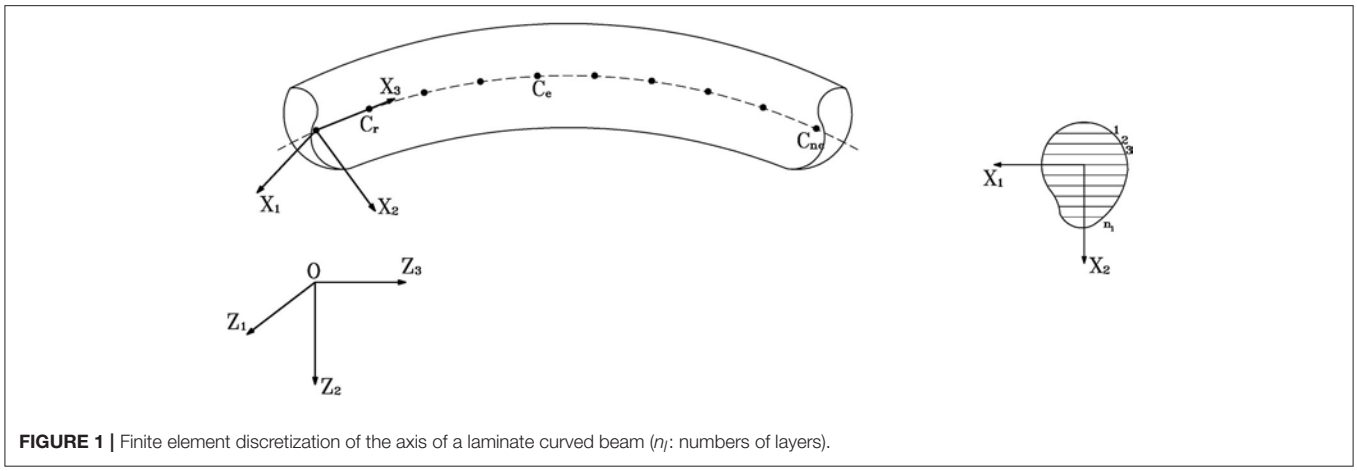

FIGURE 1 | Finite element discretization of the axis of a laminate curved beam (n_l: numbers of layers).

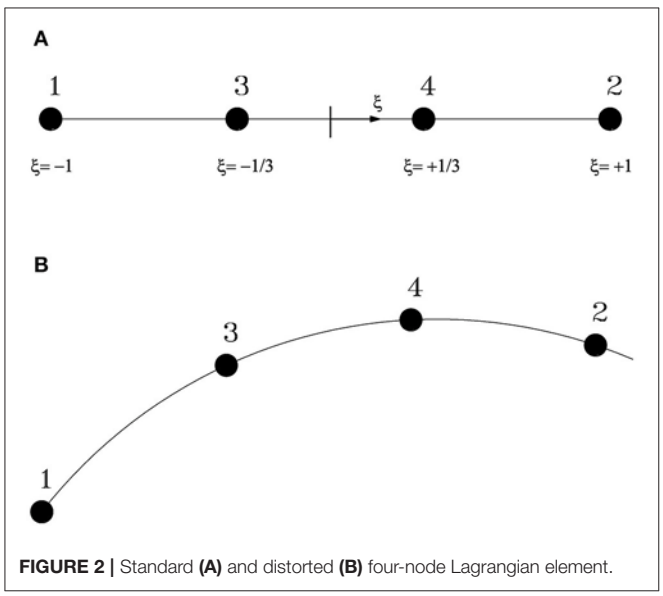

FIGURE 2 | Standard **(A)** and distorted **(B)** four-node Lagrangian element.

Equation (6) leads us to obtain the following approximation of the generalized strains

$$\hat{\boldsymbol{E}}_e^h(\boldsymbol{U}_e) = \hat{\boldsymbol{E}}_e^{(1)h}(\boldsymbol{U}_e) + \frac{\boldsymbol{1}}{\boldsymbol{2}}\hat{\boldsymbol{E}}_e^{(2)h}(\boldsymbol{U}_e, \boldsymbol{U}_e) \tag{10}$$

where

$$\hat{\boldsymbol{E}}_e^{(1)h}(\boldsymbol{U}_e) = \boldsymbol{B}_o \boldsymbol{U}_e \tag{11}$$

$$\hat{\boldsymbol{E}}_e^{(2)h}(\boldsymbol{U}_e, \delta\boldsymbol{U}_e) = \boldsymbol{B}_L(\boldsymbol{U}_e)\,\delta\boldsymbol{U}_e$$

$\boldsymbol{B}_0$ and $\boldsymbol{B}_L(\boldsymbol{U}_e)$ being the following $\sigma \times M$ matrices

$$\boldsymbol{B}_0 = [\boldsymbol{B}_{01}, \boldsymbol{B}_{02}, \ldots, \boldsymbol{B}_{0n}],$$

$$\boldsymbol{B}_L(\boldsymbol{U}_e) = \boldsymbol{A}(\boldsymbol{U}_e)\,\boldsymbol{G}. \tag{12}$$

The $\sigma \times m$ submatrices $\boldsymbol{B}_{0_I}$ in Equation $(12)_1$ are given by

$$\boldsymbol{B}_{o_I} = \begin{bmatrix} \boldsymbol{B}_{o_I}^{Ev} & \mathbf{B}_{o_I}^{E\varphi} & \mathbf{0} \\ \mathbf{0} & \boldsymbol{B}_{o_I}^{\Theta\phi} & \mathbf{0} \\ \mathbf{0} & \mathbf{0} & \mathbf{0} \\ \mathbf{0} & \mathbf{0} & \boldsymbol{B}_{o_I}^{ww} \\ \mathbf{0} & \mathbf{0} & \boldsymbol{B}_{o_I}^{w'w'} \end{bmatrix}, \tag{13}$$

where

$$\boldsymbol{B}_{o_I}^{Ev} = \boldsymbol{B}_{o_I}^{\Theta\phi} = \begin{bmatrix} N_1' & 0 & 0 \\ 0 & N_1' & N_1/R \\ 0 & -N_1/R & N_1' \end{bmatrix}, \quad \boldsymbol{B}_{o_I}^{E\varphi} = \begin{bmatrix} 0 & -N_1' & 0 \\ N_1 & 0 & 0 \\ 0 & 0 & 0 \end{bmatrix},$$

$$\boldsymbol{B}_{o_I\,[m_w \times m_w]}^{ww} = diag\,(N_I\, N_I \ldots N_I),$$

$$\boldsymbol{B}_{o_I\,[m_w \times m_w]}^{w'w'} = diag\,(N_I'\, N_I' \ldots N_I'). \tag{14}$$

The matrices $\boldsymbol{A}$ and $\boldsymbol{G}$, which appear in Equation $(12)_2$, are instead given by

$$\boldsymbol{A}(\boldsymbol{U}_e)_{[\sigma \times 9]} = \begin{bmatrix} \boldsymbol{A}(\boldsymbol{U}_e) \\ \mathbf{0} \end{bmatrix}, \quad \boldsymbol{G}_{[9 \times M]} = [\boldsymbol{G}_1, \boldsymbol{G}_2, \ldots, \boldsymbol{G}_n], \tag{15}$$

where

$$\boldsymbol{G}_{I\,[9 \times m]} = [\overline{\boldsymbol{G}}_I, \boldsymbol{0}], \overline{\boldsymbol{G}}_{I\,[9 \times 6]} = \begin{bmatrix} N_1' & 0 & 0 & 0 & 0 & 0 \\ 0 & N_1' & 0 & 0 & 0 & 0 \\ 0 & 0 & N_1 & 0 & 0 & 0 \\ 0 & 0 & 0 & N_1 & 0 & 0 \\ 0 & 0 & 0 & 0 & N_1 & 0 \\ 0 & 0 & 0 & 0 & 0 & N_1 \\ 0 & 0 & 0 & N_1' & 0 & 0 \\ 0 & 0 & 0 & 0 & N_1' & 0 \\ 0 & 0 & 0 & 0 & 0 & N_1' \end{bmatrix}, \tag{16}$$

$$\boldsymbol{A}\,(\boldsymbol{U}_e)_{[9\times 9]} =$$

$$\begin{bmatrix}
0 & \phi_3 & \frac{\phi_3}{R} & \frac{\phi_3}{2} & 0 & \left(\nu_2{}' + \frac{\nu_3}{R} + \frac{\phi_1}{2}\right) & 0 & 0 & 0 \\
-\phi_3 & 0 & 0 & 0 & \frac{\phi_3}{2} & \left(-\nu_1{}' + \frac{\phi_2}{2}\right) & 0 & 0 & 0 \\
\nu_1{}' & \left(\nu_2{}' + \frac{\nu_3}{R}\right) & \left(\frac{\nu_2{}'}{R} + \frac{\nu_3}{R^2}\right) & 0 & 0 & 0 & 0 & 0 & 0 \\
\left(-\phi_3{}' + \frac{\phi_2}{R}\right) & 0 & 0 & 0 & \left(\frac{\nu_1{}'}{R} - \frac{\phi_2}{R} + \frac{\phi_3{}'}{2}\right) & \left(\frac{\phi_2{}'}{2} + \frac{\phi_3}{R}\right) & 0 & \frac{\phi_3}{2} & \left(-\nu_1{}' + \frac{\phi_2}{2}\right) \\
0 & \left(-\phi_3{}' + \frac{\phi_2}{R}\right) & \left(-\frac{\phi_3{}'}{R} + \frac{\phi_2}{R^2}\right) & \left(-\frac{\phi_3{}'}{2} + \frac{\phi_2}{2R}\right) & \left(\frac{\nu_2{}'}{R} + \frac{\nu_3}{R^2} + \frac{\phi_1}{2R}\right) & -\frac{\phi_1{}'}{2} & -\frac{\phi_3}{2} & 0 & \left(-\nu_2{}' - \frac{\nu_3}{R} - \frac{\phi_1}{2}\right) \\
0 & 0 & 0 & \left(-\frac{\phi_2{}'}{2} - \frac{\phi_3}{2R}\right) & \frac{\phi_1{}'}{2} & -\frac{\phi_1}{2R} & \frac{\phi_2}{2} & -\frac{\phi_1}{2} & 0 \\
0 & 0 & 0 & 0 & \left(-\frac{\phi_3{}'}{R} + \frac{\phi_2}{R^2}\right) & \left(\frac{\phi_2{}'}{R} + \frac{\phi_3}{R^2}\right) & 0 & \left(\phi_2{}' + \frac{\phi_3}{R}\right) & \left(\phi_3{}' - \frac{\phi_2}{R}\right) \\
0 & 0 & 0 & 0 & \left(-\frac{\phi_3{}'}{R} + \frac{\phi_2}{R^2}\right) & 0 & \phi_1{}' & 0 & \left(\phi_3{}' - \frac{\phi_2}{R}\right) \\
0 & 0 & 0 & 0 & 0 & \frac{\phi_1{}'}{R} & \left(\phi_2{}' + \frac{\phi_3}{R}\right) & \phi_1{}' & 0
\end{bmatrix} \tag{17}$$

FINITE ELEMENT ANALYSIS OF THE STABILITY OF COMPOSITE CURVED BEAMS

Path-Following Procedure

Let us consider the variational formulation of the equilibrium equations. The use of Equations (6, 10, 11) allows us to set such equations into the following discrete form

$$\begin{aligned}
\delta\Pi^h \;&=\; \delta\mathbf{U}^T\mathbf{R}(\mathbf{U},\lambda) \\
&= \textstyle\sum_{e=1}^{n_e}\left\{\delta\boldsymbol{U}_e^T\int_{-1}^{1}\left[\boldsymbol{B}_0^T+\boldsymbol{B}_L^T\,(\boldsymbol{U}_e)\right]\hat{\boldsymbol{D}}\left[\boldsymbol{B}_0+\tfrac{1}{2}\boldsymbol{B}_L\,(\boldsymbol{U}_e)\right]\boldsymbol{U}_e J d\xi\right\} \\
&-\lambda\sum_{e=1}^{n_e}\left\{\delta\boldsymbol{U}_e^T\int_{-1}^{1}\boldsymbol{N}^T\left[\hat{\boldsymbol{q}}_e^{(1)}+\hat{\boldsymbol{q}}_e^{(2)}\,(\boldsymbol{U}_e)\right]J d\xi\right\} \\
&-\lambda\sum_{I=1}^{n_n}\left\{\delta\hat{\boldsymbol{u}}_I^T\left[\hat{\boldsymbol{Q}}_I^{(1)}+\hat{\boldsymbol{Q}}_I^{(2)}\left(\hat{\boldsymbol{u}}_I\right)\right]\right\}=0
\end{aligned} \tag{18}$$

where Π^h is the discretized functional of the total potential energy Π; $\delta\Pi^h$ is the first variation of Π^h with increment $\delta\boldsymbol{U}$; $\boldsymbol{R}(\boldsymbol{U},\lambda)$ (residuai vector) is the Gateaux derivative of Π^h with respect to $\boldsymbol{U}$ $\left(\boldsymbol{R}=D_U\Pi^h\right)$.

On accounting for a possibility of non-linear elastic response of the material, we assume that the elasticity matrix $\hat{\boldsymbol{D}}$, whose elements are the resultants and the resultant moments of the local elastic moduli (Fraternali et al., 2013), depends on the deformation of the beam ($\hat{\mathbf{D}}=\hat{\mathbf{D}}\,(\boldsymbol{U})$).

Equation (18) can also be written in the following compact form

$$\delta\boldsymbol{U}^T\boldsymbol{R}\,(\boldsymbol{U},\lambda)=\delta\boldsymbol{U}^T\left\{\boldsymbol{K}\,(\boldsymbol{U})\,\boldsymbol{U}-\lambda\left[\boldsymbol{Q}^{(1)}+\boldsymbol{Q}^{(2)}\,(\boldsymbol{U})\right]\right\}=0, \tag{19}$$

where $\mathbf{K}(\mathbf{U})$ is the $N\times N$ global (secant) stiffness matrix, which derives from the assembly of the element stiffness matrices $\mathbf{K}_e$ ($e=1,\,2,\ldots,\,n_e$). Such matrices are defined by the equations

$$\boldsymbol{K}_e\,(\boldsymbol{U}_e)\,(\boldsymbol{U}_e)=\int_{-1}^{1}\left[\boldsymbol{B}_0^T+\boldsymbol{B}_L^T\,(\boldsymbol{U}_e)\right]\hat{\boldsymbol{S}}\,(\boldsymbol{U}_e)\,J d\xi, \tag{20}$$

where $\hat{\boldsymbol{S}}$ is the generalized stress vector

$$\hat{\boldsymbol{S}}\,(\boldsymbol{U}_e)=\hat{\boldsymbol{D}}\left[\boldsymbol{B}_0+\frac{1}{2}\boldsymbol{B}_L\,(\boldsymbol{U}_e)\right]\boldsymbol{U}_e, \tag{21}$$

while $\boldsymbol{Q}^{(1)}$ and $\boldsymbol{Q}^{(2)}(\boldsymbol{U})$ are the global force vectors, which derive from the assembly of the element vectors

$$\boldsymbol{Q}_e^{(1)}=\int_{-1}^{1}N^T\hat{\boldsymbol{q}}_e^{(1)}Jd\xi,\quad \boldsymbol{Q}_e^{(2)}\,(\boldsymbol{U}_e)=\int_{-1}^{1}N^T\hat{\boldsymbol{q}}_e^{(2)}\,(\boldsymbol{U}_e)Jd\xi, \tag{22}$$

and the nodal force vectors $\hat{\boldsymbol{Q}}_I^{(1)}$ and $\hat{\boldsymbol{Q}}_I^{(2)}$ $\left(\hat{\boldsymbol{u}}_I\right)$ $(I=1,\,2,\,\ldots,\,n_n)$.

Due to the arbitrariness of $\delta\boldsymbol{U}$, Equation (19) is equivalent to the following nonlinear system of N equations

$$\boldsymbol{R}\,(\boldsymbol{U},\lambda)=\boldsymbol{K}\,(\boldsymbol{U})\,\boldsymbol{U}-\lambda\left[\boldsymbol{Q}^{(1)}+\boldsymbol{Q}^{(2)}\,(\mathbf{U})\right]=\mathbf{0}, \tag{23}$$

which can be solved by employing one of the algorithms known in literature as path-following methods (for an overview of such methods (see e.g., Riks, 1972). The basic idea of path-following methods is to append a constraint Equation $f\,(\boldsymbol{U},\lambda)=0$ to (23). Here, following Bathoz and Dhatt (1979), we adopt a displacement control and assume

$$f\,(\boldsymbol{U})=\boldsymbol{e}_p^T\boldsymbol{U}-\mathrm{u}=0, \tag{24}$$

where $\boldsymbol{e}_p$ is the vector of $\Re^N$ which has only the pth component different from zero and equal to 1, while μ is a prescribed value of the pth component of $\boldsymbol{U}$. Therefore, we are led to solve the extended system

$$\boldsymbol{R}^*\,(\boldsymbol{U},\lambda)=\begin{Bmatrix}\boldsymbol{R}\,(\boldsymbol{U},\lambda)\\ \boldsymbol{e}_p^T\boldsymbol{U}-\mu\end{Bmatrix}=0, \tag{25}$$

The linearization of Equation (25) by the Newton-Raphson method gives the system of incremental equilibrium equations

$$\boldsymbol{R}^*\,(\boldsymbol{U}+\Delta\boldsymbol{U},\lambda+\Delta\lambda)=\boldsymbol{R}^*\,(\boldsymbol{U},\lambda)+\begin{bmatrix}D_U\boldsymbol{R} & D_\lambda\boldsymbol{R}\\ \boldsymbol{e}_p^T & 0\end{bmatrix}\begin{Bmatrix}\Delta\boldsymbol{U}\\ \Delta\lambda\end{Bmatrix}=0, \tag{26}$$

The matrix $D_U\boldsymbol{R}$, which is usually referred to as tangent stiffness matrix and denoted by $\boldsymbol{K}_T$, is given in the **Appendix**. Concerning the vector $D_\lambda\boldsymbol{R}$, from Equation (23) we deduce

$$D_\lambda \boldsymbol{R} = -\left[\boldsymbol{Q}^{(1)} + \boldsymbol{Q}^{(2)}(\boldsymbol{U})\right]. \tag{27}$$

The non-symmetric system (26), that we rewrite in the form

$$\begin{bmatrix} \boldsymbol{K}_T & -\left(\boldsymbol{Q}^{(1)} + \boldsymbol{Q}^{(2)}\right) \\ \boldsymbol{e}_p^T & 0 \end{bmatrix} \begin{Bmatrix} \Delta \boldsymbol{U} \\ \Delta\lambda \end{Bmatrix} = -\begin{Bmatrix} \boldsymbol{R}(\boldsymbol{U},\lambda) \\ \boldsymbol{e}_p^T \boldsymbol{U} - \mu \end{Bmatrix}, \tag{28}$$

can be solved by a procedure known in literature as bordering algorithm (see e.g., Keller, 1977). Such algorithm and the overall procedure for the solution of the extended system (25) are described in **Table 1**.

In particular, if the first predictor $\boldsymbol{U}$ satisfies the constraint (24), Equation (31) reduces to

$$\Delta\lambda = \frac{\boldsymbol{e}_p^T \Delta \boldsymbol{U}_R}{\boldsymbol{e}_p^T \Delta \boldsymbol{U}_Q} \tag{34}$$

We point out that, since we proceed by displacement control, we apply the above iterative procedure in incremental steps. Within the generic step, say the ith one, we increment by δ the displacement component $\boldsymbol{U}_p$ which exhibited the largest variation in the previous step. We hence set in the extended system (25)

$$\mu = \boldsymbol{e}_p^T \boldsymbol{U}^{i-1} + \delta \tag{35}$$

and begin the new iteration loop by assuming the predictor $\tilde{\boldsymbol{U}} = \boldsymbol{U}^{i-1} + \delta \boldsymbol{e}_p$, $\tilde{\lambda}=\lambda^{i-1}$, which satisfies Equation (24).

Computation of Stability Points

In the current section we get a finite-element approximation of the problem of computing stability points based on the Trefftz criterion (Trefftz, 1930).

TABLE 1 | Bordering algorithm.

Algorithm
Assure a predictor $\tilde{\boldsymbol{U}}$, $\tilde{\lambda}$ for $\boldsymbol{U}$, λ and evaluate
$\tilde{\boldsymbol{R}} = \boldsymbol{R}\left(\tilde{\boldsymbol{U}},\tilde{\lambda}\right), \tilde{\boldsymbol{K}}_T = \boldsymbol{K}_{\boldsymbol{T}}\left(\tilde{\boldsymbol{U}},\tilde{\lambda}\right), \tilde{\boldsymbol{Q}}^{(2)} = \boldsymbol{Q}^{(2)}\left(\tilde{\boldsymbol{U}}\right)$. (29)
Repeat (setting $\tilde{\boldsymbol{U}}=\boldsymbol{U}$, $\tilde{\lambda}=\lambda$)
From $(28)_1$ compute the partial solutions
$\Delta \boldsymbol{U}_Q = \tilde{\boldsymbol{K}}_T^{-1}\left(\boldsymbol{Q}^{(1)} + \boldsymbol{Q}^{(2)}\right), \Delta \boldsymbol{U}_R = -\tilde{\boldsymbol{K}}_T^{-1}\tilde{\mathbf{R}}$. (30)
Solve $(28)_2$ for $\Delta\lambda$
$\Delta\lambda = -\frac{\boldsymbol{e}_p^T \Delta \boldsymbol{U}_R + \left(\boldsymbol{e}_p^T \tilde{\boldsymbol{U}} - \mu\right)}{\boldsymbol{e}_p^T \Delta \boldsymbol{U}_Q}$ (31)
Compute total displacement increment by
$\Delta \boldsymbol{U} = \Delta\lambda \Delta \boldsymbol{U}_Q + \Delta \boldsymbol{U}_R$, (32)
update: $\boldsymbol{U}=\tilde{\boldsymbol{U}} + \Delta \boldsymbol{U}$, $\lambda=\tilde{\lambda} + \Delta\lambda$
until
$\frac{\left\| \boldsymbol{R}^*(\boldsymbol{U},\lambda) \right\|}{\left\| \lambda(\boldsymbol{Q}^{(1)} + \boldsymbol{Q}^{(2)}(\boldsymbol{U})) \right\|} \leq tol$ (33)

Within the previous settings, we obtain the following discrete equation

$$D_U^2 \prod_e^h (\boldsymbol{U},\lambda)\, \boldsymbol{U}_1 \delta \boldsymbol{U} = \delta \boldsymbol{U}^T \boldsymbol{K}_T(\boldsymbol{U},\lambda)\, \boldsymbol{U}_1 = 0 \tag{36}$$

which must be satisfied by every variation $\delta\boldsymbol{U}$.

A point $\boldsymbol{U}$, λ such that Equation (36) holds for some $\boldsymbol{U}_1$ is usually called stability point, while $\boldsymbol{U}_1$ is called buckling mode (or eigenvector) associated with $\boldsymbol{U}$, λ.

Due to the arbitrariness of $\delta\boldsymbol{U}$, Equation (36) is equivalent to the system of N Equations

$$\boldsymbol{K}_T(\boldsymbol{U},\lambda)\, \boldsymbol{U}_1 = 0 \tag{37}$$

In the following we will denote $\boldsymbol{U}_1$ by $\boldsymbol{V}$. In order to exclude the trivial case $\boldsymbol{V}=\boldsymbol{0}$, it is necessary to append a constraint equation $l(\boldsymbol{V}) = 0$ to system (37). Possible choices of such an equation are

$$\|\boldsymbol{V}\| - 1 = 0 \tag{38}$$

$$\boldsymbol{e}_p^T \boldsymbol{V} - V_0 = 0 \tag{39}$$

V_0 being a fixed (non-zero) value of the pth component of $\boldsymbol{V}$. In this work we make use of Equation (39) and, after having reduced $\boldsymbol{K}_T$ to an upper triangular matrix (by Gauss elimination technique), we identify the index p with the equation number where the lowest diagonal term of the reduced stiffness matrix appears. In this way we prevent the pth component of $\boldsymbol{V}$ becoming exceedingly large. Concerning V_0, we set

$$V_0 = \frac{\boldsymbol{e}_p^T \boldsymbol{V}_0}{\|\boldsymbol{V}_0\|} \tag{40}$$

$\boldsymbol{V}_0$ being the initial approximation to $\boldsymbol{V}$.

Stability points can be classified in limit (or turning) and bifurcation points (Budiansky, 1974). Following Spence and Jepson (Spence and Jepson, 1985) we can distinguish between the two cases by using the following criteria

$$\text{Bifurcation point:} \quad \boldsymbol{V}^T\left(\boldsymbol{Q}^{(1)} + \boldsymbol{Q}^{(2)}(\boldsymbol{U})\right) = 0 \tag{41}$$

$$\text{Limit point:} \quad \boldsymbol{V}^T\left(\boldsymbol{Q}^{(1)} + \boldsymbol{Q}^{(2)}(\boldsymbol{U})\right) \neq 0 \tag{42}$$

An efficient procedure for the computation of stability points has been proposed by Simo and Wriggers (1990). It consists of solving the extended system

$$\boldsymbol{R}^{**}(\boldsymbol{U},\boldsymbol{V},\lambda,\mu) = \begin{Bmatrix} \boldsymbol{R}(\boldsymbol{U},\lambda) \\ \boldsymbol{K}_{\boldsymbol{T}}(\boldsymbol{U},\lambda)\, \boldsymbol{V} \\ \boldsymbol{e}_p^T \boldsymbol{V} - V_0 \\ \boldsymbol{e}_p^T \boldsymbol{U} - \mu \end{Bmatrix} = \boldsymbol{0} \tag{43}$$

which derives from the addition of Equations (37, 39) to the system of non-linear equilibrium Equations (25).

Since the tangent stiffness matrix becomes progressively ill-conditioned as the solution approaches the stability point, where $\boldsymbol{K}_T$ is singular, from a numerical point of view it is convenient to

transform the extended system (43) into the following equivalent form Simo and Wriggers (1990)

$$\boldsymbol{R}_{\eta}^{**}(\boldsymbol{U},\boldsymbol{V},\lambda,\mu)=\left\{\begin{array}{c}\boldsymbol{R}(\boldsymbol{U},\lambda)+\eta\left(\boldsymbol{e}_p^T\boldsymbol{U}-\mu\right)\boldsymbol{e}_p\\ \boldsymbol{K_T}(\boldsymbol{U},\lambda)\,\boldsymbol{V}+\eta\left(\boldsymbol{e}_p^T\boldsymbol{V}-V_0\right)\boldsymbol{e}_p\\ \boldsymbol{e}_p^T\boldsymbol{V}-V_0\\ \boldsymbol{e}_p^T\boldsymbol{U}-\mu\end{array}\right\}=\boldsymbol{0},\quad(44)$$

η being an arbitrary positive number. The linearization of Equation (44) by the Newton-Raphson method leads us to obtain the set of incremental equations

$$\left[\begin{array}{cccc}\boldsymbol{K}_{T_\eta} & 0 & -\boldsymbol{Q} & -\eta\boldsymbol{e}_p\\ D_U(\boldsymbol{K}_T\boldsymbol{V}) & \boldsymbol{K}_{T_\eta} & D_\lambda(\boldsymbol{K}_T\boldsymbol{V}) & \boldsymbol{0}\\ \boldsymbol{0}^T & \boldsymbol{e}_p^T & 0 & 0\\ \boldsymbol{e}_p^T & \boldsymbol{0}^T & 0 & -1\end{array}\right]\left\{\begin{array}{c}\Delta\boldsymbol{U}\\ \Delta\boldsymbol{V}\\ \Delta\lambda\\ \Delta\mu\end{array}\right\}$$
$$=\left\{\begin{array}{c}\boldsymbol{R}(\boldsymbol{U},\lambda)+\eta\left(\boldsymbol{e}_p^T\boldsymbol{U}-\mu\right)\boldsymbol{e}_p\\ \boldsymbol{K}_{T_\eta}(\boldsymbol{U},\lambda)\,\boldsymbol{V}-\eta V_0\boldsymbol{e}_p\\ \boldsymbol{e}_p^T\boldsymbol{V}-V_0\\ \boldsymbol{e}_p^T\boldsymbol{U}-\mu\end{array}\right\}\quad(45)$$

where $\boldsymbol{Q}=\boldsymbol{Q}^{(1)}+\boldsymbol{Q}^{(2)}(\boldsymbol{U})$, while

$$\boldsymbol{K}_{T\eta}(\boldsymbol{U},\lambda)=\boldsymbol{K}_T(\boldsymbol{U},\lambda)+\eta\boldsymbol{e}_p\boldsymbol{e}_p^T\ (p\text{ not summed})\quad(46)$$

is a rank-one updated stiffness matrix. The solution of the non-symmetric system (45) can be obtained by a bordering algorithm similar to that described in the previous section Path-Following Procedure. **Table 2** shows this algorithm and the global procedure for the solution of the extended system (44).

We furnish the expressions of the vectors $\boldsymbol{h}_j$ ($j=1,\ldots,4$), which appear in Equations (50), in the **Appendix**.

Overall Algorithm for Stability Analysis

We compute the pre-buckling and post-buckling equilibrium paths of a laminated beam by combining the procedures described in Sections Path-Following Procedure and Computation of Stability Points.

More precisely, denoted the initial stiffness matrix by $\boldsymbol{K}_0$ (see the **Appendix**) and an arbitrary numeric value by λ_0, we consider the couple λ_0, $\boldsymbol{U}_0=\lambda_0\boldsymbol{K_0^{-1}}\boldsymbol{Q}^{(1)}$ as the initial predictor of the first equilibrium state.

We hence correct this predictor as described in section Path-Following Procedure and keep computing equilibrium states along the primary path. We check for the sign of the tangent stiffness matrix determinant in correspondence of each state, which is a simple operation since the solution of the extended system (25) requires the factorization (i.e., the triangular decomposition) of $\boldsymbol{K}_T$.

If the sign of $\det\boldsymbol{K}_T$ changes between two successive states, say i and $i+1$, a stability point has passed. We hence switch from the path-following procedure to the procedure for computing stability points.

In particular we assume $\tilde{\boldsymbol{U}}=\mathbf{U}^{i+1}$, $\tilde{\boldsymbol{V}}=\boldsymbol{V}_0=\boldsymbol{K}_0^{-1}\boldsymbol{e}_p$, $\tilde{\lambda}=\lambda^{i+1}$, $\tilde{\mu}=\boldsymbol{e}_p^T\,\mathbf{U}^{i+1}$ (for the meaning of the index p see the beginning of section Computation of Stability Points).

TABLE 2 | Bordering algorithm.

Algorithm

Assume a predictor $\tilde{\boldsymbol{U}}$, $\tilde{\boldsymbol{V}}$, $\tilde{\lambda}$, $\tilde{\mu}$ and evaluate

$$\tilde{\boldsymbol{R}}=\boldsymbol{R}\left(\tilde{\boldsymbol{U}},\tilde{\lambda}\right),\ \tilde{\boldsymbol{K}}_{T_\eta}=\boldsymbol{K}_{T_\eta}\left(\tilde{\boldsymbol{U}},\tilde{\lambda}\right),\ \tilde{\boldsymbol{Q}}^{(2)}=\boldsymbol{Q}^{(2)}\left(\tilde{\boldsymbol{U}}\right).\quad(47)$$

Repeat (setting $\tilde{\boldsymbol{U}}=\boldsymbol{U}$, $\tilde{\boldsymbol{V}}=\boldsymbol{V}$, $\tilde{\lambda}=\lambda$, $\tilde{\mu}=\mu$)

From $(45)_1$ compute the partial solutions

$$\Delta\boldsymbol{U}_1=\tilde{\boldsymbol{K}}_{T_\eta}^{-1}\left(\boldsymbol{Q}^{(1)}+\tilde{\boldsymbol{Q}}^{(2)}\right)$$
$$\Delta\boldsymbol{U}_2=-\tilde{\boldsymbol{K}}_{T_\eta}^{-1}\tilde{\boldsymbol{R}}$$
$$\Delta\boldsymbol{U}_3=-\tilde{\boldsymbol{K}}_{T_\eta}^{-1}\boldsymbol{e}_p\quad(48)$$

From $(45)_2$ compute the partial solutions

$$\boldsymbol{q}_1=\tilde{\boldsymbol{K}}_{T_\eta}^{-1}\boldsymbol{h}_1\quad(49)$$
$$\boldsymbol{q}_2=\tilde{\boldsymbol{K}}_{T_\eta}^{-1}\boldsymbol{h}_2$$
$$\boldsymbol{q}_3=\tilde{\boldsymbol{K}}_{T_\eta}^{-1}\boldsymbol{h}_3$$
$$\boldsymbol{q}_4=\tilde{\boldsymbol{K}}_{T_\eta}^{-1}\boldsymbol{h}_4$$

where

$$\boldsymbol{h}_1=-D_U(\boldsymbol{K}_T\boldsymbol{V})\,\Delta\boldsymbol{U}_1$$
$$\boldsymbol{h}_2=-D_U(\boldsymbol{K}_T\boldsymbol{V})\,\Delta\boldsymbol{U}_2$$
$$\boldsymbol{h}_3=-D_U(\boldsymbol{K}_T\boldsymbol{V})\,\Delta\boldsymbol{U}_3$$
$$\boldsymbol{h}_4=-D_\lambda(\boldsymbol{K}_T\boldsymbol{V})\quad(50)$$

Compute $\Delta\lambda$ and $\Delta\mu$.

The increments $\Delta\lambda$ and Δu can be computed from Equations $(45_3$ to $45)_4$, which can be written as

$$\left[\begin{array}{cc}\boldsymbol{e}_p^T(\boldsymbol{q}_1+\boldsymbol{q}_4) & \eta\,\boldsymbol{e}_p^T\boldsymbol{q}_3\\ \boldsymbol{e}_p^T\,\Delta\boldsymbol{U}_1 & \eta\,\boldsymbol{e}_p^T\,\Delta\boldsymbol{U}_3-1\end{array}\right]\left\{\begin{array}{c}\Delta\lambda\\ \Delta u\end{array}\right\}=\left\{\begin{array}{c}g_1\\ g_2\end{array}\right\}\quad(51)$$

where

$$g_1=V_0-\boldsymbol{e}_p^T\left[\boldsymbol{q}_2+\eta\,V_0\,\Delta\boldsymbol{U}_3+\eta\,\left(\mu-\boldsymbol{e}_p^T\tilde{\boldsymbol{U}}\right)\boldsymbol{q}_3\right]$$
$$g_2=\mu-\boldsymbol{e}_p^T\left[\tilde{\boldsymbol{U}}+\Delta\boldsymbol{U}_2+\eta\,\left(\mu-\boldsymbol{e}_p^T\tilde{\boldsymbol{U}}\right)\Delta\boldsymbol{U}_3\right]\quad(52)$$

Compute $\Delta\boldsymbol{U}$ and $\Delta\boldsymbol{V}$ from the equations

$$\Delta\boldsymbol{U}=\Delta\lambda\Delta\boldsymbol{U}_1+\Delta\boldsymbol{U}_2+\eta\,\left(\mu\,\Delta\mu-\boldsymbol{e}_p^T\tilde{\boldsymbol{U}}\right)\Delta\boldsymbol{U}_3$$
$$\Delta\boldsymbol{V}=-\tilde{\boldsymbol{V}}+\Delta\lambda\,(\boldsymbol{q}_1+\boldsymbol{q}_4)+\boldsymbol{q}_2+\eta\left[\,\left(\mu+\Delta\mu-\boldsymbol{e}_p^T\tilde{\boldsymbol{U}}\right)\boldsymbol{q}_3+V_0\,\Delta\boldsymbol{V}_3\right]\quad(53)$$

and update: $\boldsymbol{U}=\tilde{\boldsymbol{U}}+\Delta\boldsymbol{U}$, $\boldsymbol{V}=\tilde{\boldsymbol{V}}+\Delta\boldsymbol{V}$, $\lambda=\tilde{\lambda}+\Delta\lambda$, $\mu=\tilde{\mu}+\Delta u$.

until $\dfrac{\left\|\boldsymbol{R}_\eta^{**}(\boldsymbol{U},\boldsymbol{V},\ \lambda,\mu)\right\|}{\left\|\lambda(\boldsymbol{Q}^{(1)}+\boldsymbol{Q}^{(2)}(\boldsymbol{U}))\right\|}\le tol\quad(54)$

Once the stability point $\boldsymbol{U}_c$, λ_c has been computed, we check if it is a limit or a bifurcation point. In the case of a limit point we come back to the path-following procedure to complete the primary path. In the case of a bifurcation point, we switch to the secondary (or bifurcated) path by adding to $\boldsymbol{U}_c$ a vector proportional to the eigenvector $\boldsymbol{V}$

$$\boldsymbol{U}=\boldsymbol{U}_c+\zeta\,\frac{\boldsymbol{V}}{\|\boldsymbol{V}\|}\quad(55)$$

ζ being a scaling factor to be determined in such a way that it results $\boldsymbol{R}(\boldsymbol{U},\lambda_c)\le tol$.

We then follow the secondary path using the path-following procedure and arrest the calculations when the cross-section rotations or the shear strains are more than moderately large or the axial strains are more than infinitesimal (18).

NUMERICAL RESULTS

We present in this section several numerical results relative to the evaluation of the stability points and to the post-buckling behavior of straight and curved beams.

In all the examples we supposed the beam cross-section to be rectangular with lengths H_1 and H_2 along the directions X_1 and X_2, respectively. We denoted the cross-section area by $A = H_1 H_2$, the moments of inertia by I_1 and I_2, the polar moment of inertia by I_G and the De Saint Venant torsional rigidity by J_t

$$I_1 = \frac{H_1 H_2^3}{12}, I_2 = \frac{H_1^3 H_2}{12}, \mathrm{I_G} = I_1 + I_2, \mathrm{J_t} = \frac{H_1^3 H_2}{3}. \quad (56)$$

Concerning the expression of the warping function w, we examined the following three cases:

No Warping (NW): $w = 0$

Warping Function (W1): $w = w_{11} X_1 X_2$

Warping Function (W3): $w = w_{20} X_1^2 + w_{11} X_1 X_2 + w_{02} X_2^2 + w_{30} X_1^3 + w_{21} X_1^2 X_2 + w_{12} X_1 X_2^3 + w_{03} X_2^3$.

We used cubic Lagrangian finite elements and a four-point Gauss quadrature formula to compute the tangent stiffness matrix and its derivatives. By this choice we avoided the numerical inconvenient known in literature as shear and membrane (or inplane) locking (see e.g., Prathap and Bhashyam, 1982; Reddy and Averill, 1990).

We always assumed that the external loads retain their directions during the deformation of the beam (dead loading).

BIFURCATION POINTS OF ISOTROPIC, STRAIGHT AND CURVED BEAMS

In order to assess the accuracy of our numerical model, we firstly present some results concerned with bifurcation points of isotropic straight and curved beams. They can be compared with those available in the relevant literature and corresponding to classical beam theories (see e.g., Timoshenko and Gere, 1961; Brush and Almroth, 1975). We assumed a ratio $E/G = 0.385$ between Young's and shear moduli.

The first example deals with a circular ring submitted to a radial dead load of intensity q, which is uniformly distributed along the centerline. We discretized one half of the ring by 20 finite elements imposing the following boundary conditions (no warping was considered)

$$v_1 = v_2 = v_3 = \phi_1 = \phi_2 = \phi_3 = 0 \quad \text{for } X_3 = 0,$$
$$v_1 = v_3 = \phi_1 = \phi_2 = \phi_3 = 0, \quad \text{for } X_3 = \pi R, \quad (57)$$

where R is the initial radius of the centerline. In particular, the ratios $H_1/H_2 = 2, R/H_2 = 20$ were considered.

According to Donnel' s theory (see e.g., Brush and Almroth, 1975), the first bifurcation point occurs at a load level $q_{bif} = 4\,E\,I_1/R^3$ and the buckling mode corresponds to an ovalization of the ring.

It has to be remarked that the first bifurcation point occurs at a sensibly different load level $q_{bif} = 3\,E\,I_1/R^3$ if the external load remains orthogonal to the axis during the deformation of the ring (see e.g., Timoshenko and Gere, 1961; Brush and Almroth, 1975).

TABLE 3 | Convergence behavior or the first bifurcation point or a circular ring submitted to a radial dead load q uniformly distributed along the centerline ($H_1/H_2 = 2, R/H_2 = 20$, 20 element mesh).

Iteration	$\eta = 0$		$\eta = (D_{op} - D_p) \times 10$		$\eta = (D_{op} - D_p) \times 1000$	
	λ	ε	λ	ε	λ	ε
1	4.3056	0.1822	4.3056	0.6018×10	4.3056	0.6069×10^{3}
2	4.2871	0.1645×10^{-2}	4.2871	0.1643×10^{-2}	4.2871	0.1645×10^{-2}
3	3.9886	0.1022×10^{-3}	3.9891	0.1154×10^{-3}	3.9916	0.1327×10^{-3}
4	3.9883	0.4035×10^{-5}	3.9888	0.4821×10^{-6}	3.9887	0.1010×10^{-5}
5	3.9892	0.3295×10^{-5}	3.9888	0.1920×10^{-8}	3.9888	0.4257×10^{-6}
6	3.9887	0.2094×10^{-3}			3.9888	0.1920×10^{-8}
7	3.9889	0.4045×10^{-3}				

$\lambda = \frac{q_{bif} R^3}{E I_1}$

dimensionless residual $\varepsilon = \frac{\|\boldsymbol{R}_\eta^{**}\|}{\|\lambda\, \boldsymbol{Q}\|}$

Table 3 shows the numerical convergence of the solutions of the extended system (44) for increasing values of the parameter η.

Denoting by D_p the least diagonal term of the factorized tangent stiffness matrix and by D_{op} the corresponding term in the factorized initial stiffness matrix $\boldsymbol{K}_0$, in our numerical experiments we set $\eta = 0$, $\eta = (D_{op} - D_p) \times 10$ and $\eta = (D_{op} - D_p) \times 1000$.

As already observed by Simo and Wriggers (1990), for $\eta = 0$ the results exhibit oscillations near the bifurcation point, while for $\eta > 0$ they converge in a stable way to the value $3.9888\, EI_1/R^3$.

Table 3 also shows that in the latter case the solution is rather insensitive to the value of η.

The small difference existing between our and Donnel's bifurcation load can be justified observing that Donnel's theory does not account for shear deformation and for the quadratic terms in X_1 and X_2 of the axial strain E_{33}, which are instead present in our model. In all the subsequent numerical applications we $\eta = (D_{op} - D_p) \times 10$.

The second example we considered deals with the classical case of a simply supported straight beam loaded by a compressive force at one end ($X_3 = L$). **Table 4** compares the bifurcation loads computed by using the present theory with those corresponding to Euler's theory ($P_{Eul} = \pi^2\, EI_1/L^2$) and Timoshenko's theory, for several the values of the ratio L/H_2, assuming $H_1/H_2 = 2$. Upon putting $\rho = \chi\, P_{Eul}/GA$ ($\chi = 1.2$ shear correction factor), we considered both the exact values deriving from Timoshenko's Theory

$$\frac{P_{bif}}{P_{Eul}} = \frac{-(4+3\rho) + \sqrt{(4+3\rho)^2 + 16\rho}}{2\rho} \quad (58)$$

and the approximate ones (see e.g., Timoshenko and Gere, 1961)

$$\frac{P_{bif}}{P_{Eul}} = \frac{1}{1+\rho}. \quad (59)$$

TABLE 4 | First bifurcation load of a simply supported, axially loaded straight beam for several ratios L/H_2 ($H_1/H_2 = 2$, 20 element mesh).

	$\lambda_{bif}=P_{bif}/P_{Eul}$					
L/H_2	ETT[a]	ATT[b]	PTNWNΓ[c]	PTW3NΓ[d]	PTNWΓ[e]	PTW3Γ[f]
5	0.90892	0.90700	0.92127	0.90741	0.89622	0.88437
10	0.97516	0.97501	0.97909	0.97500	0.97143	0.96756
20	0.99364	0.99363	0.99465	0.99358	0.99261	0.99164
40	0.99840	0.99840	0.99868	0.99840	0.99817	0.99790
100	0.99974	0.99974	0.99981	0.99976	0.99971	0.99966

[a] *Exact Timoshenko's Theory.*
[b] *Approximate Timoshenko's Theory.*
[c] *Pres.Th.-No warping-No Γ terms.*
[d] *Pres.Th.-W3 warping-No Γ terms.*
[e] *Pres.Th.-No warping-Γ terms incl.*
[f] *Pres.Th.-W3 warping-Γ terms incl.*

Concerning the comparisons between our and classical theories, we stressed the influences of warping and quadratic terms in X_1, X_2 of the axial strain E_{33} (Γ terms). It has to be remarked that our theory turns into a first-order shear deformation theory with no shear correction factor ($\chi = 1$) in absence of warping and Γ terms.

Table 4 shows that our results corresponding to a cubic warping function and absence of Γ terms closely approximate those by Timoshenko. Furthermore, the influence of Γ terms is found to be appreciable (up to 2.7%) for thick beams. We took into account Γ deformation terms in all the successive numerical applications.

We complete this first group of numerical results by showing some further examples concerned with lateral buckling of straight bars and semicircular arches.

We firstly considered a narrow simply supported beam transversally loaded at the middle point and a narrow cantilever transversally loaded at the free end ($H_1/H_2 = 0.1$, $L/H_2 = 10$). The kinematical boundary conditions of the first case are

$$\begin{aligned} v_1 = v_2 = v_3 = \phi_3 = 0 \quad &\text{for } X_3 = 0, \\ v_1 = v_2 = \phi_3 = 0 \quad &\text{for } X_3 = L, \end{aligned} \tag{60}$$

Three positions of the load were considered: load at the centroid, load at the extrados ($X_1 = 0$, $X_2 = -H_2/2$) and load at the intrados ($X_1 = 0, X_2 = H_2/2$). The last two cases obviously give rise to a deformation-dependent loading ($\boldsymbol{Q}^{(2)}(\boldsymbol{U}) \neq \boldsymbol{0}$).

Table 5 shows a comparison between the first bifurcation points computed within the present theory and those corresponding to the classical Prandtl's theory (See e.g., Timoshenko and Gere, 1961).

In the context of the present theory, we adopted a bilinear warping function ($W1$) and assumed both a linear and a (geometrically) nonlinear pre-buckling behavior (the first was treated by discarding the part $\boldsymbol{K}_L$ of the tangent stiffness matrix, see the **Appendix**).

We also generalized Prandtl's theory in order to include a nonlinear pre-buckling behavior. This was obtained by using our model, neglecting shear deformation, warping and Γ terms and making the torsional stiffness equal to GJ_t.

TABLE 5 | First lateral bifurcation point of a simply supported beam loaded by a transverse force **Q** at the middle point and of a cantilever loaded by a transverse force **Q** at the free end ($H_1/H_2 = 0.1$, $L/H_2 = 10$, 20 element mesh).

		CT-LPB	PT-LPB	CT-NLPB	PT-NLPB
LOAD AT THE CENTROID					
simple supported	$v_m/L \times 100$	0.4380	0.4483	0.4401	0.4520
	λ_{bif}	16.940	16.902	17.020	17.040
cantilever	$v_f/L \times 100$	1.6600	1.7240	1.7026	1.7776
	λ_{bif}	4.0130	4.1840	4.1159	4.2695
LOAD AT THE EXTRADOS					
simple supported	$v_m/L \times 100$	0.4053	0.4152	0.4071	0.4183
	λ_{bif}	15.752	15.654	15.745	15.772
cantilever	$v_f/L \times 100$	1.5912	1.6647	1.6337	1.6993
	λ_{bif}	3.8513	3.9910	3.9422	4.0737
LOAD AT THE INTRADOS					
simple supported	$v_m/L \times 100$	0.4656	0.4832	0.4743	0.4874
	λ_{bif}	18.127	18.215	18.346	18.376
cantilever	$v_f/L \times 100$	1.7199	1.8099	1.7621	1.8459
	λ_{bif}	4.1747	4.3559	4.2683	4.4428

CT, Classical Theory.
PT, Present Theory.
v_m, *middle point in-plane displacement.*
v_f, *free end in-plane displacement.*
$\lambda_{bif} = \frac{Q_{bif}L^2}{\sqrt{EI_2 GJ_t}}$.
LPB, Linear Pre-Buckling; NLPB, Nonlinear Pre-Buckling.

TABLE 6 | First lateral bifurcation load of a hinged and a clamped semicircular arch loaded by a radial dead load q uniformly distributed along the centerline ($H_1/H_2 = 0.1$, $R/H_2 = 10$, 20 element mesh).

	$\lambda_{bif}=\frac{q_{bif}R^3}{EI_2}$	
	Classical theory	**Present theory**
hinged arch	1.9358	1.9361
clamped arch	13.514	13.774

It has to be remarked that the present theory assumes a torsional rigidity equal to GI_G (as in the De Saint Venant theory of torsion without warping) and takes into account warping effects by introducing in the displacement field a polynomial warping function.

It is evident that our numerical results agree better with those by Prandtl when the warping is unconstrained, as in the case of the simply supported beam. On the contrary, in the second example (cantilever), our and Prandtl's results somewhat differ due to the presence of the restraint which doesn't allow the warping of the built-in end.

Further on we remark that the assumption of a linear pre-buckling behavior, as in the original Prandtl's theory, is less accurate for the cantilever than for the simply supported beam. Indeed, in the first case the in-plane displacements are sensibly higher than in the second case and produce moderate rotations.

Finally, **Table 6** shows the bifurcation loads of hinged and clamped narrow semicircular arches ($v_1 = v_2 = v_3 = \phi_3 = 0$ for $X_3 = 0$, πR in the first case). The load consists of a uniform radial dead load along the centerline.

The results of the present theory are compared with those given in Timoshenko and Gere (1961), which are relative to the classical beam theory. In particular, the first ones correspond to the choice of a bilinear warping function (W1).

CONCLUDING REMARKS

This work has developed a finite element model of the moderate rotation theory (MRT) of laminated composite beams proposed in Fraternali et al. (2013), and its application to the computation of nonlinear equilibrium paths and stability points of a variety of numerical examples. The proposed model describes laminated composite beams with arbitrary curvature of the beam axis, and takes into account shear deformation, warping effects, in-plane and out-of-plane instability. For the straight and curved beams examples analyzed in the present study, we conclude the following:

(i) the moderate rotation theory (MRT) and the classical beams theories correlate very well in almost all isotropic cases;
(ii) the influence of warping effects on the bifurcation load is generally pretty high for beams made up of composite materials.

Future work will apply the model presented in this work to a wide collection of technically relevant case-studies, with special emphasis on the study of the stability of light-weight roof structures and arch bridges, which make use of laminated composite beams (Fraternali et al., 2013).

AUTHOR CONTRIBUTIONS

IM led the numerical part of the study. MM supervised the numerical part of the study. AA led the mechanical modeling part of the study. FF supervised all tasks.

ACKNOWLEDGMENTS

IM, AA, and FF gratefully acknowledge financial support from the Italian Ministry of Education, University and Research (MIUR) under the Departments of Excellence grant L.23 2/2016.

SUPPLEMENTARY MATERIAL

The Supplementary Material for this article can be found online at: https://www.frontiersin.org/articles/10.3389/fbuil.2018.00057/full#supplementary-material

REFERENCES

Ascione, L., Berardi, V. P., Giordano, A., and Spadea, S. (2013). Local buckling behavior of FRP thin-walled beams: a mechanical model. *Comp Struct*. 98, 111–120. doi: 10.1016/j.compstruct.2012.10.049

Ascione, L., Giordano, and, A., and Spadea, S. (2011). Lateral buckling of pultruded FRP beams. *Compos B Eng*. 42, 819–824. doi: 10.1016/j.compositesb.2011.01.015

Bathoz, I. L., and Dhatt, G. (1979). Incremental displacement algorithms for non-linear problems. *Int. J. Num. Meth. Engng*. 14, 1262–1267. doi: 10.1002/nme.1620140811

Bencardino, F., Rizzuti, L., Spadea, G., and Swamy, R. N. (2012). Implications of test methodology on post-cracking and fracture behavior of steel fibre reinforced concrete. *Compos. B Eng*. 46, 31–38. doi: 10.1016/j.compositesb.2012.10.016

Brush, D. O., and Almroth, B. O. (1975). *Buckling of Bars, Plates and Shells*. New York, NY: McGraw-Hill.

Budiansky, B. (1974). "Theory of buckling and post-buckling behavior of elastic structures," in *Advances in Applied Mechanics*, eds Chia-Shun Yih (New York, NY: Academic Press), 1–65.

Feo, L., and Fraternali, F. (2000). On a moderate rotation theory of thin-walled composite beams. *Compos. B. Eng*. 31, 141–158. doi: 10.1016/S1359-8368(99)00079-7

Feo, L., and Mancusi, G. (2010). Modeling shear deformability of thin-walled composite beams with open cross-section. *Mech. Res. Commun*. 37, 320–325. doi: 10.1016/j.mechrescom.2010.02.005

Fraternali, F. (2007). Free discontinuity finite element models in two-dimensions for in-plane crack problems. *Theor. Appl. Fract. Mech*. 47, 274–282. doi: 10.1016/j.tafmec.2007.01.006

Fraternali, F., Angelillo, M., and Fortunato, A. (2002). A lumped stress method for plane elastic problems and the discrete-continuum approximation. *Int. J. Solids Struct*. 39, 6211–6240. doi: 10.1016/S0020-7683(02)00472-9

Fraternali, F., Ciancia, V., Chechile, R., Rizzano, G., and Feo, L. (2011). Incarnato, L. Experimental study of the thermo-mechanical properties of recycled PET fiber reinforced concrete. *Comp. Struct*. 93, 2368–2374. doi: 10.1016/j.compstruct.2011.03.025

Fraternali, F., Farina, I., Polzone, C., Pagliuca, E., and Feo, L. (2012). On the use of R-PET strips for the reinforcement of cement mortars. *Compos. B. Eng*. 46, 207–210. doi: 10.1016/j.compositesb.2012.09.070

Fraternali, F., Negri, M., and Ortiz, M. (2010). On the convergence of 3D free discontinuity models in variational fracture. *Int. J. Fract*. 166, 3–11. doi: 10.1007/s10704-010-9462-0

Fraternali, F., Spadea, S., and Ascione, L. (2013). Buckling behavior of curved composite beams with different elastic response in tension and compression. *Compos. Struct*. 100, 280–289, doi: 10.1016/j.compstruct.2012.12.021

Keller, H. B. (1977). "Numerical solution of bifurcation and nonlinear eigenvalue problems," in *Applications of Bifurcation Theory,* eds P.H. Rabinowitz (New York, NY: Academic Press), 359–384.

Markkula, S., Malecki, H. C., and Zupan, M. (2013). Uniaxial tension and compression characterization of hybrid CNS-glass fiber-epoxy composites. *Comp. Struct*. 95, 337–345. doi: 10.1016/j.compstruct.2012.07.013

Mascolo, I., Fulgione, M., and Pasquino, M. (in press). Lateral torsional buckling of compressed open thin walled beams: experimental confermations. *Int. J. Mansory Res. Innovat*.

Mascolo, I., and Pasquino, M. (2016). Lateral-torsional buckling of compressed highly variable cross section beams. *Curved. Al. Layer. Struct*. 3443, 146–153. doi: 10.1515/cls-2016-0012

Nomizu, K., and Kobayashi, S. (1963). *Foundations of Differential Geometry*. New York, NY: Wiley.

Özütok, A., and Madenci, E. (2017). Static analysis of laminated composite beams based on higher-order shear deformation theory by using mixed-type finite element method. *Int. J. Mech. Sci*. 130, 234–243. doi: 10.1016/j.ijmecsci.2017.06.013

Prathap, G., and Bhashyam, G. (1982). Reduced integration and the shear-flexible beam element. *lnt.J. Num. Meth. Engng*. 18, 195–210. doi: 10.1002/nme.1620180205

Reddy, J. N. (1992). *An Introduction to the Finite Element Method*, 2nd Edn. New York, NY: McGraw-Hill.

Reddy, J. N., and Averill, R. C. (1990). On the behavior of plate elements based on the first-order shear deformation theory. *Engng. Comput*. 7, 57–74. doi: 10.1108/eb023794

Riks, E. (1972). The application of newton's method to the problem of elastic stability. *J. Appl. Mech*. 39, 1060–1066. doi: 10.1115/1.3422829

Roberts, T. M., and Al-Ubaidi, H. (2001). Influence of shear deformation on restrained torsional warping of pultruded FRP bars of open cross-section. *Thin-Walled Struct.* 39, 395–414. doi: 10.1016/S0263-8231(01)00009-X

Schmidt, B., Fraternali, F., and Ortiz, M. (2009). Eigenfracture: an eigendeformation approach to variational fracture. *Siam. J. Multiscale Model. Simul.* 7, 1237–1266. doi: 10.1137/080712568

Simo, J. C., and Wriggers, P. (1990). A general procedure for the direct computation of turning and bifurcation points. *int. J. Num. Meth. Engng*. 30, 155–176. doi: 10.1002/nme.1620300110

Spence, A., and Jepson, A. D. (1985). Folds in the solution of two parameter systems and their calculation, Pan. I, SIAM *J. Num. Anal*. 22, 347–368. doi: 10.1137/0722021

Timoshenko, S. P., and Gere, J. M. (1961). *Theory of Elastic Stability*. New York, NY: McGraw-Hill.

Trefftz, E. (1930). "Über die Ableitung der Stäbilitats-kriterien des elastischen Gleichgewichtes aus der elasticitäts theorie endlicher Deformationen," in *Proceedings of the Third international Congress for Applied Mechanics* (Stockholm), 44–50.

Viera, R. F., Virtuoso, F. B. E., and Pereira, E. B. R. (2013). A higher order thin-walled beam model including warping and shear modes. *Int. J. Mech. Sci.* 66, 67–82. doi: 10.1016/j.ijmecsci.2012.10.009

Conflict of Interest Statement: The authors declare that the research was conducted in the absence of any commercial or financial relationships that could be construed as a potential conflict of interest.

NOTATION

We report below the list of the main notations used in the text. Throughout this paper we use boldface character to denote numerical vectors and matrices; we also use the superscript T to denote the transpose of a vector or a matrix.

C	axis curve of a laminated beam
L	length of C
$X_3 \in [0, L]$	line coordinate along C
$R\ (X_3)$	curvature radius of C at the generic point
$\Sigma\ (X_3)$	generic cross-section of the beam
$X_1,\ X_2$	orthogonal coordinates on Σ with origin at the centroid
$H_1,\ H_2$	dimensions along $X_1,\ X_2$ of a rectangular cross-section
$\boldsymbol{v}\ (X_3) = \{v_1,\ v_2,\ v_3\}^T$	displacement vector of the generic point of C
$\boldsymbol{\phi}\ (X_3) = \{\phi_1,\ \phi_2,\ \phi_3\}^T$	vector associated with the skew part of $\boldsymbol{\Sigma}$-moderate rotation tensor
$\boldsymbol{w}\ (X_3) = \{w_1,\ w_2,\ w_3\}^T$	vector collecting warping function coefficients
m_w	number of warping coefficients
$\hat{\boldsymbol{u}}\ (X_3) = \left\{\boldsymbol{v}^T,\ \boldsymbol{\phi}^T,\ \boldsymbol{w}^T\right\}^T$	generalized displacement vector
$m = 6 + m_w$	number of generalized displacements
$\hat{\boldsymbol{E}}\ (\hat{\boldsymbol{u}})$	vector collecting generalized strains
$\hat{\boldsymbol{E}}^{(1)}\ (\hat{\boldsymbol{u}}),\ \frac{1}{2}\hat{\boldsymbol{E}}^{(2)}\ (\hat{\boldsymbol{u}}, \hat{\boldsymbol{u}})$	linear and quadratic parts of $\hat{\boldsymbol{E}}$
$\hat{\boldsymbol{S}}$	vector collecting generalized stresses
$\sigma = 9 + 2\ m_w$	number of generalized stresses and deformations
$\hat{\boldsymbol{D}}$	$\sigma \times \sigma$ elasticity matrix
λ	load multiplier
$\hat{\boldsymbol{q}}^{(1)}, \hat{\boldsymbol{q}}^{(2)}\ (\boldsymbol{u})$	vectors of first-order and second-order generalized forces per unit of length of C
$\hat{\boldsymbol{Q}}_l^{(1)}, \hat{\boldsymbol{Q}}_l^{(2)}\ (\boldsymbol{U}_l)$	vectors of first-order and second-order generalized forces applied at the cross- section Σ_l
n_e	number of elements of the finite element mesh
C_e	generic finite element
n	number of nodes of C_e
$n_n = n_e \times (n-1) + 1$	total number of nodes of the finite element mesh
$M = m \times n$	number of degrees of freedom per element
$\boldsymbol{U}_e$	M-dimensional nodal displacement vector of C_e
$\boldsymbol{K}_e\ (\boldsymbol{U}_e)$	$M \times M$ secant stiffness matrix of C_e
$\hat{\boldsymbol{Q}}_e^{(1)}, \hat{\boldsymbol{Q}}_e^{(2)}\ (\boldsymbol{U}_e)$	first-order and second-order nodal force vectors of C_e
N	total number of equations
$\boldsymbol{U}$	N-dimensional global displacement vector
$\boldsymbol{K}\ (\boldsymbol{U})$	$N \times N$ global secant stiffness matrix
$\hat{\boldsymbol{Q}}^{(1)}, \hat{\boldsymbol{Q}}^{(2)}\ (\boldsymbol{U})$	first-order and second-order global force vectors
$\boldsymbol{R}\ (\boldsymbol{U}, \lambda)$	residual vector
$\boldsymbol{K}_T\ (\boldsymbol{U}, \lambda)$	tangent stiffness matrix
$\Re^{\boldsymbol{N}}$	field of real numbers
$\|\cdot\|$	norm operator in $\Re^{\boldsymbol{N}}$
tol	fixed tolerance

Given a scalar function $f\ (\boldsymbol{U}, \lambda) : \Re^N \times \Re \rightarrow \Re$, we denote by $D_U f$ the vector which represents the Gateaux derivative of f with respect to $\boldsymbol{U}$

$\boldsymbol{V}^T D_U F = \lim_{\gamma \rightarrow 0}\ \frac{1}{\gamma}\left[f\ (\boldsymbol{U} + \gamma\ \boldsymbol{V},\ \lambda) - f\ (\boldsymbol{U},\ \lambda)\right],\ \forall\ \boldsymbol{V}\ \in \Re^N,$

and by $D_\lambda f$ the partial derivative of f with respect to λ.

Similarly, given a vector function $\boldsymbol{R}\ (\boldsymbol{U}, \lambda) : \Re^N \times \Re \rightarrow \Re^N$, we denote by $D_U \boldsymbol{R}$ the $N \times N$ matrix which represents the Gateaux derivative of $\boldsymbol{R}$ with respect to $\boldsymbol{U}$

$D_U \boldsymbol{R}\ \boldsymbol{V} = \lim_{\gamma \rightarrow 0}\ \frac{1}{\gamma}\left[\boldsymbol{R}\ (\boldsymbol{U} + \gamma\ \boldsymbol{V},\ \lambda) - \boldsymbol{R}\ (\boldsymbol{U},\ \lambda)\right],\ \forall\ \boldsymbol{V}\ \in\ \Re^N,$

and by $D_\lambda \boldsymbol{R}$ the partial derivative of $\boldsymbol{R}$ with respect to λ.

Finally, in the case of a scalar function $f\ (\boldsymbol{U},\ \lambda)$, we denote by $D_U^2 f$ the bilinear operator

$D_U^2 f\ \boldsymbol{V}_1\ \boldsymbol{V}_2 = \boldsymbol{V}_2^T\ D_U\left(D_U f\right)\ \boldsymbol{V}_1, \forall\ \boldsymbol{V}_1, \boldsymbol{V}_2\ \in \Re^N.$

frontiers in Built Environment

ORIGINAL RESEARCH
published: 30 October 2018
doi: 10.3389/fbuil.2018.00063

Free Vibration Analysis of Variable Cross-Section Single-Layered Graphene Nano-Ribbons (SLGNRs) Using Differential Quadrature Method

Subrat Kumar Jena and Snehashish Chakraverty**

Department of Mathematics, National Institute of Technology Rourkela, Rourkela, India

In this article, free vibration of the variable cross-section (non-uniform) single-layered graphene nano-ribbons (SLGNRs) is investigated by using the Differential Quadrature Method (DQM). Here width of the cross-section is assumed to vary exponentially along the length of the nano-ribbon. Euler–Bernoulli beam theory is considered in conjunction with the nonlocal elasticity theory of Eringen. Step by step procedure is included and MATLAB code has been developed to obtain the numerical results for different scaling parameters as well as for four types of boundary conditions. Convergence study is carried out to illustrate the efficiency of the method and obtained results are validated with known results in special cases showing good agreement. Further, numerical as well as graphical results are depicted to show the effects of the nonuniform parameter, nonlocal parameter, aspect ratio and edge conditions on the frequency parameters.

Keywords: SLGNR, euler-bernoulli beam theory, DQM, vibration, variable cross-section

OPEN ACCESS

Edited by:
Vagelis Plevris,
OsloMet – Oslo Metropolitan University, Norway

Reviewed by:
Ahmad Partovi Meran,
Necmettin Erbakan University, Turkey
Francesco Tornabene,
Università degli Studi di Bologna, Italy
Metin Aydogdu,
Trakya University, Turkey

****Correspondence:***
Subrat Kumar Jena
sjena430@gmail.com
Snehashish Chakraverty
sne_chak@yahoo.com

Specialty section:
This article was submitted to Computational Methods in Structural Engineering, a section of the journal Frontiers in Built Environment

Received: *30 August 2018*
Accepted: *11 October 2018*
Published: *30 October 2018*

Citation:
Jena SK and Chakraverty S (2018) Free Vibration Analysis of Variable Cross-Section Single-Layered Graphene Nano-Ribbons (SLGNRs) Using Differential Quadrature Method. Front. Built Environ. 4:63. doi: 10.3389/fbuil.2018.00063

INTRODUCTION

Application of nanomaterials has expanded in the area of physics, chemistry, engineering, and nanotechnology because of their special properties like mechanical, electrical and electronic (Dai et al., 1996). As a result of these properties, nanomaterials play very significant roles in various nano-mechanical systems and nanomaterials. These materials include nanowires, nanoparticles, nanoribbons, nanotubes etc. Various applications concerning CNT reinforced structure like reinforced beam, plate etc. can be found in the literatures (Tornabene et al., 2016, 2017; Banic et al., 2017; Fantuzzi et al., 2017). One may also get detail information about nanobeams and nanoplates in the book (Chakraverty and Behera, 2016). Among these nanostructures, single-layered graphene nano-ribbons viz. nanobeams attract more attention due to their great potential in engineering applications. Graphene nanoribbons (Geim and Novoselov, 2007; Geim, 2009; Novoselov et al., 2012) are graphene nanostrip with width less than 50 nm. For the first time, Mitsutaka Fujita and coauthors introduced Graphene ribbons as a theoretical model to examine the edge and nanoscale size effect in graphene (Fujita et al., 1996; Nakada et al., 1996; Wakabayashi et al., 1999). Reddy et al. (2006) investigated equilibrium configuration and continuum elastic properties of finite sized graphene. GNRs possess additional advantages over graphene sheets. These advantages include high aspect ratio, ultra-thin width, and opening band gap. So, one must have appropriate knowledge about the mechanical behaviors for accurate prediction of vibration characteristics. So far, many researchers have developed various nonclassical continuum theories such as couple stress theory, strain gradient theory, micropolar theory, and nonlocal elasticity theory. Out of these

nonclassical continuum theories, nonlocal elasticity theory developed by Eringen (1972), has been extensively used in the vibration.

Non-uniformity of nanomaterials is very useful in designing of many nanoelectromechanical systems (NEMS) devices such as oscillators, clocks, and sensor devices. In order to make a NEMS device more efficient, nanobeams with non-uniform cross-sections should be used. To be able to use non-uniform nanobeams, mechanical behaviors in both static and dynamic conditions should be known. So, vibration analysis is important for many NEMS devices. Aydogdu et al. (2018) investigated vibration of axially functionally graded nanorods and beams with a variable nonlocal parameter and these variations are assumed in the material properties viz. elasticity modulus, density, and nonlocal parameter. Ece et al. (2007) investigated the vibration of an isotropic beam with an exponentially varying width along the length of the beam. Mirzabeigy (2014) studied free vibration analysis of variable cross-section beams resting on elastic foundation and under axial force by using a semi-analytical approach. Transverse vibration of beam of linearly variable depth with edge crack was Modeled of Chaudhari and Maiti (1999). Attarnejad and Shahba (2011) used dynamic basic displacement functions for free vibration analysis of centrifugally stiffened tapered beams. A nonlocal version of Euler-Bernoulli beam in conjunction with Eringen's nonlocal elasticity was studied by Peddieson et al. (2003). Wang et al. (2007) investigated analytical solutions for vibration of nonlocal Euler-Bernoulli and Timoshenko nanobeams. Application of nonlocal theories for bending, buckling and vibration of beams can be seen in Reddy (2007) and Aydogdu (2009) and vibration analysis of Euler-Bernoulli nanobeams by using finite element method can be found in Eltaher et al. (2013). Hosseini Hashemi and Bakhshi Khaniki (2016) investigated an analytical solution for free vibration of a variable cross-section nonlocal nanobeam. The free transverse vibration of cracked Euler- Bernoulli nanobeams based on nonlocal elasticity model was studied by Loya et al. (2009). Beni et al. (2014) studied the transverse vibration of cracked nano-beam based on modified couple stress theory. Further, Bagdatli (2015) presented the non-linear vibration of nanobeams. Now, literature related to development of various approaches of Differential Quadrature (DQ) method have also been briefly mentioned herein.

For the first time, Bellman and Casti (1971) introduced the Differential Quadrature (DQ) method in the year 1971. Therefore, this powerful technique is being used for solving linear and nonlinear differential equations arising in various dynamic problems. Later, Bert et al. (1988) used this method for solving the dynamical problem arising in the field of structural dynamics. Since then, this method is applied by various researchers for solving different types of structural problems such as linear or nonlinear. Different authors introduced various procedures to use edge conditions in the DQ method. In this regard, for the first time, Bert et al. (Jang et al., 1989) proposed δ technique to use edge conditions. In this case (Shu, 2000), one may observe that one edge condition is used at the boundary point whereas other edge condition is at a distance δ from the boundary point. This δ technique may be suitable for the C-C edge but this is not useful for S-S and S-C edge conditions. In order to eradicate the shortcomings of the above approach, Bert further presented a new technique in applying edge conditions which may be found in Bert et al. (1993, 1994), Wang and Bert (1993), Wang et al. (1993), Bert and Malik (1996). In this technique, one just needs to implement one boundary condition numerically while the other edge condition can be obtained from the DQ weighting coefficient matrices. Similarly, Tornabene et al. surveyed several methods under the heading of strong formulation finite element method (SFEM) which can be found in Tornabene et al. (2015).

To the best of the present authors' knowledge, this article provides first time the frequency parameters of the variable cross-section (non-uniform) single-layered graphene nano-ribbons (SLGNRs) by using Differential Quadrature Method (DQM). In this article, Euler-Bernoulli beam theory in conjunction with nonlocal elasticity theory has been considered to illustrate the effects of the nonuniform parameter, nonlocal parameter, aspect ratio and edge condition on the frequency parameter.

REVIEW OF NONLOCAL ELASTIC THEORY

Nonlocal stress tensor σ at a given point x in conjunction to nonlocal elasticity theory can be expressed as Murmu and Adhikari (2010)

$$\sigma(x) = \int_V K\left(\left|x' - x\right|, \alpha\right) \tau \, dV(x') \tag{1}$$

where τ is the classical stress tensor, $K\left(\left|x' - x\right|, \alpha\right)$ the nonlocal modulus, and $\left|x' - x\right|$ the Euclidean distance. One may note that the volume integral is considered over the region V. Here α is the material constant and it depends on both external and internal characteristic lengths.

From Hooke's law, one may have

$$\tau(x) = C(x) : \varepsilon(x) \tag{2}$$

where C is the fourth order elasticity tensor, ε is the classical strain tensor and: denotes double dot product.

It may be noted that Equation (1) is the integral constitutive relation and it is very complicated to solve. Hence we need an equivalent form of this equation which may be expressed as Murmu and Adhikari (2010)

$$\left(1 - \alpha^2 L^2 \nabla^2\right)\sigma = \tau, \quad \alpha = \frac{e_0 a}{L} \tag{3}$$

where ∇^2 is the Laplace operator, e_0 is a material constant, a is an internal characteristic length and L is the external characteristic length of the nanostructure. Here $e_0 a$ is the nonlocal parameter which shows scale effect on the nanostructures.

MATHEMATICAL FORMULATION OF THE PROPOSED MODEL

In this study, the Euler–Bernoulli beam theory along with the nonlocal elasticity theory of Eringen (1972) has been considered for the investigation. In this regard, one must have adequate

knowledge about energies. Strain energy U for local elasticity may express as

$$U = \frac{1}{2}\int_0^L \int_A \sigma_{xx}\varepsilon_{xx}\, dA\, dx, \tag{4}$$

where σ_{xx} is the normal stress, L is the length and A is the cross-section area. The strain-displacement relation is given as

$$\varepsilon_{xx} = -z\frac{\partial^2 w}{\partial x^2}, \tag{5}$$

where ε_{xx} is the normal strain and w is the deflection function. Substituting Equation (5) in Equation (4), one may obtain

$$U = -\frac{1}{2}\int_0^L M\frac{\partial^2 w}{\partial x^2}\, dx, \tag{6}$$

where $M = \int_A z\sigma_{xx}dA$, is the bending moment. In this study, the free harmonic motion is considered viz. we take $w = w_0(x)\ \sin\ \omega t$, where ω is the natural frequency of vibration. Using free harmonic motion in Equation (6), we may obtain the strain energy U as

$$U = -\frac{1}{2}\int_0^L M\frac{d^2 w_0}{dx^2}\, dx. \tag{7}$$

The kinetic energy T is given as

$$T = \frac{1}{2}\int_0^L \rho A\omega^2 w_0^2\, dx, \tag{8}$$

where ρ is the mass density and A is the area.

Using Hamilton's principle and setting the co-efficient of δw_0 to zero, one may obtain the governing equation as

$$\frac{d^2 M}{dx^2} = -\rho A\omega^2 w_0. \tag{9}$$

Based on Eringen's nonlocal elasticity theory, the nonlocal constitutive relation for EBT may be expressed as

$$M - \mu\frac{d^2 M}{dx^2} = -EI\frac{d^2 w_0}{dx^2} \tag{10}$$

where μ is the nonlocal parameter which can be expressed as $\mu = (e_0 a)^2$ with e_0 and a denoting material constant and internal characteristic length respectively, I is the second moment of area and E is Young's modulus. By using Equation (9) and Equation (10), M may be expressed as

$$M = -EI\frac{d^2 w_0}{dx^2} + \mu\left(-\rho A\omega^2 w_0\right) \tag{11}$$

Structural members with variable cross section play very significant role in civil, mechanical, and aeronautical engineering. Since we have considered the width of the cross-section is varied exponentially along the length of the nanoribbon, so we will have (Hosseini Hashemi and Bakhshi Khaniki, 2016)

$$A(x) = A_0 e^{nx} \quad \text{and} \quad I(x) = I_0 e^{nx} \tag{12}$$

where, n is the non-uniform parameter, I_0 and A_0 are the second moment of area and cross-section of nanoribbon respectively. Using Equation (11) along with Equation (12) in Equation (9), one may obtain the governing equation in terms of displacement as

$$EI_0\frac{d^4 w_0}{dx^4} + 2nEI_0\frac{d^3 w_0}{dx^3} + EI_0\left(n^2 + \frac{\rho A_0\mu\omega^2}{EI_0}\right)\frac{d^2 w_0}{dx^2} + 2\rho A_0\mu\omega^2 n\frac{dw_0}{dx} + \rho A_0\omega^2 w_0(\mu n^2 - 1) = 0 \tag{13}$$

Let us introduce the following non-dimensional terms
$X = \frac{x}{L}$ = Dimensionless co-ordinate
$W = \frac{w_0}{L}$ = Dimensionless transverse displacement
$\lambda^2 = \frac{\rho A_0\omega^2 L^4}{EI_0}$ = Frequency parameter
$\alpha = \frac{e_0 a}{L}$ = Dimensionless non-local parameter
$\eta = nL$ = Dimensionless non-uniform parameter.

Using the above non-dimensional terms in Equation (13), we obtain the nondimensionalized form of the governing differential equation as Hosseini Hashemi and Bakhshi Khaniki (2016)

$$\frac{d^4 W}{dX^4} + 2\eta\frac{d^3 W}{dX^3} + \eta^2\frac{d^2 W}{dX^2} = \lambda^2\left\{\left(1 - \alpha^2\eta^2\right)W - \alpha^2\frac{d^2 W}{dX^2} - 2\alpha^2\eta\frac{dW}{dX}\right\} \tag{14}$$

Next, we introduce an overview of the differential quadrature method.

DIFFERENTIAL QUADRATURE METHOD

In this investigation, Quan and Chang (1989) approach is taken into consideration along with Chebyshev-Gauss-Lobatto grid points which are expressed as

$$X_i = \frac{1}{2}\left[1 - \cos\left(\frac{i-1}{N-1}.\pi\right)\right]. \tag{15}$$

One may express the derivatives of displacement function $W(X)$ at a given discrete point i as Behera and Chakraverty (2015)

$$\begin{aligned} W'_i &= \sum_{j=1}^{N} A_{ij} W_j \\ W''_i &= \sum_{j=1}^{N} B_{ij} W_j \\ W'''_i &= \sum_{j=1}^{N} C_{ij} W_j \\ W_i^{IV} &= \sum_{j=1}^{N} D_{ij} W_j \end{aligned} \tag{16}$$

where $i = 1, 2, \ldots, N$ and N is the number of discrete grid points.

Here A_{ij}, B_{ij}, C_{ij}, and D_{ij} are the weighting coefficients of the first, second, third and fourth derivatives respectively.

Determination of Weighting Coefficients

Computation of weighting coefficient matrix $A = (A_{ij})$ plays significant role in DQ method. As per Quan and Chang 's approach, the matrix $A = (A_{ij})$ can be computed by the following procedure.

For $i \neq j$

$$A_{ij} = \frac{1}{X_j - X_i} \prod_{\substack{k=1 \\ k\neq i \\ k\neq j}}^{N} \frac{X_i - X_k}{X_j - X_k} \quad i = 1, 2, \ldots, N \;\; j = 1, 2, \ldots, N \tag{17}$$

for $i = j$

$$A_{ii} = \sum_{\substack{k=1 \\ k\neq i}}^{N} \frac{1}{X_i - X_k} \quad i = 1, 2, \ldots, N. \tag{18}$$

After weighting coefficients of first-order derivatives are computed, one may easily get the weighting coefficients of higher order derivatives by simple matrix multiplication which is given as

$$B = B_{ij} = \sum_{k=1}^{N} A_{ik} A_{kj} \tag{19}$$

$$C = C_{ij} = \sum_{k=1}^{N} A_{ik} B_{kj} \tag{20}$$

$$D = D_{ij} = \sum_{k=1}^{N} A_{ik} C_{kj} = \sum_{k=1}^{N} B_{ik} B_{kj}. \tag{21}$$

Application of Boundary Conditions

Four classical boundary conditions such as *SS*, *CS*, *CC*, and *CF* are taken into consideration in the present study where the letters *S*, *C*, and *F* denote simply supported, clamped and free edge conditions respectively.

Let us now denote

$$A = \begin{bmatrix} A_{11} & A_{12} & \cdots & A_{1,N-1} & A_{1,N} \\ A_{21} & A_{22} & \cdots & A_{2,N-1} & A_{2,N} \\ \vdots & \vdots & & \vdots & \vdots \\ A_{N1} & A_{N2} & \cdots & A_{N,N-1} & A_{N,N} \end{bmatrix}$$

$$\bar{A} = \begin{bmatrix} 0 & A_{12} & \cdots & A_{1,N-1} & 0 \\ 0 & A_{22} & \cdots & A_{2,N-1} & 0 \\ \vdots & \vdots & & \vdots & \vdots \\ 0 & A_{N2} & \cdots & A_{N,N-1} & 0 \end{bmatrix}$$

$$\bar{A}_1 = \begin{bmatrix} 0 & A_{1,2} & \cdots & A_{1,N} \\ 0 & A_{2,2} & \cdots & A_{2,N} \\ \cdots & \cdots & \cdots & \cdots \\ 0 & A_{N,2} & \cdots & A_{N,N} \end{bmatrix}$$

$$\bar{A}_2 = \begin{bmatrix} A_{1,1} & A_{1,2} & \cdots & A_{1,N-1} & 0 \\ A_{2,1} & A_{2,2} & \cdots & A_{2,N-1} & 0 \\ \cdots & \cdots & \cdots & \cdots & \cdots \\ A_{N,1} & A_{N,2} & \cdots & A_{N-1,N-1} & 0 \end{bmatrix}.$$

The weighting coefficients of higher order derivatives for different edge conditions are given below.

Simply Supported-Simply Supported

$$\{W'\} = [\bar{A}]\{W\}.$$
$$\{W''\} = [A][\bar{A}]\{W\} = [\bar{B}]\{W\} \text{ with } \bar{B} = [A][\bar{A}].$$
$$\{W'''\} = [\bar{A}]\{W'''\} = [\bar{A}][\bar{B}]\{W\} = [\bar{C}]\{W\}.$$
$$\{W^{IV}\} = [A]\{W'''\} = [A][\bar{C}]\{W\} = [\bar{B}][\bar{B}]\{W\} = [\bar{D}]\{W\}$$

where $[\bar{D}] = [\bar{B}][\bar{B}]$ or $[\bar{D}] = [A][\bar{C}]$.

Clamped-Simply Supported

$$\{W'\} = [\bar{A}]\{W\}$$
$$\{W''\} = [\bar{A}_1]\{W'\} = [\bar{A}_1][\bar{A}]\{W\} = [\bar{B}]\{W\} \text{ with } [\bar{B}] = [\bar{A}_1][\bar{A}].$$
$$\{W'''\} = [\bar{A}_2]\{W''\} = [\bar{A}_2][\bar{B}]\{W\} = [\bar{C}]\{W\} \text{ with } [\bar{C}] = [\bar{A}_2][\bar{B}].$$
$$\{W^{IV}\} = [A]\{W'''\} = [A][\bar{C}]\{W\} = [\bar{D}]\{W\} \text{ with } [\bar{D}] = [A][\bar{C}].$$

Clamped-Clamped

$$\{W'\} = [\bar{A}]\{W\}$$
$$\{W''\} = [\bar{A}]\{W'\} = [\bar{A}][\bar{A}]\{W\} = [\bar{B}]\{W\} \text{ with } [\bar{B}] = [\bar{A}][\bar{A}].$$
$$\{W'''\} = [A]\{W''\} = [A][\bar{B}]\{W\} = [\bar{C}]\{W\} \text{ with } [\bar{C}] = [A][\bar{B}].$$
$$\{W^{IV}\} = [A]\{W'''\} = [A][\bar{C}]\{W\} = [\bar{D}]\{W\} \text{ with } [\bar{D}] = [A][\bar{C}].$$

TABLE 1 | Comparisons of first fundamental frequency parameter (λ) for SS Nano beam.

μ	Present	Reddy, 2007	Aydogdu, 2009	Eltaher et al., 2013
0	9.8696	9.8696	9.8696	9.8696
1	9.4159	9.4159	9.4124	9.4159
2	9.0195	9.0195	9.0133	9.0195
3	8.6693	8.6693	8.6611	8.6693
4	8.3569	8.3569	8.3472	8.3569

TABLE 2 | Comparisons of first fundamental frequency parameter (λ) for SS Nanobeam.

μ	Aydogdu, 2009	Eltaher et al., 2013	Present
0	9.8696	9.8798	9.8696
1	9.7498	9.4238	9.7500
2	9.6343	9.0257	9.63473
3	9.5228	8.6741	9.5234
4	9.4150	8.3606	9.4158

TABLE 3 | Comparisons of frequency parameter $\left(\sqrt{\lambda}\right)$ for SS case.

$\alpha = e_0a/L$ / Mode	1st Mode		2nd Mode		3rd Mode		4th Mode		5th Mode	
	Present	Wang et al., 2007	Present	Wang et al., 2007	Present	Wang et al., 2007	Present	Wang et al., 2007	Present	Wang et al., 2007
0	3.1416	3.1416	6.2832	6.2832	9.4248	9.4248	1.566	1.566	15.708	15.708
0.1	3.0685	3.0685	5.7817	5.7817	8.0400	8.0400	9.9161	9.9161	11.5111	11.5111
0.3	2.6800	2.6800	4.3013	4.3013	5.4422	5.4422	6.3630	6.3630	7.1568	7.1568

TABLE 4 | Comparisons of frequency parameter $\left(\sqrt{\lambda}\right)$ for CS case.

$\alpha = e_0a/L$ / Mode	1st Mode		2nd Mode		3rd Mode		4th Mode		5th Mode	
	Present	Wang et al., 2007	Present	Wang et al., 2007	Present	Wang et al., 2007	Present	Wang et al., 2007	Present	Wang et al., 2007
0	3.9266	3.9266	7.0686	7.0686	10.2102	10.2102	13.3518	13.3518	16.4934	16.4934
0.1	3.8209	3.8209	6.4649	6.4649	8.6517	8.6517	10.469	10.469	12.018	12.018
0.3	3.2828	3.2828	4.7668	4.7668	5.8371	5.8371	6.7143	6.7143	7.4773	7.4773

TABLE 5 | Comparisons of frequency parameter $\left(\sqrt{\lambda}\right)$ for CC case.

$\alpha = e_0a/L$ / Mode	1st Mode		2nd Mode		3rd Mode		4th Mode		5th Mode	
	Present	Wang et al., 2007	Present	Wang et al., 2007	Present	Wang et al., 2007	Present	Wang et al., 2007	Present	Wang et al., 2007
0	4.7300	4.7300	7.8532	7.8532	10.9956	10.9956	14.1372	14.1372	17.2787	17.2787
0.1	4.5945	4.5945	7.1402	7.1402	9.2583	9.2583	11.016	11.016	12.520	12.520
0.3	3.9184	3.9184	5.1963	5.1963	6.2317	6.2317	7.0482	7.0482	7.7955	7.7955

Clamped-Free

$$\{W'\} = [\bar{A}_1]\{W\}$$

$$\{W''\} = [\bar{A}_1]\{W'\} = [\bar{A}_1][\bar{A}_1]\{W\} = [\bar{B}]\{W\} \text{ with } [\bar{B}] = [\bar{A}_1][\bar{A}_1].$$

$$\{W'''\} = [\bar{A}_2]\{W''\} = [\bar{A}_2][\bar{B}]\{W\} = [\bar{C}]\{W\} \text{ with } [\bar{C}] = [\bar{A}_2][\bar{B}].$$

$$\{W^{IV}\} = [\bar{A}_2]\{W'''\} = [\bar{A}_2][\bar{C}]\{W\} = [\bar{D}]\{W\} \text{ with } [\bar{D}] = [\bar{A}_2][\bar{C}].$$

Substituting the expression of Equation (16) into Equaion (14), one may obtain generalized eigenvalue problem as

$$[S]\{W\} = \lambda^2[T]\{W\} \tag{22}$$

where S is the stiffness matrix and T is the mass matrix.

NUMERICAL RESULTS AND DISCUSSIONS

Equaion (22) is solved by using a MATLAB program which is developed by the authors and frequency parameters $\sqrt{\lambda}$ have been obtained. DQ method has been implemented along with the boundary conditions in the coefficient matrix. Following parameters (Reddy et al., 2006) are taken for the computational purpose.

$$E = 1.012\,TPa, \quad L = 10, \quad \text{Poisson's ratio } (\nu) = 0.245,$$
$$\text{and unless mentioned } \frac{L}{h} = 10.$$

Validation

For validation of present method, we consider a nanobeam with uniform cross-section viz. results of fundamental frequency parameter (λ) are then compared with (Reddy, 2007; Aydogdu, 2009; Eltaher et al., 2013) for different nonlocal parameters (μ) which are presented in **Tables 1**, **2**. In **Table 1**, aspect ratio (L/h) is taken as 10. Similarly, in **Table 2**, fundamental frequency parameter (λ) for SS nanobeam is compared with (Aydogdu, 2009; Eltaher et al., 2013) with an aspect ratio (L/h) as 20. Again results are compared with (Wang et al., 2007) for different $\alpha = \frac{e_0a}{L}$ which are presented in **Tables 3**–**6**. From these **Tables 1**–**6**, one may observe close agreement of results with those available in the literature.

Convergence

A minimum number of grid points have been obtained by studying convergence to obtain the final results. In order to show how the solution is affected by the grid points,

TABLE 6 | Comparisons of frequency parameter $\left(\sqrt{\lambda}\right)$ for CF case.

$\alpha = e_0a/L$ / Mode	1st Mode		2nd Mode		3rd Mode		4th Mode		5th Mode	
	Present	Wang et al., 2007	Present	Wang et al., 2007	Present	Wang et al., 2007	Present	Wang et al., 2007	Present	Wang et al., 2007
0	1.8751	1.8751	4.6941	4.6941	7.8548	7.8548	10.9955	10.9955	14.1372	14.1372
0.1	1.8792	1.8792	4.5475	4.5475	7.1459	7.1459	9.2569	9.2569	11.016	11.016
0.3	1.9154	1.9154	3.7665	3.7665	5.2988	5.2988	6.1385	6.1385	7.1450	7.1450

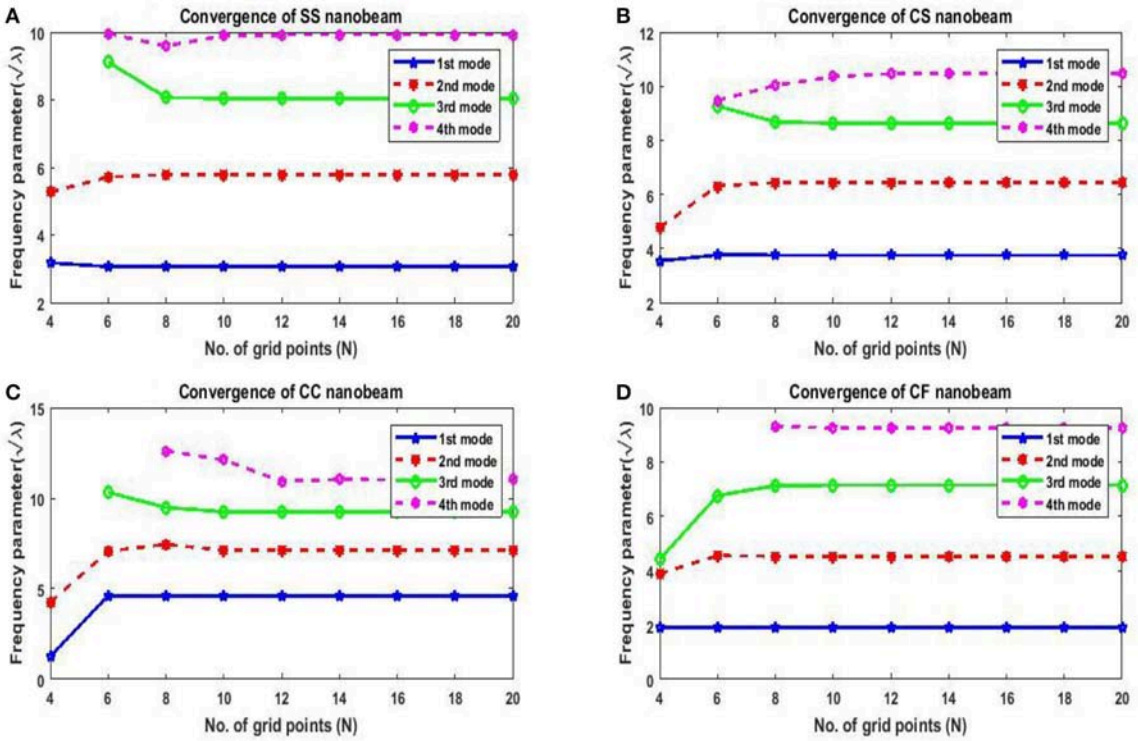

FIGURE 1 | Variation of frequency parameters with number of terms for SS, CS, CC, and CF conditions. **(A)** Convergence of SS Nanobeam. **(B)** Convergence of CS Nanobeam. **(C)** Convergence of CC Nanobeam. **(D)** Convergence of CF Nanobeam.

TABLE 7 | Convergence for SS case.

N	$\sqrt{\lambda_1}$	$\sqrt{\lambda_2}$	$\sqrt{\lambda_3}$	$\sqrt{\lambda_4}$
4	3.1757	5.2692	–	–
6	3.0647	5.7140	9.1157	9.9598
8	3.0650	5.7839	8.0678	9.5855
10	3.0650	5.7839	8.0429	9.9002
12	3.0650	5.7839	8.0421	9.9171
14	3.0650	5.7839	8.0421	9.9177
16	3.0650	5.7839	8.0421	9.9177
18	3.0650	5.7839	8.0421	9.9177
20	3.0650	5.7839	8.0421	9.9177

TABLE 8 | Convergence for CS case.

N	$\sqrt{\lambda_1}$	$\sqrt{\lambda_2}$	$\sqrt{\lambda_3}$	$\sqrt{\lambda_4}$
4	3.5411	4.7682	–	–
6	3.7592	6.3183	9.2660	9.4740
8	3.7550	6.4284	8.6839	10.0281
10	3.7552	6.4359	8.6309	10.3517
12	3.7552	6.4357	8.6336	10.4583
14	3.7552	6.4357	8.6333	10.4556
16	3.7552	6.4357	8.6333	10.4559
18	3.7552	6.4357	8.6333	10.4559
20	3.7552	6.4357	8.6333	10.4559

variations of the frequency parameters $(\sqrt{\lambda})$ with number of grid points (N) are shown in **Figure 1** and in **Tables 7–10** for SS, CS, CC, and CF cases respectively. Here, we have considered $L = 10$, $\eta = 0.5$ and $\mu = 1$. From this figure, one may note that with an increase in number of grid points, the convergence is achieving fast. One may also observe that 12 grid points are sufficient to get the converged results.

TABLE 9 | Convergence for CC case.

N	$\sqrt{\lambda_1}$	$\sqrt{\lambda_2}$	$\sqrt{\lambda_3}$	$\sqrt{\lambda_4}$
4	1.2706	4.2537	–	–
6	4.6198	7.0750	10.3179	–
8	4.5975	7.4555	9.4853	12.6027
10	4.5987	7.1200	9.2525	12.1127
12	4.5986	7.1451	9.2616	10.9317
14	4.5986	7.1435	9.2606	11.0373
16	4.5986	7.1436	9.2607	11.0154
18	4.5986	7.1436	9.2607	11.0175
20	4.5986	7.1436	9.2607	11.0175

TABLE 10 | Convergence for CF case.

N	$\sqrt{\lambda_1}$	$\sqrt{\lambda_2}$	$\sqrt{\lambda_3}$	$\sqrt{\lambda_4}$
4	1.9018	3.8806	4.4163	–
6	1.9171	4.5549	6.7626	–
8	1.9171	4.5274	7.1286	9.3090
10	1.9171	4.5284	7.1447	9.2490
12	1.9171	4.5284	7.1447	9.2605
14	1.9171	4.5284	7.1447	9.2597
16	1.9171	4.5284	7.1447	9.2597
18	1.9171	4.5284	7.1447	9.2597
20	1.9171	4.5284	7.1447	9.2597

TABLE 11 | Frequency parameter $\left(\sqrt{\lambda}\right)$ for SS case for different nonlocal parameter.

μ	$\sqrt{\lambda_1}$	$\sqrt{\lambda_2}$	$\sqrt{\lambda_3}$	$\sqrt{\lambda_4}$
0	3.1377	6.2850	9.4266	12.5680
1	3.0650	5.7839	8.0421	9.9177
2	3.000	5.4348	7.3031	8.8012
3	2.9414	5.1707	6.8133	8.1204
4	2.8881	4.9604	6.4534	7.6414
5	2.8393	4.7869	6.1720	7.2770

Effect of Nonlocal Parameter

In this subsection, the first four frequency parameters $\left(\sqrt{\lambda}\right)$ of nanobeam are obtained for different nonlocal parameters. We have taken the values of nonlocal parameter as 0, 1, 2, 3, 4, $5nm^2$. In this study, classical boundary conditions such as SS, CS, CC, and CF are considered for investigation. Both tabular and graphical results are depicted by taking other parameters such as non-uniform parameter (η) as 0.5 and $L = 10$ nm. First four frequency parameters of SS, CS, CC, and CF edges for different nonlocal parameters are presented in **Tables 11–14**. From these tables, one may observe that frequency parameters decrease with increase in nonlocal parameter except first fundamental frequency parameter of CF nanobeams. One may also notice that frequency parameters increase with increase in mode number. Here one important point is to note that CC nanobeams are having highest frequency parameters than other set of boundary conditions. **Figure 2** shows variation of frequency parameters $\left(\sqrt{\lambda}\right)$ with nonlocal parameters for different edge conditions such as SS, CS, CC, and CF.

TABLE 12 | Frequency parameters $\left(\sqrt{\lambda}\right)$ for CS case for different nonlocal parameters.

μ	$\sqrt{\lambda_1}$	$\sqrt{\lambda_2}$	$\sqrt{\lambda_3}$	$\sqrt{\lambda_4}$
0	3.8593	7.0356	10.1877	13.3348
1	3.7552	6.4357	8.6333	10.4559
2	3.6634	6.0279	7.8240	9.2697
3	3.5817	5.7240	7.2934	8.5513
4	3.5082	5.4846	6.9057	8.0473
5	3.4416	5.2885	6.6037	7.6645

TABLE 13 | Frequency parameters $\left(\sqrt{\lambda}\right)$ for CC case for different nonlocal parameters.

μ	$\sqrt{\lambda_1}$	$\sqrt{\lambda_2}$	$\sqrt{\lambda_3}$	$\sqrt{\lambda_4}$
0	4.7336	7.8561	10.9979	14.1390
1	4.5986	7.1436	9.2607	11.0174
2	4.4805	6.6661	8.3759	9.75553
3	4.3758	6.3135	7.8022	8.9952
4	4.2821	6.0375	7.3857	8.4628
5	4.1975	5.8125	7.0627	8.0587

TABLE 14 | Frequency parameters $\left(\sqrt{\lambda}\right)$ for CF case for different nonlocal parameters.

μ	$\sqrt{\lambda_1}$	$\sqrt{\lambda_2}$	$\sqrt{\lambda_3}$	$\sqrt{\lambda_4}$
0	1.9074	4.6532	7.8249	10.9722
1	1.9171	4.5284	7.1447	9.2597
2	1.9272	4.4103	6.6866	8.3720
3	1.9377	4.2975	6.3535	7.7845
4	1.9487	4.1895	6.1007	7.3456
5	1.9602	4.0855	5.9037	6.9929

Effect of Non-uniform Parameter

Effect of the non-uniform parameter η on first four frequency parameters is analyzed by taking non-uniform parameter η as 0, 0.2, 0.4, 0.6, 0.8, and 1. **Tables 15–18** depict frequency parameters of SS, CS, CC, and CF edges for different non-uniform parameters and **Figure 3** illustrates the variation of frequency parameters with non-uniform parameter η for classical boundary conditions SS, CS, CC, and CF. Here, computation is done with nonlocal parameter $\mu = 1nm^2$ and $L = 10$. It is evident from the **Figure 3** and **Tables 15–18** that the frequency parameters decrease with increase in the non-uniform parameter for the fundamental frequency of SS condition while other modes are increasing. With the increase in non-uniform parameter, frequency parameters decrease for all mode of CS edge whereas this is exactly opposite in case of CC nanoribbons. For the CF case, fundamental frequency increases, second mode decreases, and other modes show random behavior with increase in the non-uniform parameter.

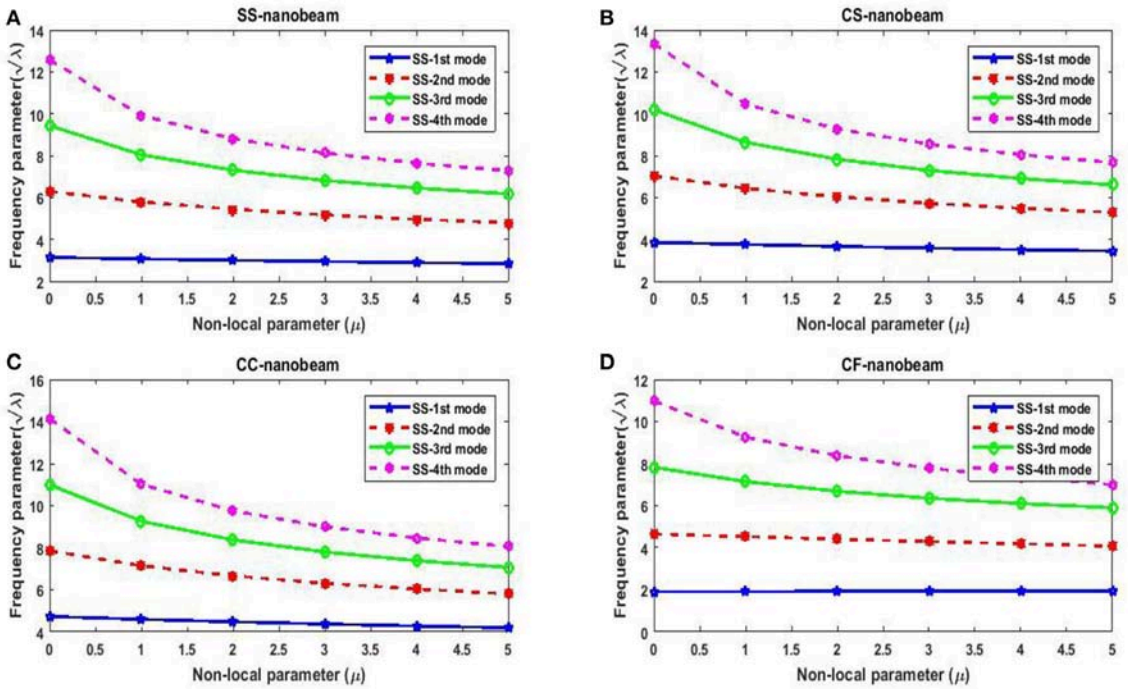

FIGURE 2 | Variation of frequency parameter with nonlocal parameter. **(A)** Variation of Nonlocal parameter for SS Nanobeam. **(B)** Variation of Nonlocal parameter for CS Nanobeam. **(C)** Variation of Nonlocal parameter for CC Nanobeam. **(D)** Variation of Nonlocal parameter for CF Nanobeam.

TABLE 15 | Frequency parameter $\left(\sqrt{\lambda}\right)$ for SS case for different non-uniform parameters.

η	$\sqrt{\lambda_1}$	$\sqrt{\lambda_2}$	$\sqrt{\lambda_3}$	$\sqrt{\lambda_4}$
0	3.0685	5.7816	8.0399	9.9161
0.2	3.0679	5.7820	8.0403	9.9163
0.4	3.0662	5.7831	8.0413	9.9171
0.6	3.0634	5.7850	8.0430	9.9184
0.8	3.0595	5.7876	8.0454	9.9202
1	3.0545	5.7909	8.0485	9.9225

TABLE 16 | Frequency parameters $\left(\sqrt{\lambda}\right)$ for CS case for different non-uniform parameters.

η	$\sqrt{\lambda_1}$	$\sqrt{\lambda_2}$	$\sqrt{\lambda_3}$	$\sqrt{\lambda_4}$
0	3.8208	6.4648	8.6516	10.4687
0.2	3.7944	6.4525	8.6438	10.4632
0.4	3.7682	6.4411	8.6366	10.4582
0.6	3.7421	6.4306	8.6302	10.4537
0.8	3.7161	6.4210	8.6245	10.4498
1	3.6900	6.4124	8.6196	10.4464

TABLE 17 | Frequency parameters $\left(\sqrt{\lambda}\right)$ for CC case for different non-uniform parameters.

η	$\sqrt{\lambda_1}$	$\sqrt{\lambda_2}$	$\sqrt{\lambda_3}$	$\sqrt{\lambda_4}$
0	4.5944	7.1402	9.2583	11.0157
0.2	4.5951	7.1407	9.2587	11.0160
0.4	4.5971	7.1424	9.2598	11.0168
0.6	4.6005	7.1450	9.2617	11.0181
0.8	4.6053	7.1488	9.2644	11.0199
1	4.6114	7.1537	9.2678	11.0223

TABLE 18 | Frequency parameters $\left(\sqrt{\lambda}\right)$ for CF case for different non-uniform parameters.

η	$\sqrt{\lambda_1}$	$\sqrt{\lambda_2}$	$\sqrt{\lambda_3}$	$\sqrt{\lambda_4}$
0	1.8791	4.5474	7.1458	9.2568
0.2	1.8951	4.5412	7.1460	9.2585
0.4	1.9105	4.5332	7.1454	9.2595
0.6	1.9224	4.5231	7.1438	9.2597
0.8	1.9278	4.5107	7.1414	9.2591
1	1.9237	4.4958	7.1381	9.2577

Effect of Length-to-Height Ratio

In this subsection, the effect of length-to-height ratio (L/h) on the first four frequency parameters has been analyzed for the classical boundary conditions such as SS, CS, CC, and CF. First four frequency parameters of nanobeam are given in **Tables 19–22** for different L/h (10, 20, 30, 40, 50). Here, computation is done with $\mu = 1nm^2$ and $\eta = 0.5$. Graphical results are presented in **Figure 4**, where variation of first four frequency parameters with L/h has been shown. From these tables, one may observe that frequency parameters increase with increase in length-to-height ratio except fundamental frequency parameter of CF nanobeams.

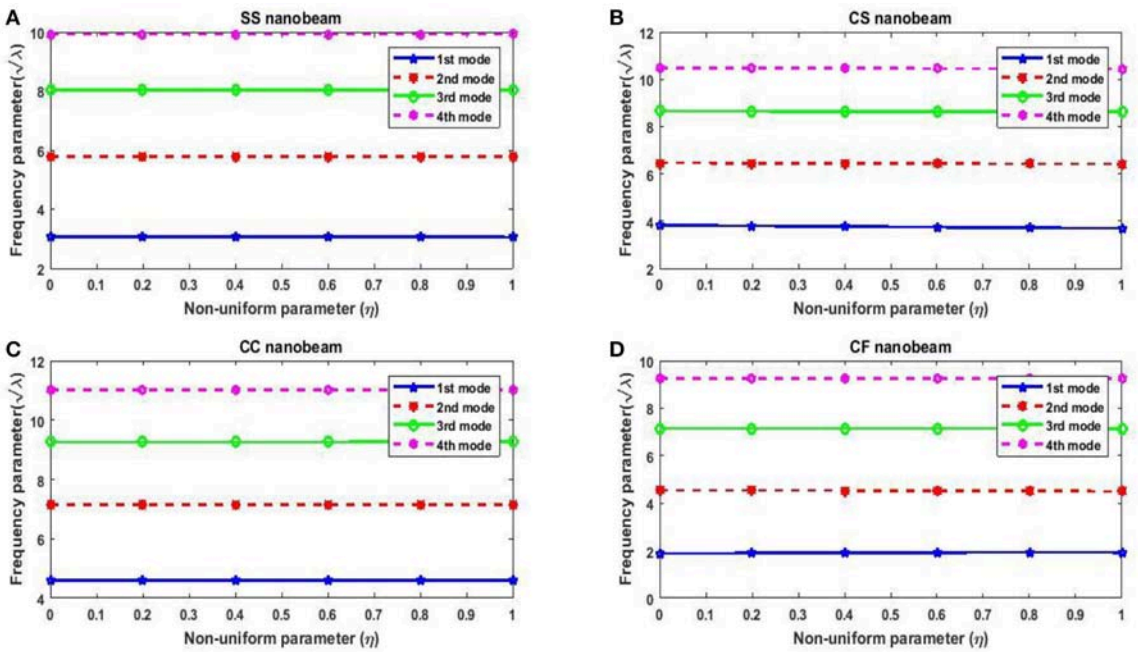

FIGURE 3 | Variation of frequency parameter with non-uniform parameter. **(A)** Variation of Non-uniform parameter for SS Nanobeam. **(B)** Variation of Non-uniform parameter for CS Nanobeam. **(C)** Variation of Non-uniform parameter for CC Nanobeam. **(D)** Variation of Non-uniform parameter for CF Nanobeam.

TABLE 19 | Frequency parameters $\left(\sqrt{\lambda}\right)$ for SS case for different length-to-height ratio.

L/h	$\sqrt{\lambda_1}$	$\sqrt{\lambda_2}$	$\sqrt{\lambda_3}$	$\sqrt{\lambda_4}$
10	3.0650	5.7839	8.0421	9.9177
20	3.1187	6.1390	8.9659	11.5651
30	3.1292	6.2180	9.2075	12.0704
40	3.1329	6.2468	9.3002	12.2758
50	3.1346	6.2604	9.3448	12.3771

TABLE 20 | Frequency parameters $\left(\sqrt{\lambda}\right)$ for CS case for different length-to-height ratio.

L/h	$\sqrt{\lambda_1}$	$\sqrt{\lambda_2}$	$\sqrt{\lambda_3}$	$\sqrt{\lambda_4}$
10	3.7552	6.4357	8.6333	10.4559
20	3.8320	6.8590	9.6642	12.2326
30	3.8471	6.9543	9.9379	12.7857
40	3.8524	6.9893	10.0434	13.0118
50	3.8549	7.0058	10.0942	13.1236

TABLE 21 | Frequency parameters $\left(\sqrt{\lambda}\right)$ for CC case for different length-to-height ratio.

L/h	$\sqrt{\lambda_1}$	$\sqrt{\lambda_2}$	$\sqrt{\lambda_3}$	$\sqrt{\lambda_4}$
10	4.5986	7.1436	9.2607	11.0174
20	4.6981	7.6449	10.4067	12.9317
30	4.7177	7.7588	10.7149	13.5354
40	4.7246	7.8006	10.8342	13.7835
50	4.7279	7.8204	10.8918	13.9063

TABLE 22 | Frequency parameters $\left(\sqrt{\lambda}\right)$ for CF case for different length-to-height ratio.

L/h	$\sqrt{\lambda_1}$	$\sqrt{\lambda_2}$	$\sqrt{\lambda_3}$	$\sqrt{\lambda_4}$
10	1.9171	4.5284	7.1447	9.2597
20	1.9098	4.6213	7.6246	10.3932
30	1.9084	4.6389	7.7328	10.6956
40	1.9080	4.6452	7.7724	10.8123
50	1.9078	4.6480	7.7911	10.8686

Effect of Boundary Conditions

One need to have adequate knowledge about boundary conditions for designing engineering structures. It helps designers to gather important information without carrying out detail experimental investigation. Therefore, it is quite important to study the effect of boundary conditions on frequency parameter. **Figure 5** illustrates variation of frequency parameter with nonlocal parameter for different boundary conditions. The values of other parameters are taken as $L = 10nm$ and $\eta = 0.5$. One may observe from the figure that CC nanobeams are having highest frequency parameter whereas CF nanobeams possess the lowest frequency parameter.

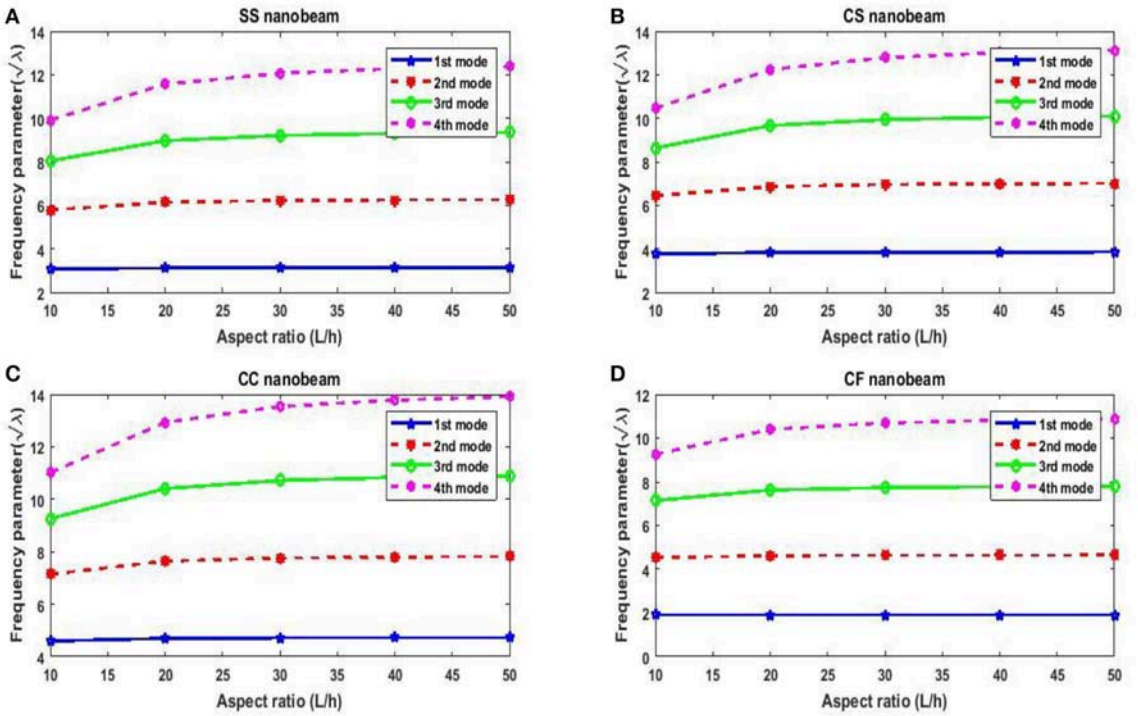

FIGURE 4 | Variation of frequency parameter with length-to-height ratio. **(A)** Variation of L/h for SS Nanobeam. **(B)** Variation of L/h for CS Nanobeam. **(C)** Variation of L/h for CC Nanobeam. **(D)** Variation of L/h for CF Nanobeam.

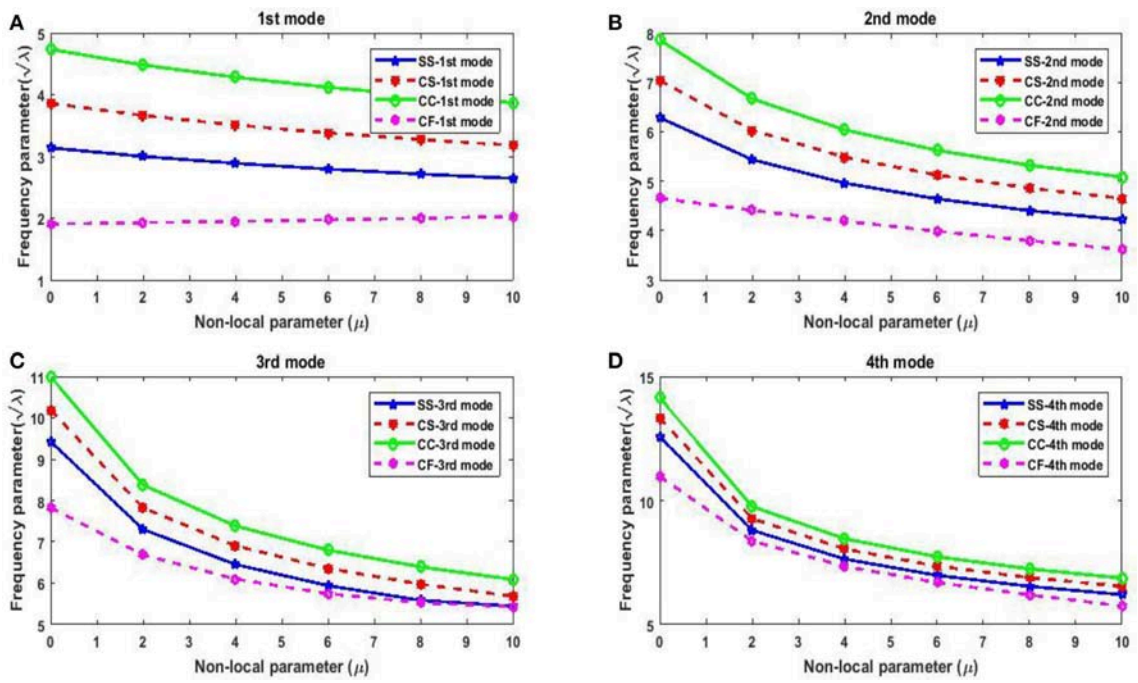

FIGURE 5 | Variation of frequency parameter with boundary condition. **(A)** Variation of boundary condition for 1st mode. **(B)** Variation of boundary condition for 2nd mode. **(C)** Variation of boundary condition for 3rd mode. **(D)** Variation of boundary condition for 4th mode.

CONCLUSIONS

Free vibration of the variable cross-section (non-uniform) single-layered graphene nano-ribbons (SLGNRs) is investigated using the Differential Quadrature Method (DQM). Euler–Bernoulli beam theory is considered in conjunction with the nonlocal elasticity theory of Eringen. In this study, width of the cross-section is varying exponentially along the length of the nano-ribbon while other parameters are kept constant. Complete procedure of Differential Quadrature Method (DQM) is depicted clearly including application of boundary conditions and MATLAB code has been developed to obtain the numerical results for different scaling parameters as well as for four types of boundary conditions. Numerical as well as graphical results are presented to show the effects of the nonlocal parameter, non-uniform parameter, aspect ratio and the boundary conditions on the frequency parameters. one may observe that the effect of the nonlocal parameter is more in higher modes and another interesting observation is that fundamental frequency (1st mode) parameter of the cantilever (CF) nanobeam does not decrease with increase in nonlocal parameters whereas frequency parameters of other modes of nanobeam decrease with increase in nonlocal parameters. Frequency parameters decrease with increase in the non-uniform parameter for the fundamental frequency of SS condition while other modes are increasing. With the increase in non-uniform parameter, frequency parameters decrease for all mode of CS edge whereas this is exactly opposite in case of CC nanoribbons. For the CF case, fundamental frequency increases, second mode decreases, and other modes show random behavior with increase in the non-uniform parameter. One may also conclude that frequency parameters increase with increase in length-to-height ratio (aspect ratio) except fundamental frequency parameter of CF nanobeam. Moreover, it is also found that clamped (CC) case possesses highest frequency parameters and cantilever (CF) nanobeam possesses the lowest among all other types of boundary conditions.

AUTHOR CONTRIBUTIONS

All authors listed have made a substantial, direct and intellectual contribution to the work, and approved it for publication.

ACKNOWLEDGMENTS

The authors are thankful to Defence Research & Development Organization(DRDO), Ministry of Defence, New Delhi, India (Sanction Code: DG/TM/ERIPR/GIA/17-18/0129/020) for the funding to carry out the present research work.

REFERENCES

Attarnejad, R., and Shahba, A. (2011). Dynamic basic displacement functions in free vibration analysis of centrifugally stiffened tapered beams; a mechanical solution. *Meccanica* 46, 1267–1281. doi: 10.1007/s11012-010-9383-z

Aydogdu, M. (2009). A general nonlocal beam theory: its application to nanobeam bending, buckling and vibration. *Phys. E* 41, 1651–1655. doi: 10.1016/j.physe.2009.05.014

Aydogdu, M., Arda, M., and Filiz, S. (2018). Vibration of axially functionally graded nanorods and beams with a variable nonlocal parameter. *Adv. Nano Res.* 6, 257–278. doi: 10.12989/anr.2018.6.3.257

Bagdatli, S. M. (2015). Non-linear vibration of nanobeams with various boundary condition based on nonlocal elasticity theory. *Composites Part B. Eng.* 80, 43–52. doi: 10.1016/j.compositesb.2015.05.030

Banic, D., Bacciocchi, M., Tornabene, F., and Ferreira, A. J. M. (2017). Influence of winkler-pasternak foundation on the vibrational behavior of plates and shells reinforced by agglomerated carbon nanotubes. *Appl. Sci.* 7, 1–55. doi: 10.3390/app7121228

Behera, L., and Chakraverty, S. (2015). Application of Differential Quadrature method in free vibration analysis of nanobeams based on various nonlocal theories. *Comput. Math. Appl.* 69, 1444–1462. doi: 10.1016/j.camwa.2015.04.010

Bellman, R., and Casti, J. (1971). Differential quadrature and long-term integration. *J. Math. Anal. Appl.* 34, 235–238. doi: 10.1016/0022-247X(71)90110-7

Beni, Y. T., Jafaria, A., and Razavi, H. (2014). Size effect on free transverse vibration of cracked nano-beams using couple stress theory. *Int. J. Eng. Trans. B Appl.* 28, 296–305. doi: 10.5829/idosi.ije.2015.28.02b.17

Bert, C., Wang, X., and Striz, A. (1994). Static and free vibrational analysis of beams and plates by differential quadrature method. *Acta Mech.* 102, 11–24. doi: 10.1007/BF01178514

Bert, C. W., Jang, S. K., and Striz, A. G. (1988). Two new approximate methods for analyzing free vibration of structural components. *AIAA J.* 26, 612–618. doi: 10.2514/3.9941

Bert, C. W., and Malik, M. (1996). The differential quadrature method for irregular domains and application to plate vibration. *Int. J. Mech. Sci.* 38, 589–606. doi: 10.1016/S0020-7403(96)80003-8

Bert, C. W., Xinwei, W., and Striz, A. G. (1993). Differential quadrature for static and free vibration analyses of anisotropic plates. *Int. J. Solids Struct.* 30, 1737–1744.

Chakraverty, S., and Behera, L. (2016). *Static and Dynamic Problems of Nanobeams and Nanoplates, 1st Edn.* Singapore: World Scientific Publishing Co.

Chaudhari, T., and Maiti, S. (1999). Modelling of transverse vibration of beam of linearly variable depth with edge crack. *Eng. Fract. Mech.* 63, 425–445. doi: 10.1016/S0013-7944(99)00029-6

Dai, H., Hafner, J. H., Rinzler, A. G., Colbert, D. T., and Smalley, R. E. (1996). Nanotubes as nanoprobes in scanning probe microscopy. *Nature* 384, 147–150. doi: 10.1038/384147a0

Ece, M. C., Aydogdu, M., and Taskin, V. (2007). Vibration of a variable cross-section beam. *Mech. Res. Commun.* 34, 78–84. doi: 10.1016/j.mechrescom.2006.06.005

Eltaher, M. A., Alshorbagy, A. E., and Mahmoud, F. F. (2013). Vibration analysis of Euler-Bernoulli nanobeams by using finite element method. *Appl. Math. Model.* 37, 4787–4797. doi: 10.1016/j.apm.2012.10.016

Eringen, A. C. (1972). Nonlocal polar elastic continua. *Int. J. Eng. Sci.* 10, 1–16. doi: 10.1016/0020-7225(72)90070-5

Fantuzzi, N., Tornabene, F., Bacciocchi, M., and Dimitri, R. (2017). Free vibration analysis of arbitrarily shaped Functionally Graded Carbon Nanotube-reinforced plates. *Composites Part B* 115, 384–408. doi: 10.1016/j.compositesb.2016.09.021

Fujita, M., Wakabayashi, K., Nakada, K., and Kusakabe, K. (1996). Peculiar localized state at zigzag graphite edge. *J. Phys. Soc. Jpn.* 65, 1920–1923.

Geim, A. K. (2009). Graphene: status and prospects. *Science* 324, 1530–1534. doi: 10.1126/science.1158877

Geim, A. K., and Novoselov, K. S. (2007). The rise of graphene. *Nat. Mat.* 6, 183–191. doi: 10.1038/nmat1849

Hosseini Hashemi, S., and Bakhshi Khaniki, H. (2016). Analytical solution for free vibration of a variable cross-section nonlocal nanobeam. *Int. J. Eng.* 29, 688–696. doi: 10.5829/idosi.ije.2016.29.05b.13

Jang, S. K., Bert, C. W., and Striz, A. G. (1989). Application of differential quadrature to static analysis of structural components. *Int. J. Num. Methods Eng.* 28, 561–577. doi: 10.1002/nme.1620280306

Loya, J., Lopez-Puente, J., Zaera, R., and Fernández-Sáez, J. (2009). Free transverse vibrations of cracked nanobeams using a nonlocal elasticity model. *J. Appl. Phys.* 105, 78–86. doi: 10.1063/1.3068370

Mirzabeigy, A. (2014). Semi-analytical approach for free vibration analysis of variable cross-section beams resting on elastic foundation and under axial force. *Int. J. Eng. Trans. C Aspects* 27, 455–463. doi: 10.5829/idosi.ije.2014.27.03c.05

Murmu, T., and Adhikari, S. (2010). Nonlocal transverse vibration of double-nanobeam-systems. *J. Appl. Phys.* 108:083514. doi: 10.1063/1.3496627

Nakada, K., Fujita, M., Dresselhaus, G., and Dresselhaus, M. S. (1996). Edge state in graphene ribbons: nanometer size effect and edge shape dependence. *Phys. Rev.* B 54:17954. doi: 10.1103/PhysRevB.54.17954

Novoselov, K. S., Fal'ko, V. I., Colombo, L., Gellert, P. R., Schwab, M. G., and Kim, K. A. (2012). Roadmap for graphene. *Nature* 490, 192–200. doi: 10.1038/nature11458

Peddieson, J., Buchanan, G. R., and McNitt, R. P. (2003). Application of nonlocal continuum models to nanotechnology. *Int. J. Eng. Sci.* 41, 305–312. doi: 10.1016/S0020-7225(02)00210-0

Quan, J., and Chang, C. (1989). New insights in solving distributed system equations by the quadrature method— Analysis, I. *Comput. Chem. Eng.* 13, 779–788. doi: 10.1016/0098-1354(89)85051-3

Reddy, C. D., Rajendran, S., and Liew, K. M. (2006). Equilibrium configuration and continuum elastic properties of finite sized graphene. *Nanotechnology* 17, 864–870. doi: 10.1088/0957-4484/17/3/042

Reddy, J. (2007). Nonlocal theories for bending, buckling and vibration of beams. *Int. J. Eng. Sci.* 45, 288–307. doi: 10.1016/j.ijengsci.2007.04.004

Shu, C. (2000). *Differential Quadrature and its Application in Engineering*. Singapore: Springer. doi: 10.1007/978-1-4471-0407-0

Tornabene, F., Fantuzzi, N., and Bacciocchi, M. (2017). Linear static response of nanocomposite plates and shells reinforced by agglomerated carbon nanotubes. *Composites Part B* 115, 449–476. doi: 10.1016/j.compositesb.2016.07.011

Tornabene, F., Fantuzzi, N., Bacciocchi, M., and Viola, E. (2016). Effect of agglomeration on the natural frequencies of functionally graded carbon nanotube-reinforced laminated composite doubly-curved shells. *Composites Part B* 89, 187–218. doi: 10.1016/j.compositesb.2015.11.016

Tornabene, F., Fantuzzi, N., Ubertini, F., and Viola, E. (2015). Strong formulation finite element method based on differential quadrature: a survey. *Appl. Mech. Rev.* 67:020801. doi: 10.1115/1.4028859

Wakabayashi, K., Fujita, M., Ajiki, H., and Sigrist, M. (1999). Electronic and magnetic properties of nanographite ribbons. *Phys. Rev.* B 59:8271. doi: 10.1103/PhysRevB.59.8271

Wang, C., Zhang, Y., and He, X. (2007). Vibration of nonlocal timoshenko beams. *Nanotechnology* 18, 105–113. doi: 10.1088/0957-4484/18/10/105401

Wang, X., and Bert, C. (1993). A new approach in applying differential quadrature to static and free vibrational analyses of beams and plates. *J. Sound Vib.* 162, 566–572. doi: 10.1006/jsvi.1993.1143

Wang, X., Bert, C., and Striz, A. (1993). Differential quadrature analysis of deflection, buckling, and free vibration of beams and rectangular plates. *Comput. Struct.* 48, 473–479. doi: 10.1016/0045-7949(93)90324-7

Conflict of Interest Statement: The authors declare that the research was conducted in the absence of any commercial or financial relationships that could be construed as a potential conflict of interest.

frontiers in Built Environment

ORIGINAL RESEARCH
published: 26 November 2018
doi: 10.3389/fbuil.2018.00069

An Iterative Parallel Solver in GPU Applied to Frequency Domain Linear Water Wave Problems by the Boundary Element Method

Jorge Molina-Moya, Alejandro Enrique Martínez-Castro and Pablo Ortiz*

Department of Structural Mechanics and Hydraulic Engineering, University of Granada, Edificio Politécnico, Granada, Spain

In this paper a parallel iterative solver based on the Generalized Minimum Residual Method (GMRES) with complex-valued coefficients is explored, with applications to the Boundary Element Method (BEM). The solver is designed to be executed in a GPU (Graphic Processing Unit) device, exploiting its massively parallel capabilities. The BEM is a competitive method in terms of reduction in the number of degrees of freedom. Nonetheless, the BEM shows disadvantages when the dimension of the system grows, due to the particular structure of the system matrix. With difference to other acceleration techniques, the main objective of the proposed solver is the direct acceleration of existing standard BEM codes, by transfering to the GPU the solver task. The CUDA programming language is used, exploiting the particular architecture of the GPU device for complex-valued systems. To explore the performances of the solver, two linear water wave problems have been tested: the frequency-dependent added mass and damping matrices of a 3D floating body, and the Helmholtz equation in a 2D domain. A NVidia GeForce GTX 1080 graphic card has been used. The parallelized GMRES solver shows reductions in computing times when compared with its CPU implementation.

Keywords: GMRES (generalized minimal residual) algorithm, CUDA (compute unified device architecture), GPU (CUDA), floating bodies, boundary element method - BEM

OPEN ACCESS

Edited by:
John T. Katsikadelis, National Technical University of Athens, Greece

Reviewed by:
Alejandro Jacobo Cabrera Crespo, University of Vigo, Spain
Aristophanes John Yiotis, National Technical University of Athens, Greece

****Correspondence:***
Alejandro Enrique Martínez-Castro
amcastro@ugr.es

Specialty section:
This article was submitted to Computational Methods in Structural Engineering, a section of the journal Frontiers in Built Environment

Received: *02 August 2018*
Accepted: *07 November 2018*
Published: *26 November 2018*

Citation:
Molina-Moya J, Martínez-Castro AE and Ortiz P (2018) An Iterative Parallel Solver in GPU Applied to Frequency Domain Linear Water Wave Problems by the Boundary Element Method. Front. Built Environ. 4:69. doi: 10.3389/fbuil.2018.00069

1. INTRODUCTION

The Boundary Element Method (BEM) is a numerical technique to obtain approximated solutions of partial differential equations. The origins of the method comes from Finite Element Method (FEM) ideas in the 1970s. The paper by Cheng and Cheng (2005) shows the previous works and the initials of the BEM. The birth date of the technique is considered in 1963, with the first paper by Jaswon and Porter (1963). The first BEM conference was held at Southampton University in 1978, and and the first book was published in the same year, by Brebbia (1978). With refference to three-dimensional boundary value problem, the basic idea of the BEM is the use of boundary integral equations for primary variables at internal points (e.g., displacements, or potentials), and its extension to boundary points after a limit-to-the-boundary process. The integrals are interpreted in the sense of the Cauchy Principal Values (primary variables) or the Hadamard Finite Parte (derived variables). To solve a boundary value problem, a mesh is defined at the boundary, and the integral equation is used at *collocation points*. A fully-populated coefficient system matrix is obtained. Comparing to the FEM, the BEM is a boundary method, in the sense that the numerical

discretization is carried out at reduced spatial dimension (e.g., in three-dimensional problems, a mesh is required only at the surfaces). This reduced dimension leads to smaller linear systems, less computer memory requirements, and more efficient computation.

The BEM is particularly well suited in wave problems due to mesh reduction and the natural treatment of radiation boundary conditions. Thus, it is an efficient competitor of some particuar techniques, such as the partition of unity method in diffraction and refraction problems (Ortiz and Sánchez, 2001; Ortiz, 2004) in the Finite Element Method.

The classical book by Brebbia and Dominguez (1996) explain the basic BEM theory and applications for potential and solid mechanics. The book by Bonnet Bonnet (1999) is a recent reference, with applications to solid and fluid mechanics. In the specific context of fluid mechanics, Hess (1990) introduced the *panel method*, which is equivalent to BEM techniques; the book by Brebbia and Partridge (1992) is focused on particular BEM topics for fluid mechanics.

Besides the inherent advantages, the BEM shows some disadvantages for systems with large number of degrees of freedom. In the standard BEM, the system matrix is fully populated, without symmetry or sparsity structures. This causes that the main bottleneck in computing times comes from the solver task. The use of acceleration iterative solvers, popular in FEM (e.g., the conjugate gradient) can not be used in BEM. For large system of equations this problem is crucial and makes the standard BEM not competitive with respect to other domain techniques, such as the Finite Element Method. This is particularly notorious in wave problems in the frequency domain, where the system matrix is complex-valued and fine meshes with large number of degrees of freedom are required.

In the BEM literature several acceleration techniques have been developed for large systems. The review paper by Liu et al. (2012) shows historical aspects and recent advances in acceleration methods for the BEM. A first approach consists on the multipole expansion of the Green functions, with an iterative solver. This is known as the Fast Multipole Method (FMM). The FMM has been regarded as one of the top 10 algorithms in scientific computing and has progressed very significantly. It was first introduced by Rokhlin (1985) in potential problems. The tutorial by Liu and Nishimura (2006) explain the basic algorithm and implementation details. The FMM has been extended to other fields: in elastostatic, Liu (2008) develops the algorithm for hipersingular 2D boundary integral equations in multidomain problems; Djojodihardjo (2010) considers the use of the FMM in FEM-BEM acoustic-structural interaction; in 3D time-harmonic elastodynamics, Chaillat and Bonnet (2013) review the basic developments in FMM; in electromagnetism, the book by Gumerov and Duraiswami (2005) shows a detailed exposition of the FMM applied to the solution of the general three-dimensional Helmholtz equation. The book by Liu (2009) covers the basic FMM algorithms for potential, elastostatics, Stokes flow and acoustic waves. Fortran codes are included.

When the FMM is implemented in a code based on the sequential use of the Central Processing Unit (CPU) for a system with N unknowns, the computing times is considerably reduced, with times $\mathcal{O}\left(N^{1.5}\right)$, or even $\mathcal{O}\left(N \log_2 N\right)$ with a multilevel approach (see López-Portugués et al., 2012).

The implementation of the FMM algorithm requires a strong redesign of an existing code: a new hierarchical mesh of reference points must be created, and the multipole expansion modifies the way in which the system matrices are computed. The method is also dependent on the kind of multipole expansion of the Green function. The multipole expansion is not unique, and it is not available for any Green function. As a consequence, the FMM is not a general method. In the literature there have been developed different strategies to accelerate a BEM code, independent on the Green function. Such techniques can be classified into two groups: the pFFT (pre-corrected Fast Fourier Transformation) and the ACA (Adaptive Cross Approximation).

The pFFT method was proposed in 1997 by Phillips (1997); Phillips and White (1997), in the context of potential problems, with Laplace and Helmhotz equations as the governing equation. It has been extended to other fields in the BEM: Stokes equation, linear elasticity, coupled electrostatic and elasticity, Poisson, dynamics and quasi-linear equations (described in Liu et al., 2012). In the pFFT the algorithm does not depend on the Green function, and its implementation is easy. The computing time in a sequential CPU implementation are $O(N) + O(N_g \log_2 N_g)$, with N_g the number of nodes of an auxiliary mesh, which is required by the method.

The ACA method (Lu et al., 2004; Benedetti et al., 2008) is in the context of methods in which the improvement comes from the acceleration of the solver, with the use of hierarchical matrices, introduced by Hackbusch (1999) . The system matrix is approximate by a low-rank expansion.

The Generalized Minimum Residual Method (GMRES) is an iterative solver for the general use in the BEM. It was introduced by Saad and Shultz (1986). It is based on Krylov subspaces approximations. The main attraction of the GMRES comes from its direct use with fully-populated matrices, typical in the collocation BEM. Its use is widely extended, as a direct solver or to accelerate other fast methods, as FMM or AKA. Leung and Walker (1997) developed a combined GMRES with Dual Compensation method in 3D elastostatics. In multipole BEM, Margonari and Bonnet (2005) developed a combined BEM-FEM method in 3D elastostatics; the GMRES is used to solve the linear system of equations, and the FMM to accelerate the matrix-vector multiplications. In AKA, Brancati et al. (2009) combine the use of hierarchical matrices with GMRES in acoustics.

In comparison with the FMM, pFFT, or ACA, the main advantage of the GMRES is its use as a direct solver; it does not require modifications of an existing BEM code respect to the collocation schema and generation of the system matrices. The computational cost of the GMRES is $\mathcal{O}\left(N^2\right)$.

Recent advances in computing hardware have extended the implementation of parallelization to improve the solver performances. The parallelizaction can be carried out in multi-core CPU (Central Processing Unit) systems. In addition, the use of the Graphics Processing Unit (GPU) for massive parallelization is extending nowadays. Its first use comes from the Graphics processors developed by NVIDIA, and the computing languaje CUDA (Computer Unified Device

Architecture) Sanders and Kandrot (2010). Thus, a new computing paradigm has been developed for numerical analysis, based on heterogeneous massive parallel computation (Kirk and Hwu, 2012). This paradigm requires a new global vision of codes, by splitting the global tasks in blocks which are best suited to be executed in the CPU, and blocks which are best suited to be executed in massive parallel GPU processors.

The use of the GPU to accelerate the BEM is a recent trend since 2009. Hamada and Takahashi (2009) show the use of the GPU in the collocation stage, in acoustic wave problems governed by the Helmholtz equation. Wang et al. (2011), used the GPU to accelerate both the collocation task and the solver stage, in elastostatics problems, with the Dual-Compensation GMRES solver. Wang et al. (2013) used the GPU with the FMM to develop an adaptive solver in 3D elasticity. In the context of the standard collocation mehtod, the use of the GPU to perform the global matrix assembly and the LU factorization is reported in the work by D'Azevedo and Nintcheu Fata (2012).

In the context fluid dynamics and meshless methods, Kelly et al. (2014) explore a GPU implementation of an incompressible Navier-Stokes code based on a Radial-Basis Function Collocation Meshless Method for two-fluid flows. For compressive flows, Ma et al. (2014) show a GPU implementation.

The acceleration of the GMRES in GPU is explored by Li and Saad (2013) for sparse matrices; in this paper, the BEM is not considered. Geng and Jacob (2013) states the acceleration of vector-matrix products in the GMRES. In the literature, the development of acceleration techniques based on the GPU for the GMRES are focused on real-variable (simple or double precision).

This paper explores the acceleration of the BEM based on the acceleration of the GMRES solver, in the GPU, for complex-valued systems with a fully-populated matrix, that arises in linear water wave problems. The interest of the topic covers fluid and fluid-structure interaction analysis. The generation of the system matrix is implemented in the CPU. The main idea of the acceleration scheme is the use of direct BEM codes, in which the CPU is used to assemble the system matrix, and the GPU is used to solve the linear system of equations. At this point, the basic GMRES algorithm is explored, in which a preconditioner has not been implemented.

This paper is organized as follows: in section 2 the basic wave problems are described; section 3 shows the parallelization algorithm, describing the tasks to be run in the CPU and the GPU; section 4 show the numerical benchmark; section 5 shows the main conclusions of the work.

2. BASIC EQUATIONS

2.1. Mass and Damping Matrices of a Floating Body

The first problem is centered in the computation of the mass and damping matrices in a fluid-solid interaction problem. The analysis of a moving solid floating in a moving fluid due to gravity waves is considered. The solution can be obtained by splitting the wave problem into a diffraction and a set of refraction problems, in which the rigid-body modes of displacement are considered. This decomposition can be found in classical references in water waves, as described in Mei et al. book Mei et al. (2005). In the diffraction problem, the solid is fixed in an incidental potential field, giving the actions (forces and moments) which excites the solid. In the radiation problems, the floating body is excited by a time-harmonic force following the rigid-body degrees of freedom; a potential problem is stated at the fluid, considering the prescribed boundary condition at the velocity field in the boundary with the body. The mass and damping matrices are obtained by integration at the fluid-solid inter-phase.

With relation to **Figure 1**, and the reference system $\mathcal{R}\{0; x, y, z\}$, it is considered a 3D floating body in a fluid domain Ω in which the interphase surface with the solid is S_B. Potential flow is considered at the fluid, with $\Phi(\mathbf{x})$ the velocity potential function, with $\mathbf{x} = (x, y, z)$ a vector representing the coordinates of a point in the fluid domain, in an eulerian framework. Considering the complex-valued variable, the potential can be split into a spatial and temporal functions,

$$\Phi(\mathbf{x}, t) = \phi(\mathbf{x})\, \mathrm{e}^{-\mathrm{i}\,\omega\, t} \tag{1}$$

with $\mathrm{i} = \sqrt{-1}$ and ω the angular frequency. Function $\phi(\mathbf{x})$ can be decomposed into a diffraction term and six radiation components (rigid-body modes),

$$\phi(\mathbf{x}) = \phi^D(\mathbf{x}) + \sum_{i=1}^{6} V_i \phi_i(\mathbf{x}) \tag{2}$$

with V_i the participation factors of the rigid-body motions.

Each potential $\phi_i(\mathbf{x})$ is governed by an independent Laplace equation,

$$\Delta\phi_i(\mathbf{x}) = 0 \tag{3}$$

with $\Delta = \left(\frac{\partial^2}{\partial x^2} + \frac{\partial^2}{\partial y^2} + \frac{\partial^2}{\partial z^2}\right)$ the Laplace operator.

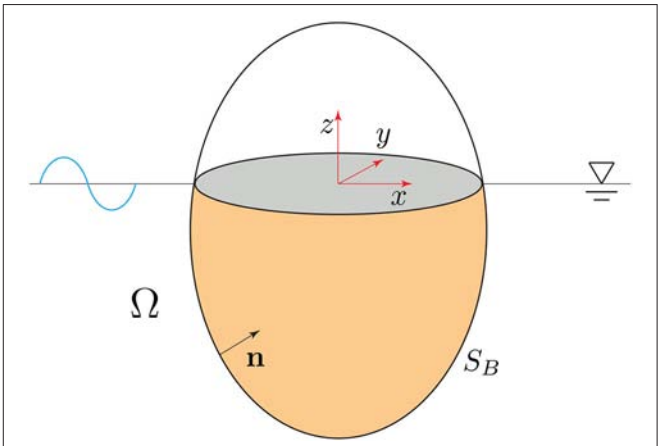

FIGURE 1 | Floating body.

The free-surface and non-permeable boundary conditions are imposed at $z = 0$ and $z = -h$, respectively

$$\frac{\partial \phi_i}{\partial z} - \frac{\omega^2}{g}\,\phi_i = 0 \quad \text{in } z = 0 \tag{4}$$

$$\frac{\partial \phi_i}{\partial z} = 0 \quad \text{in } z = -h \tag{5}$$

with g the gravity acceleration constant. At the interphase, both velocities at the solid and fluid are equal. Thus,

$$\frac{\partial \phi_i}{\partial \mathbf{n}} = -\mathrm{i}\,\omega\, V_i\ (\mathbf{a}_i \cdot \mathbf{n}) \quad \text{in } S_B \tag{6}$$

with $\mathbf{n}$ the unitary normal vector exterior to the fluid domain, and $\mathbf{a}_i$ the velocity vector due to a unitary-amplitude oscillation given at the i degree-of-freedom. Last, the Sommerfeld radiation boundary condition is given as,

$$\lim_{r\to\infty}\left(\frac{\partial \phi_i}{\partial r} - \mathrm{i}\,k\,\phi_i\right) = 0 \tag{7}$$

with $r = \sqrt{x^2 + y^2}$, and k the wavenumber, which verifies the following dispersion equation,

$$\omega^2 = g\,k\,\tanh\left(k\,h\right) \tag{8}$$

The mass matrix components (μ_{ij}) and added damping (λ_{ij}) are obtained by integration.

$$\mu_{ij} = \rho \int_{S_B} \mathrm{Re}\left[\phi_i\ (\mathbf{a}_j \cdot \mathbf{n})\right]\, dS \tag{9}$$

$$\lambda_{ij} = \rho\,\omega \int_{S_B} \mathrm{Im}\left[\phi_i\ (\mathbf{a}_j \cdot \mathbf{n})\right]\, dS \tag{10}$$

With ρ the fluid density.

2.2. Mild-Slope Equation

The second selected problem is centered in the propagation of gravity waves in a three-dimensional fluid domain characterized by a slow-varying depth profile. The governing equation is known as the Mild-Slope equation, proposed by Berkhoff (1972, 1976), in the context of harbor problems. This problem has been solved by numerical methods by the Finite Element Method (e.g., Ortiz and Pastor, 1990; Ortiz and Sánchez, 2001; Ortiz, 2004) for refraction-diffraction. In the BEM literature the domain formulation is explored for particular cases. Isaacson and Qu (1990) develop a method based on Green functions and BEM techniques for predicting the wave field in a harbor containing partially reflecting boundaries. Liu (2001) solves the numerical prediction of combined difraction and refraction ocean waves by use of a Dual Reciprocity BEM (DRBEM).

With reference to **Figure 2**, a velocity potential $\Phi(\mathbf{x}, t)$ is considered. The free surface is characterized by the function $\varsigma(x, y, t)$. Function $h(x, y)$ represents the varying depth. In the frequency domain, the complex potential $\phi(\mathbf{x})$ (1) is introduced. Thus, function $\varsigma(x, y, t)$ can be written as:

$$\varsigma(x, y, t) = \eta(x, y)\,\mathrm{e}^{-\mathrm{i}\,\omega\, t} \tag{11}$$

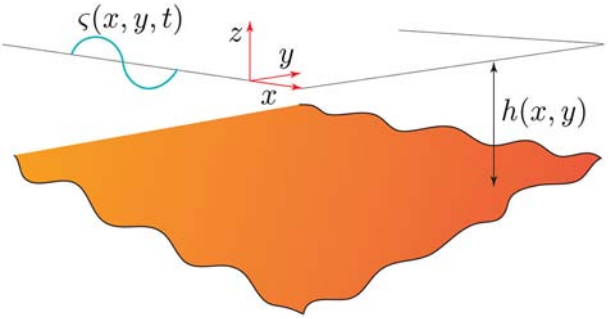

FIGURE 2 | Parameter definition in the Mild-slope problem.

The complex-valued function $\eta(x, y)$ represents the wave height, interpreted as a perturbation of the free surface respect to the rest position.

Potential $\phi(\mathbf{x})$ verifies the Laplace equation, analogous to (3). The impermeable boundary condition at the bottom depth can be written as,

$$\frac{\partial \phi}{\partial z} + \nabla\phi \cdot \nabla h = 0 \quad \text{in } z = -h(x, y) \tag{12}$$

with ∇ the gradient operator in the spatial coordinates (x, y). The free-surface condition can be written as,

$$\frac{\partial \phi}{\partial z} - \frac{\omega^2}{g}\phi = 0 \quad \text{in } z = 0 \tag{13}$$

For the particular case of constant-depth, it can be proved Chamberlain and Porter (1995) that function $\eta(x, y)$ verifies the Helmholtz equation,

$$\Delta\eta(x, y) + k^2\eta(x, y) = 0 \tag{14}$$

with k the wave length, for which the dispersion Equation (8) is verified.

2.3. Boundary Element Formulation

To approximate the solution by the BEM, the first step is the statement of a Boundary Integral Equation (BIE). For an internal point, (3), and considering the potential ϕ, the BIE is

$$\phi(\mathbf{x}) + \int_S \frac{\partial G(\mathbf{x};\,\mathbf{y})}{\partial \mathbf{n}}\,\phi(\mathbf{y})\,\mathrm{d}S(\mathbf{y}) = \int_S G(\mathbf{x};\,\mathbf{y})\,\frac{\partial \phi(\mathbf{y})}{\partial \mathbf{n}}\,\mathrm{d}S(\mathbf{y}) \tag{15}$$

with $\mathbf{x} \in \Omega$, $\mathbf{y} \in S$, and $G(\mathbf{x};\,\mathbf{y})$ is the Green function of the problem; for the three-dimensional Laplace equation, the Green function is,

$$G(\mathbf{x};\,\mathbf{y}) = \frac{1}{4\pi\, r(\mathbf{x};\,\mathbf{y})} \tag{16}$$

with $r(\mathbf{x};\,\mathbf{y})$ the euclidean distance from point $\mathbf{x}$, or *collocation point* to the *observation point* $\mathbf{y}$.

The BIE for a smooth boundary point $\mathbf{x} \in S$ is obtained after a limit-to-the-boundary process (Brebbia and Dominguez, 1996; Bonnet, 1999)

$$\frac{\phi(\mathbf{x})}{2} + \int_S \frac{\partial G(\mathbf{x};\mathbf{y})}{\partial \mathbf{n}} \phi(\mathbf{y})\, \mathrm{d}S(\mathbf{y}) = \int_S G(\mathbf{x};\mathbf{y}) \frac{\partial \phi(\mathbf{y})}{\partial \mathbf{n}} \mathrm{d}S(\mathbf{y}) \quad (17)$$

Both BIEs (15, 17) are valid for the Helmholtz Equation (14), considering a bi-dimensional domain and replacing variable ϕ by η, with the Green function,

$$G(x;y) = \frac{1}{2\pi} K_0(\mathrm{i}\, k\, r) \quad (18)$$

with K_0 the modified Bessel function order 0. In Isaacson and Qu (1990) it is derived an alternative expression for this Green function in the context of the Mild-slope equation. In case of variable-depth, the Dual Reciprocity Method (Liu, 2001) leads to a BEM formulation.

Equation (17) is used in a standard collocation method. After the boundary discretization, and integral evaluation, it is obtained the basic matrix formulation, as follows

$$\mathbf{H}\,\mathbf{U} = \mathbf{G}\,\mathbf{Q} \quad (19)$$

with $\mathbf{H}$ and $\mathbf{G}$ two matrices, and $\mathbf{U}$ and $\mathbf{Q}$ vectors with degrees-of-freedom in potential ϕ or flux $\frac{\partial \phi}{\partial \mathbf{n}}$, respectively. After the application of the prescribed boundary condition, the linear system of equations is obtained,

$$\mathbf{A}\,\mathbf{X} = \mathbf{B} \quad (20)$$

The evaluation of the integrals depends on the type of shape functions selected to interpolate the potential or flux variables (Brebbia and Dominguez, 1996), with particularities for singular or quasi-singular integration. In this paper constant elements have been considered, due to its widely use in the literature about acceleration techniques in BEM.

3. A PARALLEL GMRES WITH CUDA

3.1. The Generalized Minimum Residual Method

In this section the restarted GMRES (van der Vorst, 2003) is described. With reference to system (20), the first step in the GMRES solver is the definition of an initial solution vector, $\mathbf{X}_0$. Thus, a first residual is defined as $\mathbf{r}_0 = \mathbf{B} - \mathbf{A} \cdot \mathbf{X}_0$. **Algorithm 1** describes the steps of the restarted GMRES, in which a new initial point $\mathbf{X}_0$ is set after m steps, unless the convergence criteria is reached. This technique allows important reductions in memory and computing times. In the context of this paper, the GMRES schema has been adapted to incorporate complex-valued matrices and operations.

With reference to **Algorithm 1**, vector $\mathbf{e_1}$, length m, is a unitary vector, in which the first position is 1 and 0 the other positions. The dot products with complex-valued components are interpreted in the sense of the inner product in a Hilbert

Algorithm 1: Restarted GMRES

1: $\mathbf{r} = \mathbf{B} - \mathbf{A} \cdot \mathbf{X}_0$ for an initial approximation $\mathbf{X}_0$
2: **for** $j = 1, 2, \ldots$ **do**
3: $\beta = |\mathbf{r}|$
4: $\mathbf{v_1} = \mathbf{r}/\beta$
5: $\hat{\mathbf{B}} = \beta \mathbf{e_1}$
6: **for** $i = 1, 2, \ldots, m$ **do**
7: $\mathbf{w} = \mathbf{A} \cdot \mathbf{v_i}$
8: **for** $k = 1, \ldots, i$ **do**
9: $h_{k,i} = \bar{\mathbf{v}}_\mathbf{k} \cdot \mathbf{w}$
10: $\mathbf{w} = \mathbf{w} - h_{k,i}\mathbf{v_k}$
11: **end for**
12: $h_{i+1,i} = |\mathbf{w}|$
13: $\mathbf{v_{i+1}} = \mathbf{w}/h_{i+1,i}$
14: $u_{1,i} = h_{1,i}$
15: **for** $k = 2, \ldots, i$ **do**
16: $\gamma = c_{k-1}u_{k-1,i} + \bar{s}_{k-1}h_{k,i}$
17: $u_{k,i} = -s_{k-1}u_{k-1,i} + c_{k-1}h_{k,i}$
18: $u_{k-1,i} = \gamma$
19: **end for**
20: $\delta = \sqrt{|u_{i,i}|^2 + |h_{i+1,i}|^2}$
21: **if** $|u_{i,i}| < |h_{i+1,i}|$ **then**
22: $\mu = u_{i,i}/h_{i+1,i}$
23: $\tau = \overline{\mu}/|\mu|$
24: **else**
25: $\mu = h_{i+1,i}/u_{i,i}$
26: $\tau = \mu/|\mu|$
27: **end if**
28: $c_i = |u_{i,i}|/\delta$
29: $s_i = |h_{i+1,i}|\,\tau/\delta$
30: $u_{i,i} = c_i u_{i,i} + \bar{s}_i h_{i+1,i}$
31: $\hat{b}_{i+1} = -s_i \hat{b}_i$
32: $\hat{b}_i = c_i \hat{b}_i$
33: $\omega = |\hat{b}_{i+1}|$
34: **if** $\omega/|\mathbf{B}| \leq$ Tolerancia **then**
35: $n_r = i$
36: $y_{n_r} = \hat{b}_{n_r}/u_{n_r,n_r}$
37: Ir a línea 41
38: **end if**
39: **end for**
40: $n_r = m$
41: $y_{n_r} = \hat{b}_{n_r}/u_{n_r,n_r}$
42: **for** $k = n_r - 1, \ldots, 1$ **do**
43: $y_k = \left(\hat{b}_k - \sum_{i=k+1}^{n_r} u_{k,i}y_i\right)/u_{k,k}$
44: **end for**
45: $\mathbf{X} = \mathbf{X}_0 + \sum_{i=1}^{n_r} y_i \mathbf{v}_i$
46: $\omega_2 = |\mathbf{B} - \mathbf{A} \cdot \mathbf{X}|$
47: **if** $\omega_2/|\mathbf{B}| \leq$ Tolerancia **then**
48: Solution obtained $\rightarrow$ End
49: **end if**
50: $\mathbf{r} = \mathbf{B} - \mathbf{A} \cdot \mathbf{X}$
51: **end for**

space. Thus, if **a** and **b** are complex-valued vector, the dot product is defined as follows,

$$\mathbf{a} \cdot \mathbf{b} = \sum \overline{a_i} \cdot b_i. \tag{21}$$

with $\overline{a_i}$ the complex-conjugate of term a_i. The sum (21) is extended to the dimension of the complex vector.

The norm $|\mathbf{v}|$ is defined in terms of the previously defined product,

$$|\mathbf{v}| = \sqrt{\sum \overline{v_i} v_i} \tag{22}$$

The stopping criterion is an important aspect in solver iterative algorithms. In the context of this work, a dimensionless norm has been considered, reported in Frayssé et al. (1998).

$$\frac{|\mathbf{r}|}{\alpha\,|\mathbf{x}| + \chi} \leq \text{Tolerance} \tag{23}$$

with α and χ two parameters to be set up by the user. In this paper, parameters $\alpha = 1$ and $\chi = 0$ have been considered.

3.2. GPU Parallelization With CUDA

In the GMRES, the most demanding operation is the calculation of the matrix-vector products. The parallelization of these products has been implemented in CUDA programming languaje and run in the GPU. The GPU is a device with specific resources that must be considered in the design of the algorithms.

Computing times are sensitive to particular aspects, such as the use of the shared memory, registers per thread and the block-threads structure of the computing grid Kirk and Hwu (2012). These parameters determine the occupancy[1] of the GPU. CUDA allows the code to be optimized for each particular GPU device, which cause portability and scalability of the generated codes. To adapt the execution parameters to each singular GPU, the CUDA *Occupancy Calculator* developed by NVidia has been used. Given the shared memory and the number of registers per thread, the highest value of number of threads per block are optimized for any particular GPU device.

Figure 3 shows the global schema for the proposed solver. The operations are grouped into four steps: two of them are carried out in the CPU, and two into the GPU device.

Algorithm 2 is implemented with CUDA to be run in the GPU. This algorithm is focused on control of the matrix-vector products. Given a matrix **M** and vector **V**, the grid structure is determined depending on the matrix and vector dimensions, for maximum GPU occupancy. In general, for systems with large number of degrees of freedom it is required the use of more than one block per row, in order to balance the number of operations required to process each row. However, when more than one block is required per row, results computed at each block must to be reduced to a unique value per row.

[1]Number of simultaneous threads computed by multiprocessor divided by the maximum allowed.

After the definition of these setup parameters, the memory transfer operations between GPU and CPU must be minimized. In this sense, the system matrix in the BEM code is fully populated; thus, no compression methods are available, and all the components of the matrix must be transferred to the GPU. This transference is carried out by splitting the matrix in sub-matrices. Each sub-matrix block is transferred to the GPU, in which the matrix-vector product is carried out.

Algorithm 3 describes the first set of operations run in the GPU. Each thread is used to carry out the product of the matrix elements by the vector. Results are stored in a local vector in the shared memory at each block. The reading/writing access to the shared memory are faster than global memory.

The next step is the addition of the vector elements in each thread in the shared memory, obtaining a unique value per block. This addition is stored in a vector **R** in the global memory of the GPU.

Algorithm 2: Matrix-Vector product - Main (CPU)

```
1:  Input M: Matrix
2:  Input V: Vector
3:  Input N: Matrix dimension
4:  Set TB, number of Threads per Block
5:  Set BR, number of Blocks per Row
6:  Set memory and copy Vector V to the GPU
7:  Set memory and define vector R, dimension N·BR
8:  if Total memory < GPU memory then
9:     Set memory and copy Matrix M to the GPU
10:    i=0
11:    Call Algorithm 3 with a block mesh BR×N
12: else
13:    Set Number of Steps = NS
14:    Set NR, Number of Rows to be activated in each
       multiplication step
15:    for i=0,1,...,NS-1 do
16:       Allocate memory and copy NR rows of Matrix M to the
          GPU
17:       Call Algorithm 3 with a mesh of BR×NR blocks
18:       Free memory from GPU occupied by the NR rows
19:    end for
20: end if
21: if BR>1 then
22:    Call Algorithm 4 with a mesh, with number of threads ≥
       N
23: end if
24: Copy the computed vector from GPU to CPU
25: Free all the global memory in GPU
```

The second step to be carried out in the GPU is described by **Algorithm 4**. The aim of this part is the addition of the individual values obtained at each block, in order to give the resulting vector. This part is only required in case of defining more than one block per row of matrix M. The last step is copying the *N* first elements in vector **R** to the RAM memory in CPU.

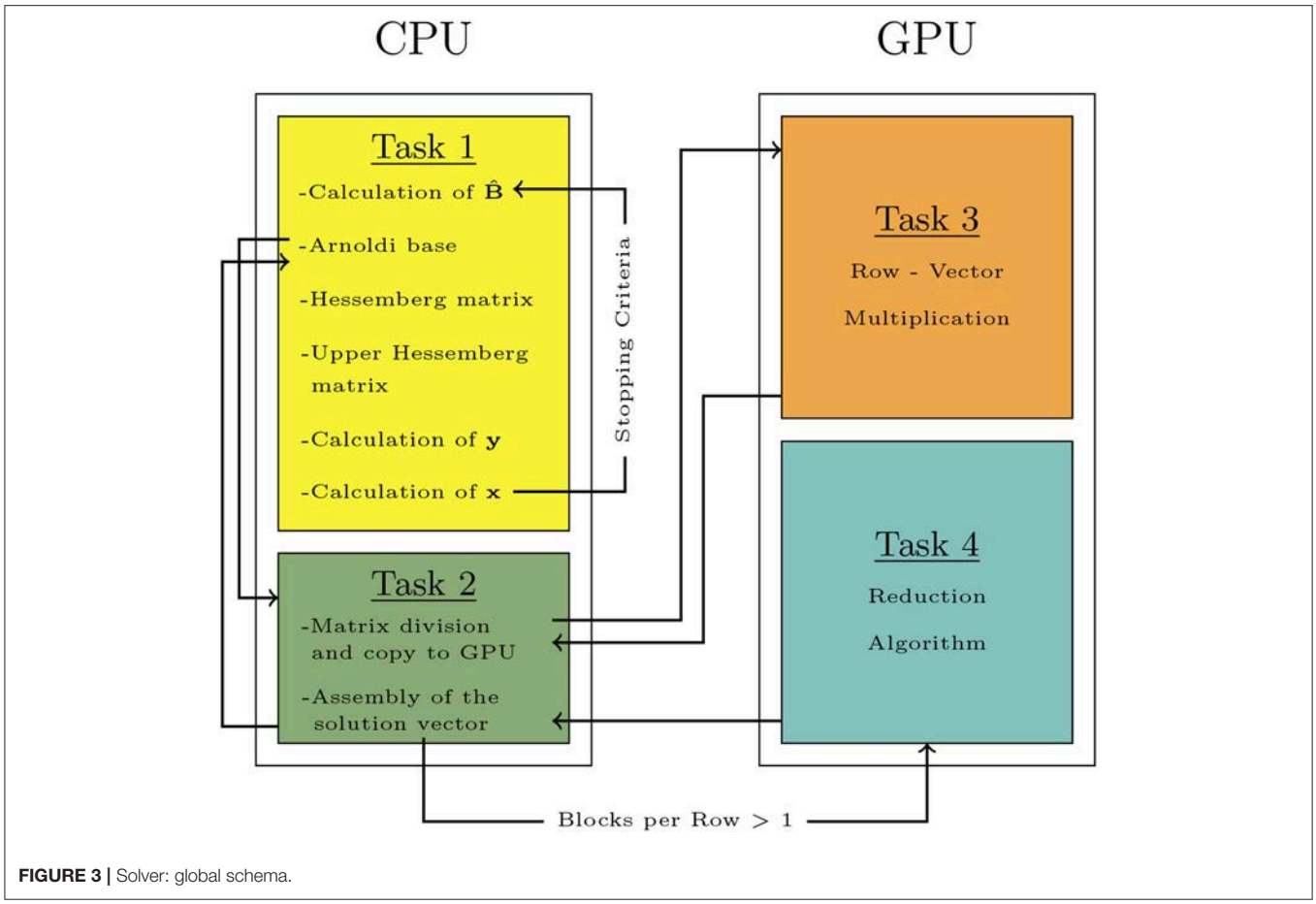

FIGURE 3 | Solver: global schema.

4. NUMERICAL TESTS

The proposed GMRES has been implemented in C++ and CUDA, in the context of two BEM codes. The main objective of the tests is the direct comparison of the computing times required by the parallel GPU solver, compared with a pure sequential CPU implementation. Tests are designed to measure the performances of the parallel solver in the GPU. Thus, the CPU operations have not been parallelized. No additional compiler optimizations have been used in CPU, which could cause wrong conclusions about computing times associated with the tested algorithms.

The NVidia GeForce GTX 1080 graphic card has been used, with a compute capability 6.1, 8GB in global memory, 48KB of shared memory per block, and 20 multiprocessors type SPMD (Single Program Multiple Data), with 128 CUDA cores per multiprocessor. CUDA 10 version has been used. The GPU allows a maximum of 1024 threads per block and 2048 threads per multiprocessor. For **Algorithm 3**, the code allocates 22 registers per thread and the required shared memory is 16 bytes (size of a double precision complex number) per thread. On the other hand, for **Algorithm 4**, the code computes 28 registers per thread and no shared memory is required. With these values, the occupancy calculator selects 1,024 threads per block with 100% occupancy. The CPU is an Intel i7-6800K processor.

The *Salome* mesher (http://www.salome-platform.org/) has been used to generate the three-dimensional meshes in the floating body problem. The post-processing software *Paraview* (http://www.paraview.org/) has been used to visualize the results.

4.1. Added Mass of a Floating Cylinder

This first example is in the context of fluid-solid interaction analysis. In this problem, term μ_{11} in (9), corresponding to a time-harmonic movement in direction x, is solved. The floating body is a cylinder, shown in **Figure 4**, as a function of the wavelength. This problem has an analytic solution in terms of a normal modes expansion (Bhatta, 2003). The objective is the observation of the dependence on the frequency on the computing times at a fixed mesh.

The number of elements of the computing mesh is 7568, shown in **Figures 5** and **6**. Constant three-node elements are used. The minimum element size has been selected according to a criterium dependent on the minimum wavelength, associated with the higher frequency. Ten elements per minumum wavelength have been considered.

The Laplace Equation (3), with the boundary conditions given by Equations (4–6) have been considered. The radiation condition (7) has been set in a simplified way Ortiz and Pastor (1990), because the Green function considered does not fulfill the

Algorithm 3: Matrix-Vector Product - GPU product

```
Store in the shared memory, given a vector of HB elements (MC)
id1=threadIdx.x+blockIdx.x·blockDim.x
id2=threadIdx.x
while id1 < N do
    MC[id2]+=M[blockIdx.y][id1]·V[id1]
    id1+=blockDim.x·gridDim.x
end while
Thread synchronization
Set integer: j=blockDim.x/2
while j ≠ 0 do
    if id2 < j then
        MC[id2]+=MC[id2+j]
    end if
    Thread synchronization
    j=j/2
end while
if id2=0 then
    R[i·NF+N·blockIdx.x+blockIdx.y]=MC[0]
end if
```

Algorithm 4: Matrix-Vector Product - Reduction in (GPU)

```
id=blockDim.x·blockIdx.x+threadIdx.x
if id < N then
    for j=1,2,. . .,BF-1 do R[id]+=R[id+N·j]
    end for
end if
```

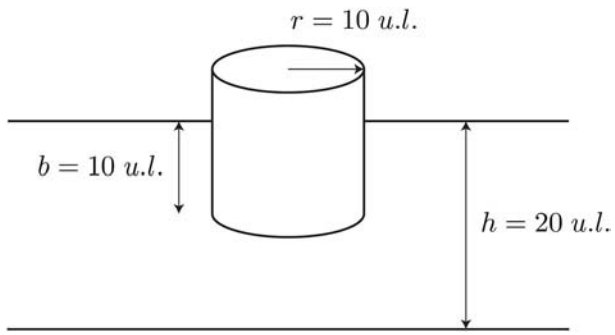

FIGURE 4 | Floating cylinder.

radiation boundary condition. An external boundary has been defined in $r = 250$ u.l. (units of length), for which relation (7) is established. In this way, a complex-valued boundary condition is given, which allows progressive waves in the solution. This approximation avoids matching with an external solution based on a normal-mode expansion, with a good approximation in the frequency range tested.

Figure 7 shows the results for the added mass. Values computed by integration (9) are compared, when potential function is obtained by the BEM or by the analytic solution

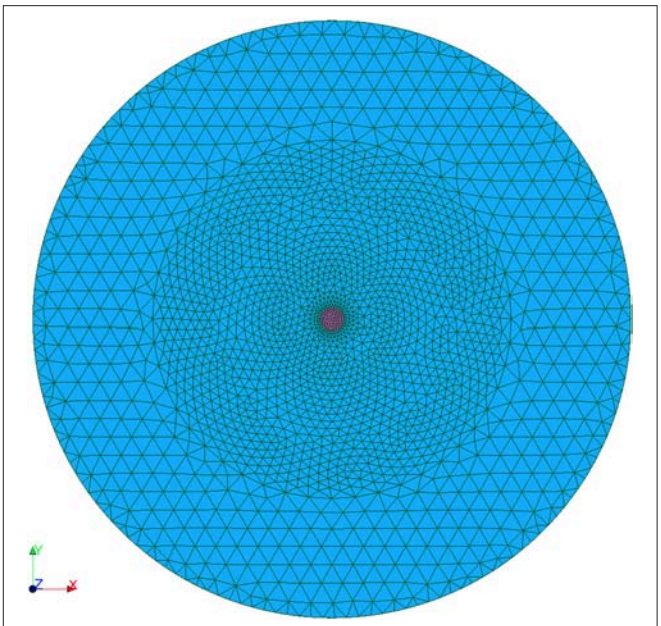

FIGURE 5 | Floating body problem. 3D Mesh, seen from above.

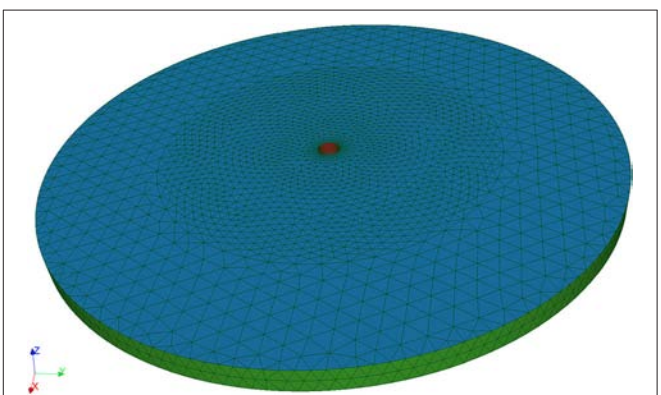

FIGURE 6 | Floating body problem. 3D Mesh, perspective.

reported in Bhatta (2003). The dimensionless variable kr is shown in abscissas, in which r is the cylinder radius and k the wavenumber. The Y-axis represents the dimensionless values of the added mass μ_{11}. Small differences between the added mass values are observed, less than 2%. Note that the comparison is in integrated values of the computed potential, and not in the potential itself. Both solutions includes representation errors; the analytic solution is given in series form, in which the singular behavior in corner is not included (Guzina et al., 2006). In contrast, the BEM solution is obtained with constant elements, and the radiation boundary condition is imposed in an approximate form.

Table 1 shows the computing times required, as a function of the wavelength. Column *CPU* shows the times required by the GMRES in CPU (sequential). Column *GPU* shows the computing times required by the GMRES in GPU. The last column shows

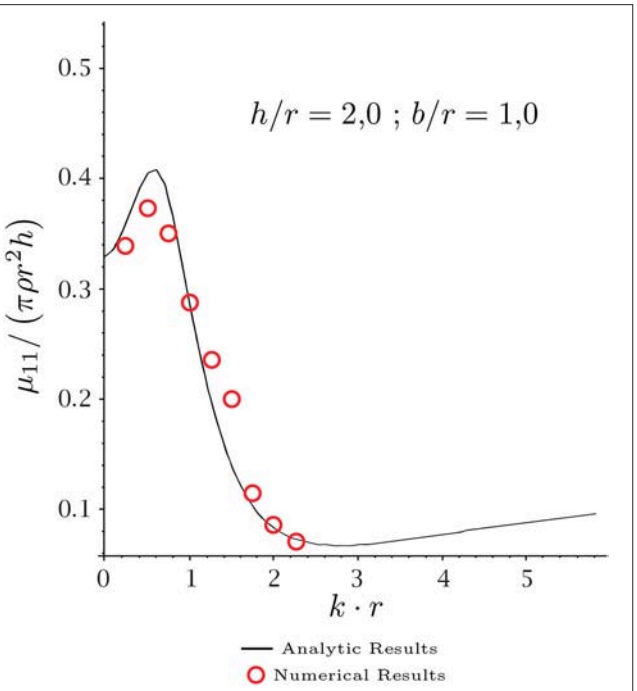

FIGURE 7 | Added mass μ_{11}, as a function of $k \cdot r$.

TABLE 1 | Computing times in the floating cylinder problem.

Wavenumber	CPU (s)	GPU (s)	Speedup
0.025	73.12	7.14	10.24
0.050	138.48	14.04	9.86
0.075	236.68	26.31	9.00
0.100	392.63	50.04	7.85
0.125	598.39	89.36	6.70
0.150	932.56	165.50	5.63
0.175	1614.29	368.86	4.38
0.200	3302.82	1047.79	3.15
0.225	3946.75	1352.72	2.92

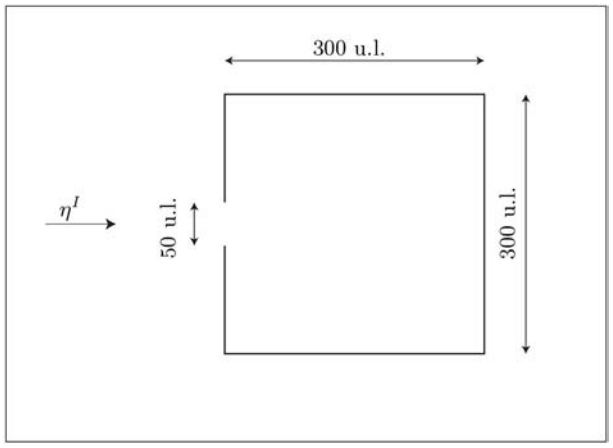

FIGURE 8 | Harbor configuration.

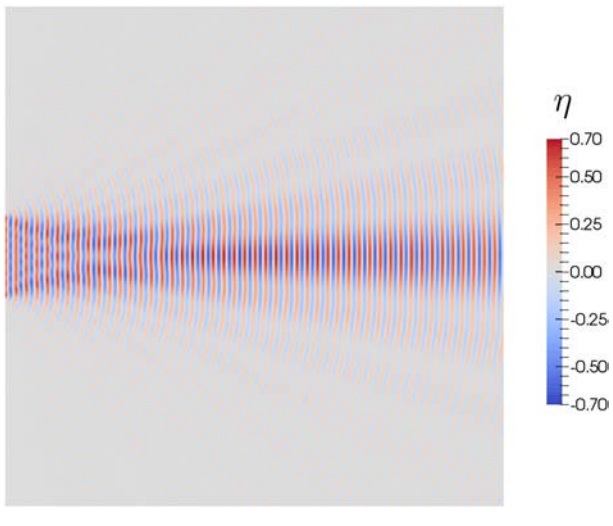

FIGURE 9 | Internal solution for η.

the *speedup*, computed as the rate between the CPU and GPU times. It is observed a dependence in the computing times with respect to the wavelength. The parallel GMRES is more effective at low frequencies. This is due to the fixed mesh considered in all the tests, with constant elements. The solution with constant elements is poor for high frequency. The GMRES algorithm shows poor convergence, and more iterations are required. At low frequency, fast convergence is observed.

4.2. Internal Harbor Oscillations

In this section, the Mild-Slope equation is solved by the BEM, to characterize the internal waves in a harbor. This problem has been studied by Isaacson and Qu (1990); the same conditions have been adopted in this paper.

Figure 8 shows the harbor geometry. The incidental wave η^I is characterized by a period 2.0 u.t (units of time), amplitude 0.5 u.l. (units of legth) and a propagation direction perpendicular to the harbor opening. Absorbing boundaries are considered at the harbor. Constant depth, 20 u.l. is considered.

The Helmholtz Equation (14) is solved, for the wave elevation η. The numerical results obtained for η inside the harbor domain are shown in **Figure 9**. Note that this case corresponds with a high frequency problem, with short wavelengths.

In this problem different meshes have been used, in order to observe the efficiency of the GPU parallelization when the number of degrees of freedom is increased. **Table 2** shows the computing times; column *DOF* reports the number of degrees of freedom in the system; column Collocation shows the computing time required by the BEM to generate the system matrix and vector; columns *CPU* y *GPU* show the computing times required by the GMRES solved in CPU or GPU, respectively. The last column shows the speedup of the GPU solver.

TABLE 2 | Harbor oscillations.

DOF	Collocation (s)	CPU (s)	GPU (s)	Speedup
1,250	1.66	4.79	1.19	4.03
2,500	6.54	22.14	3.93	5.63
3,750	14.81	55.84	8.37	6.67
5,000	26.17	107.83	14.40	7.49
7,500	58.67	266.92	31.63	8.44
10,000	103.84	510.12	56.58	9.02
15,000	232.82	1276.89	131.66	9.70
20,000	415.31	2460.94	240.60	10.23

Computing times.

Numerical results shows that computing times required by the collocation BEM (both in CPU) are one order less to the computing times required to solve the linear system of equations. It is also shown that the GPU solver is more efficient for large number of degrees of freedom. For small number of degrees of freedom, the bottleneck comes from time required to transfer memory from CPU to the global memory in GPU. The speedup increases for large number of degrees of freedom, even in systems with 15,000 and 20,000 equations, in which the product matrix-vector is carried out by blocks, with multiple memory transferences from GPU to CPU.

5. CONCLUDING REMARKS

In this paper, a GPU implementation of the GMRES algorithm is presented in the context of the BEM with fully-populated matrices and with complex-valued arguments. It is explored an interesting field related to the acceleration techniques for the BEM in the frequency domain. With difference to other acceleration techniques for the BEM (FMM, pFFT or ACA), the proposed approach does not require modifications in the main program, which computes the system matrix and the right vector. This allows the use of standard BEM codes, with the solver task transferred to the GPU.

The GMRES version described here does not include a preconditioner. The use of preconditioners in the GMRES and BEM is an important aspect for particular problems with poorly conditioned matrices. In the context of this paper, numerical tests have been designed to show the performances of the proposed solver. The development of a general preconditioned GMRES in GPU for the BEM is out of the scope of this paper.

The acceleration is carried out by a main task controlled in the CPU, which allows the massive parallelization of the matrix-vector products in the GPU. The CUDA programming language has been used to implement an adaptive solver, in the sense that the generated code is optimized for the particular GPU device in which it is compiled. The generated solver is portable and scalable for future GPU devices. All the different GPU and CPU tasks are described in algorithmic language.

Numerical tests show time reductions when compared with a standard CPU solver. In the context of the BEM, the inherent reduction in the number of degrees of freedom (only at the boundary) causes that the standard collocation method, with a direct assembly of the system matrix and right vector, is extended among the different numerical codes for a wide number of applications. For such codes, the proposed solver represents an easy way to obtain time reductions in computing times by transferring the solver task to the GPU. Due to the fast development of the GPU systems, with improvements in the number of cores, increasing the device memories and improving the speed of the memory transferences, the proposed GPU solver shows an interesting way of acceleration, with future improvements depending on the device developments.

AUTHOR CONTRIBUTIONS

AM-C conceived of the presented idea. JM-M, AM-C, and PO developed the theoretical formalism and designed the numerical tests. JM-M developed the presented algorithms and implemented them on a computational framework. He also performed the calculations and generated tables and figures. JM-M, AM-C, and PO contributed to the final version of the manuscript.

ACKNOWLEDGMENTS

We appreciate the partial financial support from the MINECO/FEDER project BIA2015-64994-P.

REFERENCES

Benedetti, I., Aliabadi, M., and Daví, G. (2008). A fast 3D dual boundary element method based on hierarchical matrices. *Int. J. Solids. Struct.* 45, 2355–2376. doi: 10.1016/j.ijsolstr.2007.11.018

Berkhoff, J. C. W. (1972). "Computation of combined refraction-diffraction," in *Proceedings of the 13th International Conference on Coastal Engineering* (Vancouver, BC), 471–490.

Berkhoff, J. C. W. (1976). *Mathematical Models for Simple Harmonic Linear Water Wave Models; Wave Refraction and Diffraction*. Ph.D. thesis, Delf University of Technology.

Bhatta, D. D. (2003). Surge Motion on a floating cylinder in water of finite depth. *Int. J. Math. Math. Sci.* 2003, 3643–3656. doi: 10.1155/S0161171203209285

Bonnet, M. (1999). *Boundary Integral Equation Methods for Solids and Fluids*. Chichester: Wiley.

Brancati, A., Aliabadi, M. H., and I., B. (2009). Hierarchical adaptive cross approximation GMRES technique for solution of acoustic problems using the boundary element method. *Comput. Model. Eng. Sci.* 43, 149–172. doi: 10.3970/cmes.2009.043.149

Brebbia, C. (1978). *The Boundary Element Method for Engineers*. New York, NY: Pentech Press; Halstead Press.

Brebbia, C., and Dominguez, J. (1996). *Boundary Elements: An Introductory Course*. Southampton: WIT Press.

Brebbia, C. A., and Partridge, P. W. (1992). *Boundary Elements in Fluid Dynamics*. Southampton: Springer.

Chaillat, S., and Bonnet, M. (2013). Recent advances on the fast multipole accelerated boundary element method for 3D time-harmonic elastodynamics. *Wave Motion* 50, 1090–1104. doi: 10.1016/j.wavemoti.2013.03.008

Chamberlain, P. G., and Porter, D. (1995). The modified mild-slope equation. *J. Fluid Mech.* 291, 393–407. doi: 10.1017/S0022112095002758

Cheng, A. D. H., and Cheng, D. T. (2005). Heritage and early history of the boundary element method. *Eng. Anal. Boundary Elem.* 29, 268–302. doi: 10.1016/j.enganabound.2004.12.001

D'Azevedo, E., and Nintcheu Fata, S. (2012). On the effective implementation of a boundary element code on graphics processing units using an out-of-core LU algorithm. *Eng. Anal. Boundary Elem.* 36, 1246–1255. doi: 10.1016/j.enganabound.2012.02.014

Djojodihardjo, H. (2010). "Further development in the application of fast multipole boundary element method for unified BEM-FEM acoustic-structural coupling," in *61st International Astronautical Congress 2010, IAC 2010*, vol. 4, Prague, 3417–3429.

Frayssé, V., Giraud, L., and Gratton, S. (1998). *A Set of Flexible-GMRES Routines for Real and Complex Arithmetics*. Technical report, Centre Européen de Recherche et de Formation Avancée en Calcul Scientifique TR/PA/98/20.

Geng, W., and Jacob, F. (2013). A GPU-accelerated direct-sum boundary integral Poisson–Boltzmann solver. *Comput. Phys. Commun.* 184, 1490–1496. doi: 10.1016/j.cpc.2013.01.017

Gumerov, N. A., and Duraiswami, R. (2005). *Fast Multipole Methods for the Helmholtz Equation in Three Dimensions*. Amsterdam: Elsevier.

Guzina, B. B., Pak, R. Y. S., and Martínez-Castro, A. (2006). Singular boundary elements for three-dimensional elasticity problems. *Eng. Anal. Bound. Elem.* 30, 623–639. doi: 10.1016/j.enganabound.2006.02.010

Hackbusch, W. (1999). A sparse matrix arithmetic based on hierarchical matrices. Part I: introduction to hierarchical matrices. *Computing* 62, 89–108. doi: 10.1007/s006070050015

Hamada, T. and Takahashi, T. (2009). GPU-accelerated boundary element method for Helmholtz equation in three dimensions. *Int. J. Numer. Meth. Eng.* 80, 1295–1321. doi: 10.1002/nme.2661

Hess, J. L. (1990). Panel methods in computational fluid dynamics. *Annu. Rev. Fluid Mech.* 22, 255–274. doi: 10.1146/annurev.fl.22.010190.001351

Isaacson, M., and Qu, S. (1990). Waves in a harbour with partially reflecting boundaries. *Coast. Eng.* 14:193–214. doi: 10.1016/0378-3839(90)90024-Q

Jaswon, M. A., and Porter, A. R. (1963). An integral equation solution of the torsion problem. *Proc. R. Soc.* 273, 237–246. doi: 10.1098/rspa.1963.0085

Kelly, J. M., Divo, E. A., and Kassab, A. J. (2014). Numerical solution of the two-phase incompressible Navier–Stokes equations using a GPU-accelerated meshless method. *Eng. Anal. Boundary Elem.* 40, 36–49. doi: 10.1016/j.enganabound.2013.11.015

Kirk, D., and Hwu, W. (2012). *Programming Massively Parallel Processors: A Hands-on Approach*. Cambridge, MA: Morgan Kaufmann.

Leung, C., and Walker, S. P. (1997). Iterative solution of large three-dimensional BEM elastostatic analyses using the GMRES technique. *Int. J. Numer. Meth. Eng.* 40, 2227–2236. doi: 10.1002/(SICI)1097-0207(19970630)40:12<2227 :AID-NME154>3.0.CO;2-Z

Li, R., and Saad, Y. (2013). GPU-accelerated preconditioned iterative linear solvers. *J. Supercomput.* 63, 443–466. doi: 10.1007/s11227-012-0825-3

Liu, H.-W. (2001). *Numerical Modelling of the Propagation of Ocean Waves*. Ph.D. thesis, University of Wollongong.

Liu, Y. (2009). *Fast Multipole Boundary Element Method*. New York, NY: Cambridge University Press.

Liu, Y., and Nishimura, N. (2006). The fast multipole boundary element method for potential problems: a tutorial. *Eng. Anal. Bound. Elem.* 30, 371–381. doi: 10.1016/j.enganabound.2005.11.006

Liu, Y. J. (2008). A fast multipole boundary element method for 2D multi-domain elastostatic problems based on a dual BIE formulation. *Comput. Mech.* 42, 761–773. doi: 10.1007/s00466-008-0274-2

Liu, Y. J., Mukherjee, S., Nishimura, N., Schanz, M., Ye, W., Sutradhar, A., et al. (2012). Recent advances and emerging applications of the boundary element method. *Appl. Mech. Rev.* 64, 1–38. doi: 10.1115/1.4005491

López-Portugués, M., López-Fernández, J., Menéndez-Canal, J., Rodríguez-Campa, A., and Ranilla, J. (2012). Acoustic scattering solver based on single level FMM for multi-GPU systems. *J. Parallel Distr. Com.* 72, 1057–1064. doi: 10.1016/j.jpdc.2011.07.013

Lu, T., Wang, Z., and Yu, W. (2004). Hierarchical block boundary-element method (HBBEM): a fast field solver for 3-D capacitance extraction. *IEEE T. Microw. Theory* 52, 10–19. doi: 10.1109/TMTT.2003.821228

Ma, Z., Wang, H., and Pu, S. (2014). GPU computing of compressible flow problems by a meshless method with space-filling curves. *J. Comput. Phys.* 263, 113–135. doi: 10.1016/j.jcp.2014.01.023

Margonari, M. and Bonnet, M. (2005). Fast multipole method applied to the coupling of elastostatic BEM with FEM. *Comput. Struct.* 83, 700–717. doi: 10.1016/j.compstruc.2004.09.007

Mei, C. C., Stiassnie, M., and Yue, D. K. P. (2005). *Theory and Applications of Ocean Surface Waves*. London: World Scientific Publishing Company.

Ortiz, P. (2004). Finite Elements using a plane-wave basis for scattering of surface water waves. *Philos. Trans. R. Soc. A.* 362, 525–540. doi: 10.1098/rsta.2003.1333

Ortiz, P., and Pastor, M. (1990). Un modelo numérico de refracción-difracción de ondas en zonas costeras. *Rev. Int. Metod. Numer.* 6, 409–436.

Ortiz, P., and Sánchez, E. (2001). An improved partition of unity finite element model for diffraction problems. *Int. J. Numer. Meth. Eng.* 50, 2727–2740. doi: 10.1002/nme.161

Phillips, J. R. (1997). *Rapid Solution of Potential Integral Equations in Complicated 3–Dimensional Geometries*. Ph.D. thesis, MIT.

Phillips, J. R., and White, J. K. (1997). A Pre-Corrected-FFT Method for Electrostatic Analysis of Complicated 3–D Structures. *IEEE Trans. Comput. Aided Des.* 16, 1059–1072. doi: 10.1109/43.662670

Rokhlin, V. (1985). Rapid solution of integral equations of classical potential theory. *J. Comput. Phys.* 60, 187–207. doi: 10.1016/0021-9991(85)90002-6

Saad, Y., and Shultz, M. (1986). GMRES: a generaliced minimal residual algorithm for solving non-symmetric linear systems. *SIAM J. Sci. Stat. Comput.* 7, 856–869. doi: 10.1137/0907058

Sanders, J., and Kandrot, E. (2010). *CUDA by Example*. Boston, MA: Addison-Wesley.

van der Vorst, H. (2003). *Iterative Krylov Methods for Large Linear System*. Cambridge, UK: Cambridge University Press.

Wang, G., Wang, Q. F., and Wang, Y. J. (2011). GPU based boundary element analysis for 3D elastostatics with GMRES-DC algorithm solving system equations. *Adv. Mat. Res.*, 308–310, 2345–2348. doi: 10.4028/www.scientific.net/AMR.308-310.2345

Wang, Y., Wang, Q., Wang, G., Huang, Y., and Wang, S. (2013). An adaptive dual-information FMBEM for 3D elasticity and its GPU implementation. *Eng. Anal. Boundary Elem.* 37, 236–249. doi: 10.1016/j.enganabound.2012.09.012

Conflict of Interest Statement: The authors declare that the research was conducted in the absence of any commercial or financial relationships that could be construed as a potential conflict of interest.

frontiers in Built Environment

ORIGINAL RESEARCH
published: 27 November 2018
doi: 10.3389/fbuil.2018.00056

Boundary Integral Formulation of Frictionless Contact Problems Based on an Energetic Approach and Its Numerical Implementation by the Collocation BEM

Christos G. Panagiotopoulos[1], *Vladislav Mantič*[2]*, *Israel G. García*[2] and *Enrique Graciani*[2]

[1] Institute of Applied & Computational Mathematics, Foundation for Research and Technology-Hellas, Heraklion, Greece,
[2] Grupo de Elasticidad y Resistencia de Materiales, Escuela Técnica Superior de Ingeniería, Universidad de Sevilla, Sevilla, Spain

OPEN ACCESS

Edited by:
Vagelis Plevris, OsloMet - Oslo Metropolitan University, Norway

Reviewed by:
Ivan Argatov, Technische Universität Berlin, Germany
Andreas Kampitsis, Faculty of Engineering, Imperial College London, United Kingdom
Cyril Fischer, Institute of Theoretical and Applied Mechanics (ASCR), Czechia

***Correspondence:**
Vladislav Mantič
mantic@us.es

Specialty section:
This article was submitted to Computational Methods in Structural Engineering, a section of the journal Frontiers in Built Environment

Received: *03 July 2018*
Accepted: *28 September 2018*
Published: *27 November 2018*

Citation:
Panagiotopoulos CG, Mantič V, García IG and Graciani E (2018) Boundary Integral Formulation of Frictionless Contact Problems Based on an Energetic Approach and Its Numerical Implementation by the Collocation BEM. Front. Built Environ. 4:56. doi: 10.3389/fbuil.2018.00056

A unified methodology to solve problems of frictionless unilateral contact as well as adhesive contact between linear elastic solids is presented. This methodology is based on energetic principles and is casted to a minimization problem of the total potential energy. Appropriate boundary integral forms of the energy are defined and the quadratic problem form of the contact problem is proposed. The problem is solved by the collocation boundary element method (BEM). To solve the quadratic problem two algorithms are developed, both being variants of the well-known conjugate gradient algorithm. The difference between them is given by the explicit construction or not of the quadratic-problem matrix. This matrix has the same physical meaning as the stiffness matrix commonly used in the context of the finite element method (FEM). Both symmetric and non-symmetric formulations of this matrix are presented and discussed, showing that the non-symmetric one provides more accurate results. The present procedure, in addition to its interest by itself, can also be extended to problems where dissipative phenomena take place such as friction, damage and plasticity. Essential steps of the numerical implementation are briefly presented and the numerical solutions of some standard problems of frictionless contact are given and compared to those obtained by other well-known BEM and FEM procedures for contact problems.

Keywords: unilateral frictionless contact, adhesive contact, linear elasticity, boundary element method, stiffness matrix in BEM, total potential energy minimization

1. INTRODUCTION

Contact problems (Johnson, 1985), often present in engineering applications, represent one of the most important and interesting topics of mechanics. Contact between deformable bodies is a complex and inherently non-linear problem. It is essentially a boundary phenomenon which has a strong effect on stress and displacement fields in the vicinity of the boundary of the contacting bodies. Phenomenologically one of the simplest models of contact is given by the Signorini (1959) contact condition, that imposes the strict non-penetrability of the bodies in contact. After early studies by Hertz (1896), many contact problems have been solved analytically. However,

complicated geometries or loads, as well as, more complex interfacial conditions (e.g., adhesion, cohesion, friction, etc.), require the use of numerical methods (Wriggers, 2006; Yastrebov, 2013). Unilateral frictionless contact problems for deformable bodies are usually numerically solved by the finite element method (FEM) or boundary element method (BEM).

For crack onset and growth modeling (see Panagiotopoulos et al., 2013; Roubíček et al., 2013), the first two authors with coworkers developed an energy based procedure implemented by BEM. In these applications, contact between crack faces should be considered, hence it is important to present in detail the theoretical background as well as details of the numerical procedure for problems of unilateral (i.e., Signorini) and adhesive frictionless contact. Hereinafter, this framework is referred to as **E***nergetic approach for the solution of elastic* **C***ontact problems by* **BEM** (EC-BEM).

Unilateral frictionless contact stands for the case where there is no other material in the interfaces (=contact zones) between elastic bodies. For this case the (Signorini, 1959) condition models the exact non-penetrability of the bodies in contact, by the following relations, Eck et al. (2005):

- The relative normal displacement at the interface cannot be larger than the initial distance between the bodies in contact.
- Stresses can be transmitted only if contact takes place.
- Only compressive normal tractions can be transmitted through the contact zone.

Adhesive unilateral contact is represented by bodies connected across their common interfaces by a continuous distribution of springs, similar to the Winkler spring model, with (possibly) distinct normal and tangential elastic stiffnesses whose values range from zero to infinity.

Several approaches for solving contact problems by BEM were developed in the past. In engineering literature an approach based on *incremental-iterative procedures* was developed and widely used from the very beginning (see París and Garrido, 1989; Katsikadelis and Kokkinos, 1993; París et al., 1995), among others. In this approach successive increments of load are applied and the Signorini contact condition is verified in each step by an iterative procedure. A BEM methodology for frictionless contact problems, based on the strong formulation of the problem, where the position of contact zones is defined through geometrical parameters is presented in Méchain-Renaud and Cimetière (2000).

In contrast to these approaches, the present approach for solving frictionless contact problems is based on general *energetic* considerations. Usually this approach requires the minimization of the potential energy under unilateral constraints on displacements (Gurtin, 1972; Lazaridis and Panagiotopoulos, 1987; Panagiotopoulos and Lazaridis, 1987), although different approaches may also be found (see Kalker and Randen, 1972), where instead of the potential energy the minimum enthalpy principle is employed, formulated as a boundary integral equations method, valid for frictionless contact problems in the absence of dissipative processes.

In the present work the contact problem is modeled as a *quasi-static* and *rate-independent* process, (Wriggers and Panagiotopoulos, 1972) (neglecting inertial and viscous forces) for linear elastic solids. In section 2 the energetic approach employed is presented. In section 3, the energetic principles formulated in boundary integral forms amenable to numerical implementation are introduced. A particular BEM implementation is presented in section 4. A procedure for computation of matrices in an explicit form that may be used in quadrature programming algorithms is described in section 5. Some details for analysis of a possible contact between elastic bodies, through interface elements, are presented in section 6, while specific features of the minimization algorithms are described in sections 7 through 10. Finally, in section 11, results of two-dimensional multi-region simulations are presented and compared to solutions obtained by other BEM and FEM techniques available in the literature, showing that the present framework is suitable to confront problems of contact between elastic bodies.

2. THEORETICAL BACKGROUND

Consider a finite number N of linear elastic bodies possibly in frictionless contact. Let these bodies be represented by mutually disjoint subdomains $\Omega^i \subset \mathbb{R}^2$ $(i=1,...,N)$ with Lipschitz boundaries $\partial\Omega^i = \Gamma^i$ (see **Figure 1**) and the unit outward normal and tangential vectors ν^i and τ^i, with $\tau^i = (-(\nu^i)_2, (\nu^i)_1)$.

Let $\mathbb{C}^{(i)}$ denote the elastic stiffness tensor of subdomain Ω^i, $u^i(x,t)$ the time dependent displacements on Ω^i, $e^i(u^i) = \frac{1}{2}\left((\bigtriangledown u^i)^T + \bigtriangledown u^i\right)$ the small strain tensor, $\sigma^i(u^i) = \mathbb{C}^{(i)} e^i(u^i)$ the stress tensor, $p^i(u^i) = \sigma^i(u^i)\nu^i$ the boundary tractions, $\sigma_n^i = p^i(u^i)\nu^i$ and $\sigma_t^i = p^i(u^i)\tau^i$ the normal and tangential component of boundary tractions, respectively.

Let $\Gamma_j^i \subset \Gamma^i$ denote the part of the boundary Γ^i which possibly can contact with Ω^j $(j = 0,...,N$ and $j \neq i)$, referred to as potential contact zone of Ω^i with Ω^j. We also consider a possible contact with a rigid obstacle on a part of Γ^i denoted as Γ_0^i.

We assume that the rest of Γ^i is partitioned into the Dirichlet and Neumann parts of the boundary, Γ_{D}^i and Γ_{N}^i, respectively. Time-dependent boundary displacement and traction vectors, $u_{\mathrm{D}}^i(x,t)$ and $p_{\mathrm{N}}^i(x,t)$, are prescribed on Γ_{D}^i and Γ_{N}^i, respectively. Thus, e.g., any admissible displacement $u^i(x,t)$ on Ω^i has to be equal to the prescribed displacement $u_{\mathrm{D}}^i(x,t)$ on Γ_{D}^i. Let

$$\Gamma_{\mathrm{D}} = \bigcup_{1\leq i\leq N} \Gamma_{\mathrm{D}}^i \text{ and } \Gamma_{\mathrm{N}} = \bigcup_{1\leq i\leq N} \Gamma_{\mathrm{N}}^i. \tag{1}$$

In the simplest case of conforming or receding contact with a zero initial gap, Γ_j^i can be equal to Γ_i^j, but in general, e.g., in the case of advancing contact or a positive gap, they do not coincide. The initial contact zone (in the undeformed configuration) between subdomains Ω^i and Ω^j, and also the active contact zone (the set of points on each subdomain which will enter in contact in the deformed configuration) both should be included in Γ_j^i and Γ_i^j. Specially, Γ_j^i and Γ_i^j may be larger than $\partial\Omega^i \cap \partial\Omega^j$ for modeling an advancing contact.

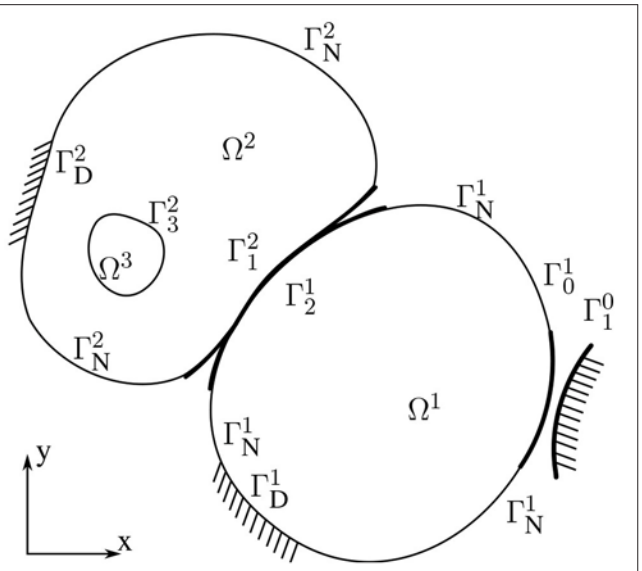

FIGURE 1 | Schematic illustration of the geometry and of the notation for the 2D case of $N = 3$ subdomains in contact including a rigid obstacle.

We assume that an intermediate contact surface, denoted as $\Gamma_{ij} = \Gamma_{ji}$, can be defined for each couple of potential contact zones, with one-to-one and onto (bijective) and continuous mappings (projections) between Γ_j^i, Γ_i^j and Γ_{ij}. A discretized version of such mappings is briefly introduced in section 6. A recent comprehensive revision of different projection techniques for a general contact configuration can be found in Yastrebov (2013). Additionally a normal direction is defined at each point of Γ_{ij} by a unit normal vector $\nu_j^i (= -\nu_i^j)$ (outward with respect to Ω^i). Recall that all Γ_j^i, Γ_i^j and Γ_{ij} are defined in the undeformed configuration. In the simplest case of conforming or receding contact with a zero initial gap, typically, $\Gamma_j^i = \Gamma_i^j = \Gamma_{ij}$.

The contact zone Γ_C in the present problem is defined by the union of all intermediate contact surfaces

$$\Gamma_C = \bigcup_{0 \le i < j \le N} \Gamma_{ij}. \tag{2}$$

The initial normal distance (gap) between some points $x^i \in \Gamma_j^i$ and $x^j \in \Gamma_i^j$ corresponding each other by the above defined mappings is given by the scalar gap function $g_{ij} = (x^j - x^i)\nu_j^i$ defined on the intermediate contact surface Γ_{ij}. A positive value of the gap function means an initial separation whereas a negative value means an initial overlapping between the bodies in contact. This gap function is denoted as g_n on Γ_C.

Similarly, we also define $[u]_{ij} = u^j(x^j) - u^i(x^i)$ on Γ_{ij} as the signed difference of displacements (displacement jump) between some points $x^i \in \Gamma_j^i$ and $x^j \in \Gamma_i^j$ corresponding each other by the above defined mappings. The normal and tangential components $[u]_n$ and $[u]_t$ on Γ_C, respectively, are defined as $[u]_n = [u]_{ij}\nu_j^i$ and $[u]_t = [u]_{ij}\tau_j^i$. According to this definition, $[u]_n$, referred to as opening, decreases when subdomains Ω^i and Ω^j are getting closer, and $[u]_n + g_n \ge 0$ should hold. $[u]_t$ is referred to as sliding. Therefore, $[u]_{ij} = [u]_n\nu_j^i + [u]_t\tau_j^i$. In fact, the model does not depend on the chosen orientation, and indices i and j are omitted when displacement jump is defined on Γ_C. The relations between the components of the tractions and displacement jump on a unilateral contact surface are shown in **Figure 2**, which indicates that $\sigma_n \le 0$ if $[u]_n + g_n = 0$ (contact), no overlapping being allowed, whereas $\sigma_n = 0$ if $[u]_n + g_n > 0$ (separation), and $\sigma_t = 0$ in both cases.

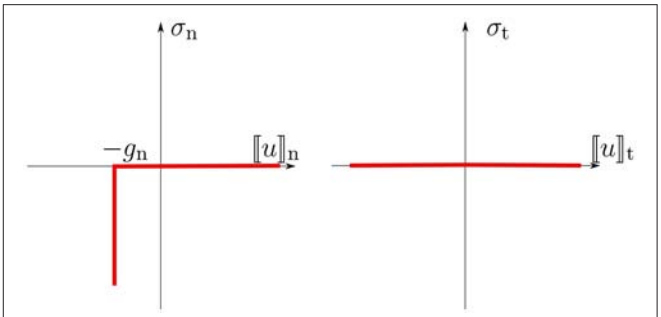

FIGURE 2 | Constitutive relations for the unilateral frictionless contact considered.

The elastic strain energy $\mathscr{E}$ stored in the volume $\Omega = \bigcup_{1 \le i \le N} \Omega^i$ is

$$\mathscr{E}(u) = \sum_{i=1}^{N} \mathscr{E}^i(u^i) = \sum_{i=1}^{N} \int_{\Omega^i} \frac{1}{2} \mathbb{C}^{(i)} e^i(u^i) : e^i(u^i)\, \mathrm{d}\Omega. \tag{3}$$

Then, the total potential energy functional, also referred to as the stored energy functional, is defined as

$$\Pi(t,u) = \begin{cases} \mathscr{E}(u) - \mathscr{W}(t,u) & \text{if } u = u_D \text{ on } \Gamma_D, \\ & [u]_n \ge -g_n \text{ on } \Gamma_C, \\ \infty & \text{elsewhere,} \end{cases} \tag{4}$$

where, $\mathscr{W}(t,u) = \sum_{i=1}^{N} \int_{\Gamma_N^i} u^i(x,t) \cdot p_N^i(x,t)\, \mathrm{d}S$ gives the work of external forces in Ω, the body forces being neglected for the sake of simplicity.

According to Fichera (1964, see also Kalker and Randen, 1972; Panagiotopoulos and Lazaridis, 1987), the minimizer $u(t)$ of the total potential energy functional $\Pi(t,u)$ at each time t is the solution of the unilateral frictionless contact considered.

Remark 1 (Adhesive unilateral frictionless contact). We refer to adhesive unilateral frictionless contact as the case where a continuous distribution of springs exists on an interface, i.e., a contact zone. The normal and tangential elastic stiffnesses of an interface, $\kappa_n \ge 0$ and $\kappa_t \ge 0$, respectively, may have different values (**Figure 3**). The interface response is considered frictionless, since no frictional dissipation of energy is considered, the tangent stiffness describing an adhesive elastic behavior. The elastic energy stored in such an adhesive interface (layer) is

$$\mathscr{E}_C(u) = \mathscr{E}_{Cn}(u) + \mathscr{E}_{Ct}(u), \tag{5}$$

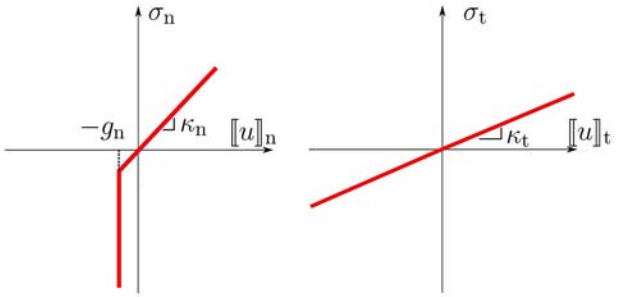

FIGURE 3 | Constitutive relations for the adhesive unilateral contact considered.

where the components corresponding to the normal and tangential directions, respectively, are

$$\mathscr{E}_{Cn}(u) = \begin{cases} \int_{\Gamma_C} \frac{\kappa_n}{2} [u]_n{}^2 \, dS & \text{if } [u]_n \geq -g_n \text{ on } \Gamma_C, \\ \infty & \text{elsewhere,} \end{cases} \tag{6}$$

and

$$\mathscr{E}_{Ct}(u) = \int_{\Gamma_C} \frac{\kappa_t}{2} [\![u]\!]_t^{\,2} \, dS. \tag{7}$$

The total potential energy is augmented by the elastic energy stored in the adhesive interface layer giving

$$\Pi(t,u) = \mathscr{E}(u) + \mathscr{E}_C(u) - \mathscr{W}(t,u). \tag{8}$$

The relations between the components of the tractions and displacement jump on an adhesive interface layer are shown in **Figure 3**, which indicates that $\sigma_n \leq 0$ if $[u]_n + g_n = 0$ (contact), whereas $\sigma_n = \kappa_n [u]_n$ if $[u]_n + g_n > 0$ (separation). Additionally, $\sigma_t = \kappa_t [u]_t$ in shear. In this case, g_n represents the width of the adhesive layer. If $[u]_n > 0$ then the layer is under tensile stresses and we do not allow to break it, whereas if $[u]_n < 0$ then the layer is under compressive stresses and we assume a linear behavior until the two domains enter in contact, no overlapping being allowed.

It is easy to realize, that for vanishing interface stiffnesses, $\kappa_n \to 0$ and $\kappa_t \to 0$, the above described Signorini unilateral contact model is recovered, cf. **Figures 2**, **3**.

3. ENERGY PRINCIPLES IN BOUNDARY INTEGRAL FORMS

For given body forces F^i in the elastic domain Ω^i, the following equilibrium condition holds:

$$-\text{div}\sigma^i(u^i) = F^i \quad \text{in } \Omega^i,$$

which multiplied by some virtual displacement field $\tilde{u}^i$ and integrated by parts over Ω^i gives

$$\int_{\Omega^i} \sigma^i(u^i) : \epsilon^i(\tilde{u}^i) \, d\Omega - \int_{\Gamma^i} \sigma^i(u^i) \cdot \nu^i \tilde{u}^i \, dx = \int_{\Omega^i} F^i \tilde{u}^i \, d\Omega. \tag{9}$$

This expression may be seen as the principle of virtual work, for virtual displacements $\tilde{u}^i$. The dependence of stresses and subsequently tractions on displacements is explicitly indicated in the notation used. By assuming zero body forces (F^i=0) (in the present work) and choosing $\tilde{u}^i$=u^i, the volume integral in (3) is replaced by the boundary integral

$$\mathscr{E}^i(u^i) = \frac{1}{2} \int_{\Gamma^i} u^i p^i(u^i) \, dS. \tag{10}$$

Furthermore, the total potential energy for Ω^i is

$$\Pi^i(t,u^i) = \mathscr{E}^i(u^i) - \int_{\Gamma_N{}^i} u^i(x,t) p_N^i(x,t) \, dS. \tag{11}$$

In order to formulate the problem as a quadratic programming problem involving boundary values only, we further proceed manipulating (11). Similar formulations may be found in Antes and Panagiotopoulos (1992) (see chapter 8), where also a proof of existence and uniqueness of solutions is provided, and in Aour et al. (2007), however without the extent and the analysis introduced in the present work.

In the following, the BVP for a sub-domain Ω^i is considered in a similar way as in Panagiotopoulos et al. (2013). Hereinafter in this section we will omit superindex *i*, for the sake of simplicity. Let u_η and p_η, respectively, denote the displacement and traction solutions of this BVP restricted to Γ_η, η = C, D and N, e.g. $u_C = u|_{\Gamma_C}$ and $p_D = p|_{\Gamma_D}$. We study here a mixed-type operator $\mathscr{M}$ which formally assigns (p_C, p_D, u_N) to the known boundary data (u_C, u_D, p_N) of the original BVP $\mathscr{P}^O$ shown in **Figure 4**, and may be partitioned using the following block structure as

$$\begin{pmatrix} p_C \\ p_D \\ u_N \end{pmatrix} = \begin{pmatrix} \mathscr{M}_{CC} & \mathscr{M}_{CD} & \mathscr{M}_{CN} \\ \mathscr{M}_{DC} & \mathscr{M}_{DD} & \mathscr{M}_{DN} \\ \mathscr{M}_{NC} & \mathscr{M}_{ND} & \mathscr{M}_{NN} \end{pmatrix} \begin{pmatrix} u_C \\ u_D \\ p_N \end{pmatrix}. \tag{12}$$

The columns of the aforementioned block operator $\mathscr{M}$ are associated to the sub-problems $\mathscr{P}^\eta$ defined in **Figure 4**. The displacement solution of a subproblem $\mathscr{P}^\eta$ is denoted as u^η. From the principle of superposition the displacement solution of the full problem $\mathscr{P}^O$ may be reconstructed by the sum:

$$u = u^C + u^D + u^N. \tag{13}$$

In view of (10) and (11), the total potential energy for the mixed type BVP $\mathscr{P}^O$ may be written in an expanded form as

$$\Pi(t,u) = \frac{1}{2} \int_{\Gamma_C} u_C(u) p_C(u) dS + \frac{1}{2} \int_{\Gamma_D} u_D p_D(u) dS - \frac{1}{2} \int_{\Gamma_N} u_N(u) p_N dS, \tag{14}$$

where we tacitly assumed that u fulfills the Dirichlet and Neumann boundary conditions. By substituting the unknown data for problem $\mathscr{P}^O$ from (12), the total potential energy can be written as

$$\Pi(t,u_C) = \frac{1}{2} \Big(\int_{\Gamma_C} u_C \mathscr{M}_{CC} u_C \, dS + \int_{\Gamma_C} u_C \mathscr{M}_{CD} u_D \, dS + \int_{\Gamma_C} u_C \mathscr{M}_{CN} p_N \, dS$$

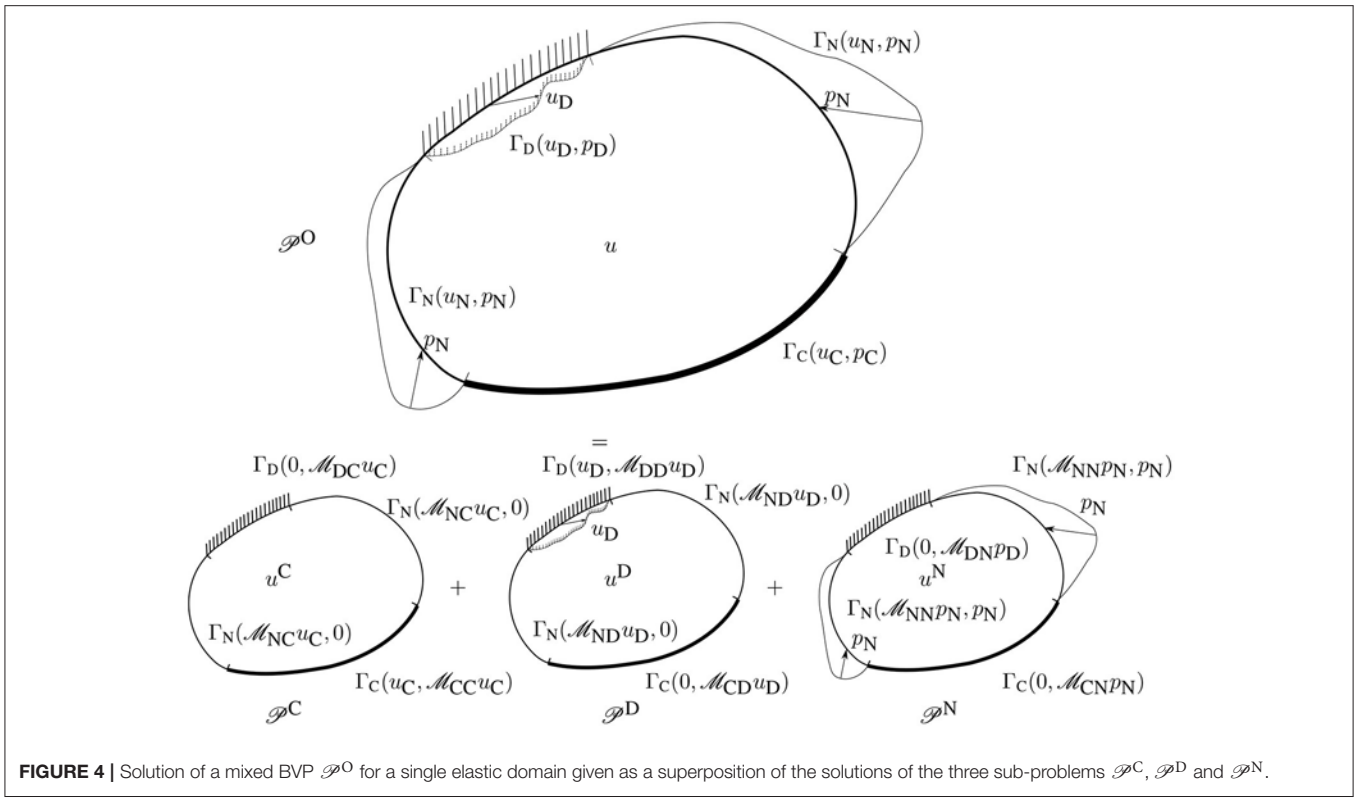

FIGURE 4 | Solution of a mixed BVP $\mathscr{P}^O$ for a single elastic domain given as a superposition of the solutions of the three sub-problems $\mathscr{P}^C$, $\mathscr{P}^D$ and $\mathscr{P}^N$.

$$+\int_{\Gamma_D} u_D.\mathscr{M}_{DC}u_C\,dS+\int_{\Gamma_D} u_D.\mathscr{M}_{DD}u_D\,dS+\int_{\Gamma_D} u_D.\mathscr{M}_{DN}p_N\,dS$$
$$-\int_{\Gamma_N} p_N.\mathscr{M}_{NC}u_C\,dS-\int_{\Gamma_N} p_N.\mathscr{M}_{ND}u_D\,dS-\int_{\Gamma_N} p_N.\mathscr{M}_{NN}p_N\,dS\Big). \quad (15)$$

From (15) it is clear, that since, at time t, u_D and p_N are a priori known prescribed values, the total potential energy is actually a function of only the contact displacements u_C. We further modify (15) in order to keep the unknown contact displacements u_C in the integrals on Γ_C part only, by utilizing the following *reciprocity* relations between the elastic solutions of $\mathscr{P}^C$ and $\mathscr{P}^N$

$$-\int_{\Gamma_N} p_N.\mathscr{M}_{NC}u_C\,dS=\int_{\Gamma_C} u_C.\mathscr{M}_{CN}p_N\,dS \quad (16)$$

as well as between the solutions of $\mathscr{P}^C$ and $\mathscr{P}^D$,

$$\int_{\Gamma_D} u_D.\mathscr{M}_{DC}u_C\,dS=\int_{\Gamma_C} u_C.\mathscr{M}_{CD}u_D\,dS. \quad (17)$$

A similar reciprocal relation holds true for the solutions of $\mathscr{P}^N$ and $\mathscr{P}^D$,

$$-\int_{\Gamma_N} p_N.\mathscr{M}_{ND}u_D\,dS=\int_{\Gamma_D} u_D.\mathscr{M}_{DN}p_N\,dS. \quad (18)$$

Notice a somewhat surprising presence of the negative sign in (16) and (18). It should be mentioned that (16), (17) and (18) hold only approximately in the case of numerical solution of the pertinent problems.

Substituting the relations (16) and (17) into the expression (15) gives

$$\Pi(t,u_C)=\int_{\Gamma_C} u_C\Big(\frac{1}{2}\mathscr{M}_{CC}u_C+\mathscr{M}_{CD}u_D+\mathscr{M}_{CN}p_N\Big)\,dS+\frac{1}{2}\int_{\Gamma_D} u_D.\mathscr{M}_{DD}u_D\,dS$$
$$+\frac{1}{2}\int_{\Gamma_D} u_D.\mathscr{M}_{DN}p_N\,dS-\frac{1}{2}\int_{\Gamma_N} p_N.\mathscr{M}_{ND}u_D\,dS-\frac{1}{2}\int_{\Gamma_N} p_N.\mathscr{M}_{NN}p_N\,dS \quad (19)$$

The present problem can be defined now in an explicit form as a quadratic programming problem. By observing here that the last four integrals in (19) are constant with respect to u_C, we may omit them in the minimization procedure since they do not have influence on the minimizer of the total potential energy. This leads to the following simplified expression including only the variable part of the total potential energy functional (for the sake of simplicity the notation of this functional is kept the same):

$$\Pi(t,u_C)=\underbrace{\frac{1}{2}\int_{\Gamma_C} u_C.\mathscr{M}_{CC}u_C\,dS}_{\mathscr{A}(u_C)}+\underbrace{\int_{\Gamma_C} u_C\Big(\mathscr{M}_{CD}u_D(t)+\mathscr{M}_{CN}p_N(t)\Big)\,dS}_{-\,b(t,u_C)} \quad (20)$$

After a suitable discretization of u_C by means of a linear combination of standard vector shape-functions

$$u_C(x)=\sum_{i=1}^{M_C}\phi_i(x)\xi_i \quad (21)$$

where M_C is the number of displacement degrees-of-freedom (DOFs), typically nodal values of displacement components, on the contact zone Γ_C. The expression in (20) may be rewritten as an algebraic representation of the corresponding quadratic function

$$\Pi(t,\boldsymbol{\xi}) = \frac{1}{2}\boldsymbol{\xi}^T\mathbf{A}\boldsymbol{\xi} - \boldsymbol{\xi}^T\mathbf{b}(t), \tag{22}$$

where $\boldsymbol{\xi}$ is a vector of the nodal displacements u_C on Γ_C, and $\mathbf{A}$ is a kind of the boundary stiffness matrix associated to Γ_C.

Recall that (20), (21) and (22) refer to a single domain. Then, the total potential energy for the assemblage of N bodies is defined as follows

$$\Pi = \sum_{i=1}^{N} \Pi^i(t, u_C^i). \tag{23}$$

This leads to the fact that the algebraic representation of the total potential energy Π for the assemblage in of N bodies in (23) adopts the same form as in (22), however, with the matrix $\mathbf{A}$ defined as a block diagonal matrix formed by the individual matrices $\mathbf{A}^i$ for subdomains Ω^i,

$$\mathbf{A} = \text{block-diag}\left\{\mathbf{A}^1, \ldots, \mathbf{A}^N\right\}, \tag{24}$$

and similarly the vector $\mathbf{b}$ defined as a block vector by formed by the individual vectors $\mathbf{b}^i$ for Ω^i

$$\mathbf{b}^T = \left\{(\mathbf{b}^1)^T, \ldots, (\mathbf{b}^N)^T\right\}. \tag{25}$$

4. BOUNDARY ELEMENT METHOD

As can be seen, the possibilities for a numerical implementation of the above framework are quite wide, the key issue is the approximation of the operators $\mathscr{M}^i_{CC}$, $\mathscr{M}^i_{CD}$ and $\mathscr{M}^i_{CN}$ for each subdomain Ω^i. Several numerical methods, such as the finite element method (FEM) or boundary element method (BEM), may be utilized. Since the adjacent bodies represented by Ω^i ($i =, 1, \ldots, N$), possibly in contact, are linearly elastic, collocation BEM or symmetric Galerkin BEM provide an intrinsic advantage herein. In the present implementation, the collocation BEM has been adopted.

The BEM is closely related to the map between the prescribed boundary conditions in displacements or tractions and the unknown boundary displacements or tractions. In pure Dirichlet and Neumann boundary-value problems (BVPs), these maps are called *Steklov-Poincaré* and *Poincaré-Steklov maps*, respectively, and BEM can be considered as an approach to discretize these maps. In the present computational procedure, the role of the BEM analysis, applied to each subdomain Ω^i separately (which, in fact, makes this problem very suitable for parallel computers), is to solve the corresponding BVPs on each Ω^i. For this goal, we numerically solve the *Somigliana displacement identity* (see París and Cañas, 1997; Aliabadi, 2002),

$$c^i_{ml}(y)u^i_m(y) + \oint_{\Gamma^i} u^i_m(x)T^i_{ml}(x,y)\,\mathrm{d}S_x = \int_{\Gamma^i} p^i_m(x)U^i_{ml}(x,y)\,\mathrm{d}S_x, \tag{26}$$

where $y \in \Gamma^i$ and $u^i_m(x)$ and $p^i_m(x)$ denote the m-component of displacement and traction vectors, respectively. The weakly singular integral kernel $U^i_{ml}(x,y)$, two-point tensor field, given by the Kelvin fundamental solution (free-space Green's function) represents the displacement at x in the m-direction originated by a unit point force at y in the l-direction in the unbounded linear-elastic medium defined by $\mathbb{C}^{(i)}$. The strongly singular integral kernel $T^i_{ml}(x,y)$, two-point tensor field, represents the corresponding tractions at x in the m-direction. The coefficient-tensor $c^i_{ml}(y)$ of the free-term is a function of the local geometry of the boundary Γ^i at y, and may be evaluated by a closed analytical formula for isotropic elastic solids (see Mantič, 1993). The symbol $\oint$ in (26) stands for the Cauchy principal value of an integral.

Consider a discretization of the boundary Γ^i by a boundary element mesh, which is also used to define a suitable discretization of boundary displacements $u^i(x)$ and tractions $p^i(x)$ by interpolations of their nodal values along Γ^i denoted as $\mathbf{u}^i$ and $\mathbf{p}^i$, respectively. By imposing (collocating) the Somigliana identity (26) at all boundary nodes (called collocation points) we set the BEM system of linear equations for Γ^i, typically written as $\mathbf{H}^i\mathbf{u}^i = \mathbf{G}^i\mathbf{p}^i$ (see París and Cañas, 1997; Aliabadi, 2002). The solution of this system provides the unknown nodal values of boundary displacements and tractions.

In the present computational implementation of BEM, straight elements with piecewise linear continuous interpolation for displacements and piecewise linear (possibly discontinuous) interpolation for tractions are adopted, respectively. On the Γ_C part of the boundaries, usually standard continuous interpolation for tractions is used.

In the context of BEM, operators $\mathscr{M}^i_{IJ}$, of (12), with I, J=C, D and N do not need to be explicitly constructed, since what we actually need are the resultant tractions or displacements for each sub-problem, as also shown in **Figure 4**. Thus, we need to solve these three sub-problems for each subdomain Ω^i by BEM.

5. EXPLICIT COMPUTATION OF THE MATRIX A AND VECTOR B

The matrix $\mathbf{A}$ in (22) has the physical meaning of a *boundary stiffness matrix* for a subdomain. Several established techniques may be utilized for its computation, a survey of such techniques based on the BEM may be found in Hartmann (1981) and Tullberg and Bolteus (1982). Hereinafter a new methodology for computing $\mathbf{A}$ is introduced. This methodology is consistent with the present energetic approach and leads directly to a symmetric form of $\mathbf{A}$. From (20), the quadratic form $\mathscr{A}$ and linear form b write as

$$\mathscr{A}(\boldsymbol{\xi}) = \frac{1}{2}\boldsymbol{\xi}^T\mathbf{A}\boldsymbol{\xi} = \frac{1}{2}\sum_{i,j=1}^{M_C} a_{ij}\xi_i\xi_j, \tag{27}$$

$$b(\boldsymbol{\xi}) = \boldsymbol{\xi}^T\mathbf{b} = \sum_{i=1}^{M_C} b_i\xi_i, \tag{28}$$

with M_C being the number of displacement DOFs on the contact zone Γ_C.

Choosing $\boldsymbol{\xi}^{(i)}$ defined as

$$\xi_i^{(i)} = 1, \xi_j^{(i)} = 0, \forall j \neq i, \tag{29}$$

then (27) simplifies to

$$\mathscr{A}(\boldsymbol{\xi}^{(i)}) = \frac{1}{2} a_{ii} \rightarrow a_{ii} = \sum_{k,l=1}^{M_C} \xi_k^{(i)} \xi_l^{(i)} \int_{\Gamma_C} \phi_k \mathscr{M}_{CC} \phi_l \, \mathrm{d}S. \tag{30}$$

Solving the above problem $\mathscr{P}^C$ by BEM sequentially for all $i = 1, \ldots, M_C$, and by utilizing the first integral of (20), we may compute all the diagonal components a_{ii} of matrix $\mathbf{A}$.

Furthermore, in order to compute the non-diagonal components a_{ij} we choose $\boldsymbol{\xi}^{(i,j)}$ defined as

$$\xi_i^{(i,j)} = \xi_j^{(i,j)} = 1, \xi_m^{(i,j)} = 0, \forall m \neq i, j, \tag{31}$$

then, similarly to (30),

$$\mathscr{A}(\boldsymbol{\xi}^{(i,j)}) = \frac{1}{2} \left(a_{ii} + a_{jj} + a_{ij} + a_{ji} \right) = \frac{1}{2} a_{ii} + \frac{1}{2} a_{jj} + a_{ij} \tag{32}$$

$$= \frac{1}{2} \sum_{k,l=1}^{M_C} \xi_k^{(i,j)} \xi_l^{(i,j)} \int_{\Gamma_C} \phi_k \mathscr{M}_{CC} \phi_l \, \mathrm{d}S. \tag{33}$$

Having computed the diagonal elements a_{ii} we may compute from the last equation also the non-diagonal elements, considering $a_{ij} = a_{ji}$, by

$$a_{ij} = \frac{1}{2} \left(\sum_{k,l=1}^{M_C} \xi_k^{(i,j)} \xi_l^{(i,j)} \int_{\Gamma_C} \phi_k \mathscr{M}_{CC} \phi_l \, \mathrm{d}S - a_{ii} - a_{jj} \right). \tag{34}$$

Similarly, solving the above problems $\mathscr{P}^D$ and $\mathscr{P}^N$ by BEM, the computation of vector b is carried out by using the first set of vectors $\boldsymbol{\xi}^{(i)}$ and computed by the second integral in (20), and its components are given as

$$b(\boldsymbol{\xi}^{(i)}) = b_i \rightarrow b_i = -\sum_{k=1}^{M_C} \xi_k^{(i)} \int_{\Gamma_C} \phi_k \left(\mathscr{M}_{CD} u_D + \mathscr{M}_{CN} p_N \right) \mathrm{d}S.$$

A more direct relation of the matrix $\mathbf{A}$ to a respective stiffness matrix could be understood for the case of a single domain where the whole boundary Γ coincides with Γ_C (see also section 10). Although by the procedure described above a direct symmetric stiffness matrix may be constructed, this matrix was found to lack the properties of *equilibrium* and *rigid motion representation*, which are satisfied only approximately and although after a mesh refinement their fulfillment is improved nevertheless they are not fully satisfied. A further detailed study of the properties of this matrix is given in section 10. Additionally in section 9, some alternative modified procedure in order to construct a non-symmetric matrix $\mathbf{A}$ together with the reasoning of its necessity is proposed and discussed.

6. THE CONTACT DESCRIPTION VIA INTERFACE ELEMENTS

Usually, a unilateral frictionless contact law is defined by a geometric condition of non-penetration (also referred to as compatibility of displacements), a static condition of no tension and no friction and equilibrium of forces (see Renaud and Feng, 2003). In the context of small displacements deformation, we may write the non-penetration condition in the normal direction associated to the surfaces under contact (see below). The exact portion of the boundaries Ω^i and Ω^j which will really contact, the so-called active contact zone, is a priori unknown, for this reason initially we consider Γ_j^i and Γ_i^j as potential contact boundaries, which should include the points of the active contact zone (see **Figure 1**).

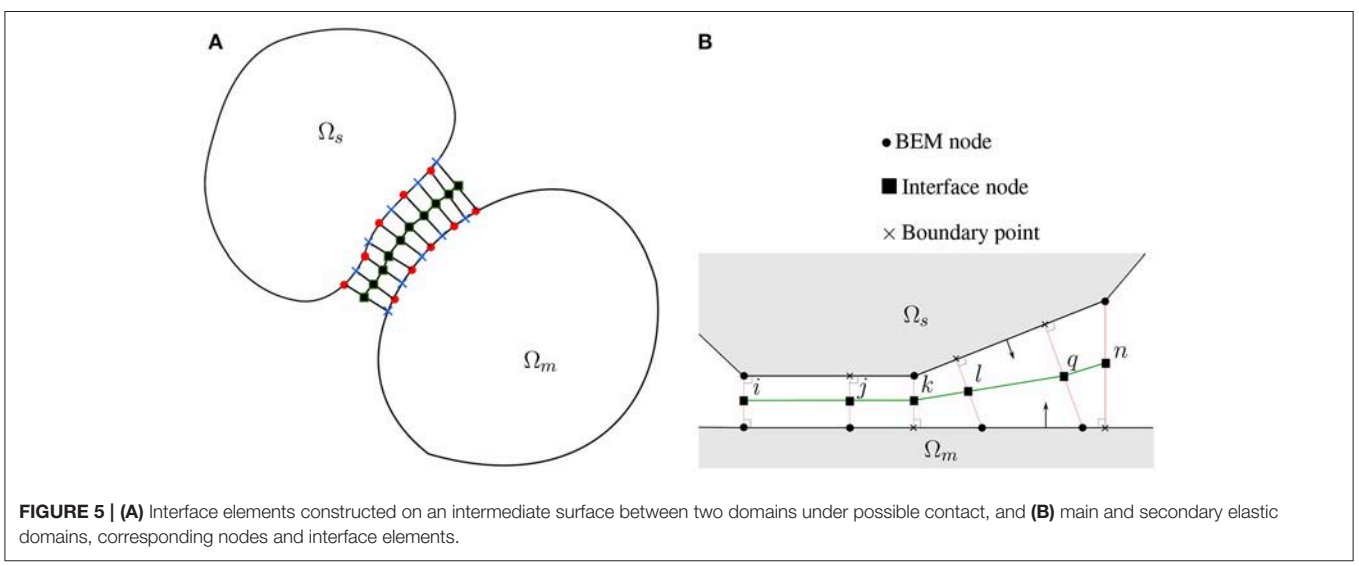

FIGURE 5 | (A) Interface elements constructed on an intermediate surface between two domains under possible contact, and **(B)** main and secondary elastic domains, corresponding nodes and interface elements.

The establishment of relations that impose the non-penetration also referred to as *Signorini* condition, is one of the most crucial parts of the present formulation. Some of the BEM formulations for contact problems enforce compatibility of displacements on one of the domains, while on the other the equilibrium is enforced (cf. Blázquez et al., 1998b; Graciani et al., 2005). These equilibrium conditions might be given in weak sense instead of their strong form (see Blázquez et al., 1998a). In the present methodology only compatibility conditions are enforced between the bodies in potential contact, by establishing the non-penetration condition which include the evaluation of the displacement jump $[u]$ and gap g_n along Γ_C, while the equilibrium of contact tractions arises through the enforcement of the principle of minimum of the total potential energy.

The interconnection of the subdomains as well as the consideration of Signorini kinematical conditions is succeeded by the intermediate surface discretized by interface elements, as shown in **Figure 5A**. Let us consider an intermediate surface between two bodies. The gap g_n, at this surface may be considered as finite or zero valued. For each node of the interface elements we define a local reference system and each relative displacement may have an opening (normal) and sliding (tangential) component. In the case of contact problems of two deformable bodies where only small changes in the geometry are assumed and also the mesh of each elastic domain is a conforming one, it is possible to incorporate the contact constraints on a purely nodal basis. However, for the general case of nodes being arbitrarily distributed along the potential contact zone between two bodies, which can occur, e.g., when automatic meshing is used for these bodies, further consideration must be taken into account in the definition of Signorini contact conditions. Such techniques have been developed in the case of BEM in Blázquez et al. (1998b), Graciani et al. (2005), Blázquez et al. (2006), Graciani et al. (2009), and Vodička (2000). Nevertheless, the necessity of non-conforming algorithms may also occur in small displacements contact problems and conforming discretizations as shown in Blázquez and París (2009). The non-penetration conditions for the case of non-conforming mesh are considered in the normal direction of the intermediate surface at interface nodes. Each interface node, related to a pair of the adjacent BEM node and boundary point, the latter may coincide with a BEM node or just be located on a BEM element as depicted in **Figure 5B**. For the latter case, the displacements of the boundary point are computed by the respective displacements of the nodes of this BEM element. The Signorini conditions, that also take into account a possible initial gap (or a finite thickness of the adhesive layer) are imposed on the normal displacements of those pairs. We will write here the conditions taken into account for two different cases referring to **Figure 5B**. In the first case, the BEM node is denoted as i_m (main) and the adjacent boundary point coincides with another BEM node denoted as i_s (secondary), and the following condition is taken into account:

$$\left[u^m(i_m) - u^s(i_s)\right]_n \geq -g_n(i). \tag{35}$$

In the next case, the BEM node is denoted as l_m (main) and the adjacent boundary point, denoted as l_s (secondary), does not coincide with any BEM node (see **Figure 5B**), then the following condition is taken into account:

$$\left[u^m(l_m) - u^s(l_s)\right]_n \geq -g_n(l) \Rightarrow$$
$$\left[u^m(l_m) - \frac{L_{ln}}{L_{kn}}u^s(k_s) - \frac{L_{kl}}{L_{kn}}u^s(n_s)\right]_n \geq -g_n(l). \tag{36}$$

The entire set of such equations may be given in a more compact algebraic form in terms of new variables

$$f_i = c_{ij}u_j, \tag{37}$$

where f_i is given by the i^{th} constraint expression, c_{ij} is the so-called *constraint matrix* and u_j are the components of normal displacements on the potential contact zone, which are the only variables included in the minimization procedure for the frictionless contact as will be shown in the following section. The inclusion of the tangential components of displacements on the contact zone in the case of adhesive frictionless contact is straightforward and will be omitted here for the sake of brevity.

7. MINIMIZATION OF TOTAL POTENTIAL ENERGY

As shown in section 2, the contact problem can be formulated as a minimization problem of the total potential energy functional defined in (4). In section 3 appropriate boundary integral forms of this functional were derived in order to generate a pure boundary value problem, as in (10) or (11), which was further manipulated in order to derive a quadratic functional in (20). In section 1 it was assumed, that the problem is a quasi-static one (neglecting inertial and viscous effects), introducing by this way a (pseudo)time variable t into the stored energy functional in (4). Finally, in section 6 it was shown that in order to define the minimization problem as a *simple bound constrained* one it is advantageous to work with variables f_i defined by (37). Making a time discretization by adopting, for simplicity only and without loss of generality, an equidistant partition of $[0, T]$ with a fixed time-step $\tau > 0$, assuming $T/\tau \in \mathbb{N}$, the minimization of the total potential energy functional defined in (4) leads to the following (formally written) recursive minimization problem:

$$\left.\begin{array}{l}\text{minimize } \mathscr{F}^k(f) = \Pi(k\tau, u(f)) \\ \text{subject to } f \geq -g\end{array}\right\} \tag{38}$$

to be solved successively for $k = 1, ..., T/\tau$. Here, f is the vector defined by Equation (37) and g the vector that contains the gap values.

For the numerical resolution of the above minimization problem there are two possible approaches, always taking into account the transformation in (37), the first is to directly minimize the objective function of type given in (11). In this case we may use a general algorithm for bound-constraint optimization problems, such as the L-BFGS-B by Zhou et al.

(1997). However, it is usually advantageous to solve the problem as a quadratic one and for this reason we utilize (23) or its algebraic form as in (22). A variety of algorithms for quadratic programming may be found in Dostál (2009). Notice that, using the algebraic form of (22), the problem may be stated as a Linear Complementarity Problem (LCP), cf. (Gakwaya et al., 1992; Stavroulakis and Antes, 1997), and may be solved, for example, by Lemke's algorithm. For the present EC-BEM computer implementation, we use a modified conjugate gradient method which does not need an explicit form of matrix **A** and vector **b** in (22) and directly minimizes (23). Its pseudocode is given in **Table 1**. Nevertheless, also the conventional conjugate gradient method is reproduced in **Table 2** following Dostál (2009). A further discussion on differences between these two variants of the conjugate gradient algorithm is given in section 9.

Regardless of the minimization algorithm we use, except if it would be a derivative free algorithm, we always need to calculate the partial derivatives of the potential energy Π. An alternative to compute these derivatives would be to use finite differences but such an approach was proved to be extremely time consuming. For this reason, we set up an analytical computation of derivatives of Π. By applying the chain rule of differentiation we obtain

$$\frac{\partial \Pi}{\partial f_i} = \frac{\partial \Pi}{\partial u_j}\frac{\partial u_j}{\partial f_i}, \tag{39}$$

and by inverting (37)

$$u_i = r_{ij} f_j, \tag{40}$$

where $r_{ij} = (c^{-1})_{ij}$, which substituted into (39) leads to

$$\frac{\partial \Pi}{\partial f_i} = \frac{\partial \Pi}{\partial u_j} r_{ji}. \tag{41}$$

Having established the quadratic formula for (23), the derivatives in (41) can be easily defined. In section 8 we give a more general treatment on how to define the derivatives of the total potential energy (11) with respect to a displacement component.

TABLE 1 | (**M1**) Conjugate gradient method (CG) adapted for EC–BEM.

Given a quadratic form $\mathscr{A}(\mathbf{x})$ and a linear form $b(\mathbf{x})$
with $\mathbf{x} \in \mathbb{R}^n$
Step 0. {Initialization.}
Choose $\mathbf{x}^0 \in \mathbb{R}^n$, set $\mathbf{g}^0 = \mathscr{A}'_x(\mathbf{x}^0) - b'_x(\mathbf{x}^0)$,
$\mathbf{p}^1 = \mathbf{g}^0$, $k = 1$
Step 1. {Conjugate gradient loop.}
while $\| \mathbf{g}^{k-1} \| > \epsilon$
Solve BEM for displacements $\mathbf{p}^k$ on Γ_C
$\alpha^k = \| \mathbf{g}^{k-1} \|^2 / \mathscr{A}(\mathbf{p}^k)$
$\mathbf{x}^k = \mathbf{x}^{k-1} - \alpha^k \mathbf{p}^k$
$\mathbf{g}^k = \mathbf{g}^{k-1} - \alpha^k \mathscr{A}'_x(\mathbf{p}^k)$
$\beta^k = \| \mathbf{g}^k \|^2 / \| \mathbf{g}^{k-1} \|^2$
$\mathbf{p}^k = \mathbf{p}^{k-1} - \beta^k \mathbf{p}^k$
$k = k + 1$
end while
Step 2. {Return the solution.}
$\hat{\mathbf{x}} = \mathbf{x}^k$

TABLE 2 | (**M2**) Conjugate gradient method (CG).

Given a matrix **A**
and a vector **b** with $\mathbf{x} \in \mathbb{R}^n$
Step 0. {Initialization.}
Choose $\mathbf{x}^0 \in \mathbb{R}^n$, set $\mathbf{g}^0 = \boldsymbol{A}\,\mathbf{x}^0 - \mathbf{b}$, $\mathbf{p}^1 = \mathbf{g}^0$, $k = 1$
Step 1. {Conjugate gradient loop.}
while $\| \mathbf{g}^{k-1} \| > \epsilon$
$\alpha^k = \| \mathbf{g}^{k-1} \|^2 / \frac{1}{2}(\mathbf{p}^k)^T \mathbf{A}\,\mathbf{p}^k$
$\mathbf{x}^k = \mathbf{x}^{k-1} - \alpha^k \mathbf{p}^k$
$\mathbf{g}^k = \mathbf{g}^{k-1} - \alpha^k \mathbf{A}\,\mathbf{p}^k$
$\beta^k = \| \mathbf{g}^k \|^2 / \| \mathbf{g}^{k-1} \|^2$
$\mathbf{p}^k = \mathbf{p}^{k-1} - \beta^k \mathbf{p}^k$
$k = k + 1$
end while
Step 2. {Return the solution.}
$\hat{\mathbf{x}} = \mathbf{x}^k$

8. DERIVATIVES OF THE TOTAL POTENTIAL ENERGY WITH RESPECT TO DISPLACEMENTS

When the minimization problem (38) is formulated as a quadratic programming problem, derivatives of Π, for a single domain, with respect to the degrees-of-freedom (DOFs) of displacements u_C on the potential contact zone can be easily computed.

However, we might also treat the minimization problem as a general one. In that case we might need the derivatives of Π as given in (11). The total potential energy functional Π from (11), for a single domain, is a function of u defined on Γ, but it also contains the tractions p, which are functions of displacements, i.e., $p(u)$, and for this reason the derivatives with respect to u cannot be computed in a straightforward manner. The displacement and traction variables, according to the BEM formulation, are discretized for $x \in \Gamma$ as

$$u(x) = \sum_i \phi_i(x) u_i, \tag{42a}$$

$$p(x) = \sum_i \psi_i(x) p_i, \tag{42b}$$

where $\phi_i(x)$ and $\psi_i(x)$ are the vector shape-functions associated to DOFs i defining the boundary values of displacements and tractions, respectively. The partial derivative of the total potential energy with respect to a DOF u_i is the functional derivative with the test function being the vector shape-function ϕ_i associated to this DOF

$$\frac{\partial \Pi(u)}{\partial u_i} = \lim_{\delta u_i \to 0} \frac{\Pi\left(u + \phi_i(x)\,\delta u_i\right) - \Pi(u)}{\delta u_i}, \tag{43}$$

where utilizing (11) leads to

$$\begin{aligned}
&\Pi\left(u+\phi_i(x)\,\delta u_i\right)=\\
&\frac{1}{2}\int_\Gamma p\big(u(x)+\phi_i(x)\delta u_i\big)\left(u(x)+\phi_i(x)\delta u_i\right)\,\mathrm{d}x\\
&-\int_{\Gamma_\mathrm{N}}\big(u(x)+\phi_i(x)\delta u_i\big)p_\mathrm{N}\,\mathrm{d}x=\\
&\frac{1}{2}\int_\Gamma\big(p\big(u(x)\big)u(x)+p\big(u(x)\big)\phi_i(x)\delta u_i+p\big(\phi_i(x)\big)u(x)\delta u_i\\
&+p\big(\phi_i(x)\big)\delta u_i^2\phi_i(x)\big)\,\mathrm{d}x\\
&-\int_{\Gamma_\mathrm{N}}\left(p_\mathrm{N}u(x)+p_\mathrm{N}\phi_i(x)\delta u_i\right)\mathrm{d}x,
\end{aligned}\tag{44}$$

where the linearity of the tractions $p(u)$ with respect to the displacements u was used. Note that the term in the above integral which includes a higher order term (δu_i^2) is dropped out in the limit in (43). Introducing the above expression in (43) leads to

$$\begin{aligned}
\frac{\partial\Pi(u)}{\partial u_i}&=\frac{1}{2}\int_\Gamma\Big(p\big(u(x)\big)\phi_i(x)+p\big(\phi_i(x)\big)u(x)\Big)\,\mathrm{d}x\\
&-\int_{\Gamma_\mathrm{N}}p_\mathrm{N}\phi_i(x)\,\mathrm{d}x=\int_\Gamma p\big(u(x)\big)\phi_i(x)\,\mathrm{d}x\\
&-\int_{\Gamma_\mathrm{N}}p_\mathrm{N}\phi_i(x)\,\mathrm{d}x,
\end{aligned}\tag{45}$$

where the reciprocity between the two states: $\big((u(x),p\big(u(x)\big)\big)$ and $\big(\phi_i(x),p\big(\phi_i(x)\big)\big)$ was used. Equation (45), after introducing also (42b) (actually the tractions computed by the (numerical) solution of the Dirichlet problem with the boundary conditions given by u on Γ), will result in the following formula, for a single domain, appropriate for the EC-BEM implementation:

$$\frac{\partial\Pi(u)}{\partial u_i}=\int_\Gamma\psi_j(x)\phi_i(x)p_j\,\mathrm{d}x-\int_{\Gamma_\mathrm{N}}\psi_j(x)\phi_i(x)p_{\mathrm{Nj}}\,\mathrm{d}x.\tag{46}$$

The integration in (46) does not need to be extended all over the boundary Γ since ψ_j and ϕ_i are local vector shape-functions whose support is given only by the boundary elements associated to the DOFs j and i, respectively. Taking also into account that, for the minimization problem under study, the relevant DOF are associated to Γ_C and their support is a part of Γ_C, supp $\phi_i\subset\Gamma_\mathrm{C}$, Equation (46) can be further simplified as

$$\frac{\partial\Pi(u)}{\partial u_i}=\int_\Gamma\psi_i(x)\phi_i(x)p_i\,\mathrm{d}x.\tag{47}$$

This expression gives the relevant numerically computed gradient of the potential energy in the present problem in terms of the numerically computed boundary tractions on Γ_C.

9. A CRITICAL COMPARISON OF ALGORITHMS M1 AND M2

In **Tables 1**, **2** of section 7, two variants of the conjugate gradient method considered, M1 and M2, respectively, were described by pseudocodes, where M2 is the original version introduced by Dostál (2009). The main difference between these two variants, is that in M1 we do not explicitly calculate the matrix **A**, since instead of using the vector-matrix-vector product $\frac{1}{2}\mathbf{x}^T\mathbf{A}\mathbf{x}$ and the matrix-vector product $\mathbf{A}\mathbf{x}$, we use the quadratic form $\mathscr{A}(\mathbf{x})$ and the derivative $\mathscr{A}'(\mathbf{x})$. In reference to M2, we initially need to compute the matrix **A**, as it is described in section 5 (actually it is the Step 0 in **Table 2**), which might be time consuming, but then the rest of the procedure, that is actually the conjugate gradient loop, showed to be fast enough. On the contrary, for M1 the initialization (Step 0) is direct and fast, however each time we need to compute the value of the quadratic form $\mathscr{A}(\mathbf{x})$ and its derivative $\mathscr{A}'(\mathbf{x})$, that is in each k^{th} step of the conjugate gradient loop (Step 1 in **Table 1**), a BEM solution is required. Nevertheless, the influence BEM matrices need to be computed only once, for all the iterations and time steps. Additionally, having decomposed the matrix of the linear algebraic system of equations produced by BEM (e.g., by LU- or QR-decomposition), each time that the solution of this system is required, only a back-substitution takes place.

Details of the algorithms for constrained minimization problems can be found in Dostál (2009). In this work, for both variants of the conjugate algorithms, we employed Polyak's algorithm for bound constrained minimization (Algorithm 5.2 in Dostál, 2009), for which the number of iterations is bounded by $\tilde{N}=n^2 2^n$, while for the standard conjugate gradient algorithm by $N=n$, with n being the number DOFs, i.e., the order of the matrix **A**. However, according to Dostál (2009), this bound for Polyak's algorithm may be considered too pessimistic.

It was found, in this work, that in M2 the usage of the symmetric matrix described in section 5, leads to exactly the same results for the energy calculation as in M1, i.e., $\mathscr{A}(\mathbf{x})=\frac{1}{2}\mathbf{x}^T\mathbf{A}\mathbf{x}$. However, the accuracy of the results for displacements and tractions was worse in M2 using the symmetric matrix than in M1, especially for points near a change of boundary condition type (that is from Γ_C to Γ_N). Previously, similar observations were made in BEM by de Paula and Telles (1989) and Tullberg and Bolteus (1982), when the symmetric stiffness matrices was chosen instead of the non-symmetric one. We conclude that the source of this lose of accuracy in our context is because the numerically computed derivatives (gradient) of the quadratic form used in M1 and M2 may be quite different, i.e., $\mathscr{A}'(\mathbf{x})\neq\mathbf{A}\mathbf{x}$, when the symmetric matrix **A** is used in M2 and if in M1, instead of computing explicitly the gradient of the quadratic form, we use its expression in terms of the boundary tractions according to section 8. In order to overcome this difficulty in M2 application we proceed to construct a consistent non-symmetric matrix $\tilde{\mathbf{A}}$ for its usage in M2.

In Antes and Panagiotopoulos (1992), it is claimed that the stiffness matrix constructed by BEM should be symmetric due to Betti's theorem, and not because of the numerical method used to compute the unit displacement response. This might be equivalent with our consideration here, that the reciprocity statements in the context of a numerical implementation of BEM are only approximately valid. In order to construct the non-symmetric matrix $\tilde{\mathbf{A}}$, we solve by BEM a problem, for each ith DOF of displacements on Γ_C, such that each time this is the only non zero component and equal to the unit value. The ith column

of the $\tilde{\mathbf{A}}$ matrix consists of the derivatives $\frac{\partial \mathscr{A}}{\partial u_j}$, with u_j being a DOF of displacements on Γ_C.

It can be shown, and also it was numerically verified, that the matrix $\mathbf{A}$ of section 5, is the symmetric part of matrix $\tilde{\mathbf{A}}$ constructed here, i.e., $\mathbf{A} = \frac{\tilde{\mathbf{A}}^T + \tilde{\mathbf{A}}}{2}$.

10. PROPERTIES OF THE SYMMETRIC AND NON-SYMMETRIC BEM MATRICES: A AND Ã

As mentioned in **Table 2**, the matrix $\mathbf{A}$ is assumed to be symmetric and positive definite. However, it is well known that it is possible to apply the conjugate gradient method of Hestenes and Stiefel (1952) also to non-symmetric systems after a minor modification of the method (e.g., solving $\tilde{\mathbf{A}}^T\tilde{\mathbf{A}}\boldsymbol{\xi} = \tilde{\mathbf{A}}^T\mathbf{b}$ instead of $\tilde{\mathbf{A}}\boldsymbol{\xi} = \mathbf{b}$). The well established and reported fact of a convergence property reduction in the conjugate gradient method for nonsymmetric, Saad and Schultz (1985), and general inconsistent systems, Axelsson (1980), did not have any significant influence on the numerical examples studied here. The linear system matrix computed by the collocation BEM, using the procedure described in section 5, may not be positive definite even if it is symmetric. Actually, this is the case when the Dirichlet and potential contact boundary parts, Γ_D and Γ_C, are empty, whereas a non-empty Dirichlet part guarantees also the positive definiteness.

In order to numerically explore properties of the eigensystem of the BEM system matrix, we consider a circular elastic body of radius $r = 5.0$, whose Young's modulus is $E = 1000.0$ and Poisson's ratio $\nu = 0$. Assuming the entire boundary of the body as a potential contact zone, i.e., $\Gamma_C = \Gamma$, we construct the matrix $\mathbf{A}$ as described in section 5, and compute its eigenvalues and eigenvectors. It is observed that three small, possibly negative, eigenvalues exist which approximate the theoretically zero eigenvalues associated to the three rigid body motions of the circular domain. Two negative eigenvalues have almost equal value of −6.116E-6, and correspond to translations, whereas the third one is several orders of magnitude smaller, taking the value of 7.395E-9 and corresponds to a rotation. In **Figure 6** deformed shapes given by some eigenvectors of the matrix $\mathbf{A}$ are plotted, for the above defined circular body. Note that for n nodes we have $2n$ kinematic DOFs and eigenvectors.

In **Figure 7** (left) it is shown how the theoretically zero eigenvalues associated to rigid body translations are approximated by the two equal and small (possible negative) eigenvalues of the symmetric and non-symmetric BEM matrices $\mathbf{A}$ and $\tilde{\mathbf{A}}$, respectively, for a refinement of the boundary element mesh. The absolute values of the numerically computed eigenvalues are plotted in logarithmic scale. These eigenvalues are negative for the symmetric matrix $\mathbf{A}$. Recall that the number of nodes is one half of the number of DOFs. We may observe that these two small eigenvalues are numerically zero regardless discretization in the case of the non-symmetric matrix $\tilde{\mathbf{A}}$. Thus, the symmetric matrix $\mathbf{A}$ describes the rigid body motions only approximately (an approximation which is improved with a mesh refinement), while in the case of the non-symmetric matrix $\tilde{\mathbf{A}}$ these rigid body motions are well represented. Finally, in **Figure 7** (right) the largest and smallest positive eigenvalues for a mesh refinement are plotted, for both matrices $\mathbf{A}$ and $\tilde{\mathbf{A}}$, a very good agreement being observed.

In order to numerically study the influence of the application of $\mathbf{A}$ instead of $\tilde{\mathbf{A}}$ in BEM calculations, we present the following trivial example whose solution is a rigid body translation. A quadrangular domain is considered with zero tractions on the right and left sides, thus they belong to Γ_N. On the upper side, which belongs to Γ_D, positive normal displacements (in the outward normal direction) are prescribed together with zero horizontal displacements. The bottom side is in frictionless contact with an obstacle, thus it belongs to Γ_C. This problem is quite trivial, since the solution is a rigid body translation in the vertical direction with zero tractions along the whole boundary of the domain. Recall, that in the present computational implementation, both displacements and tractions along the bottom side are considered as unknowns. **Figure 8** (left) shows that numerically zero horizontal displacements are obtained, and similarly **Figure 8** (right) shows that the vertical displacements accurately represent the rigid body translation by applying the method M1, and also by applying the method M2 where however the non-symmetric matrix $\tilde{\mathbf{A}}$ is used. On the other hand, when the symmetric matrix $\mathbf{A}$ is used in the method M2, both results for horizontal and vertical displacements are not so accurate although they improve with the mesh refinement. The main difference from the exact solution is observed near the corners where Γ_C intersects with Γ_N.

11. NUMERICAL EXAMPLES

A numerical implementation of EC-BEM for both cases of contact was accomplished using an in-house BEM software (Panagiotopoulos, 2017) developed, mainly by the first author, in Java programming language. Linear continuous elements with two nodes are used for the analysis of several examples assuming plane strain conditions. The results obtained by this code are compared with the results obtained by 2D BEM codes developed previously by Blázquez et al. (1998a,b, 2006), and Graciani et al. (2005) in which standard techniques of BEM for contact problems essentially based on the so-called displacement and load scaling techniques (recently also referred to as Sequential Linear Analysis, SLA) (París and Blázquez, 1994) are deployed, as well as by the commercial FEM code ANSYS.

The energetic implementation of the first case of contact described, the Signorini contact, is tested in section 11.1 by solving two problems: one of them with receding contact, in section 11.1.1, and another with advancing contact in section 11.1.2. The case of adhesive unilateral contact is tested in section 11.2 with a similar problem to that used as example of receding contact to test the numerical solution of the Signorini contact problem.

11.1. Numerical Examples to Test the Signorini Contact Implementation

11.1.1. A Case of Receding Signorini Contact

The first problem studied is shown in **Figure 9**. The geometry is composed by two rectangular solids Ω_1 and Ω_2 in frictionless

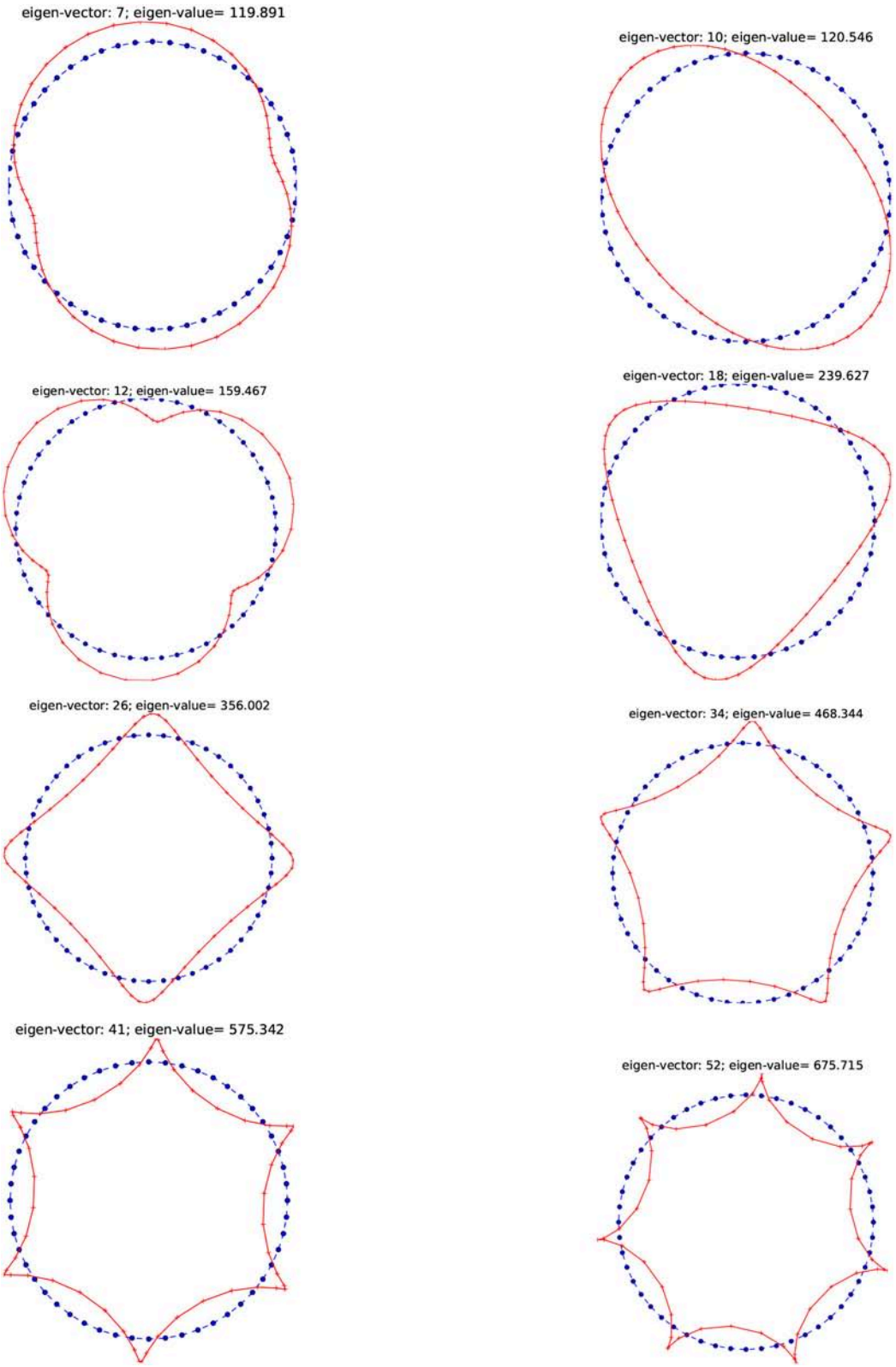

FIGURE 6 | Some of the eigenvalues and the corresponding eigenvectors of the symmetric BEM matrix **A** represented by the deformed shapes for the circular body.

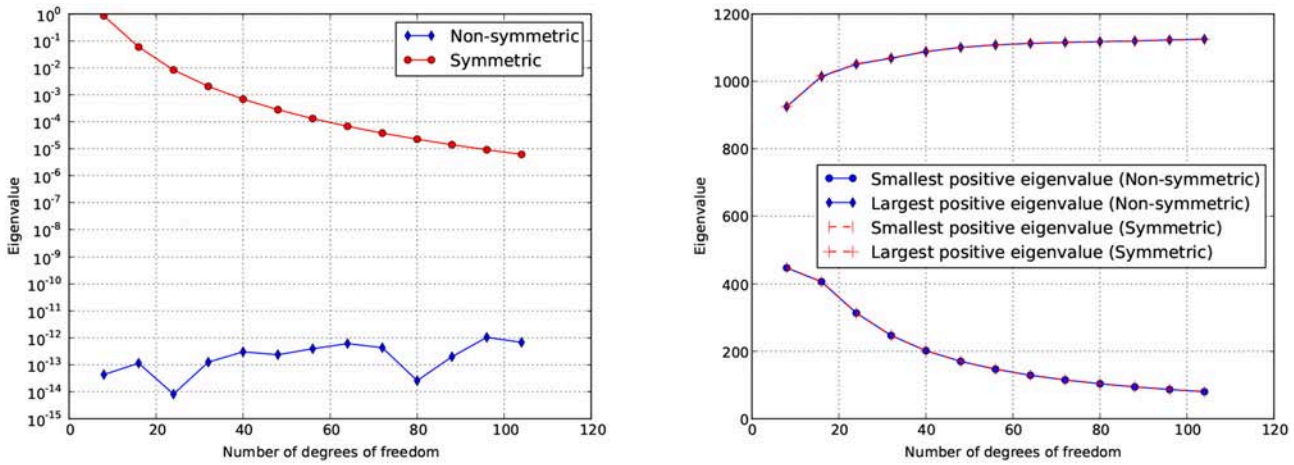

FIGURE 7 | Left: Absolute values of the two equal and small eigenvalues (associated to rigid body translations) of the BEM matrices **A** and $\tilde{\mathbf{A}}$ for a mesh refinement. **Right**: The largest and smallest positive eigenvalues of **A** and $\tilde{\mathbf{A}}$ for a mesh refinement.

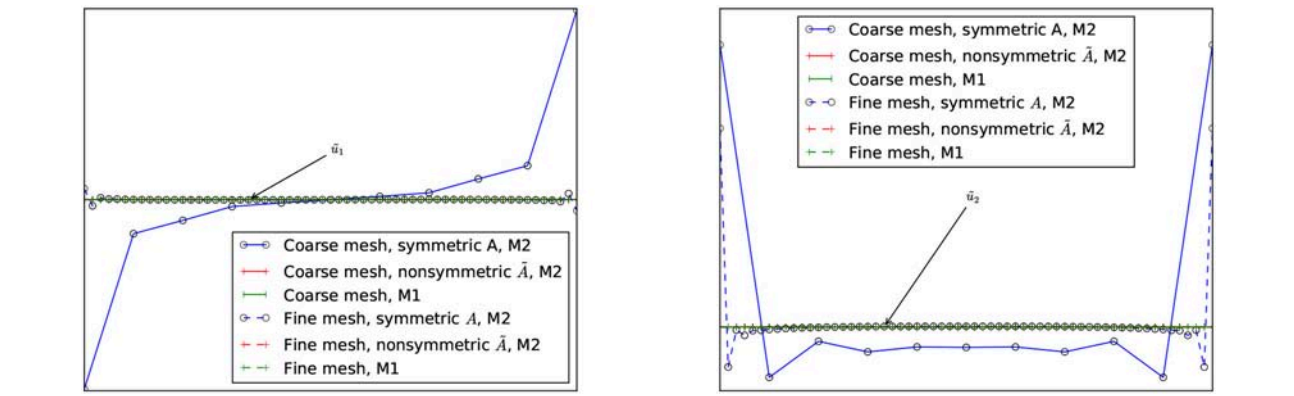

FIGURE 8 | Numerical results along the contact zone, for the trivial contact problem whose solution is a vertical rigid body translation. **Left**: Horizontal displacements, $\tilde{u}_1$ represents the exact zero horizontal displacement. **Right**: Vertical displacements, $\tilde{u}_2$ represents the exact vertical displacement.

contact. The shorter rectangle Ω_1, located below, has dimensions $(L_7 + L_8 + L_9) \times h_1$, see **Table 3** for lenght values. Vertical and horizontal displacements are restrained, respectively, along a horizontal segment of length L_1 at the lower edge and the lower-left corner of the rectangle. A larger rectangle Ω_2 with dimensions $\sum_{i=1}^{6}(L_i) \times h_2$ is located at the top. Its vertical and horizontal displacements are restrained, respectively, along an horizontal segment at the lower edge and the upper-right corner. In addition, a uniform vertical displacement u_D is imposed along a segment with dimension L_3 at the upper edge of this rectangle. A segment of length L_8 along the common edge of both solids is defined as potential contact zone, while L_7 and L_9 are assumed to be traction free zones, since separation of the solids is expected, thus, no interpenetration of solids happens along L_7 and L_9. The material of both solids is assumed to be linear elastic and isotropic with properties of aluminum shown in **Table 3**.

In the case of the BEM models presented below, the mesh used is set by the number of elements n_i with $i = 1, 2, ..., 9$

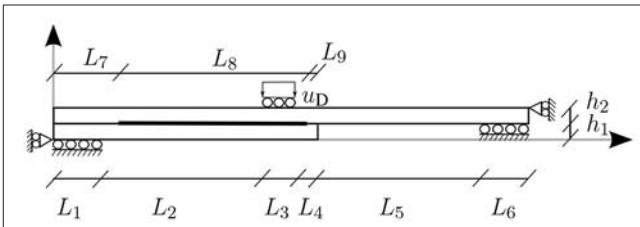

FIGURE 9 | Representation of the receding problem studied: Two beams in contact, Ω_1 and Ω_2, subjected to bending.

corresponding to the segment of length L_i and n_{h1} and n_{h2} corresponding to the segments with lengths h_1 and h_2 respectively. Element length is constant along each segment. In the case of the FEM model, solids are meshed in such a way that the nodes along their edges coincide with those in BEM models. Values for the different meshes used here are presented in **Table 4**.

TABLE 3 | Geometry, elastic properties and the imposed displacements.

Model	A	B
L_7 (m)	0	0.32
L_8 (m)	0.8	0.1
L_9 (m)	0	0.38
u_D (mm)	0.035	
$E_1 = E_2$ (GPa)	70	
$\nu_1 = \nu_2$	0.35	
L_1 (m)	0.1	
L_2 (m)	0.55	
L_3 (m)	0.1	
L_4 (m)	0.05	
L_5 (m)	0.5	
L_6 (m)	0.1	
h_1 (m)	0.05	
h_2 (m)	0.05	

TABLE 4 | Values for the variables n_i.

Mesh:	1	2	3	4
n_1	20	20	20	20
n_2	110	110	110	110
n_3	20	20	20	20
n_4	10	10	10	10
n_5	100	100	100	100
n_6	20	20	20	20
n_7	0	64	64	64
$n_8(\Omega_1)$	160	20	20	60
$n_8(\Omega_2)$	160	20	40	120
n_9	0	76	76	76
n_{h1}	10	10	10	10
n_{h2}	10	10	10	10

Along the potential contact zone defined between both solids, two distinct types of contact are considered: (a) unilateral frictionless Signorini contact analyzed in this section, as well as (b) adhesive unilateral frictionless contact shown in section 11.2.

Firstly, computation is carried out taking the model A with the mesh 1 (see **Tables 3**, **4** respectively). The boundary of the domain Ω_1 is discretized by 340 elements, and that of Ω_2 by 580 elements. The EC-BEM computation works with 160 interface elements along the segment denoted as L_8, requiring the optimization of a quadratic problem of 322 DOFs. Note that n_8 in **Table 4** is the same for both solids, so the mesh along the potential contact zone is conforming.

The model is solved by applying the above algorithm. **Figure 10** shows the deformed shape, with the scale factor of 500, predicted by the EC-BEM. Note that the potential contact zone is divided into three regions: two segments at both extremes of the initial contact zone where both solids are separated and an active contact zone in the central segment.

The numerical results along the potential contact zone are of most interest. **Figure 11** shows the normal tractions and relative normal displacements along this boundary part. The central region has compressive tractions and null opening, as expected. On the contrary, normal tractions are almost zero along the regions with a positive relative normal displacement. It is interesting to recall that, in any iteration, during the minimization in the EC-BEM procedure the initial potential contact zone is assumed as a Dirichlet boundary part. According to this, the simultaneity between compressive tractions and null opening or null tractions and positive opening is not explicitly imposed by the algorithm used, as in most contact algorithms. However, the results obtained show that these conditions are well predicted by the energy optimization procedure.

Results from the EC-BEM algorithm described here are compared in **Figure 12** with the results computed for the same problem with a classic point method algorithm implemented in BEM and the code ANSYS using an Augmented Lagrange algorithm. Note that the agreement between the predictions is accurate in spite of the strong qualitative difference between the different algorithms. The most significant difference is the presence of fictitious oscillations predicted by the EC-BEM at the extremes of contact zone, which do not appear in other numerical results. Also in **Figure 12**, a second solution obtained by the EC-BEM algorithm and a finer mesh (mesh 2 in **Table 4**), where additionally a reduced potential contact zone (model B) was assumed, is shown. As can be seen there, the oscillations are reduced, together with the maximum values of the fictitious tensional tractions.

Previous results were obtained using conforming meshes along the potential contact zone. Results obtained with non-conforming meshes are presented in the following. However, strategies presented here for non-conforming meshes are very simple, more advanced formulations may be combined with the present framework for contact problems using energetic principles.

In order to evaluate the influence of a non-conforming mesh on the results obtained by the present algorithm, a computation with the model B and the mesh 3 (see **Tables 3**, **4** respectively) is carried out. Mesh 3 as well as mesh 4, which have a reduced potential contact zone given by L_8, are defined in view of results of the previous analysis. The number of elements along the potential contact zone of Ω_2 (top) is twice that of Ω_1 (bottom).

As can be seen in **Figure 13**-top, the normal tractions along the contact boundary of Ω_2, which is the one with finer mesh, present some oscillation around the smooth solution of tractions of Ω_1. This behavior does not depend on the choice of *main* and *secondary* domain, a distinction which actually is just auxiliary. Note that, this oscillatory behavior reduces with mesh refinement. In order to observe the reduction of these oscillation, a finer mesh, at the contact boundaries, is employed (mesh 4 in **Table 4**), maintaining the ratio of number of elements at both sides of the contact zone. **Figure 13**-bottom shows the comparison of tractions along the boundary of Ω_2 for the coarser and finer mesh. Note that these oscillations are slightly reduced.

11.1.2. A Case of Advancing Signorini Contact

The indentation of a half cylinder against an elastic foundation is considered. This is an advancing contact problem as the length of

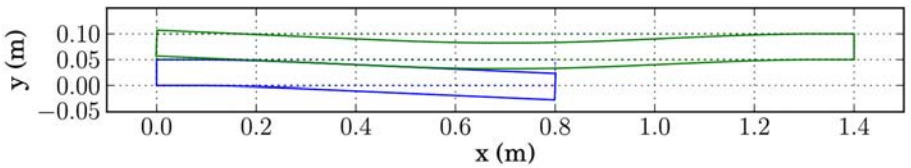

FIGURE 10 | Deformed shape for example A with Signorini contact, with the scale factor of 500.

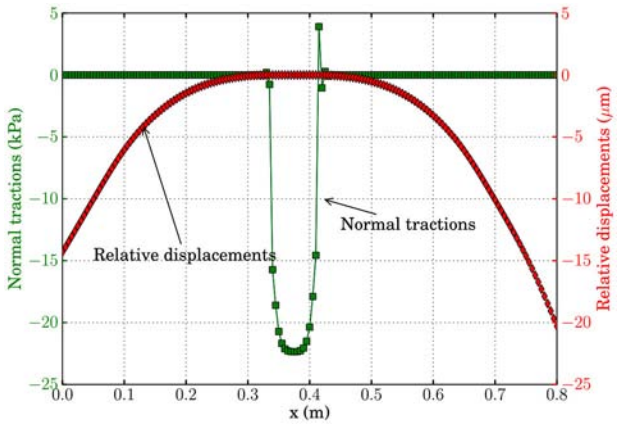

FIGURE 11 | Normal tractions and the relative normal displacements computed along the potential contact zone by the algorithm EC-BEM, for both domains Ω_1 and Ω_2.

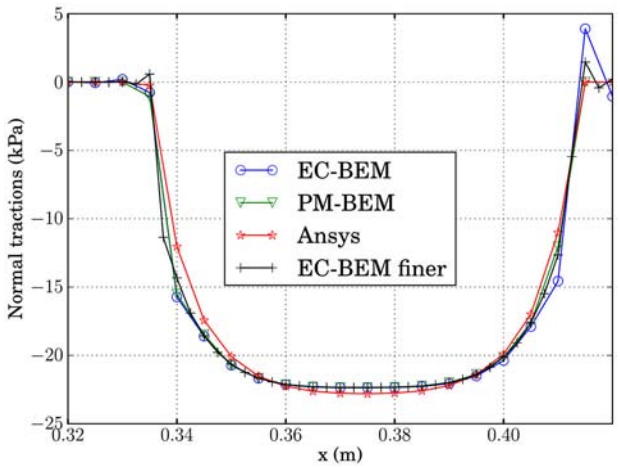

FIGURE 12 | Comparison of tractions computed along the contact zone by the algorithm described here (EC-BEM) and the point method with BEM (PM-BEM) and the FEM code ANSYS using an Augmented Lagrange algorithm. The EC-BEM solution corresponds to model A with Mesh 1, while a finer one also included here, for model B with Mesh 2 (see **Tables 3**, **4**, respectively).

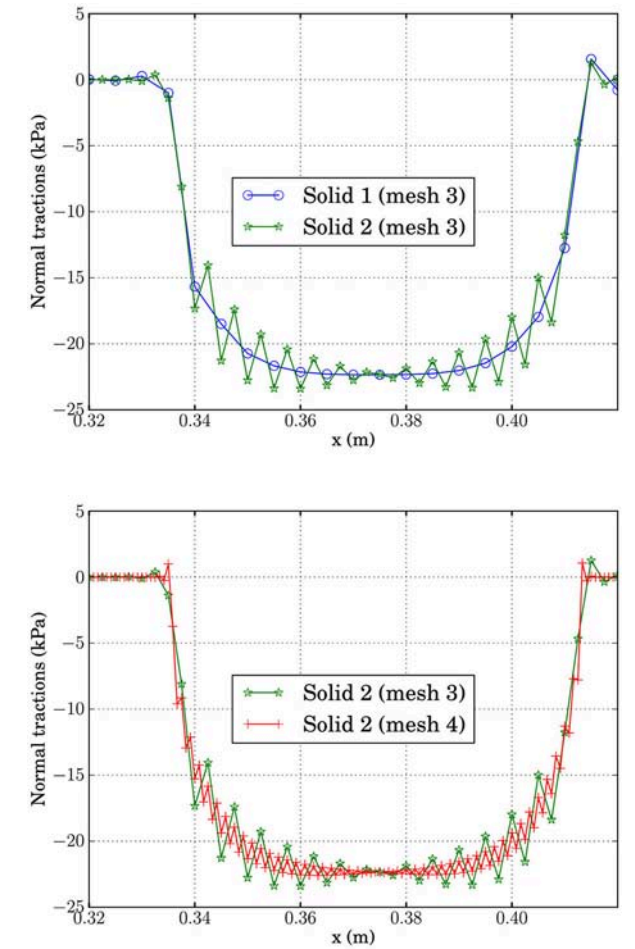

FIGURE 13 | Normal tractions computed along the potential contact zone by EC-BEM, for both domains and for two non-conforming Meshes 3 and 4 of **Table 4**, with $u_D = 0.035$ mm.

the contact zone depends on the value of the prescribed loading. The problem geometry, shown in **Figure 14**, is composed by a rectangle with dimensions $L_1 \times h_1$ and a half circle with radius h_2. The potential contact zone is defined by the length L_2 and the angle ϕ for the rectangle and the circle respectively. Vertical u_D and null horizontal displacements are imposed along the whole straight edge of the half circle.

Linear elastic and isotropic behavior is assumed for both solids, values of Young's moduli E and Poisson's ratios ν being given in **Table 5**, where also the geometrical dimensions can be found. The number of elements along each boundary part are detailed in **Table 6**. Frictionless Signorini contact

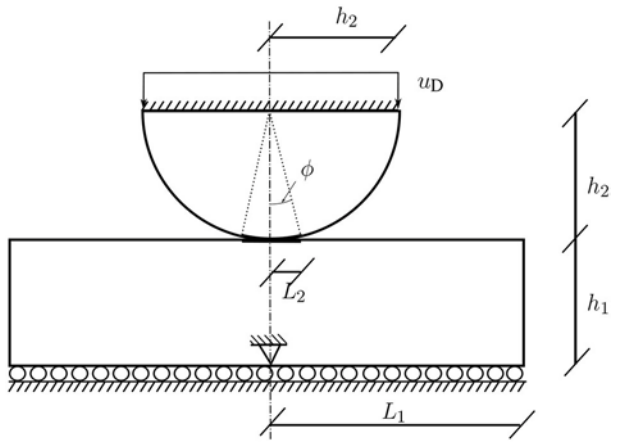

FIGURE 14 | A half elastic cylinder on an elastic rectangle.

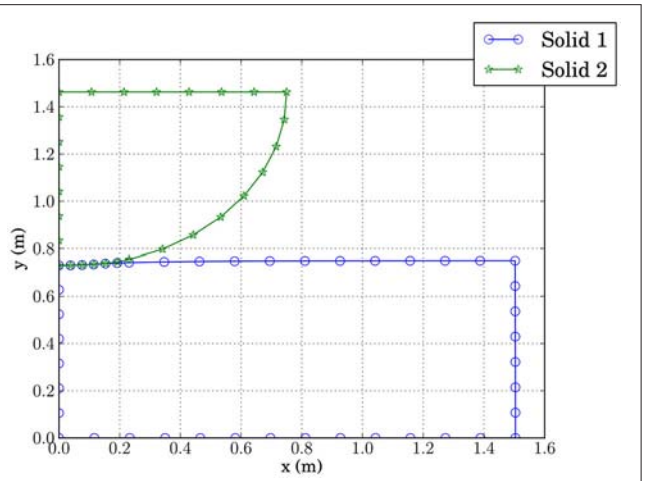

FIGURE 15 | Deformed shape predicted by EC-BEM for Mesh 1 of **Table 6**.

TABLE 5 | Geometry, elastic properties and imposed displacements.

Model	A	B
u_D (mm)	37.5	37.5
$E_1 = E_2$ (GPa)	70	70
$\nu_1 = \nu_2$	0.35	0.35
L_1 (m)	1.5	1.5
L_2 (m)	$h_2 \sin\phi$	$h_2 \sin\phi$
h_1 (m)	0.75	0.75
h_2 (m)	0.75	0.75
ϕ (°)	18	45

TABLE 6 | Values for the variables n_i defining the different meshes.

Mesh	1	2	3
n_1	13	26	94
n_2	6	12	100
n_{h1}	7	13	47
n_{h2}	7	13	47
n_ϕ	6	12	100
$n_{90°-\phi}$	8	16	53
$n_{L_1-L_2}$	11	22	61

is considered on the potential contact zone. Due to the fact that this is an advancing contact problem, we are interested in tracking the evolution of the load, which is a non-linear function of the prescribed displacements. In the numerical solution the vertical displacement is introduced by increasing 10 times this displacement in a monotonic way leading to the value u_D shown in **Table 5** at the step 10.

The problem is solved using the EC-BEM code described above with the mesh 1 (see **Table 6**), where n_1, n_2, n_{h1} and n_ϕ correspond to the number of elements on the boundary part defined by L_1, L_2, $h1$ and ϕ respectively. $n_{90°-\phi}$ is the number of elements along the arc of the half cylinder which is not a potential contact zone and $n_{L_1-L_2}$ is the number of elements at the two parts of the upper edge of the rectangle which are not potential contact zones.

The deformed shape predicted by this code is represented in **Figure 15**. Consequently, as expected, the vertical displacement imposed on the half circle results in its indentation onto the rectangle. A part of the potential contact zone is in active contact.

In a similar way to the example described in section 11.1.1 and for comparison purposes, the problem is solved by the BEM code implementing a classic algorithm of contact by Blázquez et al. (1998a, 2006). The results of the deformed shape around the contact zone for both meshes in **Table 6** are represented in **Figure 16**. Results obtained by the codes using different meshes (see **Table 6**) and distinct lengths of the potential contact zone (see **Table 5**). The aim of this figure is to compare both algorithms, and, for that reason, results obtained with the same mesh are grouped. Macroscopically both solutions for EC-BEM and PM-BEM show a very good agreement. However, it is interesting to see in the detailed plot of solutions for mesh 1, plotted in **Figure 17**, that results for EC-BEM, even for this coarse mesh, show a very good agreement with the Reference solution.

A comparison of tractions along the potential contact zone predicted by EC-BEM, PM-BEM and the reference solution is represented in **Figure 18**. In this figure, unlike those described previously, results are grouped by the method, in order to evaluate the influence of the mesh on the results for each method. Notice that both codes present more accurate results for finer meshes, thus confirming the expected solution convergence with mesh refinement.

The resultant force along the upper part Γ_D of the half cylinder can be estimated from the results of tractions predicted by both methods. In particular, we focus on the vertical component F_y of this force because it is the only one which produces work since horizontal displacements are zero by the

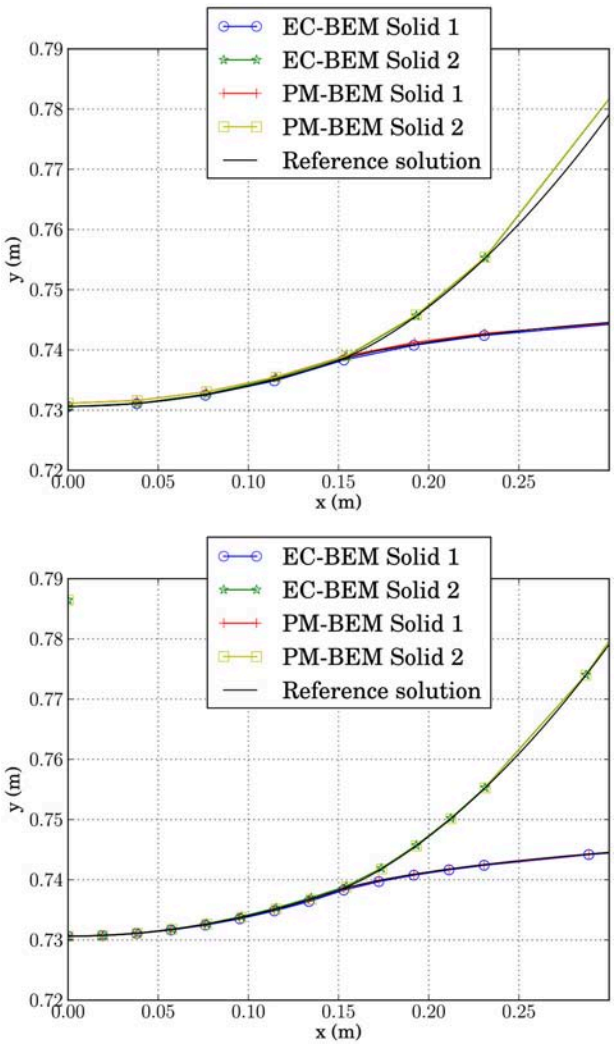

FIGURE 16 | Comparison of the deformed boundaries around the contact zone predicted by EC-BEM, for two different meshes (Mesh 1 and 2 of **Table 6** in the top and bottom plot, respectively) with the Reference solution by PM-BEM (using Mesh 3 of **Table 6**).

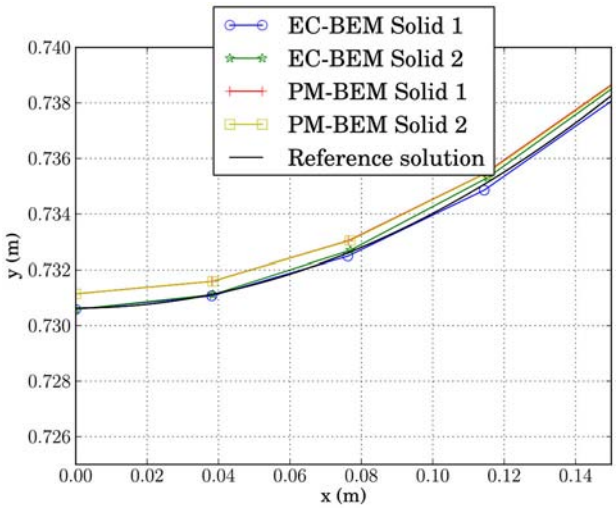

FIGURE 17 | Detailed comparison of the deformed boundaries around the contact zone predicted by EC-BEM and PM-BEM for coarse meshes (Meshes 1 and 2 of **Table 6**) together with the Reference solution by PM-BEM (using Mesh 3 of **Table 6**).

boundary conditions. This value is calculated by the integration of stresses over Γ_D,

$$F_y = \int_{\Gamma_D} \sigma_{yy} \mathrm{d}x \tag{48}$$

where σ_{yy} represent the normal tractions at the nodes. The integral is calculated by a standard quadrature.

The values of the resultant force F_y, calculated for the 10 steps by both codes, are represented in **Figure 19** as a function of the vertical displacement imposed. Both codes predict that stiffness is increasing with the vertical displacement, as typical for the Hertz contact problems. The reason is that the contact zone between both solids is enlarging, with a consequence that the global system becomes stiffer.

11.2. Numerical Examples to Test the Adhesive Contact Implementation

This section aims to compare the results obtained by the energetic approach and commercial FEM code (ANSYS, 2010) in the case of the elastic contact described in section 2. To this effect, the problem of receding contact studied above is solved again, this time with the contact conditions of the adhesive elastic contact.

The problem represented in **Figure 9** is studied with the properties of model A, see **Table 3**, and the mesh 1, see **Table 4**. The stiffness parameters, assumed for this example, are κ_n=150 GPa/m and κ_t=0.

Results from the EC-BEM computations for displacements and tractions along the boundary between both solids are presented in **Figure 20**. As expected, zones with tensions correspond to positive relative displacements (external zones for example) and zones with compressions correspond to vanishing relative displacements (zones adjacent to the previous ones). In this case, a strongly complex zone is predicted at the center of the boundary, which will be studied below.

For comparison purposes, the problem is solved using the FEM code (ANSYS, 2010) setting the contact properties in the following way:

- Contact behavior: No separation (always)
- Contact: Surface to surface
- Contact algorithm: Penalty method
- Contact detection: At nodal points (normal from contact nodes)
- Opening contact stiffness (KFOP): κ_n

Results for tractions in the solids obtained by ANSYS and the EC-BEM code are compared in **Figure 21**. In the upper figure we can observe that the agreement along the four zones

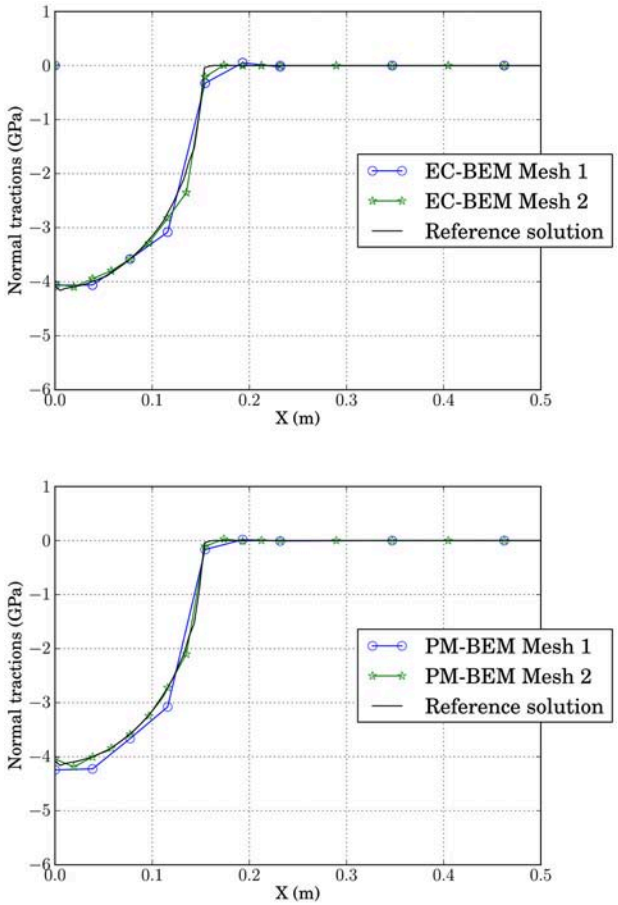

FIGURE 18 | Comparison of the normal tractions computed by EC-BEM and PM-BEM along the interface for different meshes.

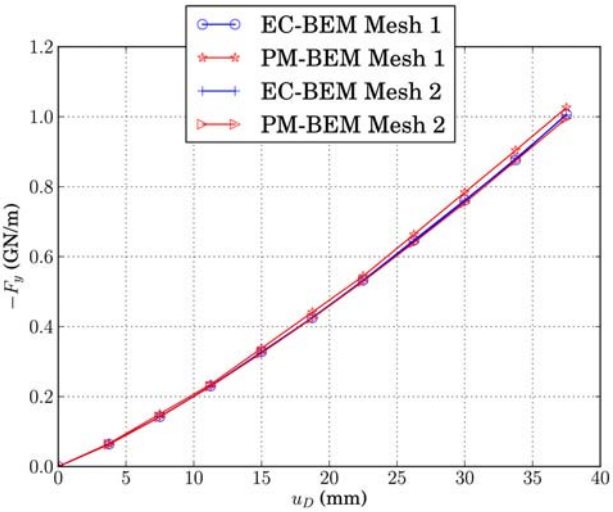

FIGURE 19 | Force F_Y predicted by both methods as a function of the imposed vertical displacement u_D.

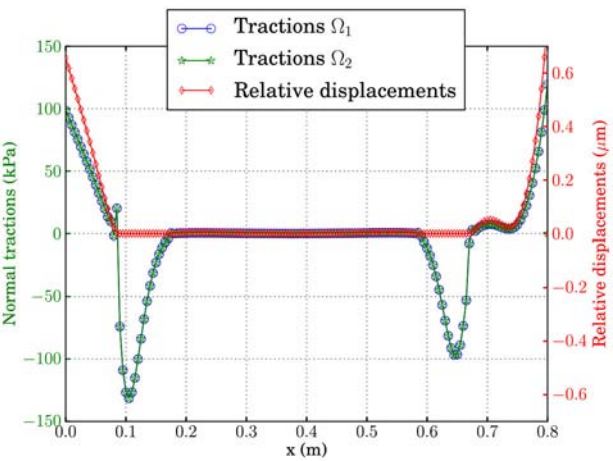

FIGURE 20 | Normal tractions and normal relative displacements along the potential contact zone in the example of **Figure 9** with the adhesive elastic contact computed by EC-BEM, and with $u_D = 0.035$ mm.

described above is accurate. It is interesting to focus on the zone in the middle of the boundary where tractions looks like vanishing at the scale of the upper figure. Lower figure shows the complexity of this zone, which is composed by two lateral regions where both solids are separated and a central region where both solids are under contact (compression). The agreement between both results is reasonable in spite of the very small scale compared to the tractions obtained on the whole boundary.

A subsequent analysis is carried out by multiplying the displacement u_D by 100 without modifying any other parameters in both codes. In this case, the results from the energetic approach presented here remain qualitatively similar, whereas the results from ANSYS present some problems to match the complex central zone. To the knowledge of authors, this could be solved by modifying some of the values of the key-options which configure the contact algorithm of ANSYS. This shows the robustness of the energetic approach compared to other contact algorithms, where convergence depends on the value of certain non-physical parameters of the numerical model.

12. CONCLUDING REMARKS

A novel approach for contact problems of elastic bodies was presented. This method is based on the energy principles expressed by boundary integrals. The solution of contact problems is obtained by the minimization of the total potential energy. Appropriate algorithms to solve the quadratic problems were presented. The cases of conforming as well as non-conforming meshes for contact zone were addressed.

Numerical examples, showing the suitability of the present framework to solve typical contact problems were examined,

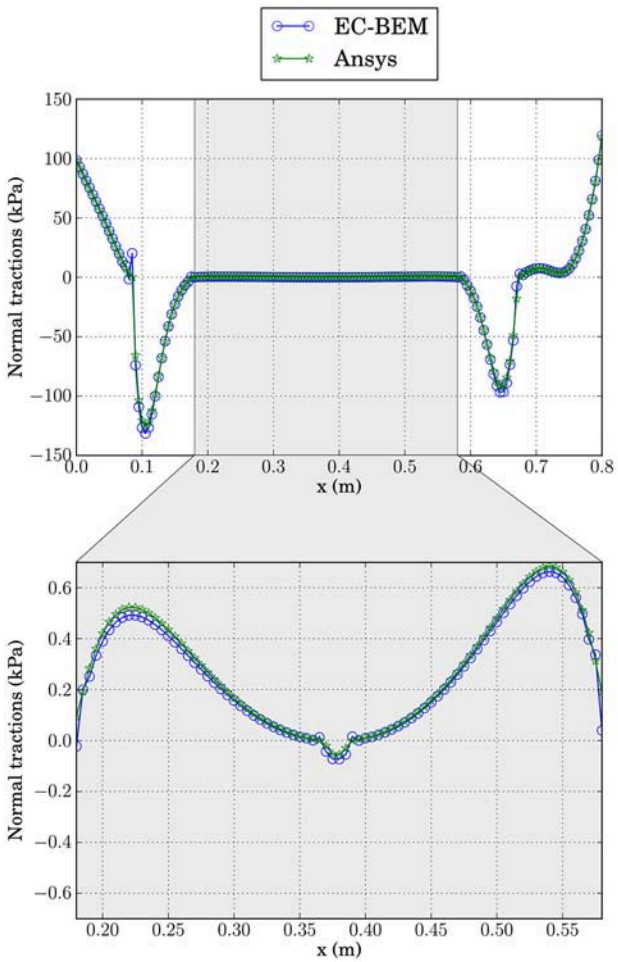

FIGURE 21 | Comparison of the normal tractions computed by EC-BEM and ANSYS for the adhesive elastic contact, with $u_D = 0.035$ mm.

and also successfully compared to other well established BEM methodologies as well as a commercial FEM code.

The proposed framework can be easily incorporated to existing BEM or FEM codes. Possible extension to the case of elastodynamics, where instead of the principle of virtual work we may use the principle of virtual power in order to compute the total energy (kinetic plus elastic), using only boundary values, of tractions and velocities, is possible. For this it might be convenient to utilize a formulation such as that introduced in Panagiotopoulos and Manolis (2010, 2011).

Finally, the present framework is found to be very useful in the case where also dissipative mechanisms exist on the boundaries or common interfaces of elastic bodies. In such cases we may apply energetic approaches to solve the corresponding non-linear problems as was shown in previous publications by some of the present authors (e.g., Panagiotopoulos et al., 2013).

AUTHOR CONTRIBUTIONS

All authors listed have made a substantial, direct and intellectual contribution to the work, and approved it for publication.

FUNDING

The authors acknowledge the support by the Junta de Andalucía and European Social Fund (Proyecto de Excelencia TEP-4051), the Spanish Ministry of Science and Innovation (Project MAT2009-14022), the Spanish Ministry of Economy and Competitiveness and European Regional Development Fund (Projects MAT2012-37387 and MAT2015-71036-P), and Spanish Ministry of Education (FPU grant AP2009-3968). Furthermore, CP acknowledges the financial support of the Stavros Niarchos Foundation within the framework of the project ARCHERS (Advancing Young Researchers' Human Capital in Cutting Edge Technologies in the Preservation of Cultural Heritage and the Tackling of Societal Challenges).

ACKNOWLEDGMENTS

The authors would like to express their gratitude to Prof. Tomáš Roubíček of the Charles University of Prague, as well as to Dr. Roman Vodička from the Technical University of Košice, for fruitful discussions.

REFERENCES

Aliabadi, M. H. (2002). *The Boundary Element Method: Applications in Solids and Structures*. Chichester, UK: Wiley.

ANSYS (2010). *ANSYS Mechanical APDL Contact Technology Guide Release 13.0*. Canonsburg, PA: Ansys, Inc.

Antes, H., and Panagiotopoulos, P. D. (1992). *The Boundary Integral Approach to Static and Dynamics Contact Problems. Equality and Inequality Methods*, Vol. 108 of *International Series of Numerical Mathematics*. Basel: Birkhauser Verlag.

Aour, B., Rahmani, O., and Nait-Abdelaziz, M. (2007). A coupled FEM/BEM approach and its accuracy for solving crack problems in fracture mechanics. *Int. J. Solids Struct.* 44, 2523–2539. doi: 10.1016/j.ijsolstr.2006.08.001

Axelsson, O. (1980). Conjugate gradient type methods for unsymmetric and inconsistent systems of linear equations. *Linear Algebra Applic.* 29, 1–16. doi: 10.1016/0024-3795(80)90226-8

Blázquez, A., Mantič, V., and París, F. (2006). Application of BEM to generalized plane problems for anisotropic elastic materials in presence of contact. *Eng. Anal. Bound. Elements* 30, 489–502. doi: 10.1016/j.enganabound.2005.07.006

Blázquez, A., and París, F. (2009). On the necessity of non-conforming algorithms for "small displacement" contact problems and conforming discretizations by BEM. *Eng. Anal. Bound. Elements* 33, 184–190. doi: 10.1016/j.enganabound.2008.05.003

Blázquez, A., París, F., and Cañas, J. (1998a). Interpretation of the problems found in applying contact conditions in node-to-point schemes with boundary element non-conforming discretizations. *Eng. Anal. Bound. Elements* 21, 361–375. doi: 10.1016/S0955-7997(98)00024-1

Blázquez, A., París, F., and Mantič, V. (1998b). BEM solution of two-dimensional contact problems by weak application of contact conditions with non-conforming discretizations. *Int. J. Solids Struct.* 35, 3259–3278. doi: 10.1016/S0020-7683(98)00016-X

de Paula, F. A., and Telles, J. (1989). A comparison between point collocation and Galerkin for stiffness matrices obtained by boundary elements. *Eng. Anal. Bound. Elements* 6, 123–128. doi: 10.1016/0955-7997(89)90025-8

Dostál, Z. (2009). *Optimal Quadratic Programming Algorithms: With Applications to Variational Inequalities*, Vol. 23 of *Springer Optimization and Its Applications*. New York, NY: Springer Science+Business Media.

Eck, C., Jarušek, J., and Krbec, M. (2005). *Unilateral Contact Problems. Variational Methods and Existence Theorems*. Boca Raton, FL: Chapman & Hall; CRC; Taylor & Francis Group.

Fichera, G. (1964). Problemi elastostatici con vincoli unilaterali: il problema di signorini con ambigue condizioni al contorno. *Mem. Accad. Naz. Lincei* VIII, 91–140.

Gakwaya, A., Lambert, D., and Cardou, A. (1992). A boundary element and mathematical programming approach for frictional contact problems. *Comput. Struct.* 42, 341–353. doi: 10.1016/0045-7949(92)90030-4

Graciani, E., Mantič, V., París, F., and Blázquez, A. (2005). Weak formulation of axi-symmetric frictionless contact problems with boundary elements. application to interface cracks. *Comput. Struct.* 83, 836–855. doi: 10.1016/j.compstruc.2004.09.011

Graciani, E., Mantič, V., París, F., and Varna, J. (2009). Numerical analysis of debond propagation in the single fibre fragmentation test. *Compos. Sci. Technol.* 69, 2514–2520. doi: 10.1016/j.compscitech.2009.07.006

Gurtin, M. E. (1972). *The Linear Theory of Elasticity*, Vol. VIa/2 of *Handbuch der Physik*. Berling: Springer-Verlag.

Hartmann, F. (1981). The derivation of stiffness matrices from integral equations. *Appl. Math. Model.* 5, 355–365. doi: 10.1016/S0307-904X(81)80058-3

Hertz, H. (1896). *Miscellaneous Papers on the Contact of Elastic Solids*. Trans. D. E. Jones (London: McMillan).

Hestenes, M. R., and Stiefel, E. (1952). Methods of conjugate gradients for solving linear systems. *J. Res. Natl. Bur. Stand.* 49, 409–436. doi: 10.6028/jres.049.044

Johnson, K. L. (1985). *Contact Mechanics*. Cambridge: Cambridge University Press.

Kalker, J., and Randen, Y. V. (1972). A minimum principle for frictionless elastic contact with application to non-Hertzian half-space contact problems. *J. Eng. Math.* 6, 193–206. doi: 10.1007/BF01535102

Katsikadelis, J., and Kokkinos, F. (1993). Analysis of composite shear walls with interface separation, friction and slip using bem. *Int. J. Solids Struct.* 30, 1825–1848. doi: 10.1016/0020-7683(93)90236-Z

Lazaridis, P. P., and Panagiotopoulos, P. D. (1987). Boundary variational "principles" for inequality structural analysis problems and numerical applications. *Comput. Struct.* 25, 35–49. doi: 10.1016/0045-7949(87)90216-1

Mantič, V. (1993). A new formula for the C-matrix in the Somigliana identity. *J. Elastic.* 33, 191–201. doi: 10.1007/BF00043247

Méchain-Renaud, C., and Cimetière, A. (2000). Influence of a curvature discontinuity on the pressure distribution in two-dimensional frictionless contact problems. *Int. J. Eng. Sci.* 38, 197–205. doi: 10.1016/S0020-7225(99)00018-X

Panagiotopoulos, C. G. (2017). *Symplegma: Java Components for Computational Mechanics and Numerical Modelling*. Available online at: http://symplegma.org/

Panagiotopoulos, C. G., and Manolis, G. D. (2010). Velocity-based reciprocal theorems in elastodynamics and BIEM implementation issues. *Arch. Appl. Mechan.* 80, 1429–1447. doi: 10.1007/s00419-009-0376-0

Panagiotopoulos, C. G., and Manolis, G. D. (2011). Three-dimensional BEM for transient elastodynamics based on the velocity reciprocal theorem. *Eng. Anal. Bound. Elements* 35, 507–516. doi: 10.1016/j.enganabound.2010.09.002

Panagiotopoulos, C. G., Mantič, V., and Roubíček, T. (2013). BEM solution of delamination problems using an interface damage and plasticity model. *Computat. Mechan.* 51, 505–521. doi: 10.1007/s00466-012-0826-3

Panagiotopoulos, P. D., and Lazaridis, P. P. (1987). Boundary minimum principles for the unilateral contact problems. *Int. J. Solids Struct.* 23, 1465–1484. doi: 10.1016/0020-7683(87)90064-3

París, F., and Blázquez, A. (1994). On the displacement and load scaling techniques in contact problems using bem. *Bound. Elements Commun.* 5, 15–17.

París, F., Blázquez, A., and Cañas, J. (1995). Contact problems with nonconforming discretizations using boundary element method. *Comput. Struct.* 57, 829–839. doi: 10.1016/0045-7949(95)92007-5

París, F. and Cañas, J. (1997). *Boundary Element Method, Fundamentals and Applications*. Oxford: Oxford University Press.

París, F., and Garrido, J. A. (1989). An incremental procedure for friction contact problems with the boundary element method. *Eng. Anal. Bound. Elements* 6, 202–213. doi: 10.1016/0955-7997(89)90019-2

Renaud, C., and Feng, Z.-Q. (2003). BEM and FEM analysis of Signorini contact problems with friction. *Comput. Mechan.* 31, 390–399. doi: 10.1007/s00466-003-0441-4

Roubíček, T., Mantič, V., and Panagiotopoulos, C. G. (2013). A quasistatic mixed-mode delamination model. *Disc. Cont. Dynam. Syst. S* 6, 591–610. doi: 10.3934/dcdss.2013.6.591

Saad, Y. and Schultz, M. H. (1985). Conjugate gradient-like algorithms for solving nonsymmetric linear systems. *Math. Comput.* 44, 417–424. doi: 10.1090/S0025-5718-1985-0777273-9

Signorini, A. (1959). Questioni di elasticità non linearizzata e semilinearizzata. *Rendiconti di Matematica e delle sue Applicazioni* 18, 95–139.

Stavroulakis, G. E., and Antes, H. (1997). Nondestructive elastostatic identification of unilateral cracks through BEM and networks. *Comput. Mechan.* 20, 439–451. doi: 10.1007/s004660050264

Tullberg, O., and Bolteus, L. (1982). "A critical study of different boundary element stiffness matrices," in *Boundary Element Methods in Engineering*, ed C. A. Brebbia (Berling: Springer–Verlag), 621–635.

Vodička, R. (2000). The first and the second–kind boundary integral equation systems for solution of frictionless contact problems. *Eng. Anal. Bound. Elements* 24, 407–426. doi: 10.1016/S0955-7997(00)00012-6

Wriggers, P. (2006). *Computational Contact Mechanics, 2nd Edn.* Berling: Springer.

Wriggers, P., and Panagiotopoulos, P. D. (1972). *New Developments in Contact Problems*, Vol. 384 of *CISM courses and lectures*. NewYork, NY: Springer Wien.

Yastrebov, V. A. (2013). *Numerical Methods in Contact Mechanics*. London, UK: ISTE Ltd and Wiley.

Zhou, C., Byrd, R. H., Lu, P., and Nocedal, J. (1997). Algorithm 778: L-BFGS-B: Fortran subroutines for large-scale bound-constrained optimization. *ACM Trans. Math. Soft.* 23, 550–560. doi: 10.1145/279232.279236

Conflict of Interest Statement: The authors declare that the research was conducted in the absence of any commercial or financial relationships that could be construed as a potential conflict of interest.

frontiers in Built Environment

ORIGINAL RESEARCH
published: 10 December 2018
doi: 10.3389/fbuil.2018.00075

Hybrid Micro-Modeling Approach for the Analysis of the Cyclic Behavior of RC Frames

Gianni Blasi[1,2], *Flavia De Luca*[2]* *and Maria Antonietta Aiello*[1]

[1] Department of Innovation for Engineering, University of Salento, Lecce, Italy, [2] Department of Civil Engineering, University of Bristol, Bristol, United Kingdom

The present study is aimed at developing a hybrid approach to consider the effect of concrete cracking on the hysteretic response of RC frames. The mechanical behavior of the concrete is defined according to the smeared cracking approach, while discrete cracking surfaces are included in the geometrical model. The interface behavior of the discrete cracking surfaces is defined by the combination of contact and cohesive elements. The proposed approach is adopted in ABAQUS to simulate an experimental test on a double cantilever column for the calibration of the numerical model. Therefore, a test conducted on a RC portal and modeled numerically for the first time is simulated. Numerical and experimental results are compared in terms of hysteretic force-displacement behavior and cumulative dissipated energy, in order to assess the reliability of the proposed model in simulating the energy dissipation capacity of RC members subjected to lateral cyclic loading. The hybrid modeling approach proposed allows an accurate description of the stress distribution and a fairly satisfactory matching of the hysteretic behavior with a reasonable compromise in terms of computational effort.

Keywords: reinforced concrete frames, cyclic behavior, hysteretic response, micro-modeling, abaqus, hybrid micro-model

OPEN ACCESS

Edited by:
Vagelis Plevris, OsloMet–Oslo Metropolitan University, Norway

Reviewed by:
Michalis Fragiadakis, National Technical University of Athens, Greece
Francesco Tornabene, Università degli Studi di Bologna, Italy
Zeljana Nikolic, University of Split, Croatia

***Correspondence:**
Flavia De Luca
flavia.deluca@bristol.ac.uk

Specialty section:
This article was submitted to Computational Methods in Structural Engineering, a section of the journal Frontiers in Built Environment

Received: *08 August 2018*
Accepted: *22 November 2018*
Published: *10 December 2018*

Citation:
Blasi G, De Luca F and Aiello MA (2018) Hybrid Micro-Modeling Approach for the Analysis of the Cyclic Behavior of RC Frames. Front. Built Environ. 4:75. doi: 10.3389/fbuil.2018.00075

INTRODUCTION

Finite element (FE) analysis is widely adopted in earthquake engineering, particularly when dealing with systems with a high number of degrees of freedom (DOF), representing the structural configuration of buildings. On the other hand the simulation of the seismic response of RC structures through finite element analysis can be complex and challenging. This is mainly caused by the difference between the mechanical response of concrete and steel rebars and by their consequent complex interaction. In numerical studies, either micro- or macro-modeling approaches are usually adopted depending on the aim of the study, which can require the accurate simulation of several phenomena influencing the response of the frames. Macro-models generally adopt simplified formulation which implicitly consider the influence of the micro-mechanical interaction phenomena on the response of the elements/materials. This approach leads to a significant simplification of the numerical problem. In micro-modeling approaches, the micro-mechanical interaction phenomena are explicitly modeled numerically (e.g., Karavelić et al., 2017; Sinaie et al., 2018) and generally high computational efforts are required. Therefore, when the target of the analysis is global behavior of RC structures, generally macro-models are preferred (e.g., Vamvatsikos and Fragiadakis, 2010; De Risi et al., 2017). This is mainly due to the substantial reduction of the computational effort required with respect to micro- and meso-models. In the

last decades, large numbers of macro-models have been developed, able to accurately reproduce the response of RC members. On the other hand, for the accurate reproduction of stress/strain distribution in the elements subjected to cyclic loads, micro- and meso-models still represent the best option. The latter approach represents the compromise between micro- and macro-modeling, featuring a simplification of the numerical problem aimed at accurately evaluate only the phenomena which are object of the analysis. For this reason, the difference between macro- and meso-models can't be unambiguously defined. In macro-models, RC frames are usually modeled through beam elements, while both micro- and meso-models generally feature solid or shell elements to represent the concrete region, whereas the steel reinforcement is simulated with embedded beam/truss elements (e.g., Viswanathan et al., 2014; Redmond et al., 2018).

Mechanical models for concrete and steel, available in most of the FE platforms, allow reproducing the stress-strain response under monotonic loading and the degradation of the strength and stiffness due to cyclic loading. The mechanical response of the steel is generally reproduced adopting a symmetric bi-linear behavior, characterized by kinematic or isotropic hardening laws; even if in some cases the compressive response is modified to take into account the buckling phenomenon on rebars.

Although the simulation of the concrete response is more challenging; as well-known, the compressive behavior is characterized by a post peak softening slope, influenced by different parameters, such as the confinement (Mander et al., 1988), while the tensile response is generally composed of an elastic branch up to the tensile strength of the concrete, followed by concrete cracking.

The post-cracking response of concrete can be simulated adopting the smeared cracking approach (Lotfi and Shing, 1991; Lee and Fenves, 1998), where cracks are not explicitly defined in the geometry of the model but they are implicitly considered in the mechanical response of the material.

The smeared cracking approach has been widely adopted in numerical studies to reproduce the monotonic response of RC frames (Sinaei et al., 2012; Sümer and Aktaş, 2015; Ors et al., 2016); although this mechanical model is not always able to accurately reproduce the response of concrete under cyclic loading.

The discrete cracking approach is an alternative method to reproduce the crack opening in the concrete (Dolbow et al., 2001; Giner et al., 2009), it generally allows high simplifications of the mechanical model adopted for the concrete. Discrete cracks develop in the mesh once the tensile strength or the cracking energy is attained and they can be explicitly identified in the post processing.

The two methods discussed allow the accurate reproduction of the effects of crack development in concrete members, but, in many cases, they are time consuming and lead to convergence issues.

Furthermore, when dealing with the cyclic behavior of the concrete members, the effects of the cyclic opening and closure of the cracks should be considered in the numerical simulation; in the smeared cracking approaches, this leads to a significant increase of the complexity of the mechanical model (Koutromanos and Shing, 2012; Redmond et al., 2018), while the eXtended Finite Element Method (XFEM) requires the definition of a contact law along the cracking surfaces, which is not pre-defined in the geometrical model (Yu et al., 2016).

The present study is aimed at proposing a hybrid approach using ABAQUS (Dassault Systemes, 2016) which combines the discrete cracking approach and the smeared cracking approach. The cracking surfaces are pre-defined in the numerical model by splitting the geometry in different "macro blocks"; along the cracking surfaces, cohesive and contact laws are defined, in order to simulate the crack opening and closure, respectively.

This approach makes possible to simplify the definition of the mechanical response of the concrete, since the cyclic opening/closure is not implicitly taken into account in the tensile behavior definition. Furthermore, since the cracking paths are predefined in the geometry, the contact and cohesive laws are only defined for specific surfaces in the geometry, leading to a significant reduction of the computational efforts.

The proposed approach is aimed at reproducing the hysteretic response of RC members subjected to cyclic lateral loading. In order to assess the reliability of the proposed model, a test on a double cantilever column was simulated (Ohue et al., 1985) by proposing different modeling approaches. The monotonic and hysteretic response of the numerical simulations were compared to the experimental results with a particular focus on the influence of the adopted model on the accuracy of the reproduction of the shape of the hysteresis loops. Then, a recent experimental test on a RC portal conducted by Verderame et al. (2016) is modeled numerically for the first time in order to assess preliminarily the reliability of the proposed approach. Hysteretic force-displacement response is evaluated and the numerical and experimental results are compared, in order to assess the accuracy of the simulation of the cyclic loops.

MICRO-MODELING OF RC FRAMES—ISSUES IN THE SIMULATION OF THE CYCLIC BEHAVIOR

Most of the mechanical models available on FE platforms to simulate the behavior of the concrete take into account the significant asymmetry of the response in compressive and tensile direction. The compressive stress-strain relationship of the concrete is represented through a non-linear formulation (**Figure 1A**) whose parameters depend on the reinforcement details, as the post-peak softening response, being highly influenced by the transverse reinforcement (Mander et al., 1988). On the other hand, the tensile behavior definition depends on the approach adopted to simulate the concrete cracking.

The response of RC members under cyclic lateral loading is indeed highly influenced by the cracking of concrete, which modifies the energy dissipation capacity. The pinching effect characterizing the flexural response of frames is caused by the cyclic closure/opening of cracks, leading to a significant reduction of the stiffness in the load-inversion phase, due to the closure of the cracks. Depending on the adopted approach, the cyclic loops characterizing the lateral response of a RC frame

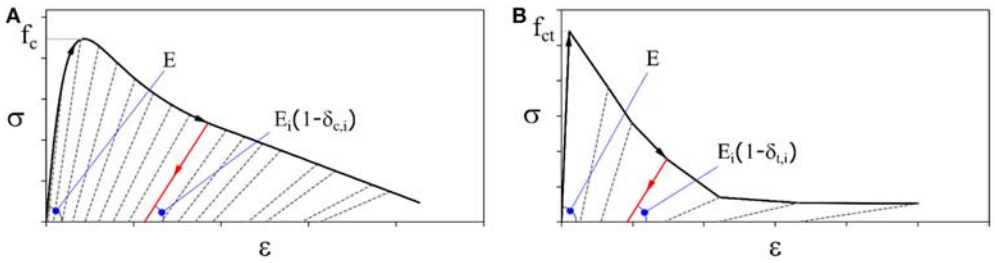

FIGURE 1 | Example of mechanical model for concrete in compression **(A)** and tension stiffening **(B)**.

can be reproduced in different ways, explained in the following section.

The Smeared Cracking Approach

In the smeared cracking approach, the development of cracks in the concrete is considered by defining a post-peak tensile response of the material. Thus, rather than tracking individual "macro" cracks in the geometrical model, the presence of cracks is considered implicitly by modifying the stress and the material stiffness associated with the integration point. After the attainment of the tensile strength of the concrete (f_{ct}), a post-peak softening branch (tension stiffening) simulates the progressive degradation due to the crack openings. Tension stiffening is reported in **Figure 1B** and can follow either linear or exponential laws.

In this approach, the simulation of the crack closure, requires an increase of the complexity of the material model (Koutromanos and Shing, 2012) and, as said before, highly influences the dissipation capacity of the frame members.

As reported in **Figure 1B**, once unloading takes place, after the crack has opened, the unloading branch stiffness is equal to the elastic stiffness, reduced by a factor δ_t that takes into account the degradation due to damage. As soon as the elastic displacement is restored, the crack closure stage begins and a significant reduction of the stiffness up to the complete closure of the crack is observed. At this point, the elastic stiffness is restored and compression takes place; the variation of the stiffness during the load inversion phase (pinching) is more marked in case of relevant crack patterns in RC members.

The analytical formulation to simulate the monotonic response of concrete usually requires the definition of two yielding surfaces; the first one is referred to the end of the elastic branch in compression, at which the linear stress-strain law turns into an exponential one. The second yielding surface is referred to the end of the elastic slope in tension, where tension stiffening takes place.

The model proposed by Oliveira and Lourenço (2004) was adopted in finite-element analysis of masonry structures to simulate the cyclic behavior of interface elements; although the same formulation can be used for concrete. The cyclic response is defined by the adoption of two auxiliary yielding surfaces moving within the monotonic yielding surface, representing the unloading/reloading phase.

The monotonic surfaces are active when either only monotonic loading has occurred or the stress point reaches the monotonic yielding surfaces during an unloading process. The proposed model was validated by comparisons with experimental results of uniaxial tests on concrete and was assessed to be highly reliable to simulate all the phenomena characterizing the cyclic response of asymmetric materials as concrete.

In some cases, mechanical models available in finite-element software packages are unable to simulate the response under cyclic loads, particularly in case of large tensile strain/displacement (**Figure 2A**); compression stiffness recovery in the reloading phase can occur earlier than expected, depending on the criterion adopted in the model to discern the transition from tension. As observed by Nikaido et al. (2015), if the compression stiffness recovery is detected at zero stress point, the pinching effect simulation can be challenging, since the crack closure cannot be accurately reproduced in the numerical model (as shown in **Figure 2B**).

In other cases, the auxiliary yielding surfaces are not even defined and the stiffness degradation, representing the cracking closure, does not take place.

If the mechanical model is unable to produce a satisfactory simulation of the pinching effect, a significant mismatch is obtained in the numerical simulation of the flexural response of RC members in terms of energy dissipation, since cracking of the concrete leads to a noticeable decrease of the energy dissipated.

The Discrete Cracking Approach

In the discrete cracking approach, the cracking process is ruled by cracks developed in the geometrical model; the most used modeling approaches are the extended finite element method and the adoption of cohesive elements to express the post-cracking response of the concrete.

The XFEM was developed by Moës and Belytschko (2002); it allows to significantly simplify the definition of the tensile response in the mechanical model of the material. The cracking path is generated by adding discontinuous basis functions to standard basis functions for nodes where cracking energy/displacement is computed, in order account for the displacements due to crack opening. The main advantage in the XFEM is that no update of the mesh is required to track the crack path, thus, the mesh-dependency of the results is significantly reduced with respect to a smeared cracking approach.

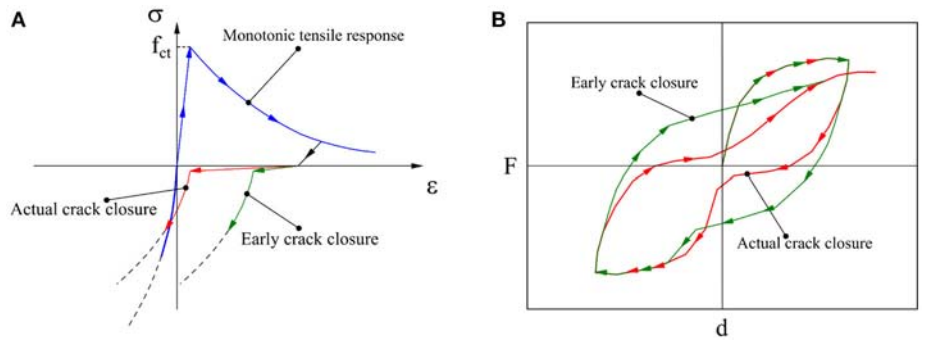

FIGURE 2 | Effect of the cracking closure simulation **(A)** in the mechanical model and **(B)** in the global response showing the pinching effect.

Since the XFEM allows to model the discontinuity in a displacement field along the crack path, the simulation of the crack growth requires an accurate definition of the fracture modes; generally, the cracking path is computed adopting the mixed mode in order to consider not only the response under uniaxial traction (Ballatore et al., 1990). Dolbow et al. (2001) also incorporated friction laws in order to simulate more accurately the crack growth under compression, which is an important feature when dealing with cyclic response of the frame members.

Since the crack path is not pre-defined, the accurate simulation of the cyclic response of reinforced concrete members requires the inclusion of contact laws in order to consider the effect of the crack closure. This assumption generally leads to high computational effort, and in many cases can cause convergence issues, particularly when dealing with RC members with embedded rebars, for which multiple crack paths are expected to develop under cyclic lateral loading.

Discrete cracking approaches adopting cohesive elements rather than XFEM have been also widely adopted in the literature (Bocca et al., 1991). The so-called discrete interelement cracks require remeshing in the model after the generation of the cracks, since the path is defined between the elements. This method is similar to the XFEM since the crack path is not pre-defined and can lead to high computational efforts as well as convergence issues. Notwithstanding the discussed issues, it was used specifically to simulate the lateral response of reinforced concrete members as well as crack growth in ductile materials (Tvergaard and Hutchinson, 1996; Gullerud et al., 2000).

The so-called intraelement approach features the incorporation of embedded discontinuities in the geometry (Belytschko et al., 1988), to simulate the post cracking response of the material. This approach allows the pre-definition of the crack paths, identified by a preliminary analysis of the stress distribution along the member, in order to define the regions where cracks are most likely to develop. Despite this approach reduces the complexity of the model, in some cases the preliminary definition of the crack paths may be difficult, as in the case of RC members subjected to cyclic loading.

In the study proposed by Yu et al. (2016), the simulation of the pinching effect characterizing the flexural cyclic response of a RC column, was conducted providing a novel modeling approach, developed through combination of the XFEM, to detect the crack paths in concrete, traction-separation cohesive laws to simulate the post-cracking response, and contact elements to take into account the clack closure process. A satisfactory simulation of the experimental response of RC frame members was obtained and the comparison between experimental and numerical hysteretic loops demonstrated the high reliability of the model in simulating the pinching effect.

An alternative discrete cracking approach for the simulation of the lateral response of RC members was proposed by Stavridis and Shing (2010). Triangular elements were connected with double-node interface elements, simulating the post cracking behavior of the concrete. The model was validated by comparing numerical results with experimental tests on infilled frames, showing a good match with the experimental backbone curve (Stavridis and Shing, 2010; Redmond et al., 2018).

A similar approach was recently developed from Zivaljic et al., 2013, combining triangular plane-stress elements with discrete cracking interfaces to reproduce concrete cracking and embedded one-dimensional elements simulating steel rebars. The bar slip was also considered by defining a pre- and post-cracking mechanical model for steel. The proposed model was adopted for the simulation of several reinforced concrete elements and was assessed to be very reliable in reproducing the crack paths in concrete (Zivaljic et al., 2013; Živaljić and Nikolić, 2014; Nikolić et al., 2017).

Also in this cases, a satisfactory simulation of the pinching required a complex mechanical model for interfaces elements, increasing the computational efforts.

THE SIMULATION OF THE HYSTERETIC RESPONSE IN THE PROPOSED APPROACH

As discussed in section Micro-Modeling of RC Frames—Issues in the Simulation of the Cyclic Behavior, the main issues in the simulation of the cyclic response of RC members under lateral loading are related to the pinching effect; when the post cracking behavior is defined in the mechanical model of the material, the process of crack closure requires a significant increase of

the complexity of the formulation, while in discrete cracking approaches, the cracking closure must be simulated by the inclusion of contact laws, which can lead to convergence issues. XFEM method was assessed to be reliable when simulating the lateral response of RC members under monotonic lateral loads even if the post-cracking behavior of the concrete is not defined in the material model (Zi and Belytschko, 2003). On the other hand, the adoption of this method requires an oversimplification of the response of the material in compression, which in many cases was assumed to be linear elastic (Dolbow et al., 2001; Liao and Huang, 2015). When analyzing the non-linear response of frame members experiencing displacements far beyond the yielding point, the simplified assumption on the compressional behavior of the material becomes questionable and the post-peak actual response of the element can be mismatched.

Description of the Numerical Model

In the numerical model developed using ABAQUS, an equivalent bi-dimensional system is proposed to simulate the cyclic lateral behavior of a RC portal. 4-node bilinear shell elements with reduced integration (CPE4R) are adopted for concrete, while both longitudinal and transverse rebars are modeled using linear truss elements (T2D2), embedded in the concrete geometry (**Figure 3A**).

The mechanical behavior of the concrete is defined adopting a Concrete smeared cracking model available in the software. As evidenced by Nikaido et al. (2015), the latter is unable to accurately simulate the crack closure process, since earlier compressive stiffness restore occurs in the unloading phase when the tensile deformation is relevant. Thus, a combination of the smeared and discrete cracking approach is adopted to simulate the pinching effect.

A bilinear kinematic hardening relationship was adopted for the definition of the mechanical behavior of the steel rebars, assuming a symmetric response in tension and compression.

In order to accurately define the compressive response of the concrete, the well-consolidated and widely adopted formulation proposed by Mander et al. (1988) was considered; which takes into account the transversal reinforcement ratio to define the ductility and strength capacity of the material. The tensile response was assumed to be elastic-perfectly-plastic with no tension stiffening, since the crack opening was modeled following a discrete approach by the adoption of cohesive laws. The model was implemented by direct input of the stress-strain backbone curve in the mechanical model available in the software (*Concrete damaged plasticity*); the parameters required for the definition of the plastic flow and the yield function are assumed considering values suggested from the literature (Lubliner et al., 1989; Lee and Fenves, 1998).

The Interface Interaction

According to different experimental and numerical studies (Sneed et al., 2016; Duan et al., 2017), flexural cracks are most likely to develop along the discontinuity surfaces, represented by the transversal rebars running through the concrete. Thus, in the proposed model, discrete crack paths are preliminarily defined in the geometry.

The path initiation position corresponds to the stirrups in the frame (**Figure 3B**), while the inclination is defined according to the variable strut inclination truss model (EN 1992-1-1, 2004; Fardis, 2009), assuming an angle of inclination of the compression stress field equal to 21.8°. Moreover, in order reduce the computational efforts, the paths are only included in the zones with the highest value of flexural moment. The geometry of concrete members is divided in different "macro-blocks," whose interaction is defined through cohesive and contact relationships.

The interface zone between the macro blocks is divided in three parts, as shown in **Figure 3B**; the external parts represent the crack paths, while the central part is a rough connection assumed as the center of the rotation of each block. The assumption of a central rough connection means that cracks in the members can only evolve up to the external boundaries of the central zone; as consequence, the latter must be adequately restricted, in order to assume that the collapse of the member is attained before cracks develop up to the central zone.

Depending on the direction of the load, the two external zones are characterized by compression and tension stress regime, respectively (**Figure 3B**); thus, either cohesive or contact laws are activated along the surfaces, on the basis of the stress regime.

The contact law is defined in order to simulate the complete closure of the crack, when the elastic compression stiffness is restored. The augmented Lagrange method (Powell, 1969) is adopted to compute the contact stress, while the contact stiffness is automatically defined depending on the stiffness of the elements experiencing the contact. This approach also allows to take into account the compressive stiffness reduction due to cyclic

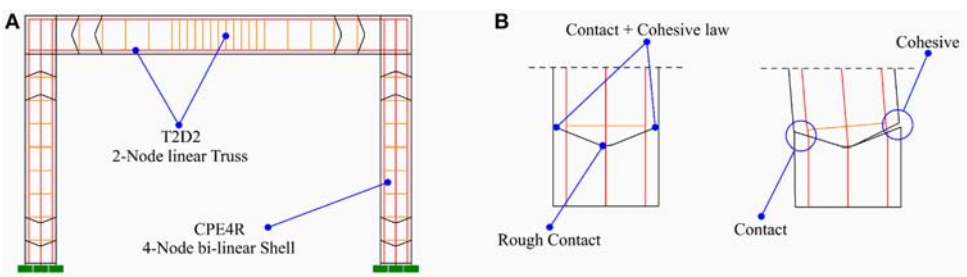

FIGURE 3 | (A) Numerical model and **(B)** interface interaction.

loading, by including compressive degradation in the mechanical model of the concrete.

The stiffness factor for the contact surfaces is assumed to be unitary, both for external and central surfaces.

In the initial stage, no gap exists between the blocks, and all the contact surfaces are in a closed status; since for the external zones separation of the surfaces is expected, the contact detention is ruled by the definition of a minimum gap between the nodes, this assumption assures contact elements being active every time that surfaces cyclically experience contact.

Once traction takes places along the surface, the separation between the surfaces follows a stress-displacement law, obtained as a function of the post-cracking stress-strain relationship of concrete, reported in **Figure 2A**.

The first elastic branch is defined considering the stiffness of the shell elements, thus, it takes into account the stiffness degradation by including a degrading tensile law in the mechanical model of the concrete.

The stress limit at the end of the elastic branch is equal to the tensile strength of the concrete. The post-peak behavior is ruled by an exponential law, according to analytical models expressing the tensile response of concrete available in the literature (Pramono and Willam, 1989; Mehta and Monteiro, 2006). In this study, an exponent equal to three is assumed to define the softening branch after the attainment of the tensile stress. Once the displacement between the surfaces reaches the residual limit, the cohesive law is inactive, meaning that no stress-displacement relationship exists between the surfaces. At this stage, once the load is reversed, the closure of the crack is represented by a displacement with zero-stress variation along the elements, making possible to simulate the pinching effect in the global response of the frame. As said before, once the crack is completely closed, the elastic compressive stiffness is partially restored, according to the compressive degradation law defined in the mechanical model of the material.

By this procedure, the pinching effect is "lumped" in the cracking interfaces; beside this, the effect of the cracking of the concrete on the flexural response in terms of strength is still considered in the whole model, by the definition of a tensile strength limit for the concrete, as well as tension stiffening.

NUMERICAL SIMULATION OF QUASI-STATIC CYCLIC TEST ON RC PORTAL

The numerical model developed was firstly validated considering the experimental test conducted on a double-cantilever column by Ohue et al. (1985). The column tested (named non-ductile column or NDC), reported in **Figure 4** featured a cross section equal to 200 × 200 mm and a height equal to 800 mm. The longitudinal reinforcement was composed of 2 + 2 rebars with 16 mm diameter, while transverse reinforcement was realized adopting 5.5 mm stirrups with spacing equal to 50 mm.

Axial load was applied on the top of the column to simulate the presence of the gravity loads. The cyclic lateral load was applied in displacement-control and it was composed of 9 load steps, each of them characterized by two fully reversed cycles at the same displacement amplitude.

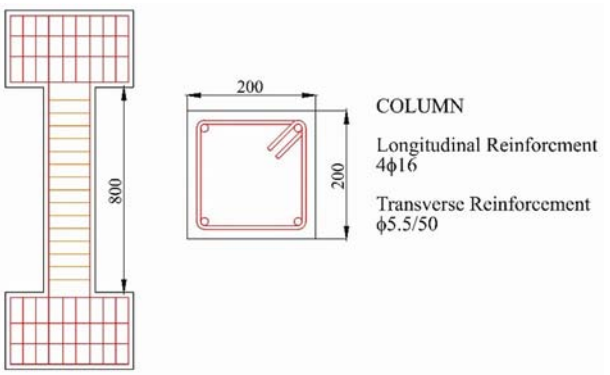

FIGURE 4 | Description of the NDC specimen tested by Ohue et al. (1985).

A mixed shear-flexural failure mode of the specimen was observed in the test, featuring major shear cracks at a displacement amplitude equal to 17.5 mm (drift equal to 2.2%).

In order to assess the reliability of the proposed model in predicting the lateral behavior of RC portals, a campaign available in literature and never modeled numerically, was considered to carry out a numerical simulation. The reinforced concrete frame (named ductile frame or DF) tested by Verderame et al. (2016) was designed according to provisions of the Italian seismic code NTC08 (2008), in order to simulate the behavior of seismic designed frames.

In DF (**Figure 5**), the longitudinal reinforcement of the beam is symmetric and made of three top and three bottom 10 mm bars. 12 mm bars were used for the column reinforcement, in order to follow the capacity design approach. Transverse reinforcement of the beam and the columns was composed of 6 mm stirrups, whose spacing was equal to 100 mm in all the three elements and 50 mm in the "critical zones," i.e., the end regions of columns and beams and in the mid span of the beam.

The experimental test was carried out by the application of cyclic lateral load at the mid-span of the beam; the loading protocol was composed of fully reversed displacement-controlled load cycles, whose displacement amplitude was increased at each load step up to the failure of the specimen. For each load step, three fully reversed cycles were executed.

The axial load was applied on top of the column during the quasi-static cyclic tests, to simulate gravity loads due to the presence of higher floors in a five-story building.

In the test, the first damage was characterized by flexural cracking at the beam ends. By increasing the displacement amplitude, flexural cracks developed in the column ends, too. The peak lateral strength was attained after the widening of the flexural cracks in beam ends and in the bottom of the columns. As expected for seismic designed frames, the collapse mechanism was caused by major cracking in beams, according to a strong column/weak beam mechanism behavior. The failure of the

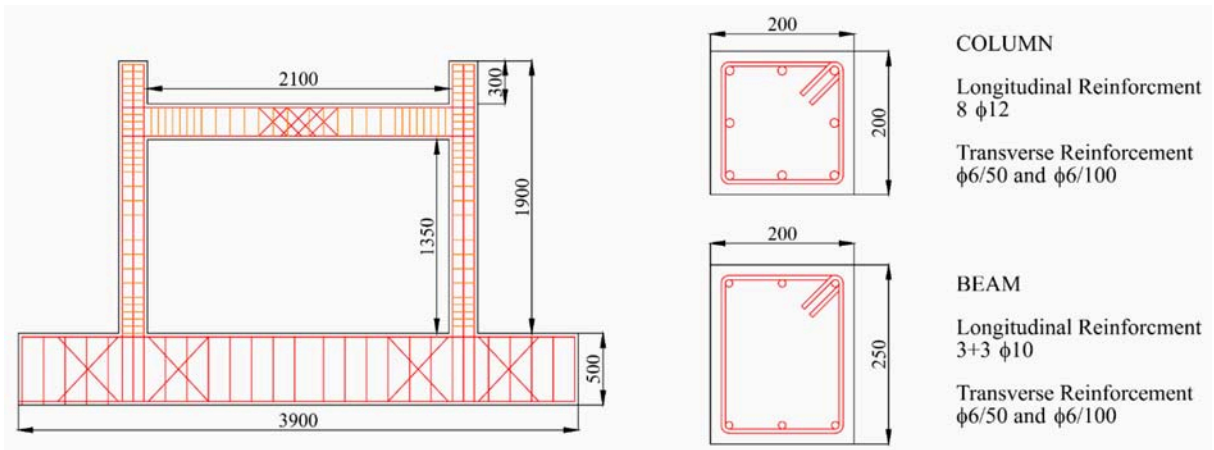

FIGURE 5 | Description of the DF specimen tested by Verderame et al. (2016).

specimen was attained at a drift Δ_f equal to 5.3% (see Verderame et al., 2016 for further details).

Numerical Simulation of the Tests in ABAQUS

In the numerical simulation in ABAQUS, different configurations of the finite element model are analyzed, in order to evaluate the influence of the proposed modeling approach on the numerical results. A Finite-Element "standard" (FES) model is firstly developed, with the aim of assessing the accuracy of the material model available in ABAQUS in simulating the pinching effect. The only difference between FES model (reported in **Figure 6A**) and the Finite-Element model with macro Blocks (FEB) model proposed in section Description of the Numerical Model is the absence of the macro blocks in the geometry, meaning that a fully smeared cracking approach is adopted, without the definition of contact and cohesive laws to simulate the cyclic opening and closure of cracks, leading to a high simplification of the numerical problem.

In FES model, the size of shell elements is assumed equal to 50 mm in the whole geometry, while, in FEB model, it is gradually reduced from 50 to 10 mm in proximity to the interfaces between the macro blocks. Referring to the truss elements adopted to simulate longitudinal rebars, a length equal to the stirrups spacing is assumed.

Furthermore, referring to FEB model, two different configurations were developed (**Figures 6B,C**) for the test considered; in order to analyse the influence of the simulation of bond between concrete and steel rebars on the accuracy of the simulation of the hysteretic loops characterizing the lateral response of the portal.

In the first configuration (FEB_1), the end zones of beams and columns are divided in two macro blocks, meaning that two discrete cracking surfaces are included. Bar slip is not considered and the truss elements are embedded in the concrete region. In the second configuration (FEB_2), which features the same number of blocks adopted for FEB_1, bar slip is modeled through linear elastic connectors between trusses representing longitudinal rebars and shell elements. The mechanical behavior of the connectors is defined according to CEB-FIP (2010).

It is worth mentioning that the same approach was adopted for each of the experimental tests simulated, even if **Figure 6** is referred to the model adopted for the portal tested by Verderame et al. (2016). The double-cantilever model for the simulation of the test by Ohue et al. (1985) featured an encastre restraint for both the bottom and the top nodes of the column.

A dynamic analysis adopting implicit method was carried out; monotonic and cyclic displacements were applied on top of the frame and the column as boundary condition to reproduce the loading protocol applied in the experimental tests, while the base shear at the fixed supports was computed during post-processing in order to plot monotonic and cyclic load-displacement relationships.

Comparison Between Numerical and Experimental Results

The numerical simulation of the test on the NDC confirms the low reliability of the mechanical model of the concrete available in the software in simulating the cyclic response of reinforced concrete columns. Firstly a monotonic push-over analysis was carried out, in order to obtain the monotonic response of each model developed (**Figure 7**). No significant variation in observed in terms of yielding strength and pre-yielding stiffness for FES and FEB_1, confirming the equivalence of the two models in the simulation of monotonic behavior.

On the other hand, FEB_2 model featured a lower stiffness due to the bar slip. The variation of the yielding strength with respect to the experimental test is equal to +1.5, +.2%, and +1.1% for FES, FEB_1, and FEB_2, respectively. The elastic stiffness increased by 13% for both FES and FEB_1 while a decrease of 36% was observed for FEB_2. The FES and FEB_1 featured a hardening response leading to an increase of the ultimate strength with respect of the experimental results. This feature suggests that the strength degradation obtained in the experimental test could be

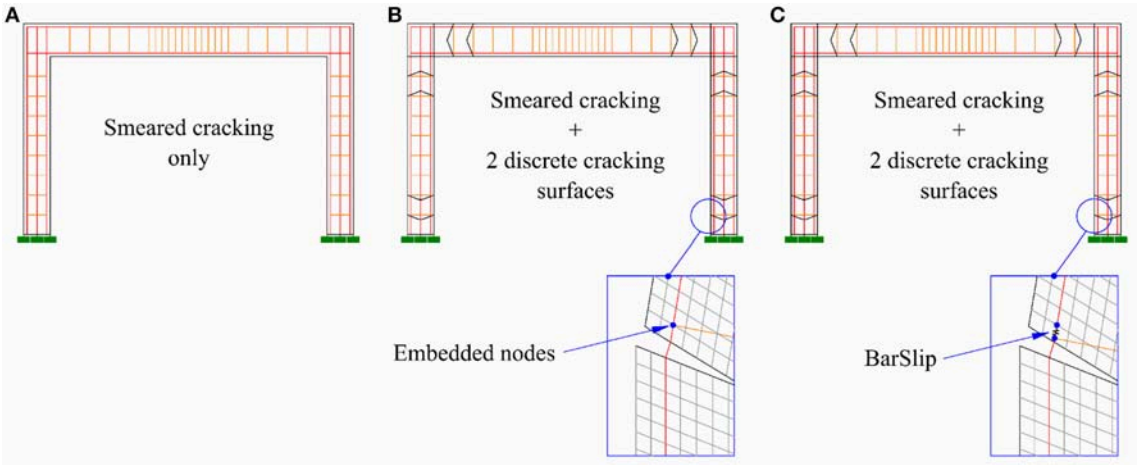

FIGURE 6 | Illustration of **(A)** FES model, **(B)** FEB_1 model, and **(C)** FEB_2 model.

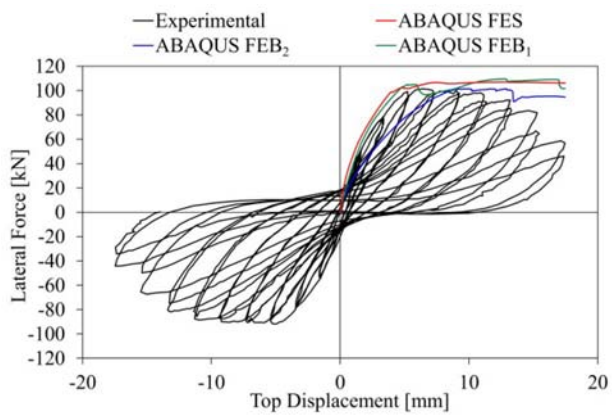

FIGURE 7 | Comparison between the monotonic response of the three FE model developed and the cyclic experimental response of NDC.

an effect of the cyclic loading, therefore it couldn't be reproduced through a push-over analysis. On the other hand, the strength degradation obtained in FEB_2 simulation, was caused by the bar slip, leading to a softening behavior and a higher accuracy of the simulation in terms of strength.

The comparison between the hysteretic response of FES and FEB_1 and the experimental test is reported in **Figure 8**. The introduction of the macro-block in the model leads to a significant reduction of the energy dissipation and the elastic stiffness of the backbone curve with respect to the FES model. Furthermore, the pinching effect observed in the experimental response is only simulated in FEB_1, confirming the limit of the original model for the concrete in accurately simulate the cracking closure process. Lastly, the isotropic hardening of the reinforcement steel observed in FES simulation led to a significant increase of the maximum strength with respect to the experimental test as well as to the corresponding maximum strength obtained from the push-over analysis. Referring to FES, the maximum strength obtained increased by 14% with respect to the experimental result (+7% with respect to the monotonic response), Also in FEB_1 model the isotropic hardening affected the global response in the first cycles, as evidenced by the different shape of the hysteretic loops comparing numerical and experimental response for low displacement amplitude. The increase in maximum strength observed for FEB_1 was 11% comparing to experimental test (+3% with respect to the monotonic response). Despite being affected by the isotropic hardening model of the reinforcement steel, the cyclic response of FEB_1 featured pinching effect and a satisfactory simulation of the experimental response was obtained comparing to experimental curve.

The introduction of the bond between steel rebars and concrete led to a significant increase of the accuracy of the experimental response simulation (**Figure 9**). The pinching effect simulation caused by the bar slip significantly affected the shape of hysteretic loops and led to a reliable simulation of the total energy dissipated (−19% with respect to the experimental test).

A good correspondence in terms of maximum strength was also observed, with a difference of 4.1% between numerical and experimental results. On the other hand, the inclusion of the bond in the numerical model affected the elastic stiffness, which was 45% lower in the numerical simulation.

The total energy dissipated, ED is reported in **Table 1**. In the FES a significantly higher value is obtained with respect to the ED of the experimental test (+252%), due to the absence of pinching and the isotropic hardening effect obtained in the model. For FEB_1 and FEB_2, a higher accuracy in the simulation of the crack opening/closure due to the presence of the macro-blocks led to a satisfactory matching of the experimental curve and, consequently, the ED. Furthermore, the bar slip simulation characterizing the FEB2 approach reduced the influence of the cyclic response of the reinforcement steel on the global behavior of the column.

The numerical simulation of the test on the DF specimen shows a significant variation of the results depending on the

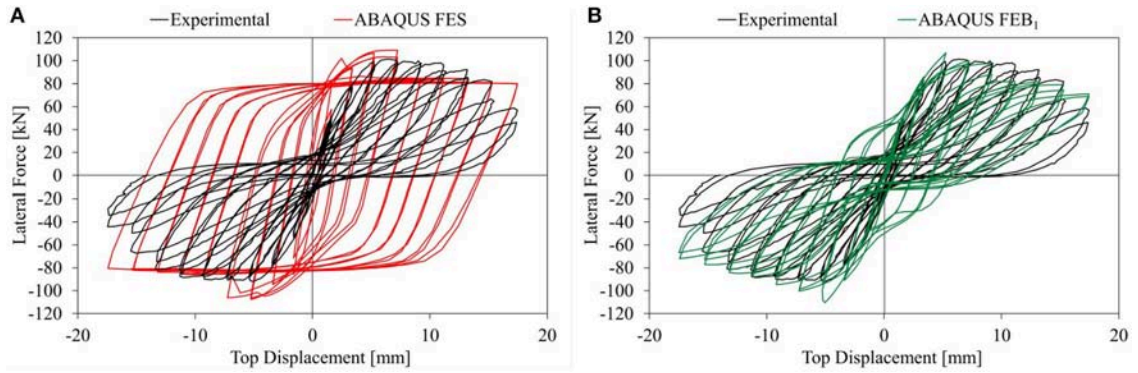

FIGURE 8 | Numerical simulation of NDC adopting **(A)** FES model and **(B)** FEB_1 model.

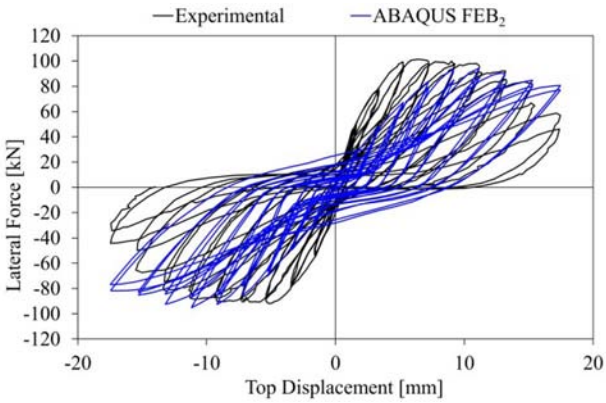

FIGURE 9 | Numerical simulation of NDC adopting FEB_2 model.

TABLE 1 | Total energy dissipated for experimental test and numerical models referring to NDC.

	Experimental test	ABAQUS FES	ABAQUS FEB_1	ABAQUS FEB_2
ED [kNm]	9.59	33.72	12.22	7.81

modeling approach adopted. The hysteretic force-displacement (F-d) behavior obtained considering the FES model (**Figure 10A**) confirms the assessments made in previous sections. No pinching effect is observed in the cyclic response of the frame, leading to a significant increase of the energy dissipated in the numerical model with respect to the experimental test. Furthermore, isotropic hardening effect is observed in hysteretic loops obtained from the numerical simulation, caused by the influence of the cyclic behavior of steel rebars on the lateral response of the frame.

In FEB_1 (**Figure 10B**), the bar slip is not simulated since embedded constraints were adopted between the nodes of shell and truss elements. For this reason, an increase of the maximum lateral stiffness is obtained in the numerical model compared to the experimental test. The absence of bar slip increases the influence of the rebar deformation on the strain developed in the shell elements, and the crack opening is not adequately simulated. On the other hand, higher quality of the matching of the experimental test can be observed in terms of strength and stiffness, even if the pinching effect is not simulated.

Comparing FES results to experimental ones, an increase of 199 and 24% is obtained in terms of elastic stiffness, E_k, and yielding strength, F_y, respectively. Considering FEB_1, the F_y is 11% higher than the value obtained from the test, while E_k increases by 111%.

For FEB_2 model (**Figure 11**), a better matching of the experimental results is obtained both in terms of strength and stiffness. The simulation of the bond leads to a significant reduction of the elastic stiffness with respect to FEB_1 (−64%), while bar slip was found to have a sensible influence on the pinching effect.

Comparing experimental to numerical results, an increase of 10% is obtained for F_y considering FEB_2, while the elastic stiffness decreases by 23%. It is worth saying that FEB_2 simulation is the only one which features a decrease of the elastic stiffness with respect to the experimental test.

Lastly, the energy dissipation capacity is also computed for the analyzed frame. The cumulative dissipated energy (CDE), evaluated as the sum of the areas of the hysteretic loops in the F-d response, is reported in **Figure 12**. Considering FES and FEB_1, a significant increase of energy dissipated is observed even for low displacement amplitude, while in case of FEB_2, a very satisfactory match is obtained in the early stage.

This assessment is confirmed by the comparison of the hysteretic loops of **Figures 10**, **11**.

The pinching effect is more noticeable in the first loops in case of FEB_2, while the more the displacement amplitude increases, the more the difference between the experimental and the numerical CDE increases.

This effect could be caused by the increase of the strain in shell elements adjacent to the cracking surface for high displacement amplitudes.

For high displacements, the interaction between the stress components in shell elements adjacent to the crack leads to a significant increase of the strain, causing a distortion of the geometry in the crack closure phase. For this reason, the cyclic

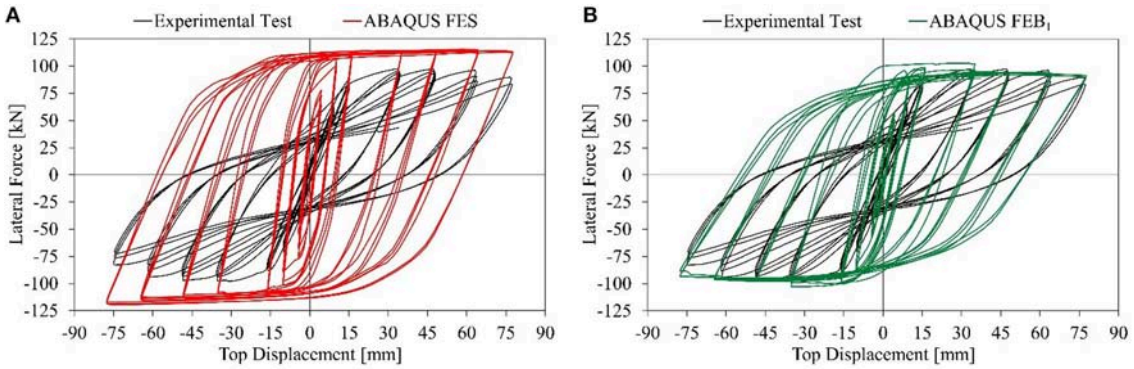

FIGURE 10 | Numerical simulation of DF adopting **(A)** FES model and **(B)** FEB_1 model.

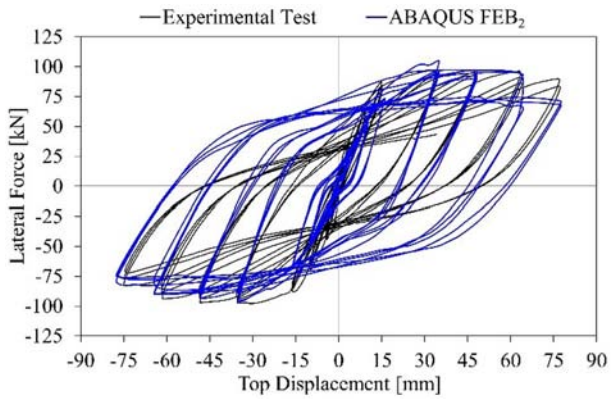

FIGURE 11 | Numerical simulation of DF adopting FEB_2 model.

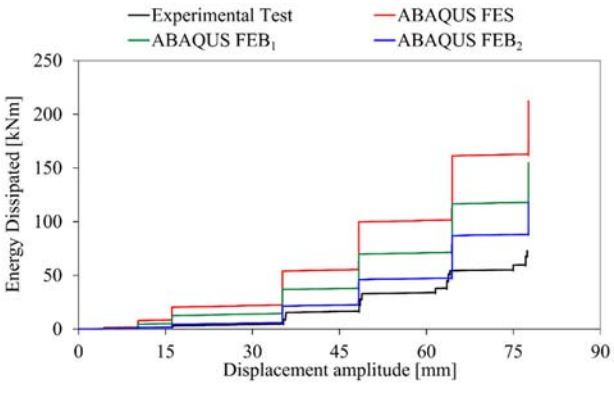

FIGURE 12 | Cumulative dissipated energy obtained for experimental test and numerical models.

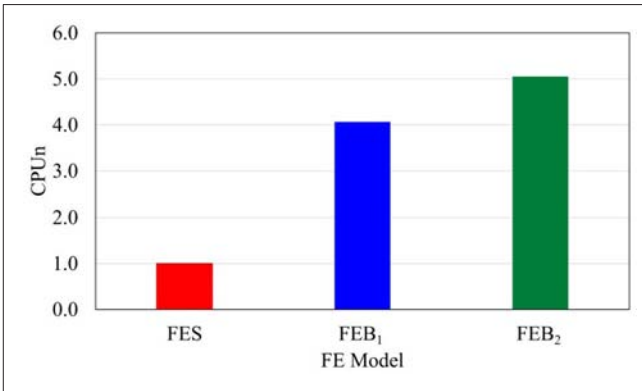

FIGURE 13 | CPU time comparison between FES, FEB_1, and FEB_2.

TABLE 2 | Total energy dissipated for experimental test and numerical models referring to DF.

	Experimental test	ABAQUS FES	ABAQUS FEB_1	ABAQUS FEB_2
ED [kNm]	73.02	228.16	159.58	118.25

loops obtained for high displacement amplitude are significantly influenced by the hysteretic behavior of the steel, which is not characterized by pinching.

The total energy dissipated, ED, is reported in **Table 2**. As expected, ED in the FES and FEB_1 models is significantly higher with respect to the ED of the experimental test, due to the absence of pinching and because of the higher stiffness obtained in these simulations. For FEB_2, a better simulation is obtained, confirming the need of accounting for the bar slip in the simulation of the hysteretic response when dealing with reinforced concrete members.

The efficacy of the proposed model was also assessed by comparing CPU time of the numerical analysis (**Figure 13**). Since the time is significantly influenced by the processor clock rate, the comparison is provided in terms normalized CPU time (CPU_n) referring to the FES model, which is the simplest configuration developed.

As expected, the absence of the discrete cracks in the FES model led to a significant reduction of the CPU time with respect of both FEB_1 and FEB_2. The presence of the macro blocks and, consequently, the inclusion of contact and cohesive laws

increased by 307% the solver time, while by including the bond between concrete and steel rebars the increase was 405%.

Even if more complex and more computationally demanding, the FEB_2 model is still an appealing and simply-to-model alternative for FE analyses with reduced effort with respect to more complex approaches (e.g., Stavridis and Shing, 2010; Yu et al., 2016).

CONCLUSIONS

Different numerical studies focussed on the seismic response of reinforced concrete members pointed out the issues when attempting to accurately reproduce the effects of the cyclic opening and closure of the cracks in concrete when adopting meso- and micro-modeling approaches. In different finite element platforms, mechanical models simulating the concrete tensile response as well as extended finite element methods available allow to accurately reproduce the crack opening process but lead to a significant increase of the computational efforts as well as convergence issues when simulating the effects of the crack opening on the cyclic response of the frames. Furthermore, in some cases the results obtained adopting a smeared cracking approaches show a significant difference compared to the actual behavior observed in experimental tests.

The hybrid modeling approach proposed in the present study was assessed to significantly improve the accuracy of the simulation of the hysteretic loops characterizing the lateral behavior of reinforced concrete members. The smeared cracking approach adopted to define the mechanical response of the concrete was combined with a discrete cracking approach through the introduction of pre-defined cracking path in the regions subjected to higher values of tensile stress.

Contact and cohesive interaction laws were adopted to define the mechanical response along the cracking paths in order to simulate the cyclic crack opening and closure. Two different configurations of the proposed model were developed, in order to evaluate the influence of the simulation of the bond on the accuracy of the matching of the experimental hysteresis loops. The simulation of the test on the double cantilever column evidenced the major limits of the existing model of the concrete in simulating the pinching effect. A better result was obtained adopting the proposed modeling approaches, although the simulation of the bond significantly affected the elastic stiffness. The comparison with a portal frame experimental test available in the literature also showed that the adoption of the smeared cracking approach results in a numerical model unable to accurately reproduce the hysteretic response, while the introduction of discrete cracking paths leads to a better fit of the experimental results in terms of strength and stiffness.

Also in this case, again, the simulation of the bond was found to be fundamental to better reproduce the pinching effect and to obtain a fair matching in terms of energy dissipation capacity.

Despite the significant improvement in the simulation, results of the most sophisticated model with bond showed that for high drift amplitudes the stress developed in shell elements along the cracking surface led to a distortion of the geometry of the concrete region. Consequently, the hysteretic loops corresponding to higher imposed displacement are mostly influenced by the behavior of the steel and pinching becomes less pronounced.

The results obtained are useful to lay the basis for the development of hybrid models to be adopted for the numerical simulation of the cyclic behavior of reinforced concrete members having fairly sustainable computational efforts. Further studies will be conducted in order to increase the accuracy of the simulation even for higher displacement amplitudes.

AUTHOR CONTRIBUTIONS

GB, FD, and MA conceived of the presented idea. All of the authors contributed to the development of the numerical model and carried out a literature review. All authors discussed the results and contributed to the final manuscript.

FUNDING

This work was supported by the Royal Society International Exchange Scheme. Award Number: IE161016. Project: Cumulative damage of masonry infills caused by anthropogenic earthquakes.

REFERENCES

Ballatore, E., Carpinteri, A., Ferrara, G., and Melchiorri, G. (1990). Mixed mode fracture energy of concrete. *Eng. Fract. Mech.* 35, 145–157. doi: 10.1016/0013-7944(90)90192-J

Belytschko, T., Fish, J., and Engelmann, B. E. (1988). A finite element with embedded localization zones. *Comput. Methods Appl. Mech. Eng.* 70, 59–89. doi: 10.1016/0045-7825(88)90180-6

Bocca, P., Carpinteri, A., and Valente, S. (1991). Mixed mode fracture of concrete. *Int. J. Solids Struct.* 27, 1139–1153. doi: 10.1016/0020-7683(91)90115-V

CEB-FIP (2010). *fib Model Code for Concrete Structures*. Ecublens: fib—fédération internationale du béton.

Dassault Systemes (2016). *Abaqus Theory Manual*. Vélizy-Villacoublay.

De Risi, M. T., Ricci, P., and Verderame, G. M. (2017). Modelling exterior unreinforced beam-column joints in seismic analysis of non-ductile RC frames. *Earthq. Eng. Struct. Dyn.* 46, 899–923. doi: 10.1002/eqe.2835

Dolbow, J., Moës, N., and Belytschko, T. (2001). An extended finite element method for modeling crack growth with frictional contact. *Comput. Methods Appl. Mech. Eng.* 190, 6825–6846. doi: 10.1016/S0045-7825(01)00260-2

Duan, A., Li, Z., Zhang, W., and Jin, W. (2017). Flexural behaviour of reinforced concrete beams under freeze–thaw cycles and sustained load. *Struct. Infrastruct. Eng.* 13, 1350–1358. doi: 10.1080/15732479.2016.1268172

EN 1992-1-1(2004). *Eurocode 2: Design of Concrete Structures—Part 1-1: General Rules and Rules for Buildings*. Brussels: European Standard.

Fardis, M. N. (2009). *Seismic Design, Assessment and Retrofitting of Concrete Buildings*. Berlin: Springer.

Giner, E., Sukumar, N., Tarancón, J. E., and Fuenmayor, F. J. (2009). An Abaqus implementation of the extended finite element method. *Eng. Fract. Mech.* 76, 347–368. doi: 10.1016/j.engfracmech.2008.10.015

Gullerud, A. S., Gao, X., Dodds, R. H. Jr., and Haj-Ali, R. (2000). Simulation of ductile crack growth using computational cells: numerical aspects. *Eng. Fract. Mech.* 66, 65–92. doi: 10.1016/S0013-7944(99)00147-2

Karavelić, E., Nikolić, M., Ibrahimbegovic, A., and Kurtović, A. (2017). Concrete meso-scale model with full set of 3D failure modes with random distribution of aggregate and cement phase. Part I: formulation

and numerical implementation. *Comput. Methods Appl. Mech. Eng.* doi: 10.1016/j.cma.2017.09.013. [Epub ahead of print].

Koutromanos, I., and Shing, P. B. (2012). Cohesive crack model to simulate cyclic response of concrete and masonry structures. *ACI Struct. J.* 109, 349–358. doi: 10.14359/51683748

Lee, J., and Fenves, G. (1998). Plastic-damage model for cyclic loading of concrete structures. *J. Eng. Mech.* 124, 892–900. doi: 10.1061/(ASCE)0733-9399(1998)124:8(892)

Liao, F., and Huang, Z. (2015). An extended finite element model for modelling localised fracture of reinforced concrete beams in fire. *Comput. Struct.* 152, 11–26. doi: 10.1016/j.compstruc.2015.02.006

Lotfi, H. R., and Shing, P. B. (1991). An appraisal of smeared crack models for masonry shear wall analysis. *Comput. Struct.* 41, 413–425. doi: 10.1016/0045-7949(91)90134-8

Lubliner, J., Oliver, J., Oller, S., and Oñate, E. (1989). A plastic-damage model for concrete. *Int. J. Solids Struct.* 25, 299–326. doi: 10.1016/0020-7683(89)90050-4

Mander, J. B., Priestley, M. J., and Park, R. (1988). Theoretical stress–strain model for confined concrete. *J. Struct. Eng.* 114, 1804–1826. doi: 10.1061/(ASCE)0733-9445(1988)114:8(1804)

Mehta, P. K., and Monteiro, P. J. M. (2006). *Concrete: Microstructure, Properties, and Materials*. SanFrancisco, CA: McGraw-Hill.

Moës, N., and Belytschko, T. (2002). Extended finite element method for cohesive crack growth. *Eng. Fract. Mech.* 69, 813–833. doi: 10.1016/S0013-7944(01)00128-X

Nikaido, Y., Mihara, Y., Sawada, S., and Takahashi, Y. (2015). Improvement and enhancement of concrete damage plasticity model. *Simulia Community Conf. Proc.* 2015, 1–10. Available online at: https://pdfs.semanticscholar.org/bf23/16970d642230cb0e98cb7cadc5b9eb6c462f.pdf

Nikolić, Ž., Živaljić, N., Smoljanović, H., and Balić, I. (2017). Numerical modelling of reinforced-concrete structures under seismic loading based on the finite element method with discrete inter-element cracks. *Earthq. Eng. Struct. Dyn.* 46, 159–178. doi: 10.1002/eqe.2780

NTC08 (2008). *Nuove Norme Tecniche per le Costruzioni*. Rome: Ministero delle Infrastrutture.

Ohue, M., Morimoto, H., Fujii, S., and Morita, S. (1985). The behavior of R.C. short columns failing in splitting bond-shear under dynamic lateral loading. *Trans. Jpn. Concr. Inst.* 7, 293–300.

Oliveira, D. V., and Lourenço, P. B. (2004). Implementation and validation of a constitutive model for the cyclic behaviour of interface elements. *Comput. Struct.* 82, 1451–1461. doi: 10.1016/j.compstruc.2004.03.041

Ors, D. M. F., Okail, H. O., and Zaher, A. H. (2016). Modeling of shear deficient beams by the mixed smeared/discrete cracking approach. *HBRC J.* 12, 123–136. doi: 10.1016/j.hbrcj.2014.11.002

Powell, M. J. D. (1969). "A method for nonlinear constraints in minimization problems," in *Optimization*, ed R. Fletcher (New York, NY: Academic Press), 283–298.

Pramono, E., and Willam, K. (1989). Fracture energy-based plasticity formulation of plain concrete. *J. Eng. Mech.* 115, 1183–1204. doi: 10.1061/(ASCE)0733-9399(1989)115:6(1183)

Redmond, L., Stavridis, A., Kahn, L., and DesRoches, R. (2018). Finite-element modeling of hybrid concrete-masonry frames subjected to in-plane loads. *J. Struct. Eng.* 144:4017178. doi: 10.1061/(ASCE)ST.1943-541X.0001913

Sinaei, H., Shariati, M., Abna, A. H., Aghaei, M., and Shariati, A. (2012). Evaluation of reinforced concrete beam behaviour using finite element analysis by ABAQUS. *Sci. Res. Essays* 7, 2002–2009. doi: 10.5897/SRE11.1393

Sinaie, S., Ngo, T. D., and Nguyen, V. P. (2018). A discrete element model of concrete for cyclic loading. *Comput. Struct.* 196, 173–185. doi: 10.1016/j.compstruc.2017.11.014

Sneed, L. H., Verre, S., Carloni, C., and Ombres, L. (2016). Flexural behavior of RC beams strengthened with steel-FRCM composite. *Eng. Struct.* 127, 686–699. doi: 10.1016/j.engstruct.2016.09.006

Stavridis, A., and Shing, P. B. (2010). Finite-element modeling of nonlinear behavior of masonry-infilled RC frames. *J. Struct. Eng.* 136, 285–296. doi: 10.1061/(ASCE)ST.1943-541X.116

Sümer, Y., and Aktaş, M. (2015). Defining parameters for concrete damage plasticity model. *Chall. J. Struct. Mech.* 1, 149–155. Available online at: http://oaji.net/articles/2015/2440-1445612389.pdf

Tvergaard, V., and Hutchinson, J. W. (1996). Effect of strain-dependent cohesive zone model on predictions of crack growth resistance. *Int. J. Solids Struct.* 33, 3297–3308. doi: 10.1016/0020-7683(95)00261-8

Vamvatsikos, D., and Fragiadakis, M. (2010). Incremental dynamic analysis for estimating seismic performance sensitivity and uncertainty. *Earthq. Eng. Struct. Dyn.* 39, 141–163. doi: 10.1002/eqe.935

Verderame, G. M., Ricci, P., Del Gaudio, C., and De Risi, M. T. (2016). "Experimental tests on masonry infilled gravity- and seismic-load designed RC frames," in *16th International Brick and Block Masonry Conference* (Padova), 1349–1358.

Viswanathan, T. S., Ganesh, G. M., and Santhi, A. S. (2014). Investigation of shear stud performance in flat plate using finite element analysis. *J. Eng. Technol. Sci.* 46, 328–341. doi: 10.5614/j.eng.technol.sci.2014.46.3.7

Yu, J., Yu, K., Shang, X., and Lu, Z. (2016). New extended finite element method for pinching effect in reinforced concrete columns. *ACI Struct. J.* 113, 689–699. doi: 10.14359/51688747

Zi, G., and Belytschko, T. (2003). New crack-tip elements for XFEM and applications to cohesive cracks. *Int. J. Numer. Methods Eng.* 57, 2221–2240. doi: 10.1002/nme.849

Živaljić, N., Nikolić, Ž, and Smoljanović, H. (2014). Computational aspects of the combined finite-discrete element method in modelling of plane reinforced concrete structures. *Eng. Fract. Mech.* 131, 362–389. doi: 10.1016/j.engfracmech.2014.10.017

Zivaljic, N., Smoljanovic, H., and Nikolic, Z. (2013)A combined finite-discrete element model for RC structures under dynamic loading. *Eng. Comput.* 30, 982–1010. doi: 10.1108/EC-03-2012-0066

Conflict of Interest Statement: The authors declare that the research was conducted in the absence of any commercial or financial relationships that could be construed as a potential conflict of interest.

frontiers in Built Environment

ORIGINAL RESEARCH
published: 07 January 2019
doi: 10.3389/fbuil.2018.00080

A Comparison of Three Different Methods for the Identification of Hysterically Degrading Structures Using BWBN Model

Ying Zhao[1], *Mohammad Noori*[1,2]*, *Wael A. Altabey*[1,3,4] *and Taher Awad*[4]

[1] International Institute for Urban Systems Engineering, Southeast University, Nanjing, China, [2] Department of Mechanical Engineering, California Polytechnic State University, San Luis Obispo, CA, United States, [3] Nanjing Zhixing Information Technology Company, Nanjing, China, [4] Department of Mechanical Engineering, Faculty of Engineering, Alexandria University, Alexandria, Egypt

Structural control and health monitoring scheme play key roles not only in enhancing the safety and reliability of infrastructure systems when they are subjected to natural disasters, such as earthquakes, high winds, and sea waves, but it also optimally minimize the life cycle cost and maximize the whole performance through the full life cycle design. In this scheme, system identification is regarded as a major technique to identify system states and related parameter variables, thus preventing degradation of structural or mechanical systems when unexpected disturbances occur. In this paper, three different strategies are proposed to identify general hysteretic behavior of a typical shear structure subjected to external excitations. Different case studies are presented to analyze the dynamic responses of a time varying shear structural system with the early version of Bouc-Wen-Baber-Noori (BWBN) hysteresis model. By incorporating a "Gray Box" strategy utilizing an Intelligent Parameter Varying (IPV) and Artificial Neural Network (ANN) approach, a Genetic algorithm (GA), and a Transitional Markov Chain Monte Carlo (TMCMC) based Bayesian Updating framework system identification schemes are developed to identify the hysteretic behavior of the structural system. Hysteresis characteristics, computational accuracy, and algorithm efficiency are further discussed by evaluating the system identification results. Results show that IPV performs superior computational efficiency and system identification accuracy over GA and TMCMC approaches.

Keywords: hysteretic behavior, BWBN model, Intelligent Parameter Varying (IPV), Genetic algorithm (GA), Transitional Markov Chain Monte Carlo simulation (TMCMC), Bayesian updating

OPEN ACCESS

Edited by:
Vagelis Plevris, OsloMet – Oslo Metropolitan University, Norway

Reviewed by:
Aristotelis E. Charalampakis, National Technical University of Athens, Greece
Eleni N. Chatzi, ETH Zürich, Switzerland

***Correspondence:**
Mohammad Noori
mnoori@outlook.com

Specialty section:
This article was submitted to Computational Methods in Structural Engineering, a section of the journal Frontiers in Built Environment

Received: *16 October 2018*
Accepted: *11 December 2018*
Published: *07 January 2019*

Citation:
Zhao Y, Noori M, Altabey WA and Awad T (2019) A Comparison of Three Different Methods for the Identification of Hysterically Degrading Structures Using BWBN Model. Front. Built Environ. 4:80. doi: 10.3389/fbuil.2018.00080

INTRODUCTION

In recent years, an increasing attention is witnessed to face the challenging issues of safety, serviceability, reliability, risk and life-cycle management, and performance improvement of structures and infrastructure due to changing and more frequently occurring natural and man-made hazards, infrastructure crisis, and sustainability issues. These disturbances are dealt with innovative technologies to enhance structural functionality and safety in various stages of research and development (Spencer, 2003; Altabey, 2017a). Several types of structures that employ control

strategies for different application scopes can be found in Constantinou et al. (1998), Soong and Spencer (2002), and Altabey (2014, 2017b,c); Altabey (2018). Proper modeling of inherent non-linearity in vast majority of structural systems plays an important role in understanding structural response under hazardous loadings. System identification is an important approach in control strategy regarded as the interface between the mathematical world of control theory and the real world of application and model abstractions (Zadeh, 1956; Ljung, 2010; Altabey, 2016, 2017d,e; Altabey and Noori, 2017a, 2018; Zhao et al., 2018), and it handles a wide range of system dynamics problem without the prior knowledge of actual system physics. The schematic diagram of system identification process is depicted in **Figure 1**.

Hysteresis can be described as the hereditary and memory nature of a non-linear or inelastic system behavior where the restoring force is dependent on both instantaneous as well as past history of deformations. In general, under cyclic loading, mechanical and structural systems are capable of dissipating considerable energy and they exhibit appreciable hysteretic behavior with hysteresis loops. Each loop enclosing the area in the restoring force vs. displacement curve depicts the energy dissipated over a complete cycle resulting from internal friction within the structural system.

Various empirical hysteresis models have been proposed in the past few decades. A class of smoothly varying hysteresis models used in engineering fields are Bouc-Wen class of hysteresis models. Bouc suggested a smooth and versatile hysteresis model for non-linear systems and hysteretic systems (Bouc, 1967; Wen, 1975, 1976, 1980, 1986, 1989; Park et al., 1986; Wen and Yeh, 1989; Ikhouane and Rodellar, 2007; Ikhouane et al., 2007; Ikhouane and Gomis-Bellmunt, 2008). Baber and Wen extended the Bouc model to take the degradation in strength or stiffness of structural systems into account (Baber and Wen, 1980). Baber-Noori, and later Noori, further extended the capabilities of Bouc-Wen model by including pinching behavior and studied the response of these systems under random excitation (Noori, 1984; Baber and Noori, 1986). Baber-Noori and subsequently Noori-Baber's work on integrating the pinching phenomenon in hysteretic behavior and extending Bouc-Wen-Baber (BWB) model was the first work in developing a smooth hysteresis model capable of taking into account strength and stiffness degradation as well as shear pinching phenomenon (Baber and Noori, 1985). BWBN was incorporated in structural design software, OpenSees developed at the University of California Berkeley (Hossain, 1995). A toolbox for computing the parameters of BWBN hysteresis model using multi-objective optimization evolutionary algorithms was also developed by SourceForge, an Open Source community (*Bouc Wen Baber Noori Model of Hysteresis, Source Forge*). Foliente showed Bouc-Wen-Baber-Noori (BWBN) model could produce previously observed inelastic behavior of wood joints and structural systems using BWBN smooth hysteresis model (Foliente, 1995; Zhao et al., 2017a,b; Noori et al., 2018). Deb et al. developed a toolbox that identifies structural parameters of Bouc–Wen–Baber–Noori hysteresis model through a noval multi-objective optimization evolutionary algorithms (MOBEAs) (Deb et al., 2002; Deb, 2013). Ortiz et al. analyzed and identified BWBN model via a multi-objective optimization algorithm (Ortiz et al., 2013). Peng et al. utilized BWBN model for identifying the parameters of a magneto-rheological damper and depicts its force-lag phenomenon (Peng et al., 2014). Muller et al. investigated the application of BWBN in their work and conducted performance-based seismic design through a Search-Based Cost Optimization (Muller et al., 2012). Chan et al. made a prediction of the hysteretic behavior of passive control systems by applying BWBN in a nonlinear-autoregressive-exogenous model (Chan et al., 2015).

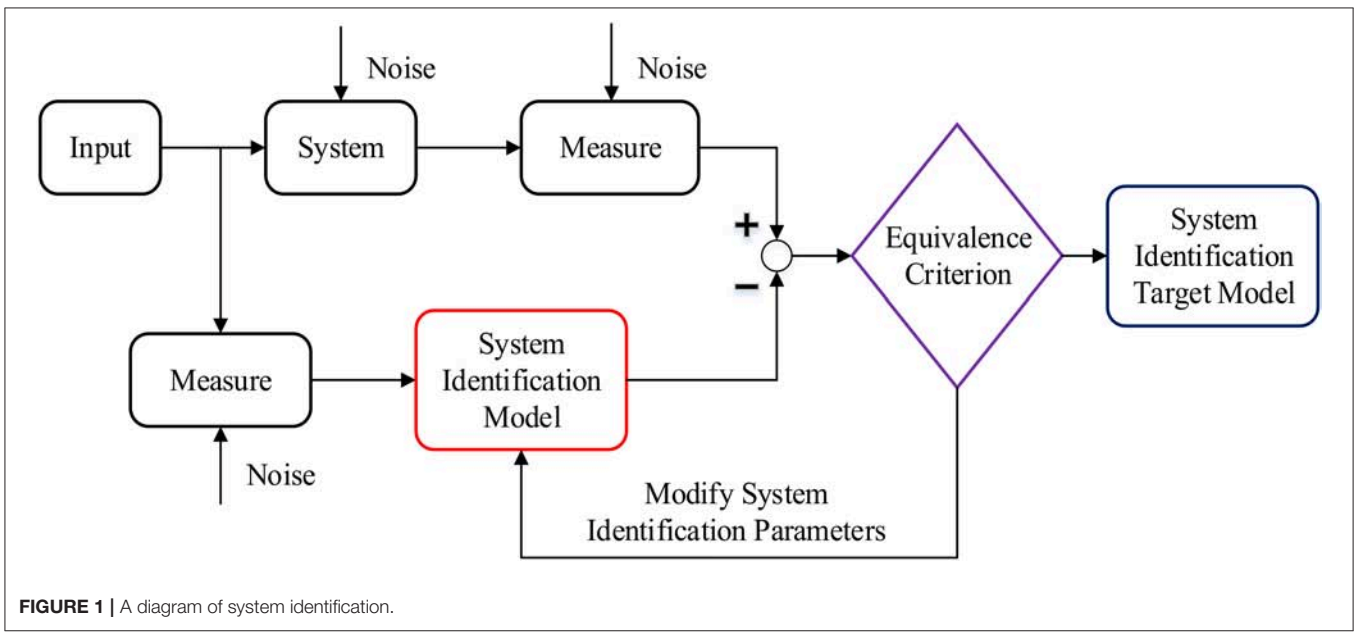

FIGURE 1 | A diagram of system identification.

Traditional artificial neural networks technique shows its superiority in the identification, monitoring, and control of complicated and non-linear dynamic systems (Narendra and Parthasarathy, 1990; Masri et al., 1992; Lu and Basar, 1998; Abouelwafa et al., 2014; Altabey and Noori, 2017b). However, a priori knowledge of the characteristics of restoring force is necessary and important for traditional parametric system identification approaches, while the non-parametric methods do not need information beforehand, lacking direct association between system dynamics and system model. In order to overcome the limitations of conventional parametric and non-parametric approaches, an noval Intelligent Parameter Varying (IPV) method was proposed, which makes full use of the embedded radial basis function networks to make an estimation of the hysteretic and inelastic characteristics of restoring forces constitutively for a multi degree of freedom system. A scaled three story base excited structure was designed to experimentally verify the non-linearity and its associated hysteresis of a structure using a displacement controlled shaking table (Saadat et al., 2003, 2004a,b, 2007). Further, a data-driven identification strategy for non-linear and hysteretic behaviors of steel wire strands was compared and verified using polynomial basis functions and neural networks. The results showed that neural networks were found more promising for the prediction of slightly pinched, hardening hysteresis, strongly pinched, hardening hysteresis, and classical quasi-linear softening hysteresis (Brewick et al., 2016). Genetic algorithms have been used for system identification of non-linear and hysteretic systems. The application of Real Coded Genetic Algorithms (RCGA) was demonstrated and applied to fit curves of synthetic and experimentally obtained Bouc-Wen hysteresis loops for a sandwich composite material (Hornig and Flowers, 2005). Different real coded genetic algorithms and their related criteria for efficiently identifying non-linear systems are regards as non-classical and optimized identification techniques (Monti et al., 2009). A Bayesian probabilistic framework was proposed to detect damage of continuous monitored structures by incorporating load-dependent Ritz vectors as an alternative to modal vectors (Sohn, 1998). A large body of work was conducted to track, estimate and identify structural parameters, system status and hysteretic and degrading behavior of structures using Kalman filters, extended Kalman filters and unscented Kalman filters (Jeen-Shang and Yigong, 1994; Yang et al., 2006; Wu and Smyth, 2007, 2008; Chatzi and Smyth, 2009; Chatzi et al., 2010; Lei and Jiang, 2011; Mu et al., 2013; Kontoroupi and Smyth, 2017; Erazo and Nagarajaiah, 2018). Traditional Markov Chain Monte Carlo approach in conjunction with Bayesian updating method were applied for structural response predictions and performance reliability evaluation (Yuen and Katafygiotis, 2001; Zhang and Cho, 2001; Beck and Au, 2002). Later, a transitional Markov Chain Monte Carlo (TMCMC) approach was developed by designing optimized sampling strategy from a series of intermediate probability density functions (PDFs) that converge to the target PDF, thus avoiding sampling difficulties. The TMCMC theory and algorithm were verified and demonstrated through the performance of the developed sampling approach, different PDFs as well as higher dimensional problems (Ching and Chen, 2007; Muto, 2007; Muto and Beck, 2008; Worden and Hensman, 2012; Zheng and Yu, 2013; Behmanesh and Moaveni, 2014; Green, 2015; Green et al., 2015; Ortiz et al., 2015).

It is a major barrier to successfully design hysteretic structures against degradation under severe cyclic loading. Most structural systems degrade with significant hysteresis, for example wood structures, dams, highways, reinforced concrete towers, steel bridges are critical and key elements of our built environment. In spite of their obvious importance, and their huge rehabilitation and replacement costs, design, construction, and analysis of the majority of these structures requires overly simplistic or in some cases flawed assumptions regarding hysteretic evolution. Development of a practical structural degrading identification approaches is much deserving. A comparative study of online and offline identification strategies for UAVs were discussed, and it is found that online approach is more adaptive to changes but with lower prediction accuracy (Puttige and Anavatti, 2007). Therefore, offline learning is employed in this paper. Based on what was discussed in the introduction above, the main contributions of the research are to present a three story hysteretically degrading shear structure by incorporating BWBN slip lock hysteresis to represent the hysteretic restoring forces in this system. This BWBN model will be capable of producing all significant and prominent features of structural strength and stiffness degradations as well as slip lock behavior, and conduct a comparative study using three system identification approaches including an Intelligent Parameter Varying Artificial Neural Network developed in an earlier research work by a group that involved one of the authors (a "gray box" model that considers linear as well as non-linear parts of the dynamic system), genetic algorithm optimization method, and a novel TMCMC statistical approach.

The comparative study of the aforementioned approaches for system identification and their application in a structural system using *BWBN MODEL* is an original work. To the best of the authors' knowledge such comparative study has not been reported in the literature.

STRUCTURAL SYSTEM MODELING AND SYSTEM IDENTIFICATION

BWBN Hysteresis Model

The model employed herein is an earlier version of BWBN hysteresis degradation model, which incorporates the previous smooth system degrading element by Bouc as modified by Baber and Wen in series with a slip-lock element (a non-linear hardening spring) developed by Baber and Noori. Under cyclic excitation, degradation manifests itself in the evolution of progressively varying hysteresis loops. A non-linear system governed by Equation (1) is given with the incorporation of BWBN model.

$$m\ddot{x} + c\dot{x} + R = F(t) \tag{1}$$

$$R = \alpha kx + (1-\alpha)\, kz \tag{2}$$

$$\dot{z} = \frac{A\dot{x}_1 - \nu\left[\beta\,|\dot{x}_1|\,|z|^{n-1}\, z + \gamma\dot{x}_1\,|z|^n\right]}{\eta} \tag{3}$$

$$\dot{x}_2 = \sqrt{\frac{2}{\pi}}\frac{s}{\sigma}\exp\left[-\frac{z^2}{2\sigma^2}\right]\dot{z} \tag{4}$$

$$\dot{\varepsilon} = (1-\alpha)\,k\dot{x}z \tag{5}$$

$$s = \delta_s\varepsilon \tag{6}$$

$$(x = x_1 + x_2) \tag{7}$$

where, parameters m, c, k are, respectively, the mass, damping, and stiffness coefficients, and parameters $\ddot{x}$, $\dot{x}$, x are quantities that describe the system acceleration, velocity and displacement, and R is the restoring force and $F(t)$ is the ambient excitation. Parameter α is the weighting value denoting the ratio of post-elastic to initial stiffness. Parameters A, β, and γ are basic hysteresis shape control parameters. Parameter z is the hysteretic displacement, and n is the degree of the sharpness of yield. Strength and stiffness degradation coefficients are, respectively denoted by $\nu(\delta_\nu)$ and $\eta(\delta_\eta)$. Parameters x_1 and x_2 are Bouc-Wen hysteretic system displacement and the additional displacement that considers slip-lock behavior. Parameter ε is the measure of the combined effect of duration and severity of the energy dissipated through hysteresis, σ is a measure of the sharpness of the peak of the hysteresis, and δ_s measures the slip magnitude. All 10 parameters are essential to produce the common features of hysteretic behavior. It would be very helpful if a small number of unspecified parameters for system identification can be reduced in that large numbers of parameters increase the uncertainty of convergence for updating parameters in search space. It was proved that the redundancy of specific hysteresis parameters can be eliminated through mathematical transformations in the parameter space devised to freeze them without affecting the system response (Ma et al., 2004; Charalampakis and Koumousis, 2008a,b; Charalampakis and Dimou, 2010).

Structural System Modeling

Restoring force curves of reinforced or steel structures show complex hysteresis characteristics, revealing material non-linearity, crack opening and closing, bond and slip between steel bars and concrete and low cycle fatigue that result in structural strength and stiffness degradation. The hysteresis model used herein considers the specific case appropriate for both strength and stiffness degradations, and slip-lock behavior of restoring hysteretic forces of the structure. All the restoring forces of the structure are assumed to follow the BWBN hysteresis model. The structural system considered in this study is a shear type model subjected to ambient sinusoidal wave and ElCentro seismic excitation as input signals $\ddot{x}_g$. The ground excitation motion $\ddot{x}_g$ makes an integral transformation to be incorporated into the structural equations. The structural system mainly includes three lumped mass coupled subsystems, as shown in **Figure 2**. These masses are lumped at floor (floor m_i), levels and these floors are assumed and constrained to only move laterally. The restoring force R_i , in conjunction with the stiffness between the adjacent floors, are represented by dampers and springs, with the corresponding coefficients c_i and k_i, respectively. The time varying system yields energy dissipation due to the hysteretic behavior of the inner structure.

For this three story shear structure, the equations of motion are represented by Equations (8–10):

$$m_3\ddot{x}_3 + c_3(\dot{x}_3 - \dot{x}_2) + R_3 = 0 \tag{8}$$

$$m_2\ddot{x}_2 + c_2(\dot{x}_2 - \dot{x}_1) + R_2 - c_3(\dot{x}_3 - \dot{x}_2) - R_3 = 0 \tag{9}$$

$$m_1\ddot{x}_1 + c_1(\dot{x}_1 - \dot{x}_g) + R_1 - c_2(\dot{x}_2 - \dot{x}_1) - R_2 = 0 \tag{10}$$

System Identification Theory

A typical system identification framework mainly has two components including system itself and system identification model. By defining an equivalence criterion, the parameters of the system identification model are updated via a comparison with the original system, until the system identification model will be eventually equivalent to the original system. System identification approaches used in this paper include intelligent parameter varying based approach, GA based approach and transitional markov chain monte carlo (TMCMC) based approach. IPV approach employs ANNs and establishes a "Gray Box" system, where the original system parameters are replaced by the parameters of ANNs, and the system structure is replaced by ANNs. For GA and TMCMC methods, they are used to optimize and identify the parameters of system model, which is regarded as an approximate model of the original real system. The

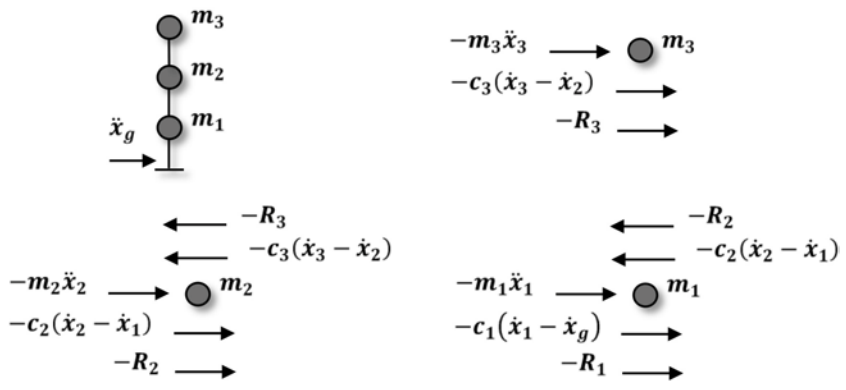

FIGURE 2 | Structural lumped mass model.

theoretical background for the three approaches are presented in the following subsections.

Intelligent Parameter Varying Based System Identification

Artificial neural network (ANN) is a non-linear and adaptive information processing system composed of large numbers of neuron units. A radial basis function (RBF) neural network is employed to build the intelligent parameter varying model. In ANN architecture, the Euclidean distance between the clustering center and input vector is calculated and the result is activated to pass through the output layer. The activation function is Gaussian output function and is formulated as:

$$g_j = \exp\left(-\frac{\sum_{i=1}^{n}\left(x_i - c_j\right)^2}{\sigma_j^2}\right) \tag{11}$$

where g_j is the output of the j^{th} unit in the hidden layer, x_i is the input data fed to the network, c_j is the center of the j^{th} unit in the input space, and σ_j is the width of the j^{th} function. $j = 1, 2, \cdots, m$. Parameter m is the number of the centers of neurons, and n represents the dimension of the input space. Linearly weighted summation of hidden layer node outputs produces the output nodes. Therefore, the output of the network is calculated by:

$$y = \sum_{j=1}^{n} w_j g_j \tag{12}$$

where w_j is the weight of the j^{th} node.

The objective is to find a series of weights that minimize the square of error between the actual and desired network outputs, i.e.,:

$$E\left(k\right) = \frac{1}{2}\sum_{j=1}^{N}\left(d\left(k\right) - y\left(k\right)\right)^2 \tag{13}$$

where $d(k)$ is the desired output and $y(k)$ the actual output of RBF and $j = 1, 2, \cdots, N$, and N is the number of data sets. There are commonly two approaches for utilizing ANNs, i.e., supervised and unsupervised learning. In supervised approach the input and the referred output are usually known. The network then processes the input values and makes a comparison between its resulting output and the desired output. The network system makes the errors propagate back through different layers, causing the system to adjust tuned weights which control the network. This process repeats over and over until all the weights are continually tweaked in an appropriate way. During the training process of a network the connection weights are continually refined to a specific generalization level and a good network performance level. In unsupervised training, the system itself must then decide what features and how many features need to be extracted to group the input data, which is often referred to as self-organization or adaption. Herein, we use the non-supervised learning algorithm to acquire the centers and variance of radial basis function, and meanwhile the least mean squared error is acquired by using supervised learning algorithm. The response of the hysteretic system is used as the desired signal, and the error between the desired signal and the simulated signal is back propagated to modify the weights and threshold values of neural network model.

Parametric system identification approaches have been widely used but in most published literature in this area a priori knowledge of the characteristics depicting the behavior of restoring force is required. Non-parametric approaches generally do not need information beforehand but they typically lack direct associations between system dynamics and associated model. When ANNs are implemented using the "Black Box" approach, little of the system information might be obtained from the traditional techniques due to the fact that the "Black Box" only considers system input and output. Intelligent Parameter Varying (IPV) method preserves the benefits of both traditional parametric and non-parametric approaches, and utilizes the embedded radial basis function as the activation of neurons to estimate the constitutive characteristics of inelastic and hysteretic restoring forces for a multi degree of freedom structural system.

IPV technique, i.e., a gray box approach (**Figure 3**) that incorporates the advantages of both "White Box" and "Black Box" approaches, was developed in such a way that the model structure can be determined using the first principle (Equations 18–20), while non-linear and adaptive learning capabilities of ANNs can be used to identify the non-linear, time varying system's dynamics (Equations 24–26) that would be difficult to model and identify using the traditional "White Box" and "Black Box" (Saadat et al., 2003, 2004a,b, 2007).

A non-linear system with full state measurement represented by the Linear Parameter Varying (LPV) model structure is given by:

$$\dot{x} = f_1\left(x, u\right) \cdot x + f_2\left(x, u\right) \cdot u \tag{14}$$

$$y = x \tag{15}$$

The IPV approach introduced herein would preserve the model structure inherent in Equation (14) without requiring a priori representations of non-linearities $f_1(x, u)$ and $f_2(x, u)$. Instead, these terms would be represented by separate artificial neural networks $g_1(x, u, w_1)$ and $g_2(x, u, w_2)$ as depicted in Equations (16, 17):

$$\dot{x} = g_1\left(x, u, w_1\right) \cdot x + g_2\left(x, u, w_2\right) \cdot u \tag{16}$$

$$y = x \tag{17}$$

By modeling the non-linearities $f_1(x, u)$ and $f_2(x, u)$ via separate artificial neural networks $g_1(x, u, w_1)$ and $g_2(x, u, w_2)$, the model structure (Equations 16, 17) is preserved. Therefore, the relationship between the model structure and artificial neural network parameters is preserved. The structural model is preserved by incorporating ANN, preserving a portion of information of the structural model. The IPV approach preserves the direct association between the construction of ANN and the system dynamics, used for structural health monitoring for system identification.

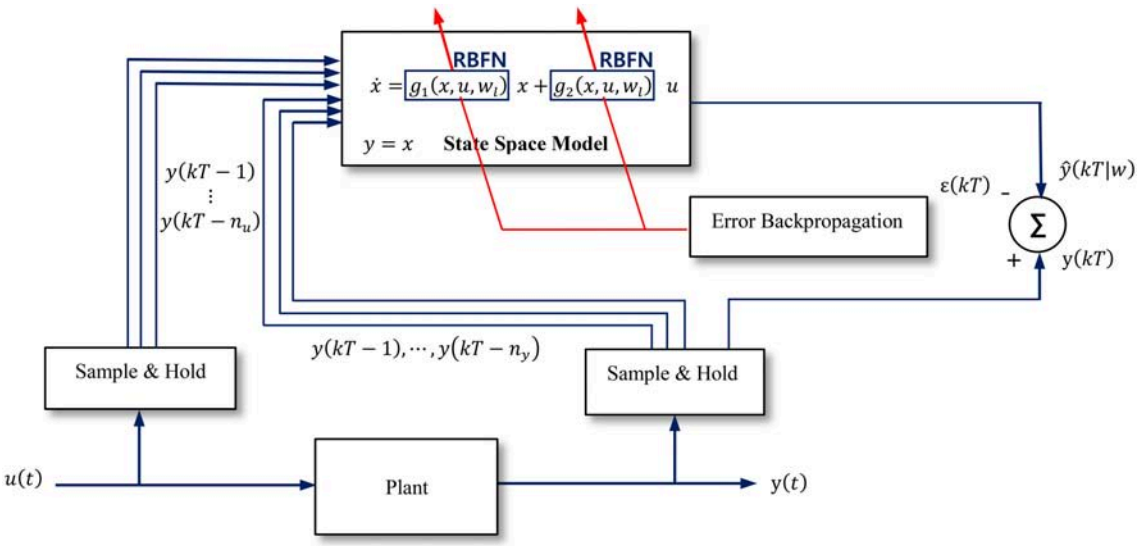

FIGURE 3 | System identification using gray box.

Based on first principle, system dynamics can be transformed to the following form:

$$-c_3(\dot{x}_3-\dot{x}_2)-R_3-m_3\ddot{x}_g=m_3\ddot{u}_3 \quad (18)$$

$$-c_2(\dot{x}_2-\dot{x}_1)-R_2+c_3(\dot{x}_3-\dot{x}_2)+R_3-m_2\ddot{x}_g=m_2\ddot{u}_2 \quad (19)$$

$$-c_1(\dot{x}_1-\dot{x}_g)-R_1+c_2(\dot{x}_2-\dot{x}_1)+R_2-m_1\ddot{x}_g=m_1\ddot{u}_1 \quad (20)$$

where u_1, u_2, u_3, respectively represent the relative displacements of each floor, i.e., $u_1 = x_1 - x_g$, $u_2 = x_2 - x_g$, $u_3 = x_3 - x_g$.

$$-R_3-m_3\ddot{x}_g=m_3\ddot{u}_3 \quad (21)$$

$$-R_2+R_3-m_2\ddot{x}_g=m_2\ddot{u}_2 \quad (22)$$

$$-R_1+R_2-m_1\ddot{x}_g=m_1\ddot{u}_1 \quad (23)$$

The stiffness and damping terms are lumped into restoring forces, since in the hysteresis models the restoring force R associates with the lateral relative displacement x_r and the restoring displacement z, where z is expressed by the function of lateral relative velocity $\dot{x}_r$.

The modeling for the restoring forces using radial basis function based neural network is as follows:

$$\hat{R}_3 = g_3(\ddot{u}_3, \ddot{x}_g) \quad (24)$$

$$\hat{R}_2 = g_2(\ddot{u}_2, \ddot{x}_g, \hat{R}_3) \quad (25)$$

$$\hat{R}_1 = g_1(\ddot{u}_1, \ddot{x}_g, \hat{R}_2) \quad (26)$$

where, $\hat{R}_1, \hat{R}_2, \hat{R}_3$ represent, respectively, the identified restoring forces through the training of ANN as shown in **Figure 4**.

Genetic Algorithm Based System Identification

Genetic algorithm (GA) is an approach that searches the global optimal solution by simulating a natural evolution process. The objective function can be formulated as the normalized mean square error (MSE) of the predicted time history $\tilde{y}(t|p)$ as compared to the reference time history $y(t)$. Herein, the acceleration response signal is employed as the time history series. The purpose of the following optimization approach is to minimize the difference (or the error) between predicted time history and the referred time history. The hysteretic structural system objective function is introduced below:

$$OF(p) = \frac{\sum_{i=1}^{n}\left(y(t_i)-\tilde{y}(t_i|p)\right)^2}{N\sigma_y^2} \quad (27)$$

where p is a parameter vector, σ_y^2 the variance of the reference history, and N the number of points used. Sum of three acceleration response signal differences of the hysteretic structural system is used as the objective function. The optimization problem can be stated as the minimization of the objective function $OF(p)$ when the parameter vector has the following side constraints as:

$$x_{LB} \le p \le x_{UB} \quad (28)$$

where x_{LB} and x_{UB} are vectors defining the lower and the upper values of the model parameters, respectively. The basic strategy for the parameter identification using GA is shown in **Figure 5**. GA operates starting from a population of the potential solutions to a representive problem, and one population is composed of numbers of individuals coded by genes. Each individual is chromosomes with the characteristics of entity. GA initializes on a population of individuals (coded candidate solutions to the problem) that are manipulated by some operators such as selection, crossover, and mutation. In short, the selection process drives the search direction toward the region of best individuals, and the cross operator combines individuals to generate offsprings.

If it is indispensable to make selection and crossover operators converge toward the optimum, mutation alters one or more gene values (individuals) in a chromosome from its initial state, thus, maintaining genetic diversity from one generation of a population to the next. In this way, a complete exploration of global search space is forced by algorithm within the search space. Each individual in the population is represented as chromosome, indicating the collection of parameters are supposed to identify. GA adopts an elitist strategy, which consists of the preservation of the most fit individuals obtained in the current generation. Population representation and initialization generate population and individuals, and the initialized value will be assigned to the parameter space for solving the hysteretic system model. The fitness function is established by using the prediction error between the simulated signal response and predicted signal response. After a series of successive mathematical operators for optimization, the next generational loop begins.

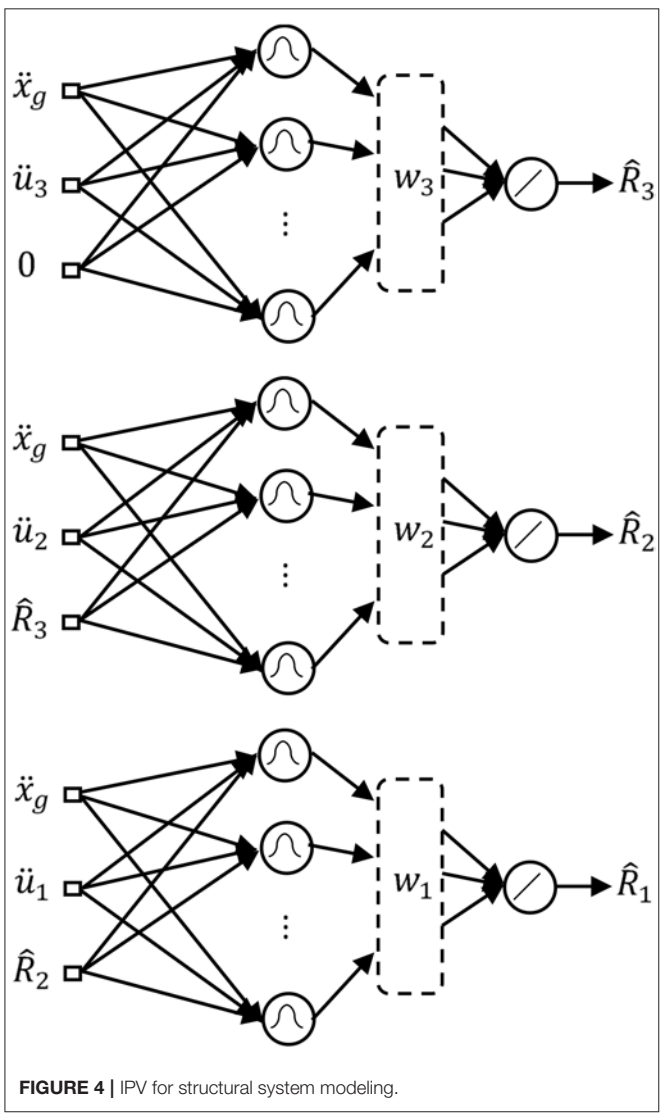

FIGURE 4 | IPV for structural system modeling.

Transitional Markov Chain Monte Carlo Based System Identification

Markov Chain Monte Carlo (MCMC) is an analytic approach which replaces numerical integration through summation over numbers of samples generated from iteration. A Markov chain is a stochastic process where one state is transformed to another state after a sufficiently long sequence of transition procedure. The next state is conditionally based on the last state. A key property of Markov chain is that the starting state has no influence on the state of the chain via a series of sequential transitions. The chain reaches its steady state at a specific point

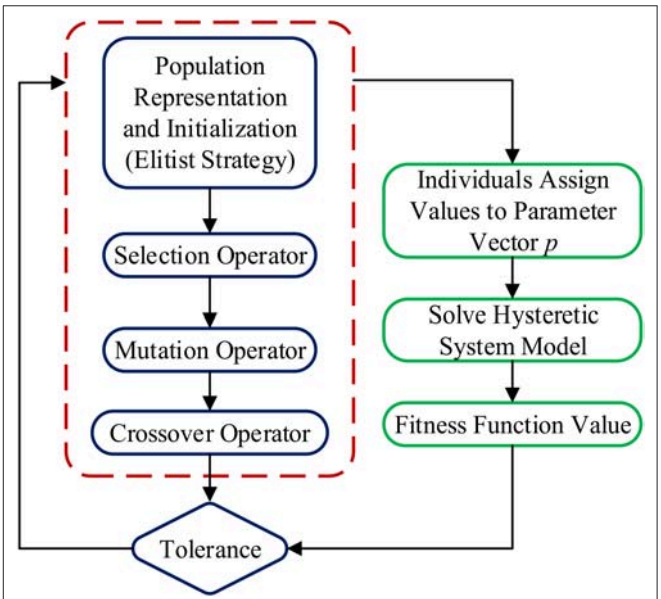

FIGURE 5 | A flow chart of system identification using GA.

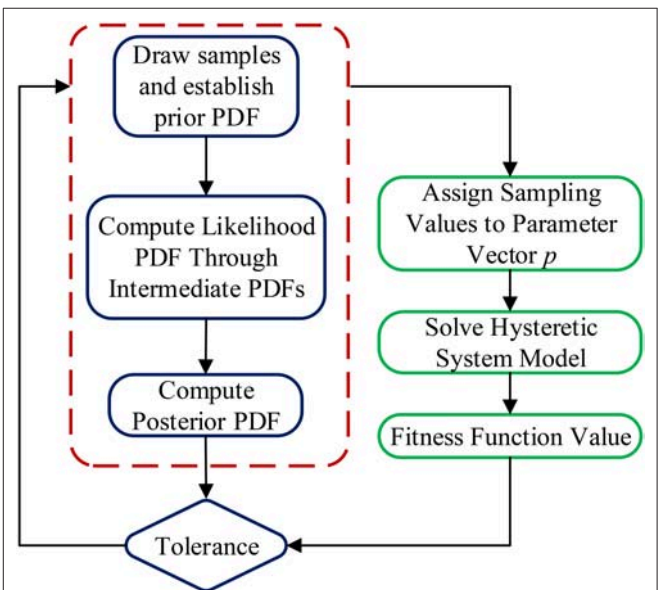

FIGURE 6 | TMCMC based system identification strategy.

where it reflects sampling distribution from stationary status. The principle of Monte Carlo simulation is applied for the integration to approximate the expected complex distribution status of numbers of samples. By increasing the number of samples, the approximation accuracy can be measured and achieve a desired value, which mainly depends on the independence of the samples.

Markov chain involves a stochastic sequential process where a series of states can be sampled from some stationary distributions while Monte Carlo sampling can make an estimation of various characteristics of a specific distribution. The goal of MCMC is to design a Markov chain to meet the target distribution of the chain which is what we are interested in sampling from.

Transitional Markov Chain Monte Carlo Theory (TMCMC) is introduced to avoid the difficulty of sampling from complicated target probability distributions (e.g., multimodal PDFs, PDFs with flat manifold, and very peaked PDFs) but sampling from a series of intermediate PDFs that converge to the target PDF and are easier to sample.

Bayesian Inference describes a process of solving posterior density functions given the likelihood and prior probability. The target probabilistic model can be depicted by M, D is the data acquired from the system, and the uncertain parameters of the model are described as θ. Sampling from the posterior PDF of θ conditioned on D is the aim of the Baysian model updating, which is given as:

$$f(\theta|M,D) = \frac{f(D|M,\theta)\cdot f(\theta|M)}{f(D|M)} = \frac{f(D|M,\theta)\cdot f(\theta|M)}{\int f(D|M,\theta)\cdot f(\theta|M)\cdot d\theta} \tag{29}$$

where $f(\theta|M)$ is the prior PDF of θ, $f(D|M,\theta)$ is the likelihood of D given θ, and $f(D|M)$ is the evidence of the model M.

Bayesian model updating generally employs simulation based methods in that it is effective to obtain samples from $f(\theta|M,\theta)$, which can be estimated at a specific quantity of interest $E(g|M,D)$ based on the Law of Large Number.

$$E(g|M,D) \approx \frac{1}{N}\sum_{k=1}^{N} g(\theta_k) \tag{30}$$

where $\{\theta_k : k = 1,2,\cdots,N\}$ represents a set of N samples from $f(\theta|M,D)$. Consider the equation as follow:

$$f(\theta|M,D) \propto f(\theta|M)\cdot f(D|M,\theta) \tag{31}$$

It is usually difficult to sample from $f(\theta|M,D)$ using Importance Sampling (*IS*) and Metropolis–Hastings (*MH*) in that it is not so easy to understand the geometry of the likelihood $f(D|M,\theta)$. To converge to the target PDF $f(\theta|M,D)$ from the prior PDF $f(\theta|M)$, a series of intermediate PDFs are constructed as the following:

$$f_j(\theta) \propto f(\theta|M)\cdot f(D|M,\theta)^{p_j},\ j = 0,1,\cdots,m$$
$$0 = p_0 < p_1 < \cdots < p_m = 1 \tag{32}$$

Note that $f_0(\theta) = f(\theta|M)$, $f_m(\theta) = f(\theta|M,D)$.

TABLE 1 | Parameter assignment for different cases.

Approach	Case	Parameter	m_1	m_2	m_3	k_1	k_2	k_3	c_1	c_2	c_3	A	α	β	γ	n	δ_ν	$\delta_\nu 1$	δ_η	$\delta_\eta 1$	σ	δ_s
IPV	Sin	–	1.0	1.0	1.0	10	10	10	0.05	0.05	0.05	1	0.01	2	2	1	0	1.5	0	1.5	0.01	0.05
	ElCentro	–	1.0	1.0	1.0	20	20	20	0.05	0.05	0.05	1	0.01	2	2	1	0	3	0	3	0.01	0.05
GA	Sin	True Value	1.0	1.0	1.0	10	10	10	0.05	0.05	0.05	1	0.01	2	2	1.5	0	1.5	0	1.5	0.01	0.05
		Lower bound	–	–	–	5	5	5	0.01	0.01	0.01	0.1	0.001	0.1	0.1	1	0	0.1	0	0.1	0.001	0.01
		Upper bound	–	–	–	15	15	15	0.1	0.1	0.1	2	0.02	4	4	2	0.1	3	0.1	3	0.02	0.1
	ElCentro	True Value	1.0	1.0	1.0	20	20	20	0.05	0.05	0.05	1	0.01	2	2	1.5	0	3	0	3	0.01	0.05
		Lower bound	–	–	–	15	15	15	0.01	0.01	0.01	0.1	0.001	0.1	0.1	1	0	0.1	0	0.1	0.001	0.01
		Upper bound	–	–	–	25	25	25	0.1	0.1	0.1	2	0.02	4	4	2	0.1	6	0.1	6	0.02	0.1
TMCMC	Sin	True Value	1.0	1.0	1.0	10	10	10	0.05	0.05	0.05	1	0.01	2	2	1.5	0	1.5	0	1.5	0.01	0.05
		Lower bound	–	–	–	5	5	5	0.01	0.01	0.01	0.1	0.001	0.1	0.1	1	0	0.1	0	0.1	0.001	0.01
		Upper bound	–	–	–	15	15	15	0.1	0.1	0.1	2	0.02	4	4	2	0.1	3	0.1	3	0.02	0.1
	ElCentro	True Value	1.0	1.0	1.0	20	20	20	0.05	0.05	0.05	1	0.01	2	2	1.5	0	3	0	3	0.01	0.05
		Lower bound	–	–	–	15	15	15	0.01	0.01	0.01	0.1	0.001	0.1	0.1	1	0	0.1	0	0.1	0.001	0.01
		Upper bound	–	–	–	25	25	25	0.1	0.1	0.1	2	0.02	4	4	2	0.1	6	0.1	6	0.02	0.1

In IPV approach, the number of hidden layer neurons is assigned 20, the initial weights are assigned with random values, and the minimum training speed is assigned 0.9.
In GA approach, the population size is assigned 100, the elite count is 10, and crossover fraction is 0.6, and the generation is 30.
In TMCMC approach, the sampling points are assigned 5000, and the scaling factor is assigned 0.2.

where the index j denotes the stage number. Although the geometry changing from $f(\theta|M)$ to $f(\theta|M, D)$ is large, the status of two changing adjacent intermediate PDFs is small. It is efficient to sample from $f_{j+1}(\theta)$ according to the previous sample from $f_j(\theta)$ through this small change.

The function $f_j(\theta)$ is used to extract samples and make an estimation of the PDF itself as a kernel density function (KDF), a combination of weighted Gaussian functions centered at the samples. The kernel density function can be regarded as the proposal PDF of the MH method to sample from $f_{j+1}(\theta)$. This will subsequently and ultimately result in $f(\theta|M, D)$ samples. This approach is called adaptive Metropolis–Hastings (AMH) algorithm. Given that the proposal PDF (KDF) function is fixed, rendering the MH method is as similar as IS, not efficient in high dimension situation.

It is a totally different strategy for TMCMC to acquire $f_{j+1}(\theta)$ samples based on $f_j(\theta)$ samples, KDF method is replaced by a resampling algorithm. It covers a battery of resampling stages, with each stage completing the following, given N_j samples from $f_j(\theta)$, depicted by $\{\theta_{j,k} : k = 1, \cdots, N_j\}$, acquire samples from $f_{j+1}(\theta)$, depicted by $\{\theta_{j+1,k} : k = 1, \cdots, N_{j+1}\}$. It can be calculated by the following in a more easier way, with the samples $\{\theta_{j,k} : k = 1, \cdots, N_j\}$ from $f_j(\theta)$. The "plausibility weights $(w(\theta_{j,k}))$" of these samples regarding $f_{j+1}(\theta)$ can be computed by:

$$w(\theta_{j,k}) = \frac{f(\theta_{j,k}|M) f(D|M, \theta_{j,k})^{p_{j+1}}}{f(\theta_{j,k}|M) f(D|M, \theta_{j,k})^{p_j}} = f(D|M, \theta_{j,k})^{p_{j+1}-p_j}, \quad k = 1, \cdots, N_j \tag{33}$$

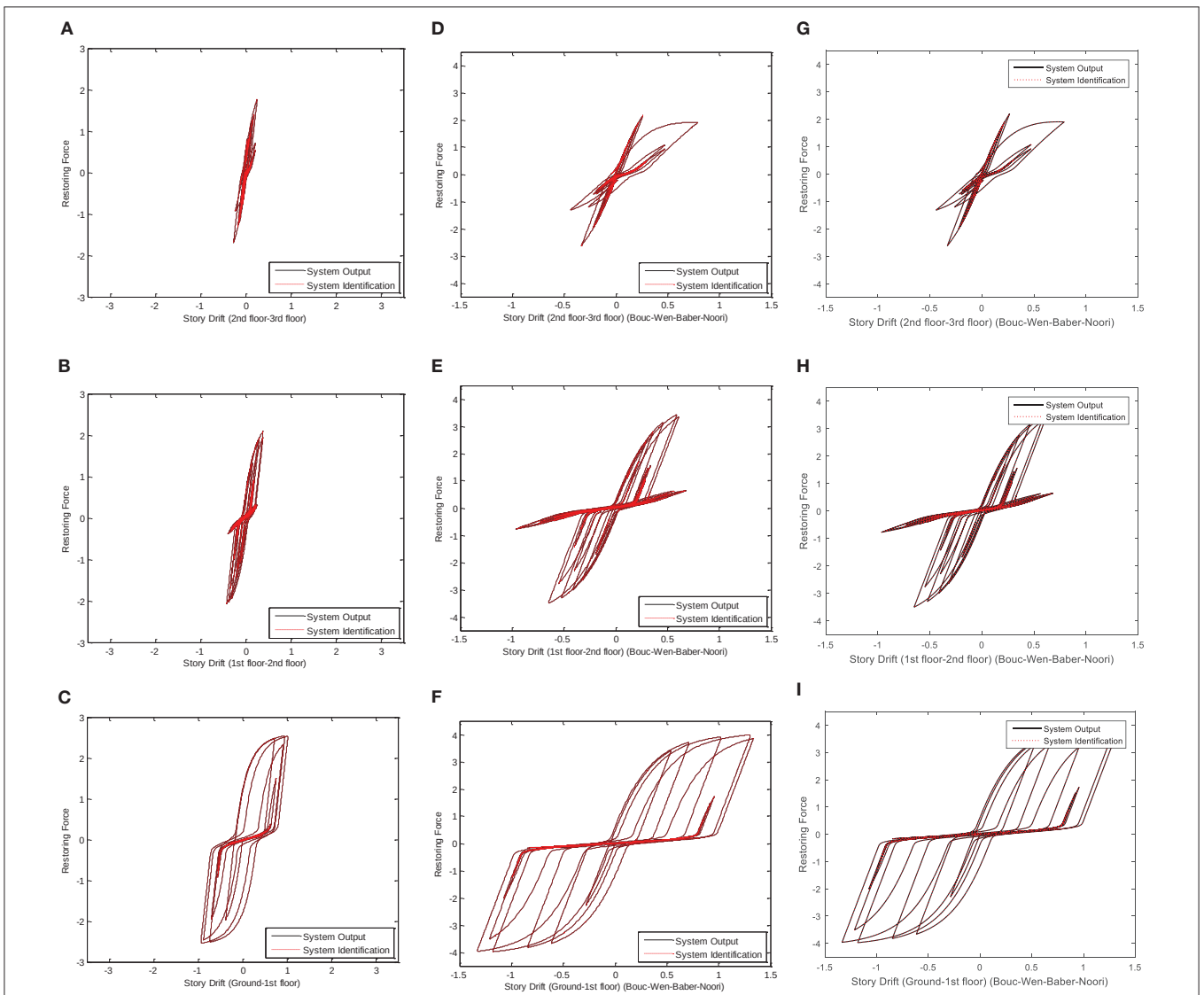

FIGURE 7 | System identification results (Sin) **(A–C)** IPV, **(D–F)** GA, **(G–I)** TMCMC.

Based on the normalized weights, the uncertain parameters can be resampled, i.e. let: $\theta_{j+1,\,k} = \theta_{j,\,l}$ and *w.p.* $\frac{w(\theta_{j,\,l})}{\sum_{l=1}^{N_j} w(\theta_{j,\,l})}$ $k = 1, \cdots, N_{j+1}$

where "with probability" is represented by *w.p.* and pacifier index is denoted as l. It is shown that if N_j and N_{j+1} achieve a relatively large quantity, $\{\theta_{j+1,\,k} : k = 1, \cdots, N_{j+1}\}$ will be distributed as $f_{j+1}(\theta)$. Moreover, $w(\theta_{j,\,k})$ is expected as the following value:

$$E[w(\theta_{j,\,k})] = \int w(\theta) \cdot f_j(\theta) \cdot d\theta = \int f(D|M,\,\theta)^{p_{j+1}-p_j} \cdot f_j(\theta) \cdot d\theta = \int f(D|M,\,\theta)^{p_{j+1}-p_j} \cdot \frac{f(\theta|M) f(D|M,\,\theta)^{p_j}}{f(\theta|M) f(D|M,\,\theta)^{p_j} d\theta} \cdot d\theta = \frac{\int f(\theta|M) f(D|M,\,\theta)^{p_{j+1}} d\theta}{\int f(\theta|M) f(D|M,\,\theta)^{p_j} d\theta} \quad (34)$$

Therefore, $\sum_{k=1}^{N_j} w(\theta_{j,\,k})/N_j$ is the automatically unbiased estimation made for $\frac{\int f(\theta|M) f(D|M,\,\theta)^{p_{j+1}} d\theta}{\int f(\theta|M) f(D|M,\,\theta)^{p_j} d\theta}$. According to the results above, the following method is used to sample from $f(\theta|M, D)$ and make an estimation of $f(D|M)$.

More precisely, with probability $w(\theta_{j,\,k})/\sum_{l=1}^{N_j} w(\theta_{j,\,l})$, by using a covariance matrix equal to the scaled version of the estimated covariance matrix of $f_{j+1}(\theta)$, a Markov chain sample

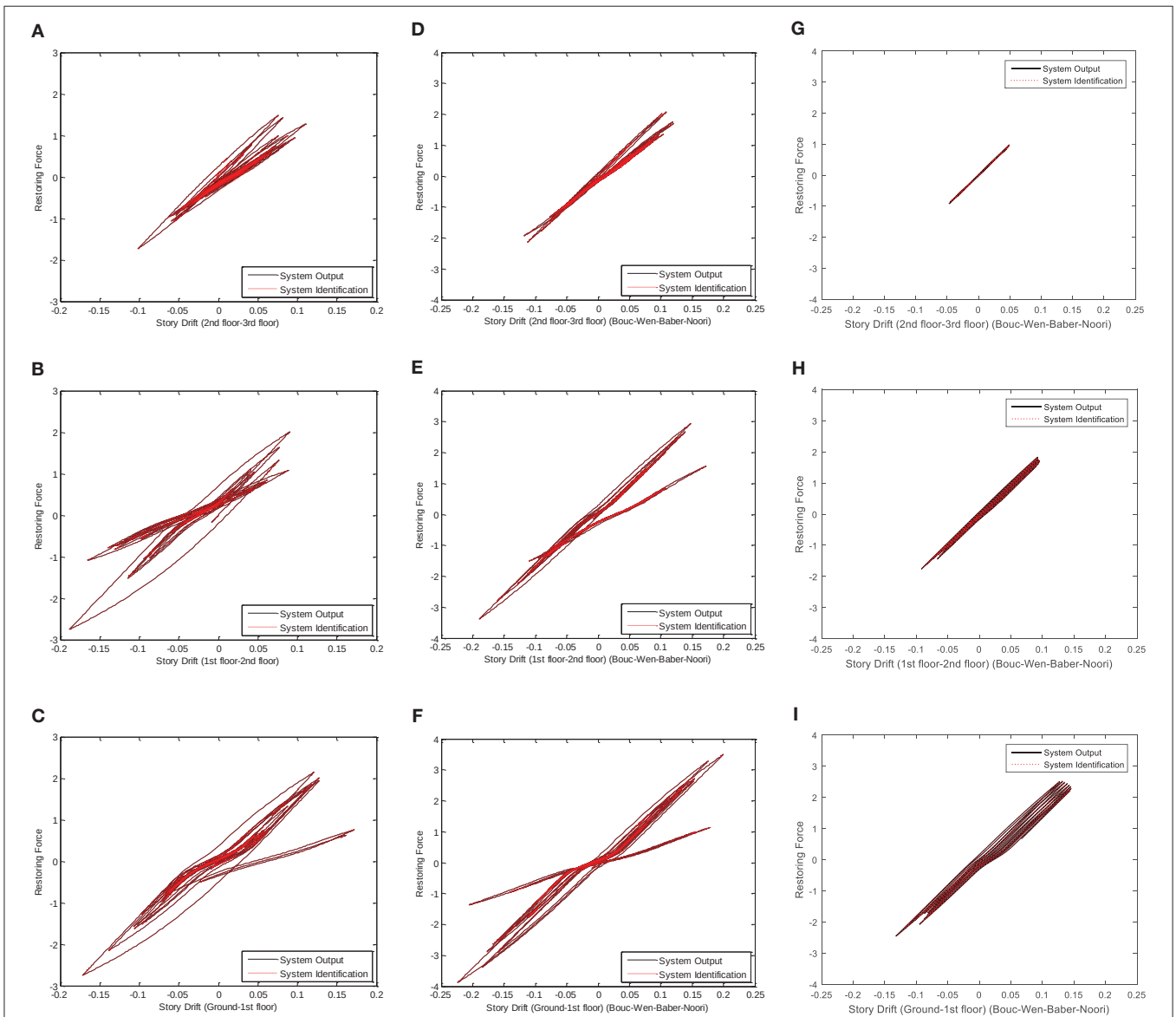

FIGURE 8 | System identification results (ElCentro) **(A–C)** IPV, **(D–F)** GA, **(G–I)** TMCMC.

in the k^{th} chain can be generated from a Gaussian proposal PDF centered at the current sample of the k^{th} chain:

$$\sum_j = \beta^2 \sum_{k=1}^{N_j} w\left(\theta_{j,\,k}\right) \left\{ \theta_{j,\,k} - \left[\frac{\sum_{j=1}^{N_j} w\left(\theta_{j,\,l}\right) \theta_{j,\,l}}{\sum_{j=1}^{N_j} w\left(\theta_{j,\,l}\right)} \right] \right\} \times \left\{ \theta_{j,\,k} - \left[\frac{\sum_{j=1}^{N_j} w\left(\theta_{j,\,l}\right) \theta_{j,\,l}}{\sum_{j=1}^{N_j} w\left(\theta_{j,\,l}\right)} \right] \right\}^T \quad (35)$$

where β is the prescribed scaling factor, $\sum_j = product\ of\ \beta^2$ and the estimated covariance of $f_{j+1}(\theta)$. The rejection rate is chosen as the value β, and MCMC may probably achieve a larger value accordingly. The value 0.2 is found to be more reasonable for the scaling parameter β.

It is essential to choose $\left\{p_j : j = 1, \cdots, m-1\right\}$. The larger value of p is desirable to make the transition between the intermediate adjacent PDFs smoother. The number of intermediate stages achieves a huge value if the increase of p-values has slow change rates.

The degree of uniformity of the plausibility weights $\left\{w\left(\theta_{j,\,k}\right) : k = 1, \cdots, N_j\right\}$ can appropriately indicate how close $f_{j+1}(\theta)$ approaches $f_j(\theta)$, so p_{j+1} should be chosen so that the coefficient of variation (COV) of the plausibility weights can be equivalent to a prescribed threshold. The Bayesian inference framework for system identification is established (**Figure 6**) for structural model updating, which is regarded as a determinant reason for choosing the most suitable model parameters related to the hysteretic behavior of the structures by minimizing the difference between the predicted structural response and the simulated structural response. For the hysteretic structural model, the uncertain model parameters are selected as the ones that need to be updated through Bayesian inference (Equation 31) by drawing samples of parameters from the posterior PDF of parameters.

The TMCMC based Bayesian Updating algorithm is coded and implemented to establish the computational environment via exchange of data between the model and the algorithm. The evolution of parameter updating process is that, the samples from the prior PDFs are approximately uniformly distributed in the model parameter space at the first stage $(p_0 = 0)$. Through applying Bayesian inference with TMCMC probabilistic simulations, the samples eventually populate well in the high probability region of the posterior PDFs close to the true model parameters at the last stage $(p_m = 1)$.

TMCMC approach is employed to make an identification of the parameters of Bouc-Wen class models, henceforth represented by the vector $\theta \leq \Theta \subseteq R^d$. The appropriate choice of θ reflects the corresponding non-linear and hysteretic behavior of structure. By applying Bayesian model updating, the major advantage is that the result gives a probability distribution expressing the likelihood probability distribution of different parameters rather than yielding a single value for θ. It is clear that the evolution of the model parameter variation represents the Bayesian inference process.

TABLE 2 | Parameter identification error for different cases.

Approach	SNR	Case	k_1	k_2	k_3	c_1	c_2	c_3	A	α	β	γ	n	δ_ν	$\delta_{\nu 1}$	δ_η	$\delta_{\eta 1}$	σ	δ_S
GA	–	Sin	4.26%	−3.76%	−7.89%	−2.82%	1.00%	2.50%	2.05%	0.90%	0.78%	−3.10%	−2.77%	Inf	−2.04%	Inf	2.46%	−0.30%	−1.74%
		ElCentro	−1.13%	0.41%	−1.41%	−0.44%	−0.88%	2.94%	1.07%	4.20%	0.31%	0.39%	2.03%	Inf	0.43%	Inf	−2.86%	5.10%	0.80%
	30	Sin	3.78%	−2.82%	−6.63%	1.26%	1.94%	2.30%	3.29%	−1.40%	−1.63%	0.04%	−4.73%	Inf	0.58%	Inf	4.42%	−4.60%	−0.96%
		ElCentro	−1.07%	0.60%	−0.79%	−0.48%	0.96%	2.30%	0.65%	−2.90%	1.95%	−1.75%	2.86%	Inf	−0.97%	Inf	−1.61%	2.50%	−1.32%
	10	Sin	4.56%	2.92%	−5.99%	−3.15%	−2.59%	2.60%	−3.29%	0.98%	−1.69%	−0.68%	3.56%	Inf	0.67%	Inf	−5.68%	3.80%	−1.12%
		ElCentro	−2.09%	−1.87%	−1.18%	−0.88%	0.69%	−1.87%	1.04%	2.78%	−1.80%	1.77%	−2.91%	Inf	1.01%	Inf	−1.57%	−2.38%	1.45%
TMCMC	–	Sin	5.63%	3.72%	−2.90%	−6.60%	−5.40%	−0.20%	1.99%	−7.00%	−0.70%	−3.94%	−5.43%	Inf	6.09%	Inf	2.67%	−9.00%	8.00%
		ElCentro	−4.76%	−4.83%	−5.87%	−2.40%	−7.80%	−8.80 %	5.16%	9.00%	−6.07%	−9.49%	0.45%	Inf	−0.37%	Inf	−8.81%	−9.00%	−6.80%
	30	Sin	5.57%	−3.69%	−3.01%	6.79%	5.47%	−0.53%	2.03%	6.45%	0.44%	−4.72%	−5.46%	Inf	−6.16%	Inf	−2.70%	−9.18%	−8.52%
		ElCentro	−4.77%	−4.88%	5.37%	2.83%	−6.99%	8.40%	5.22%	−9.17%	−6.54%	−9.55%	0.75%	Inf	0.47%	Inf	−8.99%	9.16%	−7.01%
	10	Sin	5.05%	3.70%	−3.03%	−6.88%	5.51%	0.69%	−1.98%	6.37%	−0.55%	−4.80%	−5.12%	Inf	6.23%	Inf	−2.76%	9.25%	−8.63%
		ElCentro	−4.79%	4.68%	−5.67%	−2.84%	−7.35%	8.83%	−5.63%	9.27%	−7.04%	9.79%	−1.37%	Inf	2.09%	Inf	−7.38%	−8.42%	8.32%

IPV approach does not have error analysis of structural system parameter since the structural parameters are substituted by the architecture of neural network.

Inf means the relative value of parameter identification accuracy cannot be computed in that there is a value assigned zero, but the absolute value of parameter identification accuracy can be calculated.

To make a restriction of the parameter space Θ, two side constraint vectors $\theta_{\min}$ and $\theta_{\max}$ are defined such that:

$$\theta_{\min}(i) \leq \theta(i) \leq \theta_{\max}(i) \qquad 1 \leq i \leq d \tag{36}$$

The vector θ has specific constraints such that the generated initial samples can determine the feasible values that the parameters can take. By defining prior PDF of θ a uniform distribution between the likelihood PDF and side constraints are regarded as the prediction error assumed as Gaussian function distributed with unknown variance and zero mean. The prediction error is described as the error between the predicted system response and the simulated system response given by:

$$f(D|\theta) = \prod_{i=1}^{l} \frac{1}{\sigma_{acc}\sqrt{2\pi}} \exp\left[-\frac{1}{2\sigma_{acc}^2}\left(\frac{x(t_i) - \hat{x}(t_i|\theta)}{S_{acc}(t_i)}\right)^2\right] \tag{37}$$

where σ_{acc}^2 is the variance of the prediction errors and S_{acc} is the weighting function used to normalize the acceleration response of the hysteretic system. To achieve computational convenience, the log-likelihood function $lnf(D|\theta)$ is employed in the actual implementation of the TMCMC algorithm as:

$$\begin{aligned} lnf(D|\theta) = &-\frac{1}{2}N_t \ln(2\pi) - N_t \ln(\sigma_{acc}) \\ &- \frac{1}{2\sigma_{acc}^2}\left(\frac{x(t_i) - \hat{x}(t_i|\theta)}{S_{acc}(t_i)}\right)^2 \end{aligned} \tag{38}$$

The j^{th} stage of parameter evolution process by correspondingly choosing the values of p_j can be shown as the contours of PDF $f_j(\theta)$.

NUMERICAL ANALYSIS OF SYSTEM IDENTIFICATION

Parameter Settings

Table 1 lists the parameter assignments of the structural system associated with BWBN hysteresis model for different cases. The mass coefficient of each floor is 1 kg, stiffness coefficient 10 N/m (sin) and 20 N/m (ElCentro), damping coefficient 0.05 N/(m/s) for each floor, respectively.

For hysteresis model, $A = 1$, $\alpha = 0.01$, $\beta = 2$, $\gamma = 2$, $n = 1$ (IPV), $n = 1.5$ (GA and TMCMC), $\delta_\upsilon = 0$, $\delta_{\upsilon 1} = 1.5$ (sin) and 3 (ElCentro), $\delta_\eta = 0$, $\delta_{\eta 1} = 1.5$ (sin) and 3 (ElCentro), $\sigma = 0.01$, $\delta_s = 0.05$. Damage occurrences are assumed at 30 s, 60 s, 100 s (sin) and 10 s, 20 s, 40 s (ElCentro) when both the strength degradation factor δ_υ and stiffness degradation factor δ_η change to $\delta_{\upsilon 1}$and $\delta_{\eta 1}$, respectively. For GA and TMCMC approaches, parameter initial values are assigned between the corresponding lower and upper bounds before the optimization processes. Parameters are updated between the two bounds of parametric searching space, and eventurally achieve the exact values.

Numerical Analysis Results

Figures 7, **8** show the restoring force identification results when the structure is subjected to sinusoidal signal and

TABLE 3 | Correlation coefficient analysis for different cases.

Approach	SNR	Case	R-t3	R-t2	R-t1	R-x3	R-x2	R-x1	Running time(s)
IPV	–	Sin	1.0000	1.0000	1.0000	1.0000	1.0000	1.0000	85.11
		ElCentro	1.0000	1.0000	1.0000	1.0000	1.0000	1.0000	93.33
	30	Sin	0.9978	0.9991	0.9996	0.9978	0.9991	0.9996	89.93
		ElCentro	0.9969	0.9985	0.9991	0.9969	0.9985	0.9991	96.05
	10	Sin	0.8708	0.9273	0.9566	0.8708	0.9273	0.9566	95.67
		ElCentro	0.8243	0.8936	0.9314	0.8243	0.8936	0.9314	108.98
GA	–	Sin	0.9958	0.9964	0.9987	0.9958	0.9964	0.9997	901.31
		ElCentro	0.9667	0.9770	0.9869	0.9667	0.9770	0.9869	911.52
	30	Sin	0.9944	0.9952	0.9967	0.9944	0.9952	0.9967	908.25
		ElCentro	0.9662	0.9810	0.9859	0.9662	0.9810	0.9859	916.26
	10	Sin	0.8435	0.8924	0.9312	0.8435	0.8924	0.9312	927.76
		ElCentro	0.8012	0.8370	0.8994	0.8012	0.8370	0.8994	929.19
TMCMC	–	Sin	0.9983	0.9986	0.9988	0.9983	0.9986	0.9988	64812.36
		ElCentro	0.9925	0.9932	0.9957	0.9925	0.9932	0.9957	64901.47
	30	Sin	0.9108	0.9138	0.9259	0.9108	0.9138	0.9259	65012.69
		ElCentro	0.9018	0.9092	0.9129	0.9018	0.9092	0.9129	65109.53
	10	Sin	0.8360	0.8401	0.8498	0.8360	0.8401	0.8498	66409.77
		ElCentro	0.8209	0.8275	0.8302	0.8209	0.8275	0.8302	68014.28

The running time of system identification programs is computed using Samsung computer [Win 7 Ultimate, Processor: Intel (R), Xeon (R), CPU E3-1231 v3 @3.4G Hz, RAM: 8G, System type: 64 operating system].

ElCentro signal, respectively. Black curve represents the restoring force of the original structural system while the red curve represents the identified restoring force using IPV, GA, and TMCMC approaches. For the case of sinusoidal excitation, the identification results show that the degradation phenomenon of restoring forces of 2nd−3rd floor and 1st−2nd floor are more evident compared with ground-1st floor by using all of the three approaches. For the case of ElCentro excitation, the identification results show that the degradation phenomenon of restoring forces existing in all adjacent floors by using IPV and GA methods is more evident compared with that using TMCMC method. The hysteresis curves rotate accordingly when damage occurs. More results in details are discussed in the next section.

DISCUSSIONS

Choice of Signal Excitation Type and Objective Function

Both sinusoidal excitation signal and ElCentro excitation signal are used as input signals to the system identification of hyestetic system. The frequency of sin signal is single and history curve is smooth and periodic variation. The ElCentro wave is stochastic, non-periodic, and non-steady state, and this represents the other type of excitation which is totally counter to harmonic wave such as sin signal. These two types of signals are employed to the response analysis and verification of the generalization capability of three different algorithms for identifying restoring forces of hysteretic structure. In addition, the establishment of objective functions employed in the GA and TMCMC are formulated through the combination of desired and simulated acceleration signal differences of all three degrees of freedom.

Parameter Choice for System Identification

Table 2 shows the parameter identification error using GA and TMCMC for the case of noise free, SNR = 30 and SNR = 10 (SNR = signal noise ratio). These error represents the relative error between the "true value" and "identified value." All errors are no more than 10%. Generally for the cases with higher SNR they perform better parameter identification results since the disturbance of noise to signal is low. From **Figures 7**, **8**, and **Table 2**, for the noise free case, it is shown that during the degradation process (damage evolution), strength degradation factor δ_υ changes from 0 to 1.4695 (sin,GA) /3.0130 (ElCentro,GA) /1.5913 (sin,TMCMC) /2.9890 (ElCentro,TMCMC), and stiffness degradation factor δ_η changes from 0 to 1.5370 (sin,GA)/2.9142 (ElCentro,GA)/1.5400 (sin,TMCMC)/2.7357 (ElCentro,TMCMC).

The hysteresis loop rotates clockwise with a certain degree, indicating large non-linearity and considerable degradation. However, from the identification results, it is also found that in the sin excitation case, the hysteresis loop exhibits better slip-lock phenomenon, and can absorb more energy than the case of ElCentro excitation. Noise corrupted cases have similar parameter identification results.

Table 3 shows the analysis of correlation coefficients for different cases. For the cases with small SNR, the identification effectiveness is not relatively good compared with noise free and

TABLE 4 | Degradation parameter assignment for different cases.

Approach	Case	Parameter	Group 1				Group 2				Group 3				Group 4				Group 5			
			δ_υ	$\delta_{\upsilon 1}$	δ_η	$\delta_{\eta 1}$	δ_υ	$\delta_{\upsilon 1}$	δ_η	$\delta_{\eta 1}$	δ_υ	$\delta_{\upsilon 1}$	δ_η	$\delta_{\eta 1}$	δ_υ	$\delta_{\upsilon 1}$	δ_η	$\delta_{\eta 1}$	δ_υ	$\delta_{\upsilon 1}$	δ_η	$\delta_{\eta 1}$
IPV	Sin	–	0	1.5	0	1.5	0	1.8	0	1.8	0	2.1	0	2.1	0	2.4	0	2.4	0	2.7	0	2.7
	ElCentro	–	0	3	0	3	0	3.3	0	3.3	0	3.6	0	3.6	0	3.9	0	3.9	0	4.2	0	4.2
GA	Sin	True value	0	1.5	0	1.5	0	1.5	0	1.5	0	1.5	0	1.5	0	1.8	0	1.8	0	2.1	0	2.1
		Lower bound	0	0.1	0	0.1	0	0.5	0	0.5	0	1	0	1	0	0.1	0	0.1	0	0.1	0	0.1
		Upper bound	0.1	3	0.1	3	0.1	2.5	0.1	2.5	0.1	2	0.1	2	0.1	3.6	0.1	3.6	0.1	4.2	0.1	4.2
	ElCentro	True value	0	3	0	3	0	3	0	3	0	3	0	3	0	3.3	0	3.3	0	3.6	0	3.6
		Lower bound	0	0.1	0	0.1	0	1	0	1	0	2	0	2	0	0.1	0	0.1	0	0.1	0	0.1
		Upper bound	0.1	6	0.1	6	0.1	5	0.1	5	0.1	4	0.1	4	0.1	6.6	0.1	6.6	0.1	7.2	0.1	7.2
TMCMC	Sin	True value	0	1.5	0	1.5	0	1.5	0	1.5	0	1.5	0	1.5	0	1.8	0	1.8	0	2.1	0	2.1
		Lower bound	0	0.1	0	0.1	0	0.5	0	0.5	0	1	0	1	0	0.1	0	0.1	0	0.1	0	0.1
		Upper bound	0.1	3	0.1	3	0.1	2.5	0.1	2.5	0.1	2	0.1	2	0.1	3.6	0.1	3.6	0.1	4.2	0.1	4.2
	ElCentro	True value	0	3	0	3	0	3	0	3	0	3	0	3	0	3.3	0	3.3	0	3.6	0	3.6
		Lower bound	0	0.1	0	0.1	0	1	0	1	0	2	0	2	0	0.1	0	0.1	0	0.1	0	0.1
		Upper bound	0.1	6	0.1	6	0.1	5	0.1	5	0.1	4	0.1	4	0.1	6.6	0.1	6.6	0.1	7.2	0.1	7.2

Data in the gray area represents that for the same case, it has the same "true value" but different lower and upper bounds.

higher SNR (R-t is the restoring force-time relationship, and R-x is the restoring force-relative displacement relationship).

In this paper, IPV is a radius basis neural network which is a completely data-driven approach, while GA and TMCMC are not fully data-driven in that they assign the identification model within specific initial parameter intervals and then update and search to optimize structural model.

IPV method performs better identification results due to its adaptive learning capability and anti noise property in the noise environment. From computational time, it can be concluded that the IPV approach is a more efficient identification method compared with GA and TMCMC methods. Concretely, for the case of noise free, the computational time for GA and TMCMC are 9.59 and 760.51% longer than IPV (sin), and 8.77 and 694.40% longer than IPV (ElCentro). Similar results are also shown in noise corrupted cases. This demonstrates IPV method has higher computational efficiency than GA and TMCMC approaches.

Strength and stiffness degradation parameters are both very important in the hysteresis model, which determine the hysteretic behavior of structural systems. **Table 4** lists five groups of parameter assignments regarding the variance of strength and stiffness degradation coefficients. The objective of setting these cases is studying the influence of change of degradation parameters on system identification accuracy.

To simulate damage occurrence, for IPV approach, strength degradation factor δ_υ and stiffness degradation factor δ_η change from 1.5 to 1.8, 2.1, 2.4, and 2.7, respectively (sin), while change from 3 to 3.3, 3.6, 3.9, and 4.2, respectively (ElCentro). For GA (sin) method, for the first three groups, the true value of strength degradation factor δ_υ and stiffness degradation factor δ_η keep fixed value 1.5 but the lower and upper bound change from 0.1–3 to 0.5–2.5 and 1–2, respectively. For the last two groups, the true value of strength degradation factor δ_υ and stiffness degradation factor δ_η are 1.8 and 2.1, respectively but the lower and upper bound correspondingly change from 0.1 to 3.6 and 0.1 to 4.2, respectively.

For GA (ElCentro) method, for the first three groups, the true value of strength degradation factor δ_υ and stiffness degradation factor δ_η keep fixed value 3 but the lower and upper bound

TABLE 5 | Correlation coefficient analysis (IPV).

Approach	Group	SNR	Case	R-t3	R-t2	R-t1	R-x3	R-x2	R-x1	Running time(s)
IPV	1	–	Sin	1.0000	1.0000	1.0000	1.0000	1.0000	1.0000	85.11
			ElCentro	1.0000	1.0000	1.0000	1.0000	1.0000	1.0000	93.33
		30	Sin	0.9978	0.9991	0.9996	0.9978	0.9991	0.9996	89.93
			ElCentro	0.9969	0.9985	0.9991	0.9969	0.9985	0.9991	96.05
		10	Sin	0.8708	0.9273	0.9566	0.8708	0.9273	0.9566	95.67
			ElCentro	0.8243	0.8936	0.9314	0.8243	0.8936	0.9314	108.98
	2	–	Sin	1.0000	0.9999	1.0000	1.0000	0.9999	1.0000	89.01
			ElCentro	1.0000	1.0000	1.0000	1.0000	1.0000	1.0000	92.17
		30	Sin	0.9975	0.9984	0.9993	0.9975	0.9984	0.9993	95.11
			ElCentro	0.9957	0.9960	0.9971	0.9957	0.9960	0.9971	98.02
		10	Sin	0.8567	0.8580	0.8700	0.8567	0.8580	0.8700	104.78
			ElCentro	0.8108	0.8179	0.8244	0.8108	0.8179	0.8244	115.90
	3	–	Sin	0.9999	1.0000	1.0000	0.9999	1.0000	1.0000	88.97
			ElCentro	0.9999	1.0000	1.0000	0.9999	1.0000	1.0000	90.00
		30	Sin	0.9967	0.9976	0.9987	0.9967	0.9976	0.9987	96.02
			ElCentro	0.9955	0.9965	0.9973	0.9955	0.9965	0.9973	99.14
		10	Sin	0.8607	0.8678	0.8711	0.8607	0.8678	0.8711	107.37
			ElCentro	0.8236	0.8299	0.8317	0.8236	0.8299	0.8317	120.03
	4	–	Sin	1.0000	1.0000	0.9999	1.0000	1.0000	0.9999	83.12
			ElCentro	1.0000	1.0000	0.9999	1.0000	1.0000	0.9999	87.21
		30	Sin	0.9970	0.9976	0.9984	0.9970	0.9976	0.9984	95.09
			ElCentro	0.9961	0.9973	0.9979	0.9961	0.9973	0.9979	97.33
		10	Sin	0.8700	0.8736	0.8744	0.8700	0.8736	0.8744	100.20
			ElCentro	0.8301	0.8315	0.8333	0.8301	0.8315	0.8333	107.69
	5	–	Sin	1.0000	0.9999	0.9999	1.0000	0.9999	0.9999	86.09
			ElCentro	0.9999	0.9999	0.9999	0.9999	0.9999	0.9999	89.11
		30	Sin	0.9968	0.9977	0.9990	0.9968	0.9977	0.9990	93.84
			ElCentro	0.9957	0.9969	0.9980	0.9957	0.9969	0.9980	98.94
		10	Sin	0.8657	0.8672	0.8680	0.8657	0.8672	0.8680	104.55
			ElCentro	0.8489	0.8498	0.8524	0.8489	0.8498	0.8524	111.11

change from 0.1–6 to 1–5 and 2–4, respectively. For the last two groups, the true value of strength degradation factor δ_υ and stiffness degradation factor δ_η are 3.3 and 3.6, respectively but the lower and upper bound correspondingly change from 0.1 to 6.6 and 0.1 to 7.2, respectively. TMCMC parameter assignment has similar cases.

Table 5 shows the influence of change of strength and stiffness degradation parameter on system identification accuracy indicated by correlation coefficients using IPV method. For sin excitation, as the strength and stiffness degradation parameter increase from 1.5 to 2.7, the correlation coefficients do not increase or decrease for the same case, and the computational time also keep almost unchanged: (sin) Group1: 85.11–95.67 s, Group 2: 89.01–104.78 s, Group 3: 88.97–107.37 s, Group 4: 83.12–100.20 s, Group 5: 86.09–104.55 s. (ElCentro) Group 1: 93.33–108.98 s, Group 2: 92.17–115.90 s, Group 3: 90.00–120.03 s, Group 4: 87.21–107.69 s, Group 5: 89.11–111.11 s.

Table 6 shows the influence of change of strength and stiffness degradation parameter on system identification accuracy indicated by correlation coefficients using GA method. For sin excitation, when the strength and stiffness degradation parameter value is fixed at 1.5, as bounds (interval) change from 0–3 to 1–2, the correlation coefficients approach 1, indicating the system identification accuracy improves with the bound interval decreasing. The closer the bounds approach to the true value, the more accurate and deterministic the system identifiion results are. Accordingly, the computational time decreases with the bound interval decreasing. For details: Group 1: 901.31–927.76 s, Group 2: 895.66–922.22 s, Group 3: 889.73–914.73 s. When the true value of strength and stiffness degradation increases from 1.5 to 2.1 with given bounds, the identification accuracy decreases, and the computational time increases accordingly. Similar cases can also be found for ElCentro excitation signal.

Table 7 shows the influence of change of strength and stiffness degradation parameter on system identification accuracy indicated by correlation coefficients using TMCMC method. For sin excitation, when the strength and stiffness degradation parameter value is fixed at 1.5, as bounds (interval) change from 0–3 to 1–2, the correlation coefficients approach 1, indicating the

TABLE 6 | Correlation coefficient analysis (GA).

Approach	Group	SNR	Case	R-t3	R-t2	R-t1	R-x3	R-x2	R-x1	Running time(s)
GA	1	–	Sin	0.9958	0.9964	0.9987	0.9958	0.9964	0.9997	901.31
			ElCentro	0.9667	0.9770	0.9869	0.9667	0.9770	0.9869	911.52
		30	Sin	0.9944	0.9952	0.9967	0.9944	0.9952	0.9967	908.25
			ElCentro	0.9662	0.9810	0.9859	0.9662	0.9810	0.9859	916.26
		10	Sin	0.8435	0.8924	0.9312	0.8435	0.8924	0.9312	927.76
			ElCentro	0.8012	0.8370	0.8994	0.8012	0.8370	0.8994	929.19
	2	–	Sin	0.9963	0.9968	0.9993	0.9963	0.9968	0.9993	895.66
			ElCentro	0.9700	0.9797	0.9888	0.9700	0.9797	0.9888	903.65
		30	Sin	0.9947	0.9958	0.9971	0.9947	0.9958	0.9971	906.59
			ElCentro	0.9668	0.9831	0.9877	0.9668	0.9831	0.9877	912.28
		10	Sin	0.8553	0.9012	0.9337	0.8553	0.9012	0.9337	922.22
			ElCentro	0.8108	0.8433	0.9042	0.8108	0.8433	0.9042	925.59
	3	–	Sin	0.9970	0.9976	0.9995	0.9970	0.9976	0.9995	889.73
			ElCentro	0.9712	0.9800	0.9923	0.9712	0.9800	0.9923	894.49
		30	Sin	0.9952	0.9967	0.9979	0.9952	0.9967	0.9979	900.01
			ElCentro	0.9711	0.9828	0.9880	0.9711	0.9828	0.9880	905.38
		10	Sin	0.8573	0.9103	0.9355	0.8573	0.9103	0.9355	914.73
			ElCentro	0.8098	0.8449	0.9098	0.8098	0.8449	0.9098	918.90
	4	–	Sin	0.9813	0.9877	0.9921	0.9813	0.9877	0.9921	917.74
			ElCentro	0.9512	0.9657	0.9703	0.9512	0.9657	0.9703	926.54
		30	Sin	0.9754	0.9779	0.9837	0.9754	0.9779	0.9837	930.07
			ElCentro	0.9534	0.9600	0.9718	0.9534	0.9600	0.9718	942.83
		10	Sin	0.8301	0.8544	0.9009	0.8301	0.8544	0.9009	951.11
			ElCentro	0.7885	0.8177	0.8836	0.7885	0.8177	0.8836	958.98
	5	–	Sin	0.9689	0.9788	0.9864	0.9689	0.9788	0.9864	926.34
			ElCentro	0.9321	0.9555	0.9688	0.9321	0.9555	0.9688	929.88
		30	Sin	0.9500	0.9633	0.9773	0.9500	0.9633	0.9773	937.48
			ElCentro	0.9412	0.9678	0.9006	0.9412	0.9678	0.9006	940.05
		10	Sin	0.9378	0.9538	0.9699	0.9378	0.9538	0.9699	956.01
			ElCentro	0.7650	0.7948	0.8305	0.7650	0.7948	0.8305	968.44

TABLE 7 | Correlation coefficient analysis (TMCMC).

Approach	Group	SNR	Case	R-t3	R-t2	R-t1	R-x3	R-x2	R-x1	Running time(s)
TMCMC	1	–	Sin	0.9983	0.9986	0.9988	0.9983	0.9986	0.9988	64812.36
			ElCentro	0.9925	0.9932	0.9957	0.9925	0.9932	0.9957	64901.47
		30	Sin	0.9108	0.9138	0.9259	0.9108	0.9138	0.9259	65012.69
			ElCentro	0.9018	0.9092	0.9129	0.9018	0.9092	0.9129	65109.53
		10	Sin	0.8360	0.8401	0.8498	0.8360	0.8401	0.8498	66409.77
			ElCentro	0.8209	0.8275	0.8302	0.8209	0.8275	0.8302	68014.28
	2	–	Sin	0.9985	0.9989	0.9990	0.9985	0.9989	0.9990	63508.90
			ElCentro	0.9930	0.9941	0.9964	0.9930	0.9941	0.9964	63132.56
		30	Sin	0.9112	0.9143	0.9265	0.9112	0.9143	0.9265	64657.77
			ElCentro	0.9034	0.9106	0.9244	0.9034	0.9106	0.9244	64789.88
		10	Sin	0.8373	0.8456	0.8543	0.8373	0.8456	0.8543	65546.11
			ElCentro	0.8215	0.8288	0.8376	0.8215	0.8288	0.8376	66444.90
	3	–	Sin	0.9988	0.9990	0.9993	0.9988	0.9990	0.9993	62109.67
			ElCentro	0.9935	0.9957	0.9970	0.9935	0.9957	0.9970	62476.67
		30	Sin	0.9118	0.9156	0.9279	0.9118	0.9156	0.9279	63157.58
			ElCentro	0.9056	0.9117	0.9279	0.9056	0.9117	0.9279	63654.59
		10	Sin	0.8384	0.8491	0.8579	0.8384	0.8491	0.8579	64111.67
			ElCentro	0.8244	0.8296	0.8383	0.8244	0.8296	0.8383	65000.78
	4	–	Sin	0.9867	0.9889	0.9902	0.9867	0.9889	0.9902	65457.89
			ElCentro	0.9756	0.9780	0.9806	0.9756	0.9780	0.9806	65989.07
		30	Sin	0.9000	0.9067	0.9138	0.9000	0.9067	0.9138	66675.88
			ElCentro	0.8923	0.8979	0.9036	0.8923	0.8979	0.9036	66899.04
		10	Sin	0.8222	0.8318	0.8440	0.8222	0.8318	0.8440	67476.68
			ElCentro	0.8016	0.8066	0.8148	0.8016	0.8066	0.8148	68698.36
	5	–	Sin	0.9659	0.9770	0.9799	0.9659	0.9770	0.9799	66780.77
			ElCentro	0.9502	0.9589	0.9664	0.9502	0.9589	0.9664	66999.75
		30	Sin	0.8879	0.8909	0.9008	0.8879	0.8909	0.9008	67376.11
			ElCentro	0.8748	0.8765	0.8800	0.8748	0.8765	0.8800	67980.04
		10	Sin	0.8117	0.8277	0.8335	0.8117	0.8277	0.8335	68780.99
			ElCentro	0.7980	0.8034	0.8110	0.7980	0.8034	0.8110	69333.56

system identification accuracy improves with the bound interval decreasing.

The closer the bounds approach to the true value, the more accurate and deterministic the system identifiion results are. Accordingly, the computational time decreases with the bound interval value decreasing, as shown in detailed cases: Group 1: 64812.36–66409.77 s, Group 2: 63508.90–65546.11 s, Group 3: 62109.67–64111.67 s. When the true value of strength and stiffness degradation increases from 1.5 to 2.1 with given bounds, the identification accuracy decreases, and the computational time increases accordingly. Similar cases can also be found for ElCentro excitation signal.

Comparison of Three Different Algorithm Principles

Intelligent Parameter Varying approach uses radial basis function to map the complex input signal to high dimensional signal, and it is a data driven mechanism. By using appropriate error back propagation mechanism, this method can design a good neural network architecture to process considerable amount of data or high parameter dimension, especially for system identification application. Genetic algorithm and Transitional Markov Chain Monte Carlo approaches are non-data-driven intelligent optimization algorithms. Genetic algorithm optimizes the parameters by using selection, crossover, and mutation operators through elitist strategy. Transitional Markov Chain Monte Carlo method employs model updating to optimize parameters through applying Bayesian inference with TMCMC probabilistic simulations, and the samples eventually populate well in the high probability region of the posterior PDFs close to the true model parameters through a series of intermediate updating processes. The latter two methods are related to optimization theory, and may not perform well (tapped in local optimum) especially when the parameter dimension is relatively large. Therefore, it is very significant to conduct a comparative study on system identification of hysteretic structures using Intelligent Parameter Varying, Genetic Algorithm and Transitional Markov Chain Monte Carlo methods.

The above discussions regarding the choice of signal excitation type, parameter choice for system identification and comparison between three different principles for system identification has

demonstrated the necessity, feasibility and importance of this research. It also illustrates the generalization of this research and proves the superiority using IPV over GA and TMCMC for system identification of hysteretic structures.

CONCLUSIONS

To better understand the hysterically degrading, structural systems using an earlier version of smoothly varying Bouc-Wen-Baber-Noori hysteresis model in this research, a detailed description of BWBN hysteresis model is presented, and the restoring force and the associated system variables are analyzed using non-linear differential equations containing different parameters. By choosing the parameters in a suitable way, it is possible to generate a large variety of different shapes of the hysteresis loops. A three floor shear structure is modeled which composes of three adjacent subsystems by associating system kinetic equations, restoring force expression and BWBN hysteresis model. By using BWB-Noori model, a new scheme is proposed to effectively and efficiently track and estimate the hysteretic restoring forces using intelligent parameter varying approach, genetic optimization algorithm and the transitional Markov Chain Monte Carlo simulation. Most importantly, comparative study by using these approaches for different cases is demonstrated through parameter error analysis and correlation coefficient analysis of system identification of time varying degrading structures. Major findings are summarized in the following statements.

(1) BWBN hysteresis model is a smoothly varying differential mathematical model, and it can reflect highly non-linear and gradual hysteretic degradation with slip lock behavior observed in numerous structural and mechanical systems, and this model can be widely used to predict the response of degradation phenomena of general structures.
(2) When employing system identification and parameter/model updating approach, the initial parameter spaces of the hysteretic system should be well assigned to satisfy the requirement of reliable system identification process. Tracking of the restoring forces for the hysteretic system using system identification approaches can accurately estimate the changing of restoring force status in time, i.e., the rotation of hysteresis loops indicates structural degradation due to abrupt damages. This proves that system identification techniques can be used as powerful tools for detecting the damage/degradation for structural health monitoring applications. Stiffness and damping terms are lumped into restoring forces represented by structural non-linearity, and this constructs effective IPV modeling.
(3) IPV, GA, and TMCMC methods are employed for the system identification of BWBN model, and a comparative study is conducted for the verification of the effectiveness of these approaches. The results show higher SNR cases have better correlation and smaller parameter errors. From the correlation analysis, we also know that IPV has better anti-noise capability than GA and TMCMC.
(4) Qualitative comparison regarding the computational time of these three different algorithms are ranked for different cases, i.e., IPV Based system identification approach < GA based system identification method << TMCMC based system identification approach. This demonstrates that compared with traditional parameter optimization and statistical methods, IPV approach is a promising, efficient and effective way for system identification and Structural Health Monitoring applications.
(5) IPV technique using the RBF based ANNs has its superior advantages over the GA based identification and the TMCMC based identification techniques for its fully data-driven adaptive learning ability for high dimensional data. Proper design of parameter initial bounds can improve the computational efficiency for GA and TMCMC approaches. The GA based identification may have relatively uncertain values for the randomness of genetic operations (selection, crossover, and mutation), while the TMCMC algorithm is based on the sampling technique that is not as effective and is uncertain, especially for the case that the system has a relatively large number of parameters.

AUTHOR CONTRIBUTIONS

YZ as Ph.D. student. MN as main supervisor. WA supervisor. TA was invited, due to his expertise in the area of Genetic Algorithms, to join the paper as a co-author. TA carefully reviewed the technical analysis and independently carried out a system ID using Genetic Algorithm. His contributions were valuable in this regard and thus, his name is added in the newly revised version.

REFERENCES

Abouelwafa, M. N., El-Gamal, H. A., Mohamed, Y. S., and Altabey, W. A. (2014). An expert system for life prediction of woven-roving GFRE closed end thick tube subjected to combined bending moments and internal hydrostatic pressure using artificial neural network. *Int. J. Adv. Mater. Res.* 845, 12–17. doi: 10.4028/www.scientific.net/AMR.845.12

Altabey, W. A. (2014). "Vibration analysis of laminated composite variable thickness plate using finite strip transition matrix technique and MATLAB verifications," in *MATLAB- Particular for Engineer*, ed K. Bennett (InTech), 583–620.

Altabey, W. A. (2016). FE and ANN model of ECS to simulate the pipelines suffer from internal corrosion. *Struct. Monit. Mainten.* 3, 297–314. doi: 10.12989/smm.2016.3.3.297

Altabey, W. A. (2017a). An exact solution for mechanical behavior of BFRP Nano-thin films embedded in NEMS. *J. Adv. Nano Res.* 5, 337–357. doi: 10.12989/anr.2017.5.4.337

Altabey, W. A. (2017b). Free vibration of basalt fiber reinforced polymer (FRP) laminated variable thickness plates with intermediate elastic support using finite strip transition matrix (FSTM) method. *J. Vibroeng.* 19, 2873–2885. doi: 10.21595/jve.2017.18154

Altabey, W. A. (2017c). Prediction of natural frequency of basalt fiber reinforced polymer (FRP) laminated variable thickness plates with intermediate elastic

support using artificial neural networks (ANNs) method. *J. Vibroeng.* 19, 3668–3678. doi: 10.21595/jve.2017.18209

Altabey, W. A. (2017d). Delamination evaluation on basalt FRP composite pipe by electrical potential change. *J. Adv. Aircraft Spacecraft Sci.* 4, 515–528. doi: 10.12989/aas.2017.4.5.515

Altabey, W. A. (2017e). EPC method for delamination assessment of basalt FRP pipe: electrodes number effect. *J. Struct. Monit. Mainten.* 4, 69–84. doi: 10.12989/smm.2017.4.1.069

Altabey, W. A. (2018). High performance estimations of natural frequency of basalt FRP laminated plates with intermediate elastic support using response surfaces method. *J. Vibroeng.* 20, 1099–1107. doi: 10.21595/jve.2017.18456

Altabey, W. A., and Noori, M. (2017a). Detection of fatigue crack in basalt FRP laminate composite pipe using electrical potential change method. *J. Phys. Conf. Ser.* 842:012079. doi: 10.1088/1742-6596/842/1/012079

Altabey, W. A., and Noori, M. (2017b). Fatigue life prediction for carbon fibre/epoxy laminate composites under spectrum loading using two different neural network architectures. *Int. J. Sustain. Mater. Struct. Syst.* 3, 53–78. doi: 10.1504/IJSMSS.2017.092252

Altabey, W. A., and Noori, M. (2018). Monitoring the water absorption in GFRE pipes via an electrical capacitance sensors. *J. Adv. Aircraft Spacecraft Sci.* 5, 411–434. doi: 10.12989/aas.2018.5.4.499

Baber, T. T., and Noori, M. N. (1985). Random vibration of degrading, pinching systems. *J. Eng. Mech.* 111, 1010–1026. doi: 10.1061/(ASCE)0733-9399(1985)111:8(1010)

Baber, T. T., and Noori, M. N. (1986). Modeling general hysteresis behavior and random vibration application. *J. Vib. Acoust.* 108, 411–420. doi: 10.1115/1.3269364

Baber, T. T., and Wen, Y. K. (1980). *Stochastic Equivalent Linearization for Hysteretic, Degrading, Multistory Strutctures*. University of Illinois Engineering Experiment Station; College of Engineering; University of Illinois at Urbana-Champaign.

Beck, J. L., and Au, S. K. (2002). Bayesian updating of structural models and reliability using Markov chain Monte Carlo simulation. *J. Eng. Mech.* 128, 380–391. doi: 10.1061/(ASCE)0733-9399(2002)128:4(380)

Behmanesh, I., and Moaveni, B. (2014). Probabilistic identification of simulated damage on the Dowling Hall footbridge through Bayesian finite element model updating. *J. Struct. Control Hlth. Monit.* 22, 463–483. doi: 10.1002/stc.1684

Bouc, R. (1967). "Forced vibration of mechanical systems with hysteresis," in *Proceedings of the Fourth Conference on Non-linear Oscillation* (Prague).

Brewick, P. T., Masri, S. F., Carboni, B., and Lacarbonara, W. (2016). Data-based nonlinear identification and constitutive modeling of hysteresis in NiTiNOL and steel strands. *J. Eng. Mech.* 142, 1–17. doi: 10.1061/(ASCE)EM.1943-7889.0001170

Chan, R., Yuen, J., Lee, E., and Arashpour, M. (2015). Application of nonlinear-autoregressive-exogenous model to predict the hysteretic behaviour of passive control systems. *J. Eng. Struct.* 85, 1–10. doi: 10.1016/j.engstruct.2014.12.007

Charalampakis, A. E., and Dimou, C. K. (2010). Identification of Bouc–Wen hysteretic systems using particle swarm optimization. *J. Comput. Struct.* 88, 1197–1205. doi: 10.1016/j.compstruc.2010.06.009

Charalampakis, A. E., and Koumousis, V. K. (2008a). Identification of Bouc–Wen hysteretic systems by a hybrid evolutionary algorithm. *J. Sound Vib.* 314, 571–585. doi: 10.1016/j.jsv.2008.01.018

Charalampakis, A. E., and Koumousis, V. K. (2008b). On the response and dissipated energy of Bouc–Wen hysteretic model. *J. Sound Vib.* 309, 887–895. doi: 10.1016/j.jsv.2007.07.080

Chatzi, E. N., and Smyth, A. W. (2009). The unscented Kalman filter and particle filter methods for nonlinear structural system identification with non-collocated heterogeneous sensing. *J. Struct. Control Hlth. Monit.* 16, 99–123. doi: 10.1002/stc.290

Chatzi, E. N., Smyth, A. W., and Masri, S. F. (2010). Experimental application of on-line parametric identification for nonlinear hysteretic systems with model uncertainty. *J. Struct. Saf.* 32, 326–337. doi: 10.1016/j.strusafe.2010.03.008

Ching, J., and Chen, Y. C. (2007). Transitional Markov Chain Monte Carlo method for Bayesian model updating, model class selection, and model averaging. *J. Eng. Mech.* 133, 816–832. doi: 10.1061/(ASCE)0733-9399(2007)133:7(816)

Constantinou, M. C., Soong, T. T., and Dargush, G. F. (1998). *Passive Energy Dissipation Systems for Structural Design and Retrofit*. Multidisciplinary Center for Earthquake Engineering Research.

Deb, K. (2013). *Bouc-Wen-Baber-Noori Model of Hysteresis*. Source Forge. Available online at: https://sourceforge.net/projects/boucwenbabernoo/

Deb, K., Pratap, A., Agarwal, S., and Meyarivan, T. (2002). A fast and elitist multi-objective genetic algorithm: NSGA-II. *IEEE J. Trans. Evol. Comput.* 6, 182–197. doi: 10.1109/4235.996017

Erazo, K., and Nagarajaiah, S. (2018). Bayesian structural identification of a hysteretic negative stiffness earthquake protection system using unscented Kalman filtering. *J. Struct. Control Hlth. Monit.* 25, 1–18. doi: 10.1002/stc.2203

Foliente, G. C. (1995). Hysteresis modeling of wood joints and structural systems. *J. Struct. Eng.* 121, 1013–1022. doi: 10.1061/(ASCE)0733-9445(1995)121:6(1013)

Green, P. L. (2015). Bayesian system identification of dynamical systems using large sets of training data: a MCMC solution. *J. Probabilist. Eng. Mech.* 42, 54–63. doi: 10.1016/j.probengmech.2015.09.010

Green, P. L., Cross, E. J., and Worden, K. (2015). Bayesian system identification of dynamical systems using highly informative training data. *J. Mech. Syst. Signal PR* 56, 109–122. doi: 10.1016/j.ymssp.2014.10.003

Hornig, K. H., and Flowers, G. T. (2005). Parameter characterization of the Bouc-Wen mechanical hysteresis model for sandwich composite materials using real coded genetic algorithms. *Int. J. Acoust. Vib.* 10:7381. doi: 10.20855/ijav.2005.10.2176

Hossain, M. R. (1995). *OpenSees Structural Design Software Command Manual for BWBN Material Model.* Avaialble online at: http://opensees.berkeley.edu/wiki/index.php/BWBN_Material

Ikhouane, F., and Gomis-Bellmunt, O. (2008). A limit cycle approach for the parametric identification of hysteretic systems. *J. Syst. Control Lett.* 57, 663–669. doi: 10.1016/j.sysconle.2008.01.003

Ikhouane, F., Mañosa, V., and Rodellar, J. (2007). Dynamic properties of the hysteretic Bouc-Wen model. *J. Syst. Control Lett.* 56, 197–205. doi: 10.1016/j.sysconle.2006.09.001

Ikhouane, F., and Rodellar, J. (2007). *Systems With Hysteresis: Analysis, Identification and Control Using the Bouc-Wen Model*. Hong Kong: John Wiley & Sons.

Jeen-Shang, L., and Yigong, Z. (1994). Nonlinear structural identification using extended Kalman filter. *J. Comput. Struct.* 52, 757–764.

Kontoroupi, T., and Smyth, A. W. (2017). Online Bayesian model assessment using nonlinear filters. *J. Struct. Control Hlth. Monit.* 24, 1–15. doi: 10.1002/stc.1880

Lei, Y., and Jiang, Y. Q. (2011). "A two-stage Kalman estimation approach for the identification of structural parameters under unknown inputs," in *The Twelfth East Asia-Pacific Conference on Structural Engineering and Construction,* 3088–3094.

Ljung, L. (2010). Perspectives on system identification. *Annu. Rev. Control* 34, 1–5. doi: 10.1016/j.arcontrol.2009.12.001

Lu, S., and Basar, T. (1998). Robust nonlinear system identification using neural-network models. *IEEE T. Neural Netw.* 9, 407–429. doi: 10.1109/72.668883

Ma, F., Zhang, H., Bockstedte, A., Foliente, G. C., and Paevere, P. (2004). Parameter analysis of the differential model of hysteresis. *J. Appl. Mech.* 71, 342–349. doi: 10.1115/1.1668082

Masri, S. F., Chassiakos, A. G., and Caughey, T. K. (1992). Structure-unknown non-linear dynamic systems: identification through neural networks. *J. Smart Mater. Struct.* 1, 45–56. doi: 10.1088/0964-1726/1/1/007

Monti, G., Quaranta, G., and Marano, G. C. (2009). Genetic-algorithm-based strategies for dynamic identification of nonlinear systems with noise-corrupted response. *J. Comput. Civil Eng.* 24, 173–187. doi: 10.1061/(ASCE)CP.1943-5487.0000024

Mu, T., Zhou, L., and Yang, J. N. (2013). Comparison of adaptive structural damage identification techniques in nonlinear hysteretic vibration isolation systems. *J. Earthq. Eng. Eng. Vib.* 12, 659–667. doi: 10.1007/s11803-013-0204-y

Muller, O., Savino, F., Rubinstein, M., and Foschi, R. O. (2012). "Performance-based seismic design: a search-based cost optimization with minimum reliability constraints," in *Structural Seismic Design Optimization and Earthquake Engineering: Formulations and Applications* 23–50. doi: 10.4018/978-1-4666-1640-0.ch002

Muto, M., and Beck, J. L. (2008). Bayesian updating and model class selection for hysteretic structural models using stochastic simulation. *J. Vib. Control* 14, 7–34. doi: 10.1177/1077546307079400

Muto, M. M. (2007). *Application of Stochastic Simulation Methods to System Identification.* Ph.D., California Institute of Technology.

Narendra, K. S., and Parthasarathy, K. (1990). Identification and control of dynamical systems using neural networks. *IEEE T. Neural Netw.* 1, 4–27. doi: 10.1109/72.80202

Noori, M. (1984). *Random Vibration of Degrading Systems With General Hysteretic Behavior*. Ph.D., University of Virginia.

Noori, M., Wang, H., Altabey, W. A., and Silik, A. I. H. (2018). A modified wavelet energy rate based damage identification method for steel bridges. *Int. J. Sci. Technol.* doi: 10.24200/sci.2018.20736

Ortiz, G. A., Alvarez, D. A., and Bedoya-Ruíz, D. (2013). Identification of Bouc-Wen type models using multi-objective optimization algorithms. *J. Comput. Struct.* 114, 121–132. doi: 10.1016/j.compstruc.2012.10.016

Ortiz, G. A., Alvarez, D. A., and Bedoya-Ruíz, D. (2015). Identification of Bouc–Wen type models using the Transitional Markov Chain Monte Carlo method. *J. Comput. Struct.* 146, 252–269. doi: 10.1016/j.compstruc.2014.10.012

Park, Y. J., Wen, Y. K., and Ang, A. (1986). Random vibration of hysteretic systems under bi-directional ground motions. *Earthq. Eng. Struct. D* 14, 543–557. doi: 10.1002/eqe.4290140405

Peng, G. R., Li, W. H., Du, H., Dengc, H. X., and Alicia, G. (2014). Modelling and identifying the parameters of a magneto-rheological damper with a force-lag phenomenon. *J. Appl. Math. Model.* 38, 3763–3773. doi: 10.1016/j.apm.2013.12.006

Puttige, V. R., and Anavatti, S. G. (2007). "Comparison of real-time online and offline neural network models for a UAV," in *IEEE International Joint Conference on Neural Networks* (Hungary), 412–417.

Saadat, S., Buckner, G. D., Furukawa, T., and Noori, M. N. (2003). "Nonlinear system identification of base-excited structures using an intelligent parameter varying (IPV) modeling approach," in *Proceedings of Smart Structures and Materials, International Society for Optics and Photonics* (San Diego, CA), 555–564.

Saadat, S., Buckner, G. D., Furukawa, T., and Noori, M. N. (2004a). An intelligent parameter varying (IPV) approach for non-linear system identification of base excited structures. *Int. J. Nonlin. Mech.* 39, 993–1004. doi: 10.1016/S0020-7462(03)00091-X

Saadat, S., Buckner, G. D., and Noori, M. N. (2007). Structural system identification and damage detection using the intelligent parameter varying technique: an experimental study. *J. Struct. Health Monit.* 6, 231–243. doi: 10.1177/1475921707081980

Saadat, S., Noori, M. N., Buckner, G. D., Furukawa, T., and Suzuki, Y. (2004b). Structural health monitoring and damage detection using an intelligent parameter varying (IPV) technique. *Int. J. Nonlin. Mech.* 39, 1687–1697. doi: 10.1016/j.ijnonlinmec.2004.03.001

Sohn, H. (1998). *A Bayesian Probabilistic Approach to Damage Detection for Civil Structures*. Ph.D., Stanford university.

Soong, T. T., and Spencer, B. F. (2002). Supplemental energy dissipation: state-of-the-art and state-of-the-practice. *Eng. Struct.* 24, 243–259. doi: 10.1016/S0141-0296(01)00092-X

Spencer, B. F. Jr, and Nagarajaiah, S. (2003). State of the art of structural control. *J. Struct. Eng.* 129, 845–856. doi: 10.1061/(ASCE)0733-9445(2003)129:7(845)

Wen, Y. K. (1975). Approximate method for nonlinear random vibration. *J. Eng. Mech.* 101, 389–401.

Wen, Y. K. (1976). Method for random vibration of hysteretic systems. *J. Eng. Mech.* 102, 249–263.

Wen, Y. K. (1980). Equivalent linearization for hysteretic systems under random excitation. *J. Appl. Mech.* 47, 150–154. doi: 10.1115/1.3153594

Wen, Y. K. (1986). Stochastic response and damage analysis of inelastic structures. *Probabilist. Eng. Mech.* 1, 49–57. doi: 10.1016/0266-8920(86)90009-3

Wen, Y. K. (1989). Methods of random vibration for inelastic structures. *J. Appl. Mech. Rev.* 42, 39–52. doi: 10.1115/1.3152420

Wen, Y. K., and Yeh, C. H. (1989). Biaxial and torsional response of inelastic structures under random excitation. *J. Struct. Saf.* 6, 137–152. doi: 10.1016/0167-4730(89)90016-7

Worden, K., and Hensman, J. J. (2012). Parameter estimation and model selection for a class of hysteretic systems using Bayesian inference. *Mech. Syst. Signal PR* 32, 153–169. doi: 10.1016/j.ymssp.2012.03.019

Wu, M., and Smyth, A. W. (2007). Application of the unscented Kalman filter for real-time nonlinear structural system identification. *J. Struct. Control Hlth. Monit.* 14, 971–990. doi: 10.1002/stc.186

Wu, M., and Smyth, A. W. (2008). Real-time parameter estimation for degrading and pinching hysteretic models. *Int. J. Nonl. Mech.* 43, 822–833. doi: 10.1016/j.ijnonlinmec.2008.05.010

Yang, J. N., Lin, S., Huang, H., and Zhou, L. (2006). An adaptive extended Kalman filter for structural damage identification. *J. Struct. Control Hlth. Monit.* 13, 849–867. doi: 10.1002/stc.84

Yuen, K. V., and Katafygiotis, L. S. (2001). Bayesian time–domain approach for modal updating using ambient data. *Probabilist. Eng. Mech.* 16, 219–231. doi: 10.1016/S0266-8920(01)00004-2

Zadeh, L. (1956). On the identification problem. *IRE Trans Circ. Theory* 3, 277–281. doi: 10.1109/TCT.1956.1086328

Zhang, B. T., and Cho, D. Y. (2001). System identification using evolutionary Markov Chain Monte Carlo. *J. Syst. Architect.* 47, 587–599. doi: 10.1016/S1383-7621(01)00017-0

Zhao, Y., Noori, M., and Altabey, W. A. (2017a). Damage detection for a beam under transient excitation via three different algorithms. *J. Struct. Eng. Mech.* 63, 803–817.

Zhao, Y., Noori, M., Altabey, W. A., and Bahram Beheshti-Aval, B. (2017b). Mode shape based damage identification for a reinforced concrete beam using wavelet coefficient differences and multi-resolution analysis. *J. Struct. Control Health Monitor.* 25, 1–41. doi: 10.1002/stc.2041

Zhao, Y., Noori, M., Altabey, W. A., and Wu, Z. (2018). Fatigue damage identification for composite pipeline systems using electrical capacitance sensors. *J. Smart Mater. Struct.* 27:8. doi: 10.1088/1361-665X/aacc99

Zheng, W., and Yu, Y. (2013). Bayesian probabilistic framework for damage identification of steel truss bridges under joint uncertainties. *Adv. Civil Eng.* 2013:307171. doi: 10.1155/2013/307171

Conflict of Interest Statement: The authors declare that the research was conducted in the absence of any commercial or financial relationships that could be construed as a potential conflict of interest.

frontiers in Built Environment

ORIGINAL RESEARCH
published: 10 January 2019
doi: 10.3389/fbuil.2018.00087

Damage Assessment by Numerical Modeling of Sant'Agostino's Sanctuary in Offida During the Central Italy 2016–2017 Seismic Sequence

Ersilia Giordano, Francesco Clementi, Andrea Nespeca and Stefano Lenci*

Department of Civil and Building Engineering, and Architecture, Polytechnic University of Marche, Ancona, Italy

The subject of this work is the Sant'Agostino Sanctuary in Offida (Italy); we investigated both the dynamic behavior and the seismic vulnerability of the complex, used nowadays in its parts as school building, oratory, and church. Offida is in central Italy; the village has been severely damaged by the last seismic events of 2016. The sanctuary was heavily damaged by the earthquake of 24 August 2016. We recurred to finite elements to estimate the vulnerability of the sanctuary and its dynamic response, considering masonry's non-linear behavior by means of proper constitutive assumptions. To estimate how the monastery bears the lateral loads related to the expected demands resulting from seismic actions (N2 method) using non-linear static analysis (Pushover), we recurred to a homogenized material and smeared cracking and crushing constitutive law. As may be remarked by observing buildings that share the same features of the sanctuary and, moreover, by comparing seismic demand vs. capacity, the structure is prone to massive damage leading to collapse. The paper underlines how advanced numerical analysis grants fundamental data on how historical masonry buildings behave under seismic action, providing a method that may easily be implemented at historic monasteries in Europe.

Keywords: FE modeling, solid elements, earthquake loading, non-linear static analysis, seismic vulnerability, damage assessment

OPEN ACCESS

Edited by:
Vagelis Plevris, OsloMet–Oslo Metropolitan University, Norway

Reviewed by:
Sameh Samir F. Mehanny, Cairo University, Egypt
Constantinos Repapis, University of West Attica, Greece

****Correspondence:***
Francesco Clementi
francesco.clementi@univpm.it

Specialty section:
This article was submitted to Computational Methods in Structural Engineering, a section of the journal Frontiers in Built Environment

Received: *25 August 2018*
Accepted: *19 December 2018*
Published: *10 January 2019*

Citation:
Giordano E, Clementi F, Nespeca A and Lenci S (2019) Damage Assessment by Numerical Modeling of Sant'Agostino's Sanctuary in Offida During the Central Italy 2016–2017 Seismic Sequence. Front. Built Environ. 4:87. doi: 10.3389/fbuil.2018.00087

INTRODUCTION

The intense seismic activity that affected many areas of Italy over the last decades clearly showed how much care should be taken of architectural heritage and its preservation. Assessing the seismic vulnerability of a monumental masonry building may be a difficult task to accomplish, considering how peculiar these structures usually are, requiring sophisticated and computationally heavy numerical models to have a proper estimation of their dynamical response under seismic action. Most recent Italian earthquakes (Umbria-Marche 1997–1998, Abruzzo 2009, Emilia-Romagna 2012, Central Italy 2016), caused irreparable damages to many elements of the architectural heritage, such as monumental buildings, churches and steeples (Ceci et al., 2010; Acito et al., 2014; Milani and Valente, 2015).

Protecting historical buildings from seismic activity plays a significant role on public safety, considering how European countries, moreover Italy, have such a various architectural heritage that is still in use, most of the times hosting strategic public functions (Asteris et al., 2014). However, such buildings obviously do not grant proper safety against seismic actions, since their design criteria do not take into account lateral resistance and ductility in favor of efficiently bearing gravity loads; housing significant functions in those structures, especially during emergencies of any kind, involves the attainment of the required safety levels (Clementi et al., 2015).

The features that all monumental masonry buildings share, such as being so complex, irregular, mainly designed to bear gravity loads and way more massive than modern architecture, make structural behavior uneasy to estimate, especially when it comes to evaluating it under seismic action. Despite its being challenging, proper modeling of masonry buildings is fundamental to seismic resistant design or to assess earthquake vulnerability. While contemporary structures are basically made of industrial based components, such as RC or steel, which make their structural behavior uniform and certain (Pierdicca et al., 2016b, 2018), ancient masonry structures require the acknowledgment of more parameters to be modeled, like floors' stiffness (diaphragm effect) or connections between orthogonal walls and structural and non-structural elements (Betti and Vignoli, 2008a, 2011; Bartoli et al., 2013; Clementi et al., 2018a).

Masonry macro elements are made of bricks bonded by mortar, so they can be seen as a composite system whose parts are characterized by a very different mechanical behavior, making structural modeling a challenging activity, as the wide range of designs available at the state of the art seems to prove (Asteris et al., 2015). No-Tension Material models and their mechanical characterization derive from the obvious fact that masonry does not offer a significant resistance to tensile stresses. To take into proper account how masonry is characterized by a non-linear response, starting from the lowest deformation levels, the hypothesis of unilateral mechanical behavior may be applied to the theories of limit analysis, leading to models able to estimate the collapse loads of masonry structures (Del Piero, 1998; Milani et al., 2007; Milani, 2011). Inelastic phenomena that affect masonry buildings under seismic action leading to local phenomena of softening, failure and strain localization, such as sliding, cracking, crushing at the mortar joints, tensile fracture of bricks, may be analyzed by means of micro-mechanical models, characterized by elasto-plastic laws (Lotfi and Shing, 1994; Lourenço and Rots, 1997) or damage theories (Luciano and Sacco, 1998). At the state of the art, many homogenization techniques are available to obtain continuum models, since representing bricks and joints would not be possible when modeling monumental buildings, leading to way too computationally heavy FEM (Zucchini and Lourenço, 2002; Lourenço, 2009; Addessi et al., 2010); these various approaches traced the path to the related macro-mechanical models, moving from the rigorous application of the homogenization theory for periodic media (Anthoine, 1995) to two-steps approximated strategies (Pande et al., 1989). Acary (2001) gives

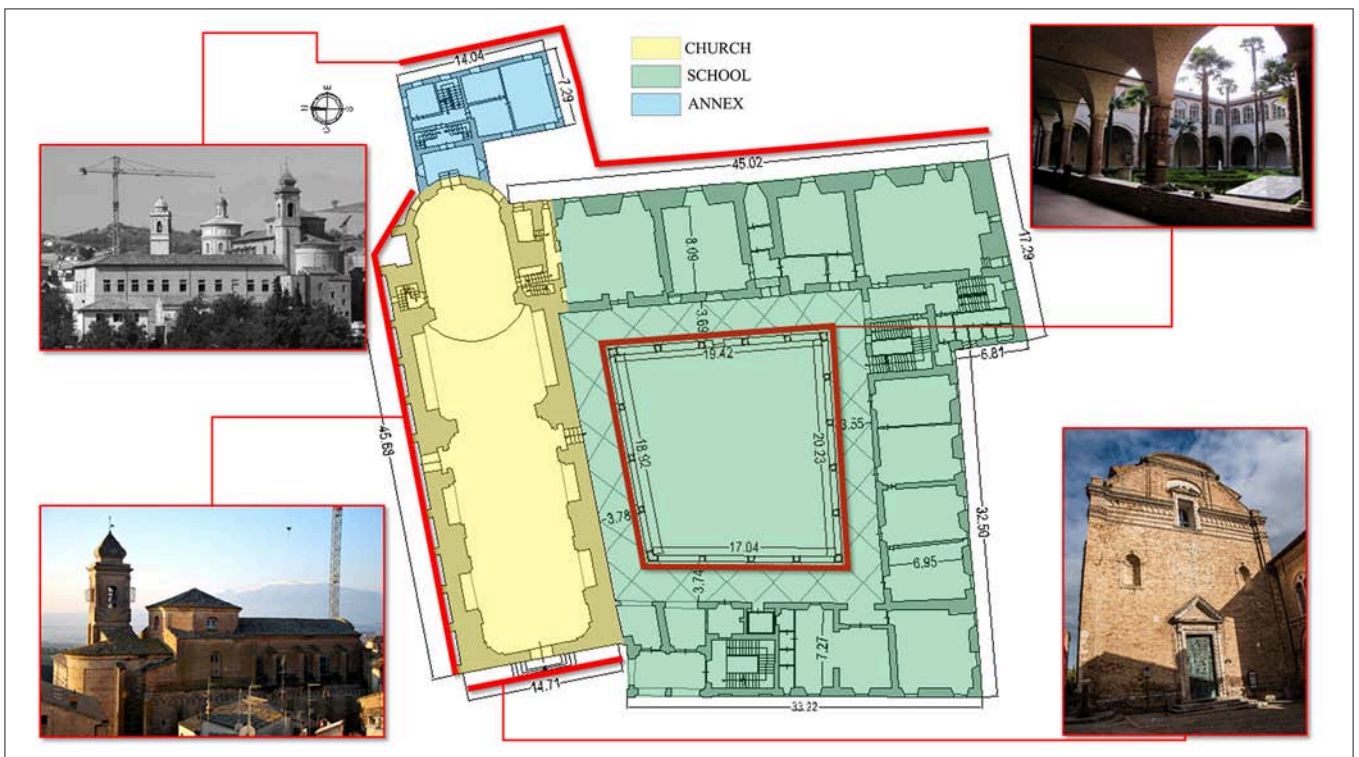

FIGURE 1 | General view of Sant' Agostino's Sanctuary.

a complete review of the homogenization techniques described above, while (Luciano and Sacco, 1997; Zucchini and Lourenço, 2002, 2004; Addessi et al., 2010) focus on historical masonry walls.

Although simplified models may be the reference to represent the structural behavior of masonry buildings and all their peculiarities, it appears challenging to apply proper simplifications while keeping the requested level of modeling accuracy. At the state of the art, we may identify three different modeling strategies. The most recurrent modeling approach we find nowadays is the Equivalent Frame Method (Caliò et al., 2012; Lagomarsino et al., 2013; Quagliarini et al., 2017), which designs the walls as an idealized frame where the non-linear response is concentrated on deformable elements connected by rigid nodes representing not usually damage prone structural components. Starting from a careful seismic phenomena observation that leads to pointing out how cracks and failure modes mostly concentrate in recurrent elements, piers and spandrels may be seen as the two main structural components, especially when it comes to analyzing the in-plane response of complex masonry walls with openings. Another frequently used approach provides for the use of finite elements schemes to model masonry structures as they were continuous; current literatures offers recurrent examples of how this modeling strategy may be applied with ease to historical buildings, such as monasteries (Lourenço et al., 2007; Betti and Vignoli, 2008a), churches (Betti and Vignoli, 2008b; Milani and Valente, 2015; Clementi et al., 2017a; Formisano et al., 2018), bridges (Betti et al., 2008), steeples or towers (D'Ambrisi et al., 2012; Minghini et al., 2014; Carpinteri et al., 2015), ancient city centers (Formisano et al., 2015). To gain exhaustive comprehension of seismic phenomena, analysis output usually comes from combining the results given by different sets of parameters, since the models are progressively refined, especially in terms of fracture and plasticity. In the two methods described above, dynamical problems are reduced to elementary static issues (equivalent pushover schemes), since equivalent horizontal static forces make up for seismic loadings. As an alternative to the Equivalent Frame Method, masonry buildings may be modeled as distinct elements in an assembly of blocks affected by unilateral frictional contacts (Jean, 1999; Clementi et al., 2018b; Poiani et al., 2018).

After carefully analyzing masonry's peculiarities, it seems clear how turning to continuous material leads to the most representative structural models, especially when those are related to irregular complexes. Many non-linear mechanisms proper of concrete structures, such as damage deriving, friction-plasticity, crushing or cohesion, are already implemented in many structural software, yet there is a blatant lack of effective instruments when it comes to design 2D and 3D non-linear models of masonry buildings.

This work aims to clearly show how delicate yet crucial it is to properly take into account the three-dimensional behavior of the complex, underlining its structural weaknesses. To obtain a representative numerical model, a preliminary survey was performed in order to get all the required parameters, such as the geometry of the structure and the mechanical properties of

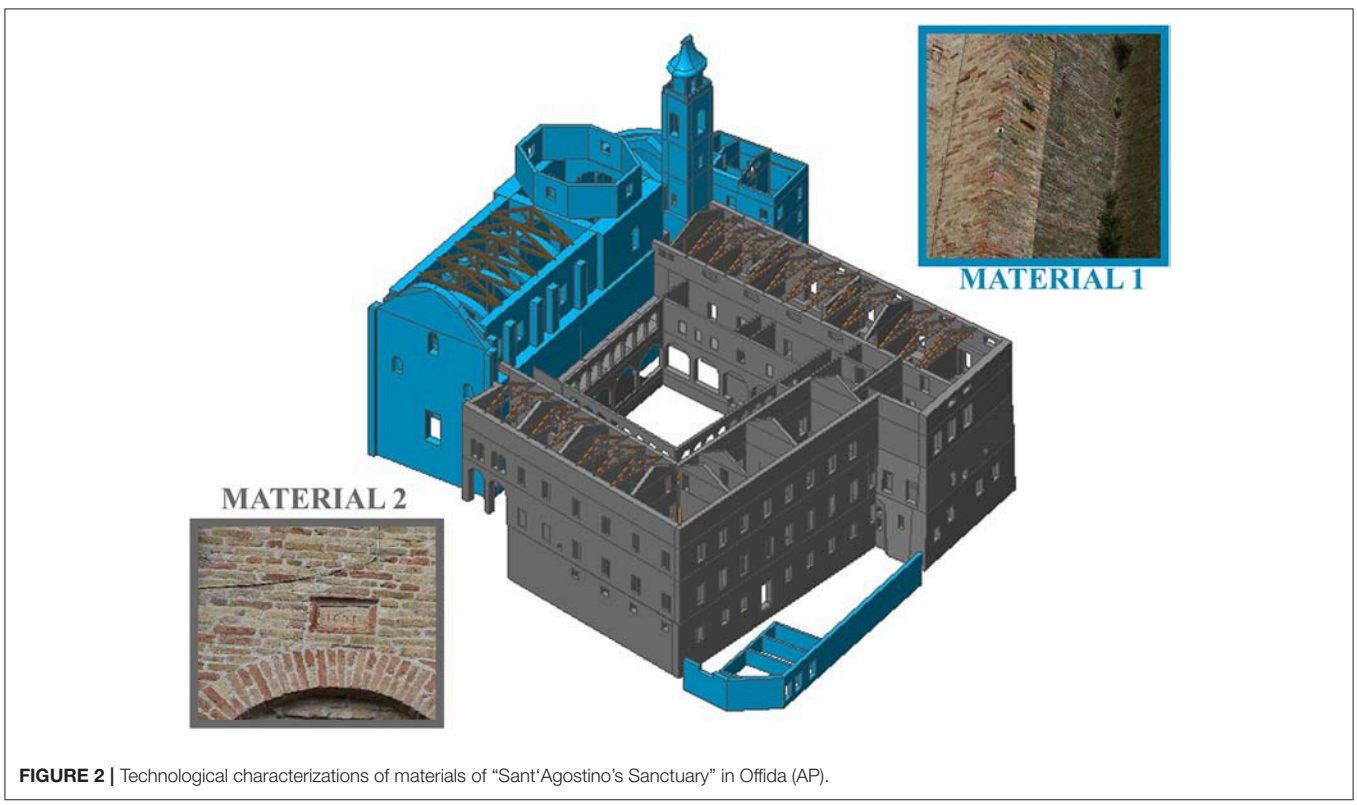

FIGURE 2 | Technological characterizations of materials of "Sant'Agostino's Sanctuary" in Offida (AP).

TABLE 1 | Mechanical characteristics of the main elements.

Knowledge level	f_c [MPa]	f_t [MPa]	γ [kN/m^3]	E [MPa]	ν	G_c [N/mm]	G_f [N/mm]	Confidence Factor (CF)
NORMAL SOLID BRICK AND LIME MORTAR—MATERIAL 1								
KL1	1.78	0.18	18	1500	0.4	1.731	0.017	1.35
GOOD SOLID BRICK AND LIME MORTAR—MATERIAL 2								
KL1	2.67	0.26	18	2250	0.4	2.299	0.023	1.35

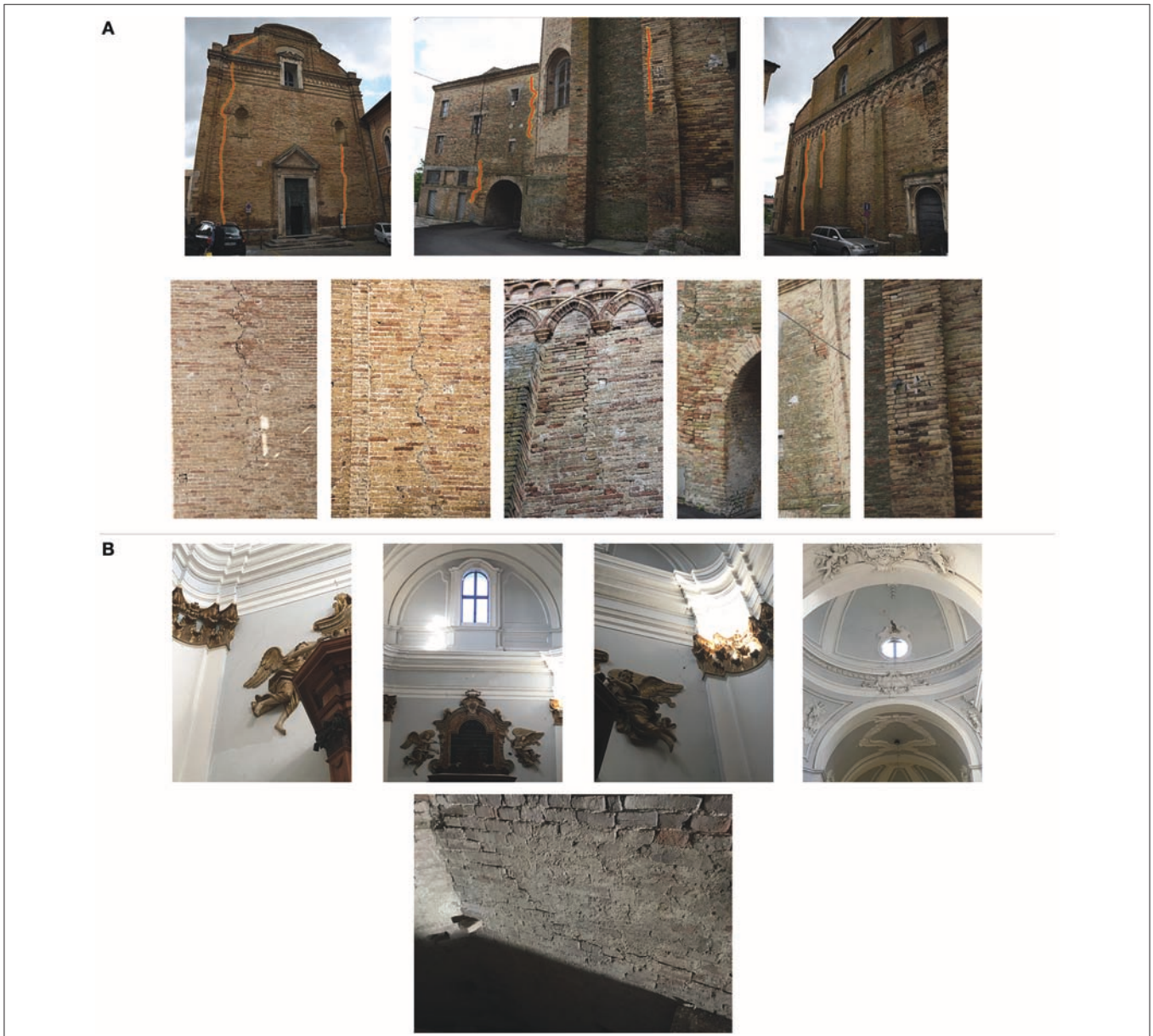

FIGURE 3 | External cracks on façade, north wall of the nave and north front of the annex **(A)** Internal cracks of the church **(B)**.

masonry material, combined with a careful historical and archival research. Once all the requested data were collected, the designed 3D finite element model, endowed with an elastic plastic (with softening) constitutive damage law, was used to perform a wide number of non-linear static analysis (Clementi et al., 2017b). To make this model and its design features useful to many other historical masonry complexes, we opted for a smeared fracture energy approach.

The paper is organized as follows. In sections Historical Developments and Description of the Building in its Current Configuration, we described the historical developments, the characteristics of the material and the geometry of the case study situated in Offida (Central Italy), which are the starting point for subsequent developments. In section Damage After Seismic Sequence of 2016 the actual damage is described. In section Structural Analysis Methodology is illustrated the modeling strategy. In section Global Seismic Behavior sensitivity analyses of the case study are described to assess the global condition of the structure. In this section also the procedure defined for isolated churches in Brandonisio et al. (2013) is applied to the monastery, constituting de facto an extension of the method to more complex structures. The paper ends with some conclusions (section Conclusions).

HISTORICAL DEVELOPMENTS

To have proper understanding of how each part composing the sanctuary developed over the centuries, a preliminary historical analysis was carried out.

The foundation of the monastery's early nucleus is dated to the XIV century, when the relics related to the Eucharistic Miracle of Lanciano arrived in Offida leading to the replacement of the original church of St. Mary Magdalene by a greater one that the Augustinians decided to name their own to St. Augustine. Its construction lasted from 1338 to 1441. The works of enlargement, from the basements, were completed during the priory of a friar Jacopo in 1441. The cloister with quadrilateral closed shape is realized during 1574 using a long line of octagonal columns, whose basements are stone capitals, and surmounted by round arches.

At the center of the abbey, we find the usual well; the cloister led to the refectory. The convent was amended several times (from 1609 to 1618) and even renewed its foundations in 1625. The façade is Baroque (1686). The interior was modified and extended in the XVIII century with a Latin cross, with a dome inside a tambour and it was decorated with late baroque stucco and valuable wooden furniture (e.g., chorus and confessionals walnut of the cabinetmaker Alessio Donati from Offida). The interiors also preserve a precious reliquary cross (the "holy cross" that protects the relic of that miracle), it operates in silver gilt made in Venice in the XIV century and another reliquary of the art of Marche region of XV century. Other significant modifications were made between 1933 and 1937.

The monastery was firstly hit by L'Aquila earthquake (April 6, 2009) with a magnitude $M_W = 6.3$. After this seismic event, the

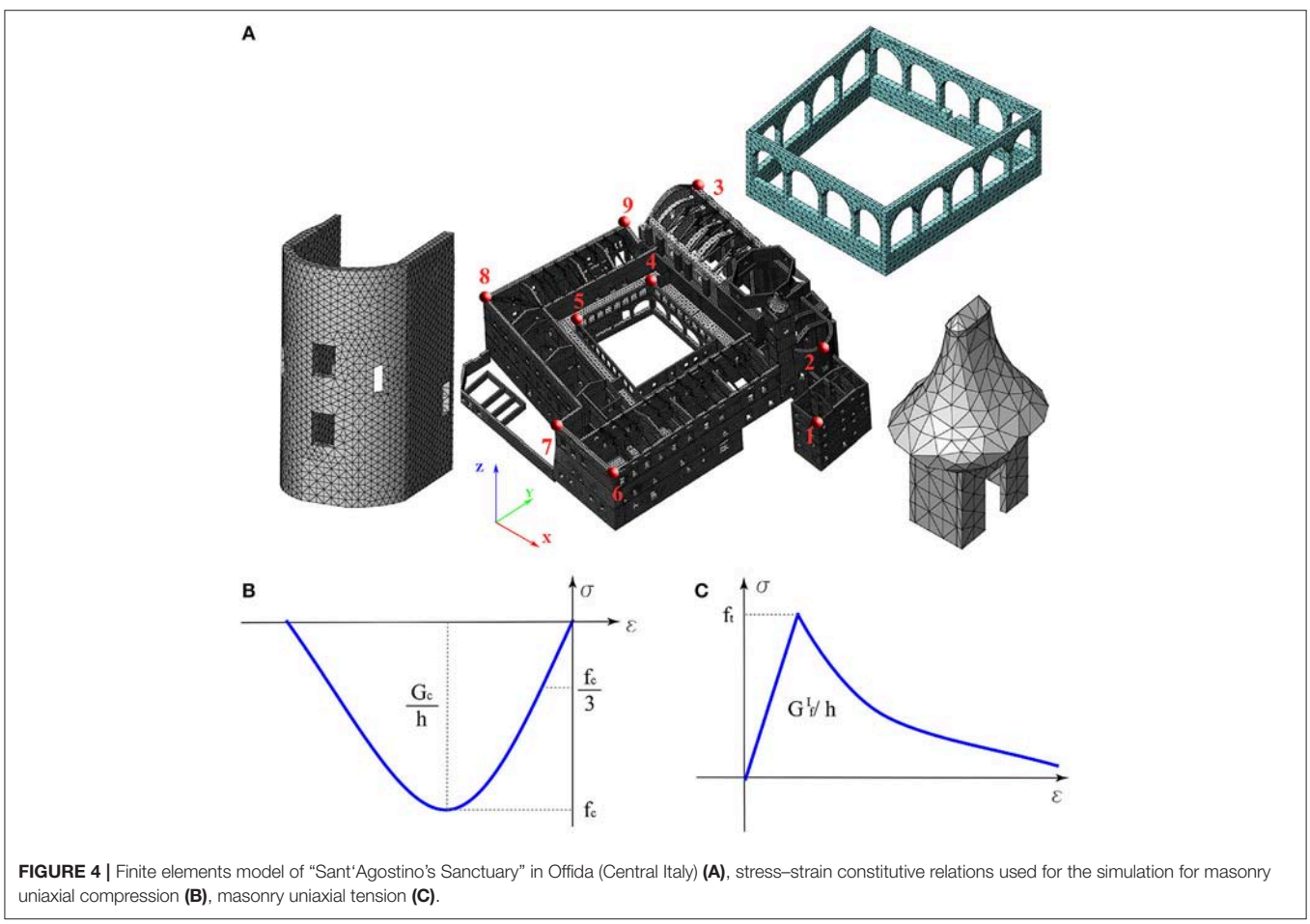

FIGURE 4 | Finite elements model of "Sant'Agostino's Sanctuary" in Offida (Central Italy) **(A)**, stress–strain constitutive relations used for the simulation for masonry uniaxial compression **(B)**, masonry uniaxial tension **(C)**.

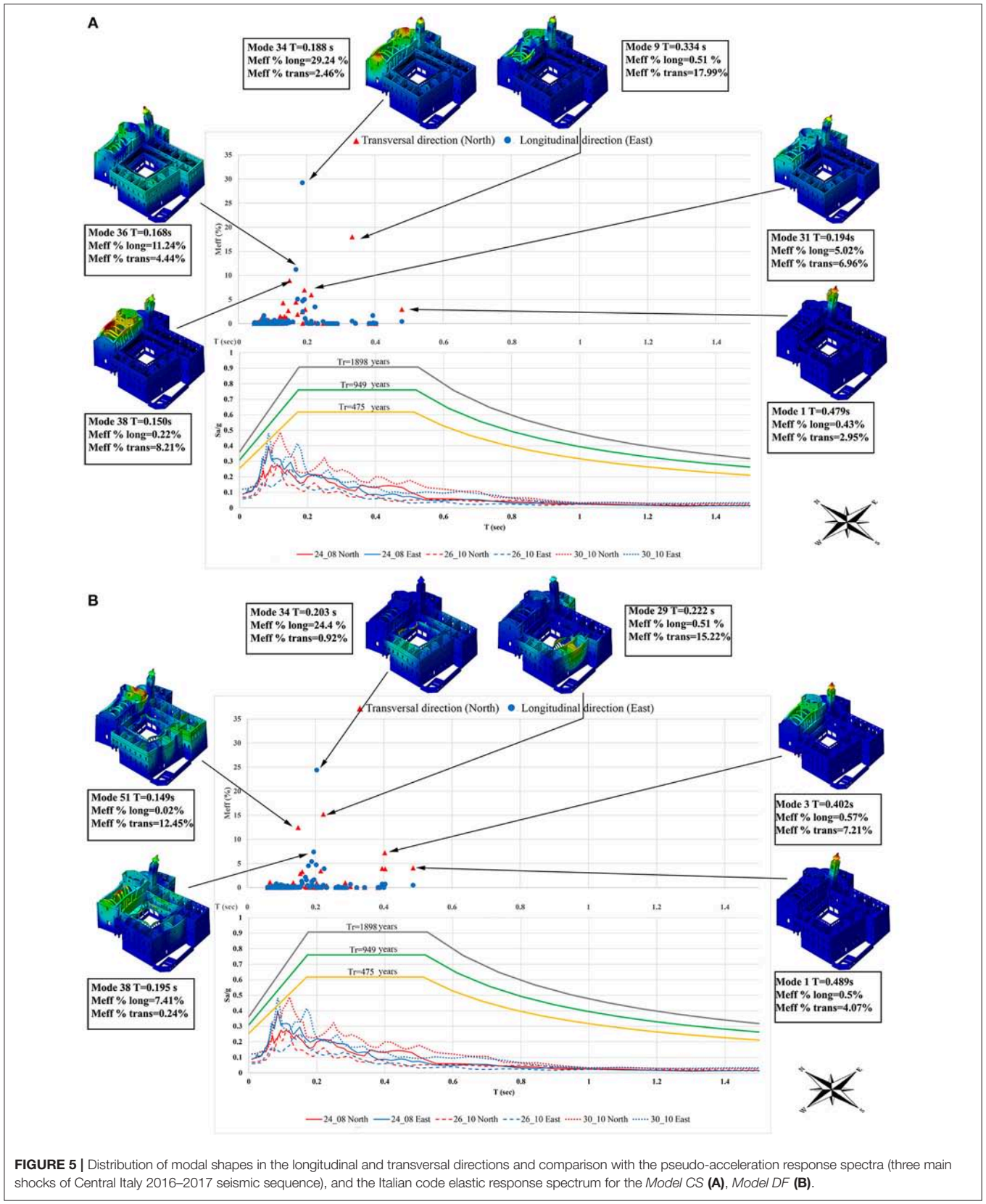

FIGURE 5 | Distribution of modal shapes in the longitudinal and transversal directions and comparison with the pseudo-acceleration response spectra (three main shocks of Central Italy 2016–2017 seismic sequence), and the Italian code elastic response spectrum for the *Model CS* **(A)**, *Model DF* **(B)**.

school building area was damaged, and other superficial cracks appeared in the main façade of the church. For this reason, in the 2010 a series of structural restorations was carried out on the buildings, except for the area of the church, which remained unchanged. A reconstruction/improvement on the three floors of the school building and an extensive re-roofing was done. Steel bracings or concrete slabs were inserted in some parts. The actual configuration is reported in **Figure 1**.

Currently, the refectory no longer exists since the rooms were turned into school classrooms, as indeed all the premises nearby the cloister. Such use began as early as 1870, after the law of confiscation of the Church's properties in 1866. The current division of the building is shown in **Figure 1.**

The church's walls linked, i.e., the masonry walls are connected from a structural point of view, to other parts of the oratory (annex) and school building, as proved by a few *in situ* tests performed on it. This means that a global analysis is appropriated for this case study.

DESCRIPTION OF THE BUILDING IN ITS CURRENT CONFIGURATION

Geometrical Survey

To ensure the preliminary data required by the study, an accurate *in situ* survey was performed on the complex, leading to a full geometry relief, focusing on structural details, such as connections between all the macro elements, characterization of masonry texture and its irregularities. As reported in section Historical Developments, the survey is completed by a historical report on how the complex developed over the centuries.

The entire area measures ∼2600 m^2 for the floor where at least three elevations are present in all parts of the structure. The main dimensions of the nave are ∼45.68 m of length, ∼14.71 m of width and a lateral-wall height (mean value) of about ∼18 m. The masonry walls' thickness is ranged between 2.55 m (nave walls) and 0.8 m (apse walls) (**Figure 1**). The church roof's structure is made of timber (nave). The masonry is composed of solid brick and lime mortar (**Figure 2**). However, the remaining parts of the monastery are also made of solid brick and lime mortar yet in a better state of preservation due to recent restorations as said in section Historical Developments. This leads to better elastic-mechanical parameters (**Table 1**).

The other portions of the building are an assemblage of horizontal rectangular zones, with a length of ∼45 m (East part) and a mean width of about ∼32 m (South and West parts). This area has three floors with a maximum height of 11 m. In the center, there is the "Portico" with square columns on solid brick with a width of 0.45 m and cross-vault at the upper sides. All these areas contain classrooms and offices of the school.

Material Characterization

We choose not to perform a complete characterization of the materials, since the annex and the monastery do not reveal any significant damage or issue nowadays, and we were on a budget. According to the current Italian Seismic Code (Ministro dei Lavori Pubblici e dei Trasporti., 2008; Circolare Ministeriale n. 617, 2009; Ministero delle Infrastrutture e dei Trasporti., 2018) this lead to the lowest Knowledge level KL1, related to a Confidence Factor (CF) equal to 1.35, as also requested by Eurocode 8 (EN 1998-3, 2010) for concrete structures.

The Italian regulation (Ministro dei Lavori Pubblici e dei Trasporti., 2008; Circolare Ministeriale n. 617, 2009; Ministero delle Infrastrutture e dei Trasporti., 2018) and its Annex C8A.2 was the reference to define the material's compressive strength, based on Table C8A.2.1 of (Circolare Ministeriale n. 617, 2009). With a Knowledge Level KL1, the related confidence factor CF = 1.35 is applied to obtain a final design compressive strength. The tensile strength of the masonry may be estimated as the 10% of the compressive resistance as reported in **Table 1**, as it is generally negligible.

DAMAGE AFTER SEISMIC SEQUENCE OF 2016

After the seismic events of 2016, the church has been seriously damaged, and it is currently being made safe to prevent collapses. The existing cracks have worsted, especially on the façade and on the transept, and new cracks have appeared on the dome and the church's roof. On the façade, two long cracks pass through the wall (**Figure 3**). The octagonal dome has cracks on all corners due to an interaction with the pushing beams of the roof; this led to a structural failure of common rafters. The transept shows vertical and diagonal cracks on north and south sides under the windows. After the seismic sequence, many cracks also appeared inside the church, especially on the nave (**Figure 3B**). The square, in front of the church, has been closed owing to the possibility of façade overturn.

STRUCTURAL ANALYSIS METHODOLOGY

Seismic assessments of monumental masonry buildings may be considered challenging, taking into account the not so obvious numerical modeling of non-linear behavior of such a no tension material itself, the complex geometrical configuration and the merely experimental characterization of its components (Pierdicca et al., 2016a). In accordance with the state of the art, we find nowadays different mechanical models and their related parameters to assess the highly non-linear behavior of masonry both in tension (low tensile capacity and consequent cracking phenomena) and compression.

The macro-modeling technique described in this paper leads to an exhaustive comprehension of all the non-linear phenomena that may affect masonry buildings under seismic action, even though its computing is still difficult to apply on a complex 3D structural system because of all the requested degrees of freedom. According to the chosen modeling technique and its features, the development of the cracks modifies the stiffness of the solid elements composing the model.

The smeared crack concept, and its FE implementation, offers a variety of possibilities, ranging from fixed single to fixed multidirectional and rotating crack approaches. Here, the distinction lies in the orientation of the crack, which is either kept constant, updated in a stepwise manner, or updated continuously

(Rots, 1991; Lourenço, 2009). Since smeared crack approaches do not require re-meshing of the model after the occurrence of cracks or a priori definition of possible locations of cracks, it is very convenient for FE models. Differently, the direct modeling of the crack into the mesh, with Linear and Non-linear Fracture mechanics models, is always accessible when the engineers deal with a small model, also for masonry or masonry-like materials (Clementi et al., 2008; Lenci et al., 2011, 2012).

Authors like (da Porto et al., 2010) used the isotropic rotating crack model to design panels composed by vertically perforated clay units and various types of joints, while (Manfredi et al., 2013) adopted a smeared crack model, to properly simulate how macro-models of brick masonry and adobe walls behave. Multi-directional fixed or rotating crack models also proved their great use in terms of debonding problems, e.g., (Ghiassi et al., 2013; Gattulli et al., 2014). Current practice shows how smeared crack models are versatile and require few preliminary data.

The non-linear behavior of the masonry panels that constitute the sanctuary is modeled by means of a Total Strain Crack Model based on fixed stress-strain law concepts provided by MIDAS FEA (Midas FEA, 2016), thus the cracking path is fixed to the direction of the principal strain vectors and kept constant during structure's loading; the panels were modeled with solid

TABLE 2 | Characteristics of main earthquakes recorded in Ascoli Piceno (ASP) station during the Central Italy seismic sequence in 2016–2017.

Seismic event	M_L	Depth (km)	Station	Class EC8	R_jb [km]	R_rup [km]	R_epi [km]	Channel NS PGA (m/s^2)	Channel EW PGA (m/s^2)
24/08/2016	6.0	8.1	Ascoli Piceno ASP	C*	31.35	31.36	37.77	0.088 g	0.087 g
26/10/2016	5.9	7.5	Ascoli Piceno ASP	C*	35.78	35.79	42.94	0.058 g	0.069 g
30/10/2016	6.1	9.2	Ascoli Piceno ASP	C*	30.18	30.18	43.95	0.12 g	0.119 g

**Indicates that site classification is not based on a direct Vs, 30 measurement.*

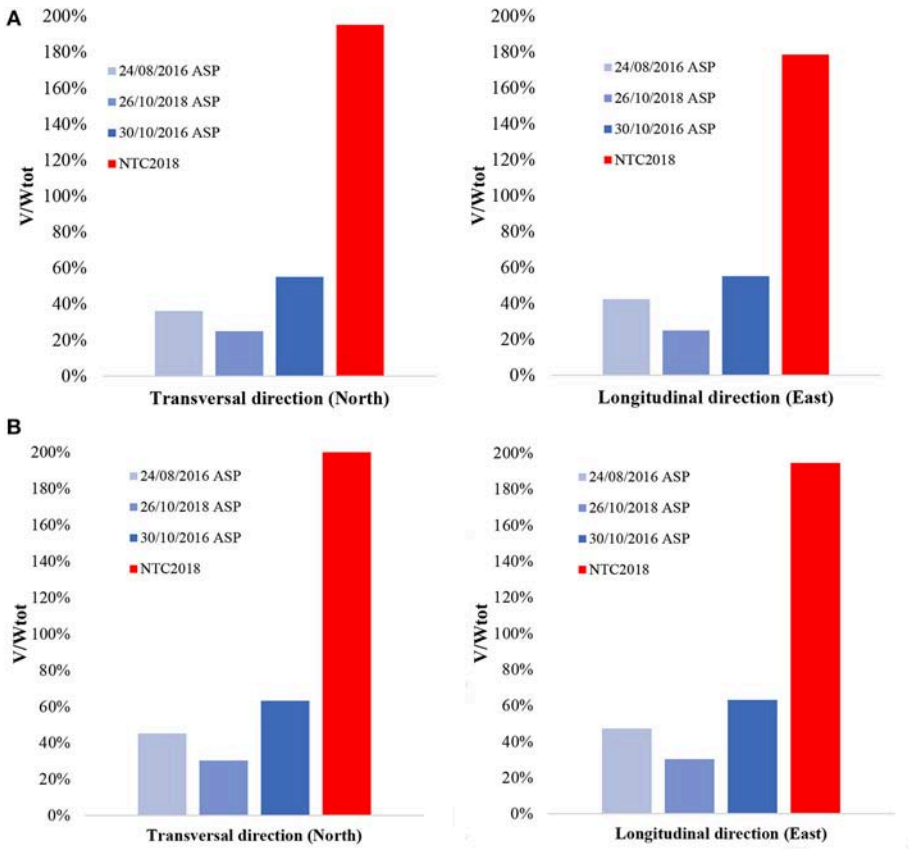

FIGURE 6 | Base shear (V) normalized to the total weight (Wtot) for *Model DF*: comparison between NTC2018 and the main shocks recorded during the 24th August 2016, 26th and 30th October 2016 for the *Model CS* **(A)**, *Model DF* **(B)**.

tetrahedron elements with 4 nodes, discretized with an optimized regular mesh (see **Figure 4A**).

The selected constitutive laws take into account the complex behavior of masonry, compression behavior is modeled by means of a parabolic hardening rule and a parabolic softening branch following the peak of resistance (**Figure 4B**) while the tension behavior is modeled by a linear hardening branch followed by a non-linear softening branch (**Figure 4C**). **Table 1** shows a report of fracture energies in compression (G_c) and tension (G_f), where *h* is the mean dimension of the mesh (Rots, 1991).

The shear retention factor (β) provides the rate of shear stiffness after cracking, which can be related to the progressive opening of the cracks or kept constant (low), in a range between 0 and 1. For the assessment described in this paper, we opted for a constant value of 0.05 as requested (Rots and de Borst, 1987; Rots, 1991).

Finite Element Model for the Global Response

The purpose of the designed numerical models was to represent all the significant features of the sanctuary, such as the geometry of the structural components with all their peculiarities and openings, the connections between all the macro elements. We also modeled the timber elements on the roofs.

One of the major focuses of the modeling phase was to choose the correct floors' in-plane stiffness, as this aspect is fundamental to comprehend structural response. According to the current Italian Standards (Ministero delle Infrastrutture e dei Trasporti., 2018), some floors which were recently restored can be considered as rigid for two coexisting reasons: solid concrete plates (i) have the minimum thickness (40 mm) and (ii) the necessary reinforcements to assure a rigid behavior (Ministero delle Infrastrutture e dei Trasporti., 2018). In other areas, differently, this assumption may not be in safe, mainly because the slabs are made of poor quality concrete or not well-connected to the peripheral walls. For this reason, two different models were analyzed, also to check the variability of the structural response due to slabs rigidity, namely:

- The model of the Current State, namely *Model CS*, where the slabs are modeled by the actual schemes;
- The model with totally Deformable Floor, namely *Model DF*, where slabs although adequately stiffened are supposed not to be connected to the peripheral walls or, the wooden slabs do not have a correct capacity design of the connector with the concrete.

After meshing, the final 3D numerical models are reported in **Figure 4A** with 94348 nodes, 454829 solid elements and a d.o.f. number of 372219 for *Model CS* and of 379062 for *Model DF*.

GLOBAL SEISMIC BEHAVIOR

According to the Italian code, the building analyzed in this paper is a "Class IV," i.e., a strategic structure, because it is currently use as school in some parts. The recurrence period ($T_{R,D}$) associated to the Limit State of Significant Damage (SLSD, or SLV in Italian) is of 1898 years, related to an expected Peak Ground Acceleration (PGA) equal to 0.283 g. The elastic response spectrum (soil type T1 and category of subsoil C are considered) is characterized by the following parameters: $S = 1.272$; $T_B = 0.175$ s; $T_C = 0.525$ s; $T_D = 2.733$ s (**Figure 5**).

The analyses were carried out using the horizontal components of different natural response spectra obtained from the time histories recorded near the city of Offida, with the objective of both assessing the damage caused to the sanctuary by the intense seismic activity affecting central Italy from august 2016 and evaluating the horizontal strength capacity. Unfortunately, the nearest station is the one in Ascoli Piceno [APS station in Italian Accelerometric Archive (ITACA)], as Offida has not been equipped with an accelerometric station. The two components responses spectrum (North direction coincide with X-direction, East direction coincides with Y-direction) used arise from the three main shocks recorded during the 2016 seismic events in that station: (i) 24/08/2016 with $M_w = 6.0$ and ML = 6.0, (ii) 26/10/2016 $M_w = 5.9$ and $M_L = 5.9$, and (iii) 30/10/2016 with $M_w = 6.5$ and $M_L = 6.1$. In **Table 2** are reported the main characteristics of the main shocks, the time histories used, the class of the site of the station, the main distance between the ASP station and the epicenter zone where (Kadas et al., 2011):

- R_jb, is the Joyner-Boore distance, known as the smallest spacing from the site to the surface projection of the rupture surface;
- R_rup, is the shortest distance between the site and the rupture surface;
- R_epi, is the distance estimated by geometric swap.

The comparison of the recorded spectrum and the elastic spectrum of building code previously defined is reported in **Figure 5**.

Linear Dynamic Analysis

Firstly, modal analysis is performed on the FEM models to identify the main frequencies, the related modal shapes and the effective modal masses ($\%M_{eff}$) of each mode of the Sanctuary in percentage respect to the total: at this moment the models are not calibrated with Ambient Vibration Surveys like those reported in Pierdicca et al. (2016a). We resorted to the Block Lanczos method to estimate the modal shapes, taking into proper account the quantum of d.o.f. of the numerical models. The monastery is affected by many local modes, and for this reason, 300 modes are considered to have more than 85% of excited mass.

In the upper part of **Figure 5A** the main modes and the associated participating masses are reported for the *Model CS*. Generally, for this model, the modal shapes distribution clearly shows how the monastery is affected by substantial out-of-plane deformations. The 34th mode has the highest participating mass in the longitudinal direction ($M_{eff} = 29.24\%$, $T = 0.188$ s) involving the timber, the bell tower, and the tambour. The 9th mode is characterized by a $M_{eff} = 17.99\%$ and a period T =

0.334 s, since it affects crosswise both the aisle's lateral walls and the steeple.

To understand the influence of rigid floors modal analysis was also performed for the *Model DF*. In this case, 300 modes involve only the 82% of the total mass due to a higher dispersion of local modes, e.g., of the walls of the porch of school, and they are reported in the upper part of **Figure 5B**. The condition without rigid floors drags more the complex of the school (see upper parts of **Figures 5A,B**) which is further stressed with small translations in the out-of-plane directions of the walls. In fact, the participating masses involved by the principal modes of *CS* and *DF Models*, i.e., the 34th and 29th, are respectively of $M_{eff} =$ 24.4% longitudinally and $M_{eff} = 15.22\%$ transversely, including both the walls of the school. Apparently, in both *Models CS* and *DF*, the 1st mode involves the bell tower in the transversal direction.

In the lower part of **Figures 5A,B** the elastic response spectra obtained from the ASP_station are reported to have a direct correlation with the attained accelerations. Modes with significant participating masses are characterized by periods in the range 0.18–0.38 s, where the response spectra have big values of accelerations. It is clearly remarkable that the masonry of the church's central aisle is always related to the high acceleration which to some extent may explain, albeit marginally, the presence of the damage observed on the structure at the end of the seismic sequence, considering that the spectral content of the ASP_station records would have been the same as that of the earthquake motion in Offida.

The Demand on the Macro-Elements

It is useful to provide the seismic demand on the entire building. In **Figure 6**, the ratio between the base shear (V) obtained in section Linear Dynamic Analysis for different response spectra [i.e., ASP_station and Italian code spectra (Ministero delle Infrastrutture e dei Trasporti., 2018)] and the total weight of the building (W_{tot}) are plotted for the transversal (X-direction) and longitudinal (Y-direction) directions for both *Models CS* and *DF*. The base shear V has been obtained using the Complete Quadratic Combination (CQC) method.

Form **Figure 6** is clear that the ratios V/W_{tot} obtained with the elastic spectrum of NTC2018 are always greater than the natural one of ASP_station, that are always in the range 22÷58%. The main observation emerging is the impossibility of being able to guarantee a high level of seismic safety, especially in comparison to the level required by the new seismic Italian law for strategic structures, for which the request of demand (and

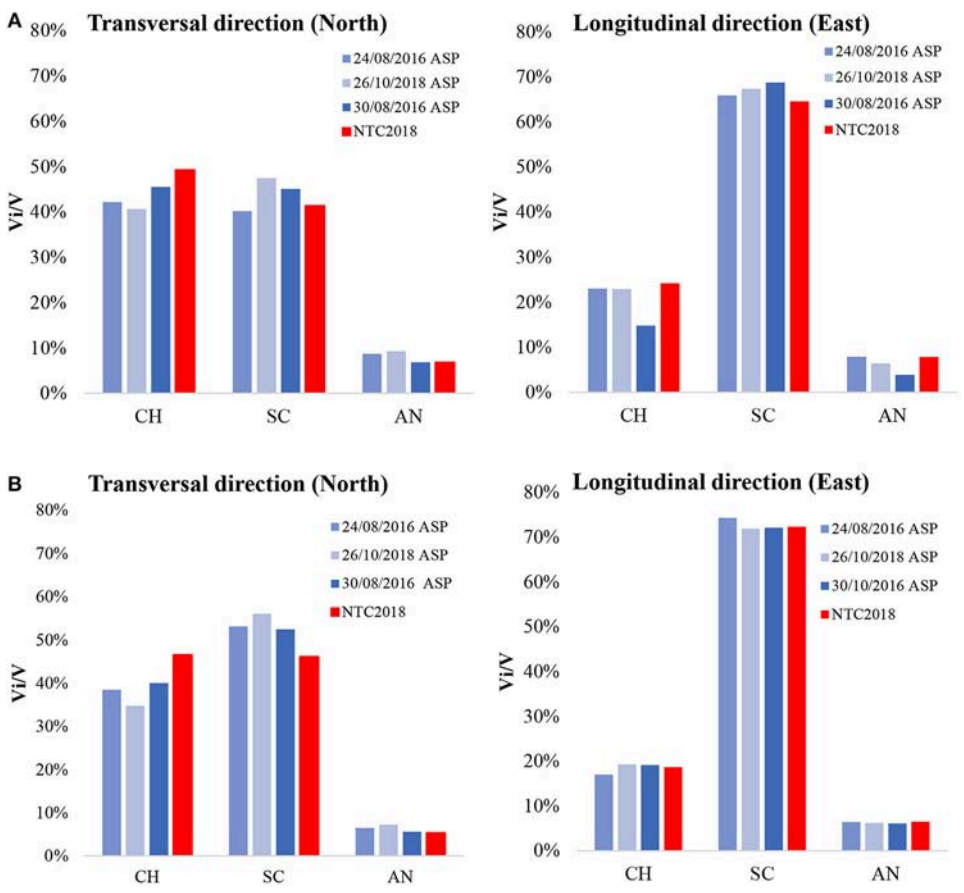

FIGURE 7 | Seismic base shear absorbed by the church (CH), the school (SC), and the annex (AN) for the *Model CS* **(A)**, *Model DF* **(B)**.

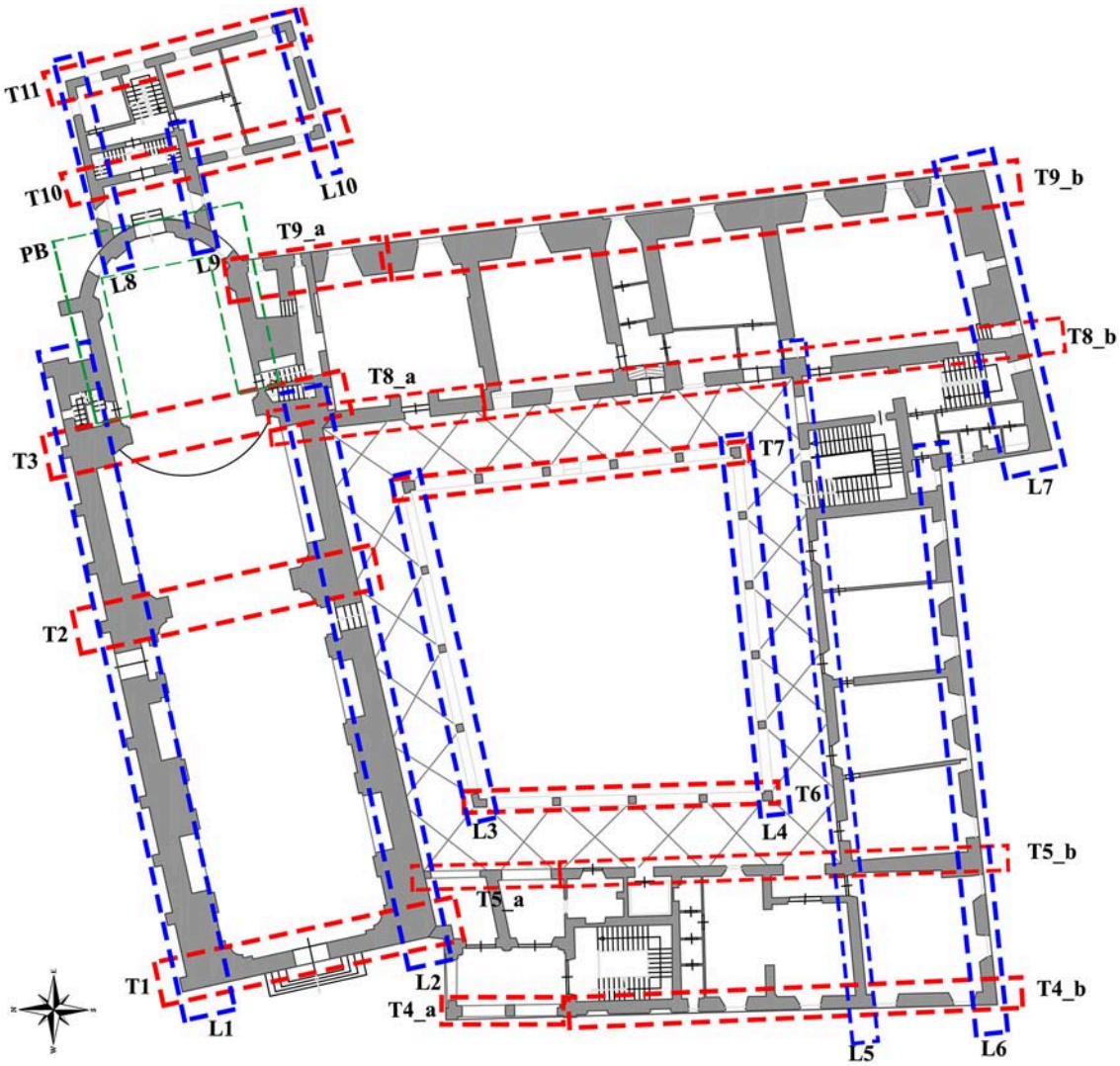

FIGURE 8 | Transversal (red) and longitudinal (blue) macro-elements.

then capacity) became very high. Additionally, the school is connected to the church which, for conservation reasons, can never undergo extensive consolidation interventions. Finally, a little reduction (∼10%) on the seismic demand in both directions is observable, and it is a direct consequence of the retrofitting interventions on the school zone, SC (**Figure 1**).

Once the seismic demand for the entire aggregate is known, to have a better perception on the real distribution of the seismic demand on the various parts of the building, we have evaluated the ratio between the base shear under each portion of the complex (Vi) and the total base shear (V), Vi/V (in percentage). The Sanctuary is divided into three main portions (see **Figure 1**): the church (CH), the school (SC) and the annex (AN). The main results, for both *Model CS* and *DF*, are displayed in **Figure 7**, showing that in longitudinal direction the shear forces are basically centered on the school building (∼70%), while in the transversal direction there is an equal behavior since both the church and the school get almost the same shear force (∼40%), Furthermore, **Figure 7** shows that the presence of rigid floors gives a better distribution of the shear force between the church and the school both in longitudinal and transversal direction. It is also evident that, in the same case, the distribution of shear is not proportional to the acceleration and the main parts of the building with higher seismic forces are the church and the school.

To evaluate the horizontal demand of each macro-element, the Sanctuary was divided into longitudinal and transversal elements as reported in **Figure 8**, with the final aim to find the most stressed wall. The ratio Vi/V (in percentage) for each macro-element in both longitudinal and transversal directions is reported in **Figure 9** for *Model CS* and *DF*.

It can be observed that, when the seismic action is applied in the transversal direction for both the models, shear forces are

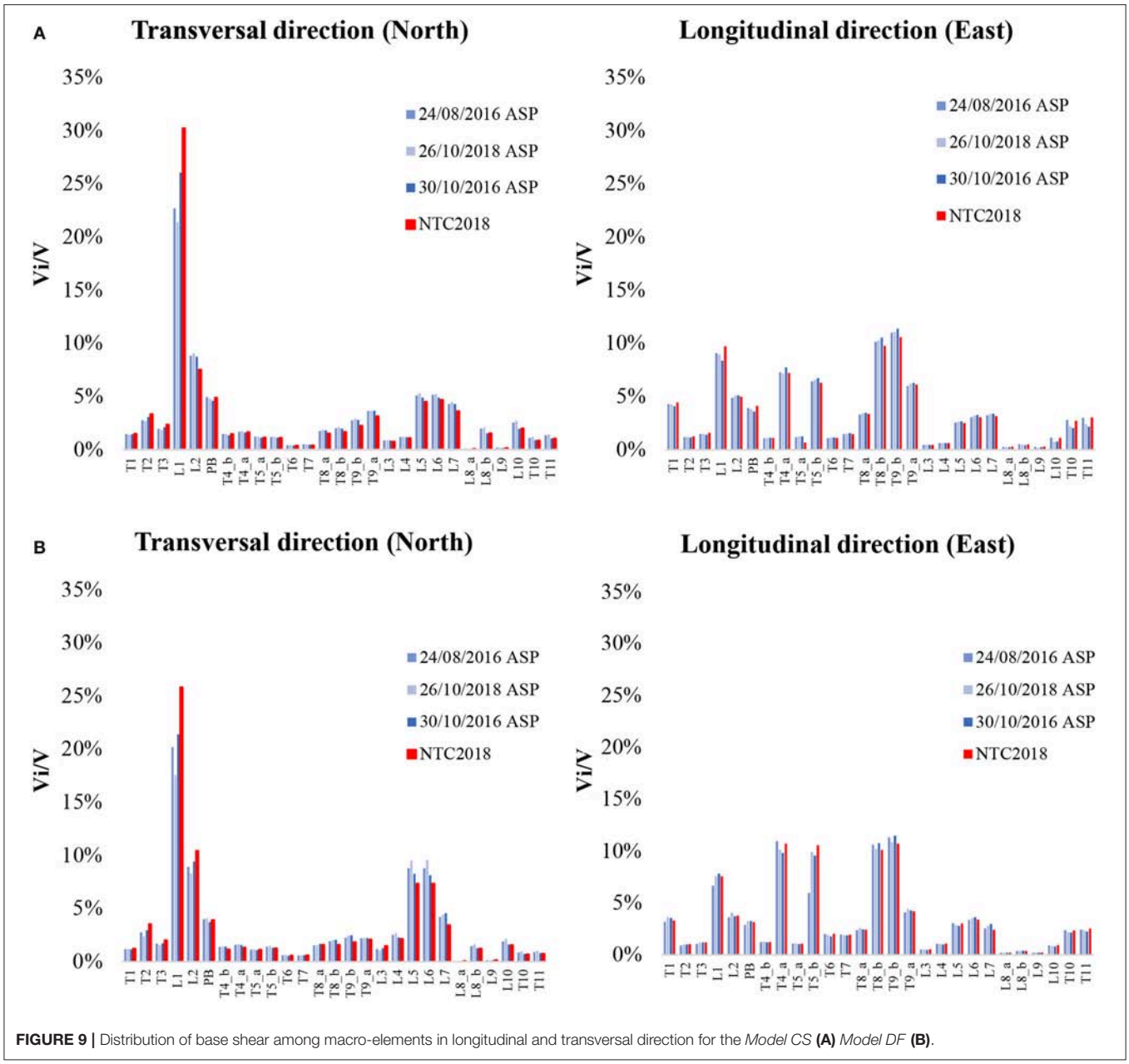

FIGURE 9 | Distribution of base shear among macro-elements in longitudinal and transversal direction for the *Model CS* **(A)** *Model DF* **(B)**.

mainly concentrated on lateral walls of the nave, namely L1, with a Vi/V ratio between 22÷30%, the presbytery (PB) ∼8÷7% and the south walls of the school with a Vi/V∼5%. On the contrary, lower forces act on internal walls, e.g., L3–L4 and T6–T7, with a ratio of <3%.

When the seismic force acts in the longitudinal direction, there are fewer differences of shear forces on the macro-elements. Major Vi/V ratios are mainly concentrated in peripheral walls with a variation concerning the transverse case of the elements most stressed (actually T4–T5 and T8–T9 with a ratio in the range 5÷10%) less of L1 which is still the one with the higher demand. This result incidentally confirms what has been observed during the recent seismic sequence of Central Italy 2016–2017 that saw in the wall L1 the one with more significant damage compared to the rest of the construction (see **Figure 3A**), an area already lightly damaged by the L'Aquila earthquake in 2009 (see section Historical Developments).

Non-linear Static Analysis: Preliminary Considerations

The non-linear static analysis method also known as pushover has been used to properly analyze the complex's seismic behavior, by monotonically increasing horizontal loads and keeping gravity loads constant. Two systems of perpendicular horizontal forces, acting at different times, were used to take into account seismic loads. These systems lead to two load distributions that may be

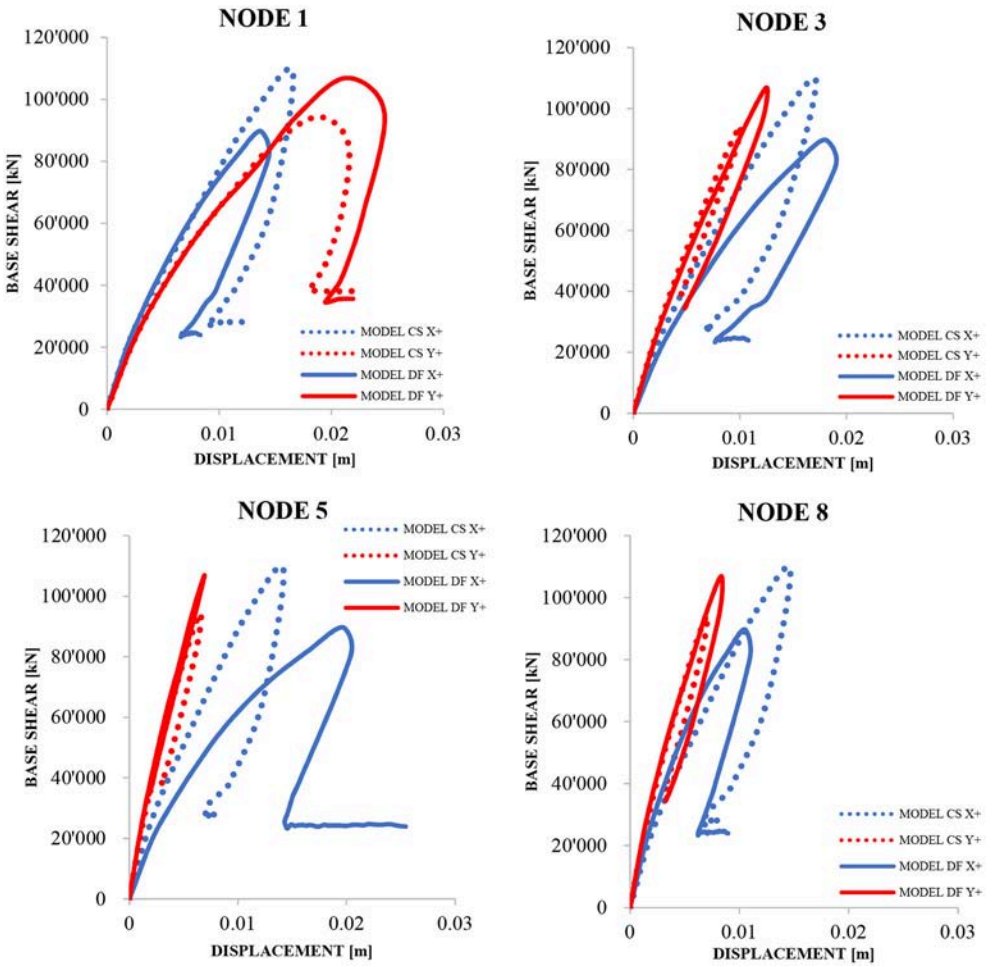

FIGURE 10 | Capacity curves at varying of control points for *Model CS* and *Model DF* in X and Y-directions.

considered two limit states of the building capacity, one related to the masses on each floor by direct proportion (PushMass) and one equivalent to the consideration of main modes involving the 85% of participating masses in both directions (PushMode).

As can be clearly remarked by considering the load distributions described above, the pushover analysis performed is merely conventional, i.e., loads applied to the building are kept constant while the structure progressively degrades during the loading, so gradual changes in modal frequencies caused by yielding and cracking on the structure during loading are not considered. Even though the invariance of static loads may lead to an overestimation in assessing masonry buildings' seismic capacity, mostly on structures affected by a high or non-uniform impairment, a conventional pushover analysis ensures a less computationally expensive alternative to non-linear dynamic analyses. It also provides substantial data on the progressive damage occurring to buildings under seismic loads, such as the cracking.

Considering the extension of the Sanctuary, the non-linear behavior has been analyzed by varying the control point (**Figure 4A**). To have a proper understanding of how the seismic response develops by modifying the floors stiffness, we used the same control points.

Pushover Analysis: First Results

To ensure clarity and brevity, the capacity curves reported in this paper are those in positive X (i.e., north-direction) and Y directions (i.e., east-direction) for PushMass load distribution **Figure 10**.

The critical load distribution for the complex, both for *Model CS* and *Model DF*, is in X-direction, transversal to the aisle. On that X-direction, most of the selected control points display a ductile behavior, while on Y-direction we mostly find a brittle aberrance. In X-direction, the condition of rigid floors produces an increase of resistance compared to the *Model DF*. In Y-direction, instead, the presence of rigid floors produces a little reduction of resistance leaving intact the stiffness and, for almost all control points, provokes a decrease of ductility. This reduction is due to an increase in the torsional effect that is going to urge the areas not

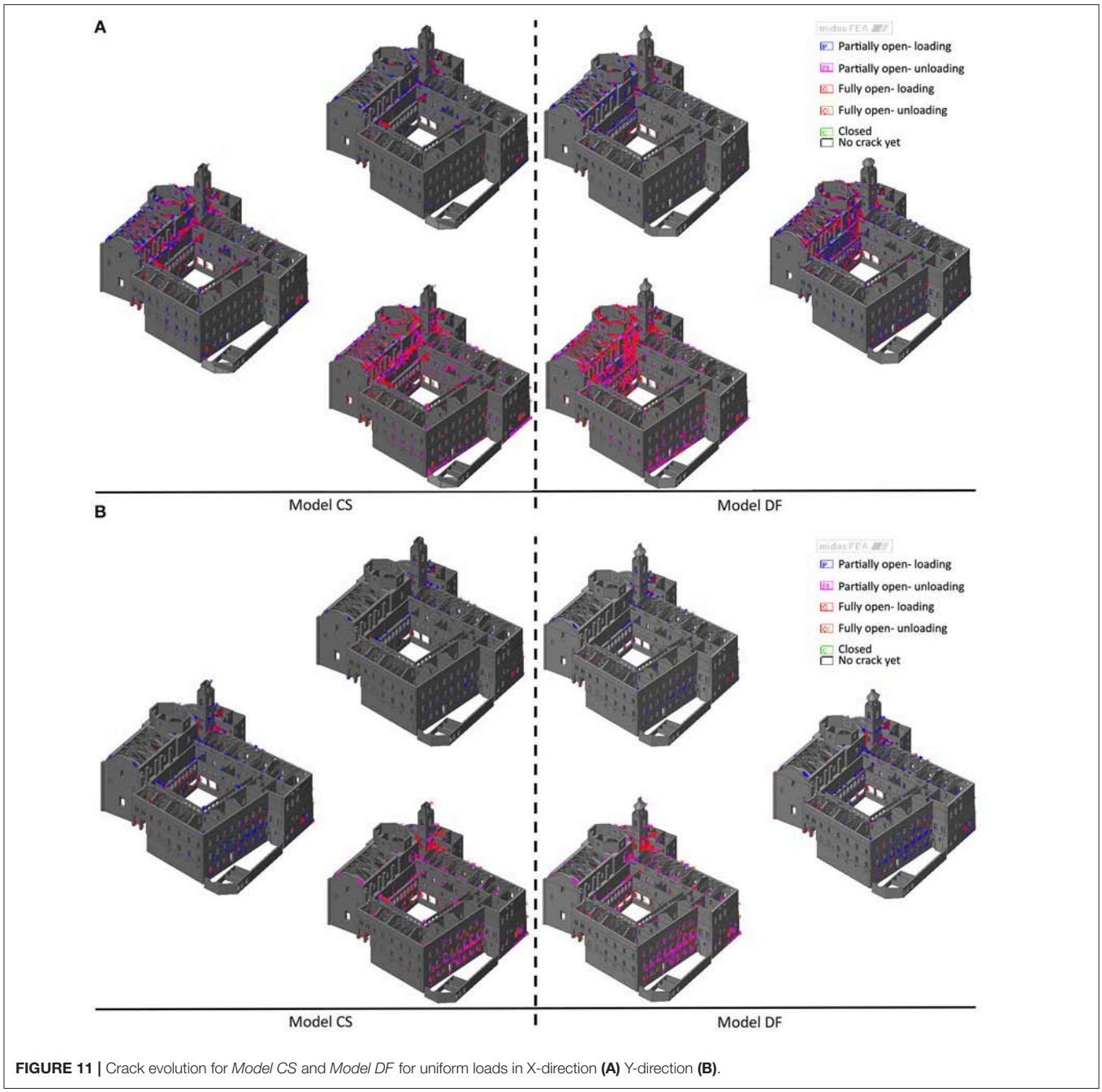

FIGURE 11 | Crack evolution for *Model CS* and *Model DF* for uniform loads in X-direction **(A)** Y-direction **(B)**.

affected by the 2010 intervention, such as the church and the oratory.

Figure 11 shows the development of the cracking in the *Model CS* and *Model DF*, due to horizontal loads. In both main directions, the first cracks appear on the walls of the nave and in the bell tower (top figures in each quarter). In X-Direction, the cracking distribution is more huge respect to Y-Direction (down figures in each quarter). Comparing *Model DF* and *Model CS* it is evident that the presence of rigid floors reduces the development of cracks, especially in X-direction where the Model CS shows less cracking in the upper section of the nave's walls sited next to the belfry (down figures in each quarter).

The Capacity of the Macro-Elements

Once the seismic demand V_i, namely the strength demand, is known for different portions and macro-elements of Sant'Agostino's Sanctuary (see section Pushover Analysis: First Results), it is possible to compare the ultimate lateral strength V_u evaluated with the pushover analysis obtaining a new ratio Vi/Vu giving us the safety levels of the analyzed portion like in Brandonisio et al. (2013). For brevity issue only the results of

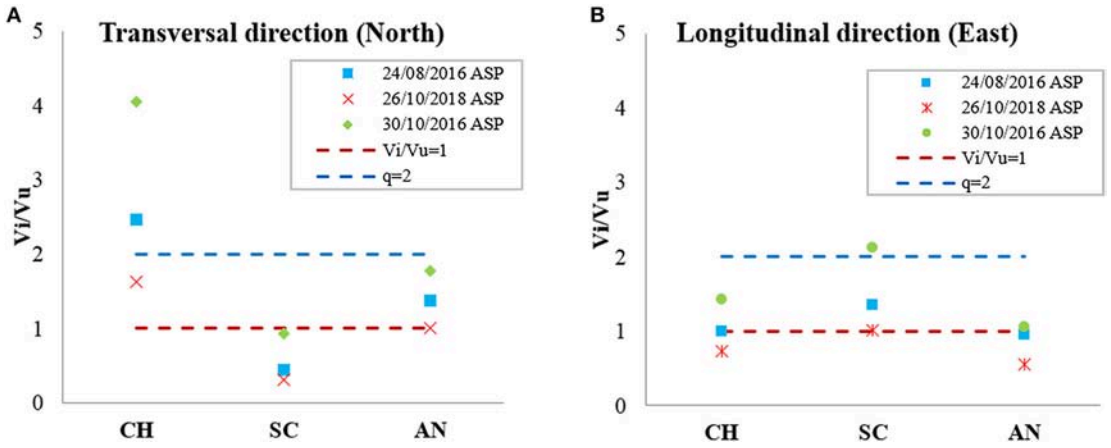

FIGURE 12 | Horizontal seismic demand (Vi) to horizontal strength capacity (Vu) ratio of the different areas of the building for the *Model CS* for transversal **(A)**, and longitudinal directions **(B)**.

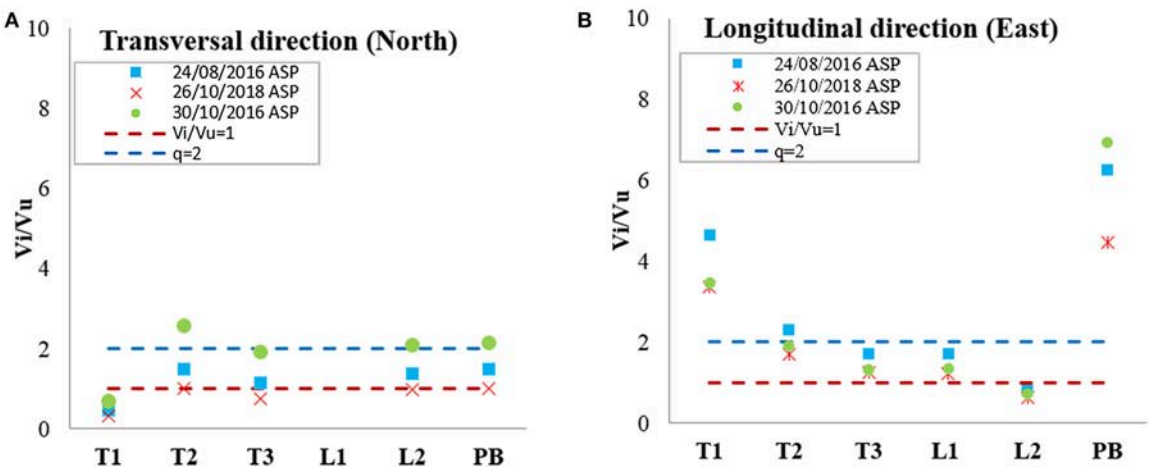

FIGURE 13 | Horizontal seismic demand (Vi) to horizontal strength capacity (Vu) ratio for different macro-elements of the church for the *Model CS* for transversal **(A)**, and longitudinal directions **(B)**.

Model CS, i.e., actual state, considering elastic spectra of the ASP_ station are described in order to have a clear assessment of the damage caused by the last seismic events that stroke Central Italy.

In **Figure 12**, there is a first general consideration on what part of the Sanctuary is more vulnerable, confirming that the major problems are in the transversal direction, i.e., X-direction, and the church (CH) is the most problematic part of the Sanctuary. In the same **Figure 12** two horizontal lines are reported corresponding to a ratio Vi/Vu = 1, i.e., the elastic limit condition, and Vi/Vu = 2 corresponding—with a good approximation—to a given level of acceptable damage, according to the behavior factor $q = 2$, as defined for masonry structure in Italian Code (Ministro dei Lavori Pubblici e dei Trasporti., 2008; Circolare Ministeriale n. 617, 2009; Ministero delle Infrastrutture e dei Trasporti., 2018).

Based on these considerations, the single macro-elements of the church have been analyzed, and the primary results are reported in **Figure 13**. After plotting Vi/Vu, limited to the value of 10 for a better comprehension, the vulnerability of the house of worship was clearly remarkable in the transversal direction, since the North wall of the nave (L1) shows the most significant values of Vi/Vu, major than 10. L1 is characterized by small stiffness due to a height of 18 m, without internal orthogonal walls and intermediate floors, and a thickness of 2.55 m. In the longitudinal direction, the ratio of Vi/Vu shows that elements more problematic are the façade (T1) and the presbytery (PB). Again, this result agrees with the appeared damage during the Central Italy 2016–2017 seismic sequence (section Damage After Seismic Sequence of 2016).

Further analyses will have to be conducted for higher knowledge levels (i.e., KL2 and KL3), which leads to greater resistance and a different spread of the damage, but this constitutes the topic of future works.

CONCLUSIONS

The paper approaches the seismic vulnerability of Sant'Agostino's Sanctuary in Offida (Ascoli Piceno), a small town in Central Italy. The complex is placed in a highly seismic region; the church portion has been considered unsafe after the earthquakes occurred with epicenters in Accumoli and Norcia, respectively on 24th August and 30th October 2016, and is now closed.

The 3D non-linear solid numerical model (NM) described in this paper gave the chance to investigate the seismic behavior of the complex using sensitivity analysis performed by varying control points and stiffness of the floors. First, the linear dynamic behavior is analyzed confirming the high presence of local modes slightly reduced by rigid floors introduced as a result of consolidation. To gain a proper understanding of the seismic demand, a linear dynamic analysis (obtained by natural and Italian code spectra) was performed not only on the entire complex but also on its main components and some macro-elements identified within the building.

Subsequently, the seismic demand has been compared with the seismic capacity, directly derived by pushover analyses, providing a good match with the most damaged parts and macro-elements of the complex after the seismic sequence of Central Italy in 2016–2017. This confirms that the procedure defined in Brandonisio et al. (2013) can offer an efficient tool to understand the safety of a whole complex and not only of isolated churches, also identifying the most vulnerable elements that are used as well to design local and global retrofitting interventions.

AUTHOR CONTRIBUTIONS

AN furnished the numerical model. EG analyzed the results. FC supervised the structural analysis. SL supervised the research. All the authors contributed to the writing of the manuscript.

REFERENCES

Acary, V. (2001). *Contribution a la modélization mécanique et numérique des edifices maconnés* (in french). Aix-en-Provence: Université de la Méditerranée - Aix-Marseille II.

Acito, M., Bocciarelli, M., Chesi, C., and Milani, G. (2014). Collapse of the clock tower in Finale Emilia after the May 2012 Emilia Romagna earthquake sequence: numerical insight. *Eng. Struct.* 72, 70–91. doi: 10.1016/j.engstruct.2014.04.026

Addessi, D., Sacco, E., and Paolone, A. (2010). Cosserat model for periodic masonry deduced by nonlinear homogenization. *Eur. J. Mech. A Solids* 29, 724–737. doi: 10.1016/j.euromechsol.2010.03.001

Anthoine, A. (1995). Derivation of the in-plane elastic characteristics of masonry through homogenization theory. *Int. J. Solids Struct.* 32, 137–163. doi: 10.1016/0020-7683(94)00140-R

Asteris, P. G., Chronopoulos, M. P., Chrysostomou, C. Z., Varum, H., Plevris, V., Kyriakides, N., et al. (2014). Seismic vulnerability assessment of historical masonry structural systems. *Eng. Struct.* 62–63, 118–134. doi: 10.1016/j.engstruct.2014.01.031

Asteris, P. G., Sarhosis, V., Mohebkhah, A., Plevris, V., Papaloizou, L., Komodromos, P., et al. (2015). "Numerical modeling of historic masonry structures," in *Handbook of Research on Seismic Assessment and Rehabilitation of Historic Structures*, eds. P. Asteris, and V. Plevris (Hershey, PA: IGI Global), 213–256.

Bartoli, G., Betti, M., and Giordano, S. (2013). *In situ* static and dynamic investigations on the "Torre Grossa" masonry tower. *Eng. Struct.* 52, 718–733. doi: 10.1016/j.engstruct.2013.01.030

Betti, M., Drosopoulos, G. A., and Stavroulakis, G. E. (2008). Two non-linear finite element models developed for the assessment of failure of masonry arches. *Comptes Rendus Mec.* 336, 42–53. doi: 10.1016/j.crme.2007.10.014

Betti, M., and Vignoli, A. (2008a). Assessment of seismic resistance of a basilica-type church under earthquake loading: modelling and analysis. *Adv. Eng. Softw.* 39, 258–283. doi: 10.1016/j.advengsoft.2007.01.004

Betti, M., and Vignoli, A. (2008b). Modelling and analysis of a Romanesque church under earthquake loading: assessment of seismic resistance. *Eng. Struct.* 30, 352–367. doi: 10.1016/j.engstruct.2007.03.027

Betti, M., and Vignoli, A. (2011). Numerical assessment of the static and seismic behaviour of the basilica of Santa Maria all'Impruneta (Italy). *Constr. Build. Mater.* 25, 4308–4324. doi: 10.1016/j.conbuildmat.2010.12.028

Brandonisio, G., Lucibello, G., Mele, E., and Luca, A. De. (2013). Damage and performance evaluation of masonry churches in the 2009 L'Aquila earthquake. *Eng. Fail. Anal.* 34, 693–714. doi: 10.1016/j.engfailanal.2013.01.021

Caliò, I., Marletta, M., and Pantò, B. (2012). A new discrete element model for the evaluation of the seismic behaviour of unreinforced masonry buildings. *Eng. Struct.* 40, 327–338. doi: 10.1016/j.engstruct.2012.02.039

Carpinteri, A., Lacidogna, G., Manuello, A., and Niccolini, G. (2015). A study on the structural stability of the Asinelli Tower in Bologna. *Struct. Control Heal. Monit.* 23, 659–667. doi: 10.1002/stc.1804

Ceci, A. M., Contento, A., Fanale, L., Galeota, D., Gattulli, V., Lepidi, M., et al. (2010). Structural performance of the historic and modern buildings of the University of L'Aquila during the seismic events of April 2009. *Eng. Struct.* 32, 1899–1924. doi: 10.1016/j.engstruct.2009.12.023

Circolare Ministeriale n. 617 (2009). *Cons. Sup. LL. PP., "Istruzioni per l'applicazione delle Nuove Norme Tecniche per le Costruzioni" di cui al decreto ministeriale del 14.01.2008*. G.U. del 26.02.2009 n. 47, supplemento ordinario n. 27 (in Italian). Rome: Consiglio Superiore Lavori Pubblici.

Clementi, F., Gazzani, V., Poiani, M., Mezzapelle, P. A., and Lenci, S. (2018a). Seismic assessment of a monumental building through nonlinear analyses of a 3D solid model. *J. Earthq. Eng.* 22, 35–61. doi: 10.1080/13632469.2017.1297268

Clementi, F., Lenci, S., and Sadowski, T. (2008). Fracture characteristics of unfired earth. *Int. J. Fract.* 149, 193–198. doi: 10.1007/s10704-008-9239-x

Clementi, F., Milani, G., Gazzani, V., Poiani, M., Cocchi, G., and Lenci, S. (2018b). "The non-smooth contact dynamics method for the analysis of an ancient masonry tower," in *14th International Conference of Computational Methods in Sciences And Engineering* (Thessaloniki, Greece), 090004.

Clementi, F., Pierdicca, A., Formisano, A., Catinari, F., and Lenci, S. (2017a). Numerical model upgrading of a historical masonry building damaged during the 2016 Italian earthquakes: the case study of the Podestà palace in Montelupone (Italy). *J. Civ. Struct. Heal. Monit.* 7, 703–717. doi: 10.1007/s13349-017-0253-4

Clementi, F., Quagliarini, E., Maracchini, G., and Lenci, S. (2015). Post-World War II Italian school buildings: typical and specific seismic vulnerabilities. *J. Build. Eng.* 4, 152–166. doi: 10.1016/j.jobe.2015.09.008

Clementi, F., Quagliarini, E., Monni, F., Giordano, E., and Lenci, S. (2017b). Cultural heritage and earthquake: the case study of "Santa Maria della Carità" in Ascoli Piceno. *Open Civ. Eng. J.* 11, 1079–1105. doi: 10.2174/1874149501711011079

da Porto, F., Guidi, G., Garbin, E., and Modena, C. (2010). In-plane behavior of clay masonry walls: experimental testing and finite-element modeling. *J. Struct. Eng.* 136, 1379–1392. doi: 10.1061/(ASCE)ST.1943-541X.0000236

D'Ambrisi, A., Mariani, V., and Mezzi, M. (2012). Seismic assessment of a historical masonry tower with nonlinear static and dynamic analyses tuned on ambient vibration tests. *Eng. Struct.* 36, 210–219. doi: 10.1016/j.engstruct.2011.12.009

Del Piero, G. (1998). Limit analysis and no-tension materials. *Int. J. Plast.* 14, 259–271. doi: 10.1016/S0749-6419(97)00055-7

EN 1998-3 (2010). *Eurocode 8: Design of Structures for Earthquake Resistance–Part 3: Assessment and Retrofitting of Buildings*. City of Brussels: Eur. Comm. Stand.

Formisano, A., Florio, G., Landolfo, R., and Mazzolani, F. M. (2015). Numerical calibration of an easy method for seismic behaviour assessment on large scale of masonry building aggregates. *Adv. Eng. Softw.* 80, 116–138. doi: 10.1016/j.advengsoft.2014.09.013

Formisano, A., Vaiano, G., Fabbrocino, F., and Milani, G. (2018). Seismic vulnerability of Italian masonry churches: the case of the Nativity of Blessed Virgin Mary in Stellata of Bondeno. *J. Build. Eng.* 20, 179–200. doi: 10.1016/j.jobe.2018.07.017

Gattulli, V., Lampis, G., Marcari, G., and Paolone, A. (2014). Simulations of FRP reinforcement in masonry panels and application to a historic facade. *Eng. Struct.* 75, 604–618. doi: 10.1016/j.engstruct.2014.06.023

Ghiassi, B., Oliveira, D. V., Lourenço, P. B., and Marcari, G. (2013). Numerical study of the role of mortar joints in the bond behavior of FRP-strengthened masonry. *Compos. Part B Eng.* 46, 21–30. doi: 10.1016/j.compositesb.2012.10.017

Jean, M. (1999). The non-smooth contact dynamics method. *Comput. Methods Appl. Mech. Eng.* 177, 235–257. doi: 10.1016/S0045-7825(98)00383-1

Kadas, K., Yakut, A., and Kazaz, I. (2011). Spectral ground motion intensity based on capacity and period elongation. *J. Struct. Eng.* 137, 401–409. doi: 10.1061/(ASCE)ST.1943-541X.0000084

Lagomarsino, S., Penna, A., Galasco, A., and Cattari, S. (2013). TREMURI program: an equivalent frame model for the nonlinear seismic analysis of masonry buildings. *Eng. Struct.* 56, 1787–1799. doi: 10.1016/j.engstruct.2013.08.002

Lenci, S., Clementi, F., and Sadowski, T. (2012). Experimental determination of the fracture properties of unfired dry earth. *Eng. Fract. Mech.* 87, 62–72. doi: 10.1016/j.engfracmech.2012.03.005

Lenci, S., Piattoni, Q., Clementi, F., and Sadowski, T. (2011). An experimental study on damage evolution of unfired dry earth under compression. *Int. J. Fract.* 172, 193–200. doi: 10.1007/s10704-011-9651-5

Lotfi, H. R., and Shing, P. B. (1994). Interface model applied to fracture of masonry structures. *J. Struct. Eng.* 120, 63–80. doi: 10.1061/(ASCE)0733-9445(1994)120:1(63)

Lourenço, P. B. (2009). "Recent advances in masonry modelling: micromodelling and homogenisation," in *Multiscale Modeling in Solid Mechanics: Computational Approaches* (London, UK: Imperial College Press), 251–294. Available online at: https://www.worldscientific.com/author/Galvanetto%2C+Ugo

Lourenço, P. B., Krakowiak, K. J., Fernandes, F. M., and Ramos, L. F. (2007). Failure analysis of Monastery of Jerónimos, Lisbon: how to learn from sophisticated numerical models. *Eng. Fail. Anal.* 14, 280–300. doi: 10.1016/j.engfailanal.2006.02.002

Lourenço, P. B., and Rots, J. G. (1997). Multisurface interface model for analysis of masonry structures. *J. Eng. Mech.* 123, 660–668. doi: 10.1061/(ASCE)0733-9399(1997)123:7(660)

Luciano, R., and Sacco, E. (1997). Homogenization technique and damage model for old masonry material. *Int. J. Solids Struct.* 34, 3191–3208. doi: 10.1016/S0020-7683(96)00167-9

Luciano, R., and Sacco, E. (1998). A damage model for masonry structures. *Eur. J. Mech. A Solids* 17, 285–303. doi: 10.1016/S0997-7538(98)80087-9

Manfredi, G., Lignola, G. P., and Voto, S. (2013). Military quarters in Nola, Italy—Caserma Principe Amedeo: damage assessment and reconstruction of a partially collapsed XVIII century complex. *Int. J. Archit. Herit.* 7, 225–246. doi: 10.1080/15583058.2011.629020

Midas FEA (2016). *Analysis and Algorithm Manual*. MIDAS Family Program.

Milani, G. (2011). Simple lower bound limit analysis homogenization model for in- and out-of-plane loaded masonry walls. *Constr. Build. Mater.* 25, 4426–4443. doi: 10.1016/j.conbuildmat.2011.01.012

Milani, G., Lourenço, P., and Tralli, A. (2007). 3D homogenized limit analysis of masonry buildings under horizontal loads. *Eng. Struct.* 29, 3134–3148. doi: 10.1016/j.engstruct.2007.03.003

Milani, G., and Valente, M. (2015). Comparative pushover and limit analyses on seven masonry churches damaged by the 2012 Emilia-Romagna (Italy) seismic events: possibilities of non-linear finite elements compared with pre-assigned failure mechanisms. *Eng. Fail. Anal.* 47, 129–161. doi: 10.1016/j.engfailanal.2014.09.016

Minghini, F., Milani, G., and Tralli, A. (2014). Seismic risk assessment of a 50 m high masonry chimney using advanced analysis techniques. *Eng. Struct.* 69, 255–270. doi: 10.1016/j.engstruct.2014.03.028

Ministero delle Infrastrutture e dei Trasporti. (2018). *DM 17/01/2018–Aggiornamento delle "Norme Tecniche per le Costruzioni"* (in italian). Rome: Ministero delle infrastrutture e dei trasporti, 1–198.

Ministro dei Lavori Pubblici e dei Trasporti. (2008). *Decreto Ministeriale 14/01/2008–Norme tecniche per le costruzioni* (in Italian). Rome: Ministero delle infrastrutture e dei trasporti.

Pande, G. N., Liang, J. X., and Middleton, J. (1989). Equivalent elastic moduli for brick masonry. *Comput. Geotech.* 8, 243–265. doi: 10.1016/0266-352X(89)90045-1

Pierdicca, A., Clementi, F., Fortunati, A., and Lenci, S. (2018). Tracking modal parameters evolution of a school building during retrofitting works. *Bull. Earthq. Eng.* doi: 10.1007/s10518-018-0483-9. [Epub ahead of print].

Pierdicca, A., Clementi, F., Isidori, D., Concettoni, E., Cristalli, C., and Lenci, S. (2016a). Numerical model upgrading of a historical masonry palace monitored with a wireless sensor network. *Int. J. Mason. Res. Innov.* 1:74. doi: 10.1504/IJMRI.2016.074748

Pierdicca, A., Clementi, F., Maracci, D., Isidori, D., and Lenci, S. (2016b). Damage detection in a precast structure subjected to an earthquake: a numerical approach. *Eng. Struct.* 127, 447–458. doi: 10.1016/j.engstruct.2016.08.058

Poiani, M., Gazzani, V., Clementi, F., Milani, G., Valente, M., and Lenci, S. (2018). Iconic crumbling of the clock tower in Amatrice after 2016 central Italy seismic sequence: advanced numerical insight. *Procedia Struct. Integr.* 11, 314–321. doi: 10.1016/j.prostr.2018.11.041

Quagliarini, E., Maracchini, G., and Clementi, F. (2017). Uses and limits of the equivalent frame model on existing unreinforced masonry buildings for assessing their seismic risk: a review. *J. Build. Eng.* 10, 166–182. doi: 10.1016/j.jobe.2017.03.004

Rots, J. G. (1991). Smeared and discrete representations of localized fracture. *Int. J. Fract.* 51, 45–59. doi: 10.1007/BF00020852

Rots, J. G., and de Borst, R. (1987). Analysis of mixed-mode fracture in concrete. *J. Eng. Mech.* 113, 1739–1758. doi: 10.1061/(ASCE)0733-9399(1987)113:11(1739)

Zucchini, A., and Lourenço, P. B. (2002). A micro-mechanical model for the homogenisation of masonry. *Int. J. Solids Struct.* 39, 3233–3255. doi: 10.1016/S0020-7683(02)00230-5

Zucchini, A., and Lourenço, P. B. (2004). A coupled homogenisation–damage model for masonry cracking. *Comput. Struct.* 82, 917–929. doi: 10.1016/j.compstruc.2004.02.020

Conflict of Interest Statement: The authors declare that the research was conducted in the absence of any commercial or financial relationships that could be construed as a potential conflict of interest.

frontiers in Built Environment

ORIGINAL RESEARCH
published: 11 January 2019
doi: 10.3389/fbuil.2018.00088

Seismic Assessment of Non-conforming Infilled RC Buildings Using IDA Procedures

Constantinos Repapis[1]* *and Christos A. Zeris*[2]

[1] Reinforced Concrete Laboratory, Department of Civil Engineering, University of West Attica, Athens, Greece, [2] Reinforced Concrete Laboratory, Department of Civil Engineering, National Technical University of Athens, Athens, Greece

The seismic performance of existing non-conforming reinforced concrete (RC) buildings is numerically investigated, taking into account the presence of clay brick masonry infill walls. The effect of infill walls on the seismic response of RC frames is widely recognised and has been a subject of numerous analytical and experimental investigations. In this context, Static Pushover analyses of typical existing RC infilled frames have established these structures' inelastic characteristics, focusing on the significant contribution of infill walls to their dynamic characteristics, overstrength, form irregularity and damage. Furthermore, more comprehensive studies of inelastic static response considered the typical variability among different generations of constructed buildings in Greece since the 60s in the form, the seismic design and detailing practice and the structural materials, with different masonry infill configurations and properties. In the present study, the results from such Static Pushover analyses are extended with Incremental Dynamic Analysis predictions using a large number of recorded base excitation from recent destructive earthquakes in Greece and abroad. Evaluation of the time history predictions and comparisons with the Static Pushover analysis findings corroborate that the presence of regular arrangements of perimeter infill walls increase considerably the stiffness and resistance to lateral loads of the infilled RC structures, while at the same time, reducing their global ductility and deformability. Fully or partially infilled RC frames can perform well, while frames with an open floor usually have the worst performance due to the formation of an unintentional soft storey. The analyses further prove that lower strength masonry provides the building with lower overstrength but higher ductility.

Keywords: non-conforming infilled RC buildings, unreinforced masonry infill walls, incremental dynamic analysis, seismic assessment, nonlinear analysis

OPEN ACCESS

Edited by:
Vagelis Plevris, OsloMet–Oslo Metropolitan University, Norway

Reviewed by:
Francesco Clementi, Università Politecnica delle Marche, Italy
Zeljana Nikolic, University of Split, Croatia
Amin Mohebkhah, Malayer University, Iran

***Correspondence:**
Constantinos Repapis
crepapis@uniwa.gr

Specialty section:
This article was submitted to Computational Methods in Structural Engineering, a section of the journal Frontiers in Built Environment

Received: *21 October 2018*
Accepted: *19 December 2018*
Published: *11 January 2019*

Citation:
Repapis C and Zeris CA (2019) Seismic Assessment of Non-conforming Infilled RC Buildings Using IDA Procedures. Front. Built Environ. 4:88. doi: 10.3389/fbuil.2018.00088

INTRODUCTION

Reinforced concrete frame structures constructed in Greece and other countries around the Mediterranean up until the 1980s, comprise a significant portion of their entire building inventory; these structures have been designed either without any seismic design considerations (primarily before the 50s), or with past generations of seismic design codes. In Greece, according to recent records, 78% of the RC buildings are designed and constructed before 1985, when there was the first modification of the seismic code towards a relatively higher conformance to currently enforced seismic standards. The first seismic design code in effect, RD59 (1959), was based on allowable stress

design procedures, prescribed relatively low service level base shear seismic coefficients, included inadequate detailing requirements and had no provisions for ductile failure response, such as weak beam vs. strong column, shear capacity design and critical region confinement in columns and shear walls. Moreover, the design method used was simplified and the quality of the structural materials was low. All these parameters, together with the loading history of the buildings (past earthquakes and/or changes in occupancy loads) introduce significant uncertainties in the expected seismic behaviour of those buildings.

Consequently, the assessment of the seismic performance of these buildings is very important, both for social and economic reasons. One common characteristic of these frames is that they are typically infilled with unreinforced clay brick masonry infill walls of different infill quality and configuration. They are relatively thicker in the perimeter frames, while they may be punctured (for openings) or discontinuous, depending on the building use; being, therefore, in full deformation compatibility with the RC frame, they contribute to its seismic response, in a manner not controlled in the seismic design. It is widely recognised, however, that the infill wall geometry and characteristics significantly influence the seismic response of infilled frames, as also observed in recent earthquakes and proven by numerous experimental and analytical studies (Fardis and Calvi, 1995; Dolšek and Fajfar, 2002; Repapis et al., 2006b).

During the past 60 years there have been extensive experimental laboratory test studies of infilled frame structures under gravity and lateral load, aiming at the identification of the infill contribution to the frame stiffness and resistance (Smith, 1966; Page et al., 1985; Prakash et al., 1993; Mehrabi et al., 1996; Negro and Verzeletti, 1996; Buonopane and White, 1999; Fardis et al., 1999; Žarnić et al., 2001; Pinto et al., 2002; Cavaleri et al., 2005; Santhi et al., 2005a; Hashemi and Mosalam, 2006; Kakaletsis and Karayannis, 2008; Basha and Kaushik, 2012; Stavridis et al., 2012; Stylianidis, 2012; Cavaleri and Di Trapani, 2014; Chiou and Hwang, 2015; Lourenço et al., 2016; Vintzileou et al., 2017; Palieraki et al., 2018). At the same time, a large number of analytical investigations of the behaviour of masonry infilled RC building structures have been pursued, at different modelling scales and levels of complexity, in order to predict the effect of masonry infills on infilled frame response and failure (Smith and Carter, 1969; Dhanasekar and Page, 1986; Fardis and Calvi, 1995; Crisafulli, 1997; Kappos and Ellul, 2000; Chrysostomou et al., 2002; Dolšek and Fajfar, 2002, 2008a,b; Repapis et al., 2006b; Borzi et al., 2008; Bakas et al., 2009; Asteris and Cotsovos, 2012; Chrysostomou and Asteris, 2012; Ellul and D'Ayala, 2012; Haldar and Singh, 2012; Lagaros, 2012; Vougioukas, 2012; Sarhosis et al., 2014; Zeris, 2014; Jeon et al., 2015; Bolea, 2016; Dumaru et al., 2016; Furtado et al., 2016; Morfidis and Kostinakis, 2017). More recently, with the advancement of testing and data acquisition hardware, together with the evolution of fast and efficient algorithms for data handling techniques, these two approaches above are jointly pursued in full scale field testing vis-à-vis the dynamic model identification (OMA) in order to establish the dynamic characteristics of full scale structures under excitation (Rainieri, 2008; Yu et al., 2017).

The effects of infills may be either beneficiary or detrimental to the seismic performance. In most cases, the presence of unreinforced masonry infills has been proved to significantly improve the seismic performance of those buildings and increase their lateral strength and stiffness. However, the positive contribution of infills may be reversed in cases of irregular distribution of the infill walls (Santhi et al., 2005b; Karayannis et al., 2011; Favvata et al., 2013). The experience gained from recent earthquakes shows that some cases of irregular distributions of infills in plan or elevation, which have not been taken into account during design, may even induce collapse of the entire building. Moreover, damage to these non-structural elements usually represents a large portion of the earthquake induced economic losses (Chiozzi and Miranda, 2017). Despite this fact, in conventional structural design of the buildings, infills are still usually treated as non-structural elements and are not taken into account or taken into account indirectly in current codes.

A number of factors are responsible for the neglect of infill walls, related to the uncertainty and difficulty in simulating the behaviour of infilled walls and an attempt to simplify calculations. Main factors are the significant uncertainties related to the large variety of infill walls and their dependence on local construction practices, the incomplete knowledge of their material properties and performance, the interaction between the surrounding frame and the infill wall and the possible failure mechanisms. Moreover, during the lifetime of a building, it is not rare that some heavy infill walls may be removed or substituted with light partitions, something that may totally change the nonlinear behaviour of the structure. Finally, another factor for ignoring the infills in order to simplify the analysis is the misleading assumption that, since infill walls provide additional strength and stiffness, they always influence positively and improve the performance of the structure.

Therefore, in seismic areas, the practice of ignoring the infill walls (apart from their weight contribution) is not always safe. Infill walls significantly increase the stiffness and strength of the frames, which could result to a possible change of the seismic demand due to the significant reduction in the fundamental period of the composite structural system, compared to the bare frame (Smith, 1966; Paulay and Priestley, 1992; Asteris et al., 2015, 2017). On the other hand, the contribution of infill walls to the lateral stiffness of the frame is significantly reduced when the structure is subjected to cyclic loading, like an earthquake, and undergoes large nonlinear cycles due to the brittle damage of infill walls (Vintzeleou and Tassios, 1989; Paulay and Priestley, 1992; Cavaleri et al., 2005; Asteris et al., 2011; Cavaleri and Di Trapani, 2014), while, furthermore, changing the entire manner that the seismic forces are taken and redistributed among the RC elements (Zeris, 2014).

Modelling of the infill walls poses many uncertainties because of the different materials involved and the many possible failure modes that need to be evaluated, with a high degree of uncertainty. In the literature several different modelling techniques have been proposed and tested for the simulation of the infills (Crisafulli, 1997; Chrysostomou et al., 2002; such as among others, Asteris et al., 2011, 2013; Chrysostomou

and Asteris, 2012; Sarhosis et al., 2014; Zeris, 2014; Furtado et al., 2016). Modelling follows an increasing level of detail and complexity, from micro to meso and macro-models. Micro and meso-scale models are based on small region finite element modelling or discrete element modelling of the infill panel brick and mortar, and are able to capture the behaviour of the infill frame with higher accuracy accounting the local infill-frame interaction (Lemos, 2007; Haldar and Singh, 2012; Sarhosis et al., 2012; Asteris et al., 2013; Zeris, 2014).

Lourenco (1996) and Attard et al. (2007) modelled masonry using continuum and interface line elements to simulate the possible fracture of bricks and mortar joints. Stavridis and Shing (2010) proposed a modelling technique combining smeared and discrete crack approaches to capture the different failure modes, including flexural and shear failure of concrete and tensile and shear fracture of mortar joints, using triangular smeared-crack elements connected with zero-thickness cohesive interface elements. Sarhosis et al. (2012) and Sarhosis and Lemos (2018) modelled the bricks as distinct blocks while the mortar joints were modelled as zero thickness interfaces. For the establishment of both in plane and out-of-plane effects, Anić et al. (2017) developed a three-dimensional computational model based on the finite element method (FEM) able to predict the in-plane and out-of-plane behaviour of masonry infilled RC frames containing openings.

More recently, the discrete element method (DEM) or the combined finite-discrete element method (DFEM) approach is being pursued, since they can address problems involving discontinuous kinematic fields, such as fracture and dislocation, sliding, large displacements, detachment of the elements, or the formation of new contacts (Yuen and Kuang, 2015; Hazay and Munjiza, 2016; Mohebkhah and Sarhosis, 2016). Smoljanovic et al. (2017) analysed confined masonry structures using the DFEM method, using a model that simulated initiation and propagation of cracks: the model, in addition to modelling masonry and confining concrete members using discrete elements, adopted zero thickness interface elements, simulating the behaviour of mortar, and through contact, cracking and masonry confinement by the RC members.

However, these models are complex, time consuming, require high computational effort and are difficult to apply for practical problems of real structures, especially in cyclic response analysis. On the other hand, macro-models are simplified models of the entire infill panels, which require less computational effort and have sufficient accuracy for entire building performance evaluation under earthquake. These models simulate the infill walls with diagonal struts acting only in compression, with a variety of macro models having been proposed based on different empirical and phenomenological formulations, which use single strut, double strut or three struts in each diagonal. Asteris et al. (2011) presented a review of the different macro models proposed in the literature.

Magenes and Pampanin (2004) performed Static Pushover (SPO) and time history analyses on frame structures designed for gravity loads and studied the influence of the infills on the seismic performance and their interaction with the joint damage mechanism. They showed that the presence of infills reduces the interstorey drift demand, while increasing the maximum floor accelerations. Moreover, the column interstorey shear contribution is consistently lower in the infilled frames, in spite of the higher interstorey shear demand and the formation of a soft-storey mechanism is delayed. However, when the infills are damaged, thereby causing a sudden reduction of the storey stiffness, a soft storey mechanism can be formed, not necessarily at the ground storey due to the interaction with joint damage. Kakaletsis and Karayannis (2008) tested seven 1/3 scaled, single storey, single bay frame specimens under cyclic horizontal loading with two qualities of infills, in order to investigate their influence; they showed that infills with openings can significantly improve the performance of RC frames, while specimens with strong infills exhibited better performance than those with weak infills.

Karayannis et al. (2011) investigated the seismic behaviour of fully and open ground storey infilled frames with beam–column joint degradation effects under nonlinear static and time history analyses, demonstrating that neglecting the possible local damage of the exterior joints may lead to erroneous conclusions and unsafe design. Furthermore, the influence of exterior joints degradation was shown to be significant for the overall behaviour of open ground frames. Basha and Kaushik (2012) tested eight half-scale specimens of masonry infilled RC frames designed in accordance with current codes and showed that the shear force of the RC columns was increased due to the infills.

Chrysostomou and Asteris (2012) proposed analytical expressions for quantifying the in-plane stiffness, strength and deformation capacity of infills, as well as simplified methods for predicting the in-plane failure mode of mainly solid panels. They further performed a parametric study to compare these methods against experimental results. Sanij and Alaghebandiyan (2012) performed SPO analysis in a three-storey infilled RC frame with three different infill arrangements, comparing three macro models for the simulation of masonry and showing that the three strut model obtained a smaller initial stiffness and increased axial forces in columns relative to the single diagonal strut model. Burton and Deierlein (2014) performed Incremental Dynamic Analysis to nonductile infilled RC frames using dual compression struts to capture the column-infill interaction that may cause shear failure of the columns. Their results indicated that it is critical to include the infill strut-column interaction and the shear degradation of columns for the accurate prediction of the collapse capacity of nonductile infill frames, otherwise the predictions are not conservative.

Zeris (2014) demonstrated the various failure types of infilled RC frames during earthquakes and reviewed the modelling conventions of infilled RC frames. He subsequently investigated their seismic response comparing nonlinear analyses using meso and macro infill models. Morfidis and Kostinakis (2017) performed nonlinear time history analysis on fifty four RC buildings with different heights, structural systems and distribution of masonry infills, for 80 bidirectional seismic sequences at different angles of incidence. They concluded that the influence of the successive earthquake phenomenon on the structural damage was higher for the infilled buildings, compared to the bare structures, while for buildings with

masonry infills, the effect of the orientation of the seismic motion was significant. Recently, Choudhury and Kaushik (2018) investigated the seismic response sensitivity to the uncertainties in different input parameters and concluded that for bare or open ground storey frames, the concrete compressive strength and column dimensions are the most important parameters affecting the response. On the other hand, for uniform infilled frames the most important parameters are the infill properties, such as the diagonal strut width and the masonry strength.

Despite the extensive analytical and experimental studies on the performance of infilled RC buildings, there is still not enough knowledge of the performance under earthquake excitation of typically encountered existing infill RC buildings, which have been designed and built according to past generation of codes with various arrangements of the infills and of the variability of their nonlinear response under actually recorded seismic base input. The aim of the present study is the assessment of the seismic performance of such non-conforming infilled RC buildings, designed according to past generations of structural design codes and construction practices, using nonlinear Incremental Dynamic Analyses (IDA) procedures (Vamvatsikos and Cornell, 2004). The influence of infill walls in the seismic performance of these buildings is quantified and the reliability of previous static pushover (SPO) predictions on these buildings designs, previously reported in Repapis et al. (2006b) is investigated. For this purpose, a set of recorded earthquake accelerograms is selected and a set of non-conforming bare and infilled RC frames is analysed in IDA, and their seismic performance is assessed, using the same limit state criteria (LC) also used previously under SPO by Repapis et al. (2006a,b), for comparison. In this way, these two assessment methodologies are compared while, furthermore, the presence of the infills in these different building types is established, based on actual earthquake excitation response.

Both global (deformation ductility, behaviour factor, overstrength, collapse mechanism formation) and local (member or infill) indices, quantifying damage of the building, are defined and are being monitored, while alternative expected failure modes, are considered in this study. Consequently, the research contribution of the present work is, to provide additional information on the vulnerability under seismic excitation of such non-conforming infilled RC structures, in order to develop possible rehabilitation and/or strengthening schemes for these structures. Furthermore, the reliability of time history predictions using IDA to establish the dependence of the monitored LCs on cyclic history and the excitation input content is demonstrated, as compared with those from inelastic static analysis predictions, which are unable to account for these.

MASONRY INFILLED RC BUILDING FORMS

All buildings considered in the present study are cast-*in-situ* RC frames with column supported beams, which are cast monolithically with the slabs. Out of a larger set of structural forms considered and analysed using SPO procedures by Repapis et al. (2006b), 13 bare and infilled RC buildings are selected in the present study in order to investigate the influence of infill walls in the seismic performance of RC buildings, using the IDA method. Three bare frames, regular in plan and elevation, comprising one typical building of the 60s (denoted K60A59), one of the 70s (denoted K70A59) and one of the 90s (denoted K60AEC8) are selected. Moreover, infilled frames of the above bare frame configurations are also examined. Letter "K" denotes a bare frame structure, while letter "T" denotes an infilled frame. "60" or "70" denotes the period of construction (frame geometry). "A" denotes a regular frame, out of a larger set of structural forms with irregularities considered in other studies (Repapis et al., 2006b; Repapis and Zeris, 2018; Zeris and Repapis, 2018) and "59" or "EC8" denotes the earthquake resistant design code in effect during construction. Both buildings of the 60 and 70s were designed according to past generation of codes (RD59, 1959), while building of the 90s according to modern codes (EC8, 2004).

Frame Characteristics

All the buildings considered consist of a plan layout four by three bays wide and they are analysed as plane frames, with four bays in the direction of the earthquake. The typical building of the 60s is five storeys high. The storey height is 3.00 m and the building has regular 3.50 m bay sizes in the two orthogonal directions. In line with the evolution of building shapes, the building of the 70s is seven storeys high, again with a storey height of 3.00 m but bay sizes equal to 6.00 m in the two orthogonal directions. Finally, the building of the 90s has the same geometry as the building of the 60s for comparison reasons. The layouts of the buildings are shown in **Figure 1**.

Influence of Masonry Infill Walls

In order to examine the influence of the layout of the perimeter frame masonry infill panels to the seismic response of the structure, fully and partially unreinforced masonry frame bays are also considered herein, assumed symmetric in plan in the response direction considered. Out of the different topological possibilities previously considered (Repapis et al., 2006b), three different arrangements of unreinforced masonry infilled frames are studied, denoted as T1–T3, as shown in **Figure 2**, since they represent the cases most commonly encountered in RC construction:

T1: Perimeter frames fully infilled over the entire height (**Figure 2A**).
T2: Perimeter frames infilled but with completely open ground storey (called pilotis) (**Figure 2B**).
T3: Perimeter frames partially infilled, with a vertically continuous window opening (**Figure 2C**).

The perimeter infill panels are 25 cm thick irrespective of the building generation, in accordance with the conventional practice of using exterior double leaf infill panels constructed of clay bricks with longitudinal holes and plaster. Single leaf interior partition walls (also denoted as moveable partitions), normally 0.10 m thick, are only included in the mass of the building and are not considered to contribute to the system that resists the earthquake forces.

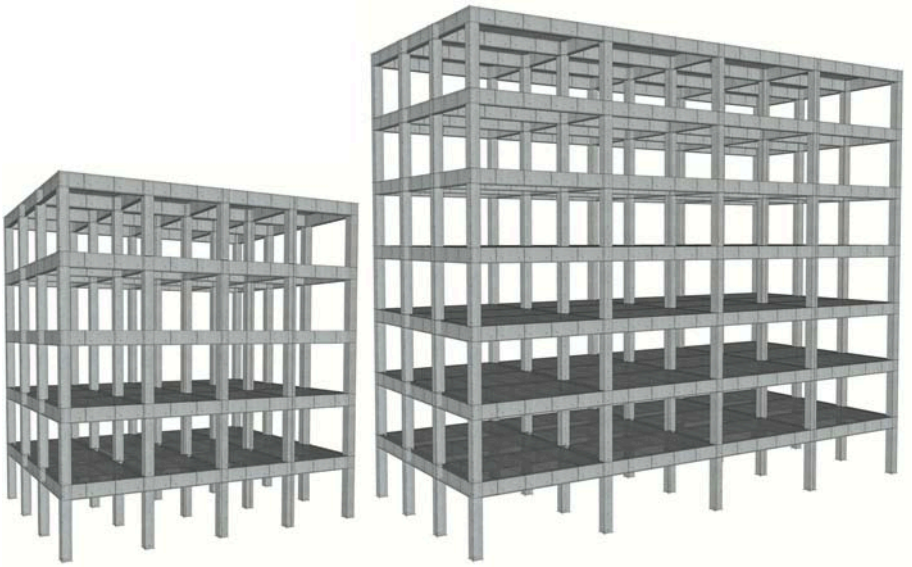

FIGURE 1 | Selected building forms of the 60 and 70s.

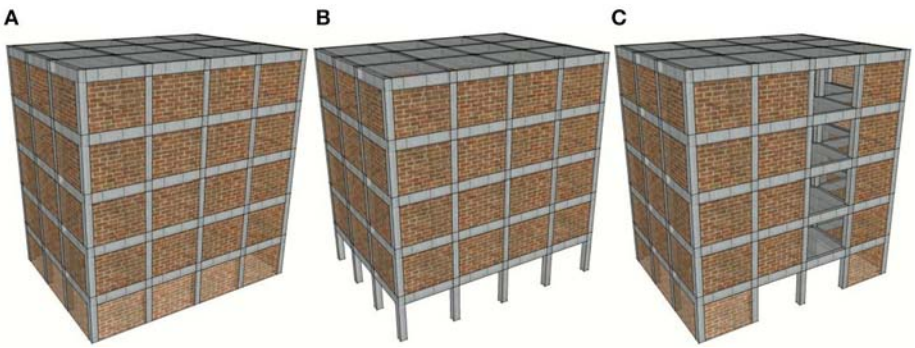

FIGURE 2 | Distribution of masonry infilled walls. **(A)** T1, **(B)** T2, **(C)** T3.

Design Characteristics

The buildings of the 60 and 70s were designed in accordance with the requirements of the first Greek Earthquake Resistant Design Code which was established in 1959 (RD59, 1959) and was based on the allowable stress design methodology. Loads were unfactored, strict requirements for detailing of the reinforcement were not specified and structural elements of the buildings of that period were characterized by widely spaced transverse reinforcement and, therefore, very little confinement. Moreover, no capacity design provisions were specified. Structural analysis methods for the buildings made use of simplifying assumptions, e.g., the beams and columns of the interior frames were designed for vertical loads and only the members of the exterior frames were designed for frame actions under both seismic and vertical loads, with the corner columns being, in addition, designed for biaxial response of the floor plans due to their mass and stiffness eccentricity.

For the definition of the seismic load a seismicity classification system that adopted three seismic zones was used, with the corresponding base shear coefficients being set equal to 4, 6, and 8% of the vertical loads (namely, dead and live loads without any reduction factors), for buildings on hard ground. The buildings of the 60 and 70s examined in this study were designed for a seismic coefficient of 4%, corresponding to seismicity Zone I. Furthermore, when seismic loading demands were verified in the design process, the allowable stresses specified in the code for vertical loads were increased to 120% of these values, as also considered herein.

Building of the 90s had the same geometry and loads as the building of the 60s (K60A59) and was designed according to EC8 (2004), as the conforming frame benchmark case. This structure was again considered to be located in the same seismicity area as the other two, characterised by an effective peak ground acceleration of 0.16 g (EC8, 2004). The commercial software package Fespa (Logismiki, 2013) capable of designing following the past and current seismic code was used for the design of all the buildings.

The design loads adopted remain the same for all buildings from the 60s through the 90s, and included: the dead loads, namely the structural self-weight and an additional uniformly distributed load equal to 1.50 kN/m^2 for floorings and the live load, which is equal to 2.00 kN/m^2, similar to the values specified in EC1 (2002). The interior masonry moveable partitions are taken into account as an additional uniform load of 1.00 kN/m^2 over the plan. The weight of the 25 cm thick perimeter infills (double wythe construction) was expressed as a uniform dead load of 3.60 kN per square meter of wall façade, imposed on the outer frame beams only.

The 60s building had a uniform slab thickness of 12 cm, beam dimensions of 20 cm by 50 and 35cm square columns at the first (ground) storey, 30 cm square columns at the second storey and 25 cm square columns from the third storey up. Building of the 70s, due to its wider spans, had a uniform slab thickness of 16 cm. Column dimensions were: 60 cm square (interior) and 90/25 cm^2 rectangular (exterior), at the first two storeys, being subsequently reduced by 10 cm (interior) and 20 cm (exterior) for every two storeys, respectively, up to the seventh storey, where the columns were 30 cm square (interior) and 35/25 cm^2 rectangular (exterior). Similarly, the dimensions of the beams were 20/60 cm^2 along the interior frames and 25/50 cm^2 along the perimeter frames. Finally, the building of the 90s has similar geometry with the building of the 60s for comparison reasons. Slab thickness is again 12 cm and beam dimensions remain 20 cm by 50 cm, but with increased reinforcement. Column dimensions increase to 40 cm square at the three lower storeys, 35 cm square at the next floor and 30 cm square at the top.

Materials of Construction

The materials of construction for building of the 60s were: (i) DIN B160 concrete having an average (cube) compressive strength of 16 MPa [this material would be classified as C10/12, in accordance with EC2 (2004)]; (ii) smooth mild steel reinforcing bars, grade DIN StI (grade S220). The allowable stress in compression of the concrete, for design under bending with axial load ranged between 6.0 and 8.4 MPa, with higher larger values specified for columns and beams, as opposed to lower allowable stresses for the slabs. Accordingly, the allowable stress in tension of the reinforcement was 140 MPa. For building of the 70s, the materials of construction were: (i) DIN B225 having an average (cube) compressive strength of 22.5 MPa [this would be classified as C12/16 per EC2 (2004)]; and (ii) ribbed high strength steel reinforcing bars, grade DIN StIII (grade S400). For this concrete grade, the allowable stress in compression of the concrete (for bending and axial load designs) ranged between 8.0 and 10.8 MPa (for columns and beams, and slabs, respectively). The allowable stress in tension of the reinforcement was, in this case, 220 MPa. Building of the 90s had materials similar to the one used in building of the 60s for comparison reasons.

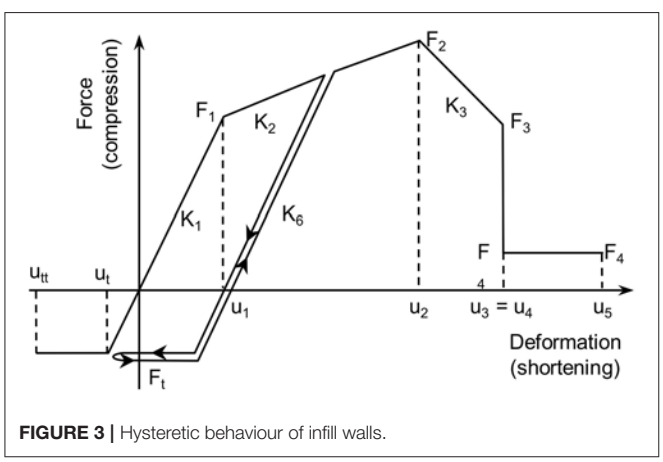

FIGURE 3 | Hysteretic behaviour of infill walls.

ANALYTICAL MODELLING

Nonlinear static and dynamic analyses were performed using the computer program Drain-2DX by Prakash et al. (1993) for the static and dynamic inelastic analysis of two-dimensional systems. The code was extended with additional finite element modelling capability in order to account for the infills. Furthermore, DrainExplorer (Repapis, 2002), a post-processing program, was developed, for processing the results of all the frame analyses. The selected buildings were regular in-plan and the frames were modelled as plane frames with rigid diaphragms in each floor. The structural mass in all cases was assumed to be lumped at the nodes and was considered, during the time history analysis, to be equal to the inertia mass due to the dead loads plus a portion only of the live load, equal to 30%. For dynamic analysis, mass proportional damping was used, with the damping coefficient determined assuming 5% critical damping in the first fundamental mode response of the cracked structure.

Structural Members Modelling

All the beams and columns of the structures were modelled using a two component concentrated plasticity line element, having bilinear hardening flexural characteristics at the end hinges. Beams were modelled as T-section beams. For the estimation of beam flexural capacities, effective slab widths equal to 1.0 and 0.5 m were assumed for internal and external frame beams respectively, for the buildings with 3.5 m bay length. For the buildings with 6.0 m bay length, these values increased to 1.30 and 0.65 m, respectively. For the estimation of the flexural characteristics of the beams in negative bending, the reinforcement in the effective width of the slab was included.

The nonlinear moment curvature characteristics were developed for all the end critical regions of beams and columns, using average material properties. Furthermore, in the columns, the dependence of these with axial load was considered. According to standard practice of construction at the 60s and 70s, top steel at the critical end sections of the beams included half plus one bent up bars from the two neighbouring midspan sections plus any top additional steel. Moreover, the reinforcement within the slab effective width was also taken into account. The bottom steel at the ends included the remaining unbent midsection bars anchored within the joint.

The average concrete strength was taken to be equal to 16 MPa for concrete grade B160, and 22.5 MPa, for concrete grade

TABLE 1 | SPO analyses results for uniform and triangular distribution of lateral loads.

Building	Prof	f_m [MPa]	T_1 [sec]	V_{max} [KN]	Ω	μ	q	δ_u [cm]	δ_{N2} [cm]	LC
K60A59	unif.	–	0.84	1012.4	1.86	1.85	2.57	6.0	6.5	θ_{pl}
	tr.	–		876.6	1.61	1.63	2.03	5.3	7.3	θ_{pl}
T160A59	unif.	2.5	0.44	2485.7	4.57	1.83	3.37	4.5	2.9	θ_{pl}
	tr.	2.5		2159	3.97	1.63	2.87	4.1	3.4	θ_{pl}
T260A59	unif.	2.5	0.51	1349	2.48	1.72	2.35	2.5	3.5	θ_{pl}
	tr.	2.5		1332	2.45	1.76	2.38	3.0	3.9	θ_{pl}
T360A59	unif.	2.5	0.52	1824	3.36	1.76	2.85	4.2	3.7	θ_{pl}
	tr.	2.5		1616	2.97	1.57	2.42	3.9	4.2	θ_{pl}
T160A59-05	unif.	0.5	0.65	1367	2.51	2.03	3.07	5.7	5	θ_{pl}
	tr.	0.5		1243	2.29	2.04	2.91	6.3	5.8	θ_{pl}
T260A59-05	unif.	0.5	0.67	1166	2.14	1.78	2.48	4.4	5.2	θ_{pl}
	tr.	0.5		1105	2.03	1.91	2.56	5.5	5.9	θ_{pl}
T360A59-05	unif.	0.5	0.69	1225	2.25	1.89	2.75	5.3	5.4	θ_{pl}
	tr.	0.5		1132	2.08	2.06	2.84	6.5	6.1	θ_{pl}
K70A59	unif.	–	1.38	2772	1.47	1.25	1.44	7.1	12.4	θ_{pl}
	tr.	–		2436	1.30	1.40	1.55	8.9	14.7	θ_{pl}
T170A59	unif.	2.5	0.72	4281	2.27	1.28	1.84	3.5	6.3	θ_{pl}
	tr.	2.5		4109	2.19	1.35	1.92	4.5	7.6	θ_{pl}
K60AEC8	unif.	–	0.63	1807	1.37	5.83	4.80	19.4	4.6	*dr*
	tr.	–		1608	1.22	7.63	5.44	27.2	5.2	*dr*
T160AEC8	unif.	2.5	0.40	3495	2.57	2.04	2.70	5.7	2.1	*Infill*
	tr.	2.5		3284	2.41	2.14	2.71	6.7	2.6	*Infill*
T260AEC8	unif.	2.5	0.45	2360	1.74	2.75	2.72	6.0	2.6	θ_{pl}
	tr.	2.5		2340	1.72	2.61	2.62	6.5	3.1	θ_{pl}
T360AEC8	unif.	2.5	0.45	2775	2.04	2.01	2.38	5.5	2.7	*Infill*
	tr.	2.5		2617	1.92	2.1	2.38	6.4	3.2	*Infill*

B225, respectively. For the reinforcing steel, the mean yield stress was assumed to be 310 MPa and 420 MPa for StI and StIII, respectively, and the average ultimate strength in tension was taken as 430 MPa and 630 MPa, respectively, with these values being measured from tests on smooth steel bars. In all cases, trilinear behaviour for the reinforcement and different constitutive models for the confined concrete core and the cover concrete were considered, in separate section analyses, performed for each member critical region prior to developing the inelastic building models. Beam-column joints were assumed to be rigid.

Infill Walls Modelling

The perimeter infill walls were modelled with equivalent pin-jointed diagonal truss elements (struts) resisting only compressive loads, with out-of-plane effects ignored. An unequal compression–tension truss finite element was used to model the infills, with a trilinear behaviour that is able to model softening with a residual strength. The trilinear envelope comprised of an initial elastic portion, a post-cracking region with positive stiffness and a softening portion, beyond the point of peak axial resistance, with negative stiffness, as shown in **Figure 3**.

The global inelastic characteristics and failure pattern of infilling masonry exhibit large uncertainty and vary significantly with the quality of construction. For the building of the 60s (K60A59) two types of masonry were selected: (i) a strong and stiff good construction quality masonry with a compressive strength f_m equal to 2.5 MPa and (ii) a weak and soft poor construction masonry with an infill compressive strength f_m equal to 0.5 MPa (buildings denoted as "−05" herein). For the buildings of the 70 and 90s, only good workmanship quality masonry with a compressive strength f_m equal to 2.5 MPa was selected. The thickness of the equivalent diagonal struts is the same as the thickness of the infill panel. Mainstone's approach was used to determine both the initial stiffness $K_{in} = K_1$ in **Figure 3** and the effective width W_{ef} of the diagonal strut (Mainstone, 1971):

$$W_{ef} = 0.175\,(\lambda_h\,H)^{-0.4}\,\sqrt{H^2 + L^2} \tag{1}$$

with,

$$\lambda_h = \sqrt[4]{\frac{E_w\,t_w\,sin(2\theta)}{4\,E_c\,I_c\,H_w}} \tag{2}$$

where E_w and E_c are the uncracked secant moduli of elasticity of the infill wall and the RC frame members, respectively, $\theta = \arctan(H_w/L_w)$ is the diagonal strut's inclination, t_w is the thickness of the infill wall, I_c is the moment of inertia of the frame columns, whereas H_w and H are the height of the infill wall (clear from slab to beam soffit) and the storey height, respectively, while L_w and L are the clear length of the infill from column to

column and the bay width, respectively. Following a proposal by Paulay and Priestley (1992) it was assumed that $E_w = 750 f_m$ for clay bricks. The initial lateral stiffness K_1, according to Mainstone (1971), is equal to

$$K_1 = \frac{E_w W_{ef} t_w}{\sqrt{H^2 + L^2}} cos^2\theta \quad (3)$$

The simplified expression by Žarnić and Gostić (1997) as given bellow, extended from an initial suggestion by Dolšek and Fajfar (2002) , was used for the evaluation of the peak resistance of the infills F_{max} in **Figure 3**. F_{max} was assumed to occur at an axial deformation of the strut u_2 equal to 0.5% of the storey height H:

$$F_{max} = 0.818 \frac{L_w t_w f_{tp}}{C_I} \left(1 + \sqrt{C_I^2 + 1}\right) \quad (4)$$

and

$$C_I = 1.925 \frac{L_w}{H_w} \quad (5)$$

where f_{tp} is the cracking strength of the infill, obtained from a diagonal compression test, and θ, L_w and H_w as previously defined. Compressive cracking forces were assumed to be equal to approximately half of the corresponding ultimate resistance, $F_1 = F_{max}/2$, following (Dolšek and Fajfar, 2002) , while the tensile strength of the infill (F_t, **Figure 3**) was assumed to be zero. The stiffness of the softening branch was taken as 10% of the initial stiffness K_1 while the residual strength F_4 was set equal to 15% of F_{max}, primarily for numerical stability.

In the results reported herein, two different levels of infill resistance F_{max} are considered only for building K60A59. For all the other case study buildings, infilled frames with relatively good quality masonry were considered only, representative of the construction pattern, the quality of the materials and the workmanship of that period.

SEISMIC ASSESSMENT USING IDA PROCEDURES

The seismic assessment of the non-conforming infilled RC buildings considered herein has been previously investigated using an SPO procedure analysis methodology described in Repapis et al. (2006a). The results of an extensive study for the seismic assessment of a wide range of regular and irregular, bare and infilled, existing RC buildings of the 60 till the 90s, using SPO, were presented in Repapis et al. (2006b). Inelastic SPO analyses were performed with both uniform and inverted triangular load profiles. Both global and local limiting performance criteria (LC) were considered (Repapis et al., 2006a,b) for performance assessment and nominal failure of the building was defined at the minimum deformation over all monitored criteria. From these analyses, the overstrength, the global ductility capacity and behaviour factor were evaluated and the failure mechanism and the critical LC were identified. Moreover, upon determination of the buildings' capacity curve, their target displacement demand was determined in accordance with the N2 methodology by Fajfar (1999) which is adopted by EC8-3 (2005), and was compared with the peak lateral deformation of the building.

In the present study, the seismic performance obtained using the IDA procedure is compared with the performance obtained from SPO procedures above, considering similar LC. For this purpose, 14 recorded base accelerograms were selected and used and, inelastic time history analyses were executed for each base excitation record and for increasing values of the recorded peak ground acceleration (PGA), until yield was exceeded and any failure LC considered was imminently reached, signifying nominal collapse. For each time history analysis, the maximum base shear and the corresponding spectral acceleration or PGA (the Intensity) are plotted against the maximum displacement or interstorey drift (the damage index), in order to establish the IDA curve for global response. Moreover, for meaningful comparison with the vulnerability predictions obtained with SPO analysis at the target point for these buildings, the time history response is also computed under all base excitations also being scaled to the design response spectral intensity, currently in effect for each building under the currently enforced regulations (EC8, 2004). For selected base inputs (e.g., record KAL18601Long), the as

TABLE 2 | Ground motion characteristics of the fourteen acceleration records used in IDA.

Record	Location and date	*PGA*	*PGV*	*VSI*	AI	t_d
		g	cm/sec	cm	cm/sec	sec
A299-1Long	Athens 1999	0.11	5.1	18.4	8.6	10.2
A299-1Tran	Athens 1999	0.16	7.1	21.1	14.5	8.4
Aigio Long	Aigio 1995	0.49	40.2	113.7	97.2	4.4
H-E06230	Imperial 1979	0.44	109.8	178.7	175.4	11.2
I-ELC-180	Imperial 1940	0.31	29.7	132.9	170.4	24.6
IZT090	Kocaeli 1999	0.22	29.8	112.3	81.3	16.6
KAL18601 Long	Kalamata 1986	0.23	30.9	106.9	54.2	6.1
KAL18601 Tran	Kalamata 1986	0.27	24.8	102.3	72.6	7.5
KOBE	Kobe 1995	0.82	81.4	417.4	839.0	10.8
KORINTHOS	Korinth 1981	0.29	23.5	123.6	85.3	16.4
KOZ19501 Long	Kozani 1995	0.22	9.2	38.8	26.4	8.0
KOZ19501 Tran	Kozani 1995	0.14	6.6	24.7	19.6	10.6
LOMA PRIETA	Loma Prieta 1989	0.64	55.1	179.6	323.8	10.2
THESSALONIKI	Thessaloniki 1978	0.14	11.4	51.8	17.2	8.7

recorded unscaled PGA intensity is also considered, since it was close to this design level intensity.

The quantification of the structural performance of the buildings is made at both global and local levels. Some response parameters of interest are the minimum elastic response spectrum acceleration intensity inducing first yield in any structural member, $(Sa)_y^{el}$, the minimum elastic response spectrum acceleration intensity inducing conventional collapse, $(Sa)_c^{el}$ and the corresponding maximum absolute values of the roof deformation δ_y and δ_u, respectively. The evolution of peak local damage and demand indices, with record intensity, is also monitored.

The available behaviour factor q and global ductility capacity μ for the buildings are evaluated using IDA, in a similar approach as in SPO, assuming that the spectral amplification remains constant with increasing intensity. The behaviour factor q is established as the ratio of the PGAs of the collapse and onset of yield earthquakes (Salvitti and Elnashai, 1996), while global ductility capacity μ as the ratio of the corresponding roof drifts, as depicted in the following Equation 6:

$$q = \frac{(Sa)_c^{el}}{(Sa)_y^{el}} \quad , \quad \mu = \frac{\delta_u}{\delta_y} \tag{6}$$

The LC at both the local and global levels, which were adopted in SPO analyses, for the estimation of conventional collapse, as described in detail in Repapis et al. (2006a), are also adopted herein for the IDA study. Consequently, during each inelastic time history analysis, the following checks were performed during step by step time history analysis:

i) Exceedance of the plastic rotation capacity of the columns at the critical regions, equal to the section's ultimate curvature under the axial load of the member (for columns) at the current time step, times the plastic hinge length (LC designated as θ_{pl}). The length of the plastic hinge was taken equal to (a) half the section effective depth or, (b) following a more refined empirical expression proposed by Paulay and Priestley (1992), whichever governed,

ii) exceedance of the member shear strength capacity under current axial load (LC designated as *V*), according to current design Code,

iii) local capacity of the masonry infill panels, assumed to be exceeded when the axial load of the equivalent diagonal struts representing the infill reaches its maximum strength (LC designated as *Infill*) and

iv) exceedance of the maximum interstorey drift (LC designated as *dr*). A limit of 1.25% was assumed for buildings of the 60 and 70s, designed for past generation of codes and 2.5% for buildings of the 90s designed according to modern codes.

Beam-column joint shear capacity was only checked in SPO analysis. It was shown that this limit criterion was not critical because other failure modes preceded.

For the automatic performance of the required time history analysis, for increasing peak ground acceleration intensity and for the evaluation of all LC in a step by step manner, the computer code DrainExplorer (Repapis, 2002) was used. The analysis input parameters are the geometry of the building and the structural materials, reinforcement detailing of all critical regions of the members, base input excitation record and its elastic response spectrum characteristics. The critical region cross-section characteristics are calculated for all members. The ground motion record is scaled automatically and Drain-2DX (Prakash et al., 1993) is called by DrainExplorer to perform the corresponding time history analysis. For each dynamic analysis at a given PGA, DrainExplorer post processes the results to check all LC at every step of the analysis, in order to identify the critical excitation for all LC. Moreover, the plastic hinge distribution, the deformed shape, the vertical interstorey drift distribution, the energy absorption among the beams, columns, and infills with height, the current state of each member, the local plastic rotations and ductility demands, the capacity check of the joints and the shear capacity ratios for each member are some of the parameters monitored in every step of the analysis and for each base input intensity.

The procedure is repeated for another scale of the ground motion, until all LC are exceeded and yield and conventional

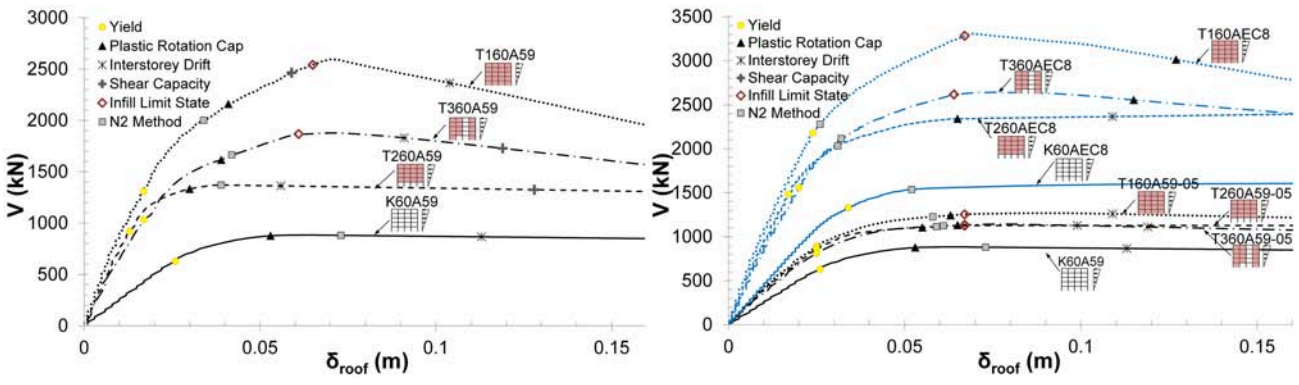

FIGURE 4 | Inelastic pushover (SPO) characteristics of bare and infilled frame structures K60A59 and K60AEC8.

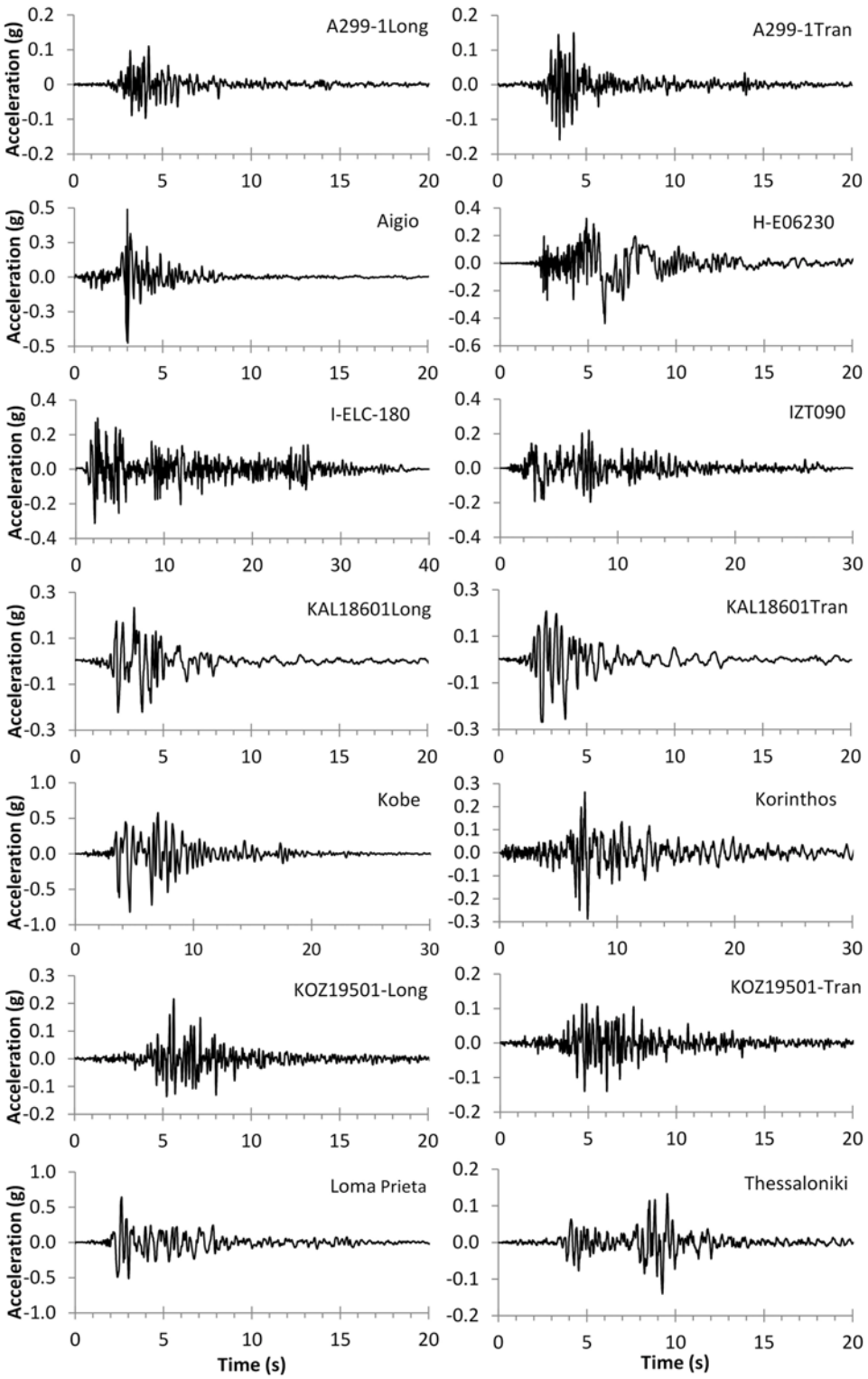

FIGURE 5 | Earthquake record time histories used in IDA analysis.

failure are identified. The upper bound of the intensity of the base excitation is reached when the predefined limiting roof displacement is exceeded. Next, additional time history analyses are performed in an iterative manner for scaled values of the PGA around the values of yield and collapse PGA, in order to evaluate with increased accuracy $(Sa)_y^{el}$ and $(Sa)_c^{el}$ and,

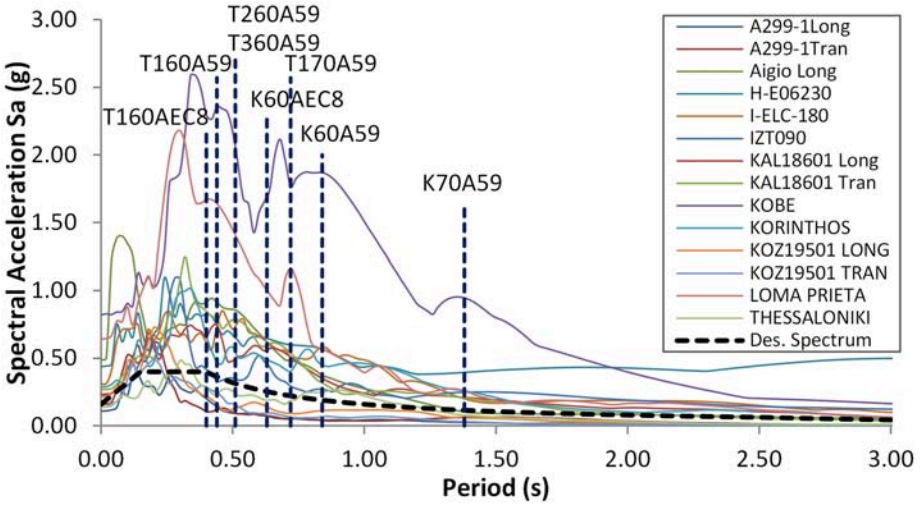

FIGURE 6 | Elastic response spectra of the as recorded accelerograms and predominant periods of the case study buildings.

therefore, the available behaviour factor q and the ductility capacity μ of the building. Finally, the entire IDA curve is traced.

NONLINEAR ANALYSES RESULTS

The inelastic analysis results following IDA for the full set of infilled plane frames, including, for comparison, their bare frame counterparts, using the set of base excitations in **Table 2**, are presented and discussed herein. For comparison, SPO analyses, previously reported on these frames (Repapis et al., 2006b), are also briefly described. The purpose of the analyses is 2-fold, namely: (i) on one hand, to investigate the seismic performance of these infilled frames, and, (ii) on the other hand, to establish the reliability of performance prediction of SPO methods to assess these structures' seismic performance under actual recorded excitations, compatible with the design assumptions currently enforced.

The graphic results of the inelastic analyses are given in **Figure 4** for the SPO studies and in **Figures 7–12** for the IDAs. All SPO derived key performance indices are also given in tabular form in **Table 1** and include, for each structural case study: (a) the assumed compressive strength of the masonry infill walls f_m strength (for the infilled frames), (b) the plane frame fundamental period T_1, obtained from modal analysis (not the effective stiffness), (c) the maximum base shear V_{max}, the corresponding overstrength Ω and the supplied behaviour factor of the building q of the equivalent bilinearized single degree of freedom (SDOF) system following the methodology proposed in Repapis et al. (2006a). Furthermore, in terms of the kinematic parameters, are given: (i) the analytically obtained peak global roof drift prediction at failure, δ_u, (ii) the target point demand δ_t, determined according to the N2 methodology by Fajfar (1999), and (iii) the corresponding ductility supply μ of the SDOF system. Finally, the controlling LC on which δ_u was established is also reported, in order to separate brittle from ductile nominal failure forms in the response.

Response Prediction Based on SPO Analyses

Prior to examining the IDA response, the SPO predictions are briefly initially examined, while, further on, the reliability of SPO to safeguard against actual earthquake response is considered by comparing SPO with IDA results. The capacity curves following inelastic plane frame SPO analyses under a triangular distribution of the lateral loads are given in **Figure 4** for the bare and infilled frame configurations, for all frames considered. In all cases, the first initiation of yield δ_y, the target point prediction using the N2 method (Fajfar, 1999) and the roof deformation levels for the different LCs are also depicted, with the minimum of which establishing the roof deformation at nominal failure δ_u for each frame (see also **Table 1**). Pushover curves for the bare and infilled frame of the 70s is out of scale and is not shown in **Figure 4**, however, they can be found in Repapis et al. (2006b) and Zeris and Repapis (2018). The results are tabulated in **Table 1** for both uniform and triangular distribution of the lateral loads. For a more detailed discussion of the use of these curves for the evaluation of the design level at allowable stress and ultimate, the overstrength and the supplied behaviour factor of each building, (see Repapis et al., 2006a,b).

Considering the SPO capacity curves it is observed that the governing LC for all bare and infilled frames is the exceedance of the plastic rotation capacity in the critical regions (θ_{pl}), with the exception of the conforming fully and partially infilled buildings T160AEC8 and T360EC8, for which infill failure is the critical LC, and for the conforming bare frame K60AEC8, for which interstorey drift limit of 2.5% is critically exceeded first, prior to all other LCs. Apart from these three buildings, infill or shear failure and interstorey drift always occur at roof deformations higher than the onset of the plastic rotation capacity LC. The

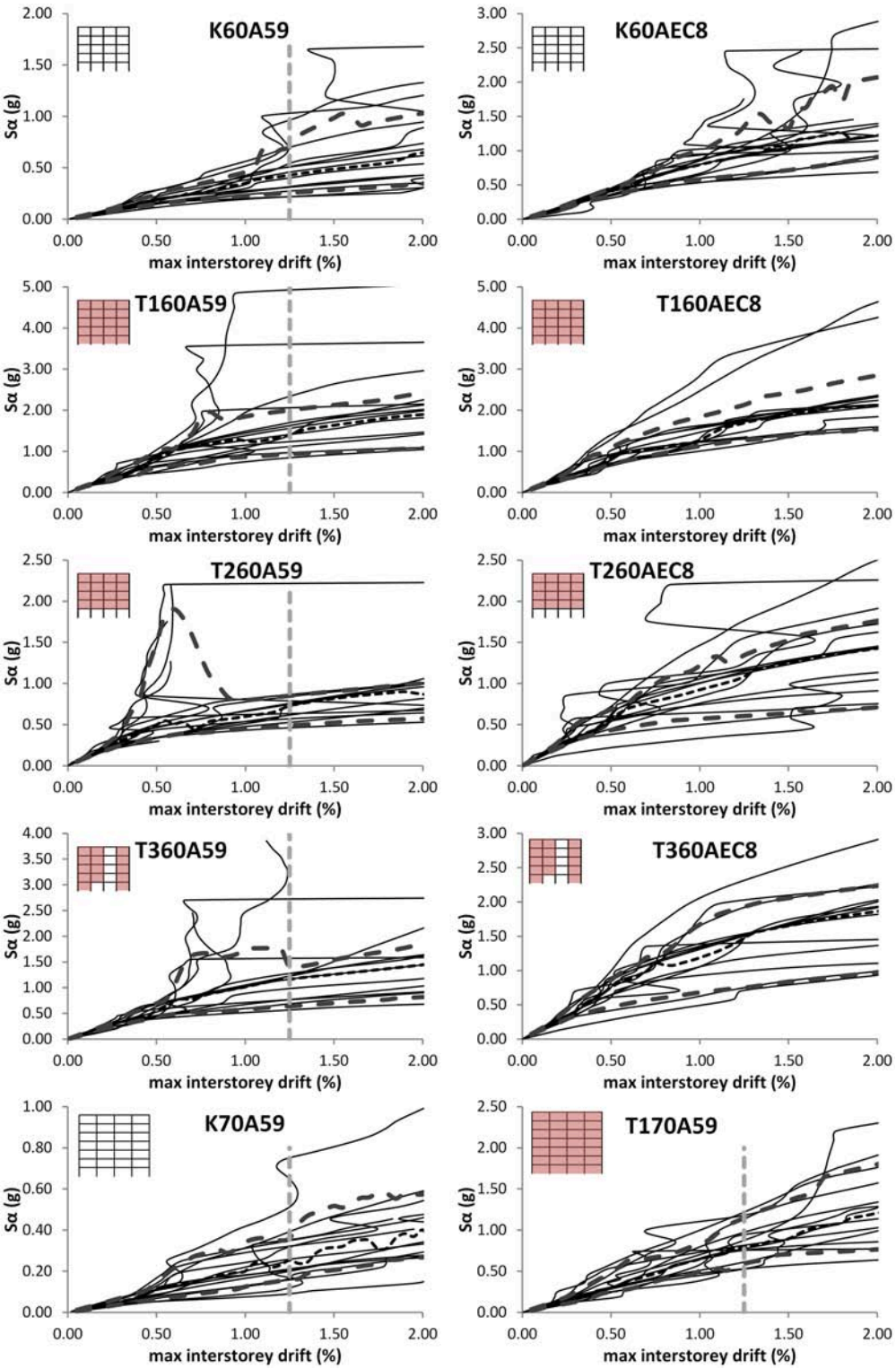

FIGURE 7 | IDA curves for the bare and infill frames considered: median, 16 and 84% fractiles for all 14 records considered.

inclusion of the infills results in a considerable increase in the initial stiffness, while also, the maximum displacement at failure of the infilled structures is decreased compared to the bare frames. Due to the interaction between the RC frame and the infills the shear strength of columns is surpassed earlier than the bare frame structures, with this LC, however, not being critical,

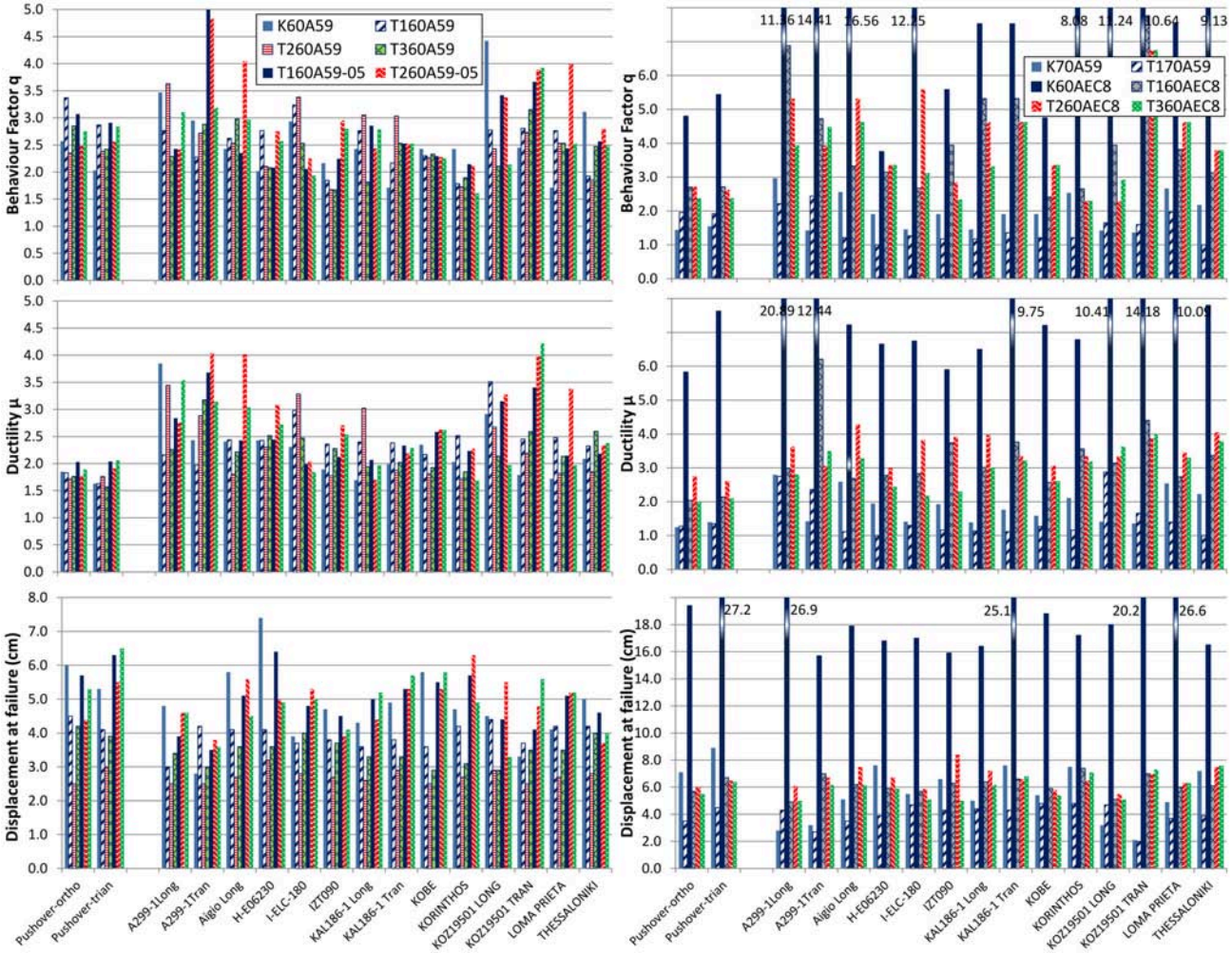

FIGURE 8 | Behaviour factor q, ductility μ and top displacement at failure evaluated from SPO and IDA analyses. (Note that building K60AEC8 results are out of scale).

since it follows the aforementioned LC of θ_{pl}. Regarding the performance of the structure, it is observed that the target point demand following the N2 method exceeds nominal failure in all non conforming frame cases, with the exception of the fully or partially infilled frames, be it with a good or a low quality infill material, whose nominal failure takes place after the target demand. Expectedly, the conforming EC8 designs are by far performing the best whether infilled or bare, and have ample reserves of deformation beyond the target demand.

Response Prediction Based on IDA

The seismic performance predictions using SPO analyses, above, are compared to the results of inelastic dynamic analyses using the IDA methodology of Vamvatsikos and Cornell (2004). To this purpose, the subject buildings were analysed in the time domain using 14 actually recorded time history base excitations, recorded during recent earthquakes in Greece and abroad. The time history traces (as recorded) for these excitations are depicted in **Figure 5**. In **Figure 6**, the linear elastic acceleration response spectra of the record set for 5% damping, are compared to the smoothed Elastic Design Response Spectrum (EDRS) prescribed in EC8 (2004) for seismicity zone I (PGA equal to 0.16 g, in the Greek National Annex of EC8), to which these building designs correspond in currently enforced seismic regulations. In the same plot are also depicted the linear elastic first mode periods of the subject buildings (denoted T_1, in **Table 1**).

For each recorded excitation, the base time history is obtained for subsequent scaling in IDA, compatible with the design seismic intensity currently enforced in the seismicity zone in which each structure is located; this scaled record excitation is obtained from the actual recording scaled so as to match the Velocity Spectrum Intensity (*VSI*) of the zone I EDRS of EC8 (2004). The as recorded record characteristics, namely: (i) PGA, (ii) the peak ground velocity (*PGV*), (iii) the record duration t_d, defined as the time elapsed between the times at the 3 and 97% limits of the Arias Intensity, (iv) the Arias Intensity (*AI*), and (v) the parameter *VSI* are also given in **Table 2**, for comparison of the characteristics of the base excitation time history set.

TABLE 3 | Behaviour factor, ductility and minimum roof drift at failure, evaluated from SPO, and IDA analyses for all the records considered, together with the mean, median, minimum, and maximum values of the entire IDA analysis set, for each building (for each frame, the predominant period, and infill strength are also noted).

	K60A59 (T_1 = 0.84 s)			T160A59 (T_1 = 0.44 s)			T260A59 (T_1 = 0.51 s)			T360A59 (T_1 = 0.52 s)			T160A59-05 (T_1 = 0.65 s)			T260A59-05 (T_1 = 0.67 s)			T360A59-05 (T_1 = 0.69 s)		
	–			f_m = 2.5 MPa			f_m = 2.5 MPa			f_m = 2.5 MPa			f_m = 0.5 MPa			f_m = 0.5 MPa			f_m = 0.5 MPa		
	q	μ	δ_u(cm)	q	μ	δ_u(cm)	q	μ	δ_u(cm)	q	μ	δ_u(cm)	q	μ	δ_u(cm)	q	μ	δ_u(cm)	q	μ	δ_u(cm)
Pushover -Unif.	2.57	1.85	6.0	3.37	1.83	4.5	2.35	1.72	2.5	2.85	1.76	4.2	3.07	2.03	5.7	2.48	1.78	4.4	2.75	1.89	5.3
-Triang.	2.03	1.63	5.3	2.87	1.63	4.1	2.38	1.76	3.0	2.42	1.57	3.9	2.91	2.04	6.3	2.56	1.91	5.5	2.84	2.06	6.5
RECORD																					
A299-1Long	3.47	3.85	4.8	2.77	2.16	3.0	3.63	3.44	2.5	2.29	2.26	3.4	2.43	2.84	3.9	2.42	2.76	4.6	3.11	3.54	4.6
A299-1Tran	2.95	2.43	2.8	2.28	1.98	4.2	2.72	2.88	2.5	2.88	3.18	3.0	5.05	3.68	3.5	4.83	4.04	3.8	3.19	3.14	3.6
Aigio Long	2.43	2.41	5.8	2.62	2.44	4.1	2.53	1.81	2.7	2.98	2.22	3.6	2.35	2.43	5.1	4.05	4.02	5.6	2.97	3.04	4.5
H-E06230	2.02	2.43	7.4	2.77	2.43	4.1	2.11	2.30	3.2	2.08	2.52	3.6	2.08	2.45	6.4	2.75	3.09	5.0	2.57	2.72	4.9
I-ELC-180	2.94	2.31	3.9	3.24	2.98	3.7	3.38	3.28	2.8	2.53	2.47	4.0	2.06	1.99	4.8	2.25	2.04	5.3	1.94	1.84	5.0
IZT090	2.16	1.89	4.7	1.85	2.36	3.8	1.67	1.78	2.7	1.67	2.28	3.7	2.25	2.12	4.5	2.95	2.71	3.9	2.80	2.54	4.1
KAL18601Long	2.43	1.70	4.3	2.77	2.40	3.6	3.05	3.02	2.6	1.81	1.94	3.3	2.86	2.07	5.0	2.44	1.71	4.4	2.79	1.98	5.2
KAL18601Tran	1.71	1.99	4.9	2.17	2.38	3.8	3.03	1.88	2.9	2.53	2.02	3.3	2.53	2.33	5.3	2.53	2.18	5.3	2.53	2.29	5.7
KOBE	2.43	2.35	5.8	2.30	2.17	3.6	2.27	1.81	2.5	2.33	1.92	2.9	2.30	2.58	5.5	2.27	2.63	5.3	2.25	2.62	5.8
KORINTHOS	2.43	2.03	4.7	1.78	2.52	4.2	1.73	1.72	2.7	1.90	1.85	3.1	2.15	2.23	5.7	2.11	2.27	6.3	1.61	1.69	4.9
KOZ19501Long	4.42	2.92	4.5	2.77	3.51	4.4	2.43	2.67	2.9	2.11	2.14	2.9	3.42	3.15	4.4	3.38	3.27	5.5	2.14	1.97	3.3
KOZ19501Tran	2.45	1.79	3.3	2.81	2.45	3.7	2.73	2.19	2.5	3.15	2.59	3.5	3.67	3.41	4.1	3.90	3.98	4.8	3.92	4.22	5.6
LOMA PRIETA	1.71	1.72	4.1	2.77	2.48	4.2	2.53	1.82	2.7	2.53	2.13	3.5	2.44	2.15	5.1	4.00	3.38	5.2	2.53	1.97	5.2
THESSALONIKI	3.11	2.09	5.0	1.93	2.32	4.2	1.85	1.85	2.8	2.47	2.60	4.0	2.57	2.18	4.6	2.80	2.34	3.7	2.50	2.37	4.0
Mean value	2.62	2.28	4.7	2.49	2.47	3.9	2.55	2.32	2.7	2.37	2.29	3.4	2.72	2.54	4.9	3.05	2.89	4.9	2.63	2.57	4.7
Median value	2.43	2.20	4.7	2.69	2.41	4.0	2.53	2.04	2.7	2.40	2.24	3.5	2.43	2.38	4.9	2.78	2.73	5.1	2.55	2.46	4.9
Min value	1.71	1.70	2.8	1.78	1.98	3.0	1.67	1.72	2.5	1.67	1.85	2.9	2.06	1.99	3.5	2.11	1.71	3.7	1.61	1.69	3.3
Max value	4.42	3.85	7.4	3.24	3.51	4.4	3.63	3.44	3.2	3.15	3.18	4.0	5.05	3.68	6.4	4.83	4.04	6.3	3.92	4.22	5.8
Standard dev.	0.72	0.57	1.1	0.44	0.37	0.4	0.60	0.62	0.2	0.44	0.35	0.4	0.82	0.53	0.8	0.8	0.8	0.8	0.6	0.7	0.8
Coef. of variation	0.28	0.25	0.24	0.18	0.15	0.09	0.23	0.27	0.07	0.19	0.15	0.11	0.30	0.21	0.16	0.28	0.27	0.15	0.22	0.28	0.16

(continued)

Table 3 | (Continued)

																		
	K70A59 (T_1 = 1.38 s)			**T170A59 (T_1 = 0.72 s)**			**K60AEC8 (T_1 = 0.63 s)**			**T160AEC8 (T_1 = 0.40 s)**			**T260AEC8 (T_1 = 0.45 s)**			**T360AEC8 (T_1 = 0.45 s)**		
	–			**f_m = 2.5 MPa**			**continued**			**f_m = 2.5 MPa**			**f_m = 2.5 MPa**			**f_m = 2.5 MPa**		
	q	***μ***	**δ_u(cm)**	***q***	***μ***	**δ_u(cm)**	***q***	***μ***	**δ_u(cm)**	***q***	***μ***	**δ_u(cm)**	***q***	***μ***	**δ_u(cm)**	***q***	***μ***	**δ_u(cm)**
Pushover -Unif.	1.44	1.25	7.1	1.95	1.28	3.5	4.80	5.83	19.4	2.70	2.04	5.7	2.72	2.75	6.0	2.38	2.01	5.5
-Triang.	1.55	1.40	8.9	1.92	1.35	4.5	5.44	7.63	27.2	2.71	2.14	6.7	2.62	2.61	6.5	2.38	2.10	6.4
RECORD																		
A299-1Long	2.97	2.97	2.80	2.21	2.75	4.3	11.36	20.89	26.9	6.88	2.98	4.9	5.31	3.63	6.1	3.94	2.81	5.0
A299-1Tran	1.43	1.43	1.42	2.44	2.36	2.7	14.41	12.44	15.7	4.73	6.21	7.0	3.94	3.07	6.7	4.48	3.49	6.2
Aigio Long	2.56	2.56	2.59	1.21	1.11	3.5	16.56	7.22	17.9	3.32	2.69	6.2	5.31	4.28	7.5	4.63	3.28	6.2
H-E06230	1.91	1.91	1.95	1.00	1.00	3.9	3.75	6.66	16.8	3.15	2.78	5.9	3.36	2.99	6.7	3.36	2.45	5.9
I-ELC-180	1.46	1.46	1.41	1.26	1.30	4.7	12.25	6.75	17.0	2.67	2.83	5.7	5.58	3.82	5.9	3.12	2.18	5.1
IZT090	1.91	1.91	1.92	1.17	1.16	4.3	5.58	5.90	15.9	3.94	3.74	6.3	2.85	3.92	8.4	2.34	2.30	5.0
KAL18601Long	1.46	1.46	1.39	1.17	1.14	4.4	7.53	6.50	16.4	5.31	3.01	6.4	4.63	3.98	7.2	3.32	3.01	6.2
KAL18601Tran	1.91	1.91	1.76	1.36	1.11	4.3	7.53	9.75	25.1	5.31	3.76	6.6	4.63	3.35	6.6	4.63	3.22	6.8
KOBE	1.91	1.91	1.59	1.21	1.27	4.8	4.75	7.21	18.8	2.41	2.57	5.9	3.35	3.06	5.8	3.35	2.61	5.4
KORINTHOS	2.53	2.53	2.11	1.21	1.16	4.8	8.08	6.78	17.2	2.65	3.56	7.4	2.30	3.34	6.5	2.30	3.18	7.1
KOZ19501Long	1.42	1.42	1.42	1.65	2.87	4.7	11.24	10.41	18.0	3.94	3.14	5.1	2.28	3.34	5.5	2.93	3.63	5.1
KOZ19501Tran	1.36	1.36	1.36	1.60	1.66	2.0	10.64	14.18	20.2	7.77	4.40	7.0	6.74	3.88	7.0	6.74	4.02	7.3
LOMA PRIETA	2.67	2.67	2.54	1.97	1.40	3.7	7.53	10.09	26.6	3.82	2.73	6.0	4.63	3.46	6.3	4.63	3.30	6.3
THESSALONIKI	2.18	2.18	2.23	1.00	1.00	3.9	9.13	7.80	16.5	3.13	3.37	6.1	3.80	4.04	7.5	3.80	3.78	7.6
Mean value	1.98	1.89	5.3	1.46	1.52	4.0	9.31	9.47	19.2	4.22	3.41	6.2	4.19	3.58	6.7	3.83	3.09	6.1
Median value	1.91	1.84	5.25	1.24	1.22	4.3	8.61	7.51	17.55	3.88	3.08	6.2	4.28	3.54	6.7	3.58	3.20	6.2
Min value	1.36	1.36	2.1	1.00	1.00	2.0	3.75	5.90	15.7	2.41	2.57	4.9	2.28	2.99	5.5	2.30	2.18	5.0
Max value	2.97	2.80	7.6	2.44	2.87	4.8	16.56	20.89	26.9	7.77	6.21	7.4	6.74	4.28	8.4	6.74	4.02	7.6
Standard dev.	0.53	0.50	1.9	0.45	0.65	0.8	3.65	4.11	4.0	1.62	0.96	0.7	1.31	0.41	0.8	1.2	0.6	0.9
Coef. of variation	0.27	0.26	0.36	0.31	0.43	0.20	0.39	0.43	0.21	0.38	0.28	0.11	0.31	0.11	0.12	0.30	0.18	0.15

Dynamic Response Variability and Global Damage Prediction

For each building and record considered, a typical IDA series involved about 20 time history analyses, leading to a total of more than 4,500 nonlinear dynamic analyses, for the entire building and record set. The results of all records' IDA analyses for all buildings are initially compared in **Figure 7**, in terms of the structures' global response under each nonlinear time history analysis, namely peak absolute interstorey drift vs. the corresponding spectral acceleration. For statistical evaluation purposes, in addition to the entire set of IDA curves the median IDA of all 14 records together with the 16 and 84% fractile plots are also depicted, together with the corresponding global LC (previously designated *dr*), namely 1.25% for non conforming frames and 2.5 % for conforming frames (off graph scale); one should stress, however, that the actual controlling LC for nominal failure, in each IDA analysis, differed for each structure and record case, with the majority of cases governed by structural LCs and followed by infill failure at higher intensities, as presented in more detail later on.

The inclusion of infills over the entire height of the building results in a considerable increase in the structure's lateral overstrength, in the case of the non conforming buildings as this is manifested by comparing the spectral intensities to reach a given storey drift, for the bare (and pilotis) frames and their infilled counterparts for all building generations: while the bare frames attain the critical drift limit of 1.25% at about 0.70 and 0.36 g (K60A59 and K70A59 frames, respectively), the corresponding fully and partially infilled frames attain this value at 2.00 g (T160A59), 0.85 g (T260A59), 1.4 g (T360A59), and 1.15 g (T170A59) respectively, namely 285, 121, 199, and 319% of the bare frame counterpart, with the corresponding ratios of peak resistance under SPO being 246, 152, 184, and 169%, respectively, for these buildings (Repapis et al., 2006b). It is therefore concluded that IDA predictions with drift limit criteria considerations generally predict higher overstrengths than SPO, except the irregularly infilled frame with the open ground storey (T2), whose performance is overly optimistic under static inelastic analysis, with the pilotis having the worst prediction errors. Fully infilled frame of the 70s has the worst prediction errors. The opposite is observed to the conforming frames, for which the IDA predictions with drift limit criteria considerations generally predict lower overstrengths than SPO.

Comparing the IDA response in **Figure 7** among the bare and infilled frames and concentrating in particular to the 84% fractile and median peak storey drifts for given spectral intensity, it is seen that the presence of the infills results in an overall reduction of the scatter between the two, compared to the bare frames; the latter structural forms (both 60 and 70s) invariably exhibit higher deviations between the two IDA curves, with increasing base input intensity–with building K70A59 being the worst in performance at relatively lower intensities. The entirely opposite holds true for the pilotis cases (the T260A59 and T260AEC8 designs offscale), for which the difference between the latter two curves is minimal at the LC *dr* level, with building T260A59 exhibiting an initially relatively stronger resistance for small storey drifts, quickly dropping, however, to the bare frame spectral acceleration levels at higher drifts, due to the soft storey: this expected response transition is actually corrected for by infilling two bays at the open ground storey (the T360A59 and T360AEC8 designs), following closer the spectral acceleration levels of the fully infilled cases; it should be mentioned at this point that infill configuration T360XX, with two infilled bays at ground storey, is being used in Greece as a possible seismic intervention scheme of existing pilotis RC buildings.

It is interesting to note further, that for each building type there exist up to four records (∼30% of the sample) for which the IDA demands increase disproportionately compared to the remaining records in the set, and dynamic instability is obtained at storey drifts over 0.5, 1.2, and 1.0% drifts for pilotis, bare and infilled frames, respectively; these records vary with building type and are consistently within the subset of A299-1, Aigio, KOZ19501, and THESSALONIKI (**Figure 7**).

Quantification of the Seismic Performance Indices

Further to the overall comparison of the IDA and SPO results based on the LC *dr* only, and given that, as subsequently discussed, the form of failure is not the same among different records and structural forms (in fact the nominal failure controlling LC varies even between IDA and the SPO prediction), the actual seismic performance predictions are subsequently considered in more detail. To that effect, the basic performance parameters used for the equivalent SDOF (re)design of RC structures, namely the provided behaviour (q) factor and ductility capacity, and the corresponding global damage index as expressed in terms of the roof displacement at failure, are compared between the SPO and IDA in **Figure 8**, with the corresponding values (and their statistics) given in **Table 3** for all the buildings and record analyses at hand. An immediate comparison between the conforming (K60AEC8) and non conforming bare frames of the 60 and 70s reveals the influence of the conforming detailing and current seismic design requirements in a resulting considerable increase in all their performance indices: compared to the bare frame (K60A59) which exhibits a median behaviour factor and global ductility of 2.4 and 2.2, the corresponding values for conforming building K60AEC8 are 8.6 and 7.5, respectively. The inclusion of the infills, however, in these frames, has the opposite effect in their seismic performance indices. Considering the corresponding median behaviour factor and global ductility values it is observed that these remain or increase to 2.7 and 2.4 (T160A59), 2.5 and 2.0 (T260A59, pilotis), 2.4 and 2.2 (T360A59, upgraded pilotis)–with even better performance of the weak infill wall pilotis (T260A59-05), while they are reduced to 3.9 and 3.0 for the fully infilled conforming frame (T160AEC8). This observation does not apply to the 70s group, which are relatively taller and have larger spans, for which the poor bare frame performance (median q and μ equal to 1.9 and 1.8, frame K70A59) compares to even lower values of median q and μ equal to 1.2 and 1.2 for the fully infilled frame T170A59. Equally importantly, the scatter in the IDA results (see, e.g., the standard deviation and coefficients of variation in **Table 3**) for fully infilled

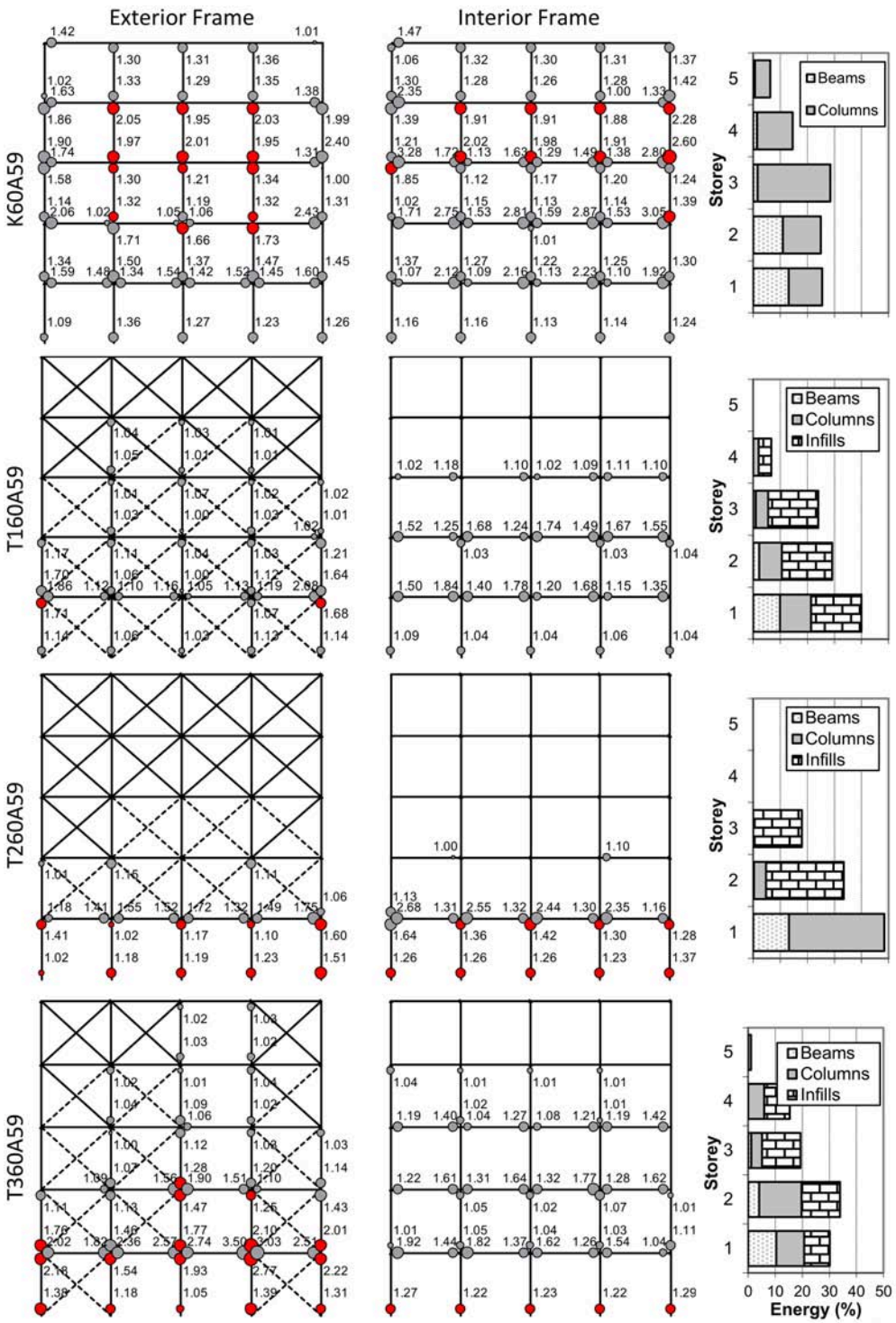

FIGURE 9 | Plastic hinge distribution, ductility rotation demands and energy absorption at the end of the analysis. KAL18601Long record (unscaled). Red plastic hinges have failed. Infills are plotted in "dashed" line if cracked.

structures is reduced to half of the bare frame for T160A59 and T160AEC8, while it increases for the corresponding 70s frames. Similar observations hold true also for the peak global roof deformations.

Compared to the SPO predictions, one again observes that median IDA values are nearly equal (K60A59) or higher (K70A59, K60AEC8) than the SPO predictions (uniform distribution), which are therefore more conservative for use

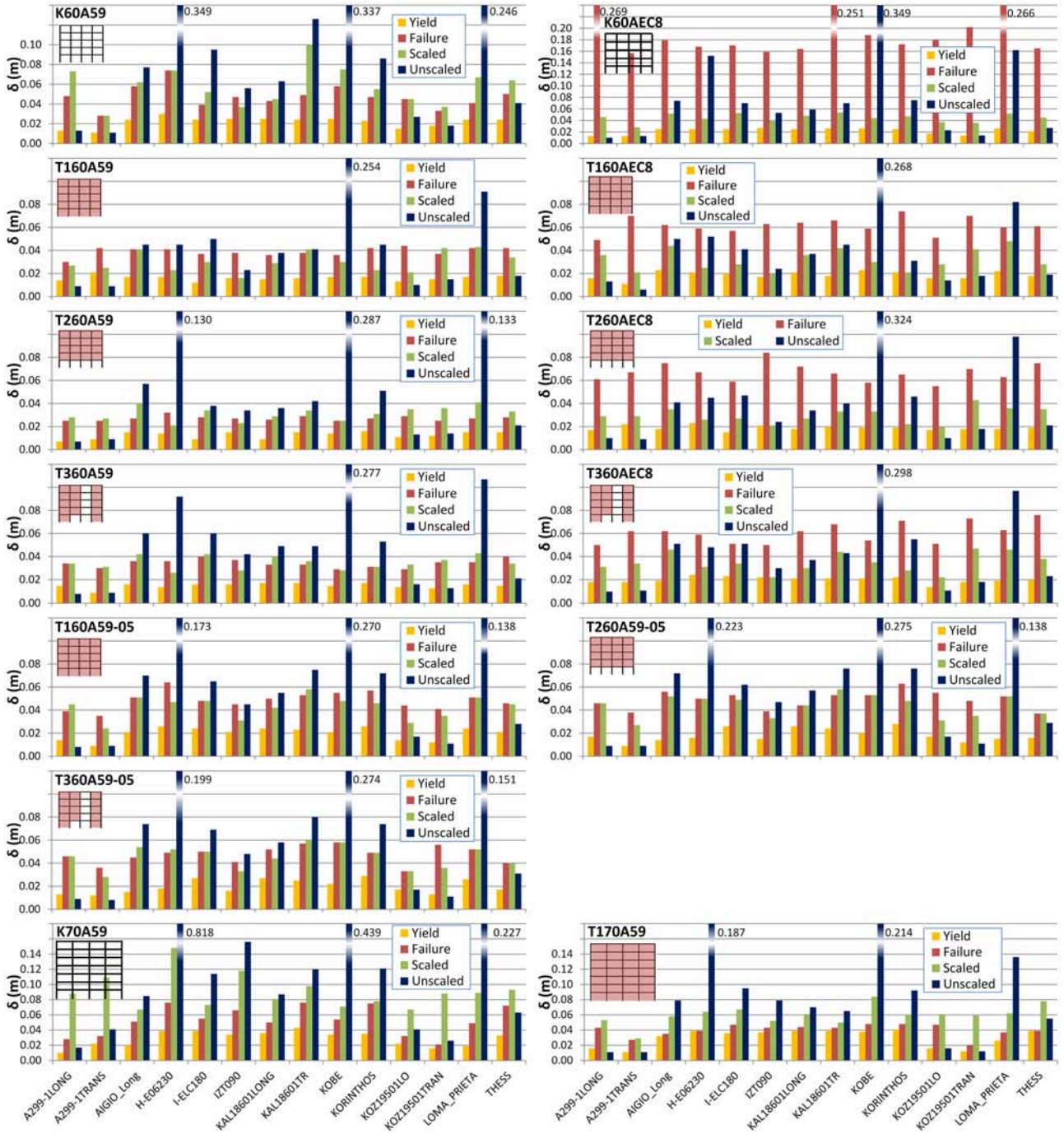

FIGURE 10 | Roof displacements from IDA analysis for the 14 records. Values for yield, failure, the scaled record to the design spectrum and the unscaled (raw) record are shown.

in redesign, yet, in this case, IDA predictions systematically are lower than the SPO predictions in the supplied behaviour factor of the non conforming frames (T160A59 and T170A59), implying that assessment and verification methods adopting the SPO values not to be conservative in the frame performance levels; again, unlike T160A59, for the 70s infilled frame the ductility marginal difference between IDA and SPO vanishes.

Local Resisting Mechanisms and Energy Absorption

This overall difference in performance of the bare and infilled frames can be qualitatively related to the distribution of resting

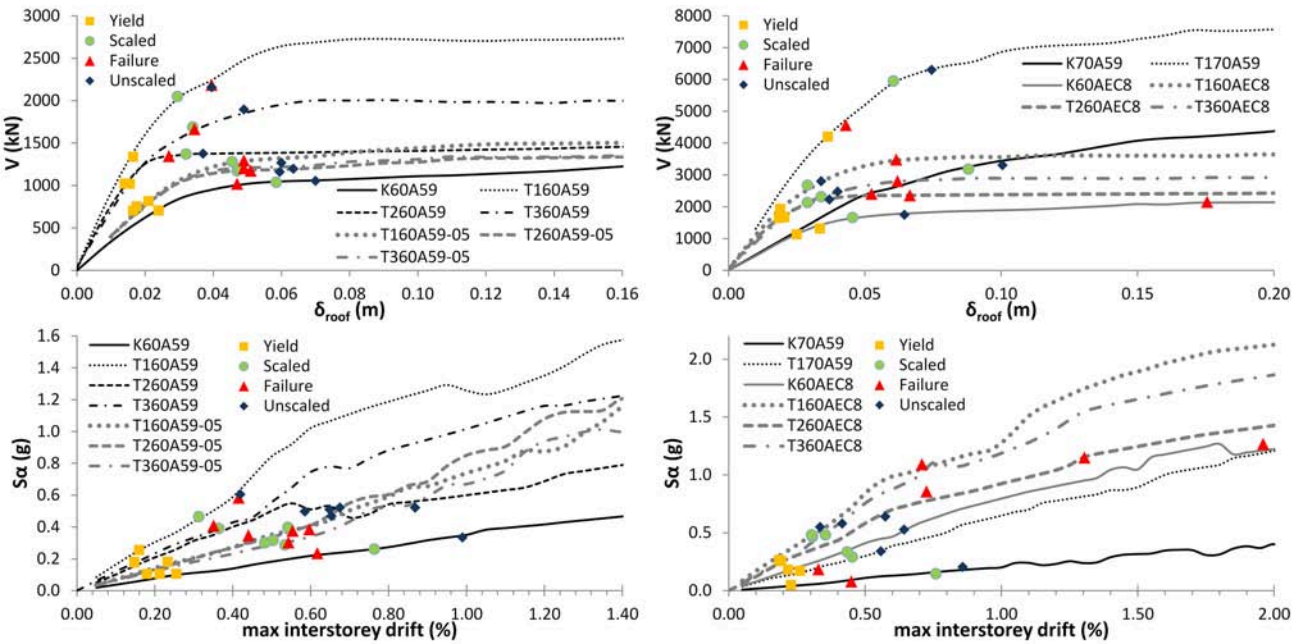

FIGURE 11 | Comparison of the median IDA intensity curves for the bare and infill frames considered in terms of the *dr* global LC.

mechanisms and their failure extent, considering in **Figure 9** the time history snapshot at the end of the analysis for the unscaled KAL18601Long record. At this instant the hinge distributions and their relative demands, the extent of cracking in the infills and the energy absorption for all the infill configurations of frame K60A59 (internal and external) are plotted. In this Figure comparisons of (i) the plastic hinge distributions between the members and the flexural ductility demands in the hinge, (ii) the possible onset of failure in the corresponding hinge, (iii) the extent of cracking in the infill struts, and (iv) the energy absorption per storey, of the beams, the columns and the infill struts, relative to the total energy absorbed, are shown. It is seen that, while the bare frame attains the maximum drift through a soft storey mechanism in the third and fourth storey and failure of the columns, with very little energy contribution from the beams, including a regular infill pattern results in the lower four storeys contributing in the energy absorption with a complete correction of the soft storey formation. Furthermore, the change in the response profile results in this case in a failure at this instant of the base column heads only, while the beams are in this case mobilized fully with higher ductility demands and no failure. The pilotis configuration follows the bare frame performance, with the exception that the soft storey formation is in this case forced to the ground storey, causing the columns to fail in this location. Again, this type of response is corrected by partially infilling two ground storey bays at the ends of the exterior frame only (case T360A59).

The peak roof deformation demands at first onset of yield and at nominal failure, is compared with the peak deformation of the as recorded and scaled record inputs for all 14 records and for each building, in **Figure 10**; furthermore, the entire demand history with increasing base input is demonstrated for these buildings considering the median IDA response in terms of roof deformation and interstorey drift in **Figure 11**. In the case of the 60s frame configurations characterised by a smaller number of floors and relatively dense column spacing, the first yield deformation does not differ among the different types of structural systems (bare frames and infilled configurations with good or weak infill masonry quality). This is not the case for K70A59 and T170A59 for which the onset of yield varies with the input content, albeit in the same manner for both building forms. Considering the deformation at failure vis-a-vis the peak deformation demand of the scaled input, one observes that: (i) both the drift and the roof deformation at first yield are fairly insensitive to the infill configuration or lack thereof, lying in the 0.2% range, (ii) in absolute value, roof or storey deformations at failure of the bare frames are lower than the corresponding deformation of the scaled earthquake record, (iii) inclusion of the infills for building K60A59 (but not K70A59) results in correcting for this deficiency in the infilled frames, with the exception of the KAL18601Long, KOZ19501TRAN and Loma Prieta records; and (iv) the infill configuration affects favourably and very strongly the safety margin between scaled input response and failure of the conforming frames, which have the most favourable response.

Form of Nominal Failure and Target Point Prediction

Since the actual form of failure (the controlling LC) varies with record and building type, the median IDA results of the peak base shear and peak roof deformation are compared with the SPO predictions for all the 60s frames (bare, infilled, pilotis, weakly infilled) in **Figure 12**, with designation, in each case, of the controlling LC. From the load resistance curve comparisons

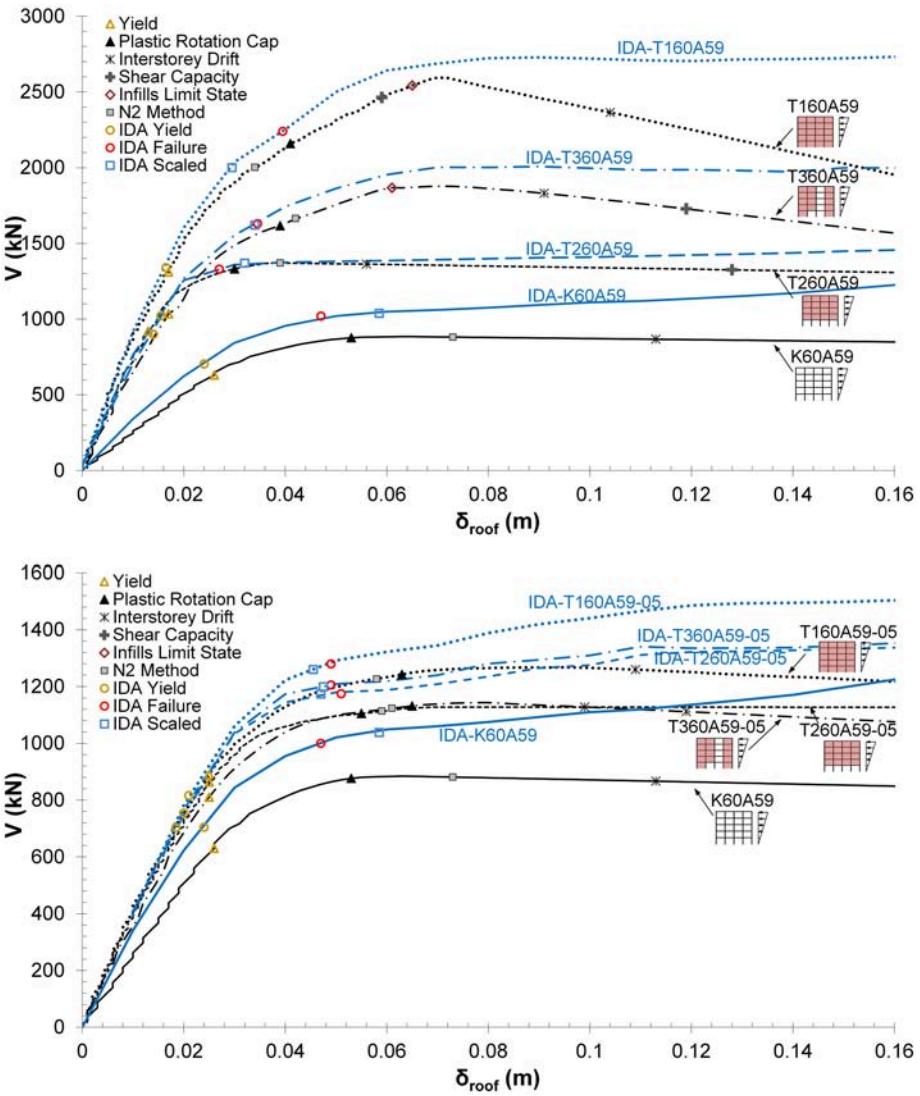

FIGURE 12 | SPO and median IDA predictions for the bare (K60A59) and infill (T160A59, T260A59 and T360A59) frames of the 60 s.

it is demonstrated clearly that the overstrength under IDA is consistently higher than SPO estimation under the triangular lateral force distribution (and closer, for K60A59 to the uniform load distribution, see Repapis et al., 2006b); the scaled input median IDA deformation demand is consistently less than nominal failure for the infilled frames (T160A59), marginally so for the partially or weakly infilled frames (T360A59 and both T160A59-05 and T360A59-05) and exceeds the deformation capacity for the bare frame and the pilotis. This difference in overstrength also results in a consistent increase of the target point prediction based on the N2 method (Fajfar, 1999) under SPO, relative to the median IDA prediction under the scaled record inputs. It should be noted, also, that the LC controlling this nominal failure differs in each case and in no case (SPO or IDA) is the infill controlling failure: in most cases flexural plastic rotations are exceeded in columns, albeit at different axial loads for the bare and infilled frames, due to the change in the structural system. This is not the case for the conforming frames. The critical LC for the conforming bare frame (K60AEC8) is the interstorey drift, while for the fully infilled (T160AEC8) and the partially infilled (T360AEC8) frames, the critical LC in most cases (SPO and IDA) is exceedance of the infill capacity. However, for the open ground storey (T260AEC8) frame, energy absorption concentrates at the open storey and critical LC is, in most cases, the failure of the ground columns.

CONCLUSIONS

The present study aims at the vulnerability assessment of non-conforming infilled RC structures of the 60 and 70s, which represent a significant portion of the whole building estate

in Greece and other seismically affected countries worldwide. The seismic performance of typical bare and infilled structures was evaluated using nonlinear pushover and time history analyses. The results from Incremental Dynamic Analysis were compared with previous analysis assessments on the same structures, based on static inelastic prediction procedures. Based on the findings of this study, the following can be concluded regarding the expected inelastic performance of typical non-conforming infilled RC buildings under seismic excitation:

- The inclusion of infills regularly distributed over the entire height of the building resulted in a considerable increase in the structure's lateral overstrength compared to the bare frame, followed by a companion reduction in their deformability. Furthermore, observed scatter of the IDA results was reduced compared to the bare frames.
- IDA overstrength predictions were higher, compared to the SPO predictions for the non conforming frames, with the opposite being observed for the conforming case. Accordingly, SPO methods overestimated the target displacement, as compared to the median value obtained using IDA. Moreover, deformation capacity was also overestimated by the SPO methods.
- The form and criterion governing failure differed among different records and structural forms. In the bare frame of the 60s a soft storey mechanism occurred between the third and fourth storeys due to the reduced dimensions of the columns, while the fully infilled frame suffered extensive damage at the lower storey infills, resulting to a soft storey at the lower two storeys. In general fully infilled frames presented a better distribution of damage along the height of the structure. Infilled frames with an open storey concentrated all the inelastic action at the base and exhibited the worst performance; introducing a few infill bays at the soft storey level provided these buildings with increased resistance, similar to the infilled frames. The plastic hinge rotation capacity of columns was the governing LC for all non-conforming bare and infilled frames. On the contrary, the critical LC was the interstorey drift for the conforming bare frame, while the capacity of the infills governed for the fully or partially infilled frames.
- IDA predictions of the basic performance parameters, such as the available behaviour factor, ductility capacity and deformation at failure exhibited high scatter, with SPO predictions being within the range of the IDA predictions. One important point regarding the building generation and form is that overall, infilled buildings of the 60s exhibited a higher ductility capacity and behaviour factor under IDA (q and μ equal to 2.4 and 2.2 for the bare frame, and 2.7 and 2.4 for the fully infilled frame, respectively) than SPO predictions, due to their relatively dense column spacing. The opposite holds true for the 70s buildings, with wider spans and more storeys, which, under SPO, had relatively worse performance than the 60s; under IDA, their median performance indices were even lower (q and μ equal to 1.9 and 1.8 for the bare frame, and 1.2 for both q and μ for the fully infilled frame, respectively) than the SPO values.
- For non-conforming bare frames of the 60 and 70s, maximum deformation capacity is smaller than the demand under the scaled record inputs. On the contrary, for fully infilled frames the deformation demand is less than nominal failure and marginally so for the partially or weakly infilled frames (T360A59 and both T160A59-05 and T360A59-05). The open ground storey (pilotis) frame (T260A59) has the worst performance, for which demand exceeds the deformation.

In view of the complexity and number of parameters involved in the evaluation of the seismic vulnerability of existing RC frame structures (both infilled and not), the findings of the present study can further be refined by considering the following modelling improvements, currently under investigation: (i) three-dimensional response effects, under different plan infill configurations, (ii) additional LCs involving, among others, the lack of proper anchorage and the buckling of the compression reinforcement, (iii) improved modelling techniques to account for modelling of the joint behaviour and the pinched cyclic characteristics of the members; and (iv) uncertainty in the quality of the materials.

AUTHOR CONTRIBUTIONS

CR formulated the problem, carried out the literature review, developed the numerical models, conducted the computation, drew the figures and wrote the paper. CZ formulated the problem, carried out the literature review, developed the numerical models, conducted the computation, drew the figures and wrote the paper.

REFERENCES

Anić, F., Penava, D., and Sarhosis, V. (2017). "Development of a three-dimensional computational model for the in-plane and out-of-plane analysis of masonry-infilled reinforced concrete frames," in *COMPDYN 2017 6th ECCOMAS Thematic Conference on Computational Methods in Structural Dynamics and Earthquake Engineering* (Rhodes Island).

Asteris, P. G., Antoniou, S. T., Sophianopoulos, D. S., and Chrysostomou, C. Z. (2011), Mathematical macromodeling of infilled frames: state of the art. *J. Struct. Eng. ASCE* 137, 1508–1517. doi: 10.1061/(ASCE)ST.1943-541X.0000384

Asteris, P. G., and Cotsovos, D. M. (2012). Numerical investigation of the effect of infill walls on the structural response of RC frames. *Open Constr. Build Tech. J.* 6, 164–181. doi: 10.2174/18748368012060 10164

Asteris, P. G., Cotsovos, D. M., Chrysostomou, C. Z., Mohebkhah, A., and Al-Chaar, G. K. (2013). Mathematical micromodeling of infilled frames: state of the art. *Eng. Struc.* 56, 1905–1921. doi: 10.1016/j.engstruct.2013. 08.010

Asteris, P. G., Repapis, C., Repapi, E., and Cavaleri, L. (2017). Fundamental period of infilled reinforced concrete frame structures, structure and infrastructure. *Engineering* 13, 929–941. doi: 10.1080/15732479.2016.1227341

Asteris, P. G., Repapis, C., Tsaris, A. K., Di Trapani, F., and Cavaleri, L. (2015). Parameters affecting the fundamental period of infilled RC frame structures. *Earthquakes Struc.* 9, 999–1028. doi: 10.12989/eas.2015.9.5.999

Attard, M. M., Nappi, A., and Tin-Loi, F. (2007). Modeling fracture in masonry. *J. Struc. Eng.* 133, 1385–1392. doi: 10.1061/(ASCE)0733-9445(2007)133:10(1385)

Bakas, N. P., Babouskos, N. G., Kokkinos, F. T., and Katsikadelis, J. T. (2009). "Influence of infill walls in the dynamic response of buildings via a B.E. Modeling," in *Proceedings of the 10th International Conference on Advances in Boundary Element Techniques* (Athens).

Basha, S. H., and Kaushik, H. B. (2012). "Evaluation of shear demand on columns of masonry infilled reinforced concrete frames," in *Proceedings of the 15th World Conference on Earthquake Engineering* (Lisbon).

Bolea, O. (2016). The seismic behaviour of reinforced concrete frame structures with infill masonry in the Bucharest area. *Energy Procedia* 85, 60–76. doi: 10.1016/j.egypro.2015.12.275

Borzi, B., Crowley, H., and Pinho, R. (2008). "The influence of infill panels on vulnerability curves for RC buildings," in *Proceedings of the 14th World Conference on Earthquake Engineering* (Beijing).

Buonopane, S. G., and White, R. N. (1999). Pseudodynamic testing of masonry infilled reinforced concrete frame. *J. Struc. Eng. ASCE* 125, 578–589. doi: 10.1061/(ASCE)0733-9445(1999)125:6(578)

Burton, H., and Deierlein, G. (2014). Simulation of seismic collapse in nonductile reinforced concrete frame buildings with masonry infills. *J. Struc. Eng.* 140:A4014016. doi: 10.1061/(ASCE)ST.1943-541X.0000921

Cavaleri, L., and Di Trapani, F. (2014). Cyclic response of masonry infilled RC frames: experimental results and simplified modeling. *Soil Dynam. Earthquake Eng.* 65, 224–242. doi: 10.1016/j.soildyn.2014.06.016

Cavaleri, L., Fossetti, M., and Papia, M. (2005). Infilled frames: developments in the evaluation of cyclic behaviour under lateral loads. *Struc. Eng. Mechan.* 21, 469–494. doi: 10.12989/sem.2005.21.4.469

Chiou, T. C., and Hwang, S. J. (2015). Tests on cyclic behavior of reinforced concrete frames with brick infill. *Earthquake Eng. Struc. Dynam.* 44, 1939–1958. doi: 10.1002/eqe.2564

Chiozzi, A., and Miranda, E. (2017). Fragility functions for masonry infill walls with in-plane loading. *Earthquake Eng. Struc. Dynam.* 46, 2831–2850. doi: 10.1002/eqe.2934

Choudhury, T., and Kaushik, H. B. (2018). Seismic response sensitivity to uncertain variables in RC frames with infill walls. *J. Struc. Eng.* 144:04018184. doi: 10.1061/(ASCE)ST.1943-541X.0002190

Chrysostomou, C. Z., and Asteris, P. G. (2012). On the in-plane properties and capacities of infilled frames. *Eng. Struc.* 41, 385–402. doi: 10.1016/j.engstruct.2012.03.057

Chrysostomou, C. Z., Gergely, P., and Abel, J. F. (2002). A six-strut model for nonlinear dynamic analysis of steel infilled frames. *Int. J. Struc. Stability Dynam.* 2, 335–353. doi: 10.1142/S0219455402000567

Crisafulli, F. J. (1997). *Seismic Behaviour of Reinforced Concrete Structures With Masonry Infills*. Ph.D. Dissertation, University of Canterbury, New Zealand.

Dhanasekar, M., and Page, A. W. (1986). "Influence of brick masonry infill properties on the behaviour of infilled frames," *Proceedings of the Institution of Civil Engineers*, London, 81(Pt 2), 593–605.

Dolšek, M., and Fajfar, P. (2002). Mathematical modelling of an infilled RC frame structure based on the results of pseudo-dynamic tests. *Earthquake Eng. Struc. Dynam.* 31, 1215–1230. doi: 10.1002/eqe.154

Dolšek, M., and Fajfar, P. (2008a). The effect of masonry infills on the seismic response of a four-storey reinforced concrete frame—a deterministic assessment. *Eng. Struc.* 30, 1991–2001. doi: 10.1016/j.engstruct.2008.01.001

Dolšek, M., and Fajfar, P. (2008b). The effect of masonry infills on the seismic response of a four storey reinforced concrete frame—a probabilistic assessment. *Eng. Struc.* 30, 3186–3192. doi: 10.1016/j.engstruct.2008.04.031

Dumaru, R., Rodrigues, H., Furtado, A., and Varum, H. (2016). Seismic vulnerability and parametric study on a bare frame building in Nepal. *Front. Built Environ.* 2:31. doi: 10.3389/fbuil.2016.00031

EC1 (2002). *European Committee for Standardization, EN-1991, Eurocode No. 1, Actions on Structures*. Brussels.

EC2 (2004). *European Committee for Standardization, EN-1992-1-1, Eurocode No. 2, Design of Concrete Structures, Part 1: General Rules and Rules for Buildings*. CEN, Brussels.

EC8 (2004). *European Committee for Standardization, EN-1998-1, Eurocode No. 8, Design of Structures for Earthquake Resistance, Part 1: General Rules, Seismic Actions and Rules for Buildings and National Annex*. CEN, Brussels.

EC8-3 (2005). European Committee for Standardization, EN-1998-3, Eurocode No. 8, *Design of Structures for Earthquake Resistance, Part 3: Assessment and retrofitting of buildings and National Annex*. CEN, Brussels.

Ellul, F., and D'Ayala, D. (2012). Realistic FE models to enable push-over non linear analysis of masonry infilled frames. *Open Constr. Build. Technol. J. Integr.* 6, 213–235. doi: 10.2174/1874836801206010213

Fajfar, P. (1999). Capacity spectrum method based on inelastic demand spectra. *Earthquake Eng. Struc. Dynam.* 28, 979–993. doi: 10.1002/(SICI)1096-9845(199909)28:9<979::AID-EQE850>3.0.CO;2-1

Fardis, M. N., Bousias, S. N., Franchioni, G., and Panagiotakos, T. B. (1999). Seismic response and design of RC structures with plan-eccentric masonry infills. *Earthquake Eng. Struct. Dynam.* 28, 173–191. doi: 10.1002/(SICI)1096-9845(199902)28:2<173::AID-EQE810>3.0.CO;2-1

Fardis, M. N., and Calvi, M. G. (1995). "Effects of infills on the global response of reinforced concrete frames," in *Procedings of the 10th European Conference on Earthquake Engineering,* Balkema, Rotterdam, 2893–2898.

Favvata, M. J., Naoum, M. C., and Karayannis, C. G. (2013). Limit states of RC structures with first floor irregularities. *Struc. Eng. Mech.* 47, 791–818. doi: 10.12989/sem.2013.47.6.791

Furtado, A., Rodrigues, H., Arêde, A., and Varum, H. (2016). Simplified macro-model for infill masonry walls considering the out-of-plane behaviour. *Earthquake Eng. Struct. Dynam.* 45, 507–524. doi: 10.1002/eqe.2663

Haldar, P., and Singh, Y. (2012). Modeling of URM infills and their effect on seismic behavior of RC frame buildings. *Open Constr. Build. Tech. J.* 6, 35–41. doi: 10.2174/1874836801206010035

Hashemi, A., and Mosalam, K. M. (2006). Shake-table experiment on reinforced concrete structure containing masonry infill wall. *Earthquake Eng. Struc. Dynam.* 35, 1827–1852. doi: 10.1002/eqe.612

Hazay, M., and Munjiza, A. (2016). "Introduction to the combined finite-discrete element method," in *Computational Modeling of Masonry Structures Using the Discrete Element Method*, eds V. Sarhosis, K. Bagi, J. Lemos, and G. Milani (Hershey, PA: IGI Global), 123–145.

Jeon, J. S., Park, J. H., and DesRoches, R. (2015). Seismic fragility of lightly reinforced concrete frames with masonry infills. *Earthquake Eng. Struc. Dynam.* 44, 1783–1803. doi: 10.1002/eqe.2555

Kakaletsis, D. J., and Karayannis, C. G. (2008). Influence of masonry strength and openings on infilled R/C frames under cycling loading. *J. Earthquake Eng.* 12, 197–221. doi: 10.1080/13632460701299138

Kappos, A. J., and Ellul, F. (2000). "Seismic design and performance assessment of masonry infilled RC frames," in *Proceedings of the 12th World Conference on Earthquake Engineering,* Auckland, paper (No. 989).

Karayannis, C. G., Favvata, M. J., and Kakaletsis, D. J. (2011). Seismic behaviour of infilled and pilotis RC frame structures with beam–column joint degradation effect. *Eng. Struc.* 33, 2821–2831. doi: 10.1016/j.engstruct.2011.06.006

Lagaros, N. D. (2012). Fuzzy fragility analysis of structures with masonry infill walls. *Open Const. and Build. Tech. J.* 6, 291–305. doi: 10.2174/1874836801206010291

Lemos, J. V. (2007). Discrete element modeling of masonry structures. *Int. J. Architec. Heritage* 1, 190–213. doi: 10.1080/15583050601176868

Logismiki, L. H. (2013), *FESPA 10 for Windows, v.5.4.0.100*. Athens.

Lourenco, P. B. (1996). *Computational Strategies for Masonry Structures*. Ph.D. thesis, Delft University of Technology, Delft.

Lourenço, P. B., Leite, J. M., Paulo-Pereira, M. F., Campos-Costa, A., Candeias, P. X., and Mendes, N. (2016). Shaking table testing for masonry infill walls: unreinforced versus reinforced solutions. *Earthquake Eng. Struc. Dynam.* 45, 2241–2260. doi: 10.1002/eqe.2756

Magenes, G., and Pampanin, S. (2004). "Seismic reponse of gravity-load design frames with masonry infills," in *Proceedings of the 13th World Conference on Earthquake Engineering* (Vancouver, BC).

Mainstone, R. J. (1971). "On the stiffness and strength of infilled frames," in *Proceedings of Institution of Civil Engineers (ICE), Supplement (IV),* Paper no. 7360, 57–90.

Mehrabi, A. B., Benson Shing, P., Schuller, M. P., and Noland, J. L. (1996). Experimental evaluation of masonry-infilled RC frames. *J. Struct. Eng. ASCE* 122, 228–237. doi: 10.1061/(ASCE)0733-9445(1996)122:3(228)

Mohebkhah, A., and Sarhosis, V. (2016). "Discrete element modeling of masonry-infilled frames," in *Computational Modeling of Masonry Structures Using the*

Discrete Element Method, eds V. Sarhosis, K. Bagi, J. Lemos, and G. Milani (Hershey, PA: IGI Global), 200–234.

Morfidis, K., and Kostinakis, K. (2017). The role of masonry infills on the damage response of R/C buildings subjected to seismic sequences. *Eng. Struc.* 131, 459–476. doi: 10.1016/j.engstruct.2016.10.039

Negro, P., and Verzeletti, G. (1996). Effect of infills on the global behavior of R/C Frames: energy considerations from pseudodynamic tests. *Earthquake Eng. Struc. Dynam.* 25, 753–773. doi: 10.1002/(SICI)1096-9845(199608)25:8<753::AID-EQE578>3.0.CO;2-Q

Page, A. W., Kleeman, P. W., and Dhanasekar, M. (1985). "An in-plane finite element model for brick masonry." in *Proceedings of a Session Held in Conjunction With Structures Congress'85* (Chicago, IL), 1–18.

Palieraki, V., Zeris, C., Vintzileou, E., and Adami, C. E. (2018). In-plane and out-of plane response of currently constructed masonry infills. *Eng. Struc.* 177, 103–116. doi: 10.1016/j.engstruct.2018.09.047

Paulay, T., and Priestley, M. N. J. (1992). *Seismic Design of Reinforced Concrete and Masonry Buildings*, New York, NY: John Wiley and Sons, Inc.

Pinto, A., Verzeletti, G., Molina, J., Varum, H., Pinho, R., and Coelho, E. (2002). *Pseudo-Dynamic Tests on Non-Seismic Resisting RC Frames (Bare and Selective Retrofit Frames),* Ispra: Joint Research Centre (JRC).

Prakash, V., Powell, G. H., and Campbell, S. (1993). *Drain-2DX: Base Program Description and User Guide, Version 1.10*, Report No. UCB/SEMM-93/17, Dept. of Civil and Environmental Engineering, University of California, Berkeley.

Rainieri, C. (2008). *Operational Modal Analysis for Seismic Protection of Structures.* Ph. D. Thesis, University of Naples "Federico II," Naples.

RD59 (1959), *Ministry of Public Works, Earthquake Design Regulation of Building Works,* Royal Decree 26/2/59, Decree 36?/26/2/59, Greece.

Repapis, C. (2002), *DrainExplorer, a Drain-2DX post-processor program, Reinforced Concrete Laboratory,* Department of Civil Engineering, National Technical University of Athens.

Repapis, C., Vintzileou, E., and Zeris, C. (2006a). Evaluation of the seismic performance of existing RC buildings: I. Suggested methodology. *J. Earthquake Eng. Imperial College Press* 10, 265–287., doi: 10.1080/13632460609350596

Repapis, C., Zeris, C., and Vintzileou, E. (2006b). Evaluation of the seismic performance of existing RC buildings: II. A case study for regular and irregular buildings. *J. Earthquake Eng. Imperial College Press* 10, 429–452, doi: 10.1080/13632460609350604

Repapis, C. C., and Zeris, C. A. (2018). Performance investigation of existing RC buildings with height irregularity using the IDA procedure. *J. Earthquake Eng.* 14, 505–523. doi: 10.1080/13632469.2018.1488777

Salvitti, L. M., and Elnashai, A. S. (1996). "Evaluation of behavior factors for RC buildings by nonlinear dynamic analysis," in *Proceedings of the 11th World Conference on Earthquake Engineering.* Acapulco, Mexico, Paper no. 2005, Elsevier Science.

Sanij, E. D., and Alaghebandiyan, R. (2012). Nonlinear earthquake response analysis of RC frames with masonry infills," in *Proceedings of the 15th World Conference of Earthquake Engineering.* Lisbon.

Santhi, M. H., Knight, G. M. S., and Muthumani, K. (2005a). Evaluation of seismic response of soft-storey infilled frames. *Comp. Concr.* 2, 423–437. doi: 10.12989/cac.2005.2.6.423

Santhi, M. H., Knight, G. M. S., and Muthumani, K. (2005b). Evaluation of seismic performance of gravity load designed reinforced concrete frames. *J. Perform. Constr. Facilities* 19, 277–282. doi: 10.1061/(ASCE)0887-3828(2005)19:4(277)

Sarhosis, V., Garrity, S., and Sheng, Y. (2012). "A computational modelling approach for low bond strength masonry," in *Proceedings of the International Conference on Structural Analysis of Historical Constructions*, SAHC 2012. Wroclaw.

Sarhosis, V., and Lemos, J. V. (2018). A detailed micro-modelling approach for the structural analysis of masonry assemblages. *Comp. Struct.* 206, 66–81. doi: 10.1016/j.compstruc.2018.06.003

Sarhosis, V., Tsavdaridis, K. D., and Giannopoulos, I. (2014). Discrete element modelling (DEM) for masonry infilled steel frames with multiple window openings subjected to lateral load variations. *Open Constr. Build. Tech. J.* 8, 93–103. doi: 10.2174/18748368014080 10093

Smith, B. S. (1966), Behavior of square infilled frames. *J. Struc. Division ASCE* 92(ST1), 381–403.

Smith, B. S., and Carter, C. (1969). A method of analysis for infilled frames, *Proc. Institut. Civil Eng.* 44, 31–48.

Smoljanovic, H., Zivaljic, N., Nikolic, Z., and Munjiza, A. (2017). Numerical model for confined masonry structures based on finite discrete element method. *Int. J. Eng. Model.* 30, 19–35. Available online at: https://hrcak.srce.hr/201719

Stavridis, A., Koutromanos, I., and Shing, P. B. (2012). Shake-table tests of a three-story reinforced concrete frame with masonry infill walls. *Earthquake Eng. Struc. Dynam.* 41, 1089–1108. doi: 10.1002/eqe.1174

Stavridis, A., and Shing, P. B. (2010). Finite-element modeling of nonlinear behavior of masonry-infilled RC frames. *J. Struc. Eng.* 136, 285–296. doi: 10.1061/(ASCE)ST.1943-541X.116

Stylianidis, K. C. (2012). Experimental investigation of masonry infilled RC frames. *Open Constr. Build. Technol. J.* 6, 194–212. doi: 10.2174/1874836801206010194

Vamvatsikos, D., and Cornell, C. A. (2004). Applied incremental dynamic analysis. *Earthquake Spectra* 20, 525–533. doi: 10.1193/1.1737737

Vintzeleou, E., and Tassios, T. P. (1989). Seismic behaviour and design of infilled RC frames. *Eur. Earthquake Eng.* 3, 22–28.

Vintzileou, E., Adami, C. E., Palieraki, V., Mouzakis, C., and Karapitta, L. (2017). "Seismic behaviour of a reinforced masonry infill made with an innovative new brick unit: results of a shaking table test," in *Proceedings of the 6th ECCOMAS International Conference on Computational Methods in Structural Dynamics and Earthquake Engineering* (COMPDYN 2017), Rhodes Island.

Vougioukas, E. (2012). Out-of-plane response of infill masonry walls. *Open Constr. Build. Tech. J.* 6, 325–333. doi: 10.2174/1874836801206010325

Yu, H., Mohammed, M. A., Mohammadi, M. E., Moaveni, B., Barbosa, A. R., Stavridis, A. et al. (2017). Structural identification of an 18-Story RC building in Nepal using post-earthquake ambient vibration and lidar data. *Front. Built Environ.* 3:11. doi: 10.3389/fbuil.2017.00011

Yuen, Y. P., and Kuang, J. S. (2015). Nonlinear seismic responses and lateral force transfer mechanisms of RC frames with different infill configurations. *Eng. Struct.* 91, 125–140. doi: 10.1016/j.engstruct.2015.02.031

Žarnić, R., and Gostić, S. (1997). "Masonry infilled frames as an effective structural sub-assemblage," in *Seismic Design Methodologies for the Next Generation of Codes*, eds P. Fajfar and H. Krawinkler (Rotterdam: Balkema), 335–346.

Žarnić, R., Gostič, S., Crewe, A. J., and Taylor, C. A. (2001). Shaking table tests of 1: 4 reduced-scale models of masonry infilled reinforced concrete frame buildings. *Earthquake Eng. Struc. Dynam.* 30, 819–834. doi: 10.1002/eqe.39

Zeris, C. (2014). "Seismic response of existing non-conforming reinforced concrete buildings with unreinforced masonry infills," in *New Trends in Seismic Design of Structures*, eds N. D. Lagaros, Y. Tsompanakis and M. Papadrakakis (Saxe-Coburg Publishers). Available online at: http://www.saxe-coburg.co.uk/pubs/pub.html?id=37

Zeris, C. A., and Repapis, C. C. (2018). Comparison of the seismic performance of existing RC buildings designed to different codes. *Earthquakes Struct. Techno-Press.* 14, 505–523. doi: 10.12989/eas.2018.14.6.505

Conflict of Interest Statement: The authors declare that the research was conducted in the absence of any commercial or financial relationships that could be construed as a potential conflict of interest.

frontiers in Built Environment

ORIGINAL RESEARCH
published: 22 February 2019
doi: 10.3389/fbuil.2019.00009

FE Modeling of Circular, Elliptic, and Triangular Isolated Slabs With a Continuous Damage Model

Gelacio Juárez-Luna and Omar Caballero-Garatachea*

Departamento de Materiales, Universidad Autónoma Metropolitana, México City, Mexico

The non-linear behavior of reinforced concrete circular, elliptic, and triangular isolated slabs was studied using computational mechanics. Concrete was modeled with a damage model which includes softening, while the behavior of the reinforcing steel was modeled with a 1D bilinear plasticity model. The constitutive models and the finite element method were validated by comparing the computed numerical results with the experimental results of a rectangular slab reported in the scientific literature. The coefficient method is proposed for its simplicity to calculate design bending moments in slabs with circular, elliptic, and triangular geometries. These coefficients were computed from the FE analysis. The layout of steel reinforcement is proposed, particularly lengths of zones for positive and negative moments, respectively. The crack paths are showed, which are depending on the boundary conditions, acting loads, and geometry of the slabs.

Keywords: slabs, damage model, finite elements, cracking, coefficient method, moment design

OPEN ACCESS

Edited by:
Vagelis Plevris,
OsloMet–Oslo Metropolitan University, Norway

Reviewed by:
Alessia Monaco,
Dipartimento di Architettura e Design, Politecnico di Torino, Italy
Francesco Tornabene,
University of Bologna, Italy
Flavia De Luca,
University of Bristol, United Kingdom

****Correspondence:***
Gelacio Juárez-Luna
gjl@azc.uam.mx

Specialty section:
This article was submitted to Computational Methods in Structural Engineering, a section of the journal Frontiers in Built Environment

Received: *24 August 2018*
Accepted: *17 January 2019*
Published: *22 February 2019*

Citation:
Juárez-Luna G and Caballero-Garatachea O (2019) FE Modeling of Circular, Elliptic, and Triangular Isolated Slabs With a Continuous Damage Model. Front. Built Environ. 5:9. doi: 10.3389/fbuil.2019.00009

INTRODUCTION

A floor is a flat structural member whose primary function is to support transverse and in plane loads and carry them to its supports. Generally, floor systems are an arrangement of panels with rectangular geometries; however, some architectural designs need slabs with other kinds of geometries. In the current provisions of the design codes, there are detailed methods for the analysis and design of slabs with rectangular geometries, including methods such as: equivalent frame, direct, coefficient method, among others. However, slabs without rectangular geometry do not have common forms of structuration neither analysis methodologies in the current design codes. Although, there are slabs with other geometries, this paper only considers circular, elliptic and triangular isolated reinforced concrete slabs.

There are mainly three models for modeling cracking: (1) fracture mechanics, which localizes the cracks, either in a line or a surface, the disadvantages of this model is that it is mainly applicable for brittle materials, where initial cracks as well as a costly re-meshing process are necessary; (2) smeared crack model, cracks occur in any point of a finite element; in this model initial cracks and re-meshing are no needed, but it may show problems of stress locking or spurious kinematic modes; (3) the embedded discontinuities model, which takes the advantages of the first two models, since it introduces the discontinuities (cracks) at any place and direction within the finite elements. These discontinuities (cracks) are not observed, but there are zones with high displacement gradients where damage is concentrated.

In the modeling of the reinforced concrete slabs, de Borst and Nauta (1985) applied the smeared crack model to study an axisymmetric slab under shear penetration, showing that cracking initiated at the bottom face of the slab and the corresponding cracking paths. Then, Kwak and Filippou (1990) modeled a square slab supported on its corners with a concentrated load at the center of the span, obtained the load *vs*. displacement curve, which was congruent with experimental results reported by Jofriet and McNeice (1971) and McNeice (1967); in the reported results by Kwak and Filippou (1990), neither the first crack load nor the cracking pattern was given. There were other proposals for modeling reinforced concrete slabs, such as Gilbert and Warner (1978), Hand et al. (1973), Hinton et al. (1981), Lin and Scordelis (1975), Wang et al. (2013) among others, most of them used the smeared crack model. Juárez-Luna and Caballero-Garatachea (2014) provides flexural design moments and cracking paths in circular, triangular and elliptic slabs, but they also used the smeared crack model for modeling cracking in concrete in the academic version of the software ANSYS (2010). Shu et al. (2015) studied the response of slabs subjected to bending with non-linear finite element analysis in the software DIANA, modeling the concrete with 3D elements and the steel reinforcement with bar elements. Juárez-Luna et al. (2015) investigates the cracking process of reinforced concrete slabs subject to vertical load. Concrete was modeled with hexahedral finite elements with embedded discontinuities; whereas steel reinforcement was modeled by 3D bar elements, placed along the edges of the solid elements. Genikomsou and Polak (2015) investigated the failures modes of reinforced concrete slab-column connections under static and pseudo-dynamic loadings by 3D non-linear finite element analyses. The comparison between experimental and numerical results, computed in ABAQUS, shows that the calibrated model properly predicts the punching shear response of the slabs. Wosatko et al. (2015) carried out numerical simulations of punching shear in a reinforced concrete slab-column, loaded as monotonically increasing imposed displacement at the column. Two regularized plastic-damage models were applied. The first model, implemented in FEAP, was refined by an additional averaging equation where gradient enhancement involves an internal length scale. In the second model, from ABAQUS, a viscoplastic strain rate was introduced. These models properly predicted punching shear behavior. Genikomsou and Polak (2017) performed finite element analyses to investigate the effect of the compressive membrane action in flat concrete slabs. Numerical results showed that the punching shear capacity of a continuous slab is higher than the capacity of a conventional isolated slab. Navarro et al. (2018) carried out a parametric study of the punching shear phenomenon in a reinforced concrete slab by non-linear numerical models based on finite elements. The slab was simulated in ABAQUS software and the model was calibrated with experimental results reported in literature. The studied parameters were: yield strength of steel reinforcement, compressive strength of concrete, flexural reinforcement, relationship between column width and slab width and slab thickness.

In this paper, reinforced concrete slabs with circular, elliptic and triangular geometries are studied by means of computer simulations to make predictions of these slabs under vertical loading and different support conditions. As it is well-known, computational methods are computer-based methods used to numerically solve mathematical models that describe physical phenomena (Plevris and Tsiatas, 2018). Firstly, linear elastic analyses of slabs with these three geometries were carried out to know the negative and positive moment zones and, consequently, the placement of negative and positive reinforcement. Then, non-linear analyses were carried out to obtain the load-displacement capacity curve as well as cracking paths. The linear elastic analyses were carried out with the software for structural analysis and design SAP2000 (CSI, 2009) and the non-linear analyses were carried out with the finite element analysis program (FEAP), developed by Taylor (2008). In the former software, the slabs were modeled with 2D shell finite elements, but in the latter software, the slabs were modeled with solid and bar finite elements in 3D. The concrete constitutive behavior was modeled with a continuous damage model, which includes different threshold values in tension and compression and also includes strain softening. The steel reinforcement constitutive behavior is modeled with a 1D rate independent plasticity model, including isotropic hardening model. It is important to point out that this damage model with different failure surface in tension and compression was formulated and validated by Juárez-Luna et al. (2014), which was also implemented by these authors in FEAP. The developed damage model does not exhibit the problem of stress locking as the smeared cracking model does; this guaranties an adequate energy release as the material fails. An experimental test of a rectangular slab, reported in the literature, was modeled to validate both constitutive models. The computed force *vs*. displacement curves at the midspan of the slab as well as cracking paths seem to be in good agreement with the experimental results. Taking avantage of the computed FE results, design suggestions for circular, elliptic and triangular slabs were included. The coefficient method is proposed for its simplicity to calculate design bending moments in these slabs. These coefficients were computed from the FE models. Steel reinforcement layout is proposed, particularly lengths of zones with only bottom reinforcement for positive moments and lengths of zones with top and bottom reinforcement for negative moments.

The outline of this paper is as follows. Section Finite Element Model gives a description of the specimens and shows the concrete and steel constitutive models used in the non-linear analyses. The section Validation shows a validation between the finite element method and the constitutive models through numerical modeling based on a laboratory experiment reported in the literature. Section Results shows linear elastic analyses with finite element method to compute the the steel reinforcement layout and non-linear analyses to compute the force-displacement curves at the midspan of the slabs; additionally, this section shows the grown of cracking on the surfaces of the slabs with simple and clamped supports. Section Design Recommendations provides design recommendations for circular, elliptic and triangular slabs. Finally, in section Conclusions, conclusions derived from this work are given.

FINITE ELEMENT MODEL

Description of the Specimens

The modeled reinforced concrete slabs with circular geometry has a diameter $d = 4.0$ m. Elliptic slab models had values of ratio of minor axis to major axis, *b/a*, equal to 0.5, 0.6, 0.7, 0.8, and 0.9, respectively, considering a constant value $a = 4\ m$ for the major axis. The triangular slab model has a height $h = 4\,m$ and base $2h/\sqrt{3}$. The studied slabs with three different geometries have a thickness of 10 cm, which satisfied the minimum thickness of the Mexican guidelines for concrete structures NTCC-17 (2017).

Initially, elastic analyses were carried out for the study of the slabs in the software SAP2000 (CSI, 2009). These models were modeled with plate finite elements, which have three degrees of freedom in each node: one translational and two rotational. Subsequently, non-linear analyses were carried out in FEAP, but these models were modeled with hexahedral solid elements and bar elements, which have three degrees of freedom in each one of their nodes. The moment distributions were computed with elastic analyses, which were used to place the steel reinforcement at the top and at the bottom zones of the slabs. On the other hand, cracking and propagation were computed with non-linear analyses.

Constitutive Models

A continuous damage model, developed by Juárez-Luna et al. (2014), was used for modeling the constitutive behavior of concrete, congruent with the experimental behavior reported in the literature, e.g., Kupfer and Gerstle (1973), as shown in **Figure 1A**. The proposed damage model uses the failure surface proposed by Oliver et al. (1990). Nevertheless, the tangent constitutive tensor developed by Juárez-Luna et al. (2014) is different to the one developed by Linero (2006). This concrete constitutive model considers strain softening after reaching the ultimate stress strength. On the other hand, the steel reinforcement was modeled with a 1D rate independent plasticity model, which has an elastic bounded space shown in **Figure 1B**, considering a bilinear curve with isotropic hardening.

The continuous damage model, developed by Juárez-Luna et al. (2014), has different failure surface in tension and compression, which is defined by the following equations:

a) Free energy density $\Psi(\epsilon, r) = \left(1 - d(r)\right)\ \Psi_0$

b) Constitutive equation $\sigma = \frac{\partial \Psi}{\partial \varepsilon} = (1 - d)C\ :\ \varepsilon$

c) Damage variable $d(r) = 1 - \frac{q}{r};\quad q \in [r_0, 0]\quad d \in [0, 1]$

d) Evolution law $\dot{r} = \gamma \begin{cases} r \in [r_0, \infty] \\ r_0 = r|_{t=0} = \frac{\sigma_y}{\sqrt{E}} \end{cases}$

e) Damage criterion
$$f(\tau_\sigma, q) = \chi \tau_\sigma - q = \chi \sqrt{\sigma : C^{-1} : \sigma} - r;\ \begin{cases} q \in [0, r_0] \\ q\big|_{t=0} = r_0 \end{cases} \quad (1)$$

f) Hardening rule $\dot{q} = H^d(r)\ \dot{r};\ H^d(r) = q^{'}(r) \leq 0$

g) Loading-unloading conditions $f < 0;\ \gamma \geq 0;\quad \gamma f = 0;\quad \gamma \dot{f} = 0$ (consistency)

where Ψ is the free energy density, ε is the strain tensor, **σ** is the stress tensor and **C** is the elastic tensor. The damage variable, *d*, is defined in terms of hardening/softening variable *q*, which is dependent on the hardening/softening parameter, *H*. The damage multiplier γ determine the loading-unloading condition, the function, $f(\tau_\sigma, q)$, bounds the elastic domain defining the damage surface in the stress space. The value, r_o, is the threshold that determines the limit of the initial elastic domain, i.e, $q = r_o$. In this damage surface, any stress state is transformed to a norm, bounded by r_o, where every stress state outside of this surface is inelastic as shown in **Figure 2**.

The tangent constitutive equation, in terms of rates, from the model in Equation (1) is:

$$\dot{\sigma} = \mathbf{C}^T :\ \dot{\varepsilon} \quad (2)$$

Where $\mathbf{C}^T$ is the continuum tangent constitutive operator, relating the stress and the strains rates, of the non-linear loading interval, which is defined by

$$\mathbf{C}^T = (1 - d)\mathbf{C} - \frac{q - H_r}{r^3}\chi^2(\mathbf{C} : \varepsilon \otimes \varepsilon : \mathbf{C}) \quad (3)$$

and for the elastic loading and unloading interval ($\dot{d} = 0$):

$$C^T = \left(1 - d\right)\ C \quad (4)$$

The parameter χ in Equation (3)

$$\chi = \phi + \left(\frac{1 - \phi}{n}\right) \quad (5)$$

where φ a is weight factor, depending on the principal stresses, σ_i, given by:

$$\phi = \frac{\sum_{i=1}^{3} \langle \sigma_i \rangle}{\sum_{i=1}^{3} |\sigma_i|} \quad (6)$$

where the Maclauy operator $< >$ and the symbol $||$ consider, respectively, the positive and the absolute magnitudes of the principal stresses. The interval of ϕ is [*0,1*], bounded by *0* for a triaxial compression ($\sigma_3 \leq \sigma_2 \leq \sigma_1 \leq 0$) and *1* for triaxial tension ($0 \leq \sigma_3 \leq \sigma_2 \leq \sigma_1$). Consequently, the corresponding interval of χ is [*1/n,1*], bounded by *1/n* for a triaxial compression and 1 for triaxial tension.

The parameter χ scales down *1/n* times the norm, as shown in **Figure 2**, in such a way it is compared with the elastic interval [*0,* r_o]. The value of $r_o = \sigma_{ut}/\sqrt{E}$ depends on the threshold value of σ_{ut} and the Young's modulus *E*. Note that the initial elastic interval is the same for 1D, 2D, and 3D problems, all with a limit point r_o, and that for a 2D principal stress state, the parameter χ takes the value of *1* in the first quadrant, *1/n* in the third quadrant and the interval [*1/n,1*] in the second and fourth quadrants.

The non-linear analyses were carried out with the software FEAP. The concrete was modeled with hexahedral elements, using the constitutive continuous damage model with different threshold value in tension and compression. The

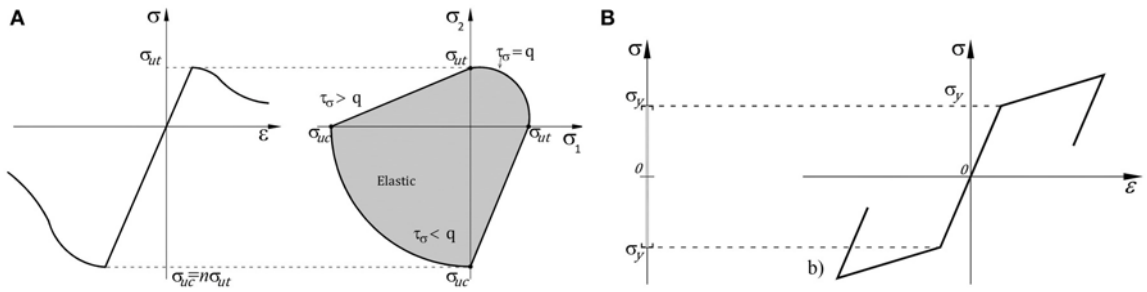

FIGURE 1 | Constitutive behavior of **(A)** plain concrete and **(B)** steel reinforcement (adapted from Juárez-Luna et al., 2014).

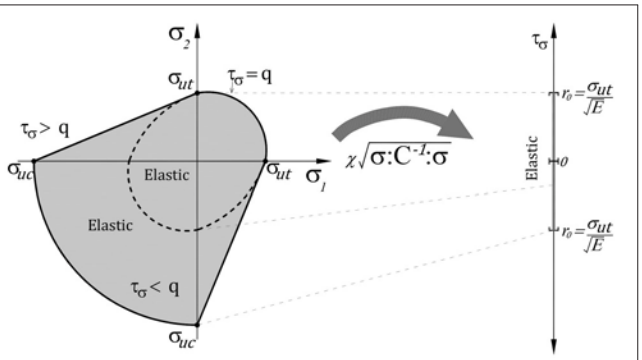

FIGURE 2 | Transformation of the stresses to a norm. (adapted from Juárez-Luna et al., 2014).

steel reinforcement was modeled with the one-dimensional bar element, which was assigned with a 1D constitutive rate independent plasticity model. Both elements have three degree of freedom per node and large deformations. The 1D elements were placed along the edges of the solid elements and joined at the same nodes to guarantee continuity. In the presented examples hereafter, modeled with bar and solid elements, perfect bond between both elements was considered.

VALIDATION

One of the six specimens tested by Girolami et al. (1970) was modeled to validate the constitutive models of concrete and steel reinforcement. The test slab was 1.829 m square and 0.044 m deep, as shown in **Figure 3A**. Vertical loads were applied on the top surface through 16 plates, which were 0.2038 m square and 0.0254 m thick, as shown in **Figure 3B**. Additionally, eight loads were applied at cantilever extensions of the beams to maintain a certain amount of restraint at the corners. The mechanical properties of the concrete are: Young's modulus $E_c = 19.90\ GPa$ and ultimate compressive strength $\sigma_{uc} = 31.026\ MPa$. The mechanical properties of the steel reinforcement are: Young's modulus $E_a = 206\ GPa$, Poisson ratio $\upsilon = 0.3$, yield stress $\sigma_y = 330.95\ MPa$ and hardening modulus $H = 2.871\ GPa$.

The steel reinforcement was placed at top and at the bottom of the slab to support a uniform design load of 7.182 kPa. The top and bottom reinforcement used in the slab consisted of 3.66 mm diameter steel bars cut from No.7 gage wire, which were spaced 10.954 cm in both orthogonal directions, as shown in **Figure 3C**. Also, the stirrups were bent from the No.7 gage steel wire as shown in **Figure 3D**. The edge beams have over-reinforced bars because other five of six specimens tested by Girolami et al. (1970) were also loaded in-plane, in addition to vertical load, perpendicular to the surface slab; the reason of the shear reinforcing in the beams is to avoid damage and to transfer the loads to the slab.

The slab geometry and the load have two axes of symmetry, so only a quarter of the slab specimen was modeled, which saves computational cost in the non-linear analysis. In the model, the degrees of freedom perpendicular to the respectively axis of symmetry were restrained. The slab was modeled with two kinds of element, the steel reinforcement was modeled with bar elements as shown in **Figure 4A**; whereas the plain concrete was modeled with hexahedral solid elements as shown in **Figure 4B**.

The experimental and numerical load-displacement curves at the midspan of the slab are compared, as shown in **Figure 5**. It is seen that both curves in the a-b trajectory are the same; however, in the b-c trajectory a backward motion in the experimental displacement curve was reported, attributed to the loads applied at the ends of the beams to provide restraint. Finally, both curves have the same path in the trajectory d-e. On the other hand, the cracking grown is shown in **Figure 6**, where cracks started at the corner on the top of the slab. Subsequently, cracking propagates overall the edges to the center, which is in agreement with the experimental results reported by Girolami et al. (1970). This example was also modeled with finite elements with embedded discontinuities by Juárez-Luna et al. (2015), where damage is localized on a surface discontinuity placed at the geometrical center of a solid element.

RESULTS

Linear Elastic Analyses for Steel Reinforcement Distribution

The computed moments of circular, elliptic and triangular slabs were carried out with linear elastic analyses using plate finite elements, as shown respectively in **Figure 7**. In these models, the reinforced concrete was modeled as an isotropic material with a Young's modulus of $E = 21.673\ GPa$ and Poisson's

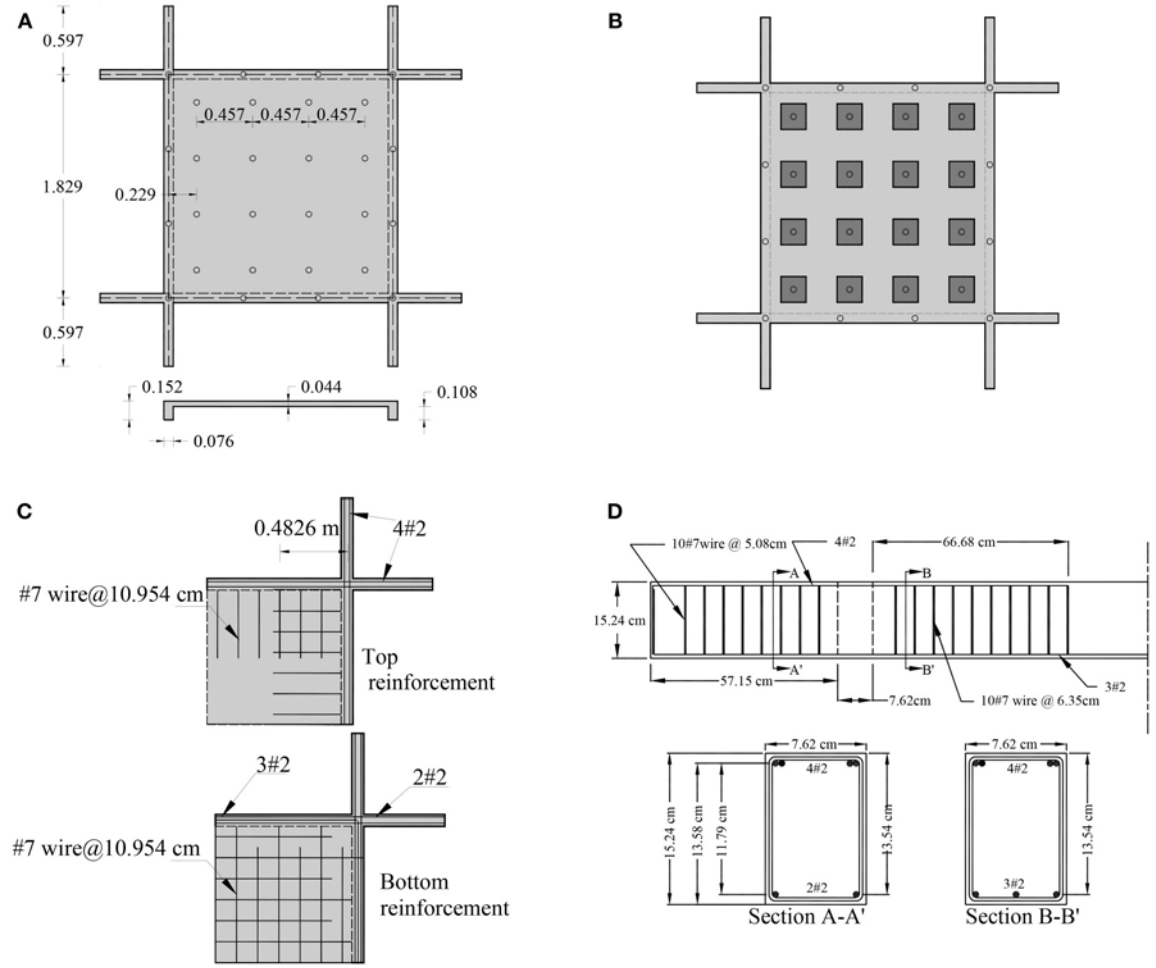

FIGURE 3 | Experimental test: **(A)** geometry in cm, **(B)** applied loads, **(C)** reinforcement of one quarter of the slab and **(D)** reinforcement of one half of a beam (adapted from Girolami et al., 1970).

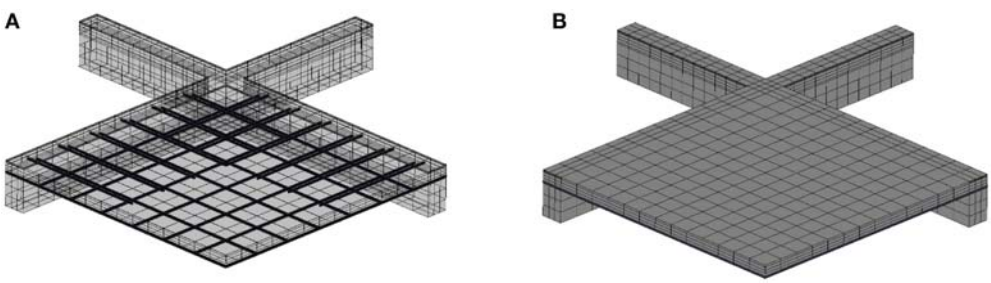

FIGURE 4 | Meshing: **(A)** steel reinforcement and **(B)** reinforced concrete.

ratio $\nu = 0.25$. In the analyses of these models, only clamped supports were considered, yielding negative moments at the edges and positive moments at the center; simple support slabs were not analyzed because this condition provides only positive moments, which needs only steel reinforcement at the bottom of the slab.

Flexural moments in the circular geometry was computed from a slab modeled with quadrilateral plate elements, avoiding triangular elements at the center of the model, which could generate numerical instability for the large element aspect ratio. According to **Figure 7A**, negative moments occurred from the edge to the dotted line, in an external ring with an approximated

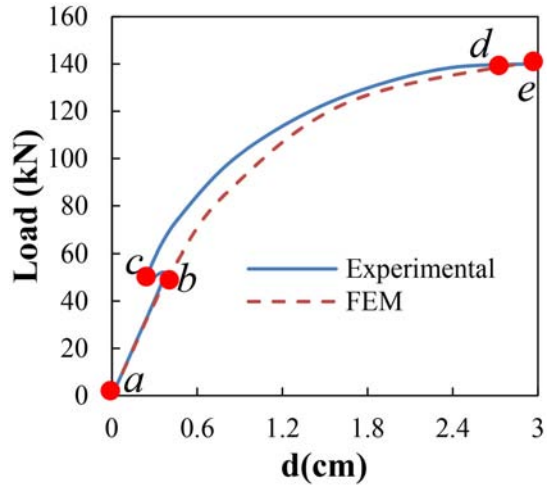

FIGURE 5 | Load vs. displacement curves.

width of one quarter of the diameter, i.e., $L_{neg} = d/4$. This length, where negative moments occurs, is analogous to the width of the external band in rectangular slabs, where the steel reinforcement is mainly placed at the top. The steel reinforcement layout was proposed as shown in **Figure 8A**, where the steel reinforcement is placed at top and bottom faces for negative and positive moments, respectively.

Flexural moments in elliptic slabs were computed from numerical models with ratio of minor axis to major axis, b/a, equal to 0.5, 0.6, 0.7, 0.8, and 0.9, respectively, but the major axis length was kept constant, $a = 4$ m. Quadrilateral plate elements were used for modeling the elliptic slab. According to the moment distribution in **Figures 7B,C**, the negative moment zones were identified from the edge to the center, having a length of $l_{neg} = a/3$ for the major axis and a length of $l_{neg} = b/3$ for the minor axis. A typical the steel reinforcement layout was proposed as shown in **Figure 8B**, in which the central zone has steel reinforcement only at the bottom, but at the edges, there is steel reinforcement at the top and at the bottom of the slab.

Flexural moments in the triangular geometry were computed from a slab modeled with quadrilateral plate elements, which has a height $h = 4$ m and base $2h/\sqrt{3}$. **Figures 7D,E** shows the lengths, which mark out the zones of negative moment at both directions: horizontal with a length of $h/3$ and vertical with a length $h/7$ at the bottom and $h/2$ at the top. The proposed steel reinforcement layout is shown in **Figure 8C**, in which the central zone has steel reinforcement only at the bottom, but at the edges, there is steel reinforcement at the top and bottom of the slab.

Non-linear Analyses

In the non-linear analyses of the slabs with FEAP, 3D solid elements were used for modeling the concrete, which has the following mechanical properties: Young's modulus $E_c = 17$ GPa, Poisson ratio $\nu = 0.20$, ultimate tensile strength $\sigma_{ut} = 5$ MPa and an ultimate compressive strength $\sigma_{uc} = 25$ MPa. The steel reinforcement has the following mechanical properties: Young's modulus of $E_a = 2.05 \times 10^5$ MPa, Poisson's ratio of $\nu = 0.30$ and yield strength $\sigma_y = 410$ MPa. Top and bottom steel reinforcement have 0.025 m of covering. The models were analyzed under two support conditions at the edges: simply supported and clamped, loaded on the surface under distributed load increments. To save computational cost in the analyses, only a quarter of the slabs were modeled, considering the two symmetry axes. The load-displacement curves computed with FEAP are compared with the curves computed in the software ANSYS (2010) reported by Juárez-Luna and Caballero-Garatachea (2014).

In the non-linear analysis of the circular slab, a model with diameter $d = 4$ m was carried out. The slab was reinforced with number 3 bars, which were spaced 0.20 m in both orthogonal directions. The steel reinforcement meshing was embedded into the solid elements as shown in **Figure 9A**, where the nodes of both kinds of elements were joined. **Figure 10** shows the load-displacement curves at the center of the span, where distributed loads of 17 and 98 kPa were needed on the slabs with simple and clamped supports, respectively, to reach a displacement of 5 cm.

The non-linear analyses of elliptic slabs were carried out considering minor axis to major axis ratios $b/a = 0.5$, 0.6, 0.7, 0.8, and 0.9. The steel reinforcement consisted of 3/8 in diameter steel bars placed at the top and at the bottom, which were spaced 0.20 m in both orthogonal directions. The steel reinforcement was modeled with bar elements. The meshing of both concrete and the embedded steel reinforcement is shown in **Figure 9B**, which were joined at the nodes. The distributed load-displacement at the center of the span curves is shown in **Figure 11**, where it is observed that the needed loading to develop a displacement at the center of the span is in inverse proportion to the ratio, b/a, for both support conditions. Furthermore, it is observed that the applied distributed load magnitude in the simple supported slab is ∼20% of the distributed load magnitude in the clamped supported slab to reach the same displacement.

Concerning to the non-linear analysis of the triangular slab, the steel reinforcement consisted of bar size of number 3 placed at the top and at the bottom and spaced 0.20 m in both orthogonal directions, which was modeled with bar elements. The concrete meshing with the embedded steel reinforcement is shown in **Figure 9C**. Taking advantage of the symmetry, only one half of the model was analyzed. The distributed load *vs.* displacement at the center of the span curves are shown in **Figure 12**, where it is observed again that the support conditions have influence in the global behavior, in such a way that the simple supported triangular slab only needs ∼20% of the distributed load in the clamped supported slab to reach the same displacement at the center.

Cracking Paths

Cracking paths are important to identify the tension stress concentration zones, which qualitatively point out the zone where the steel reinforcement must be placed. In this paper, cracking was modeled with a damage model, associated to a stresses state at the Gaussian integration points of each element, where the material reaches a failure surface. Therefore, large displacements and as consequence, strain concentration are observed where the material is damaged. In this section,

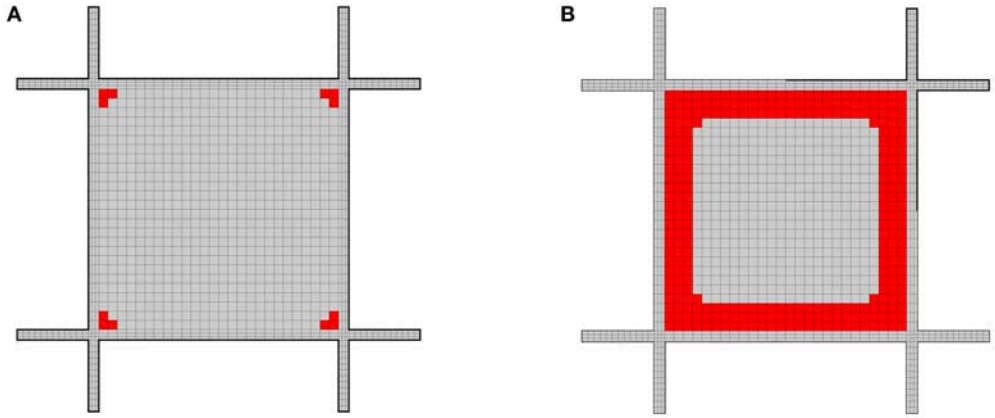

FIGURE 6 | Cracking propagation on the top surface at the: **(A)** beginning and **(B)** end.

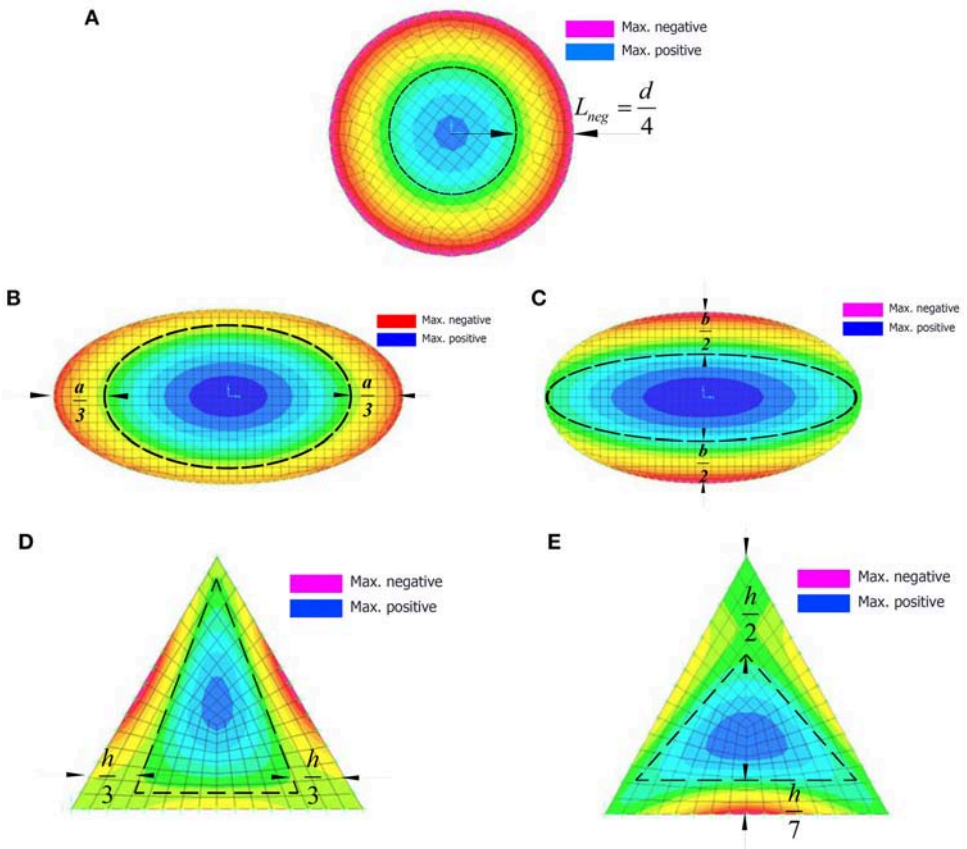

FIGURE 7 | Moment distribution in: **(A)** circular slab, **(B)** elliptic slab along horizontal strip **(C)** elliptic slab along vertical strip, **(D)** triangular slab along horizontal strip, and **(E)** triangular slab along vertical strip.

the bottom and top surfaces of the slabs show those zones where the integration points are damaged. The cracking zones caused by tension stresses are shown in red color, but crashing zones, dominated by compressive stresses, are shown in blue color.

In the clamped circular reinforced concrete slabs, cracking started along the edges on the top surface because of his axisymmetric characteristic, as shown in **Figure 13A**. Then, cracking occurs at the center of the slab on the bottom surface, see **Figure 13B**. After that, cracking grows

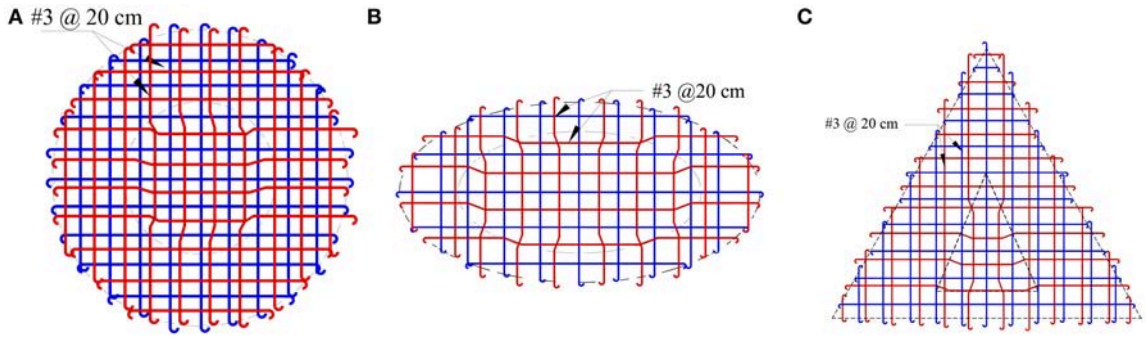

FIGURE 8 | Steel reinforcement layout in: **(A)** circular slab, **(B)** elliptic slab, and **(C)** triangular slab.

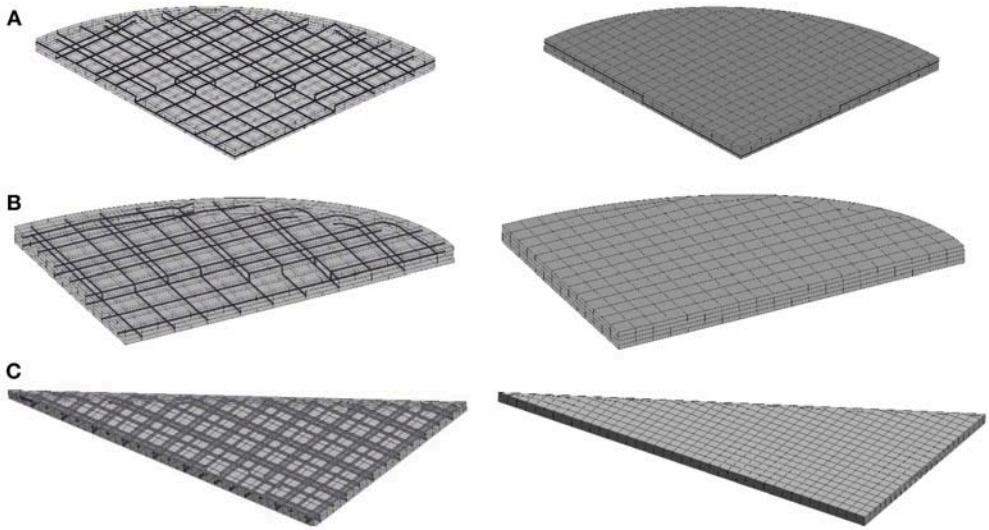

FIGURE 9 | Finite element meshing of steel reinforcement and plain concrete of: **(A)** circular slab, **(B)** elliptic slab, and **(C)** triangular slab.

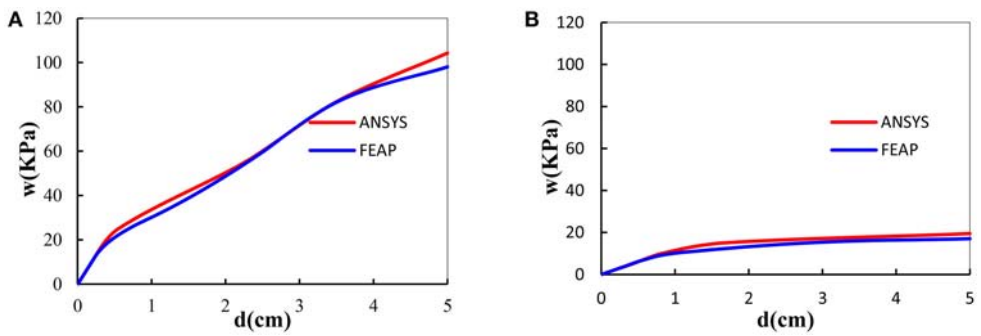

FIGURE 10 | Load vs. displacement curve at the midspan of circular slab: **(A)** clamped and **(B)** simple supported.

from the edges to the center and crushing occurs at the center on the top surface, while at the bottom surface, cracking grows from the central zone to the edges. On the other hand, in the simply supported circular slabs, cracking starts at the central zone on the bottom surface and it propagates to the edges as shown in **Figure 13D**. On the top surface, neither cracking nor crushing occurs as shown in **Figure 13C**.

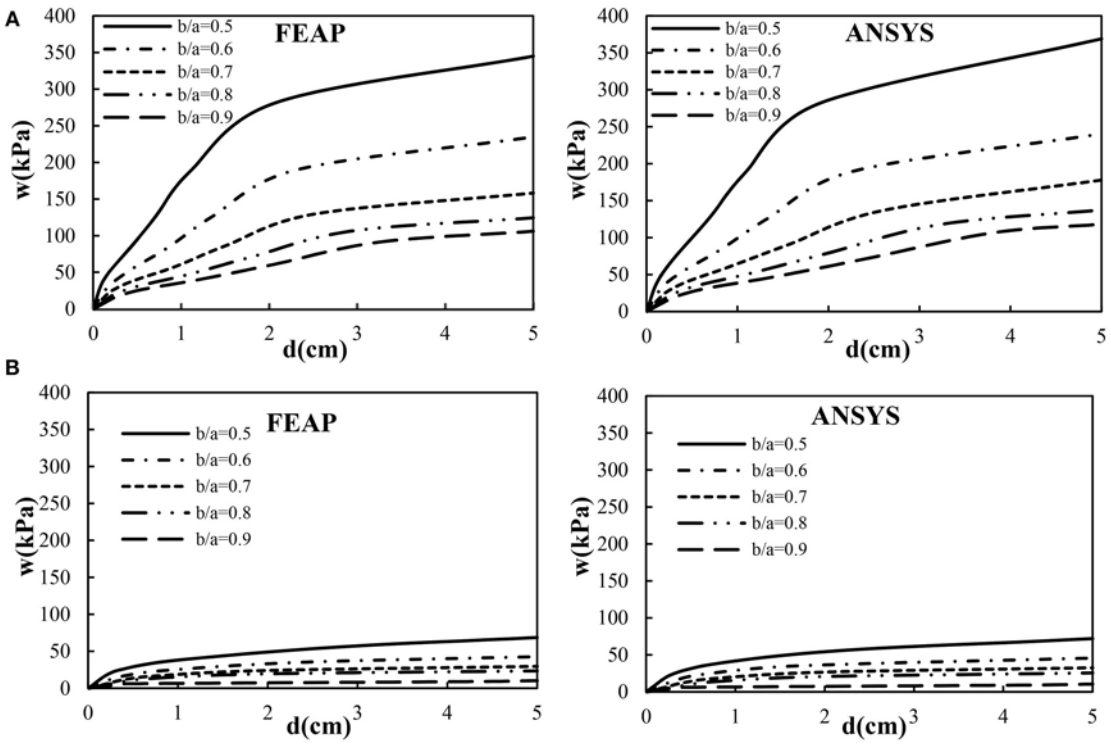

FIGURE 11 | Load vs. displacement curves at the midspan of elliptic slab: **(A)** clamped and **(B)** simple supported.

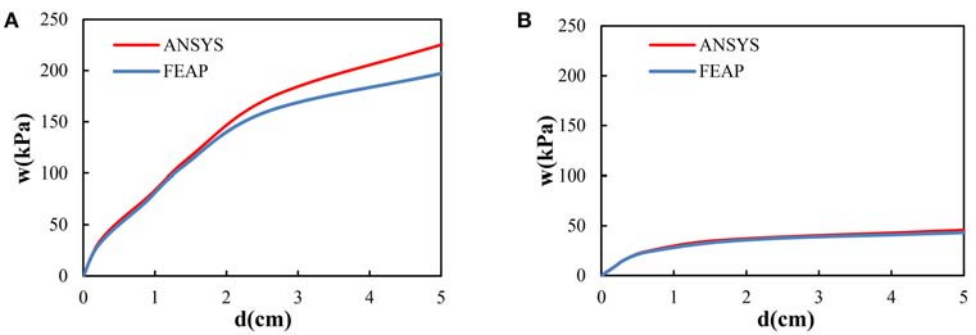

FIGURE 12 | Load vs. displacement curve at the midspan of triangular slab with $a = 4$ m: **(A)** clamped and **(B)** simple supported.

In the reinforced concrete clamped elliptic slab, cracking starts along the edges on the top surface, which are approximately perpendicular to the major axis, as shown in **Figure 14A**. Then, cracking occurs at center of the slab on the bottom surface, see **Figure 14B**. On the top surface, cracking propagation is analogous to the circular slab, since it grows from the edges to the central zone; however, at the center, crushing occurs, but on the bottom surface, cracking grows from the central zone to the edges. In the reinforced concrete simple supported elliptic slab, cracking starts on the bottom surface, as shown in **Figure 14D**. Then, it propagates from the central zone to the edges. On the top surface, neither cracking nor crushing occurs as shown in **Figure 14C**.

In the reinforced concrete clamped triangular slab, cracking starts along the three edges on the top surface, as shown in **Figure 15A**, where tension stresses are developed. Then, cracking occurs on the bottom surface at the central zone, as shown in **Figure 15B**. On the top surface, cracking propagation starts from the center of the edges to the vertexes, but on the bottom surface, it propagates from the central zone to the vertexes. On the contrary, in the reinforce concrete simple supported triangular slab, cracking starts on the bottom surface in the central zone and it propagates to the vertexes as shown in **Figure 15D**. At the same time, cracking occurs on the top surface as shown in **Figure 15C**.

In general, in reinforce concrete clamped slabs, cracking starts along the edges on the top surface. Then, it occurs at center of

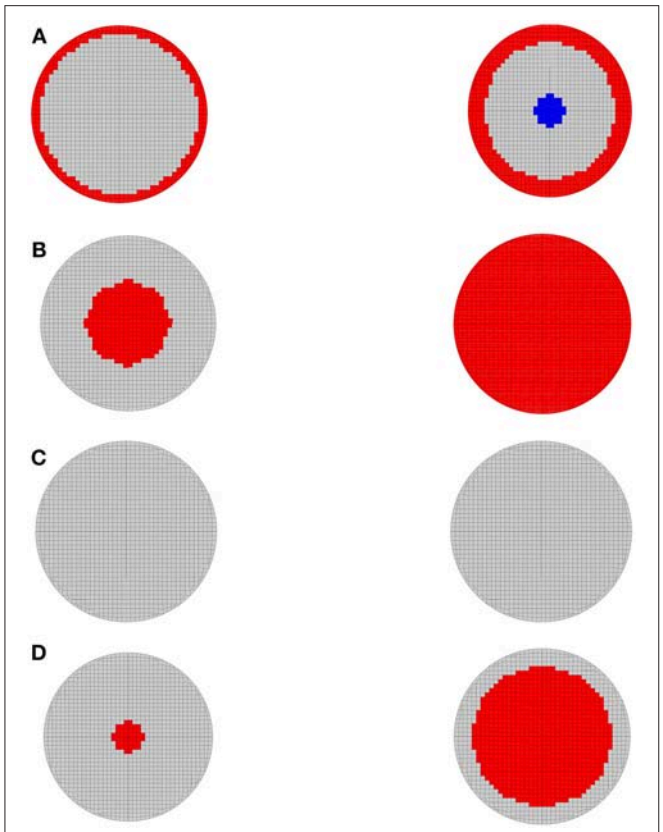

FIGURE 13 | Cracking propagation of a circular slab on the: **(A)** top-clamped, **(B)** bottom-clamped, **(C)** top-simple supported, and **(D)** bottom-simple supported.

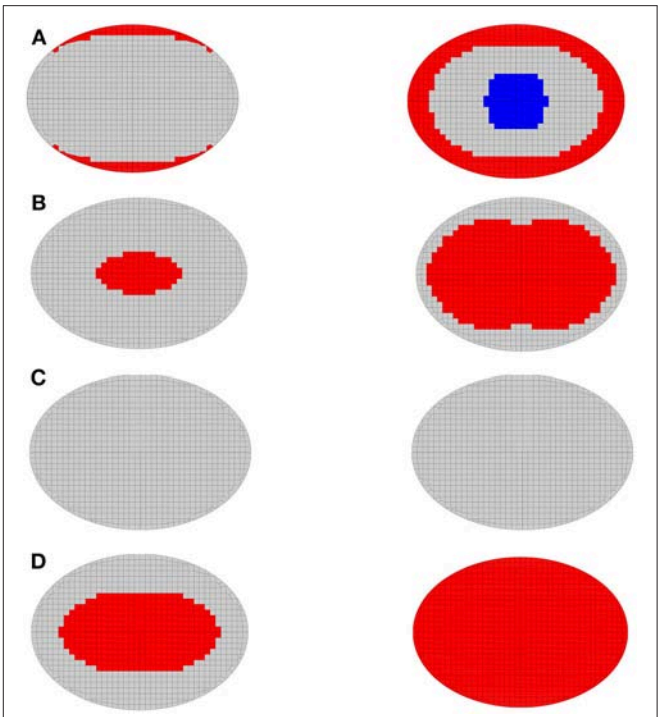

FIGURE 14 | Cracking propagation of an elliptic slab on the: **(A)** top-clamped, **(B)** bottom-clamped, **(C)** top-simple supported, and **(D)** bottom-simple supported.

the slab on the bottom surface. On the other hand, in reinforced concrete simple supported slabs, cracking occurs on the bottom surface in the central zone and it propagates to the overall surface. After that, an incipient cracking occurs at the central zone on the top surface. The fact that cracking is larger than crushing in the slab is due to the stress re-distributions and to the ultimate tensile strength, which varies from 5 to 20% of the ultimate compressive strength.

DESIGN RECOMMENDATIONS

The steel reinforcement layout for circular, elliptic and triangular slabs is proposed as shown in **Figures 7**, **8**, respectively. Top and bottom reinforcement is placed outside of the dotted line for negative moments, but only bottom reinforcement is placed inside of the dotted line for positive moments.

In this paper, the coefficient method is proposed for its simplicity to calculate design bending moments in slabs. This method to design two-way slabs supported on all sides by walls and deep beams was included in the ACI-318-63 (1963) code. The coefficient method uses a moment coefficient table for a variety of types of panels. In the coefficient method, moments for the middle strips of the slab are computed by the general formula:

$$M = \alpha w a_1^2 \tag{7}$$

where M is the design moment at the critical section considered, w is the total uniform load per square meter acting on the panel and a_1 is the short span length. The slabs meshed with solid and bar elements provided stresses at the nodes; however, the design of reinforced concrete slabs is based on moments per unit width, so moments were computed by integrating the stress function along eight elements of the overall thickness, using a linear interpolation, as shown in **Supplementary Figure 1**.

In **Supplementary Tables 1–3**, design coefficients are given for circular, elliptic and triangular geometry, respectively. These coefficients must be multiplied by $10^{-4}\ wl^2$ to obtain the flexural design moments per unit width. l is the reference length (r, b, and h for circular, elliptic and triangular slabs, respectively). Two types of construction were considered: case I, slabs built monolithically with their supports and case II, slabs not built monolithically with their supports. In the last one, negative coefficients have zero values at the edges because there are only positive moments in the slab due to the support condition. These coefficients are negative in the edges of the three geometries, but they are positive in the centre of three geometries and in point B of the triangular geometry, as shown in **Supplementary Figure 2**. The variations of the computed coefficients in the circular, elliptic and triangular slabs are shown in **Supplementary Figures 3–9**. The variations of their magnitudes are attributed to cracking in concrete and to hardening in steel reinforcement in the nonlinear range at the zones with maximum stresses of the slabs.

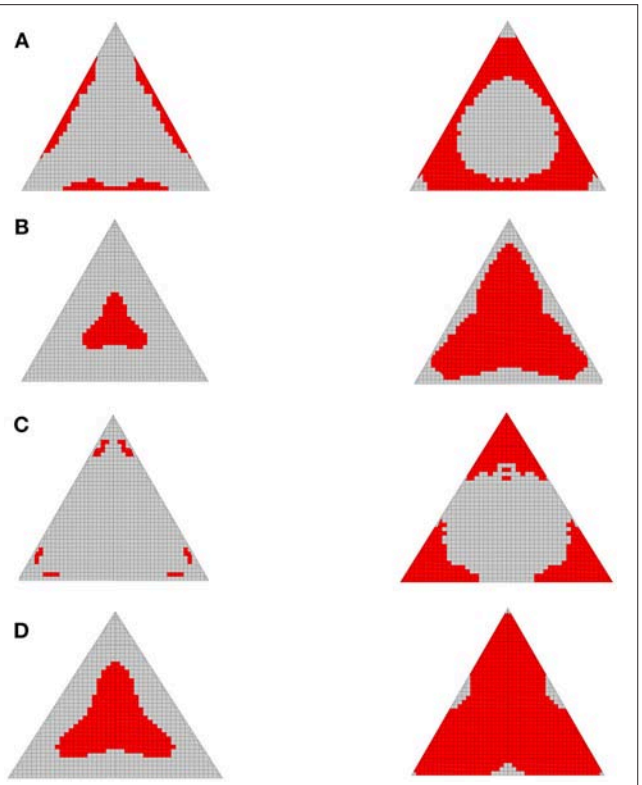

FIGURE 15 | Cracking propagation of a triangular slab on the: **(A)** top-clamped, **(B)** bottom-clamped, **(C)** top-simple supported, and **(D)** bottom-simple supported.

CONCLUSIONS

The load-displacement curves of the numerical and the experimental test reported from literature, respectively, showed a good agreement. Nevertheless, a backward motion in the experimental displacement was reported, attributed to the loads applied at the ends of the beams to provide restraint.

The yielding line method was not considered in the calculation of cracking paths or ultimate load because this method provides only values of the ultimate load, but it does not provide the cracking paths. Moreover, the aforementioned ultimate load can be greater or smaller than the ultimate load. Therefore, the computational mechanics was used because it provides the starting and the growing of damage.

The steel reinforcement layout in each slab, based on linear elastic analyses of homogenous plate elements, was adequate because there was a good approximation in the moment distribution as well as in the location and initiation of cracking in the slabs. The lengths of the steel reinforcement (positive and negative) are recommended to the design and construction of slabs with the geometries presented in this paper.

The load-displacement curves at the central zone of the slabs with the three studied geometries show that the distributed loading in the simply supported slabs was ∼20% of the distributed loading in the clamped slabs with the same displacement. The load-displacement curves computed with FEAP show good agreement with those curves computed with ANSYS (2010) byJuárez-Luna and Caballero-Garatachea (2014).

The coefficient method is proposed for its simplicity to calculate design bending moments in circular, elliptic and triangular slabs, respectively. These coefficients are tabulated, considering two types of construction: case I, slabs built monolithically with their supports and case II, slabs not built monolithically with their supports.

In general, cracking in clamped slabs occurs at the edges on the bottom surface; subsequently, it is propagated from the central zone to the edges. On the other hand, in the simply supported slabs, cracking occurs in the central zone on the bottom surface and it is propagated to the edges.

In general, the study of these complex slabs under vertical loading by computer simulations does not substitute experimental results, but it provides reasonably good approximations.

AUTHOR CONTRIBUTIONS

GJ-L and OC-G contributed to the conception and idea of the paper. The analyses of the slab models were carried out in the software FEAP by GJ-L and in the software ANSYS by OC-G. Both authors contributed to organize, read, review, and approve the submitted version.

ACKNOWLEDGMENTS

The authors acknowledge the support given by the Universidad Autonoma Metropolitana. The second author acknowledges the scholarship for his Master's studies given by CONACYT.

SUPPLEMENTARY MATERIAL

The Supplementary Material for this article can be found online at: https://www.frontiersin.org/articles/10.3389/fbuil.2019.00009/full#supplementary-material

REFERENCES

ACI-318-63. (1963). *Building Code Requirements for Structural Concrete and Commentary*. Farmington Hills, MI: American Concrete Institute.

ANSYS. (2010). *ANSYS User's Manual Version 13.0*. Canonsburg, PA: ANSYS, Inc.

CSI (2009). *SAP2000 Advanced 12.0.0*. Berkeley, CA: Computers and Structures. Inc.

de Borst, R., and Nauta, P. (1985). Non-orthogonal cracks in a smeared finite element model. *Eng. Comput.* 2, 35–46. doi: 10.1108/eb023599

Genikomsou, A. S., and Polak, M. A. (2015). Finite element analysis of punching shear of concrete slabs using damaged plasticity model in ABAQUS. *Eng. Struct.* 98, 38–48. doi: 10.1016/j.engstruct.2015.04.016

Genikomsou, A. S., and Polak, M. A. (2017). 3D finite element investigation of the compressive membrane action effect in reinforced concrete

at slabs. *Eng. Struct.* 136, 233–244. doi: 10.1016/j.engstruct.2017.01.024

Gilbert, R. I., and Warner, R. F. (1978). Tension stiffening in reinforced concrete slabs. *J. Struct. Div. ASCE* 104, 1885–1900.

Girolami, A. G., Sozen, M. A., and Gamble, W. L., (1970). *Flexural Strength of Reinforced Concrete Slabs With Externally Applied In-plane Forces.* Civil Engineering Department, University of Illinois, 176.

Hand, F. D., Pecknold, D. A., and Schnobrich, W. C. (1973). Nonlinear analysis of reinforced concrete plates and shells. *J. Struct. Div. ASCE* 99, 1491–1505.

Hinton, E., Abdel Rahman, H. H., and Zienkiewicz, O. C. (1981). *Computational Strategies for Reinforced Concrete Slab Systems.* International Association of Bridge and Structural Engineering, Colloquium on Advanced Mechanics of Reinforced Concrete, 303–313.

Jofriet, J. C., and McNeice, G. M. (1971). Finite element analysis of RC slabs, *J. Struct. Div. ASCE.* 97, 785–806.

Juárez-Luna, G., and Caballero-Garatachea, O. (2014). Determinación de coeficientes de diseño y trayectorias de agrietamiento de losas aisladas circulares, elípticas y triangulares. *Ing. Invest. Tecnol.* 15, 103–123. doi: 10.1016/S1405-7743(15)30010-X

Juárez-Luna, G., Méndez-Martinez, H., and Ruiz-Sandoval, M. E. (2014). An isotropic damage model to simulate collapse in reinforced concrete elements. *Lat. Am. J. Solids Struct.* 11, 2444–2459. doi: 10.1590/S1679-78252014001300007

Juárez-Luna, G., Tena-Colunga, A., and Ayala, G. A. (2015). Computational modelling of RC slabs fracture with an embedded discontinuity formulation. *Lat. Am. J. Solids Struct.* 12, 2539–2561. doi: 10.1590/1679-78251890

Kupfer, H. B., and Gerstle, K. H. (1973). Behavior of concrete under biaxial stresses. *J. Eng. Mech. ASCE* 99, 853–866.

Kwak, H. G., and Filippou, F. C. (1990). *Finite Element Analysis of Reinforced Concrete Structures Under Monotonic Loads*, Department of Civil Engineering, University of California, Berkeley, CA, p. 124.

Lin, C. S., and Scordelis, A. C. (1975). Nonlinear analysis of RC shells of general form. *J. Struct. Div. ASCE* 101, 523–238.

Linero, D. L. (2006). *Un Modelo del Fallo Material en el Hormigón Armado, Mediante la Metodología de Discontinuidades Fuertes de Conti-nuo y la teoría de Mezclas*. Dissertation, Escola Tècnica Superior d'Enginyers de Camins, Canals i Ports, Universidad Politécnica de Cata-luña.

McNeice, A. M. (1967). *Elastic-Plastic Bending of Plates and Slabs by the Finite Element Method*. Dissertation, London University.

Navarro, M., Ivorra, S., and Varona, F. B. (2018). Parametric computational analysis for punching shear in RC slabs. *Eng. Struct.* 165, 254–263. doi: 10.1016/j.engstruct.2018.03.035

NTCC-17. (2017). *Normas Técnicas Complementarias para Diseño de Estructuras de Concreto*. Gaceta Oficial del Distrito Federal.

Oliver, J., Cervera, M., Oller, S., and Lubliner, J. (1990). "Isotropic damage models and smeared crack analysis of concrete," in *SCI-C Computer Aided Analysis and Design of Concrete Structures*, eds N. Bićanć, and H. Mang (Swansea: Pineridge Press), 945–957.

Plevris, V., and Tsiatas, G. C. (2018). Computational structural engineering: past achievements and future challenges. *Front. Built Environ.* 4:21. doi: 10.3389/fbuil.2018.00021

Shu, J., Fall, D., Plos, M., Zandi, K., and Lundgren, K. (2015). Development of modelling strategies for two-way RC slabs. *Eng. Struct.* 101, 439–449. doi: 10.1016/j.engstruct.2015.07.003

Taylor, L. R. (2008). *A Finite Element Analysis Program (FEAP) v8.2*. Department of Civil and Environmental Engineering, University of California at Berkeley, Berkeley, CA.

Wang, Y., Dong, Y., and Zhou, G. (2013). Nonlinear numerical modeling of two-way reinforced concrete slabs subjected to fire. *Comput. Struct.* 119, 23–36. doi: 10.1016/j.compstruc.2012.12.029

Wosatko, A., Pamin, J., and Polak, M. A. (2015). Application of damage–plasticity models in finite element analysis of punching shear. *Comput. Struct.* 151, 73–85. doi: 10.1016/j.compstruc.2015.01.008

Conflict of Interest Statement: The authors declare that the research was conducted in the absence of any commercial or financial relationships that could be construed as a potential conflict of interest.

frontiers in Built Environment

ORIGINAL RESEARCH
published: 28 February 2019
doi: 10.3389/fbuil.2018.00083

Efficient Static Analysis of Assemblies of Beam-Columns Subjected to Continuous Loadings Available as Digitized Records

Aram Soroushian[1]* *and Emadoddin Majdabadi Farahani*[2]

[1] Structural Engineering Research Center, International Institute of Earthquake Engineering and Seismology, Tehran, Iran,
[2] School of Civil Engineering, College of Engineering, University of Tehran, Tehran, Iran

OPEN ACCESS

Edited by:
Nikos D. Lagaros,
National Technical University of Athens, Greece

Reviewed by:
Andreas Kampitsis,
Imperial College London, United Kingdom
Maria E. Stavroulaki,
Technical University of Crete, Greece

***Correspondence:**
Aram Soroushian
a.soroushian@iiees.ac.ir;
aramsoro@yahoo.com

Specialty section:
This article was submitted to Computational Methods in Structural Engineering, a section of the journal Frontiers in Built Environment

Received: *12 October 2018*
Accepted: *17 December 2018*
Published: *28 February 2019*

Citation:
Soroushian A and Farahani EM (2019) Efficient Static Analysis of Assemblies of Beam-Columns Subjected to Continuous Loadings Available as Digitized Records. Front. Built Environ. 4:83. doi: 10.3389/fbuil.2018.00083

Beams, beam-columns, columns, and frames, are of major importance in structural engineering, and especially buildings and infrastructures analysis and design. In some cases, these structural members are subjected to static loadings, that though are continuous with respect to the longitudinal axes, are available as digitized records. Finite element analysis of assemblies of these members may be computationally expensive when the loading is digitized densely. In order to reduce this computational effort, attention is paid to a technique originally proposed in 2008 for reduction of the computational effort in time integration analysis. In view of the convergence-based nature of this technique, in this paper, the technique is adapted to static analysis of assemblies of beam-columns subjected to digitized loadings. The good performance of the adapted technique is demonstrated from different points of view, and is compared with the performance of the technique in time integration analysis.

Keywords: accuracy, computational effort, finite elements, static analysis, beam-columns, digitized loading

INTRODUCTION

Structural systems are getting larger and behave more complicatedly day by day. Accordingly, efficient analysis of structural systems is an important concern, in areas such as optimum structural design, time history analysis, and structural control. In addition, when the structural analysis is more efficient, the pre-processing and post-processing stages may become simpler and lead to easier interpretation of the results. Some different model reduction methods are reviewed in (Besselink et al., 2013). The objective of this paper is to extend the application area of a technique proposed for more efficient time integration analysis (Soroushian, 2008) by adapting the technique to static analysis of assemblies of beam-columns (the final goal of the research, including the presentation in this paper, is to put together reductions based on the above technique in time and space).

After discretization in space, the dynamic behavior of many structural systems can be expressed as the initial value problem below (Henrych, 1990; Argyris and Mlejnek, 1991; Bathe, 1996; Belytschko et al., 2000):

$$\begin{aligned} &\mathbf{M}\ddot{\mathbf{u}} + \mathbf{f}_{\text{int}} = \mathbf{f}(t) \quad 0 \le t \le t_{\text{end}} \\ &\mathbf{u}(t=0) = \mathbf{u}_0 \\ &\dot{\mathbf{u}}(t=0) = \dot{\mathbf{u}}_0 \\ &\mathbf{f}_{\text{int}}(t=0) = \mathbf{f}_{\text{int}_0} \\ &\mathbf{Q} \le \bar{\mathbf{O}} \end{aligned} \tag{1}$$

In Equation (1), $\mathbf{M}$ is the mass matrix, $\mathbf{f}_{\text{int}}$ stands for the vector of internal forces, $\mathbf{f}(t)$ implies the external force, $\mathbf{Q}$ represents restrictions because of non-linearity, e.g., impact and elastoplastic behavior (Hughes et al., 1979; Wriggers, 2002), t, standing for the time, is the independent variable of the initial value problem, $\mathbf{u}$ is the displacement vector, each top dot implies once differentiation with respect to time, "0," as the right subscript, indicates that the argument is at its initial value, t_{end} is the total length of the time interval, and $\bar{\mathbf{O}}$ stands for a zero vector or matrix. The vector $\mathbf{f}(t)$ might be composed of components continuous in time, but available as digitized records (see **Figure 1**, where ${}_f\Delta t$ stands for the digitization step). For these cases, a technique was proposed by Soroushian (2008) to enlarge the digitization step, such that the analysis efficiency is enhanced and the analysis accuracy is practically unchanged. The technique has been implemented in analysis of different structural systems against different earthquakes by different time integration methods, considering linear and non-linear behavior, and near- and far-field earthquakes. The results evidence the good performance of the technique. Three significant applications are reviewed in **Table 1** (Nateghi and Yakhchalian, 2011; Sabzei, 2013; Bastami, 2014; Garakaninezhad and Moghadas, 2015; Hadad, 2015; Soroushian et al., 2016; Zarabimanesh, 2017; Baiani, 2018; Ghondaghsaz, 2018). In view of the convergence-based mathematics of the technique (Soroushian, 2008), it seems applicable to structural systems subjected to static loadings, that are continuous with respect to the spatial coordinates, while available as digitized records. This paper is an attempt to display the validity of this idea for assemblies of beam-columns. A real example for such an application is analysis of lengthy underground structural systems. For these systems, the soil above the structural system defines a static loading that though is actually continuous with respect to the longitudinal axis, is available as a digitized record, because of the nature of the geodetic surveys; see the last example in the Numerical Study section.

In the next section, the technique proposed in Soroushian (2008) is briefly reviewed and adapted to enlargement of the beam-column elements in finite element analysis (Hughes, 1987; Bathe, 1996; Cook et al., 2002; Zienkiewicz and Taylor, 2005; Soroushian, 2008) of assemblies of beam-columns. Afterwards, via several examples, it is shown that the adapted technique might considerably reduce the analysis computational effort at the price of negligible change of accuracy. The observations are later discussed and compared with those reported from the time integration analysis application. Eventually, the paper is concluded with a brief set of the achievements and the future perspective.

FROM STEP-ENLARGEMENT TO ELEMENT-ENLARGEMENT

Convergence to exact solution is the main essentiality of successful approximate computation (Henrici, 1962; Strikwerda, 1989). In a brief review on the technique proposed by Soroushian (2008), the basis of the technique is proper convergence (Soroushian, 2010) of the computed response to the exact response. This consideration has led to the change of the $\mathbf{f}(t)$ digitized in ${}_f\Delta t$ to the $\tilde{\mathbf{f}}(t)$ digitized in ${}_f\Delta \tilde{t}$ $(= n_f \Delta t \ , \ n \in \{2, 3, ...\})$, according to Soroushian (2017):

$$\begin{aligned} \tilde{\mathbf{f}}_i &= \tilde{\mathbf{f}}(t_i) \qquad\qquad t_i = 0,\ n\ {}_f\Delta t,\ 2n\ {}_f\Delta t,\ \ldots \\ &= \begin{cases} \mathbf{g}(t_i) & t_i = 0 \\ \frac{1}{2}\mathbf{g}(t_i) + \frac{1}{4n'}\sum_{k=1}^{n'}\left[\mathbf{g}\left(t+\frac{k}{n}\right)+\mathbf{g}\left(t-\frac{k}{n}\right)\right] & 0 \le t_i < t'_{end} \\ \mathbf{g}(t_i) & t_i = t'_{end} \end{cases} \end{aligned} \tag{2}$$

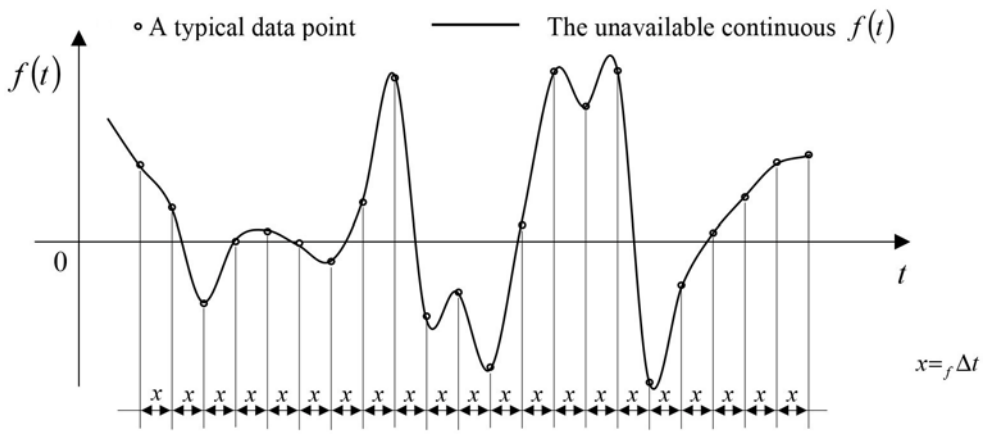

FIGURE 1 | A typical digitized component of $\mathbf{f}(t)$.

TABLE 1 | A brief report of the tests carried out on the technique proposed by Soroushian (2008).

System	Details	Computational effort reduced (%)	Change of accuracy (%)
Residential buildings	About 200 buildings structures with linear/non-linear behavior and regularity/irregularity in plan/height subjected to different earthquakes	50–90	<7
Power station, Cooling tower, Space structure, Silo	One or two of each special structure, considering linear/non-linear behavior and different near-field/far-filed earthquakes and different integration schemes	>50	<7
Milad tele-communication tower	Considering linear/non-linear behavior and different near-field/far-filed earthquakes and different integration schemes	50–70	<7

where n'can be obtained from

$$n' = \begin{cases} n-1 & \text{when } t_i = n_f \Delta t \\ \begin{cases} \frac{n}{2} & n = 2j, \quad j \in Z^+ \\ \frac{n-1}{2} & n = 2j+1, \ j \in Z^+ \end{cases} & \text{when } t_i \neq n_f \Delta t, t_i \neq t'_{end} - n_f \Delta t \\ n-1 & \text{when } t_i = t'_{end} - n_f \Delta t \end{cases} \quad (3)$$

t'_{end} stands for the only number satisfying the two relations below:

$$t_{end} \leq t'_{end} < t_{end} + n_f \Delta t \quad (4)$$

$$\frac{t'_{end}}{n_f \Delta t} \in \{1, 2, ...\} \quad (5)$$

and $\mathbf{g}(t_i)$ is available from:

$$\mathbf{g}(t_i) = \begin{cases} \mathbf{f}(t_i) & \text{when } 0 \leq t_i \leq t_{end} \\ 0 & \text{when } t_{end} \leq t_i \leq t'_{end} \end{cases} \quad (6)$$

From the parameters in Equation (2), n is still undefined. This parameter stands for the positive enlargement scale that should be set such that the enlargement does not affect the response accuracy. The broadly accepted comment for selection of the integration step of a time integration analysis, mainly based on accuracy considerations, is formulated as (McNamara, 1974; Clough and Penzien, 1993; Bathe, 1996; NZS 1170, 2004; Soroushian, 2017):

$$\Delta t \leq \text{Min}\left(\Delta t_{cr}, \ \Delta t_r, \ \frac{T}{\chi}, \ {}_f\Delta t\right) \quad (7)$$

In Equation (7), Δt_{cr} stands for the largest step providing numerical stability, Δt_r is the largest digitization step acceptable for the response, T is the smallest period with worthwhile contribution in the response, and χ is available from:

$$\chi = \begin{cases} 10 & \text{when the behavior is linear} \\ 100 & \text{when the behavior is nonlinear but not involved in impact} \\ 1000 & \text{when the behavior is involved in impact} \end{cases} \quad (8)$$

Consequently, the largest value that can be assigned to n, i.e., $n_{\max}$, is obtainable from:

$$\begin{aligned} & n_{\max} \ {}_f\Delta t \leq \text{Min}\left(\Delta t_{cr}, \ \Delta t_r, \ \frac{T}{\chi}\right) < (n_{\max} + 1) \ {}_f\Delta t \\ & n_{\max} \in \{2, 3, 4, ...\} \end{aligned} \quad (9)$$

and any positive integer larger than one and smaller than or equal to $n_{\max}$ can be assigned to n, i.e.,

$$1 < n \leq n_{\max} \quad (10)$$

Considering cases of the first relation in Equation (9), that lead to $n_{\max} = 0$ or $n_{\max} = 1$, there is no guarantee to be able to assign a value to n. In these cases, the technique proposed by Soroushian (2008) is inapplicable. In view of **Table 1**, this is a rare situation and the technique is successfully applicable to many real analyses. In order to extend the application to analysis of assemblies of beam-columns subjected to digitized static loadings on longitudinal axes of the beam-columns, the longitudinal axis of each beam-column is considered as the time axis and the digitized static loading is considered as the $\mathbf{f}(t)$ in Equations (2, 6). Considering these, the technique would be applicable when the accuracy requirements (as stated in Equation (9) for time integration) are satisfied and:

$$t'_{end} = t_{end} \quad (11)$$

Equation (11) is taken into account, because of the essentiality to preserve the geometry of the structural system. To satisfy this restriction, attention is paid to the fact that, if without the restriction, x_{end} and x'_{end} (defined in few lines), are sufficiently close, i.e.,

$$0 < \frac{x'_{end} - x_{end}}{x_{end}} << 1, \quad (12)$$

we might be able to eliminate this difference by shortening the distance between each two sequential data of the static loading, i.e., ${}_f\Delta x$, (corresponding to ${}_f\Delta t$) instead of increasing the length of the beam-column. In Equation (12), x'_{end} and x_{end} are the parameters corresponding to t'_{end} and t_{end} (in application of the technique to time integration analysis, respectively). In view of

Equation (4), for the validity of Equation (12) it is sufficient to guarantee

$$\frac{n_x \, {}_f\Delta x}{x_{end}} << 1 \tag{13}$$

where with attention to Equations (9, 10), n_x (the parameter corresponding to the n, defined for finite element analysis of beam-column assemblies) can be obtained from

$$1 < n_x \leq (n_x)_{\max}$$

$$(n_x)_{\max f}\Delta x \leq \text{Min}\,(\mathbf{OP}, \mathbf{AC}) < ((n_x)_{\max} + 1)\ {}_f\Delta x \tag{14}$$

$$n_x \in \{2, 3, 4, \ldots\} \quad , \quad (n_x)_{\max} \in \{2, 3, 4, \ldots\}$$

and **OP** and **AC** are schematic representations of the restrictions on $(n_x)_{\max}$, respectively originated in the response digitization and the response accuracy. Consequently, when Equation (13) is satisfied, we can redefine ${}_f\Delta x$ as:

$${}_f\Delta x' = {}_f\Delta x \ \frac{x_{end}}{x'_{end}} \tag{15}$$

and consider implementation of Equation (15) as a reasonable way for preserving lengths of the beam-columns in the finite element model. A question in this stage is that under Equation (13), the change of the members lengths will be negligible even if we do not implement Equation (15). Why cannot we accept the approximation because of the replacement of x_{end} with x'_{end}? In response to this question, changes of the structure's geometry can considerably change the mathematical model for the effects of geometric non-linearity (Gao and Strang, 1989; Bathe, 1996). This is true, especially when the structural members' lengths differ considerably. These changes should be avoided. Another ambiguity is on the inequality sign in Equation (13). What is the notion of the "very small"? In response to this question, it seems to the authors that because of the second order of convergence in many practical analyses, it is sufficient to satisfy

$$\frac{n_x \, {}_f\Delta x}{x_{end}} < 0.01 \tag{16}$$

Furthermore, one may ask whether the above-mentioned change in the element length can be used in time integration analysis in order to avoid replacement of t_{end} with t'_{end}. The response is negative. The reason is that different from static finite element analysis, time integration analysis has a step-by-step nature, where the error because of the change in the integration step can be accumulated to some level. In addition, in time integration analysis, the replacement of t_{end} with t'_{end} is not important.

Finally, it is worth noting that, even when Equations (13, 16) are not satisfied, the technique proposed by Soroushian (2008) is applicable by considering a small element in the end of the beam-column. This will not affect the accuracy and will trivially affect the computational effort. However, the pre-processing stage will become slightly more complicated. In view of the rareness of this condition, for the sake of brevity, the detailed discussion is left for future studies.

Consequently, provided we can assign positive integers larger than one to n_x, we would be able to implement the technique proposed by Soroushian (2008) in static finite element analysis of assemblies of beam-columns subjected to digitized excitation. The efficiency is studied next, and a complementary discussion on efficiency and determination of n_x is presented later.

NUMERICAL STUDY

Introduction

The objective of this paper is to respond to the question: Can the technique proposed by Soroushian (2008) be successful when implemented in analysis of assemblies of beam-columns subjected to static loadings, originally continuous but available as digitized records? This section presents a numerical study on the response of this question. We examine the existence of a value of n_x causing negligible change of accuracy and sufficient reduction of computational effort, regardless of Equation (14), the resulting $(n_x)_{\max}$, and the possibility of assigning fractional numbers larger than one to n_x (Soroushian et al., 2017). The accuracy is studied by depicting the responses obtained from finite element analysis and the computational effort is studied in different ways.

A Simple Example

The system under consideration in this example is the beam displayed in **Figure 2**. IPB 500 is used as the beam profile, with a moment of inertia equal to 1.072×10^5 cm^4 and a modulus of elasticity equal to 210 GPa (Gaylord et al., 1997). The digitization

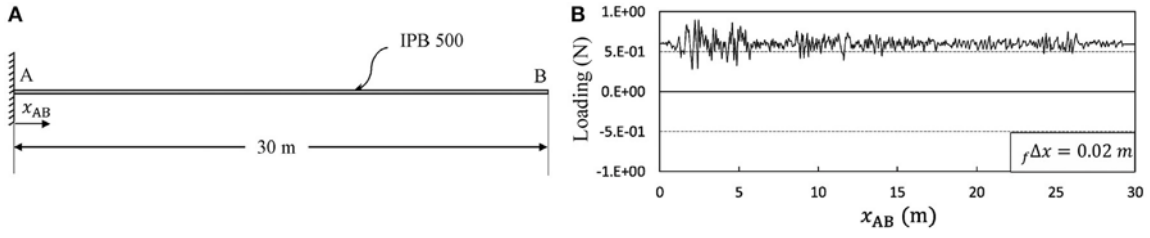

FIGURE 2 | Structural system under consideration in the first example **(A)** structural model and **(B)** digitized static loading.

step of the static loading equals ${}_f\Delta x = 0.02$ m. The analysis is carried out by two-node beam-column elements (with six and twelve degrees of freedom in two- and three-dimensional analyses, respectively) loaded uniformly along the element axis. The intensity of loading on each element equals the average of the actual loadings at the element's nodes (see **Figure 1**). First, an analysis is carried out with elements sized equal to the loading digitization step. The displacement shear and moment diagrams are depicted in **Figure 3A**. The analysis is then repeated with 4 times larger elements after implementation of the technique proposed by Soroushian (2008), considering $n = n_x = 4$, and the results are reported in **Figure 3B**.

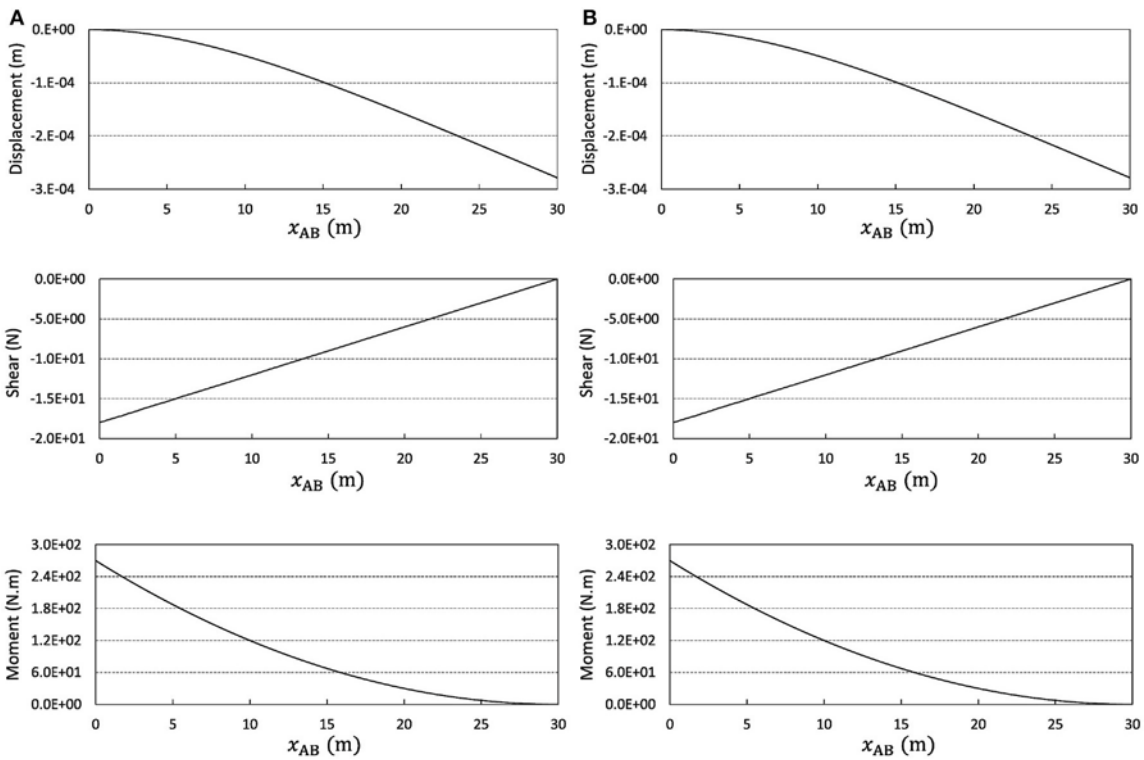

FIGURE 3 | Responses of the structural system in the first example obtained from finite element analysis using elements sized **(A)** 0.02 m and **(B)** 0.08 m.

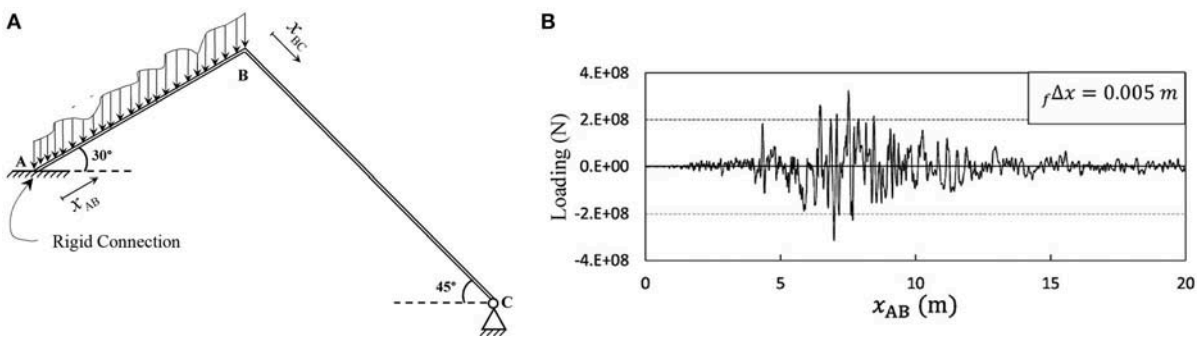

FIGURE 4 | Structural system in the second example **(A)** structural model and **(B)** loading.

TABLE 2 | Properties of the structural members in **Figure 4A**.

Beam-column	Length (m)	Profile	Modulus of Elasticity (GPa)	Moment of Inertia (cm^4)	Area (cm^2)
AB	20	IPB 500	210	1.072×10^5	239
BC	30	IPB 500	210	1.072×10^5	239

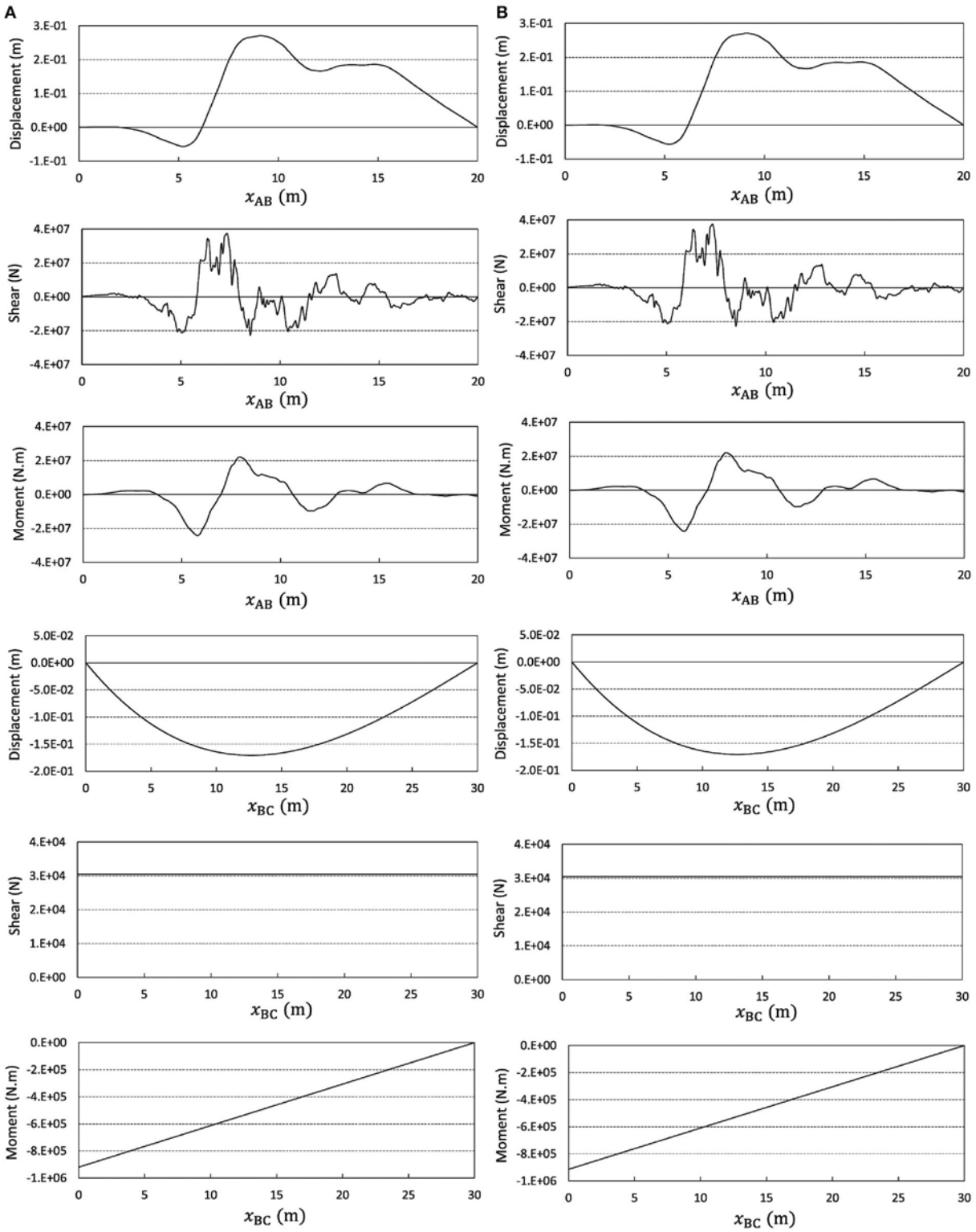

FIGURE 5 | Responses of the second example obtained from analysis with elements sized **(A)** $_f\Delta x$ and **(B)** $3_f\Delta x$.

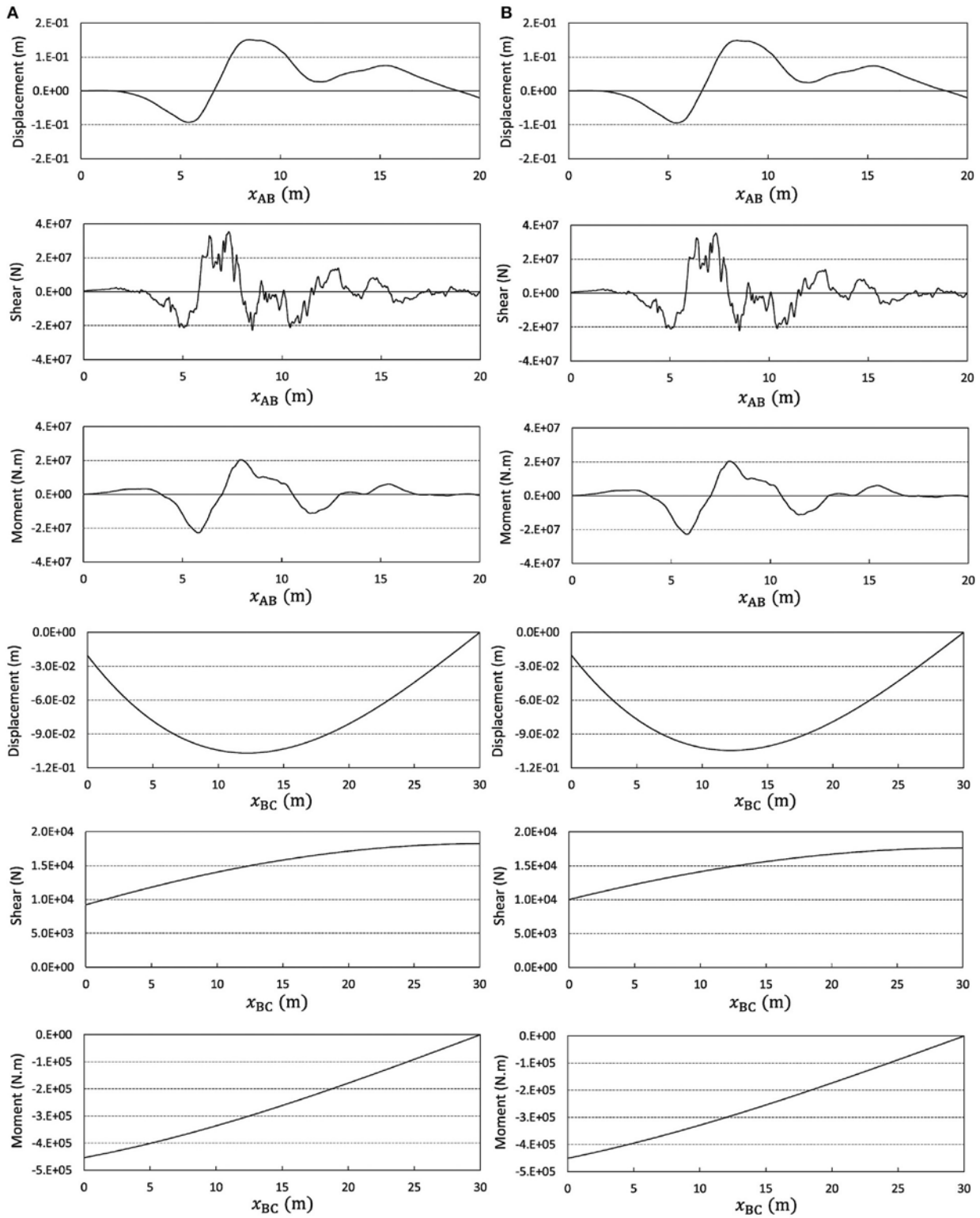

FIGURE 6 | Responses of the second example considering large displacements and obtained from analysis with elements sized **(A)** $_f\Delta x$ and **(B)** $3_f\Delta x$.

Apparently, the change of accuracy is trivial, while the reduction of the computational effort is considerable. The experience reported above clearly displays that the technique proposed for more efficient time integration analysis

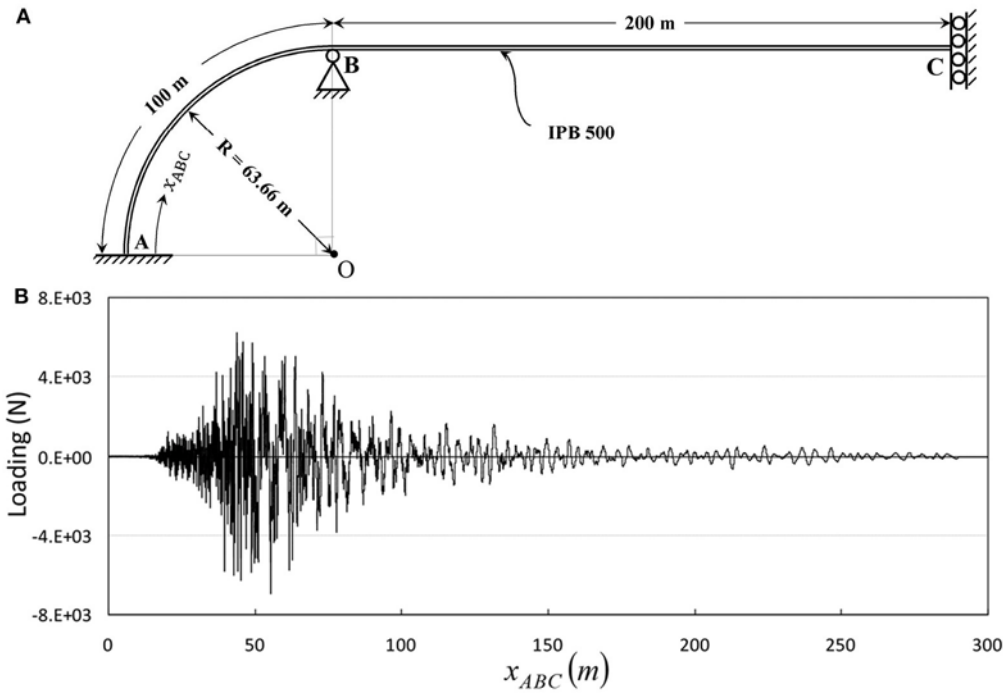

FIGURE 7 | Structural system in the third example **(A)** structural model and **(B)** loading.

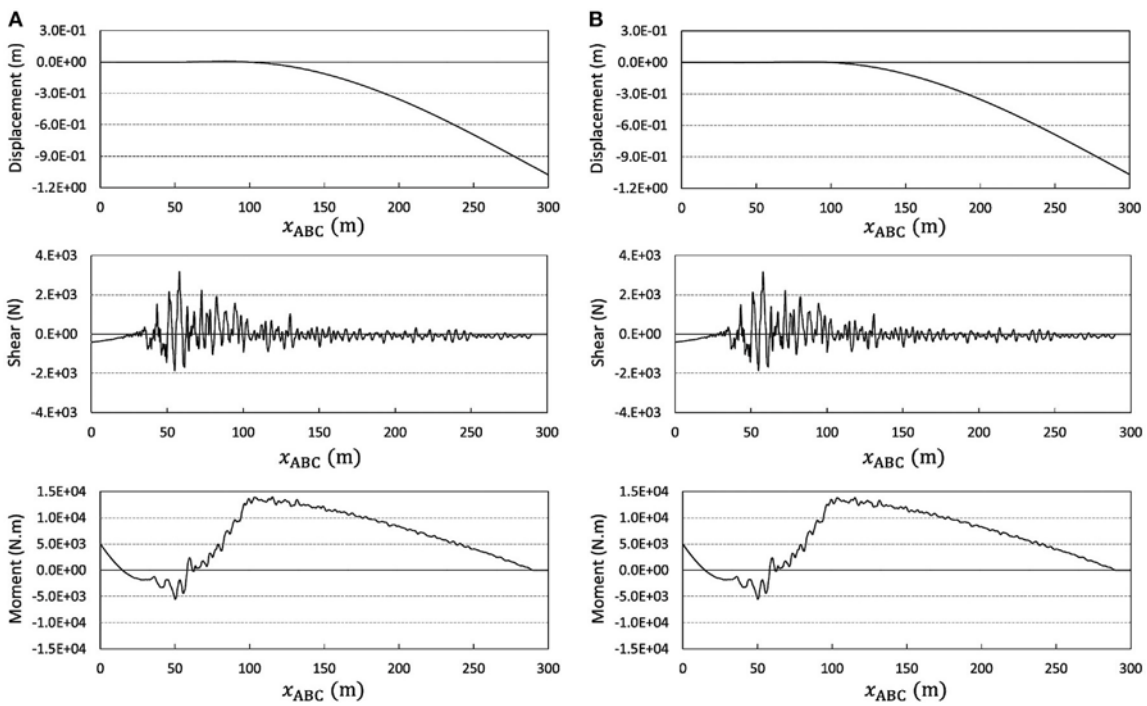

FIGURE 8 | Responses of the third example obtained from analysis with elements sized **(A)** $_f\Delta x$ and **(B)** $4_f\Delta x$.

(Soroushian, 2008) can also be effectual in enhancement of finite element analysis.

Complicated Examples

Loading Non-perpendicular to the Member Axis in Linear/Nonlinear Analysis

Consider the structural system introduced in **Figure 4A** and **Table 2**. The finite element analysis is carried out using elements similar to the previous example and sized $_f\Delta x$ (see **Figure 4B**). The results are displayed in **Figure 5A**. The analysis is repeated with 3 times larger elements and has led to **Figure 5B**. The two analyses are repeated, while considering the non-linearity because of large displacements (Gao and Strang, 1989; Bathe, 1996), and the results are reported in **Figure 6**. In view of these results, the change of accuracy is unrecognizable, regardless of the non-linearity. The two examples in this section, and specifically **Figures 5** and **6**, clearly reveal the possibility to expect good performance from the technique proposed by Soroushian (2008), when implemented in finite element analysis of static linear and static non-linear behaviors of assemblies of beam-columns subjected to digitized loadings, not necessarily perpendicular to the beam-columns axes.

Curved Beam-Column in Linear/Non-linear Analysis

The structural system under consideration is introduced in **Figure 7**, where the static loading is applied in the vertical direction regardless of the position (see **Figure 7B**). Using the element type addressed in the previous examples has led to the

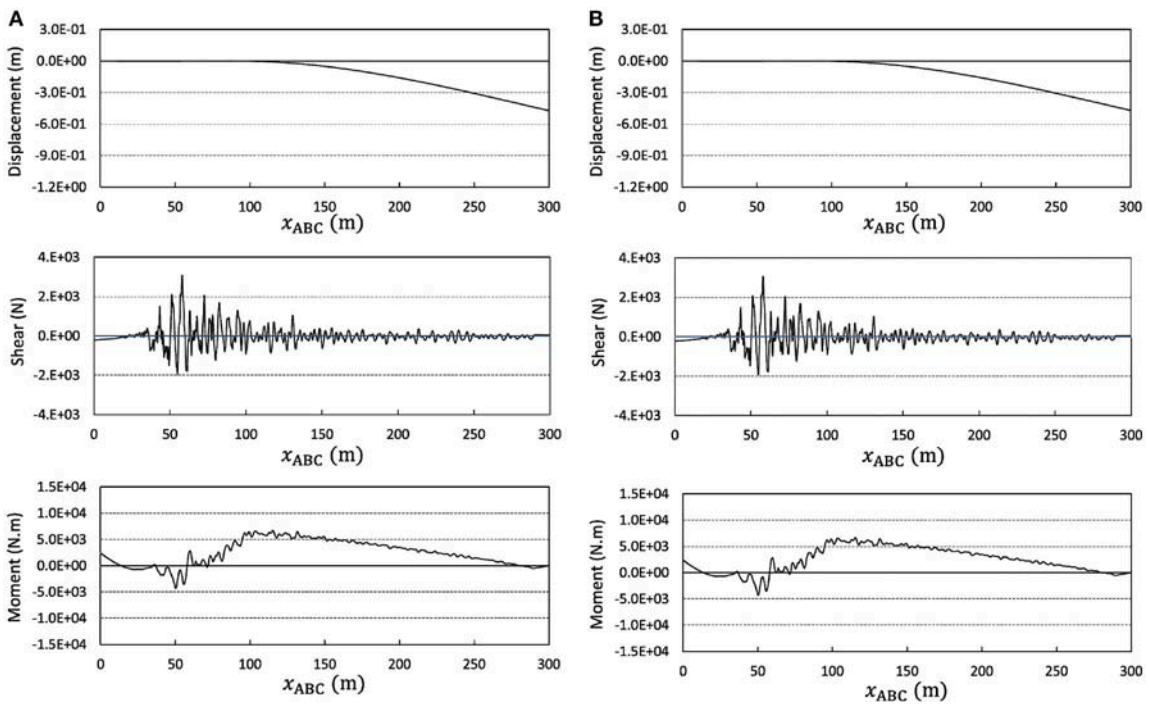

FIGURE 9 | Responses of the third example taking into account large displacements and obtained from analysis with elements sized **(A)** $_f\Delta x$ and **(B)** $4_f\Delta x$.

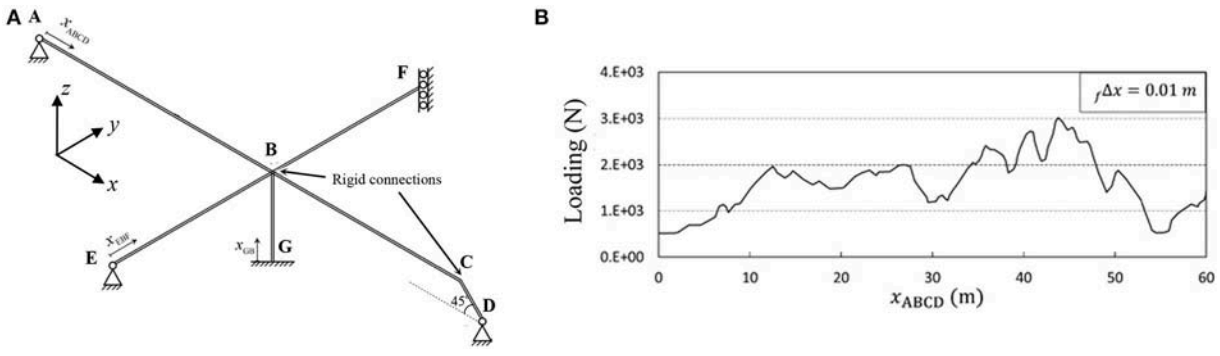

FIGURE 10 | Structural system in the last example **(A)** structural model and **(B)** loading.

TABLE 3 | Properties of the structural members in **Figure 10A**.

Beam-column	Length (m)	Profile	Modulus of Elasticity (GPa)	Moment of Inertia (cm^4)*	Area (cm^2)	Polar Moment of Inertia (cm^4)
AB	30	IPB 500	210	1.072×10^5	239	1.198×10^5
BC	25	IPB 500	210	1.072×10^5	239	1.198×10^5
CD	5	IPB 500	210	1.072×10^5	239	1.198×10^5
EB	20	IPB 500	210	1.072×10^5	239	1.198×10^5
BF	20	IPB 500	210	1.072×10^5	239	1.198×10^5
GB	10	Box 400*400*40	210	1.259×10^5	576	2.519×10^5

*Each stated value is associated with the horizontal main axis of the cross-section perpendicular to the longitudinal axis of the member.

TABLE 4 | Complementary details of the supports of the structural system displayed in **Figure 10A**.

Support	Freedom of movement or rotation
A, D	Free to rotate around the *x*, *y*, and *z* axes
E	Free to rotate around the *x* and *z* axes
F	Free to move along and rotate around the *z* axis
G	No freedom for movement or rotation

responses reported in **Figure 8**. This is another evidence for the applicability of the technique proposed by Soroushian (2008), in analysis of assemblies of beam-columns (taking into account the modification addressed in Section From Step-Enlargement to Element-Enlargement). In view of the geometry of the structure in this example, the study is repeated considering the non-linearity because of large displacements. The consequence, reported in **Figure 9**, is conceptually similar to the results of the linear analysis reported in **Figure 8**. This implies that the technique can display a good performance in different static behaviors of beam-columns, even when the beam-columns are curved.

A More Realistic Example

Consider the system introduced in **Figure 10** and **Tables 3**, and **4**, as a simplified model of a real structural system. **Figure 10B** displays a loading originated in the longitudinal profile of the Brenner Base tunnel, which is a part of the future TEN No. 5 corridor Helsinki-Valleta (Bergmeister, 2012). Via this assembly of beam-columns, and by finite element analysis with the elements in the previous examples, the performance of the technique proposed by Soroushian (2008) is tested. The consequence is reported in **Figure 11**, once again evidencing the good performance of the technique when applied to analysis of assemblies of beam-columns. Compared to previous examples, the contribution of lower frequencies is much more in this example (see **Figure 12**). This implies versatility of the technique with respect to the digitized loading. In this regard, **Figures 13**, and **14**, display a replacement of **Figures 10B**, and **11**, as an evidence for the versatility considering a specific assembly of beam-columns. Furthermore, comparison between **Figures 11** and **14** reveals that, as implied in the **AC** in Equation (14), the enlargement of the element size corresponding to trivial change of accuracy can also depend on the response.

More on the Efficiency

According to the almost perfect accuracy observed in Sections A Simple Example, Complicated Examples, and A More Realistic Example, the efficiency can be compared in view of computational effort. Accordingly, less computational effort implies more efficiency. Computational effort can be studied in terms of the in-core storage involved in the computation (Monro, 1982; Soroushian and Farjoodi, 2003; Zhou and Tamma, 2004). With attention to the details of finite element analysis (Hughes, 1987; Bathe, 1996; Cook et al., 2002; Zienkiewicz and Taylor, 2005), the storage changes with the α th power of the number of the degrees of freedom, where $2 < \alpha < 3$ (Cook et al., 2002). Consequently, the change of efficiency, *E*, because of implementation of the technique proposed by Soroushian (2008) can be addressed as

$$\frac{E_{2008}}{E_{\text{tr}}} \approx n_x^{\alpha} \left(\frac{TR_{\text{tr}}}{TR_{2008}}\right), \qquad 2 < \alpha < 3 \tag{17}$$

where *TR* stands for the run-time and the right subscripts "tr" and "2008", respectively indicate the traditional (ordinary) analysis and the analysis after implementation of the technique proposed by Soroushian (2008), considering n_x as the enlargement scale ($n = n_x$). Equation (17), together with **Figures 3**, **5**, **6**, **8**, **9**, **11**, and **14**, and **Table 5**, clearly evidence the significantly increased efficiency of the analysis after implementing the above-mentioned technique, at the price of trivial change of accuracy. Furthermore, the percentage of the enhancement of efficiency, *EE*, can be expressed as

$$EE = \left(\frac{E_{2008}}{E_{\text{tr}}} - 1\right) \times 100\% = \left(n_x^{\alpha} \frac{TR_{\text{tr}}}{TR_{2008}} - 1\right) \times 100 \tag{18}$$

which, in view of Equations (14, 17) and the fact that $TR_{\text{tr}} > TR_{2008}$, is at least 300%, for the presented finite element application ($EE_{femb} \geq 300\%$; the subscript "femb" stands for finite element analysis of beam-columns). The smallest *EE* in implementation of the technique proposed by Soroushian (2008) in time integration analysis is 100% [both when disregarding the fractional enlargement proposed by Soroushian et al. (2017)].

DISCUSSION

Static loadings addressed in Section Numerical Study vary from the slow changing loading in the last example to the rapid

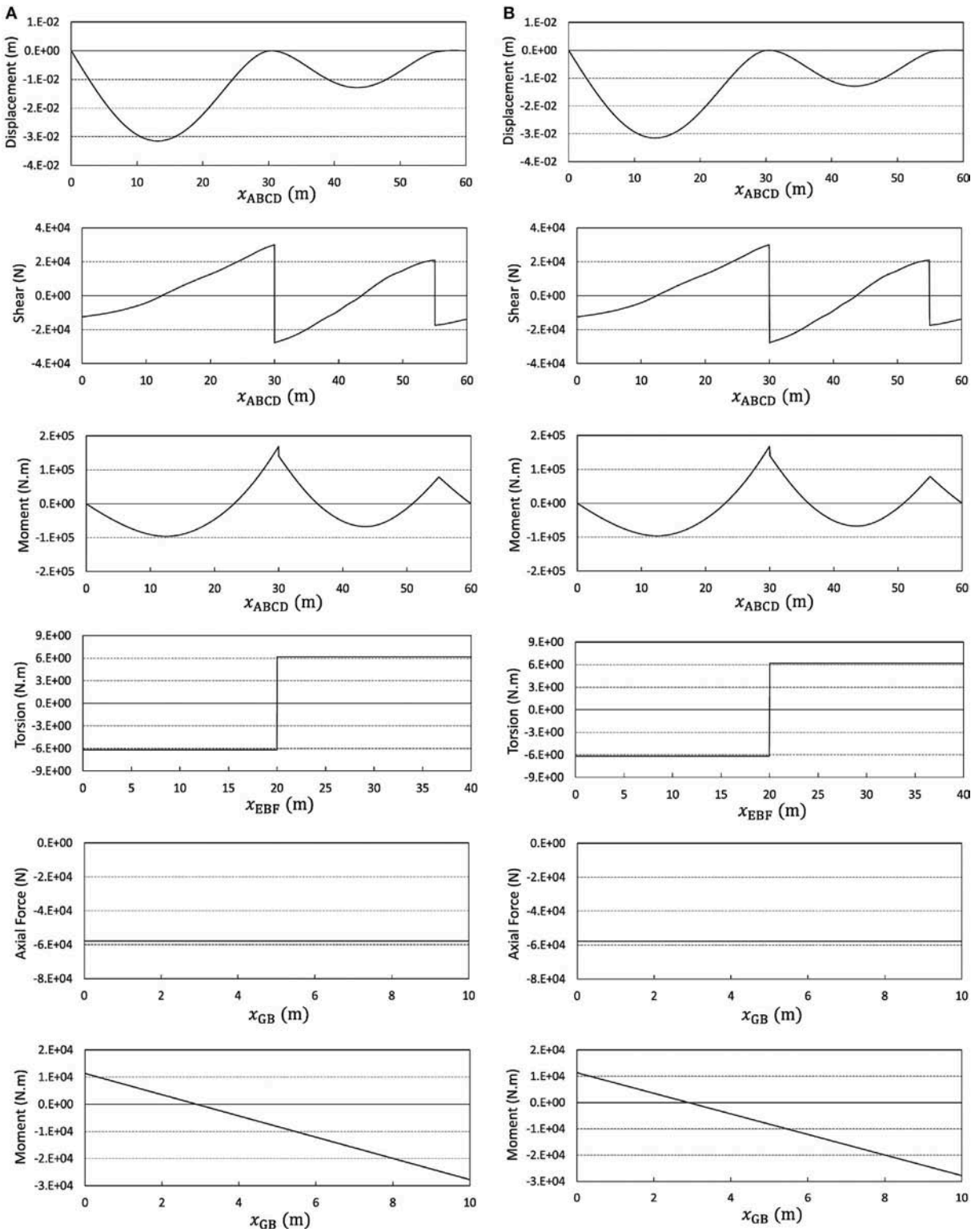

FIGURE 11 | Responses of the fourth example obtained from finite element analysis using elements sized **(A)** $_f\Delta x$ and **(B)** $4_f\Delta x$.

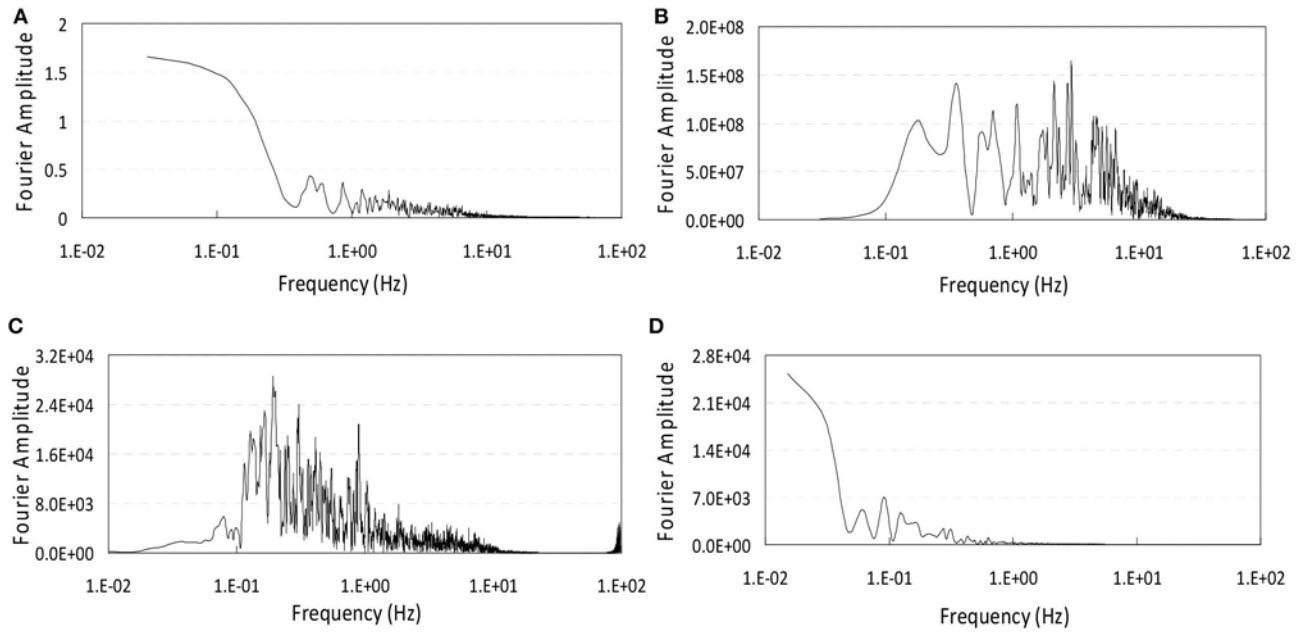

FIGURE 12 | Frequency contents of the static loadings in the **(A)** first example, **(B)** second example, **(C)** third example and **(D)** forth example.

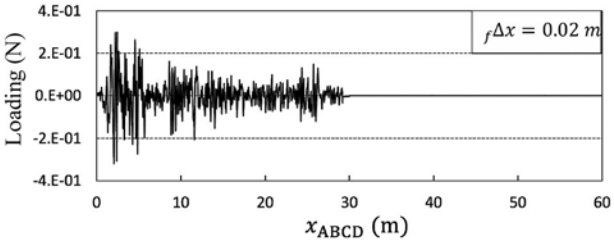

FIGURE 13 | A replacement for **Figure 10B** for further study on the versatility.

changing loadings in the second and third examples (the rapid case is rare). The technique proposed by Soroushian (2008) has been significantly successful in implementation in analysis of beam-column assemblies subjected to all of these loadings; see Sections A Simple Example, Complicated Examples, A More Realistic Example, and More on the Efficiency, and Equation (18). Even more, compared to time integration application, the enhancement because of the technique is considerably more in finite element analysis of beam-column assemblies; see Equation (17) and the corresponding relation in time integration application, i.e.,

$$\frac{E_{2008}}{E_{\text{tr}}} = \left(\frac{TR_{\text{tr}}}{TR_{2008}}\right) \approx n \tag{19}$$

Meanwhile, it is worth noting that, as obvious in Equations (17) and (19) and **Table 5**, different from time integration application, in the finite element application, the enhancement of efficiency is because of both faster analysis and less in-core storage. Considering these, further study on the extension reported in this paper is reasonable. In this regard, attention should be paid to the fact that time integration and finite element analyses are different in nature. As a main difference, while the former is a mean to analyze ordinary initial value problems, the latter is a tool for analysis of boundary value problems. Because of this difference, the invalidity of Equation (11) does not impose additional errors to time integration applications, while $x'_{end} \neq x_{end}$ may lessen the accuracy of the results in finite element analysis applications. Another considerable difference is the amount of efficiency, which can lead to:

(1) Sufficiency of upper-bounding n_x by 4 [the upper-bound for time integration analysis is 5 (Azad, 2015)], i.e.,

$$n_x \leq 4 \tag{20}$$

Assigning larger values to n_x enhances the efficiency trivially.

(2) Importance of fractional enlargement of digitization step (Soroushian et al., 2017), especially when Equation (14) leads to

$$n_x = 1 \tag{21}$$

Therefore, further study on the extension of the technique proposed by Soroushian (2008) to static analysis of structures by finite elements is of high importance. It also sounds reasonable to expect good performance, when applying the technique to dynamic finite element analysis of different structural systems. Even more, in continuation of the extension presented in this paper, the enlargement of the digitization step (Soroushian, 2008) can be tested in other analyses, in the broad range of science and engineering computation. In addition, it is

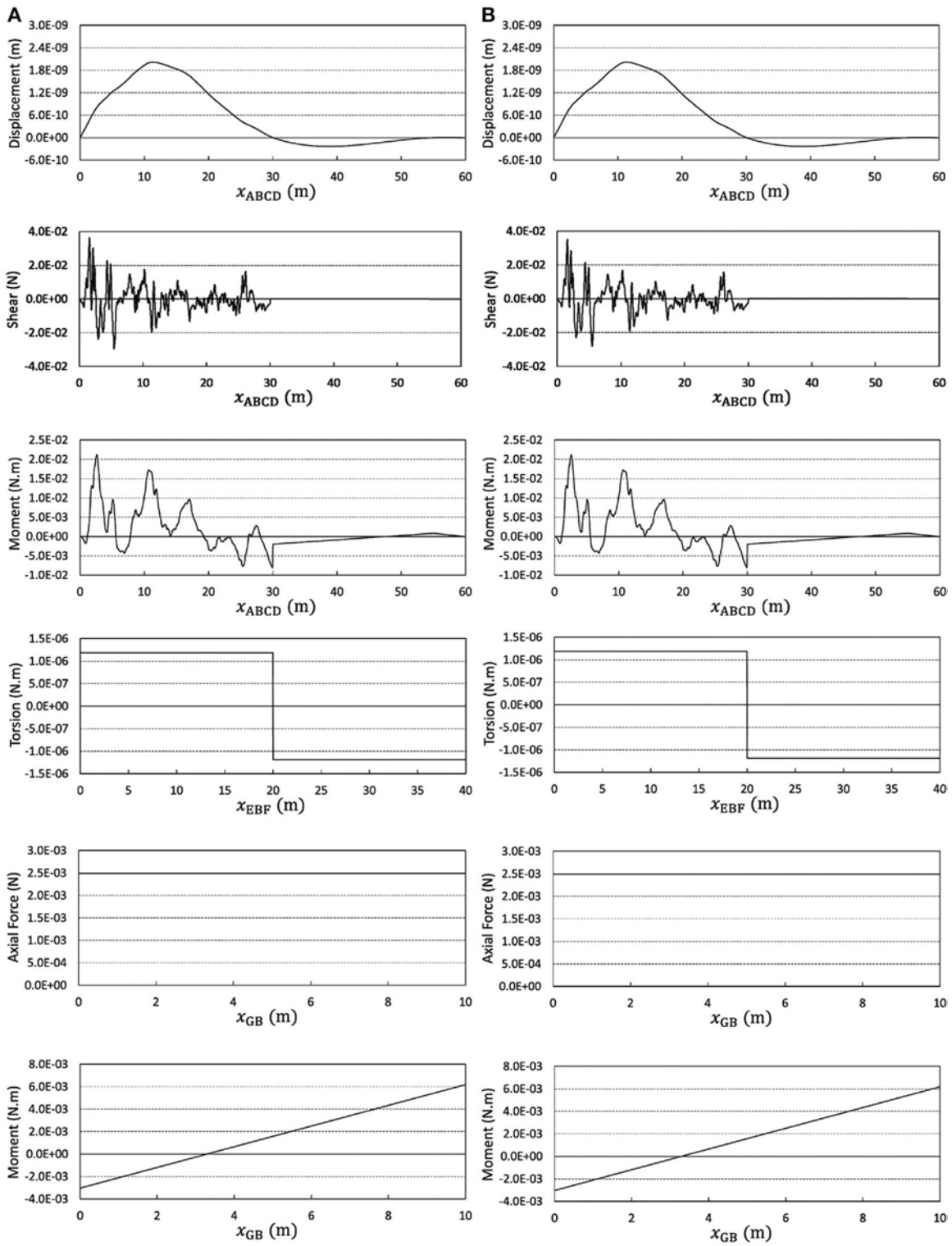

FIGURE 14 | A consequence of the replacement addressed in **Figure 13 (A)** analysis with elements sized$_f$ Δx and **(B)** analysis with elements sized 2_f Δx.

TABLE 5 | Values of n_x, TR_{tr}, and TR_{2008} in the four examples studied in Sections A Simple Example, Complicated Examples, and A More Realistic Example*.

Example	Section	n_x	TR_{tr}(s)	TR_{2008}(s)	Minimum enhancement of efficiency (%)
1	A simple example	4	5	3	2567
2 (linear)	Loading non-perpendicular to the member axis in linear/nonlinear analysis	3	16	7	1957
2 (nonlinear)	Loading non-perpendicular to the member axis in linear/nonlinear analysis	3	16	6	2300
3 (linear)	Curved beam-column in linear/nonlinear analysis	4	113	27	6596
3 (non-linear)	Curved beam-column in linear/nonlinear analysis	4	125	30	6567
4 (first loading)	A more realistic example	4	24	8	4700
4 (second loading)	A more realistic example	2	13	8	550

TR_{tr} and TR_{2008} depend on the power of the computational facility.

essential to note that, similar to time integration application, in implementation of the technique to finite element analysis, determination of the adequate amount of enlargement is not easy. The reason is the dependence of the **AC** in Equation (14) to the response.

CONCLUSIONS

The technique proposed by Soroushian (2008) has been adapted to finite element analysis of assemblies of beam-columns subjected to continuous static loadings, available as digitized records. As the main consequences,

1) The extension can be successful in linear and non-linear analyses, for different target responses, when the beam-columns are straight or curved, and the loadings are perpendicular or non-perpendicular to the axes of the beam-columns, and change gradually or sharply.
2) Implementation of the technique to static finite element analysis of structural systems may suffer from an additional source of error originated in the length of the structural members. This can be obviated by satisfying Equations (13, 16) or assigning a slightly different size to one of the elements in modeling the structural member.
3) For a specific digitization-step enlargement, enhancement of efficiency because of the technique can be considerably more in finite element analysis of beam-columns' assemblies compared to time integration analysis. A main reason is that, in the finite element analysis application, the enhancement of efficiency is via the decrease of the run-time as well as the decrease of the in-core storage. In the time integration application, only the run-time decreases.
4) The capability to enlarge the digitization step by fractional scales is very important in the finite element analysis.
5) Practically, in application of the step-enlargement technique to static finite element analysis, it is meaningless to enlarge the digitization step more than 4 times.
6) Similar to the time integration application, ambiguities exist in determination of n_x in the finite element application.

As a perspective of future, more tests on larger and more complicated assemblies of beam-columns is recommended. Further study on improvement of the existing step-enlargement technique in time integration, as well as finite element analysis, especially on clearer determination of n and n_x, is recommended. Meanwhile, extension of the step-enlargement technique to other problems and computational methods, specifically simultaneous model reduction in space and time, is a reasonable area for further research.

AUTHOR CONTRIBUTIONS

AS conceived the main idea, and the idea of preparing the paper. The draft was prepared by the collaboration of both authors. The structural analysis of the examples and the typing of the draft was done by EF. The final editing of the manuscript was done by AS.

ACKNOWLEDGMENTS

The authors sincerely appreciate the detailed comments as well as the kind attention and time of the reviewers, because of which, the quality of the paper has been enhanced significantly. The authors feel essential to also express their sincere gratitude to the editor of the paper for his managing all of the process of the paper's revision in a short time interval. Last but not the least thanks of the authors go to the typesetter(s) of the paper, who with considerable patience implemented the many changes asked by the authors.

REFERENCES

Argyris, J., and Mlejnek, H. (1991). *Dynamics of Structures, Volume 5 (Texts on Computational Mechanics)*. Amsterdam: Elsevier.

Azad, S. (2015). *A Study on Accelerating Time History Analysis of Bridges*. M.Sc. dissertation, International Institute of Earthquake Engineering and Seismology (IIEES), Iran (In Persian).

Baiani, A. (2018). *On the Possibility to Accelerate Time History Analysis of Buildings with Irregularities in Plan Because of Mass Distribution*. M.Sc. Dissertation, University of Pooyandegan Danesh, Iran (in press in Persian).

Bastami, M. (2014). "A technique for more efficient time integration applied to seismic analysis of power substation equipment," in *Paper Presented at the 11th World Congress on Computational Mechanics (WCCM XI)* (Barcelona).

Bathe, K. (1996). *Finite Element Procedures*. Upper Saddle River, NJ: Prentice-Hall.

Belytschko, T., Liu, W. K., and Moran, B. (2000). *Nonlinear Finite Elements for Continua and Structures*. New York, NY: John Wiley & Sons.

Bergmeister, K. (2012). *Brenner Base Tunnel under Construction*. Available online at: http://www.tunnel-online.info/en/artikel/tunnel_2012-01_Brenner_Base_Tunnel_under_Construction_1370791.html

Besselink, B., Tabak, U., Lutowska, A., Van de Wouw, N., Nijmeijer, H., Rixen, D. J., et al. (2013). A comparison of model reduction techniques from structural dynamics, numerical mathematics and systems and control. *J. Sound Vib.* 332, 4403–4422. doi: 10.1016/j.jsv.2013.03.025

Clough, R. W., and Penzien, J. (1993). *Dynamics of Structures*. Singapore: McGraw-Hill.

Cook, R., Malkus, D., Plesha, M., and Witt, R. (2002). *Concepts and Applications of Finite Element Analysis*. New York, NY: John Wiley & Sons.

Gao, Y., and Strang, G. (1989). Geometric nonlinearity: potential energy, complementary energy, and the gap function. *Q. Appl. Math.* 47, 487–504. doi: 10.1090/qam/1012271

Garakaninezhad, A., and Moghadas, R. K. (2015). "On the performance of a technique to accelerate time integration when applied to space structures analyses," in *Paper Presented at the 5th ECCOMAS Thematic Conference on Computational Methods in Structural Dynamics and Earthquake Engineering (COMPDYN 2015)* (Crete Island).

Gaylord, E. H., Gaylord, C. N., and Stallmeyer, J. E. (1997). *Structural Engineering Handbook*. New York, NY: McGraw-Hill.

Ghondaghsaz, H. (2018). *A Study on a Recent Technique for More Efficient Seismic Analysis Applied to Concrete and Steel Buildings*. M.Sc. dissertation, Islamic azad, University West Tehran Branch, Tehran, (in Persian).

Hadad, A. (2015). *Reducing Computational Costs in Time Integration Analyses of Buildings With Irregularities in Height Because of Mass*. M.Sc. Dissertation, International Institute of Earthquake Engineering and Seismology (IIEES), Iran (In Persian).

Henrici, P. (1962). *Discrete Variable Methods in Ordinary Differential Equations*. Upper Saddle River, NJ: Prentice-Hall.

Henrych, J. (1990). *Finite Models and Methods of Dynamics in Structures*. Amsterdam: Elsevier.

Hughes, T. J. (1987). *The Finite Element Method: Linear Static and Dynamic Finite Element Analysis*. Upper Saddle River, NJ: Prentice-Hall.

Hughes, T. J., Pister, K. S., and Taylor, R. L. (1979). Implicit-explicit finite elements in nonlinear transient analysis. *Comput. Methods Appl. Mech. Eng.* 17, 159–182. doi: 10.1016/0045-7825(79)90086-0

McNamara, J. F. (1974). Solution schemes for problems of nonlinear structural dynamics. *J. Pressure Vessel Technol.* 96, 149–155. doi: 10.1115/1.3454158

Monro, D. M. (1982). *Fortran 77*. Edward Arnold, UK.

Nateghi, F., and Yakhchalian, M. (2011). "An investigation into the effectiveness of a technique proposed for reducing computational cost of time integration in the analysis of silos seismic behaviors," in *Paper presented at the 11th US National Congress on Computational Mechanics (USNCCM 2011)* (Minneapolis, MN).

NZS 1170 (2004). *Structural Design Actions, Part 5: Earthquake Actions-New Zealand*.

Sabzei, A. (2013). *On the Performance of a Recent Technique For Seismic Analyses Computational Cost Reduction When Applied to Buildings Structural Systems*. M.Sc. dissertation, International Institute of Earthquake Engineering and Seismology (IIEES), Iran (in Persian).

Soroushian, A. (2008). A technique for time integration analysis with steps larger than the excitation steps. *Commun. Numer. Methods Eng.* 24, 2087–2111. doi: 10.1002/cnm.1097

Soroushian, A. (2010). "Proper Convergence a Concept New in Science and Important in Engineering," in *Paper Presented at the 4th International Conference from Scientific Computing to Computational Engineering* (Athens), 7–10.

Soroushian, A. (2017). "Integration step size and its adequate selection in analysis of structural systems against earthquakes," in *Computational Methods in Earthquake Engineering. Computational Methods in Applied Sciences,* Vol. 3, eds M. Papadrakakis, V. Plevris, and N. Lagaros (Cham: Springer), 285–329. doi: 10.1007/978-3-319-47798-5_10

Soroushian, A., and Farjoodi, J. (2003). More reliable responses for time integration analyses. *Struct. Eng. Mech.* 16, 219–240. doi: 10.12989/sem.2003.16.2.219

Soroushian, A., Jahani Mehrnoosh, A., Zarabimanesh, Y., Ghondaghsaz, M., Baiani, A., and Zakizade, A. (2016). "On the performance of a computational cost reduction technique when applied to cooling towers transient analysis," in *Paper Presented at the 7th European Congress on Computational Methods in Applied Sciences and Engineering (ECCOMAS VII)* (Crete Island).

Soroushian, A., Zarabimanesh, Y., Soleymani, K., and Khalkhali, S. M. (2017). "A new technique for fractional enlargement of integration steps in transient analysis against digitized excitations," in *Paper Presented at the International Conference on Structural Engineering Dynamics (ICEDyn 2017)* (Ericeira).

Strikwerda, J. C. (1989). *Finite Difference Schemes and Partial Differential Equations*. Pacific Grove: Wadsworth & Books/Cole.

Wriggers, P. (2002). *Computational Contact Mechanics*. New York, NY: John Wiley & Sons.

Zarabimanesh, Y. (2017). *On a Recent Technique for Reducing the Computational Costs in Time Integration Analyses When Applied to the Analysis of Milad Tower*. M.Sc. dissertation, International Institute of Earthquake Engineering and Seismology (IIEES), Iran (In Persian).

Zhou, K. K., and Tamma, K. K. (2004). A new unified theory underlying time dependent first-order systems: a prelude to algorithms by design. *Int. J. Numer. Meth. Eng.* 60, 1699–1740. doi: 10.1002/nme.1019

Zienkiewicz, O. C., and Taylor, R. L. (2005). *The Finite Element Method for Solid and Structural Mechanics*. Oxford: Elsevier.

Conflict of Interest Statement: The authors declare that the research was conducted in the absence of any commercial or financial relationships that could be construed as a potential conflict of interest.

frontiers in Built Environment

REVIEW
published: 15 May 2019
doi: 10.3389/fbuil.2019.00064

Shunt Piezoelectric Systems for Noise and Vibration Control: A Review

*Konstantinos Marakakis, Georgios K. Tairidis, Panagiotis Koutsianitis and Georgios E. Stavroulakis**

Computational Mechanics and Optimization Laboratory, School of Production Engineering and Management, Technical University of Crete, Chania, Greece

In this paper, the current state of the art on shunt piezoelectric systems for noise and vibration control is reviewed. The core idea behind the operation of electronic shunt piezoelectric circuits is based on their capability of transforming the dynamic strain energy of the host structure, i.e., a smart beam or plate, into electric energy, using the properties of the direct piezoelectric phenomenon and sending this energy into the electronic circuit where it can be partially consumed and transformed into heat. For this purpose, transducers which are made by piezoelectric materials are used, since such materials present excellent electromechanical coupling properties, along with very good frequency response. Shunt piezoelectric systems consist of an electric impedance, which in turn consists of a resistance, an inductance or a capacitance in every possible combination. Several types of such systems have been proposed in the literature for noise or vibration control for both single-mode and multi-mode systems. The different types of shunt circuits provide results comparable to other types of control methods, as for example with tuned mass-dampers, with certain viscoelastic materials, etc. As for the hosting structure, several studies on beams and plates connected with shunt circuits have been proposed in recent literature. The optimization of such systems can be performed either on the design and placement of the piezoelectric transducers or on the improvement and fine-tuning of the characteristics of the system, i.e., the values of the resistance, the inductance, the capacitance and so on and so forth. There are several applications of shunt systems including among others, structural noise control, vibration control, application on hard drives, on smart panels etc. Last but not least, shunt circuits can be also used for energy harvesting in order to collect the small amount of energy which is necessary in order to make the system self-sustained.

Keywords: shunt circuits, piezoelectrics, vibrations, control, acoustics

OPEN ACCESS

Edited by:
Vagelis Plevris, OsloMet – Oslo Metropolitan University, Norway

Reviewed by:
Antonio Formisano, University of Naples Federico II, Italy
Dimitrios Giagopoulos, University of Western Macedonia, Greece

****Correspondence:***
Georgios E. Stavroulakis
gestavr@dpem.tuc.gr

Specialty section:
This article was submitted to Computational Methods in Structural Engineering, a section of the journal Frontiers in Built Environment

Received: *12 January 2019*
Accepted: *29 April 2019*
Published: *15 May 2019*

Citation:
Marakakis K, Tairidis GK, Koutsianitis P and Stavroulakis GE (2019) Shunt Piezoelectric Systems for Noise and Vibration Control: A Review. Front. Built Environ. 5:64. doi: 10.3389/fbuil.2019.00064

INTRODUCTION

Smart materials, such as piezoelectrics, piezoceramics, shape memory alloys, fiber optics, electrostrictive materials, magnetostrictive materials etc. can be integrated in structural models to provide them with the smart behavior. In principle, the initial stress or strain produced by some smart element can be controlled and leads to controlled, i.e., smart, behavior of the whole composite structure. Piezoelectrics constitute a suitable technology for testing smart structure concepts, since they have almost instantaneous reaction time without hysteresis and they work in most cases within

the linarity range. An important thing here is that both sensing and actuation functions are possible due to the nature of the piezoelectric effect. This specific characteristic leads many investigators to deal with the passive control of vibrations by using devices with shunted piezoelectric elements (Thomas et al., 2009; Tairidis et al., 2018) in the form of an electric impedance.

This idea was first introduced in the innovative work of Forward (1979) who suggested the use of piezoelectric transducers in association with electric elements which he called shunt circuits for passive vibration control. The main concept consists of the transformation of the dynamic strain energy of the host structure into electric energy. This is achieved by using the direct piezoelectric effect and routing this energy into the shunt circuit where it can be partially consumed (see **Figure 1**).

In fact, shunt piezoelectric systems with an electric impedance can be very effective in structural vibration damping, thus they have been extensively studied during the past decades. Several shunting techniques have been developed based on different shunting methods, (Hollkamp, 1994; Moheimani and Fleming, 2006; Tairidis, in press), in order to deal with the energy which is produced by the structural vibrations. In these techniques, the energy is usually expressed in terms of loss factor or more often of a suitably defined damping ratio, depending on two distinct matters; the contribution of the electromechanical coupling and the design of the shunt system. Therefore, damping can be accurately predicted if the generalized coupling coefficient which describes completely the electromechanical coupling can be described (Delpero et al., 2012).

At this point, it is worth mentioning that in terms of dynamic behavior, certain types of shunt circuits present similarities with several other types of vibration control methods, as for example with tuned mass-dampers. Actually, as shown by Hagood and von Flotow (1991) and Wu (1996), among others, if the shunt circuit consists of a resistance R, i.e., it is a pure resistive shunt, the dynamic behavior of the whole system is similar to the one of a viscoelastic material. In case of resonant, i.e., resistive–inductive (RL) shunt circuit, the influence of the circuit is analogous to the one of a viscously damped dynamic vibration absorber (Viana and Steffen, 2006).

Some even more sophisticated electronic shunt circuits for the increase of the damping capability of the system have been also proposed recently, as it will be shown in the following sections. Such systems include, among others, switched shunts (Ducarne et al., 2010) and negative capacitance circuits (Marneffe and de, 2008).

PIEZOELECTRIC MATERIALS

Piezoelectric materials are very attractive functional materials in smart structures because they can directly convert mechanical energy to electrical and via versa. In 1880, the piezoelectric phenomenon discovered by Curie and Curie (1881) initially discovered the direct piezoelectric effect in the tourmaline crystals. They found that a mechanical deformation in specific directions causes opposite electrical charges on opposite crystalline faces, which are proportional to the magnitude of the mechanical deformation. This phenomenon, which was also observed in quartz and other crystals without a center of symmetry, was called a piezoelectric phenomenon (from the Greek words "πιέζειν-piezein" that means to squeeze or press and "ηλεκτον-ēlektron," which means amber, an ancient source of electric charge. This phenomenon is called the direct piezoelectric effect (as shown in **Figure 2A**). However, when an electric field is applied to the material a mechanical stress or strain is induced; this phenomenon is called the converse piezoelectric effect (see **Figure 2B**). However, the Curie brothers did not predict the reverse piezoelectric effect, which was mathematically deduced from fundamental thermodynamic principles by Lippmann (1881).

Piezoelectric materials present very good electromechanical coupling properties, as well as excellent frequency response, due to their nature. Thus, such materials have been extensively used in vibration control of smart structures, in structural health monitoring, energy harvesting, optimal positioning, etc. The direct phenomenon is mainly used in sensors (detection of structural flaws, vibration suppression, etc.) or for the harvesting of the energy which is produced by the vibrations. On the other hand, the reverse phenomenon is mainly used on actuators. Piezoelectric transducers are available in many forms and shapes, usually in thin sheets, and are capable of producing forces from applied voltages.

Piezoelectric materials exhibit, also by their nature, a non-linear behavior, which is reinforced by their complex grain and domain structure. The understanding of the properties of such materials over a large range of parameters (e.g., temperature, frequency, stresses, etc.) is essential. The knowledge of the electroelastic constitutive behavior is very important in order to predict the response of a structure with embedded piezoelectric sensors and actuators. The non-linear behavior of piezoelectric ceramics is outlined among others in Mukherjee et al. (2001) and Albareda and Pérez (2011). A focused, multidisciplinary review on the field-dependent nonlinear piezoelectricity is provided by Benjeddou (2018). The non-linear constitutive equations for piezoceramic materials are given in detail in Joshi (1992). The analytical modeling of non-linear piezoelectric transducers is investigated, among others, in Mack (2003). According to Mack (2003) a possible reason of the occurrence of non-linearities is the interaction between isotropic elements and the anisotropic piezoelectric sensor.

Optimal control of smart structures with the use of piezoelectric sensors and actuators on vibration suppression was presented in Stavroulakis et al. (2005). Two different control schemes, i.e., LQR and H_2 control, are compared. The results have shown that sufficient vibration suppression can be achieved in smarts structures with the use of piezoelectric materials.

In Buchacz et al. (2013) the control of the characteristics of a piezoelectric mechatronic system is investigated. More specifically, two examples of systems with piezoelectric transducers are considered in order to examine the suppression of vibrations; a single piezoelectric plate glued on a mechanical subsystem surface, and a piezostack, i.e., a set of piezoelectric plates vibrating in a thickness mode. In both cases, the

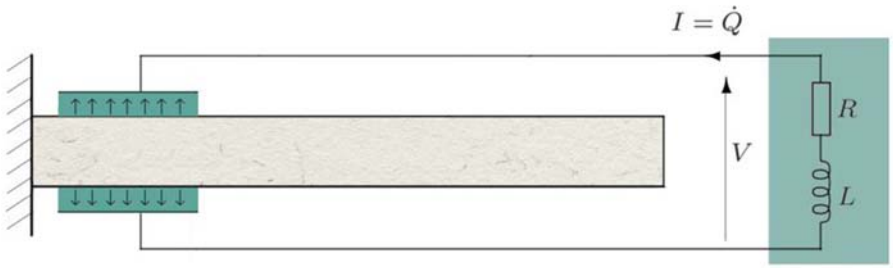

FIGURE 1 | A beam model with a resonant shunt piezoelectric circuit.

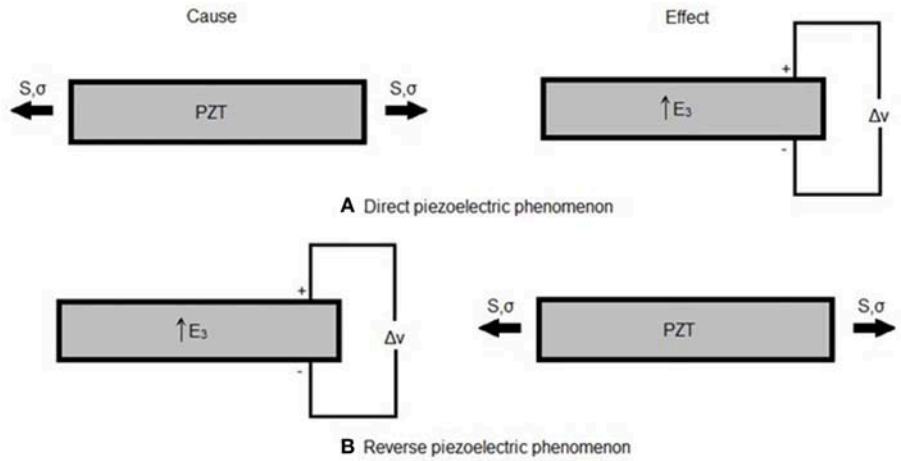

FIGURE 2 | (A) Direct piezoelectric phenomenon, **(B)** Reverse piezoelectric phenomenon.

desired characteristics of the studied systems were generated and presented.

DESCRIPTION OF SHUNT PIEZOELECTRIC SYSTEMS

Shunt systems, also known as shunt piezoelectric systems, are electric circuits connected with piezoelectric elements (e.g., PZT patches, piezoelectric transducers, etc.). Such systems are mostly passive, however, recently, also semi-passive or even active systems have been proposed.

During passive shunt control, a piezoelectric actuator is necessary in order to convert the mechanical energy, which is produced by the vibrations of the structure, into electrical energy. This energy is transferred to the electric elements of the shunt circuit in order to be destroyed, and thus to suppress the vibrations (Corr and Clark, 2003; Fleming and Moheimani, 2004).

The use of piezoelectric patches connected with resistive shunt circuits, i.e., circuits with only a resistance, was first proposed by Hagood and von Flotow (1991). The proposed formulation provided an equivalent vibration damper. Regarding structural damping, resonant shunt circuits (resistive inductive) can also be very useful for the control of single modes. These systems are characterized by the need for specific inductance and resistance values in order to reach the optimum values in terms of vibration attenuation. This is due to the fact that the passive control system uses the principle of dynamic absorbers by tuning the resonance frequency of the shunt circuit to the natural frequency of the structural system. These circuits are equivalent to vibration absorbers within a narrow frequency range.

In general, shunt circuits can be roughly classified into passive and active. Another categorization of these circuits can be into linear and nonlinear. Several approaches with resonant, resistive, capacitive, and switching shunts have been proposed (Niederberger, 2005). The most common shunt circuits are depicted in **Figure 3**.

Piezoelectric Shunt Damping

The basic principles of passive damping with shunted piezoelectric elements are analytically presented in the very recent book of Preumont (2018). Resistive, inductive and resonant shunting are examined. Moreover, several ways of tuning of such systems in terms of inductance are discussed, along with the capabilities of synchronized switch damping. The

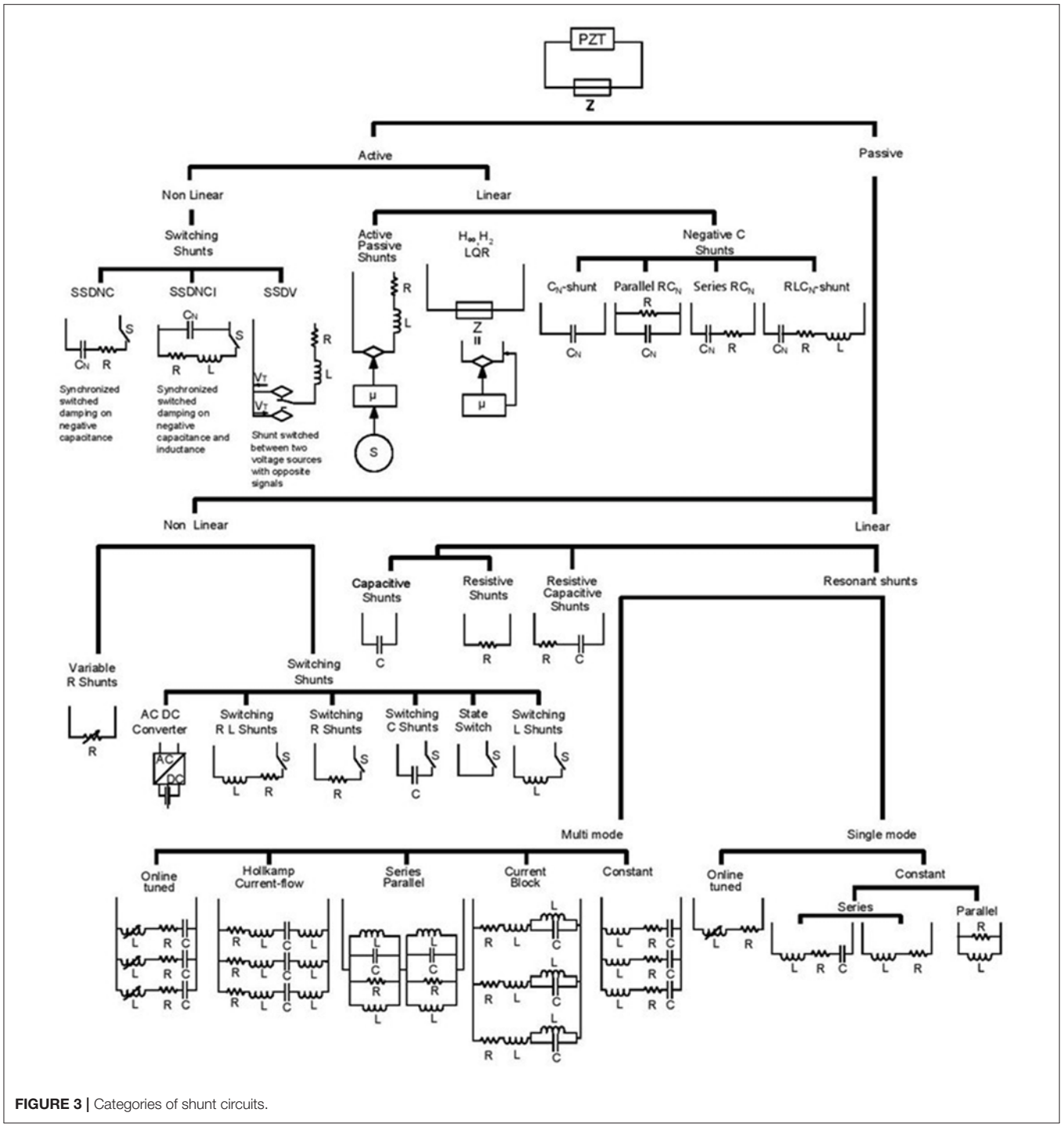

FIGURE 3 | Categories of shunt circuits.

idea of active damping with shunted piezoelectric elements is discussed, among others, in the book of Preumont (2006).

Semi-passive shunt electrical components are used for the tuning of vibration controllers in McDaid and Mace (2016). The system consists by an electromagnet with an adaptive synthetic shunt impedance. The design of the system allows self-tuning and maintenance, even when variations in excitation frequency, environmental conditions or shape properties are present. The control system consist of two different types of controllers and many algorithms for each type are used. Experiments demonstrate that the linear controller is not reliable, however, some good results are obtained for polynomial and fuzzy controllers. The proposed control system adjusts very well to variable excitation frequencies, it is stable and performs efficiently for different modifications of the system's parameters. An RC shunt, i.e., a circuit of a resistor and a capacitor, is developed, and its parameters are adapted online in order to achieve optimal tuning. The results are verified experimentally.

A semi-passive damping technique is presented in Liu and Vasic (2013). The proposed method is based on pulse-width modulation and it can significantly increase the structural damping of the system. With this method, the waveform of the piezoelectric voltage accommodates to the vibration velocity, the system has a stable voltage source and at the same time the performance is increased. The theoretical part of the investigation is also experimentally proved.

The synthesis of electromagnetic shunt impedances for vibration control of structures is studied in Behrens et al. (2004). Namely, a technique of sensor-less active shunt control for application to a mechanical vibration system is proposed. For the minimization of structural vibrations, an electrical impedance was designed and connected to an electromagnetic element. Common control tools were used to design the required shunt impedance. The application of an active shunt impedance reduced the vibration of the structure without the use of any additional feedback sensors.

As an alternative to the above, negative capacitance shunt systems have also been examined by many authors. Among others, Marneffe and de (2008) study a scheme for vibration damping with negative capacitance shunts both theoretically and experimentally. Namely, the enhancement of piezoelectric transducers by means of negative capacitive shunting is considered. Two different implementations are investigated; one in series and one in parallel. The results indicated the lack of robustness of the parallel system. From the experimental results on a truss structure it is shown that the damping which is introduced by the negative capacitance shunt system is larger than the damping which is obtained by the passive shunt circuits.

General Electromechanical Equations of Shunted Piezoelectric Systems

The general electromechanical equations which describe the behavior of piezoelectric materials are defined in the IEEE Standard on Piezoelectricity (American National Standards Institute et al., 1987):

$$\begin{Bmatrix} T \\ D \end{Bmatrix} = \begin{bmatrix} c^E & -e \\ e^t & \varepsilon^s \end{bmatrix} \begin{Bmatrix} S \\ E \end{Bmatrix} \tag{1}$$

After Hamilton's principle and discretization with finite elements for coupled electromechanical systems (Thomas et al., 2009) one has:

$$\begin{bmatrix} M & 0 \\ 0 & 0 \end{bmatrix} \begin{Bmatrix} \ddot{w} \\ \ddot{v} \end{Bmatrix} + \begin{bmatrix} C & 0 \\ 0 & 0 \end{bmatrix} \begin{Bmatrix} \dot{w} \\ \dot{v} \end{Bmatrix} + \begin{bmatrix} K & \Theta \\ \Theta^t & -C_p \end{bmatrix} \begin{Bmatrix} w \\ v \end{Bmatrix} = \begin{Bmatrix} F \\ q \end{Bmatrix} \tag{2}$$

The equation of motion of the coupled piezoelectric electromechanical system, as described in Equation (2), can be rewritten as a set of two coupled equations (Jeon, 2009a,b):

$$[M]\{\ddot{w}\} + [C]\{\dot{w}\} + [K]\{w\}] + [\Theta]\{v\} = \{F\} \tag{3}$$

$$[\Theta]^t \{w\} - \left[C_p\right]\{v\} = \{q\}$$

The first equation describes the equilibrium state of mechanical forces, while the second one gives the electromechanical state of the electric potential. These two equations are used to describe the piezoelectric passive damping force from the piezoelectric shunt damping system, which is connected with the electrodes, to the host structure.

The electric voltage across the piezoelectric patches and the shunt circuit can be represented by the current-voltage ratio in the Laplace domain:

$$V_{sh}(s) = Z_{sh}(s) \cdot I_{sh}(s) \tag{4}$$

Substituting in Equation (4) the electric current $I_{sh}(s)$ with the derivative of the electric charge $\dot{q}(s)$ from the second part of Equations (3), one obtains the relation:

$$V_{sh}(s) = Z_{sh}(s) \cdot \dot{q}(s) = Z_{sh}(s) \cdot ([\Theta]^t \{w\} s - \left[C_p\right] V_{sh}(s) s) \tag{5}$$

Solving Equation (5) for $V_{sh}(s)$, we have the relation:

$$V_{sh}(s) = \frac{Z_{sh}(s)[\Theta]^t \{w\} s}{1 + Z_{sh}(s)\left[C_p\right] s} \tag{6}$$

where s is the Laplace operator.

Substituting the Equation (6) in the first equation of Equation (3) we obtain the relationship of the shunted piezoelectric system where the additional passive piezoelectric damping force is considered:

$$[M]\{\ddot{w}\} + \left([C] + Z_{total}[\Theta][\Theta]^t\right)\{\dot{w}\} + [K]\{w\} = \{F\} \tag{7}$$

where the inherent capacitance Z_{total} of the system includes the total electric impedance of the shunted piezoelectric Z_{sh} as:

$$Z_{total} = \frac{Z_{sh}}{1 + Z_{sh}\left[C_p\right] s} \tag{8}$$

Equation (7) can be transformed into the modal domain using the following modal coordinates:

$$\{w\} = [\Phi]\{\xi\} \tag{9}$$

Substituting Equation (9) into Equation (7) and transforming into the frequency domain, one can obtain the uncoupled equations of motion for harmonic vibrations in the modal domain:

$$-\omega^2[m]\{\xi\} + j\omega([c] + Z_{total}[\Theta]) + [\kappa]\{\xi\} = \{f\} \tag{10}$$

$$\{\xi\} = (-\omega^2[m] + j\omega([c] + Z_{total}[\Theta]) + [\kappa])^{-1}\{f\} \tag{11}$$

Piezoelectric Shunt Acoustic Control

Piezoelectric shunt acoustic control is a more general term, i.e., a superset, of piezoelectric shunt damping, as it includes also systems without damping. The core idea behind this concept for vibration control of mechanical systems is depicted in **Figure 4**.

For the case of acoustic systems (see **Figure 5**), the piezoelectric transducer is embedded into the system and acoustic pressure is applied. The piezoelectric element is used

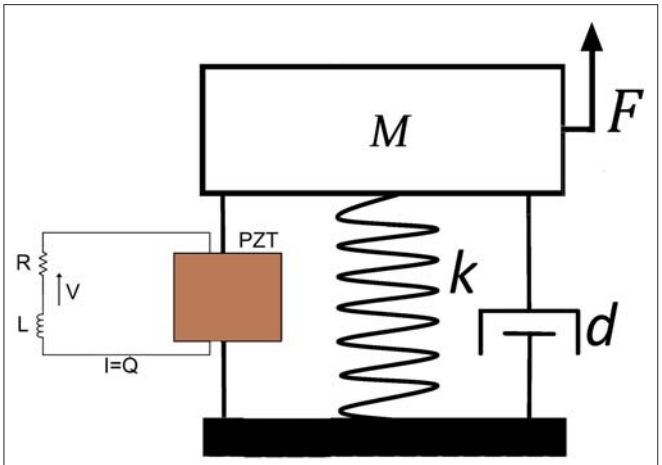

FIGURE 4 | The concept of the piezoelectric shunt acoustic control for vibration control of mechanical systems (shunt damping).

for the deterioration of acoustic signals in the same way it does for the mechanical vibrations. This approach was suggested by Forward (1979) and Forward and Swigert (1981). In these studies, a single piezoelectric element is used between the host structure and the electrical shunt circuit, in a form of a passive resistor or a resonant circuit.

The greater part of the published studies in the field of piezoelectric shunt acoustic control has mainly focused on resonant shunt circuits for the control of vibration and more specifically on vibration damping.

Shunted Piezoelectric Circuits

Single Mode Shunt Circuits

A finite element formulation, as well as, a reduced-order model is proposed for the piezoelectric shunt vibration damping of structural-acoustic systems (Deü et al., 2014). This model is used for the approximation of a fully coupled electromechanical system using modal projection techniques. The piezoelectric patches, along with bonded resonant shunt circuits, are considered for the suppression of the vibrations of the coupled system. The numerical results illustrate the accuracy and the adaptiveness of the proposed reduced-order model, regarding the requested attenuation.

Another efficient finite element formulation, along with a suitably defined set of electromechanical coupling coefficients for an elastic structure with shunted piezoelectric circuits is sought in Thomas et al. (2009). More specifically a numerical simulation with application for control, sensing and vibration reduction is conducted. In parallel, a reduced-order model using modal techniques is proposed in order to show that the electromechanical coupling coefficients are the main parameters in coupling. The results are verified by an application on a cantilever beam.

Numerical modeling of noise and vibration reduction of thin radiating structures in the low frequency range is presented from (Silva et al., 2014). Piezoelectric patches which connected with two types of electrical shunted circuits (resonant and resistive) are used for the analysis. The parameters of placement and size of the piezoelectric patches are optimized with objective the adoption of better results in terms of the reduction of structural vibrations and acoustic radiation.

In Andreaus and Porfiri (2007) the problem of the effect of variations of the electric impedance with respect to its optimal selection in an electric network for resonant piezoelectric shunting system is analyzed.

Two novel electromagnetic shunt damping vibration isolators (EMSD-VIs) are proposed in Yan and Zhang (2012). The aim of the work is the isolation of vibrations of a beam structure. A pair of electromagnetic coils along with a box-shaped spring with variable damping are used. The negative resistance is introduced in order to improve the performance of the isolation system. The design rules of the shunted negative resistance are obtained by stability analysis. An experimental validation of the proposed theoretical model is also carried out.

A detailed study which focuses on the optimization of piezoelectric actuators which are shunted with LR Impedances is presented in Berardengo et al. (2015). Namely various algorithms are used to optimize the values of the electric components of the shunt impedance in order to achieve better performance and guarantee the robustness of the whole system. The algorithms which are presented are in compliance with the tuned mass dampers theory, which is used also for comparison. Analytical and numerical results are confirmed by the ones of a corresponding experiment.

The damping of structural vibrations with piezoelectric materials and passive electrical networks is studied in the work of Hagood and von Flotow (1991). The shunted piezoelectric circuit add some frequency dependent stiffness to the system. The general model is specialized for two different circuits; one with only a resistor (resistive shunt) and one with a resistor and inductor (resonant shunt). The material presents viscoelastic behavior in the case of the resistive shunt, however, when it comes for the resonant shunt with a resistor and an inductor, an electrical resonance is introduced to the system, which in turn can be tuned to structural resonances. An experiment on a cantilevered beam is conducted and the results validate the shunted piezoelectric damping models.

Multimode Shunt Circuits

A new method regarding the use of shunted piezoelectric transducer patches (PZT) for vibration reduction of multiple modes is presented in Fleming et al. (2000). Namely, it is proposed that the vibrational mechanical energy of a structure can be consumed via an electrical impedance by the PZT patches. This method used an arbitrary impedance using a current source and a digital signal processor.

According to Viana and Steffen (2006) the analytical model of passive vibration damping using piezoelectric patches with resonant shunt circuits shows that the general behavior of shunted piezoelectric systems is similar to the classical dynamic vibration absorbers. The study presents interesting analytical and experimental data concerning the design of the interlaced circuits with synthetic inductors.

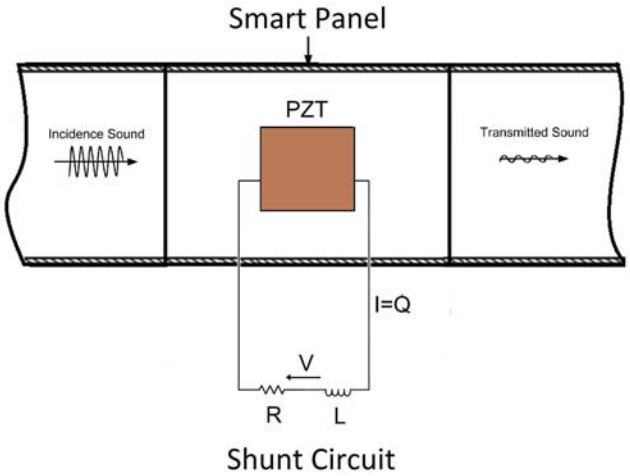

FIGURE 5 | The concept of the piezoelectric shunt acoustic control for control of noise (sound transmission) on a smart panel.

Moreover, Cheng et al. (2009) have employed a multiple current flowing electromagnetic shunt damper for semi-active vibration suppression of flexible structures. The system was electromagnetically-mechanically coupled between the electric circuit and mechanical beam vibration by using an electromagnetic transducer.

A multi-mode passive piezoelectric shunt model is proposed in Berardengo et al. (2017). The shunt damping is investigated by means of matrix inequalities, while the involved impedance is treated as a controller of the electro-mechanical system. The paper focuses on passive multi-mode vibration control in order to find the optimal impedance. The proposed method successfully overcomes the difficulties of multi-mode shunt control strategies. The results of the investigation show the capability of the matrix inequality method to provide sufficient damping. An experimental verification is also carried out.

In the work of Goldstein (2011) a method for the design and online adaptation of multimodal piezoelectric resonant shunts is discussed. The difference between the proposed method and other multi-modal shunting methods, such as current blocking and current flowing, lies to the implementation of the shunting network. Namely, a reduced number of discrete electrical components is used for the online tuning of the parameters of shunt system. The mathematical model provides the coupled equations of motion of the structure with piezoelectric elements and passive shunt networks. The design of the multimodal shunt network is presented based on passive filter synthesis methods. An experimental demonstration of the proposed multimodal self-tuning damper is also presented.

An online tuned multi -mode resonant piezoelectric shunt controller for vibration attenuation is proposed in Niederberger et al. (2004). For the optimal adjustment of the shunt parameters, the relative phase difference between a vibration reference signal and the shunt current is minimized. The proposed technique is validated by experiments. More specifically, it is demonstrated that the damping of two structural modes can be achieved at the same time. The convergence of the adjustment is quick and optimal performance in the presence of uncertainties is maintained.

In Nguyen and Pietrzko (2006) a finite element analysis of a piezo-actuated adaptive aluminum beam with vibration damping which use an electric multiple-mode shunt system is considered. Electric finite elements are used in order to simulate explicitly the R-L shunt circuit. Calculations are also extended to a multiple-mode shunt system, where each branch consists of a parallel R-L shunt circuit in series with two C-L circuits in order to block two different resonance frequencies. The results indicated that in the modified system, only the half of the circuits are needed.

Multiple-mode structural vibration control using negative capacitive shunt damping is studied in Park and Park (2003). A novel shunt piezoelectric circuit, capable of attenuating multimode vibration amplitudes by using a pair of piezoceramic patches is presented. The damping mechanism is described considering a voltage which is constrained by the impedance of the shunt circuit. The presented numerical results indicate that the piezoelectric beam model combined with a series and a parallel resistor-negative capacitor branch circuit can suppress multiple-mode vibration amplitudes over a frequency range of interest with respect to the dynamic response of the whole structure.

Multimodal passive vibration control of sandwich beams with shunted shear piezoelectric materials is investigated in Trindade and Maio (2008). The performance of a multimodal passive vibration control scheme, based on independent resistive shunt circuits, is studied. The shunt control scheme is applied on a sandwich beam core using shear piezoelectric materials. The numerical results indicate that modal damping factors of 1%-2% can be obtained for three selected vibration modes.

An F-15 panel was tested in acoustic excitation in Wu et al. (2000). The aim of proposed method was to examine the ability of the system with bonded piezoelectric elements to control and survive of high acoustic excitation levels, and to investigate the piezoelectric shunt-damping technique at these excitations. Single- and multiple-mode shunting systems were used in order to suppress the first two modes. For this purpose, many piezoelectric components, along with two shunt electric circuits were used. Experimental results are also presented with details.

The use of piezoelectric transducers, shunted with a multi-terminal network, in multimode vibration control is presented in Giorgio et al. (2009). The reduction of vibrations for one- and two-dimensional mechanical structures of shunted piezoelectric transducers with electric networks is studied. Namely, a method for controlling "n" structural modes by "n" piezoelectric transducers shunted with an electric network system is presented. The proposed technique can be classified as a virtual passive damping method.

Lastly, a different approach for the control of several modes is proposed by Tairidis (in press). According to this study, vibration control of different modes can be achieved considering a set of optimized resonant shunt piezoelectric circuits in combination with an intelligent adaptive neuro-fuzzy control system. In this approach, shunt circuits can be pre-tuned to the first four eigenfrequencies and the control system can be used for the

activation of the suitable shunt circuit, each time. This makes the whole system not only adaptive, but effective as well.

Switching Shunt Systems

An autonomous piezoelectric shunt damping system is described in Fleming et al. (2003a). More specifically, an efficient, light-weight, and small-in-size technique for implementing switched-mode piezoelectric shunt damping circuits is presented. The experimental results demonstrate the effectiveness of the shunt circuit implementation, as with the current-flowing shunt circuit, two modes of a simply supported beam were successfully reduced in amplitude by 21.6 and 21.3 dB, respectively. The development of a device which connects research and practical application is also discussed.

Another autonomous shunt circuit for vibration damping is presented in Niederberger and Morari (2006). In this study, an implementation of an autonomous switching resonant (R–L) shunt circuit for the reduction of structural vibrations is described. The resulting circuit does not require power for its operation and is almost as effective as a classic shunt. Moreover, experiments show that the damping performance is robust against temperature variations which are caused due to environmental conditions, whereas other shunt circuits lose their damping performance. The proposed system requires only a minimum number of electronic components; therefore, it can be considered as an effective solution for the control of vibrations.

A third application on autonomous shunt circuits is presented in Niederberger (2005), where a hybrid system for the development of an optimal control system for vibrational damping is studied. More specifically, the system obtains the optimal laws for the switching of the circuits. Multi-parametric programming allows to the calculation of the switching law which is necessary for the partitioning of the state-space into regions where the switch is either open or closed. The electronic shunt circuit requires a small amount of power for its operation, which in some cases can be neglected. From the experimental results it is shown that the proposed autonomous damping circuit could suppress vibrations, but it is not as effective as a standard resonant shunt circuit.

In Ducarne et al. (2010), structural vibration reduction by switch shunting of piezoelectric elements is discussed. More specifically, the study deals with modeling and optimization in terms of the reduction of structural vibrations by means of synchronized switch damping techniques on piezoelectric elements. The electrical impedance is selected either as a simple resistance, which produces a synchronized switch damping on short circuit or a resistance and an inductance in series, where a synchronized switch damping occurs on the inductor. The extra damping which is added by the piezoelectric device is also estimated. From the results it is concluded that the only parameter which needs to be optimized is the piezoelectric coupling factor. In fact, if this parameter is maximized, the damping which is added to the system is maximized as well.

In Collinger et al. (2009) a new vibration control method on beams is presented. The controller is synchronized in every change of the parameters of the system (mass, stiffness, and excitation) and dissipates the maximum amount of energy. The simulation takes into account the coupled dynamics of the structure and piezoelectric circuit to obtain the general coordinates between the sets of modes for the open- and closed-switch modulation. With this method, the time instants of the optimal switching procedure are recognized through a filtered velocity signal. A fuzzy logic algorithm is used in order to maximize depreciation. The efficacy of the method is confirmed by laboratory tests on a headlamp driven by the stimulation of the base and two piezoelectric elements attached to the beam for vibration control.

In Chen et al. (2013) a self-powered damping system based on zero-velocity crossing detection is presented. The control signal is obtained from a velocity sensor which controls the switches of the system. The system does not require any type of external energy, except from the one which is harvested using the synchronized switch damping on inductor (SSDI) technique. The proposed technique has the advantage of no delay switching time, in comparison with the one based on a voltage peak detector. The self-powered technique has been also experimentally tested.

An aggregation of the advantages and disadvantages of the several types of shunt systems which are reviewed in the present paper is outlined in **Table 1**.

From the investigations which are reviewed in the present paper, it is found that resonant shunts, i.e., circuits with inductors and resistors which are tuned around natural frequencies, are the most efficient, in terms of damping of several structures and systems.

Shunt Systems on Composite Structures

Several investigations on beam structures with piezoelectric materials connected with shunt circuits have been proposed in literature. For example, in Lossouarn et al. (2017), a possible design of inductors with high inductance values for resonant piezoelectric damping, which takes into account practical limitations which usually appear in the low frequency range is presented. The electrical elements are integrated into a piezoelectric shunt circuit which is dedicated to the control of vibrations of a cantilever beam. From the results of the analysis, it is shown that specific designs can extend the application of passive resonant shunt strategies, especially for lower frequencies.

In Isola et al. (2004), the passive damping of beam vibrations through distributed electric networks and piezoelectric transducers is studied. The aim of the paper is to present a design of a device for damping, along with experimental validation. For this purpose, two different electric networks were used; a purely resistive network and an inductive–resistive (resonant) one. The feasibility and the effectiveness of the proposed methods, in terms of structural damping, were validated through an experiment, presenting very good agreement with the numerical results.

A passive modal damping method using piezoelectric shunts is presented in Granier et al. (2002). More specifically, piezoelectric materials are used in conjunction with passive inductance-resistance-capacitance (RLC) shunt circuits in order to provide vibration damping in specific modes. The piezoelectric transducers are used for the conversion of mechanical energy into electrical, which, in turn, is consumed in the shunt circuit as heating. In order to test the circuits, an impulse

TABLE 1 | Comparison of shunt systems and methods.

Shunt systems	Advantages	Disadvantages
Single-mode	Easy to implement and tune	Limited capabilities and applicability in real-life applications, medium efficiency
Multi-mode	Wide range of applicability, easy to implement, increased efficiency	Increased complexity, hard to tune
Switching	Wide range of applicability, increased efficiency	Delay of response, increased complexity
Resistive (R)	Easy to implement and tune	Very limited capabilities and real-life applications, poor efficiency
Resonant (RL)	Easy to implement, wide range of applicability, increased efficiency	Not always easy to tune
Resistive-Inductive-Capacitive (RLC)	Wide range of applicability, increased efficiency	Not always easy to implement and tune
Negative capacitance	Increased efficiency, applicability in specialized real-life applications	Increased complexity, hard to tune
Synthetic impedance	Applicability in specialized real-life applications	Increased complexity, not always easy to tune

is applied to a simple cantilever beam and the parameters of the RLC circuit are tuned in order to provide the desired damping.

Piezoelectric RL shunt damping of flexible structures, and more specifically of piezoelectric beams, is discussed in Høgsberg and Krenk (2015b). The calibration of the involved parameters is based on the equal damping of the two eigen modes which are associated with the resonant vibration of the structure. A quasi-static contribution from the non-resonant vibration modes of the structure is also included in the analysis, which leads to explicit calibration expressions for the circuit components. A simple numerical example indicates the effectiveness of the proposed scheme.

Resonant shunt circuits with piezoelectric elements bonded on a thin beam are studied in Hassan et al. (2011). Resonant RL shunt circuits, both in series and in parallel are considered. An iterative process based on finite elements is used in order to find the optimum values of the resistance and the inductance of the system.

A piezoceramic shunted damping concept regarding testing, modeling and correlation on cantilever long beams, which are bonded with single pairs of small piezoceramic patches symmetrically on both surfaces, upper and lower, is presented in Chevallier et al. (2009). Experimental results are used for the evaluation and the assessment of the shunted damping concept of the host structure. The efficiency of the proposed technique is measured by the modal effective electromechanical coupling coefficient, which is calculated from free-vibrations analyses under short- and open-circuit formulations. ABAQUS commercial software is used for the finite element analysis.

In Fleming and Moheimani (2005), a method for the design and the implementation of high-performance piezoelectric shunt impedances in order to control mechanical vibrations is presented. The shunt impedance design can be accomplished by solving a common control problem with parameters the transducer voltage inputs and charge outputs. The impedance which occurs from the proposed method has been compared experimentally with a resonant shunt system on a cantilever beam. The results of the experiment have shown significant reduction of vibrations of the structure in the first mode of the cantilever.

In Buchacz and Płaczek (2011) a one-dimensional flexural vibrating mechatronic system is studied. The system includes a cantilever beam with piezoelectric elements connected with an electric circuit for the damping of vibrations. The Galerkin method was used to analyze the system. The damping of the structure was taken into account. Kelvin-Voigt model of materials was used for the introduction of Rheological properties. The results of the proposed method were presented in 3D graphs.

In the work of Schoeftner and Irschik (2009), passive damping and vibration suppression of beams using shaped piezoelectric layers and tuned inductive networks is studied. More specifically, the study is focused on the development of an extended Bernoulli–Euler beam theory for passive piezoelectric composite structures which considers also the presence of electric networks. From the results it is shown that control of vibrations for a cantilever beam is possible, under certain conditions for the electric elements. In another work of the same group (Schoeftner and Irschik, 2011), a comparative study of smart passive piezoelectric structures interacting with electric networks is carried out. The results from Timoshenko's beam theory are compared with finite element calculations of plane stress.

During the last three decades, several investigations on the use of piezoelectric transducers for the vibration control of thin plate-like structures have been carried out by many authors. In the work of Saravanos (1999), the damping of vibrations of composite plates with passive piezoelectric-resistor elements is studied. It is shown that, for each mode, there is an optimal value of the resistance which adds significant modal damping. Away from this optimal value the damping gradually reduces to zero.

Vibration control of plates with passive electrical dampers made of shunted piezoelectric materials is studied in Park et al. (2005). The electrical absorber, which is proposed in this paper, consists of piezoelectric patches connected with a resistor and an inductor in series and can be considered as an equivalent to the damped mechanical vibration absorber. In order to estimate the effectiveness of the absorber, the equations of motion are derived by the classical laminate plate theory and Hamilton's principle. The theoretical analysis is also experimentally validated for the

simply supported plates and the performance of the passive electrical damper is demonstrated. The resulted model can be used in many engineering applications.

Electrical tuned vibration absorbers are studied by Tondreau et al. (2014). Namely, an application of the equal-peak method to linear and non-linear RL piezoelectric shunts is presented. The major contribution of this study to the current state of the art is to propose a new optimum design of a series RL piezoelectric shunt, and at the same time to apply it on a realistic example. For this purpose, a clamped-free steel plate with piezoelectric layers is considered. The laminate structure is excited by using two piezoelectric actuators and it is shunted with two piezoelectric elements. The improvement of damping performance in the presence of structural non-linearities using a non-linear piezoelectric tuned vibration absorber is presented.

Another application of shunt circuits on smart plates is presented in Kim et al. (2000). The measured electrical impedance is the basic parameter for tuning the parameters of passive piezoelectric damping. Unlike the usual tuning method related to a mechanical vibration absorber, the proposed method uses the electrical impedance model of which parameters are found from measured impedance data. Maximization of the amount of dissipated energy at the electrical components is the basic criterion for optimization. Experiments with cantilever beams and plates shows good accordance of the proposed method with the common methods of tuning. The method can be used for structures of any shape and it is also applicable for multiple-mode piezoelectric damping with the same piezoelectric patch.

Last, but not least, in the work of Saravanos (2000) composite beams with piezoceramic patches, piezoelectric plates and laminated piezoelectric shell structures with integrated electric circuits are studied in terms of passive damping. More specifically, numerical and experimental results are presented for several structural formulations. Form the results, the dependence of piezoelectric damping on shunting resistance, structural shape, and curvature is demonstrated. An important outcome, which occurred by both the analytical and experimental studies, was that regardless of the configuration of the structure, the concept of passive piezoelectric damping is feasible and moreover, the values of the electric components can be easily tuned.

OPTIMIZATION OF SHUNT PIEZOELECTRIC SYSTEMS

Optimization of the Design and of Placement of PZT

Optimal placement and dimension optimization of shunted piezoelectric patches for vibration reduction is the object of study in Ducarne et al. (2012). The investigation is carried out through optimization procedures of the damping performance of both the geometry of the piezoelectric patches and their position in the elastic structure. Optimization is based on maximizing the modal electro-mechanical coupling factor (MEMCF) of the mechanical vibration mode on which the shunt is tuned. Several important conclusions regarding the mechanism of coupling between the piezoelectric patches and the host structure are drawn from the study. The results of the investigation are also confirmed experimentally.

In the work of Bachmann et al. (2012a), a strain energy–based finite element approach for the optimum piezoelectric patch positioning is presented. More specifically, the finite element method is used in order to provide an efficient approximation for the calculation of the coupling coefficient. The method is applied on a smart composite turbomachine blade. Two different placement positions of the piezoelectric patches are proposed. An experiment is conducted for the verification of the results on a blade structure and the coupling coefficient was compared to the calculated values. A novel optimization method based on modal strains was used to calculate both electric charge and generalized electromechanical coupling coefficient of piezoelectric patch transducers.

Actuator location optimization is also studied by Foutsitzi et al. (2013b). In this work, a numerical investigation on the optimal voltages and on the optimal placement of piezoelectric actuators for shape control of beam structures is presented. A hybrid optimization scheme, based on great deluge and genetic algorithms, is proposed. The optimal location of the piezoelectric actuators is sought considering the minimization of the error between the achieved and the desired shape of the structure. The results indicate the efficiency of the proposed method.

Last but not least, in the work of Zorić et al. (2012), a multi-objective fuzzy algorithm for the optimization of sizing and location of piezoelectric elements is proposed. Namely, the location of piezoelectric sensors and actuators on thin-walled beam structures is studied. The optimization criterion is the degree of controllability, while the whole process takes into account the involved constraints from the dynamics of the structure. The discretization is done by using the finite element method, while the optimization is based on the particle swarm method.

Optimization of Shunt Characteristics

In Thomas et al. (2012) the passive damping of vibrations in any form of construction for free and forced oscillation is studied by means of shunted piezoelectric patches. The conclusion from this research is that oscillation reduction performance depends mainly on a single parameter: the so-called modal electromechanical coupling coefficient (MEMCF) of the mechanical vibration mode. Thus, in order to optimally tune the resonant shunt system, one has to find the optimum value of this coefficient. From the experiments, a satisfactory agreement with the proposed theory is achieved.

A new method of adjusting the parameters of shunt circuits for passive piezoelectric damping of structures is presented by Kim et al. (2000). During the adjustment process, the optimal parameters of the shunts are identified from measured impedance data, to maximize the dissipated energy in the shunt circuit.

In Mokrani et al. (2015) a method for the damping of vibrations of structures with piezoelectric transducers is proposed. Specifically, the area near the natural oscillation frequency is studied using an adaptive induction scheme. Linear RL branches for damping of only one mode at a time have been

investigated. The problem is associated with the robustness of the RL branch with respect to resonant frequency variability and it was resolved by adapting the inductor value L through a controlled voltage inducer.

A novel acoustic radiation optimization method for vibrating panel-like structures with passive piezoelectric shunt circuits is presented in Jeon (2009a). The objective of the work is the minimization of the well-radiating modes generated from the panel. The optimization scheme is a mixture of the p-version finite element method, the boundary element method and the particle swarm optimization algorithm. The optimum design works like a stiffener so that well-radiating modes are shifted up. However, the optimized panel require additional damping for attenuating the peak acoustic amplitude, thus a passive shunt damping system is employed. The particle swarm optimization is used in order to achieve the optimum performance for the damping of several modes simultaneously. An experiment is also carried out and it is shown that the numerical results have good agreement with the experimental ones.

In the work of Fleming et al. (2002) a new approach aiming to provide the optimal performance and implementation of piezoelectric circuits is introduced. The method determines the resistance values by minimizing the H2 standard of the dampened system. The short circuits are normally implemented using discrete resistors, virtual inductors and Riordian gyrators. Synthetic impedance, which consists of a voltage controlled current source and a digital signal processor system, is used to synthesize the ultimate impedance of the shunt network.

In the same direction, the induction requirements of piezoelectric transducers can be reduced by adding capacitors to every piezoelectric circuit as proposed in another work of the same group (Fleming et al., 2003b). The theoretical background is presented and experimentally confirmed for two modes of a simply supported beam.

In Krenk and Høgsberg (2009) an optimal method for the design and the implementation of resonant shunt circuits in structural damping is presented. The resonant control includes a resonant shunt circuit, coupled to the structure via the feedback of a sensor and an actuator. A control system with one degree of freedom is initially investigated, and then the method is expanded to structures with many degrees of freedom. There are several multi-d.o.f. applications which vary from ideal models of piezoelectric sensors-actuators application on beams, to accelerometers-actuators devices on cables. For both cases, near-ideal response characteristics were acquired, when the quasi-static correction of the modal properties was considered.

In Park and Inman (2003) a technique which is able to reduce the amplitude of the structural vibrations by using an electrical passive damper with lower inductance, compared to previous attempts is introduced. To achieve this, a modified and amplified piezoelectric circuit, analyzing the mechanical-electrical analogies has been designed in order to provide the system with natural interpretation. The enhanced shunt circuit demonstrated, both theoretically and experimentally, that the vibration function in the concrete cantilever beam has significantly decreased.

A specific formulation for the tuning of vibration absorbers with shunted piezoelectric transducers, as an alternative to classical tuned mass dampers, is presented in Heuss et al. (2016). The characteristics of the absorber can be altered by applying a purely resistive or a resonant shunt circuit. Moreover, the tuning frequency of the damper can be adapted to the excitation frequency, considering a negative capacitance circuit, which requires only a small amount energy in order to supply the electric components of the shunt system.

In the work of Xie et al. (2014) an electromagnetic shunt damping absorber, based on electromagnetic shunt damping, is employed. The governing equations are enriched with the electromagnetic system. The main parameters of the shunt absorber are obtained by using the particle swarm optimization method. More specifically, the minimization of the response of the variance of system is sought. Both numerical and experimental results which indicate that the electromagnetic shunt damping absorber can reduce significantly the vibrations of the structure are presented.

A balance calibration system for RL piezoelectric shunts is discussed in Høgsberg and Krenk (2015a). The procedure is analytically presented. The proposed balanced calibration scheme with explicit correction for background flexibility present some significant advantages, such as equal modal damping, effective reduction of the dynamic amplification, no overshoot of piezoelectric force amplitude and explicit formulas for the system parameters in terms of structural modal properties and the desired damping ratio.

The optimization of the damping properties of electro-viscoelastic objects with external electric circuits is investigated in Matveenko et al. (2015). More specifically, the dynamic characteristics of smart structures with piezoelectric materials are optimized in terms of the resonance frequencies and the damping properties which are provided by external electric shunt circuits which, in turn, incorporate resistance, capacitance and inductance to the system. A natural vibration problem of an electroviscoelastic solid is used for the numerical investigation. Several examples are used in order to demonstrate the efficiency of the proposed method. The shunt circuits can be placed either in series, in parallel, or a combination of them. The advantage of passive piezoelectric damping lies to its capability to tune the damper in a wider frequency range in order to achieve better thermal stability.

A similar study for the optimization of vibration damping for structures with piezoelectric patches, which, however, are shunted with negative capacitance is presented in Wahid et al. (2016). Namely, the ant colony optimization algorithm is used. The frequency range of interest is presented in the context of statistical energy analysis with modal overlap. Two different resistive-negative capacitance (RC) shunt circuits; one in series and one in parallel are studied. The equation of motion is obtained using the Lagrange method, while the ant colony optimization algorithm is used to obtain the optimum values of the shunt circuit for the different frequency areas, for reducing the maximum amount of energy of the vibrating structure.

In Jeon (2009b) another optimization scheme for the improvement of a piezoelectric shunt damping system is

proposed. The objective of this work is to find the optimal electrical parameters of the shunt circuit for the structural vibration suppression of several modes. The vibration reduction is based on the idea of using the integrated p-version finite element method (p-version FEM), and the particle swarm optimization algorithm (PSO). The optimal electrical components are determined by the minimization of the objective function, which is given as the sum of the average velocity at a specific frequency range. The performance of the optimal system in terms of structural damping is shown both numerically and experimentally.

A comparative analysis of the electrical circuits used in piezo-electric passive vibration damping is conducted by Caruso (2001). The analysis is carried out by means of analyzing various electrical circuits, i.e., R-L in series, RL in parallel, and RL-C parallel shunt circuits. The optimum values of the electric variables are obtained by using the pole-placement technique, considering the inherent structural damping of the system. Experimental results, in good agreement with the numerical ones, are also reported.

A detailed study of piezoelectric shunts with a parallel resistor and inductor circuit for passive structural damping and vibration control has been made in Wu (1996). When tuning is optimum, it is easily proved that the peak amplitude of the displacement over the frequency curve of a structural mode decreases with the increase of the shunt resistance. Thus, a "plateau" is created at the area near the optimum resistance. If a further increase of the resistance is considered, the middle of the plateau also decreases, and two peaks appear around the shoulders of the plateau. Structural parameters, such as mass and stiffness, also affect the displacement. When the inductance is larger or smaller than the optimum value, a peak appears on the right or on the left shoulder, respectively.

In the same sense, the optimal electrical circuits for passive vibration damping are sought in Bisegna et al. (2006). In this paper, shunts where an inductance and a capacitance are in parallel and in series with a resistance are proposed. The main focus of the investigation lies on the optimal choice of shunt system to reduce the structural vibrations. An advantage of the proposed modulation is that higher values of the piezoelectric coupling coefficient can be obtained.

In Delpero et al. (2012) a study for the prediction of loss factor in piezoelectric shunt damping, considering the involved electromechanical parameters, is presented. More specifically, an efficient method, which is based on the analysis of the dynamic response of the structure, is proposed for the measurement of the involved coupling coefficient. The method is applied on several structures, with different shunting techniques, i.e., resonant shunts, synchronized switching systems, etc., and the numerical results are compared with the experimental ones.

In Soltani et al. (2014) the optimum tuning rules for piezoelectric shunt control are studied. The piezoelectric transducer is shunted with passive RL electric components for the vibration damping of the host structure. The performance of the proposed method was higher compared to other tuning rules for resonant circuits, even if the improvement of the electromechanical coupling parameters were slight.

Another important aspect, like the minimization of the acoustic radiation of a structure with the use of optimal shunted electrical components with piezoelectric transducers is studied in Collet et al. (2012). The aim of the research was the calculation of the optimal impedance for the reduction of the velocity of the flexural waves. Numerical experiments confirm the proposed method and show the potential for application of the research.

Last but not least, the influence of a digital synthetic impedance on vibration damping applications is studied in Nečásek et al. (2016). The paper presents a compact digital synthetic impedance for application in the field of vibration damping with constructional details. The results of the actual artificial impedance have been compared with several prescribed impedances, resulting in very good performance of the device. An experiment on a one-dimensional spring-mass vibration system, with a piezoelectric actuator incorporated as an interface between the vibration source and vibrating mass, proves the applicability of the proposed model.

APPLICATIONS OF SHUNT PIEZOELECTRIC CIRCUITS

In Kurczyk and Pawelczyk (2016) a shunt circuit with a single piezoelectric transducer and a suitably defined fuzzy system is considered for the noise control of structures. More specifically, a fuzzy inference system is used to adapt the parameters of the electrical circuit. For the optimization of the fuzzy rules, a genetic algorithm is used. The numerical results indicate the efficiency of the method, which is useful for several industrial applications.

Another application of the shunt damping is on the vibration control of hard drives. More specifically, in Lim and Choi (2007) a piezoelectric bimorph shunt damping circuit is used. In the first part of this work, the dynamic analysis and modeling of the system is described. A target vibration mode which significantly restricts the density increment of the hard drive is determined by undertaking both modal testing and finite element analysis tools. For the control of unwanted oscillations, a piezoelectric bimorph is designed and integrated into the system. The mechanical impedance here is derived from the lamination theory and the linear piezoelectric constitutive equations, while the coupling coefficient is incorporated into this impedance. From the numerical results it is shown that the displacement transmissibility can be tuned by adjusting only the coupling coefficient. This implies that the total vibration of the system can be suppressed successfully by activating the piezoelectric shunt circuits which are proposed.

A reduced-order finite element model of double sandwich panels using shunted piezoelectric patches for noise and vibration reduction is developed and presented in Larbi et al. (2016). The paper deals with the suppression of sound transmission through double laminated sandwich panels of three layers each, with viscoelastic core and an air cavity between the layers. A semi-passive piezoelectric shunt technique with resonant circuits is used for the damping of vibrations of specific resonance frequencies of the resulted coupled system. Both a full- and a reduced- order finite element formulation of

the visco-electro-mechanical acoustic system, which takes into account the frequency dependence of the viscoelastic material is presented. More specifically, the coupled system is solved considering the first real short-circuit structural modes, while a static correction is introduced in order to consider the effect of higher eigenmodes. The efficiency of the proposed scheme is illustrated by several results.

A three-hinged arch controlled by piezoelectric stack actuators and passive RL electrical circuits is presented in Pagnini and Piccardo (2016). The proposed system is considered as a simple structural model, which can be used as an ignition in order to generalize to more common civil and industrial engineering structures. The Lagrangian approach is used for the formulation, taking into account the analogy between the electrical and the mechanical model, which can guarantee multi-modal attenuation. Some preliminary results, which indicate the efficiency of the method, are also presented.

An adaptive control strategy based on passive piezoelectric shunt techniques with application to mistuned bladed disks is described in Zhou et al. (2013). Resonant shunted piezoelectric transducers are placed onto the disk between adjacent blades in order to reduce the vibrations of the blade, via the blade–disk coupling. In this study, piezoelectric damping is exploited with the objective of minimizing the blade mistuning effects using genetic algorithms. Numerical experiments indicate that a good performance is achieved.

The self-excited vibration called chatter is a problem which recurs during machining. Passive shunt circuits can increase the system's damping and thus, they can be used to control chatter. In Venter and da Silva (2016) and Venter et al. (2015), a method for reducing chatter in turning using a piezoelectric LR passive shunt strategy is proposed. Firstly, the system is evaluated without any control strategy. Then, LR passive shunts are used in the two main directions of vibration, and the response of the system is analyzed. The electromechanical coupled structure which is considered in the numerical simulations presents FRFs that are very close the experiments. Moreover, the robustness of the passive shunt control strategy for chatter reduction is discussed in Venter and da Silva (2016). Two different boundary conditions formulations are tested experimentally, and the effectiveness of the passive control strategy is shown. The results indicate the lack of robustness of the method, due to its inability to perform well for both conditions, however the damping is increased for the first experiment, where the fixation was selected in a form that the system could maintain its natural frequency.

An application on helicopter rotor blade vibration control on the basis of active/passive piezoelectric dampers is presented in Shevtsov et al. (2009). More specifically, a comparative analysis on the efficiency of the helicopter rotor blades vibration suppression was conducted both by active controlled and passive shunted piezoelectric patches. The obtained results illustrate the efficiency of the proposed method.

A passive damping of composite blades using embedded piezoelectric shunt modules is proposed in Bachmann et al. (2012b). Namely, the potential improvement of the mechanical damping of composite fan blades is sought by using two different passive damping techniques; piezoelectric shunt circuits and shape memory allow wires. From the results of the investigation, both piezoelectric shunt and shape memory alloy damping were effective in terms of passive damping for the application in open rotor fan blade applications.

The vibration damping of turbomachinery components with RL-shunted piezoelectric transducers is discussed in Mokrani et al. (2012). A design rule, capable of overcoming the high level of uncertainties, is given for the RL-shunt circuits. The performance of the proposed schemes is validated through experiments. The results indicate the simplicity, the efficiency and the robustness of the whole system. An application of piezoelectric shunt damping on circular saw blades with autonomous power supply for noise and vibration reduction is presented in Pohl and Rose (2016). Due to the thin blade and the contact of the cutting edges, circular saws suffer of vibrations and tension phenomena, thus a novel damping concept is proposed. The experimental investigation indicates a significant attenuation of the vibration amplitude over a wide range of frequencies when the system is not rotating. In the rotating condition the damping which is achieved is lower and it is limited to a narrower band.

The investigation of Min et al. (2010) focuses on the efficiency of a piezoelectric shunt vibration control of turbine blades, especially for a centrifugal rotation state. Piezoelectric patches are placed on plate specimens and two types of circuits, resistive R circuits and resonant RL circuits are used for testing. The experiments and the analyses are executed both in spinning and in non-spinning conditions. The results show the ability of shunted piezoelectric damping to suppress vibrations under centrifugal loading of turbine blades.

The shunt vibration technology was applied in Kurczyk and Pawełczyk (2018) for noise control. The aim of study was to reduce the noise which comes from outside, by damping vibration control of structures. The control vibration of walls achieved with the use of neural networks. An experimental simulation was carried out to confirm the proposed method.

The use of piezoelectric materials in combination with RL shunt circuits is investigated in Min et al. (2008). The main purpose of study was to reduce the problems of high cycle fatigue (HCF) in of turbomachinery blades which caused from vibrations. Experiments on resonant damping control with shunted piezoelectric elements with passive and active control techniques have shown that the optimal electrical components reduce significantly the vibrations.

In Rana et al. (2013) an observer-based model predictive control (OMPC) scheme is investigated in order to improve the positioning of an Atomic Force Microscope. The design of the control system takes into account the piezoelectric tube scanner (PTS) model. For the consideration of the full-state properties, a Kalman filter is used. Experimental results indicate the efficiency of the control method.

Another application of piezoelectric shunt control is discussed in Fairbairn et al. (2011). The aim of the research was the improvement of the image quality and scan rate of tapping mode Atomic Force Microscopy (AFM). The scan rate is ameliorated by degreasing the quality factor of the micro-cantilever, and the PZT shunt control is applied by using an electrical impedance in series with the cantilever tip

oscillation circuit. The conducted experiment indicates the efficiency of the proposed method in scan rate and image quality improvement.

The electrical control of elasticity with piezoelectric coupling is investigated in Date et al. (2000). When shunt circuits are connected in parallel with a piezoelectric polymer film, the dynamic elastic constant increases. Many separate electrical circuits (resistance, inductance and capacitance circuit) can be used for the measurement of the influence in the elastic constant. Experimental tests of the dynamic elastic constants validate the theoretical model. The results of the research have a particular contribution on sound absorption.

An application of shunt vibration damping is presented in Takigami and Tomioka (2005). More specifically, stationary excitation tests are carried out over a railway passenger vehicle car body for vibration control using piezoelectric transducers with shunt circuits. The experiments were conducted for different types of shunts, and the results indicate the deterioration of frequency response gain between excitation force and acceleration on the floor at the natural frequency, up to about 30%. In a similar investigation of the same group (Takigami and Tomioka, 2008), the suppression of bending vibrations of a 5 m long Shinkansen railway vehicle carbody with small piezoelectric transducers and shunt circuits is studied. The results indicate that the vibrations can be successfully reduced.

ENERGY HARVESTING WITH SHUNT CIRCUITS

A parametric study on a collocated piezoelectric beam vibration absorber and power harvester is conducted in Huang et al. (2016). More specifically, the parametric effects of a piezoelectric beam which is used both as a vibration absorber and a power harvester are investigated. A load resistance which increases with the lumped mass ratio is used in order to harvest the maximum amount of power. Experimental results have proved the existence of a best value for the resistance, however the measured harvested power values were lower than the theoretical ones, due to structural damping and possible divergence of material properties.

A novel electromagnetic resonant shunt tuned mass-damper-inerter with application on wind induced vibration control of building structures and energy harvesting is proposed in Luo et al. (2017). A single degree of freedom system is considered for the study of the performance of the damper. The effectiveness and the robustness of the proposed technique in both the frequency and time domain are shown by the numerical results.

Moreover, the effect of shunted piezoelectric control for the fine-tuning of piezoelectric power harvesters is studied in Lumentut and Howard (2015). Namely, a novel analytical technique on the modeling of shunt circuit control responses for the modification of the electromechanical piezoelectric harvesting structures is presented. The proposed technique presents self-adaptive capabilities in terms of harvesting response, for the adjustment of the frequency band, as well as of the power amplitude of the harvesting devices.

The optimization of piezoelectric energy harvesting devices in order to achieve advanced electromechanical efficiency and frequency range is discussed in Godoy et al. (2014). More specifically, some preliminary results on the topological optimization of the piezoelectric layer which is bonded to a sliding-free plate and connected to shunt circuit are presented. From the obtained results, one concludes that topology optimization of active layers can significantly increase efficiency of the system in terms of the amount of the energy which is harvested per unit mass.

An energy harvesting system for the power supply of a shunt piezoelectric system, i.e., to achieve zero energy consumption have been proposed by Tairidis et al. (2018). The shunt system is developed for the suppression of vibrations of smart structures and it usually needs a small amount of energy in order to operate. Energy harvesting can be proved very effective in this direction. In the method which is proposed by the authors, the whole implementation will be restricted only to the collection of the necessary amount of energy in order to make the system self-sustained.

CONCLUSIONS

Shunt piezoelectric systems have been extensively used for vibration and noise control during the last several years. In fact, resonant shunts are proved to be very efficient and stable for the reduction of vibration on smart piezoelectric structures, such as beams and plates. Moreover, it is proven that if the values of the electrical parameters (e.g., of the inductance, the resistance etc.) are tuned properly, a minimum number of piezoelectric patches can be sufficient. In this direction, the optimization of shunt parameters has also been an object of study in the current state of the art, either for single-mode, as well as for multi-mode shunt circuits as presented in the present review.

From the numerous applications which are reviewed in the present paper, it is clear, as well, that shunt piezoelectric systems can be very effective for several different purposes such as among others, the control of vibrations on hard drives, the noise reduction on acoustic applications, the improvement of the image quality and scan rate of tapping mode Atomic Force Microscopy and so on and so forth.

An interesting idea for further investigation is the extension of the use of Riordian gyrators, as they could possibly solve the problem of large capacitors which are needed in such systems. Moreover, adaptive and/or fuzzy controlled shunt systems as described in Tairidis (in press) should be studied further. Last but not least, shunted piezoelectric systems can be used for the fine-tuning of piezoelectric power harvesters as seen in Tairidis et al. (2018), which is

very important in the direction of designing zero energy consumption systems.

AUTHOR CONTRIBUTIONS

KM did the investigation in the framework of the preparation of his Ph.D. Thesis. GT and GS supervised the work. GT and PK supported the research work and provided with practical help.

FUNDING

 The research work of PK was supported by the Hellenic Foundation for Research and Innovation (HFRI) and the General Secretariat for Research and Technology (GSRT), under the HFRI Ph.D. Fellowship grant (GA. no. 34254).

ACKNOWLEDGMENTS

GT gratefully acknowledges the French Embassy in Greece and the French Government for the funding of his visit to the Structural Mechanics and Coupled Systems Laboratory of the institute Conservatoire national des arts et métiers though a fellowship of the program Séjours scientifiques de haut niveau for new researchers. He would also like to express his sincere gratitude to Prof. Jean-François Deü and Prof. Roger Ohayon for the hospitality at the Institute and the fruitful cooperation.

REFERENCES

Albareda, A., and Pérez, R. (2011). "Non-linear behaviour of piezoelectric ceramics." in *Multifunctional Polycrystalline Ferroelectric Materials. Springer Series in Materials Science*, eds L. Pardo and J. Ricote (Dordrecht: Springer). 681–726. doi: 10.1007/978-90-481-2875-4_15

American National Standards Institute, IEEE Ultrasonics Ferroelectrics and Frequency Control Society, Standards Committee, and Institute of Electrical and Electronics Engineers (1987). *IEEE Standard on Piezoelectricity: An American National Standard.* New York, NY: Institute of Electrical and Electronics Engineers

Andreaus, U., and Porfiri, M. (2007). Effect of electrical uncertainties on resonant piezoelectric shunting. *J. Intell. Material Syst. Struct*. 18, 477–485. doi: 10.1177/1045389X06067116

Bachmann, F., Bergamini, A. E., and Ermanni, P. (2012a). Optimum piezoelectric patch positioning: a strain energy–based finite element approach. *J. Intell. Material Syst. Struct*. 23, 1575–1591. doi: 10.1177/1045389X12447985

Bachmann, F., Oliveira, R., Sigg, A., Schnyder, V., Delpero, T., Jaehne, R., et al. (2012b). Passive damping of composite blades using embedded piezoelectric modules or shape memory alloy wires: a comparative study. *Smart Mater. Struct.* 21:075027. doi: 10.1088/0964-1726/21/7/075027

Behrens, S., Fleming, A. J., and Moheimani, S. O. (2004). "Control Orientated Synthesis of Electromagnetic Shunt Impedances for Vibration Isolation," in *3rd IFAC Symposium on Mechatronic Systems 2004* (Sydney), 301–306. doi: 10.1016/S1474-6670(17)31120-5

Benjeddou, A. (2018). Field-dependent nonlinear piezoelectricity: a focused review. *Int. J. Smart Nano Mater.* 9, 68–84 doi: 10.1080/19475411.2018.1439850

Berardengo, M., Cigada, A., Manzoni, S., and Vanali, M. (2015). Vibration control by means of piezoelectric actuators shunted with lr impedances: performance and robustness analysis. *Shock Vib*. 2015:704265. doi: 10.1155/2015/704265

Berardengo, M., Manzoni, S., and Conti, A. M. (2017). Multi-mode passive piezoelectric shun tdamping by means of matrix in equalities. *J. Sound Vib*. 405, 287–305. doi: 10.1016/j.jsv.2017.06.002

Bisegna, P., Caruso, G., and Maceri, F. (2006). "On the choice of the shunt circuit for single-mode vibration damping of piezoactuated structures," in *Mechanical Modelling and Computational Issues in Civil Engineering*. eds M. Frémond, and F. Maceri, (Berlin: Springer), (389–400). doi: 10.1007/3-540-32399-6_24

Buchacz, A., and Płaczek, M. (2011). Mechatronic system with shunted piezoelectric damper modelled with structural damping. *Proc. Appl. Mathemat. Mech.* 11, 261–262. doi: 10.1002/pamm.201110122

Buchacz, A., Płaczek, M., and Wróbel, A. (2013). Control of characteristics of mechatronic systems using piezoelectric materials. *J. Theor. App. Mech-Pol.* 51, 225–234. Available online at: http://www.ptmts.org.pl/jtam/index.php/jtam/article/view/v51n1p225

Caruso, G. (2001). A critical analysis of electric shunt circuits employed in piezoelectric passive vibration damping. *Smart Mater. Struct*. 10, 1059–1068. doi: 10.1088/0964-1726/10/5/322

Chen, Y.-Y., Vasic, D., Costa, F., Lee, C.-K., and Wu, W.-J. (2013). Self-powered semi-passive piezoelectric structural damping based on zero-velocity crossing detection. *Smart Mater. Struct.* 22:025029. doi: 10.1088/0964-1726/22/2/025029

Cheng, T. H., Wang, X. L., and Oh, I. K. (2009). "Electromagnetic multi-mode shunt damper for flexible beams based on current flowing circuit," in *Proceeding SPIE 7493, Second International Conference on Smart Materials and Nanotechnology in Engineering* (Weihai). doi: 10.1117/12.843409

Chevallier, G., Ghorbel, S., and Benjeddou, A. (2009). Piezoceramic shunted damping concept: testing, modelling and correlation. *Mec. Ind*. 10, 397–411. doi: 10.1051/meca/2009073

Collet, M., Ouisse, M., Ichchou, M. N., and Ohayon, R. (2012). Semi-active optimization of 2D wave dispersion into shunted piezo-composite systems for controlling acoustic interaction. *Smart Mater. Struct.* 21:094002. doi: 10.1088/0964-1726/21/9/094002

Collinger, J. C., Wickert, J. A., and Corr, L. R. (2009). Adaptive piezoelectric vibration control with synchronized switching. *J. Dyn. Syst. Meas Control.* 131:041006. doi: 10.1115/1.3117189

Corr, L., and Clark, W. (2003). A novel semi-active multi-modal vibration control law for a piezoceramic actuator. *J. Vib. Acoust*. 125, 214–222. doi: 10.1115/1.1547682

Curie, P., and Curie, J. (1881). Contractions et dilations produits par des tensions electriques dans les cristeaux hemieedres a faces inclines. *Comptes Rendus de l' Acad. Sci.* 93, 1137–1140.

Date, M., Kutani, M., and Sakai, S. (2000). Electrically controlled elasticity utilizing piezoelectric coupling. *J. Appl. Phys*. 87, 863–868. doi: 10.1063/1.371954

Delpero, T., Bergamini, A. E., and Paolo, E. (2012). Identification of electromechanical parameters in piezoelectric shunt damping and loss factor prediction. *J. Intell. Material Syst. Struct*. 24, 287–298. doi: 10.1177/1045389X12457253

Deü, J.-F., Larbi, W., Ohayon, R., and Sampaio, R. (2014). Piezoelectric shunt vibration damping of structural-acoustic systems: finite element formulation and reduced-order model. *J. Vib. Acoust.* 136:031007. doi: 10.1115/1.4027133

Ducarne, J., Thomas, O., and Deü, J.-F. (2010). Structural vibration reduction by swith shunting of piezoelectric elements: modelling and optimization. *J. Intell. Material Syst. Struct*. 21, 797–816. doi: 10.1177/1045389X10367835

Ducarne, J., Thomas, O., and Deü, J.-F. (2012). Placement and dimension optimization of shunted piezoelectric patches for vibration reduction. *J. Sound Vib.* 331, 3286–3303. doi: 10.1016/j.jsv.2012.03.002

Fairbairn, M. W., Moheimani, S. O., and Fleming, A. J. (2011). "Improving the scan rate and image quality in tapping mode atomic force microscopy with piezoelectric shunt control, in *Australian Control Conference* (Melbourne), 26–31.

Fleming, A., Behrens, S., and Moheimani, S. (2000). "A new approach to piezoelectric shunt damping," in *Proceeding International Symposium on Smart Structures and Microsystems* (Hong Kong).

Fleming, A., Behrens, S., and Moheimani, S. (2002). Optimization and implementation of multimode piezoelectric shunt damping systems. *IEEE/ASME T Mech*. 7, 87–94. doi: 10.1109/3516.990891

Fleming, A., and Moheimani, S. (2004). Improved current and charge amplifiers for driving piezoelectric loads, and issues in signal processing design for synthesis of shunt damping circuits. *J. Intell. Material Syst. Struct*. 15, 77–92. doi: 10.1177/1045389X04039701

Fleming, A. J., Behrens, S., and Moheimani, S. O. (2003a). "An *Autonomous Piezoelectric Shunt Damping System*. In *Proceedings Smart Structures and Materials 2003: Damping and Isolation* (San Diego).

Fleming, A. J., Behrens, S., and Moheimani, S. O. (2003b). Reducing the inductance requirements of piezoelectric shunt damping systems. *Smart Mater. Struct.* 12, 57–64. doi: 10.1088/0964-1726/12/1/307

Fleming, A. J., and Moheimani, S. O. (2005). Control orientated synthesis of high-performance piezoelectric shunt impedances for structural vibration control. *IEEE T-CST*. 13, 98–112. doi: 10.1109/TCST.2004.838547

Forward, R. L. (1979). Electronic damping of vibrations in optical structures. *Appl. Opt*. 18, 690–697. doi: 10.1364/AO.18.000690

Forward, R. L., and Swigert, C. J. (1981). Electronic damping of orthogonal bending modes in a cylindrical mast-experiment. *J. Spacecr Rock*. 18, 5–10. doi: 10.2514/3.28048

Foutsitzi, G. A., Gogos, C. G., Hadjigeorgiou, E. P., and Stavroulakis, G. E. (2013b). Actuator location and voltages optimization for shape control of smart beams using genetic algorithms. *Act* 2, 111–128. doi: 10.3390/act2040111

Giorgio, I., Culla, A., and Vescovo, D. D. (2009). Multimode vibration control using several piezoelectric transducers shunted with a multiterminal network. *Arc. Appl. Mech*. 79, 859–879. doi: 10.1007/s00419-008-0258-x

Godoy, T. C., Trindade, M. A., and Deü, J.-F. (2014). "Topological optimization of piezoelectric energy harvesting devices for improved electromechanical efficiency and frequency range," in *10th World Congress on Computational Mechanics* (São Paulo), 4003–4016. doi: 10.5151/meceng-wccm2012-19664

Goldstein, A. L. (2011). Self-Tuning multimodal piezoelectric shunt damping. *J. Braz. Soc. Mech. Sci. Eng.* 33, 428–436. doi: 10.1590/S1678-58782011000400006

Granier, J. J., Hundhausen, R. J., and Gaytad, G. E. (2002). "Passive modal damping with piezoelectric shunts," in *The 20th International Modal Analysis Conference* (Los Angeles).

Hagood, N., and von Flotow, A. (1991). Damping of structural vibrations with piezoelectric materials and passive electrical networks. *J. Sound Vib*. 146, 243–268. doi: 10.1016/0022-460X(91)90762-9

Hassan, H., Yves, B., and Razek, A. (2011). "Finite element model of a beam structure with piezoelectric patches using RL shunt circuits," in *14th International Conference on Active Systems for Dynamics Markets* (Darmstadt), (124–131).

Heuss, O., Salloum, R., Mayer, D., and Melz, T. (2016). Tuning of a vibration absorber with shunted piezoelectric transducers. *Arch. Appl. Mech.* 86, 1715–1732. doi: 10.1007/s00419-014-0972-5

Høgsberg, J., and Krenk, S. (2015a). Balanced calibration of resonant piezoelectric RL shunts with quasi-static background flexibility correction. *J. Sound Vib*. 341, 16–30. doi: 10.1016/j.jsv.2014.12.006

Høgsberg, J., and Krenk, S. (2015b). "Piezoelectric RL shunt damping of flexible structures," in *7th ECCOMAS Thematic Conference on Smart Structures and Materials*. (Ponta Delgada).

Hollkamp, J. J. (1994). Multimodal passive vibration suppression with piezoelectric materials and resonant shunts. *J. Intel. Mat. Syst Str*. 5, 49–57. doi: 10.1177/1045389X9400500106

Huang, S.-C., Tsai, C.-Y., and Liao, H.-H. (2016). Parametric study on a collocated PZT beam vibration absorber and power harvester. *J. Mech. Sci. Technol*. 30, 4877–4885. doi: 10.1007/s12206-016-1006-8

Isola, F., d., Maurini, C., and Porfiri, M. (2004). Passive damping of beam vibrations through distributed electric networks and piezoelectric transducers: prototype design and experimental validation. *Smart Mater. Struct*. 13, 299–308. doi: 10.1088/0964-1726/13/2/008

Jeon, J.-Y. (2009a). Passive acoustic radiation control for a vibrating panel with piezoelectric shunt damping circuit using particle swarm optimization algorithm. *J. Mech. Sci. Technol*. 23, 1446–1455. doi: 10.1007/s12206-009-0349-9

Jeon, J.-Y. (2009b). Passive vibration damping enhancement of piezoelectric shunt damping system using optimization approach. *J. Mech. Sci. Technol*. 23, 1435–1445. doi: 10.1007/s12206-009-0402-8

Joshi, S. P. (1992). Non-linear constitutive relations for piezoceramic materials, *Smart Mater. Struct.* 1, 80–83 doi: 10.1088/0964-1726/1/1/012

Kim, J., Ryu, Y.-H., and Choi, S.-B. (2000). New shunting parameter tuning method for piezoelectric damping based on measured electrical impedance. *Smart Mater. Struct*. 9, 868–877. doi: 10.1088/0964-1726/9/6/318

Krenk, S., and Høgsberg, J. (2009). Optimal resonant control of flexible structures. *J. Sound Vib*. 323, 530–554. doi: 10.1016/j.jsv.2009.01.031

Kurczyk, S., and Pawelczyk, M. (2016). "Structural noise control using a shunt circuit with single piezoelectric transducer and fuzzy algorithm," in *The 23rd International Congress on Sound and Vibration* (Athens).

Kurczyk, S., and Pawełczyk, M. (2018). Nonlinear structural acoustic control with shunt circuit governed by a soft-computing algorithm. *Arch. Acoust*. 43, 397–402. doi: 10.24425/123911

Larbi, W., Deü, J.-F., and Ohayon, R. (2016). Finite element reduced order model for noise and vibration reduction of double sandwich panels using shunted piezoelectric patches. *Appl. Acoust*. 108, 40–49. doi: 10.1016/j.apacoust.2015.08.021

Lim, S. C., and Choi, S. B. (2007). Vibration control of an HDD disk-spindle system utilizing piezoelectric bimorph shunt damping: I. dynamic analysis and modeling of the shunted drive. *Smart Mater. Struct*. 16, 891–900. doi: 10.1088/0964-1726/16/3/039

Lippmann, G. (1881). Principe de la conservation de l'électricité (Principle of the conservation of electricity). *Ann. de Chimie et de Physique*. 24:145. doi: 10.1038/024140b0

Liu, Y.-P., and Vasic, D. (2013). semi-passive piezoelectric structural damping based on a pulse-width modulation switching circuit. *J. Mech. Sci. Technol*. 27, 1–9. doi: 10.1007/s12206-013-0906-0

Lossouarn, B., Aucejo, M., Deü, J.-F., and Multon, B. (2017). Design of inductors with high inductance values for resonant piezoelectric damping. *Sens. Actuator A-Phys*. 259, 68–76. doi: 10.1016/j.sna.2017.03.030

Lumentut, M. F., and Howard, I. M. (2015). Effect of shunted piezoelectric control for tuning piezoelectric power harvesting system responses—analytical techniques. *Smart Mater. Struct.* 24:105029. doi: 10.1088/0964-1726/24/10/105029

Luo, Y., Sun, H., Wang, X., Zuo, L., and Chen, N. (2017). Wind induced vibration control and energy harvesting of electromagnetic resonant shunt tuned mass-damper-inerter for building structures. *Shock Vib.* 2017:4180134. doi: 10.1155/2017/4180134

Mack, O. (2003). "The non-linearity of piezoelectric force transducers and their analytical modelling," in *Proceedings, XVII IMEKO World Congress* (Dubrovnik).

Marneffe, B., de, and Preumont, A. (2008). Vibration damping with negative capacitance shunts: theory and experiment. *Smart Mater. Struct.* 17:035015. doi: 10.1088/0964-1726/17/3/035015

Matveenko, V. P., Yurlov, M. A., and Yurlova, N. A. (2015). "Optimization of the damping properties of electro-viscoelastic objects with external electric circuits," in *Mechanics of Advanced Materials*, eds V. V Silberschmidt, and V.P Matveenko (Cham: Springer), 79–100. doi: 10.1007/978-3-319-17118-0_4

McDaid, A. J., and Mace, B. R. (2016). A robust adaptive tuned vibration absorber using semi-passive shunt electronics. *IEEE Trans. Ind. Electron*. 63, 5069–5077. doi: 10.1109/TIE.2016.2554541

Min, J. B., Duffy, K. P., Choi, B. B., Morrison, C. R., Jansen, R. H., and Provenza, A. J. (2008). "A resonant damping study using piezoelectric materials," in *49th AIAA/ASME/ASCE/AHS/ASC Structures, Structural Dynamics, and Materials* (Schaumburg). doi: 10.2514/6.2008-2335

Min, J. B., Duffy, K. P., and Provenza, A. J. (2010). "Shunted piezoelectric vibration damping analysis including centrifugal loading effects," in *Structural Dynamics and Materials Conference* (Orlando), 2716. doi: 10.2514/6.2010-2716

Moheimani, R. S., and Fleming, A. J. (2006). *Piezoelectric Transducers for Vibration Control and Damping*. London: Springer-Verlag.

Mokrani, B., Bastaits, R., Viguié, R., and Preumont, A. (2012). "Vibration damping of turbomachinery components with piezoelectric transducers: Theory and Experiment," in *International Conference on Noise and Vibration Engineering, Proceedings of ISMA 2012* (Leuven), 345–356.

Mokrani, B., Burda, I., Tian, Z., and Preumont, A. (2015). "Uncertainty, adaptive inductor for vibration damping in presence of uncertainty," in *7th ECCOMAS Thematic Conference on Smart Structures and Materials* (Ponta Delgada).

Mukherjee, B. K., Ren, W., Liu, S.-F., Masys, A. J., and Yang, G. (2001). "Nonlinear properties of piezoelectric ceramics," in *Smart Structures and Materials 2001: Active Materials: Behavior and Mechanics, Proceedings of SPIE*, ed C. S. Lynch (Newport Beach, CA). doi: 10.1117/12.432738

Nečásek, J., Václavík, J., and Marton, P. (2016). Digital synthetic impedance for application in vibration damping. *Rev. Sci. Instrum.* 87:024704. doi: 10.1063/1.4942085

Nguyen, C., and Pietrzko, S. (2006). "FE analysis of a PZT-actuated adaptive beam with vibration damping using an electric multiple-mode shunt system,"

in *International Conference on Noise and Vibration Engineering, Proceedings of ISMA 2006* (Leuven), 461–472.

Niederberger, D. (2005). "Design of optimal autonomous switching circuits to suppress mechanical vibration hybrid systems: computation and control,"in *8th International Workshop, HSCC 2005* (Zurich), 511–525. doi: 10.1007/978-3-540-31954-2_33

Niederberger, D., Fleming, A., Moheimani, S. O., and Morari, M. (2004). "Online-tuned multi-mode resonant piezoelectric shunt for broadband vibration suppression," in *3rd IFAC Symposium on Mechatronic Systems 2004* (Sydney), 37, 295–300. doi: 10.1016/S1474-6670(17)31119-9

Niederberger, D., and Morari, M. (2006). An autonomous shunt circuit for vibration damping. *Smart Mater. Struct*, 15, 359–364. doi: 10.1088/0964-1726/15/2/016

Pagnini, L. C., and Piccardo, G. (2016). The three-hinged arch as an example of piezomechanic passive controlled structure. *Continu. Mech Therm*. 28, 1247–1262. doi: 10.1007/s00161-015-0474-x

Park, C. H., and Inman, D. J. (2003). Enhanced piezoelectric shunt design. *Shock Vib*. 10, 127–133. doi: 10.1155/2003/863252

Park, C. H., Kim, Y. H., and Park, H. C. (2005). Dynamic formulations of plates with shunted piezoelectric materials. *J. Intel. Mater. Syst. Struct*. 16, 971–976. doi: 10.1177/1045389X05053781

Park, C. H., and Park, H. C. (2003). Multiple-mode structural vibration control using negative capacitive shunt damping. *J. Mech. Sci. Technol*. 17, 1650–1658. doi: 10.1007/BF02983594

Pohl, M., and Rose, M. (2016). Piezoelectric shunt damping of a circular saw blade with autonomous power supply for noise and vibration reduction. *J. Sound Vib*. 361, 20–31. doi: 10.1016/j.jsv.2015.09.021

Preumont, A. (2006). Mechatronics Dynamics of Electromechanical and Piezoelectric Systems. Solid Mechanics and Its Applications. Cham: Springer.

Preumont, A. (2018). *Vibration Control of Active Structures. Solid Mechanics and Its Applications*. Cham: Springer.

Rana, M. S., Pota, H. R., and Petersen, I. R. (2013). "Advanced control of atomic force microscope for faster image scanning," in *Applied Methods and Techniques for Mechatronic Systems*, eds L. Liu, Q. Zhu, L. Cheng, Y. Wang, and D. Zhao (Berlin; Heidelberg: Springer), 371–388. doi: 10.1007/978-3-642-36385-6_19

Saravanos, D. (1999). Damped vibration of composite plates with passive piezoelectric-resistor elements. *J. Sound Vib*. 221, 867–885. doi: 10.1006/jsvi.1998.2037

Saravanos, D. (2000). Passively damped laminated piezoelectric shell structures with integrated electric networks. *AIAA J*. 38, 1260–1268. doi: 10.2514/2.1096

Schoeftner, J., and Irschik, H. (2009). Passive damping and exact annihilation of vibrations of beams using shaped piezoelectric layers and tuned inductive networks. *Smart Mater. Struct*. 18:125008. doi: 10.1088/0964-1726/18/12/125008

Schoeftner, J., and Irschik, H. (2011). A comparative study of smart passive piezoelectric structures interacting with electric networks: Timoshenko beam theory versus finite element plane stress calculations. *Smart Mater. Struct*. 20:025007. doi: 10.1088/0964-1726/20/2/025007

Shevtsov, S., Soloviev, A., Acopyan, V., and Samochenko, I. (2009). "Helicopter rotor blade vibration control on the basis of active/passive piezoelectric damping approach," in *PHYSCON* (Catania).

Silva, L., Deü, J.-F., Larbi, W., and Trindade, M. (2014). "An efficient finite element approach for reduction of structural vibration and acoustic radiation by passive shunted piezoelectric systems," in *10th World Congress on Computational Mechanics* (Sao Paulo: Blucher Mechanical Engineering Proceedings).

Soltani, P., Kerschen, G., Tondreau, G., and Deraemaeker, A. (2014). Piezoelectric vibration damping using. *Smart Mater. Struct*. 23:125014. doi: 10.1088/0964-1726/23/12/125014

Stavroulakis, G., Foutsitzi, G., Hadjigeorgiou, E., Marinova, D., and Baniotopoulos, C. (2005). Design and robust optimal control of smart beams with application on vibrations suppression. *Adv. Eng. Softw*. 36, 806–813. doi: 10.1016/j.advengsoft.2005.03.024

Tairidis, G. K. (in press). Vibration control of smart composite structures using shunted piezoelectric systems and neuro-fuzzy techniques. *J. Vib. Control*.

Tairidis, G. K., Marakakis, K., Koutsianitis, P., Foutsitzi, G., Stavroulakis, G. E., Deü, J.-F., et al. (2018). "Energy harvesting system for the power supply of a shunt piezoelectric system developed for vibration suppression," in *Proceedings of the international conference on wind energy harvesting* (Catanzaro Lido), 223–227.

Takigami, T., and Tomioka, T. (2005). Investigation to suppress bending vibration of railway vehicle carbodies using piezoelectric elements. *Q. Rep. RTRI* 46, 225–230. doi: 10.2219/rtriqr.46.225

Takigami, T., and Tomioka, T. (2008). Bending vibration suppression of railway vehicle carbody with piezoelectric elements. *J. Mech. Syst. Transp. Logist*. 1, 111–121. doi: 10.1299/jmtl.1.111

Thomas, O., Deü, J.-F., and Ducarne, J. (2009). Vibrations of an elastic structure with shunted piezoelectric patches: efficient finite element formulation and electromechanical coupling coefficients. *Int. J. Numer Meth. Eng*. 80, 235–268. doi: 10.1002/nme.2632

Thomas, O., Ducarne, J., and Deu, J.-F. (2012). Performance of piezoelectric shunts for vibration reduction. *Smart Mater. Struct*. 21:015008. doi: 10.1088/0964-1726/21/1/015008

Tondreau, G., Soltani, P., and Kerschen, G. (2014). "Electrical tuned vibration absorber: application of the equal-peak method to linear and non-linear RL piezoelectric shunts," in *25nd International Conference on Adaptive Structures and Technologies* (Hague).

Trindade, M. A., and Maio, C. E. (2008). Multimodal passive vibration control of sandwich beams with shunted shear piezoelectric materials. *Smart Mater. Struct*. 17:055015. doi: 10.1088/0964-1726/17/5/055015

Venter, G. S., and da Silva, M. M. (2016). "On the robustness of the passive shunt control strategy for chatter reduction," in *International Conference of Noise and Vibration Engineering* (Curitiba), 3721–3734.

Venter, G. S., Missura, L., and da Silva, M. M. (2015). "Reducing chatter in turning using a piezoelectric LR passive shunt strategy," in *23rd ABCM International Congress of Mechanical Engineering* (Rio de Janeiro).

Viana, F. A., and Steffen, J. V. (2006). Multimodal vibration damping through piezoelectric patches and optimal resonant shunt circuits. *J. Braz. Soc. Mech. Sci. Eng*. 28, 293–310. doi: 10.1590/S1678-58782006000300007

Wahid, A. N., Muthalif, A. G., and Nor, K. A. (2016). Investigating negative capacitance shunt circuit for broadband vibration damping and utilizing ACO for optimization. *Int. J. Circuits Electron.* 1, 168–173. Available online at: https://www.iaras.org/iaras/journals/computer-science-communications/caijce/investigating-negative-capacitance-shunt-circuit-for-broadband-vibration-damping-and-utilizing-aco-for-optimization

Wu, S.-Y. (1996). "Piezoelectric shunts with a parallel R-L circuit for structural damping and vibration control," in *Symposium on Smart Structures and Materials* (San Diego), 259–269. doi: 10.1117/12.239093

Wu, S.-Y., Turner, T. L., and Rizzi, S. A. (2000). "Piezoelectric shunt vibration damping of F-15 panel under high acoustic excitation," in *Proceedings of SPIE - The International Society for Optical Engineering* (Newport Beach).

Xie, S., Li, P., Zhang, X., and Yan, B. (2014). Vibration suppression of structure with electromagnetic shunt damping absorber. *Int. J. Appl. Electrom*. 45, 395–402. doi: 10.3233/JAE-141856

Yan, B., and Zhang, X. N. (2012). Vibration isolation of a beam via negative resistance electromagnetic shunt dampers. *J. Intell. Mater. Syst. Struct*. 23, 665–673. doi: 10.1177/1045389X12437889

Zhou, B., Thouverez, F., and Lenoir, D. (2013). An adaptive control strategy based on passive piezoelectric shunt techniques applied to mistuned bladed disks. *J. Comput. Appl. Math*. 246, 289–300. doi: 10.1016/j.cam.2012.06.023

Zorić, N. D., Simonović, A. M., Mitrović, Z. S., and Stupar, S. N. (2012). Multi-Objective fuzzy optimization of sizing and location of piezoelectric actuators and sensors. *FME Transac.* 40, 1–9. Available online at: https://www.mas.bg.ac.rs/istrazivanje/fme/vol40

Conflict of Interest Statement: The authors declare that the research was conducted in the absence of any commercial or financial relationships that could be construed as a potential conflict of interest.

frontiers in Built Environment

ORIGINAL RESEARCH
published: 26 November 2019
doi: 10.3389/fbuil.2019.00140

Selecting and Scaling of Energy-Compatible Ground Motion Records

George Papazafeiropoulos, Manolis Georgioudakis and Manolis Papadrakakis*

School of Civil Engineering, Institute of Structural Analysis and Antiseismic Research, National Technical University of Athens, Athens, Greece

We propose a novel spectra-matching framework, which employs a linear combination of raw ground motion records to generate artificial acceleration time histories perfectly matching a target spectrum, taking into account not only the acceleration but also the seismic input energy equivalent velocity. This consideration is leading to optimum acceleration time histories which represent actual ground motions in a much more realistic way. The procedure of selection and scaling of the suite of ground motion records to fit a given target spectrum is formulated by means of an optimization problem. Characteristic ground motion records of different inherent nature are selected as target spectra, to verify the effectiveness of the algorithm. In order to assess the robustness and accuracy of the proposed methodology the seismic performance of single- and multi- degree of freedom structural systems has been also considered. The portion of the seismic input energy that is dissipated due to viscous damping action in the structure is quantified. It is shown that there exists a good agreement between the target and optimized spectra for the different matching scenarios examined, regardless of the nature of target spectra, demonstrating the reliability of the proposed methodology.

Keywords: Fast Fourier Transform, genetic algorithm, artificial ground motion records, seismic input energy, selection, scaling

OPEN ACCESS

Edited by:
Vagelis Plevris, OsloMet—Oslo Metropolitan University, Norway

Reviewed by:
Afaq Ahmad, University of Engineering and Technology, Pakistan
Sameh Samir F. Mehanny, Cairo University, Egypt

****Correspondence:***
Manolis Georgioudakis
geoem@mail.ntua.gr

Specialty section:
This article was submitted to Computational Methods in Structural Engineering, a section of the journal Frontiers in Built Environment

Received: *24 September 2019*
Accepted: *08 November 2019*
Published: *26 November 2019*

Citation:
Papazafeiropoulos G, Georgioudakis M and Papadrakakis M (2019) Selecting and Scaling of Energy-Compatible Ground Motion Records. Front. Built Environ. 5:140. doi: 10.3389/fbuil.2019.00140

INTRODUCTION

The response history analysis for the seismic design and the evaluation of the performance of structures has evolved along with the rapid increase in the computational power of the various engineering software. This has enabled not only the application of a faster and more accurate linear elastic time history analysis of structures having some thousands degrees of freedom, but also of the nonlinear time history response analysis which is becoming more and more common nowadays. Traditionally, the seismic design of structures is based on a force-based and/or displacement based approach, in which the effect of the earthquake loading is quantified using the peak ground and response spectra acceleration of the corresponding ground motion record. However, the current status of the various norms regarding the selection of suitable ground motion records that meet specific requirements is rather simplified, which, despite the robustness of the various finite element models available for seismic design, may account for significant source of error in structural design. Therefore, the selection of appropriate sets of ground motion records for linear/nonlinear dynamic analysis of structures remains a challenge.

Although, large ground motion databases are today widely available, in engineering practice, the problem of record selection is tackled either through scaling a real ground motion, or generating them artificially. A state-of-the-art review on the available methods for selection and scaling of ground motion records is presented by Katsanos et al. (2010), whereas some critical issues in record selection and manipulation are presented by Iervolino et al. (2008). In case of limited availability of appropriate real acceleration time-histories, simulated strong motion records can be used (Boore, 2009; Graves and Pitarka, 2010). The generation of artificial/simulated spectrum-compatible ground motion records has some disadvantages against real ground motions. Artificial records have generally a large number of cycles of strong motion, which leads to increased energy content compared to real ground motions. Adjusting the Fourier spectrum of a real ground motion in the frequency domain with a view to matching a target spectrum at specific frequencies affects amplitude, frequency content and phasing, which generally tends to increase the total input energy. The same deficiencies are observed also in the simulated records, which may not produce similar nonlinear response in structures as real records due to unrealistic phasing as well as peaks and troughs effects (Atkinson and Goda, 2010).

An alternative formulation of the loading effect of earthquakes on structures can be based on the earthquake input energy, which is the internal product of force and displacement. Energy considerations for the seismic design of structures constitutes the basis of the energy-based seismic design (EBSD) approach and is gaining extensive attention (Uang and Bertero, 1988; Chou and Uang, 2003; Surahman, 2007; Leelataviwat et al., 2009; Jiao et al., 2011; López Almansa et al., 2013). Since in the EBSD methods the energy-absorption capacity of the structure and the input energy that comes from the ground motion are compared for seismic design, it is imperative to develop and use design energy input spectra (DEIS).

EBSD has many benefits and compensates the deficiencies related to the use of conventional acceleration or pseudo-acceleration response spectra as follows: (a) It accounts for the effects of duration of the cyclic loading of the earthquake ground motion. Therefore, it can adequately capture the different type of time histories (impulsive, non-impulsive, periodic with long-duration pulses, etc.) regarding their destructive potential. (b) It enables the quantitative evaluation of the cumulative structural damage in terms of hysteretic energy without the need to use equivalent viscous damping and/or ductility reduction. (c) There is no interdependence between the earthquake input energy and the structural resistance in terms of energy dissipation capacity. (d) The input energy that a structure experiences during an earthquake is governed primarily by its eigenperiod and mass and less by its strength or damping, except for the short-period range (Zahrah and Hall, 1984; Akiyama, 1985; Kuwamura and Galambos, 1989). This has been verified experimentally by Tselentis et al. (2010). Therefore, the input energy is a stable quantity that does not depend on many factors and thus is simpler to handle and interpret.

Given the advantages of the EBSD over the traditional approaches, the incorporation of not only acceleration spectra but also energy-based spectra for the generation of artificial ground motion records is an interesting alternative that could lead to more realistic spectrum-compatible design records (Chapman, 1999; Tselentis et al., 2010). Actually, it has been demonstrated that if the hazard is assessed on the basis of the earthquake input energy, the hazard posed by larger magnitude earthquakes contributes more to the total seismic hazard at a specific site, than that based on spectral acceleration (Tselentis et al., 2010). It is noted that the input energy spectrum that is obtained elastically is valid also for inelastic systems since the strength and plastification of the structure do not practically affect the total energy input (López Almansa et al., 2013; Dindar et al., 2015).

In this study a novel spectra-matching framework is developed, to generate artificial acceleration time histories perfectly matched a target spectrum. Apart from the well-known design acceleration spectrum that is prescribed by the various norms and guidelines, the seismic input energy equivalent velocity spectrum is also taken into account. This consideration is leading therefore to optimum acceleration time histories which represent actual motions in a much more realistic way. In order to produce elastic spectra that match as closely as possible to a given target spectrum, the procedure of selection and scaling of the suite of ground motion records to fit a given target spectrum is formulated as an optimization problem. Three characteristic ground motion records of different inherent nature are selected as target spectra, to verify the effectiveness of the proposed algorithm, ensuring that its performance is target spectrum independent assuming different matching scenarios. The optimization results have shown that there exists a good agreement between the target and optimum spectra for each case examined, regardless of the nature of target spectrum, demonstrating the reliability and performance of the proposed methodology.

NUMERICAL MODELING

The main goal of this study is to obtain artificial ground motion records by performing as minimum as possible number of operations on the raw ground motion data. These ground motion records are linearly combined together forming a suite of records. The procedure of selection and scaling of the suite of ground motion records to fit a given target spectrum is formulated as an optimization problem. In this section, the process of the raw ground motion data as well as the ingredients for the formulation of the optimization problem are presented.

Processing Raw Ground Motion Data

A linear combination of real accelerograms requires only selection and scaling of the latter and does not alter their inherent characteristics (e.g., non-stationarity, coda, phase content, etc.), which have to be preserved in order to obtain realistic artificial records as a result of the linear combination. Since the real records have various durations, linear combination cannot be applied directly to the acceleration time histories. However, it can be applied to their Fourier spectra in the frequency domain which have the same length for all motions; the resulting time history

can be obtained by the inverse Fourier transform of the Fourier spectra of a suite of m ground motion records as follows:

$$\ddot{u}_{g,c} = IFFT\left(\sum_{i=1}^{m} x_i FFT\left(\ddot{u}_{g,i}\right)\right) \tag{1}$$

where $\ddot{u}_{g,i}$ is the acceleration time history, $FFT\left(\ddot{u}_{g,i}\right)$ is its Fast Fourier Transform, x_i is the combination coefficient, respectively, of the i-th ground motion, $IFFT()$ is the inverse Fourier transform and $\ddot{u}_{g,c}$ is the linear combination of the accelerations of ground motions records in the suite. Given that the Fourier transform of any real ground motion record is a linear transformation, it can be established that Equation (1) effectively combines linearly the various records involved. In this way, the artificial time history that is generated depends only on selection and scaling of the participating ground motion records and also on the values of the combination coefficients x_i, i.e., scale factors.

It is apparent that an inverse Fourier transform of a signal in the frequency domain which is a linear combination of Fourier-transformed signals, requires a time step which has to be identical to that used for the Fourier transform of the original records, in order to obtain in this way realistic linear combinations of real ground motions. For this purpose, each record is resampled so that the fixed sampling rate of all records in the data base is unique. This fixed sampling rate (or fixed time step) is used for the inverse Fourier transform of the linear combination of the Fourier transforms of the resampled motions.

Resampling

The resampling technique is based on least-squares linear-phase finite-duration impulse-response (FIR) filter for the rate conversion. The order N_{FIR} of the FIR filter is given by:

$$N_{FIR} = 20 \cdot max\left(\Delta t_{old}, \Delta t_{new}\right) \tag{2}$$

where Δt_{old}, Δt_{new} are the time steps of the ground motion before and after conversion, respectively. The frequency-amplitude characteristics of the FIR filter approximately match those given by the relation:

$$A\left(f\right) = \begin{cases} 1 & 0 \le f \le f_0 \\ 0 & f_0 < f \le 1 \end{cases} \tag{3}$$

where A is the amplitude that corresponds to frequency f, 1 is the Nyquist frequency and f_0 is given by:

$$f_0 = 1/\max\left\{\Delta t_{old}, \Delta t_{new}\right\} \tag{4}$$

The coefficients of the FIR filter are multiplied by the coefficients of a Kaiser window of length equal to $N_{FIR} + 1$, given by:

$$w\left(n\right) = \frac{I_0\left(\beta\sqrt{1-\left(\frac{n-N_{FIR}/2}{N_{FIR}/2}\right)^2}\right)}{I_0\left(\beta\right)},\ 0 \le n \le N_{FIR} \tag{5}$$

where I_0 is the zero-th order modified Bessel function of the first kind. In this study, β parameter is selected to be equal to 5. To compensate for the delay of the linear phase filter a number of entries at the beginning of the output sequence are removed. After obtaining the FIR filter designed via a Kaiser window, the raw ground motion record is resampled based on this filter thus obtaining the modified ground motion history.

Fast Fourier Transform

The FFT of a raw motion data of Equation (1) is calculated by means of DFT (Discrete Fourier Transform). The DFT of raw motion data $\ddot{u}_g\left(t\right)$ is calculated as:

$$\bar{\ddot{u}}_g\left(k\omega\right) = \sum_{j=1}^{n} \ddot{u}_g\left(j\Delta t\right) W_n^{(j-1)(k-1)} \tag{6}$$

where $W_n = e^{-2\pi i/n}$ is one of the n roots of unity and $\omega = 1/(2n\Delta t)$. The inverse DFT of $\bar{\ddot{u}}_g\left(k\omega\right)$ is given by:

$$\ddot{u}_g\left(j\Delta t\right) = \frac{1}{n}\sum_{k=1}^{n} \bar{\ddot{u}}_g\left(k\omega\right) W_n^{-(j-1)(k-1)} \tag{7}$$

The execution time of DFT depends on the number of multiplications involved. A direct DFT evaluation takes n^2 multiplications whereas FFT takes $n\log_2 n$ multiplications. It has been proven that the n-point DFT can be obtained from two $n/2$ -point transforms, one on even input data and one on odd input data (Frigo and Johnson, 1998; FFTW). Therefore, if n is a power of 2, then it is possible to recursively apply this decomposition until only discrete Fourier transforms of single points are left.

Problem Formulation

In mathematical terms the procedure of selection, scaling and linearly combining of ground motion records to fit a given target spectrum is formulated as follows:

$$\begin{array}{ll} \text{minimize:} & f(\mathbf{x}) \\ \text{subject to:} & x_{i,\min} \le x_i \le x_{i,\max} \\ & \text{i=\{1,2,...,D\}} \end{array} \tag{8}$$

where f is the objective function to be minimized, $\mathbf{x}$ is the vector of design variables of dimension D, and $x_{i,\min}$, $x_{i,\max}$ are the lower and upper bounds of its i-th component.

Objective Function

In this study, two types of objective functions are proposed:

(a) Objective function f_{Sa} which consists a measure of the area under the curve of the deviation between the suite and the target spectral accelerations and is defined as follows:

$$f_{Sa} = \int_{T_1}^{T_2} \left|\frac{Sa_c(T) - Sa_t(T)}{Sa_t(T)}\right| p\left(T\right) dT. \tag{9}$$

where Sa_c is the spectral acceleration of the linear combination of the ground motions as obtained from Equation (1) and Sa_t is the target spectral acceleration.

(b) Objective function $f_{Sa-Siev}$ which consists a measure of the sum of the following:

- The area between the spectral acceleration curves.
- The area between the equivalent seismic absolute input energy velocity spectra curves.
- The area between the equivalent seismic relative input energy velocity spectra curves.

$f_{Sa-Siev}$ is given by:

$$f_{Sa-Siev} = \int_{T_1}^{T_2} \left(\left| \frac{Sa_c(T) - Sa_t(T)}{Sa_t(T)} \right| + \left| \frac{Siev_c^{ABS}(T) - Siev_t^{ABS}(T)}{Siev_t^{ABS}(T)} \right| + \left| \frac{Siev_c^{REL}(T) - Siev_t^{REL}(T)}{Siev_t^{REL}(T)} \right| \right) p(T)\, dT \quad (10)$$

where $Siev_c^{ABS}$, $Siev_c^{REL}$ are the spectral equivalent absolute and relative input energy velocities, respectively, of the suite of the ground motions and $Siev_t^{ABS}$, $Siev_t^{REL}$ are the target spectral equivalent absolute and relative input energy velocities, respectively. Detailed calculation of $Siev_t^{ABS}$ and $Siev_t^{REL}$ quantities can be found in Uang and Bertero (1990).

In Equations (9) and (10) and || denotes the absolute value and $p(T)$ is a linear penalty function which is biased toward the lower period range and is given by:

$$p(T) = \frac{(T - T_1) + k_p (T_2 - T)}{T_2 - T_1} \quad (11)$$

where T_1, T_2 are the lower and upper period integration limits, T is the period and k_p is a penalty constant. Although baseline correction is performed before the various spectral computations, the penalty function ensures that the displacement and velocity of the acceleration is equal to zero at the start and the end of the time history considered.

Design Variables

The design variables of the optimization problem are arranged into the vector **x** which contains $2m$ components, where m is the number of ground motion records in the suite. The first m components are the scale factors (continuous variables) used for the selected ground motions in the suite of Equation (1), and the remaining components, are the IDs (integer variables) of the corresponding selected ground motion. The lower and upper bounds, $x_{i,\min}$ and $x_{i,\max}$, respectively, of the continuous variables, $i = \{1, 2, ..., m\}$, have a significant impact on the performance of the optimization algorithm and the quality of the optimum solution. As the range of values of a design variable gets broader, the optimization algorithm shows a relaxed behavior, which can become unstable for very large upper and/or very small lower limits. Therefore, suitable values for these limits should be selected. The values selected in this study are as follows:

$$x_{i,\min} = \begin{cases} -2.0 & 1 \le i \le m \\ 1 & m+1 \le i \le 2m \end{cases} \quad (12)$$

$$x_{i,\max} = \begin{cases} 2.0 & 1 \le i \le m \\ M & m+1 \le i \le 2m \end{cases} \quad (13)$$

where M is the total number of the raw ground motions records contained in the database.

As obtained from Equations (12) and (13) the problem considered in this study is virtually a mixed-integer optimization problem and for this purpose the optimization algorithm has to be able to handle such a situation.

Mixed Integer Genetic Algorithm

Choosing the proper search algorithm for solving such problem is not a straightforward procedure. Metaheuristic search optimization algorithms achieve efficient performance for a wide range of structural optimization problems. In this study, among the plethora of metaheuristic algorithms, a genetic algorithm has been chosen to solve the underlying optimization problem, capable to handle mixed-integer nature of the design variables. This should not be considered as an implication related to the efficiency of other algorithms, since any algorithm available can be used for solving a particular optimization problem based on researcher's experience.

The Genetic Algorithm (GA) is a stochastic global search optimization method introduced by Holland (1992) which emulates the natural biological evolution. GA applies on a population of potential solutions the principle of survival of the fittest to produce better approximations to a solution. At each generation, a new set of approximations is created by the process of selecting individuals according to their level of fitness in the problem domain and breeding them together using operators borrowed from natural genetics (selection, crossover and mutation). This process leads to the evolution of individuals that are better suited to their environment than the individuals that they were created from, like in natural evolution process. The algorithm stops when a suitable criterion is met (e.g., current generation GEN equals to maximum number of generations, MAXGEN). A pseudocode of GA is described in Algorithm 1.

Algorithm 1 | The pseudocode of a GA.

Pseudocode of the GA

```
Set parameters
Generate the initial population
while GEN < MAXGEN do
        Fitness calculation
        Selection
        Crossover
        Mutation
end while
Obtain the individual with maximum fitness
return the best solution
```

For the purposes of this study, a real-valued representation is adopted as encoding strategy. The use of real-valued genes in GAs offers over binary encodings the following advantages: (i)

efficiency of the GA is increased as there is no need to convert chromosomes to phenotypes before each function evaluation, (ii) less memory is required as efficient floating point internal computer representations can be used directly, (iii) no loss in precision by discretization to binary or other values, (iv) greater freedom to use a variety of genetic operators.

Initialization of Population

The GA starts with the generation of a random initial population of individuals with uniform distribution in the initial generation. If the initial population is denoted by P_0 and its size (number of individuals) by n_P, then any element of P_0 is given by:

$$x_{i,j} = x_{j,\min} + \left(x_{j,\max} - x_{j,\min}\right) a_{RU} \tag{14}$$

where a_{RU} is a random variable with uniform distribution for which $0 \leq a_{RU} \leq 1$. It is ensured that $x_i, i = \{m+1, m+2, ..., 2m\}$ is a positive integer. In case of a duplicate integer found this is replaced by a random integer value (respecting the upper and lower bounds) different from the calculated ones in P_0.

Selection and Crossover

The stochastic universal sampling (SUS) is used as a selection function, which provides zero bias and minimum spread. SUS offers an offspring selection procedure that may lead to faster convergence to the solution of a problem than other selection methods, such as e.g., roulette wheel selection.

In addition, to avoid duplicate entries in the ground motion record identities a new crossover scheme is proposed which ensures that the linear combination of the ground motion records examined each time is comprised by unique members. This procedure is described by detail in the following:

If the crossover is performed between two random individuals at generation k, $P_{k,1} = \left\{x_{i1,j}\right\}$ and $P_{k,2} = \left\{x_{i2,j}\right\}$, the individual $P_{k+1,12}$ is produced as a result of the crossover. Initially, three set operations are performed between the two individuals:
a) Intersection between $x_{i1,j}$ and $x_{i2,j}$:

$$x_{1\cap 2} = \left\{x_{i1,j}\right\} \bigcap \left\{x_{i2,j}\right\} \tag{15}$$

b) Subtraction of $x_{i2,j}$ from $x_{i1,j}$:

$$x_{1-2} = \left\{x_{i1,j}\right\} - \left\{x_{i2,j}\right\} \tag{16}$$

c) Subtraction of $x_{i1,j}$ from $x_{i2,j}$:

$$x_{2-1} = \left\{x_{i2,j}\right\} - \left\{x_{i1,j}\right\} \tag{17}$$

The offspring $P_{k+1,12}$ will contain the intersection $x_{1\cap 2}$ which contains $n_{1\bigcap 2}$ elements and the vector $\{x_{1-2}, x_{2-1}\}_l$ which contains $l = m - n_{1\bigcap 2}$ randomly selected elements from the vector formed by concatenating the two differences $\{x_{1-2}, x_{2-1}\}$:

$$P_{k+1,12} = \left\{x_{1\bigcap 2}, \{x_{1-2}, x_{2-1}\}_l\right\} \tag{18}$$

In the case where $x_{1\cap 2} = \varnothing$ then $\{x_{1-2}, x_{2-1}\}_l = \{x_{1-2}, x_{2-1}\}$. Equations (15–18) apply both for continuous and integer design variables of the problem.

Mutation

In GA, the mutation function uses various distributions from which random numbers (perturbations) are generated and added to the components of the individual that is mutated. In this study, the perturbation of the continuous/integer design variables, is performed using a Gaussian/random uniform distribution, respectively, and are described in detail below.

Continuous variables

The mutation function of continuous design variables follows a Gaussian distribution of zero-mean with standard deviation given by the relation:

$$m_{SC,k} = m_{SC,0}\left(1 - m_{SH}\frac{k}{k_{\max}}\right) \tag{19}$$

where the standard deviation $m_{SC,k}$ is the fraction of the maximum range of possible perturbations of the design variables (i.e., scale factors) that can be added to an individual in generation k during mutation process. $m_{SC,0}$ is the scale parameter and is equal to the fraction of the maximum range of possible perturbations of the continuous variables at the initial generation (0), whereas m_{SH} is the shrink parameter which controls how fast $m_{SC,k}$ is reduced as generations evolved. Both of the parameters $m_{SC,0}$ and m_{SH} can be arbitrarily selected and their values must be between 0 and 1. $m_{SH} < 0$ or $m_{SH} > 1$ is also possible, but not recommended. For a random individual at generation k, $P_{k,1} = \left\{x_{i1,j}\right\}$ this operation can be written as follows:

$$P_{k+1,1} = \left\{x_{i1,j}\right\} + \bar{a}_{GU} m_{SC,k}, \quad 1 \leq j \leq m \tag{20}$$

where $m_{SC,k}$ is given by Equation (19) and $\bar{a}_{GU}$ is a vector with entries following a uniform Gaussian distribution.

Integer variables

The mutation function of integer design variables follows a random uniform distribution. Since the random perturbations are not integers in general, the result is rounded toward the nearest integer and then the remainder of its Euclidean division with M is extracted, to ensure that the result does not exceed M value. For a random individual at generation k, $P_{k,1} = \left\{x_{i1,j}\right\}$ this operation can be written as follows:

$$P_{k+1,1} = \mathrm{mod}\left(\left\langle\left\{x_{i1,j}\right\} + (2\bar{a}_{RU} - 1)\, m_{SC,k}\right\rangle, M\right), \quad m+1 \leq j \leq 2m \tag{21}$$

where the symbol $\langle\rangle$ is used to denote the nearest integer of the quantity contained in the brackets, $\bar{a}_{RU}$ is a vector with entries following a uniform random distribution with $0 \leq \bar{a}_{RU,j} \leq 1$, $m_{SC,k}$ is the scale parameter of mutation function (standard deviation of Gaussian distribution at the k^{th} generation), and mod() denotes the modulo operation, i.e., the remainder of the Euclidean division of between the two arguments. After application of Equation (21) the result is checked for duplicate values of integer components. If so, the duplicates are replaced by a random integer value (respecting the upper and lower bounds) different from the calculated ones.

NUMERICAL RESULTS

The effectiveness of the proposed algorithm is verified by generation of artificial accelerograms which are compliant to target spectra of different inherent nature, ensuring also the independence of the algorithm's performance from the target spectrum. More specific, the acceleration and equivalent input energy velocity response spectra of three ground motion records: (a) El Centro Terminal Substation Building record of the 1940 Imperial Valley earthquake, (b) Rinaldi record of the 1994 Northridge earthquake and (c) Sakarya—SKR record of the 1999 Kocaeli earthquake are defined as target spectra. The target spectra are associated with a far-field ground motion, a near-field ground motion which contains forward directivity effects and a near-field ground motion which contains fling-step effects, respectively (Kalkan and Kunnath, 2006). Typical characteristic of the near-field motions is the presence of high-velocity pulses, which do not exist in typical far-field ground motions. The difference between these two types of motions originates mainly from two factors: (a) the distance between the site where the earthquake is recorded and the seismic fault, (b) the orientation of the last. It is noted that the three target spectra have essentially different general configurations, a fact that results from the different inherent nature of the time histories of the three ground motions.

Two matching scenarios are considered: (i) Matching Scenario 1 (Sa matching): Matching only the spectral acceleration and (ii) Matching Scenario 2 (Sa–Vei matching): Matching both the spectral acceleration and the equivalent input energy velocity spectra (absolute and relative). In each scenario, the database is comprised of the ground motion records obtained from the European Strong Motion (ESD) database (Ambraseys et al., 2004; Iervolino et al., 2010). After a preliminary screening of the ESD database, a subset database is constructed that consists of 6026 ground motion records corresponding to horizontal earthquake components, i.e., $M = 6026$. The number m of ground motion records in the suite is set to be equal to 20 and the matching range of periods is between $T_1 = 0.1$ s and $T_2 = 4.0$ s. The penalty constant k_p is set to be equal to 50.

Furthermore, the tuning parameters of the GA are selected as follows: the population size n_p (number of individuals in each generation) is equal to 80. For reproduction, the number of individuals that are guaranteed to survive to the next generation (elite children) is equal to 5% of the population size, namely $n_E = 0.05 n_P = 4$, and the fraction of the next generation, other than elite children, that is produced by crossover (crossover fraction) is equal to 0.8, i.e., $n_C = 0.8\,(n_P - n_E) \approx 61$ individuals are produced in each generation. The number of individuals in each generation that are produced by mutation is $n_M = n_P - n_E - n_C = 15$. In the GA used in this study no migration occurs, as there are no subpopulations. As stopping criteria for the GA algorithm the maximum number of generations (MAXGEN) is used, i.e., equal to 100. A sensitivity analysis of 30 independent optimization runs is also performed followed by a statistical process on the optimized results. The sensitivity analysis represents a necessary step since the GA optimization procedure does not yield the same results when restarted due to its stochastic nature.

In all cases examined, the objective function is evaluated using OpenSeismoMatlab, an open source tool for earthquake ground motion processing (Papazafeiropoulos and Plevris, 2018). OpenSeismoMatlab performs baseline correction and generates the elastic acceleration and equivalent input energy velocity response spectra which are then used for the calculation of the objective function.

Matching Scenario 1

The optimization results for Matching Scenario 1 are depicted in **Figure 1**. For each target record, the black curve represents the target acceleration spectrum, while the red and blue curves represent the spectral acceleration that corresponds to the optimization run (out of the 30 runs) that fits best and worst to the target spectrum, respectively. The coefficient of variation (CoV) of the 30 runs for each period is also depicted by the green curve.

A good agreement is observed between the "best" and "target" spectra in all cases examined while the CoV value increases near the bounds of the matching period range. This is mostly attributed to the range of the periods involved in the calculation of the objective value [see Equations (9) and (10)] which is defined in a way that it covers the eigenperiods of a structure. This means that the period range used in the matching procedure and consequently the optimized acceleration time history are period-dependent. In this study, an extended period range is selected to highlight the applicability of the proposed methodology for a variety of structures. However, most of civil structures have eigenperiods that are concentrated near the middle of the range considered, where the CoV values are minimum and high accuracy can be achieved. Furthermore, the finite number of ground motions in the suite of the linear combination contributes to large CoV values in general. As the number of the ground motions in the suite decreases, the methodology becomes more cumbersome, since the time history given by the suite has less flexibility. Hence, as the number of the ground motions increases, the matching becomes generally better. Finally, the shape of the penalty function in Equation (11) has an important effect on the optimized response spectrum of each optimization run, since the weighting of the deviation from the target spectrum for the matching period range considered is not uniform, as has been already mentioned in the previous section.

Figure 2 shows the convergence history of the 30 independent optimization runs of Matching Scenario 1. Each curve represents the objective value of the best individual at each generation of a given optimization run. The red (blue) curve represents the evolution of the objective value that corresponds to the optimization run (out of the 30 runs) that fits best (worst) to the target spectrum.

It can be noted that in the case of El Centro earthquake the best individual of the final generation for the best independent run corresponds to roughly 14% of the objective value of the best individual of the initial generation. The best individual of the final generation for the worst independent run corresponds to roughly 40.3% of the objective value of the best individual of the initial generation. In the case of Northridge earthquake these

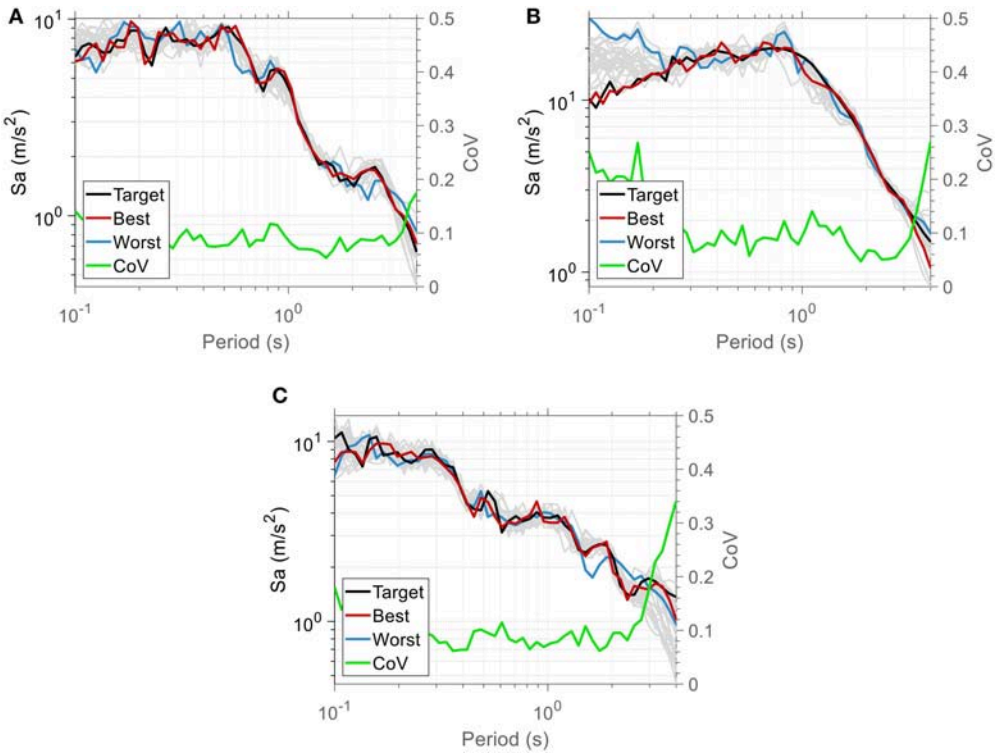

FIGURE 1 | Optimization results of Matching Scenario 1 for each target: **(A)** El Centro, **(B)** Northridge, and **(C)** Sakarya.

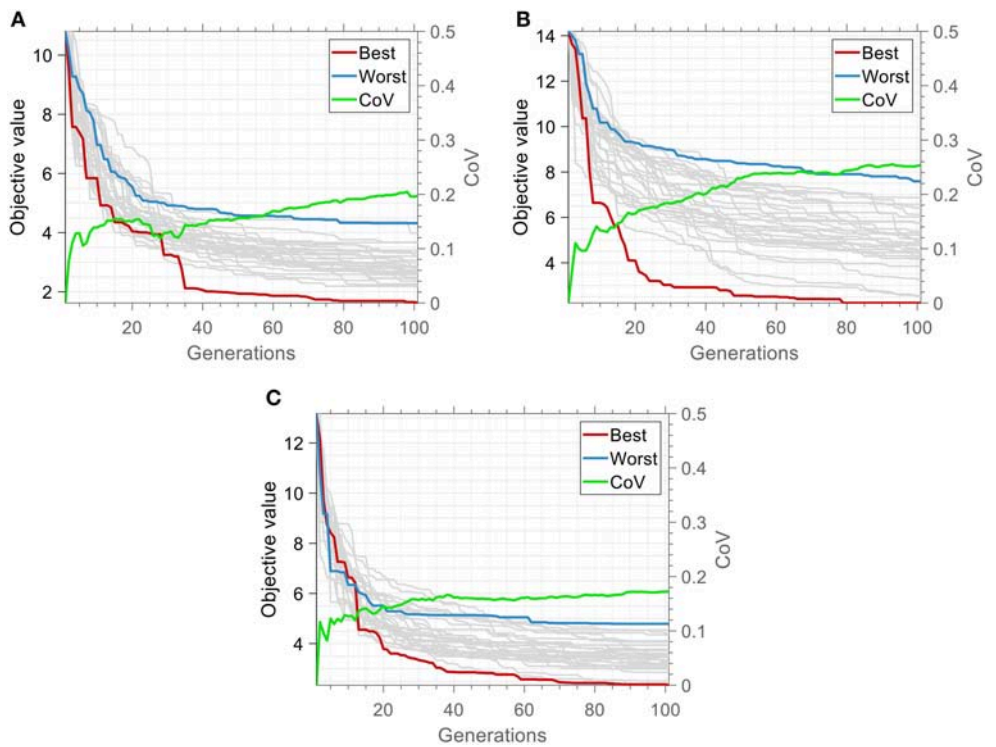

FIGURE 2 | Optimization history of the 30 independent runs of the Matching Scenario 1 for each target: **(A)** El Centro, **(B)** Northridge, and **(C)** Sakarya.

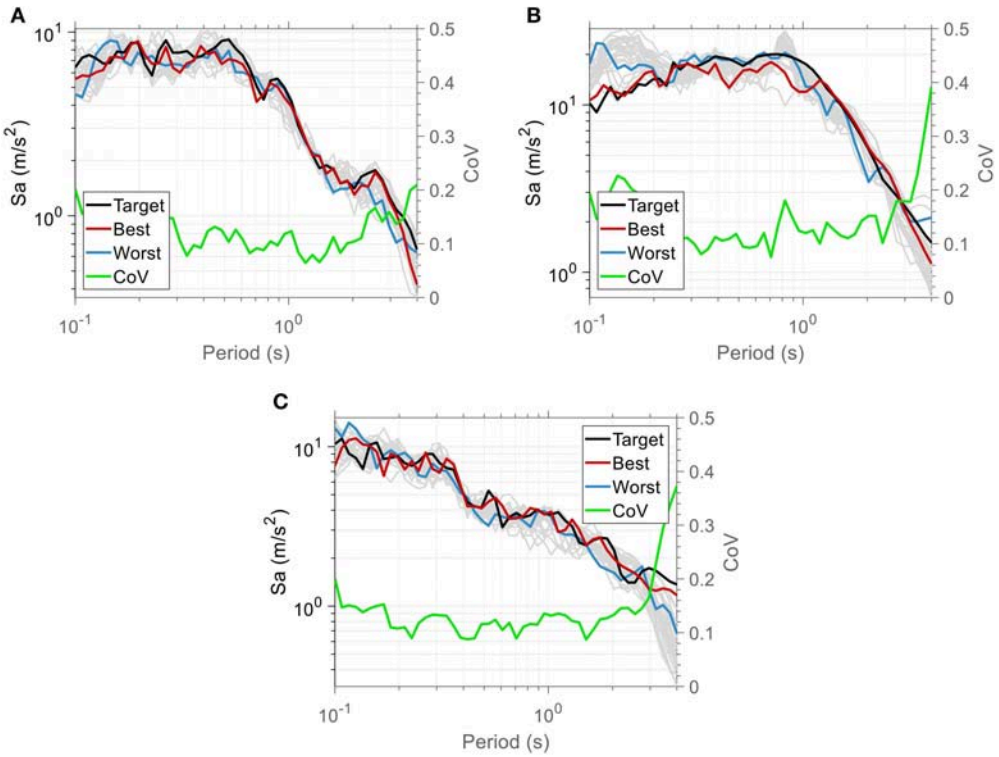

FIGURE 3 | Results of Matching Scenario 2 regarding spectral acceleration for each target: **(A)** El Centro, **(B)** Northridge, and **(C)** Sakarya.

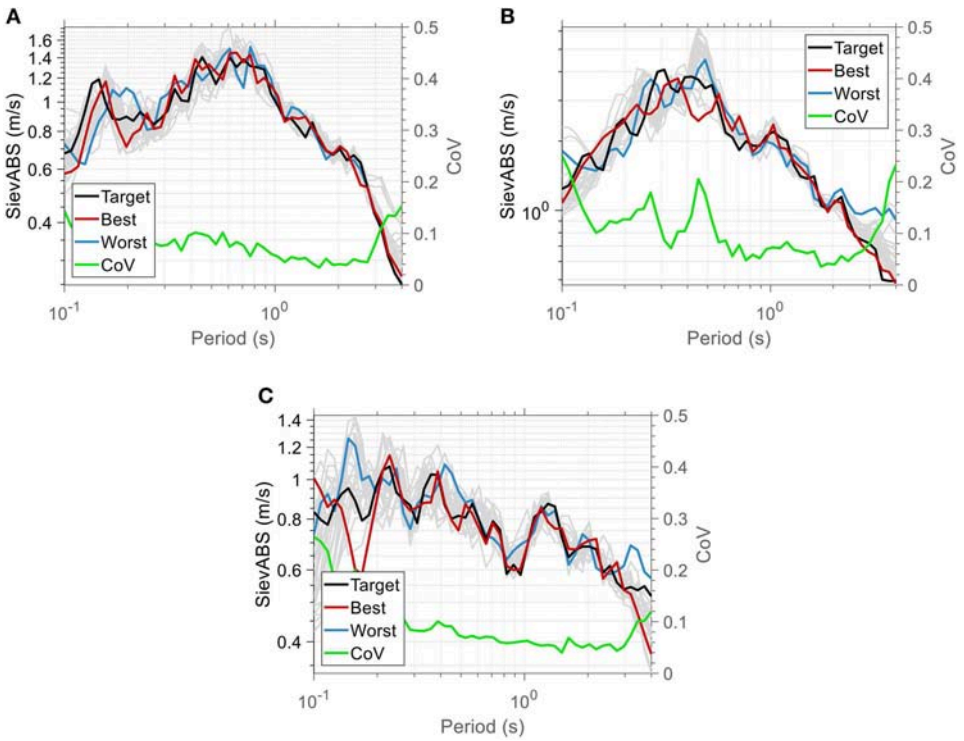

FIGURE 4 | Results of Matching Scenario 2 regarding equivalent absolute seismic input energy velocity spectra (SievABS) for each target: **(A)** El Centro, **(B)** Northridge, and **(C)** Sakarya.

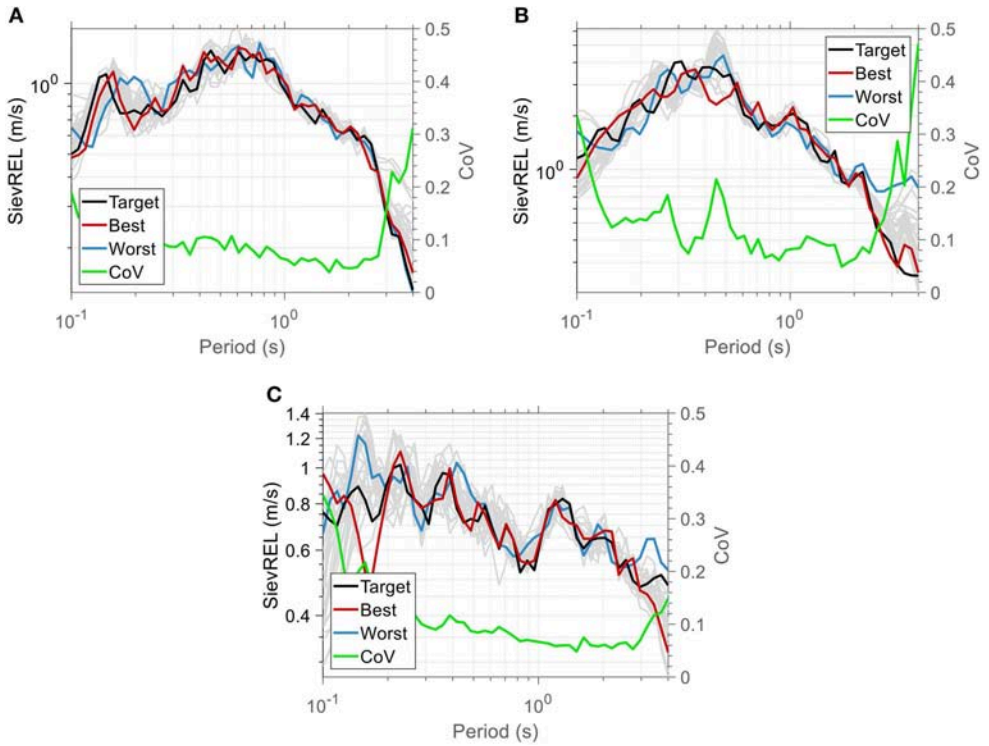

FIGURE 5 | Results of Matching Scenario 2 regarding equivalent relative seismic input energy velocity spectra (SievREL) for each target: **(A)** El Centro, **(B)** Northridge, and **(C)** Sakarya.

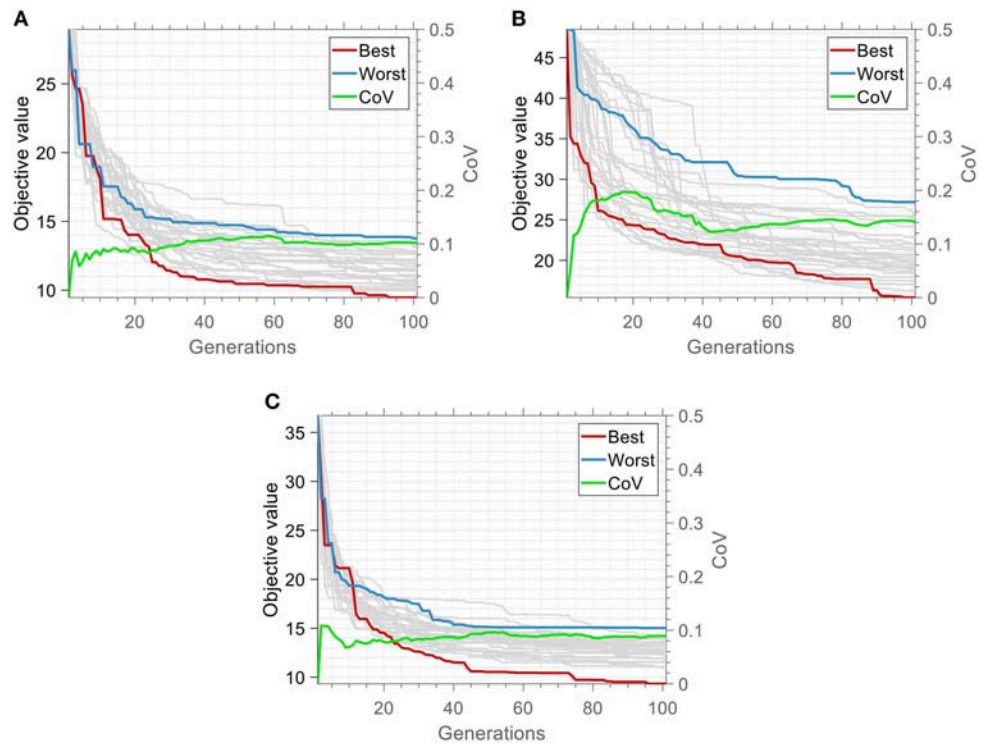

FIGURE 6 | Optimization history of the 30 independent runs of the Matching Scenario 2 for each target: **(A)** El Centro, **(B)** Northridge, and **(C)** Sakarya.

percentages are roughly equal to 16.1% and 53.6%, and in the case of Sakarya earthquake they are 17.7% and 36.9% respectively.

The trend of all convergence histories shows that the approach to the optimum value is quick and relatively smooth, which is achieved by proper adjustment of the crossover and mutation rates, in order to ensure sufficient population diversity in each generation. It seems that, while the coefficient of variation among the optimization histories increases at the early stages of the optimization process, there is a point after which it stabilizes until termination. The magnitude of the final stabilized value of the CoV value is a measure of the complexity of the optimization space. As it is expected, larger CoV values corresponds to increased diversity between the various optimization runs, in terms of the path followed by the best individual of each optimization run. The largest CoV value of the objective value of the best individual among the various optimization runs at the final generation occurs in the case of Northridge earthquake, an observation that correlates well with the large dispersion of the optimum spectra, especially in the low period range, in **Figure 1B**.

Matching Scenario 2

The optimization results for Matching Scenario 2 are depicted in **Figure 3**. Nearly the same traits that are mentioned for **Figure 1** are observed; the proposed algorithm gives higher CoV values in the lower and higher limits of the matching period range considered.

In **Figures 4**, **5**, the absolute seismic input energy equivalent velocity (S_{iev}ABS) and the relative seismic input energy equivalent velocity (S_{iev}REL) spectra for each target spectrum are presented, respectively. A very close agreement between the target and corresponding optimized spectra is also observed in this case. Although the CoV plots exhibit local peaks and troughs, all of them fluctuate around the value of 10%, regardless of the target spectrum.

In a similar rationale, **Figure 6** depicts the convergence history of the 30 independent optimization runs of Matching Scenario 2. It is apparent that in the case of El Centro

Table 1 | Normalized error of the damping energy between the optimized and the target ground motion records.

Target ground motion	Matching Scenario 1	Matching Scenario 2	Difference (%)
El Centro	0.4065	0.2794	31.3
Northridge	0.2289	0.1901	17.0
Sakarya	1.2104	0.2310	80.9

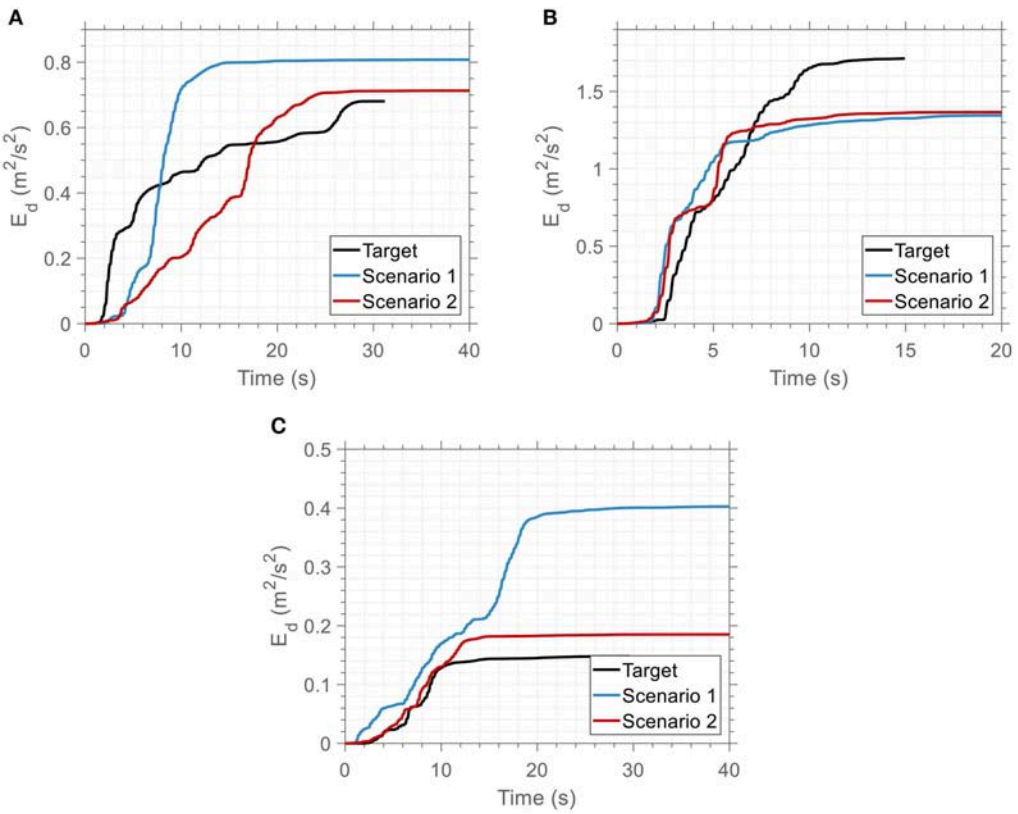

FIGURE 7 | Energy dissipated by viscous damping per unit mass over time for the optimized artificial ground motions of the two matching scenarios and for each target ground motion: **(A)** El Centro, **(B)** Northridge, and **(C)** Sakarya.

earthquake the best optimization run gives result equal to 32.8% of the best objective value of the initial population, whereas the worst result is roughly equal to 48.3% of the initial best objective value. In the case of Northridge earthquake the best and worst results are roughly equal to 32 and 55.7% respectively of the initial best objective value. Similarly, the corresponding percentages for the Sakarya earthquake are 26 and 41.1%. Interestingly, the lowest (best) percentage appears in the case of Sakarya earthquake whereas the highest (worst) percentage appears in the case of Northridge earthquake. The smooth convergence in optimization histories demonstrates the reliability of the proposed algorithm not only for matching the target spectral acceleration, but also for matching both target acceleration and target seismic input energy equivalent velocity spectra.

Table 2 | Yield displacement and ductility demand of each story for the 3-DOF and 9-DOF structural systems.

Target Ground Motion			El Centro	Northridge	Sakarya
LA3	Yield displacement [m]		0.0283	0.1681	0.0356
	Ductility demand	Story 2	1.19	0.99	0.99
		Story 3	0.62	0.48	0.49
LA9	Yield displacement [m]		0.0685	0.166	0.1193
	Ductility demand	Story 2	0.41	0.38	0.38
		Story 3	0.44	0.41	0.38
		Story 4	0.39	0.39	0.30
		Story 5	0.51	0.58	0.30
		Story 6	0.47	0.61	0.25
		Story 7	0.52	0.74	0.28
		Story 8	0.36	0.53	0.20
		Story 9	0.18	0.26	0.10

Scenarios Comparison

A one-to-one comparison between the performance of the two scenarios shows that the CoV is generally higher in Scenario 2. This occurs because the optimization problem of Scenario 1 is more "relaxed" than the Scenario 2. In Scenario 1, the objective function is related only with a single target spectrum (acceleration), while in Scenario 2 the objective function is related with three target spectra (acceleration, absolute velocity, relative velocity), at the same time. This relation establishes an indirect "constraint" which implies that, with respect to the target acceleration spectrum only, the optimized solution of Scenario 2 will have higher deviation than that of Scenario 1, which interprets the higher CoV values in **Figure 3** when compared to **Figure 1**. Consequently, in the case of Scenario

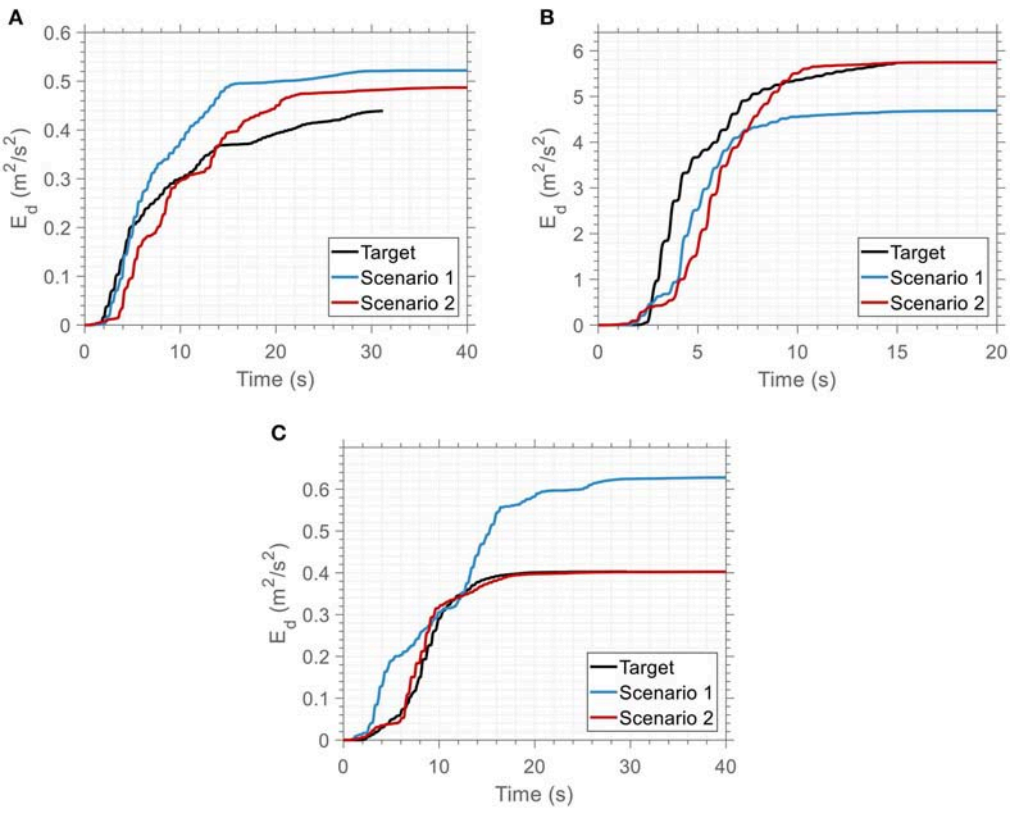

FIGURE 8 | Time variation of energy dissipated at the 1st story of the 3-DOF system for the optimized and the target ground motion records: **(A)** El Centro, **(B)** Northridge, and **(C)** Sakarya.

2 the possible "paths" of the population evolution toward the optimum are far fewer and therefore the population diversity is lower compared to Scenario 1, which explains the reduced CoV in the last generation in **Figure 6** (Scenario 2), compared to that in **Figure 2** (Scenario 1). Finally, it is noted that as the generations increase, the CoV fluctuation is smoother in the case of Scenario 2, related to the increased robustness of the algorithm in this case.

VERIFICATION OF THE PROPOSED METHODOLOGY

In order to assess the robustness and accuracy of the proposed methodology the seismic performance of single- and multi-degree of freedom structural systems has been considered. To this end, nonlinear response history analyses were conducted for the optimized accelerograms of the two Matching Scenarios as resulted for the three target ground motion records in Section 3. The response results are compared in terms of the *goodness-of-fit* with the respective response result of the target ground motion. The seismic input energy that is dissipated due to viscous damping action in the structure (damping energy) is also quantified.

Energy Definitions

The seismic input energy that is absorbed by an inelastic single degree of freedom (SDOF) structural system during an earthquake can be defined by integrating the equation of motion of the system as follows:

$$\int_0^u \ddot{u}\bar{m}du + \int_0^u \dot{u}\bar{c}du + \int_0^u f_s du = -\int_0^u \bar{m}\{I\}\ddot{u}_{g,c}du \qquad (22)$$

where $\bar{m}$ is the mass matrix, $\bar{c}$ is the viscous damping coefficient matrix, f_s is the resistance force due to stiffness, I is the unit influence vector of the structure and $\ddot{u}_{g,c}$ is the linear combination of the accelerations of ground motions records in the suite as defined in section resampling Equation (22) stands as a statement of energy balance of the system and can be rewritten as:

$$E_k(t) + E_d(t) + E_s(t) + E_y(t) = E_I(t) \qquad (23)$$

With regard to Equation (22) the first integral gives the kinetic energy E_k, the integral on the right-hand side gives the input energy E_I imparted from the ground motion to the structure and the last integral on the left-hand side is equal to the sum of the linear elastic recoverable strain energy E_s and the plastic

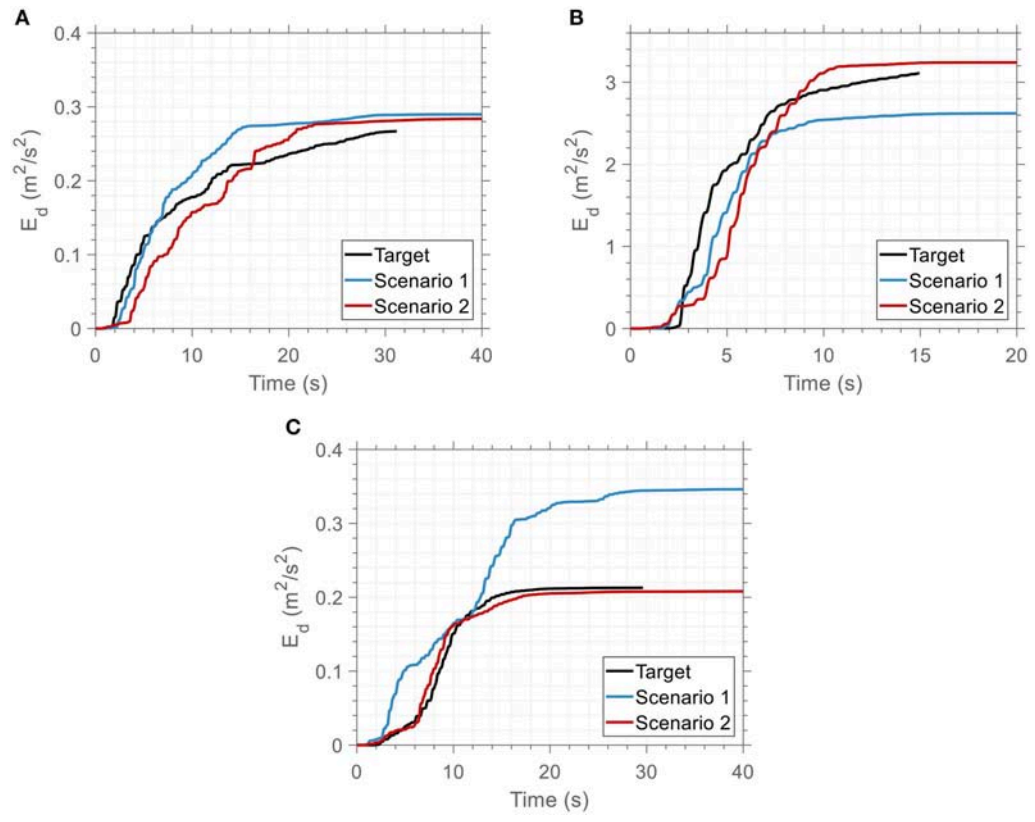

FIGURE 9 | Time variation of energy dissipated at the 2nd story of the 3-DOF system for the optimized and the target ground motion records: **(A)** El Centro, **(B)** Northridge, and **(C)** Sakarya.

irrecoverable strain energy E_y. The damping energy term E_d is defined as follows:

$$E_d(t) = \int_0^u i\bar{c}du. \tag{24}$$

The definitions of the aforementioned energy quantities are given for a structure whose mass is acted upon by a force equal to $p_{eff}(t) = -\bar{m}\{I\}\ddot{u}_{g,c}$, i.e., they are based on the consideration of the structural motion relative to the base, rather than the total motion of the structure. The two types of energy formulations (relative and absolute) are equivalent but the former is more intuitive and simplifies the calculations when it comes to multi degree of freedom (MDOF) structural systems. Equations (22–24) correspond to a SDOF system in mathematical terms and their extension to MDOF systems can be done in a straightforward manner.

SDOF System Results

Three SDOF systems involving a bilinear elastoplastic constitutive model with kinematic hardening are analyzed for each target ground motion. The eigenperiod, the critical damping ratio, the post-yield stiffness ratio (i.e., the ratio of the post-yield stiffness to the initial small strain stiffness of the structure), and the ductility demand are same for all the SDOF systems and equal to 0.5 sec, 5%, 1%, and 1.1, respectively. The three systems have different yield displacements, equal to 0.052, 0.1, and 0.025 m for the El Centro, the Northridge and the Sakarya target ground motion, respectively. The reader is referred to Papazafeiropoulos et al. (2017) for more details about the implementation of the bilinear elastoplastic constitutive model with kinematic hardening and the time integration algorithm that were used in this study.

The small ductility value specified for all target ground motions denotes that structures only with slightly nonlinear behavior are considered in this study; for cases of severely nonlinear response the scenarios presented in this study for calculation of the design artificial ground motion is an open research issue. For such cases it would be better to consider the inelastic response spectra, rather than elastic response spectra in matching scenarios. In addition, the physical properties of each SDOF system remain the same for the estimation of its dynamic response for each target ground motion as well as the optimized ground motions obtained from the two matching scenarios. Based on an arbitrarily selected value of ductility demand (equal to 1.1, to ensure a slightly nonlinear response) for each target ground motion the yield displacement that is calculated was used also for the corresponding optimized ground motions obtained from

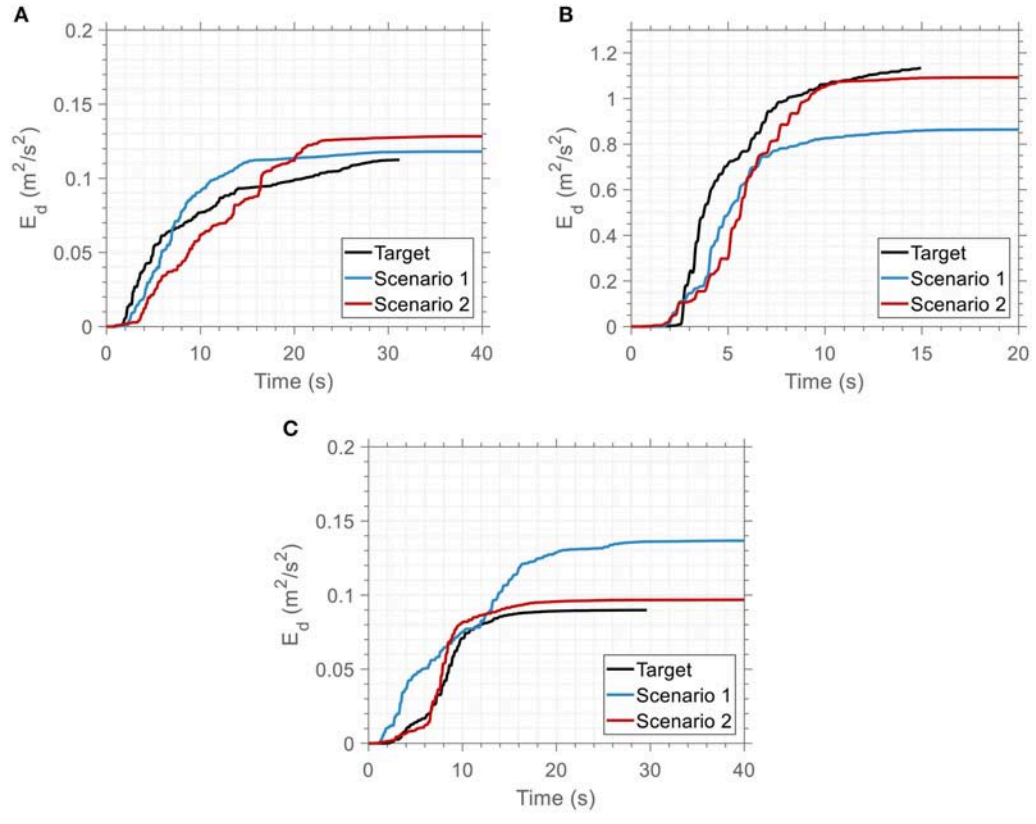

FIGURE 10 | Time variation of energy dissipated at the 3rd story of the 3-DOF system for the optimized and the target ground motion records: **(A)** El Centro, **(B)** Northridge, and **(C)** Sakarya.

the two matching scenarios in all nonlinear time history response analyses.

In **Figure 7**, the time variation of the damping energy per unit mass for each target motion and the optimized ground motion records produced from the two matching scenarios is depicted. A good agreement is observed in all cases since the damping energy of the optimized ground motion (red line) is very close to that of the respective target ground motion (black line). To quantify this agreement, the normalized error e_{ij} for the ith story (in the case of SDOF systems i is always equal to 1) and jth matching scenario, which is proportional to the area between a matching scenario and the target ground motion curves was used as a metric of this goodness-of-fit, defined as follows:

$$e_{ij} = \frac{\int_0^{T_d} \left| E_{d,i}^{j}(t) - E_{d,i}^{T}(t) \right| dt}{\int_0^{T_d} E_{d,i}^{T}(t)\, dt}. \quad (25)$$

where $E_{d,i}^{j}$ and $E_{d,i}^{T}$ is the damping energy for the jth scenario and the target ground motion, respectively.

Even in the case of Northridge target ground motion, it is indicative that the damping energy corresponding to Scenario 2 is slightly closer to the respective curve of the target motion, although there is not much difference between the two scenarios (17% as seen in **Table 1**). This fact, in combination with the large value of the dissipated energy per unit mass may be a consequence of the special characteristics of Northridge earthquake, which contains a high velocity pulse (forward directivity effect) as a near-field ground motion.

MDOF System Results

Two model buildings were analyzed as a 3-DOF and 9-DOF structural systems. More specific, the model buildings are a 3-story (LA3) and a 9-story building (LA9) designed as standard office buildings and situated on a stiff soil (soil type S2), following the local code requirements for the Los Angeles city (UBC, 1994), and according to the provisions of the FEMA/SAC project, presented in FEMA 355C (2000). The plan and elevation of their effective structural models, along with the various cross sections of its members are shown in **Supplementary Figure 1**. The perimeter moment-resisting frames act as the structural system of the building. The column bases of the moment resisting frames are considered as fixed. Furthermore, the design of the buildings for the two orthogonal directions is quite similar, and therefore only half of the structure is considered in the analysis in each case.

The benchmark buildings are simulated as a 3-DOF and a 9-DOF structural system involving the same bilinear elastoplastic constitutive model with kinematic hardening, as in the SDOF system analyzed previously. Their fundamental eigenperiods are equal to 1.01 and 2.85 sec, respectively. The post-yield stiffness ratio and critical damping ratio were set equal to 1% and 5%, respectively. The yield displacement and ductility demand of each story for the 3-DOF and 9-DOF structural systems are shown in **Table 2**. The maximum ductility at any story does not exceed the value of 2. Usually, an interpolative iterative procedure is necessary to obtain the yield displacement for a target ductility demand (Chopra, 2017). However, for each target ground motion in each building the yield displacement is assumed as uniform distributed across all stories and is calculated so that the maximum ductility demand is equal to 2 at least in one story of the building. For both of the LA3 and LA9 buildings the maximum ductility demand is observed at the first story. The ductility of the remaining stories is much lower or even lower than 1 (i.e., story remains linear elastic).

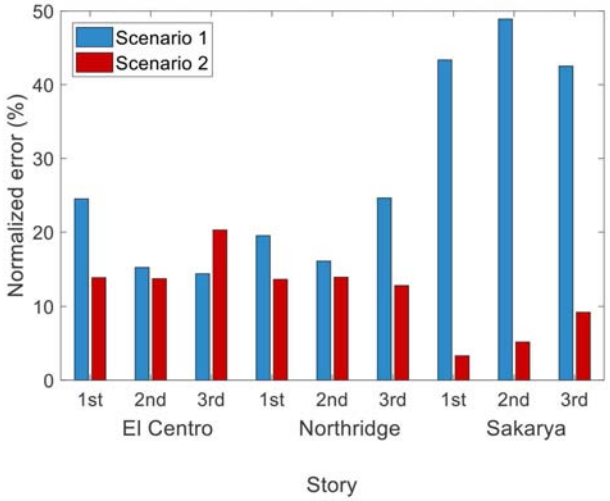

FIGURE 11 | Normalized error of the damping energy between the optimized and the target ground motion records for each floor of the 3-DOF structural system.

For each target ground motion, three nonlinear response history analyses were conducted using as excitation the target ground motion and the two optimized ground motions resulting from the two matching scenarios. **Figures 8–10** show the time history of the damping energy at the three stories of the building for each target ground motion and the optimized ground motion records. Again, a good agreement is observed in all cases since the damping energy of the optimized ground motion (red line) is very close to that of the respective target ground motion (black line).

To quantify this agreement the normalized error as defined in Equation (25) was used as a metric of this goodness-of-fit. **Figure 11** shows the normalized error of the damping energy between the optimized and the target ground motion records for each floor of the 3-DOF structural system. The min/max errors for the two scenarios are 15%/48% and 3%/20%, respectively. It is observed that the proposed algorithm (Scenario 2) yields far lower error compared to Scenario 1. Although the error of Scenario 2 remains lower, only in the case of the dynamic response of the third floor of the 3-DOF system for the El Centro target motion Scenario 2 gives greater error compared to Scenario 1 (28% higher).

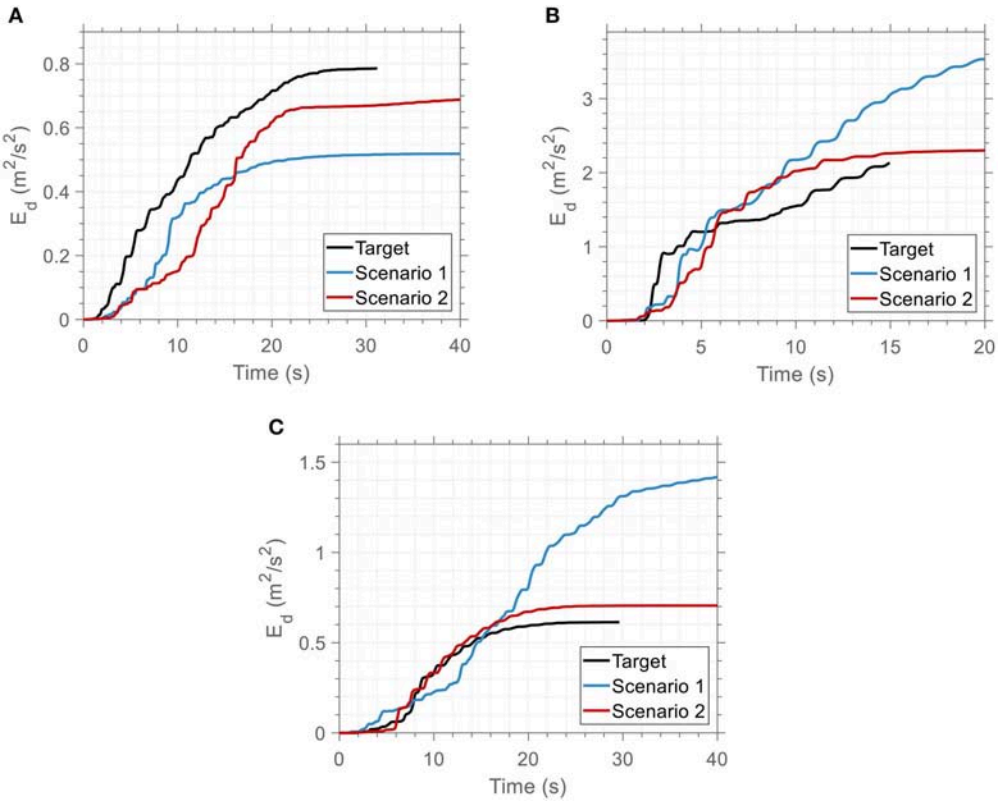

FIGURE 12 | Time variation of energy dissipated at the 1st story of the 9-DOF system for the optimized and the target ground motion records: **(A)** El Centro, **(B)** Northridge, and **(C)** Sakarya.

It is worth noting that in the case of the Sakarya target ground motion the error of the Scenario 2 is 78.3% lower compared to Scenario 1. This is directly related with the low CoV values observed in Section 3 for this specific case, a fact that also proves the robustness and accuracy of the proposed methodology.

Figure 12 shows the time history of the damping energy at a typical story (i.e., first story) of the LA9 building for each target ground motion and the optimized ground motion records. Again, a good agreement is observed in all cases since the damping energy of the optimized ground motion is very close to that of the respective target ground motion. To quantify this agreement, **Figure 13** shows the normalized error of the damping energy between the optimized and the target ground motion records for each story of the 9-DOF structural system. The min/max errors for the two scenarios are 8.2%/88.7% and 9.8%/38.5%, respectively. It is observed that the proposed algorithm (Scenario 2) yields far lower error compared to Scenario 1. The error of Scenario 2 remains higher, only in the case of the dynamic response of the upper stories of the 9-DOF system for the Northridge target motion. This deviation is attributed to the dynamic characteristics of the structural system mainly affected by the near field effects of the specific ground motion. It is worth noting that the maximum error of the Scenario 1 is 130.4% higher compared to the corresponding maximum error of the Scenario 2.

CONCLUSIONS

In this study a novel spectra-matching framework is developed, which employs a linear combination of raw ground motion records to generate artificial accelerograms. To this end, apart from the well-known design acceleration spectrum that is prescribed by the various norms and guidelines, the seismic input energy equivalent velocity spectrum is also taken into account.

This consideration is leading therefore to optimized acceleration time histories, which represent actual motions in a much more realistic way. In order to produce elastic spectra that match as closely as possible to a given target spectrum, the procedure of selection and scaling of a suite of ground motion records to fit a given target spectrum is formulated as an optimization problem. Three characteristic ground motion records of different inherent nature are selected as target spectra, to verify the effectiveness of the proposed algorithm, ensuring that its performance is not ground motion record-dependent assuming different matching scenarios. The optimization results

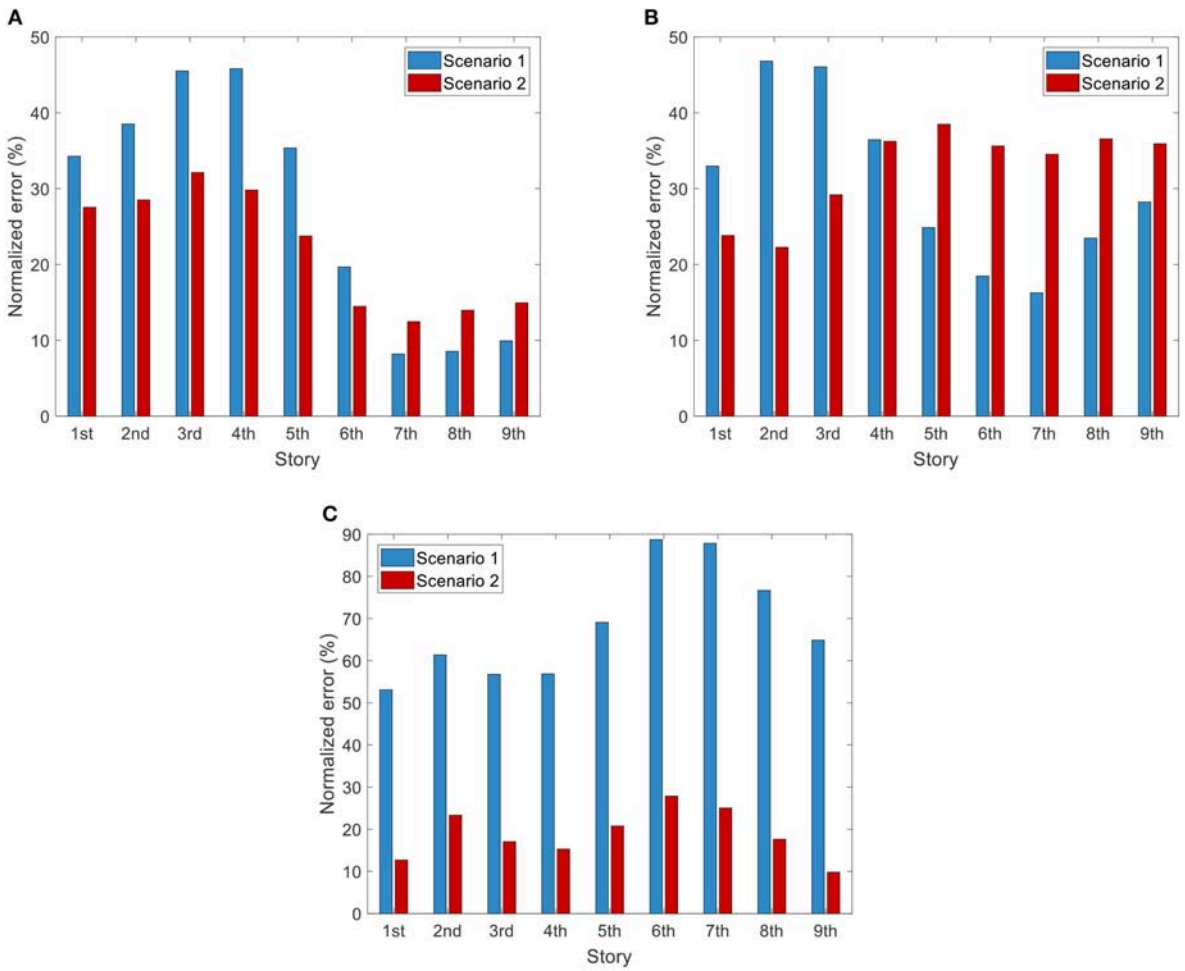

FIGURE 13 | Normalized error of the damping energy between the optimized and the **(A)** El Centro, **(B)** Northridge, and **(C)** Sakarya target ground motion records for each floor of the 9-DOF structural system.

have shown that there exists a good agreement between the target and optimized spectra for each case examined, regardless of the nature of target spectrum. Finally, it is proved that the artificially generated records are much more realistic and suitable for the seismic design of structures, since they reproduce better the real non-linear structural inelastic response in terms of the damping energy, demonstrating also the reliability and robustness of the proposed methodology.

DATA AVAILABILITY STATEMENT

The datasets generated for this study are available on request to the corresponding author.

AUTHOR CONTRIBUTIONS

GP had the research idea, drafted the article, did the data collection, contributed in the numerical analysis of the numerical examples, and wrote the paper. MG analyzed and interpreted the data, contributed in the conception and design of the work, wrote the paper, and supervised the overall research work. MP supervised the overall research work.

SUPPLEMENTARY MATERIAL

The Supplementary Material for this article can be found online at: https://www.frontiersin.org/articles/10.3389/fbuil.2019.00140/full#supplementary-material

REFERENCES

Akiyama, H. (1985). *Earthquake-Resistant Limit-State Design for Buildings*. Tokyo: University of Tokyo Press.

Ambraseys, N., Smit, P., Douglas, J., Margaris, B., Sigbjörnsson, R., and Olafsson, S. (2004). Internet site for European strong-motion data. *Bollettino di geofisica teorica ed applicata*, 45, 113–129. Available online at: http://www3.ogs.trieste.it/bgta/provapage.php?id_articolo=225

Atkinson, G. M., and Goda, K. (2010). Inelastic seismic demand of real versus simulated ground-motion records for cascadia subduction earthquakesinelastic seismic demand of real versus simulated ground-motion records for subduction earthquakes. *Bull. Seismol. Soc. Am.* 100, 102–115. doi: 10.1785/0120090023

Boore, D. M. (2009). Comparing stochastic point–source and finite–source ground–motion simulations: SMSIM and EXSIM. *Bull. Seismol. Soc. Am.* 99, 3202–3216. doi: 10.1785/0120090056

Chapman, M. C. (1999). On the use of elastic input energy for seismic hazard analysis. *Earthq. Spect.* 15, 607–635. doi: 10.1193/1.1586064

Chopra, A. K. (2017). *Dynamics of Structures, 5th Edn.* Pearson: University of California at Berkeley.

Chou, C.-C., and Uang, C.-M. (2003). A procedure for evaluating seismic energy demand of framed structures. *Earthq. Eng. Struct. Dyn.* 32, 229–244. doi: 10.1002/eqe.221

Dindar, A. A., Yalçin, C., Yüksel, E., Özkaynak, H., and Büyüköztürk, O. (2015). Development of earthquake energy demand spectra. *Earthq. Spect.* 31, 1667–1689. doi: 10.1193/011212EQS010M

FEMA 355C (2000). Federal Emergency Management Agency. *State of the Art Report on Systems Performance of Steel Moment Frames Subject to Earthquake Ground Shaking*. FFTW. Retrieved from: http://www.fftw.org (accessed November, 2019).

Frigo, M., and Johnson, S. G. (1998). "FFTW: an adaptive software architecture for the FFT," in *Paper Presented at the Proceedings of the 1998 IEEE International Conference on Acoustics, Speech and Signal Processing, ICASSP'98 (Cat. No. 98CH36181)* (Seattle, WA). doi: 10.1109/ICASSP.1998.681704

Graves, R. W., and Pitarka, A. (2010). Broadband ground-motion simulation using a hybrid approach. *Bull. Seismol. Soc. Am.* 100, 2095–2123. doi: 10.1785/0120100057

Holland, J. H. (1992). *Adaptation in Natural and Artificial Systems: An Introductory Analysis With Applications to Biology, Control, and Artificial Intelligence*. Cambridge, MA: MIT Press. doi: 10.7551/mitpress/1090.001.0001

Iervolino, I., C., and Galasso, and, E., Cosenza (2010). REXEL: computer aided record selection for code-based seismic structural analysis. *Bull. Earthq. Eng.* 8, 339–362. doi: 10.1007/s10518-009-9146-1

Iervolino, I., Maddaloni, G., and Cosenza, E. (2008). Eurocode 8 compliant real record sets for seismic analysis of structures. *J. Earthq. Eng.* 12, 54–90. doi: 10.1080/13632460701457173

Jiao, Y., Yamada, S., Kishiki, S., and Shimada, Y. (2011). Evaluation of plastic energy dissipation capacity of steel beams suffering ductile fracture under various loading histories. *Earthq. Eng. Struct. Dyn.* 40, 1553–1570. doi: 10.1002/eqe.1103

Kalkan, E., and Kunnath, S. K. (2006). Effects of fling step and forward directivity on seismic response of buildings. *Earthq. Spect.* 22, 367–390. doi: 10.1193/1.2192560

Katsanos, E., Sextos, A. G., and Manolis, G. D. (2010). Selection of earthquake ground motion records: a state-of-the-art review from a structural engineering perspective. *Soil Dyn. Earthq. Eng.* 30, 157–169. doi: 10.1016/j.soildyn.2009.10.005

Kuwamura, H., and Galambos, T. V. (1989). Earthquake load for structural reliability. *J. Struct. Eng.* 115, 1446–1462. doi: 10.1061/(ASCE)0733-9445(1989)115:6(1446)

Leelataviwat, S., Saewon, W., and Goel, S. C. (2009). Application of energy balance concept in seismic evaluation of structures. *J. Struct. Eng.* 135, 113–121. doi: 10.1061/(ASCE)0733-9445(2009)135:2(113)

López Almansa, F., Yazgan, A. U., and Benavent Climent, A. (2013). Design energy input spectra for high seismicity regions based on Turkish registers. *Bull. Earthq. Eng.* 11, 885–912. doi: 10.1007/s10518-012-9415-2

Papazafeiropoulos, G., and Plevris, V. (2018). OpenSeismoMatlab: a new open-source software for strong ground motion data processing. *Heliyon* 4:e00784. doi: 10.1016/j.heliyon.2018.e00784

Papazafeiropoulos, G., Plevris, V., and Papadrakakis, M. (2017). A new energy-based structural design optimization concept under seismic actions. *Front. Built Environ.* 3:44. doi: 10.3389/fbuil.2017.00044

Surahman, A. (2007). Earthquake-resistant structural design through energy demand and capacity. *Earthq. Eng. Struct. Dyn.* 36, 2099–2117. doi: 10.1002/eqe.718

Tselentis, G., Danciu, L., and Sokos, E. (2010). Probabilistic seismic hazard assessment in Greece–Part 2: acceleration response spectra and elastic input energy spectra. *Nat. Hazards Earth Syst. Sci.* 10, 41–49. doi: 10.5194/nhess-10-41-2010

Uang, C.-M., and Bertero, V. V. (1988). *Use of Energy as a Design Criterion in Earthquake-Resistant Design,* Vol. 88. Richmond, CA: Earthquake Engineering Research Center, University of California at Berkeley.

Uang, C.-M., and Bertero, V. V. (1990). Evaluation of seismic energy in structures. *Earthq. Eng. Struct. Dyn.* 19, 77–90. doi: 10.1002/eqe.4290190108

Uniform Building Code (UBC) (1994). *International Conference of Building Officials*. Whittier, CA.

Zahrah, T. F., and Hall, W. J. (1984). Earthquake energy absorption in SDOF structures. *J. Struct. Eng.* 110, 1757–1772. doi: 10.1061/(ASCE)0733-9445(1984)110:8(1757)

Conflict of Interest: The authors declare that the research was conducted in the absence of any commercial or financial relationships that could be construed as a potential conflict of interest.

NOMENCLATURE

A:	*amplitude*
a_{RU} :	*scalar variable with uniform random distribution with* $0 \leq a_{RU} \leq 1$
$\tilde{a}_{GU}$:	*vector with entries following a uniform Gaussian distribution*
$\tilde{a}_{RU}$:	*vector with entries following a uniform random distribution with* $0 \leq \tilde{a}_{RU} \leq 1$
$\tilde{c}$:	*viscous damping coefficient matrix*
DFT ():	*Discrete Fourier Transform*
E_d:	*Energy dissipated due to damping*
E_k:	*Kinetic energy*
E_I:	*Input energy due to earthquake*
E_s:	*Elastic recoverable strain energy*
E_y:	*Energy dissipated due to yielding*
f:	*frequency*
f_i:	*fitness value of the i-th individual*
f_S:	*force due to stiffness*
FFT ():	*Fast Fourier Transform*
I:	*unit column vector (influence vector)*
I_0:	*zeroth – order modified Bessel function of the first kind*
$IFFT$ ():	*Inverse Fast Fourier Transform*
k:	*number of generation*
$k_{\max}$:	*maximum number of generations*
k_P:	*constant for penalty of lower period bound*
k_S:	*positive integer for selection function with* $0 \leq k_S \leq n_S - 1$
$\tilde{k}$:	*small strain (initial) stiffness matrix*
M:	*number of raw accelerograms that are contained in the earthquake data base*
m:	*number of raw accelerograms combined to produce the artificial time history*
$m_{SC,0}$:	*scale parameter of mutation function (standard deviation of Gaussian distribution at the first generation) at the initial generation (0)*
$m_{SC,k}$:	*scale parameter of mutation function (standard deviation of Gaussian distribution at the first generation) at generation k*
m_{SH}:	*shrink parameter of mutation function (rate of decrease of standard deviation w.r.t. generation number)*
$\tilde{m}$:	*mass matrix*
N_{FIR}:	*order of FIR filter*
n:	*length of the Fourier transform*
$n_1 \bigcap 2$:	*number of elements of the intersection* $x_{1\cap 2}$
n_C:	*number of individuals in each generation produced by crossover*
n_E:	*number of elite individuals in each generation*
n_M:	*number of individuals in each generation produced by mutation*
n_P:	*population size*
n_S:	*number of individuals which are selected for breeding in each generation*
P_0:	*population at zeroth generation (initial)*
P_k:	*population at generation k*
$P_{k,1}$:	*first random individual belonging to population at generation k*
$P_{k,2}$:	*second random individual belonging to population at generation k*
$P_{k+1,12}$:	*offspring from crossover between* $P_{k,1}$ *and* $P_{k,2}$
p (T):	*penalty function*
p_i:	*probability of selection of the* i^{th} *individual*
r:	*rank of an individual*
Sa_c:	*spectral acceleration of the linear combination of the selected ground motions*
Sa_t:	*target spectral acceleration*
$Siev_c^{ABS}$:	*spectral equivalent absolute input energy velocity of the linear combination of the selected ground motions*
$Siev_c^{REL}$:	*spectral equivalent relative input energy velocity of the linear combination of the selected ground motions*
$Siev_t^{ABS}$:	*target spectral equivalent absolute input energy velocity*
$Siev_t^{REL}$:	*target spectral equivalent relative input energy velocity*
T:	*eigenperiod*
T_1:	*lower period limit of the various spectra*
T_2:	*upper period limit of the various spectra*
T_d:	*duration of the earthquake time history*
t:	*time*
u:	*displacement vector of the structure*
$\dot{u}$:	*velocity vector of the structure*
$\ddot{u}$:	*acceleration vector of the structure*
$\ddot{u}_{g,c}$:	*acceleration time history of the linear combination of the selected ground motions*
$\ddot{u}_{g,i}$:	*acceleration time history of the ith ground motion*
W_n:	*one of the n roots of unity*
w:	*coefficients of Kaiser window*
$x_{1\cap 2}$:	*intersection between two random individuals* $x_{i1,j}$ *and* $x_{i2,j}$
x_{1-2}:	*relative complement of individual* $x_{i2,j}$ *in individual* $x_{i1,j}$
x_{2-1}:	*relative complement of individual* $x_{i1,j}$ *in individual* $x_{i2,j}$
x_i:	*combination coefficient respectively of the* i^{th} *ground motion*
$x_{i,j}$:	j^{th} *element of the ith individual*
β:	*constant equal to 5*
Δt_{old}:	*time step of ground motion before resampling*
Δt_{new}:	*time step of ground motion after resampling*
ω:	*cyclic frequency step of the Fourier spectrum*

Advantages of publishing in Frontiers

OPEN ACCESS
Articles are free to read for greatest visibility and readership

FAST PUBLICATION
Around 90 days from submission to decision

HIGH QUALITY PEER-REVIEW
Rigorous, collaborative, and constructive peer-review

TRANSPARENT PEER-REVIEW
Editors and reviewers acknowledged by name on published articles

Frontiers
Avenue du Tribunal-Fédéral 34
1005 Lausanne | Switzerland

Visit us: www.frontiersin.org
Contact us: info@frontiersin.org | +41 21 510 17 00

REPRODUCIBILITY OF RESEARCH
Support open data and methods to enhance research reproducibility

DIGITAL PUBLISHING
Articles designed for optimal readership across devices

FOLLOW US
@frontiersin

IMPACT METRICS
Advanced article metrics track visibility across digital media

EXTENSIVE PROMOTION
Marketing and promotion of impactful research

LOOP RESEARCH NETWORK
Our network increases your article's readership